ION TRANSPORTERS AND CHANNELS IN CELLULAR PATHOPHYSIOLOGY

EDITED BY: Rossana Morabito, Alessia Remigante, Paola Gavazzo and Silvia Dossena

PUBLISHED IN: Frontiers in Cell and Developmental Biology and Frontiers in Molecular Biosciences

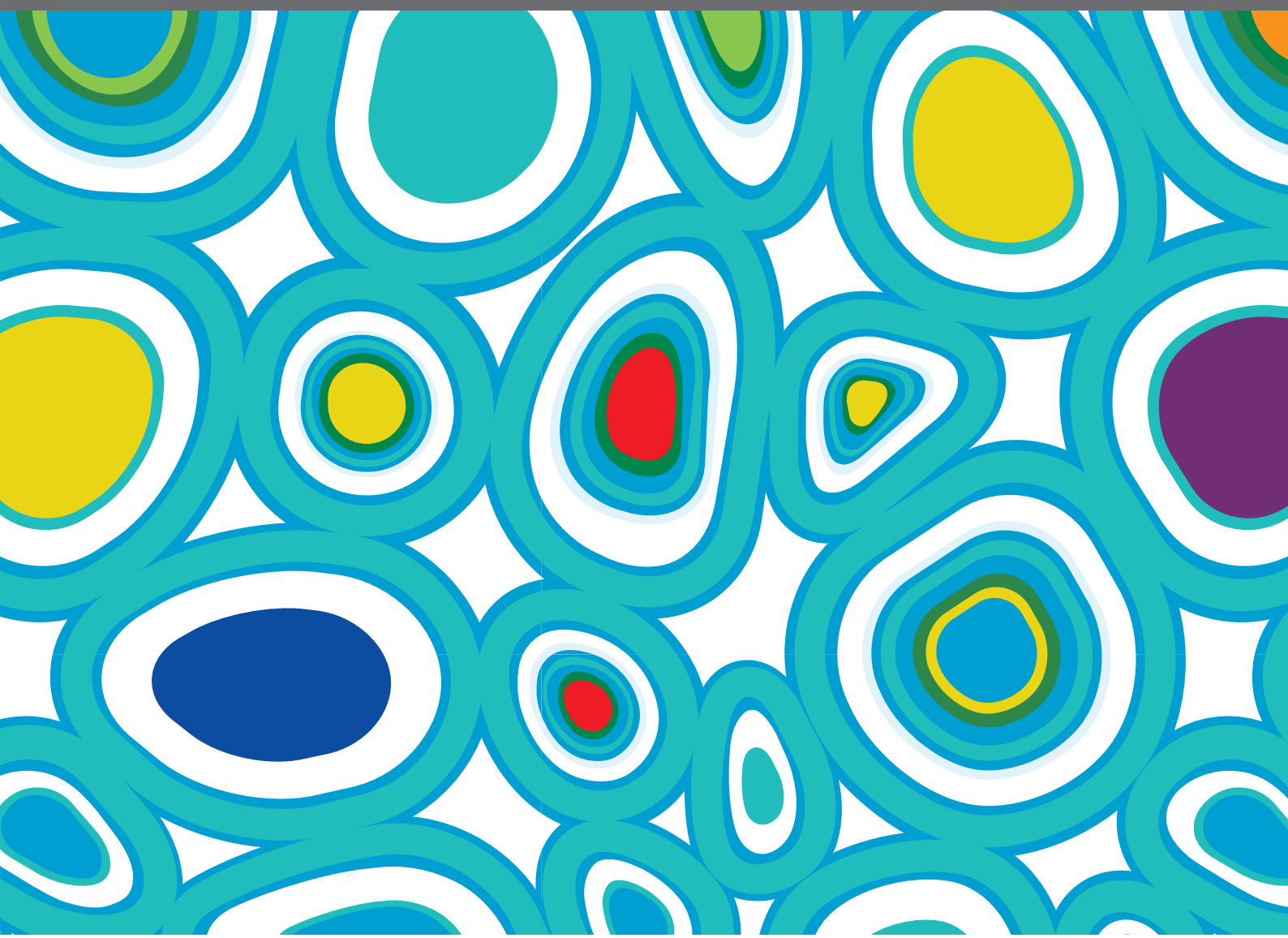

frontiers Research Topics

frontiers

ISSN 1664-8714
ISBN 978-2-83250-645-5
DOI 10.3389/978-2-83250-645-5

About Frontiers

Frontiers is more than just an open-access publisher of scholarly articles: it is a pioneering approach to the world of academia, radically improving the way scholarly research is managed. The grand vision of Frontiers is a world where all people have an equal opportunity to seek, share and generate knowledge. Frontiers provides immediate and permanent online open access to all its publications, but this alone is not enough to realize our grand goals.

Frontiers Journal Series

The Frontiers Journal Series is a multi-tier and interdisciplinary set of open-access, online journals, promising a paradigm shift from the current review, selection and dissemination processes in academic publishing. All Frontiers journals are driven by researchers for researchers; therefore, they constitute a service to the scholarly community. At the same time, the Frontiers Journal Series operates on a revolutionary invention, the tiered publishing system, initially addressing specific communities of scholars, and gradually climbing up to broader public understanding, thus serving the interests of the lay society, too.

Dedication to Quality

Each Frontiers article is a landmark of the highest quality, thanks to genuinely collaborative interactions between authors and review editors, who include some of the world's best academicians. Research must be certified by peers before entering a stream of knowledge that may eventually reach the public - and shape society; therefore, Frontiers only applies the most rigorous and unbiased reviews.
Frontiers revolutionizes research publishing by freely delivering the most outstanding research, evaluated with no bias from both the academic and social point of view. By applying the most advanced information technologies, Frontiers is catapulting scholarly publishing into a new generation.

What are Frontiers Research Topics?

Frontiers Research Topics are very popular trademarks of the Frontiers Journals Series: they are collections of at least ten articles, all centered on a particular subject. With their unique mix of varied contributions from Original Research to Review Articles, Frontiers Research Topics unify the most influential researchers, the latest key findings and historical advances in a hot research area! Find out more on how to host your own Frontiers Research Topic or contribute to one as an author by contacting the Frontiers Editorial Office: frontiersin.org/about/contact

ION TRANSPORTERS AND CHANNELS IN CELLULAR PATHOPHYSIOLOGY

Topic Editors:
Rossana Morabito, University of Messina, Italy
Alessia Remigante, University of Messina, Italy
Paola Gavazzo, Institute of Biophysics, Department of Physical Sciences and Technologies of Matter, National Research Council (CNR), Italy
Silvia Dossena, Paracelsus Medical University, Austria

Citation: Morabito, R., Remigante, A., Gavazzo, P., Dossena, S., eds. (2023). Ion Transporters and Channels in Cellular Pathophysiology. Lausanne: Frontiers Media SA. doi: 10.3389/978-2-83250-645-5

Table of Contents

frontiers | Frontiers in Cell and Developmental Biology

TYPE Editorial
PUBLISHED 17 October 2022
DOI 10.3389/fcell.2022.1049433

OPEN ACCESS

EDITED AND REVIEWED BY
Cecilia Giulivi,
University of California, Davis,
United States

*CORRESPONDENCE
Rossana Morabito,
rmorabito@unime.it

SPECIALTY SECTION
This article was submitted to Cellular Biochemistry,
a section of the journal
Frontiers in Cell and Developmental Biology

RECEIVED 20 September 2022
ACCEPTED 05 October 2022
PUBLISHED 17 October 2022

CITATION
Remigante A, Gavazzo P, Morabito R and Dossena S (2022), Editorial: Ion transporters and channels in cellular pathophysiology.
Front. Cell Dev. Biol. 10:1049433.
doi: 10.3389/fcell.2022.1049433

Editorial: Ion transporters and channels in cellular pathophysiology

Alessia Remigante[1], Paola Gavazzo[2], Rossana Morabito[1]* and Silvia Dossena[3]

[1]Department of Chemical, Biological, Pharmaceutical and Environmental Sciences, University of Messina, Messina, Italy, [2]Biophysics Institute, National Research Council, Genova, Italy, [3]Institute of Pharmacology and Toxicology, Paracelsus Medical University, Salzburg, Austria

KEYWORDS

ion channels, ion transporters, disease, kidney, heart, erythrocytes

Editorial on the Research Topic
Ion transporters and channels in cellular pathophysiology

Ion and water channels and transporters mediate the flux of ions, water, and small- and medium-size molecules across cellular membranes in response to specific stimuli. Ion transport is crucial for proper cell, tissue, and organ function, including the regulation of cardiac and neuronal activity, systemic pH, salt and water homeostasis, as well as cell proliferation, differentiation, and apoptosis. As a consequence, the impairment of any of its molecular components may have dramatic consequences for cellular and organ physiology, and eventually for human health. Therefore, the precise understanding of the mechanisms of physiological regulation and pathological dysregulation of ion transport is essential to open new avenues in therapy and drug design. The purpose of this Research Topic was to collect and contribute to the dissemination of high-quality research articles summarizing the current progress in the understanding of different aspects of ion channels and transporters, including intracellular signaling. The 10 original publications collected are well representative of the variety of roles of ion channels and transporters and highlight the multitude of the experimental models and approaches currently used to unravel their complexity. Hereafter we offer an overview of the content of the Research Topic.

Alterations in the ion transport can cause serious diseases affecting the heart and the central nervous system. Among these, sudden cardiac arrest (SCA) is a global public health problem. Most cases of SCA are caused by cardiac arrhythmias that may arise from functional changes of ion channels that underlie the cardiac action potential (AP) and can be evoked by various drugs used for the treatment of cardiac or non-cardiac conditions, including carbamazepine (CBZ). In their manuscript, Jia et al. showed a correlation between CBZ treatment and SCA and demonstrated that CBZ reduced the AP upstroke velocity by reducing the cardiac Na^+ current at therapeutic concentrations and shortened

the AP duration by reducing the L-type Ca^{2+} currents at high concentrations. Thus, these data mechanistically explain the increase of SCA risk upon CBZ exposure (Jia et al.).

Pathogenic sequence alterations in the *LMNA* gene coding for the type-V intermediate filament proteins Lamin A/C are linked to muscular dystrophies and cardiac abnormalities associated with fatal arrhythmias. De Zio et al. found that cardiomyocytes expressing the truncated Lamin A/C Q517X variant exhibit action potential abnormalities, tubulin hyper-polymerization and hyper-acetylation, and defective cell surface Nav1.5 expression. The authors provided evidence showing that pharmacological manipulation of tubulin state might represent a novel strategy in the treatment of cardiac laminopathies (De Zio et al.).

The Ca^{2+}-releasing second messenger nicotinic acid adenine dinucleotide phosphate (NAADP) mobilizes lysosomal Ca^{2+} through two-pore channels (TPCs), thereby modulating the excitation-contraction (EC) coupling in vascular smooth muscle cells and cardiomyocytes and driving the angiogenic behaviour of vascular endothelial and endothelial progenitor cells (Moccia et al., 2021). Faris et al. have examined the Ca^{2+} signalling in cardiac mesenchymal stromal cells (C-MSCs) and revealed that the NAADP-induced lysosomal Ca^{2+} release stimulates inositol-1,4,5-trisphosphate ($InsP_3$)-induced Ca^{2+} mobilization from the endoplasmic reticulum (ER) through the mechanism of Ca^{2+}-induced Ca^{2+} release. The functional interaction between acidic and neutral Ca^{2+} stores and activation of TPCs permits the C-MSC proliferation induced by extracellular signals. This pathway might offer novel therapeutic targets in cardiac repair (Faris et al.).

The role of intracellular calcium in non-excitable cells including fibroblasts is incompletely understood. Histamine could act as an inflammatory mediator in asthmatic lungs by stimulating proliferation and migration of resident fibroblasts through an increase in $[Ca^{2+}]_i$. Berra-Romani et al. investigated the mechanism whereby histamine induces intracellular Ca^{2+} signals in the human lung fibroblast cell line WI-38 and found that these signals are triggered by histamine one receptors (H1Rs) and partially contributed by H2Rs (Berra-Romani et al.). The Ca^{2+} response is mediated by $InsP_3$-induced Ca^{2+} release from the ER and maintained over time by store-operated Ca^{2+} entry. The authors suggest that pharmacological blockade of $InsP_3$ receptors and store-operated channels could represent an alternative strategy to prevent the deleterious effects of histamine on lung fibroblasts in asthmatic patients.

The K^+-Cl^- cotransporter KCC2 is expressed in neurons throughout the central nervous system and deficits in its activity have been implicated in a variety of neurological disorders, including epilepsy. Prael III et al. discovered and characterized a new class of small-molecule KCC2 potentiators and showed that pharmacological KCC2 potentiation, by itself, is sufficient to attenuate neuronal hyperexcitability in an *in vitro* model of cortical neuronal-glial co-cultures that is sensitive to anti-epileptic drugs (Prael et al.). These results pave the way to the development of KCC2-directed therapeutics for multiple neurological disorders.

Yap et al. characterized a *Dictyostelium discoideum* model of CLN7 disease, which is a form of neurodegeneration in humans linked to mutations in *MFSD8* (Yap et al.). The MFSD8 protein has been reported to transport chloride ions across the lysosomal membrane and, in their study, Yap et al. showed that the *D. discoideum* homolog of MFSD8 plays an important role in modulating a variety of cellular processes during the growth and early development of the organism.

Ion transport in the kidney is fundamental in the regulation of systemic pH and blood pressure. Ferdaus et al. show that the potassium-chloride co-transporter KCC3a co-localizes with the chloride/bicarbonate exchanger pendrin (SLC26A4) in the apical membrane of type B and non-A/non-B intercalated cells in the mouse kidney cortex (Ferdaus et al.). As metabolic alkalosis upregulated both pendrin and KCC3a, the authors suggested that KCC3a might provide a pathway for recycling of chloride ions across the apical membrane to permit bicarbonate secretion *via* pendrin. A functional interplay between these two transporters could explain the mechanism of hypokalemia in metabolic alkalosis.

Xu et al. identified the IQ motif-containing GTPase-activating protein 1 (IQGAP1) as a protein that binds to the C-terminus of pendrin and co-localizes with pendrin on the apical membrane of B-intercalated cells in the mouse kidney. Functional studies in cell-based systems demonstrated that IQGAP1 favors the plasma membrane localization of pendrin and enhances its Cl^-/HCO_3^- exchanger activity. The authors suggested that a disturbed interaction between these two proteins might contribute to pathophysiological states characterized by an altered function or trafficking of pendrin (Xu et al.).

In addition to kidneys, also the colonic epithelium, which expresses the water channel AQP3, modulates water and salt homeostasis. Centrone et al. evaluated the action of vasopressin (AVP) on the AQP3 expression and function by using selective vasopressin receptors (VRs) antagonists in human colonic HCT8 cells (Centrone et al.). dDAVP reduced AQP3 activity and cell viability in a V1aR-dependent, V2R-independent manner. Interestingly, in the colon of patients with adenocarcinoma, the expression of V1aR was significantly decreased. These findings identify the AVP-dependent AQP3 pathway as a novel target in colon diseases associated with abnormal cell growth.

Ferreira et al. characterized the regulation of red blood cells (RBC) Mg^{2+} in conditions of hyperglycemia (Ferreira et al.). Exposure of RBC to 50 mM D-glucose lowered cellular Mg^{2+} and enhanced the Na^+/Mg^{2+} exchange activity. Similar changes were also observed in RBC from individuals with type 2 diabetes (T2D) or a diabetic mouse model and were reversed by reducing the

N-glycosylation state of membrane proteins. These data show that the decreased Mg^{2+} content of RBC in T2D reflects enhanced Na^{+}/Mg^{2+} exchange and further suggest that N-deglycosylation of targets within the pathway of Mg^{2+} regulation may have therapeutic potential in treatment of the vascular complications of T2D.

To conclude, the precise understanding of the ion transport pathophysiology is predicted to favor the identification of novel therapeutic targets and strategies for conditions ranging from cardiac diseases, epilepsy, asthma, and T2D.

Author contributions

AR, PG, RM, SD writing-original draft preparation. All authors have read and agreed to the published version of the manuscript.

Conflict of interest

The authors declare that the research was conducted in the absence of any commercial or financial relationships that could be construed as a potential conflict of interest.

Publisher's note

All claims expressed in this article are solely those of the authors and do not necessarily represent those of their affiliated organizations, or those of the publisher, the editors and the reviewers. Any product that may be evaluated in this article, or claim that may be made by its manufacturer, is not guaranteed or endorsed by the publisher.

References

Moccia, F., Negri, S., Faris, P., Perna, A., De Luca, A., Soda, T., et al. (2021). Corrigendum: Targeting endolysosomal two-pore channels to treat cardiovascular disorders in the novel COronaVIrus disease 2019.. *Front. Physiol.* 12, 690189. doi:10.3389/fphys.2021.690189

frontiers in Cell and Developmental Biology

ORIGINAL RESEARCH
published: 15 March 2022
doi: 10.3389/fcell.2022.874043

Nicotinic Acid Adenine Dinucleotide Phosphate Induces Intracellular Ca^{2+} Signalling and Stimulates Proliferation in Human Cardiac Mesenchymal Stromal Cells

Pawan Faris[1], Claudio Casali[2], Sharon Negri[1], Lara Iengo[3], Marco Biggiogera[2], Angela Serena Maione[3]† and Francesco Moccia[1]*†*

[1]Laboratory of General Physiology, Department of Biology and Biotechnology "Lazzaro Spallanzani", University of Pavia, Pavia, Italy, [2]Laboratory of Cell Biology and Neurobiology, Department of Biology and Biotechnology "Lazzaro Spallanzani", University of Pavia, Pavia, Italy, [3]Vascular Biology and Regenerative Medicine Unit, Centro Cardiologico Monzino, IRCCS, Milan, Italy

OPEN ACCESS

Edited by:
Alessia Remigante,
University of Messina, Italy

Reviewed by:
Dmitry Lim,
University of Eastern Piedmont, Italy
Alessandra Rossini,
Eurac Research, Italy

***Correspondence:**
Angela Serena Maione
angela.maione@cardiologicomonzino.it
Francesco Moccia
francesco.moccia@unipv.it

†These authors have contributed equally to this work and share last authorship

Specialty section:
This article was submitted to Cellular Biochemistry, a section of the journal Frontiers in Cell and Developmental Biology

Received: 11 February 2022
Accepted: 24 February 2022
Published: 15 March 2022

Citation:
Faris P, Casali C, Negri S, Iengo L, Biggiogera M, Maione AS and Moccia F (2022) Nicotinic Acid Adenine Dinucleotide Phosphate Induces Intracellular Ca^{2+} Signalling and Stimulates Proliferation in Human Cardiac Mesenchymal Stromal Cells. Front. Cell Dev. Biol. 10:874043. doi: 10.3389/fcell.2022.874043

Nicotinic acid adenine dinucleotide phosphate (NAADP) is a newly discovered second messenger that gates two pore channels 1 (TPC1) and 2 (TPC2) to elicit endo-lysosomal (EL) Ca^{2+} release. NAADP-induced lysosomal Ca^{2+} release may be amplified by the endoplasmic reticulum (ER) through the Ca^{2+}-induced Ca^{2+} release (CICR) mechanism. NAADP-induced intracellular Ca^{2+} signals were shown to modulate a growing number of functions in the cardiovascular system, but their occurrence and role in cardiac mesenchymal stromal cells (C-MSCs) is still unknown. Herein, we found that exogenous delivery of NAADP-AM induced a robust Ca^{2+} signal that was abolished by disrupting the lysosomal Ca^{2+} store with Gly-Phe β-naphthylamide, nigericin, and bafilomycin A1, and blocking TPC1 and TPC2, that are both expressed at protein level in C-MSCs. Furthermore, NAADP-induced EL Ca^{2+} release resulted in the Ca^{2+}-dependent recruitment of ER-embedded $InsP_3Rs$ and SOCE activation. Transmission electron microscopy revealed clearly visible membrane contact sites between lysosome and ER membranes, which are predicted to provide the sub-cellular framework for lysosomal Ca^{2+} to recruit ER-embedded $InsP_3Rs$ through CICR. NAADP-induced EL Ca^{2+} mobilization via EL TPC was found to trigger the intracellular Ca^{2+} signals whereby Fetal Bovine Serum (FBS) induces C-MSC proliferation. Furthermore, NAADP-evoked Ca^{2+} release was required to mediate FBS-induced extracellular signal-regulated kinase (ERK), but not Akt, phosphorylation in C-MSCs. These finding support the notion that NAADP-induced TPC activation could be targeted to boost proliferation in C-MSCs and pave the way for future studies assessing whether aberrant NAADP signaling in C-MSCs could be involved in cardiac disorders.

Keywords: nicotinic acid adenine dinucleotide phosphate (NAADP), two-pore channels (TPCs), membrane contact sites, store operated Ca^{2+} entry, cardiac mesenchymal stem cells, proliferation

1 INTRODUCTION

Nicotinic acid adenine dinucleotide phosphate (NAADP) has emerged as a the most powerful (already in the nanomolar concentration range) Ca^{2+}-releasing second messenger in mammalian cells (Galione, 2015; Patel, 2015). NAADP elicits an increase in intracellular Ca^{2+} concentration ($[Ca^{2+}]_i$) by gating a novel family of intracellular Ca^{2+}-releasing channels, known as two-pore channels (TPCs), which present two isoforms in mammals (i.e., TPC1 and TPC2) and mobilize endo-lysosomal (EL) Ca^{2+} into the cytosol (Patel, 2015; Galione, 2019; Jin et al., 2020). Jupiter microtubule-associated homolog 2 (JPT2) (Gunaratne et al., 2021) and the RNA-binding protein, Lsm2 (Zhang et al., 2021), serve as auxiliary protein to bind NAADP and thereby contribute to mediate TPC-mediated EL Ca^{2+} release. The Ca^{2+} response to NAADP may remain spatially confined in proximity of EL vesicles (Ruas et al., 2010; Vassileva et al., 2020) or it can be amplified into a regenerative Ca^{2+} wave through the Ca^{2+}-dependent recruitment of juxtaposed ryanodine and inositol-1,4,5-trisphosphate ($InsP_3$) receptors at membrane contact sites (MCSs) between lysosomes and endoplasmic reticulum (ER) (Kinnear et al., 2004; Davis et al., 2012; Kilpatrick et al., 2013; Penny et al., 2014). Lysosomal Ca^{2+} refilling is impaired by alkalinization of the EL lumen (Ronco et al., 2015), although the mechanisms whereby intraluminal pH recharges EL vesicles with Ca^{2+} remains a controversial issue (Morgan et al., 2011; Garrity et al., 2016; Faris et al., 2018).

NAADP has been recognized as the trigger of the cellular Ca^{2+} response to extracellular stimuli in multiple tissues (Galione, 2015; Patel, 2015), including the cardiovascular system (Fameli et al., 2017; Moccia et al., 2021a; Negri et al., 2021b). NAADP-induced Ca^{2+} release through TPC2 increases the Ca^{2+} content within the sarcoendoplasmic reticulum in ventricular (Macgregor et al., 2007) and atrial myocytes (Collins et al., 2011), both at rest (Macgregor et al., 2007; Collins et al., 2011) and during β-adrenergic receptor stimulation (Macgregor et al., 2007; Collins et al., 2011; Lewis et al., 2012; Capel et al., 2015). Likewise, a flurry of reports showed that NAADP-induced intracellular Ca^{2+} signals elicit contraction in multiple types of vascular smooth muscle cells (VSMCs) (Kinnear et al., 2004; Jiang et al., 2013; Fameli et al., 2014; Trufanov et al., 2019). For instance, NAADP gates TPC2 to promote the Ca^{2+}-dependent recruitment of RyR3 and global cytosolic Ca^{2+} waves in pulmonary artery VSMCs stimulated with either endothelin-1 (Kinnear et al., 2004; Jiang et al., 2013) or angiotensin II (Lee et al., 2015). Finally, NAADP may serve as a trigger of the Ca^{2+} response to extracellular stimuli also in vascular endothelial cells (Favia et al., 2014; Zuccolo et al., 2019; Negri et al., 2021a) and circulating endothelial colony forming cells (ECFCs) (Balducci et al., 2021; Moccia et al., 2021b). Aberrant NAADP signalling in cardiac myocytes may result in arrhythmia (Nebel et al., 2013) and ischemia-reperfusion injury (Davidson et al., 2015), whereas it could lead to pulmonary artery hypertension in VSMCs (Jiang et al., 2018; Hu et al., 2021).

Once regarded as mere bystanders of the contractile function effected by neighbouring cardiac myocytes, cardiac mesenchymal stromal cells (C-MSCs) are required to maintain myocardial structure and function and, therefore, to ensure effective cardiac contraction (Brown et al., 2005; Camelliti et al., 2005). C-MSCs contribute to wound healing and fibrotic remodelling after ischemic injury (Jugdutt, 2003; Camelliti et al., 2005) and they have been put forward as a promising cellular substrate to induce cardiac repair (Bagno et al., 2018; Braunwald, 2018). Furthermore, C-MSCs could stimulate cardiac myocytes to undergo proliferation or hypertrophy depending on whether this interaction takes place during embryonic development or in the adult heart (Kakkar and Lee, 2010). Finally, C-MSCs exhibit significant immunomodulatory potential by attenuating the inflammatory response in the infarcted myocardium (Czapla et al., 2016; Diedrichs et al., 2019). In agreement with their contribution to the structural, biochemical and electro-chemical features of the myocardium, C-MSCs are involved in the pathogenic mechanisms of multiple cardiac diseases (Brown et al., 2005; Camelliti et al., 2005). For instance, C-MSCs provide a source of adipocytes (Sommariva et al., 2016; Stadiotti et al., 2017) and support fibrotic remodelling (Maione et al., 2021) in arrhythmogenic cardiomyopathy (ACM), a rare genetic disorder that is featured by fibro-fatty myocardium substitution, malignant arrhythmias, and heart failure and that can lead to sudden death in young individuals (Moccia et al., 2019). It has long been known that an increase in $[Ca^{2+}]_i$ regulates multiple functions in human MSCs (Moccia et al., 2015; Forostyak et al., 2016; Jiang et al., 2017), including proliferation (Foreman et al., 2006), migration (Peng et al., 2016), gene expression (Kawano et al., 2006), and differentiation (Kawano et al., 2006; Tao et al., 2011). However, it is still unclear whether and how NAADP evokes intracellular Ca^{2+} signals and whether lysosomal-ER MCSs do exist in C-MSCs. This information could be extremely helpful to boost the design of alternative strategies to effectively target C-MSCs in a variety of life-threatening cardiac disorders. In the present investigation, we first provided the evidence that NAADP evokes robust lysosomal Ca^{2+} mobilization, which is amplified into a global increase in $[Ca^{2+}]_i$ by $InsP_3$ receptors ($InsP_3Rs$). Transmitted electron microscopy (TEM) then revealed clearly discernible MCSs between lysosomes and ER membrane in C-MSCs. Finally, we found that NAADP-induced Ca^{2+}-dependent crosstalk between lysosomes and ER triggers the intracellular Ca^{2+} signals whereby Fetal Bovine Serum (FBS) induces cell proliferation. The role of Ca^{2+} signalling in regulating proliferation and differentiation in MSCs confer these findings the potential to provide the molecular framework for further studies aiming at manipulating C-MSCs for therapeutic purposes.

2 MATERIALS AND METHODS

2.1 Ethical Statement

This study complies with the WMA Declaration of Helsinki. The use of human cells from biopsy samples of healthy subjects

TABLE 1 | Primer sequences 5′-3′.

Gene	Forward primer	Reverse primer
TPC1	GAGTTTGGATGACGACGTGC	GAGTCGTGGATGGCATAGCT
TPC2	CTTACCGCAGCATCCAAGTC	GTAAAGCCACATCGAGCTGG
GAPDH	ATGTTCGTCATGGGTGTGAA	GTCTTCTGGGTGGCAGTGAT

(cardiomyopathies ruled out) was approved by IEO-CCM IRCCS Ethic Committee (project CCM1072). Written informed consent was obtained from all participants.

2.2 C-MSC Isolation and Culture

Cells were obtained from endomyocardial specimens and characterized as previously described (Pilato et al., 2018) and cultured with Iscove's Modified Dulbecco's Medium (Thermo Fisher Scientific, MA, United States) supplemented with 20% Fetal Bovine Serum (FBS), 10 ng/ml basic fibroblast growth factor, 10,000 U/ml Penicillin, 10,000 μg/ml Streptomycin, and 0.02 M L-Glutamine.

2.3 Solutions

Physiological salt solution (PSS) had the following composition (in mM): 150 NaCl, 6 KCl, 1.5 $CaCl_2$, 1 $MgCl_2$, 10 Glucose, 10 Hepes. In Ca^{2+}-free solution ($0Ca^{2+}$), Ca^{2+} was substituted with 2 mM NaCl, and 0.5 mM EGTA was added. Solutions were titrated to pH 7.4 with NaOH. The osmolality of the extracellular solution, as measured with an osmometer (Wescor 5500, Logan, UT, United States), was 300–310 mmol/kg.

2.4 $[Ca^{2+}]_i$ Measurements and Statistics of Ca^{2+} Signals

C-MSCs were loaded with 2 μM fura-2 acetoxymethyl ester (fura-2/AM; 1 mM stock in dimethyl sulfoxide) in PSS for 30 min at room temperature (RT). The details of the Ca^{2+} recording set-up have been described in Moccia et al. (2021b) and are reported in the **Supplementary Material**. All the experiments were performed at RT. The amplitude of intracellular Ca^{2+} release in response to each agonist (NAADP or FBS) or drug [Gly-Phe β-naphthylamide (GPN), nigericin, bafilomycin A1, and cyclopiazonic acid (CPA)] was measured as the difference between the ratio at the peak of intracellular Ca^{2+} mobilization and the mean ratio of 1 min baseline before the peak. Pooled data are given as mean ± SE and statistical significance ($p < 0.05$) was evaluated by the Student's t-test for unpaired observations or one-way Anova analysis followed by the post-hoc Dunnett's test as appropriate (Negri et al., 2021a; Remigante et al., 2021). Data relative to Ca^{2+} signals are presented as mean ± SE, while the number of cells analysed is indicated in the corresponding bar histograms.

2.5 mRNA Extraction and qRT-PCR Assay

Cell cultures were lysed in RL lysis buffer (Norgen Biotek Corp., Thorold, ON, Canada). RNA was isolated from cells by using a Total RNA Purification kit (Norgen Biotek Corp., Thorold, ON, Canada). The quantification of the isolated RNA was determined by NanoDrop spectrophotometer (ND-1000, EuroClone, Milan, Italy). Reverse transcription was conducted with SuperScript III (Invitrogen, Carlsbad, CA, United States) following the manufacturer's instructions. qRT-PCR was performed with the use of the iQTM SYBR Green Super Mix (Bio-Rad Laboratories, Hercules, CA, United States) and specific primers (reported in **Table 1**). All reactions were performed in a 96-well format with the 7900HT Fast Real-Time PCR System (Thermo Fisher Scientific, MA, United States). The relative quantities of specific mRNA were obtained with the use of the comparative Ct method and were normalized to the housekeeping gene glyceraldehyde 3-phosphate dehydrogenase (GAPDH) (Maione et al., 2021; Zuccolini et al., 2022). The expression of each target gene was assessed in triplicate (Ferrera et al., 2021; Maione et al., 2021).

2.6 Protein Extraction and Western Blot Analysis

C-MSCs were lysed in cell lysis buffer (Cell Signalling Technology, Danvers, MA, United States) supplemented with protease and phosphatase inhibitor cocktails (Sigma-Aldrich, Saint Louis, MO, United States). Total protein extracts were subjected to SDS-PAGE and transferred onto a nitrocellulose membrane (Bio-Rad, CA, United States). The membranes were blocked for 1 h at room temperature in 5% non-fat dry milk in Wash Buffer (Tris Buffer Sulfate, 0.1% Tween-20) and then incubated O/N at 4°C with the appropriate primary antibodies (reported in **Table 2**). The membranes were incubated with peroxidase-conjugated secondary antibodies (GE Healthcare, Chicago, IL, United States) for 1 h. Signals were visualized using the LiteUP Western Blot Chemiluminescent Substrate (EuroClone, Milan, Italy). Images were acquired with the ChemiDocTM MP Imaging System (Bio-Rad, CA, United States), and densitometric analysis of membranes was performed using the ImageJ software (National Institutes of Health, Bethesda, MD, United States). C-MSC proteins were normalized according to glyceraldehyde 3-phosphate dehydrogenase (GAPDH) signal.

2.7 Transmission Electron Microscopy

For transmission electron microscopy (TEM) analysis, following trypsinization cells were centrifuged at 800 rpm for 5 min and then fixed with 2.5% glutaraldehyde in culture medium, for 2 h at RT (Carriero et al., 2021). The cell pellet was then rinsed in PBS overnight, post-fixed in 1% aqueous OsO4 for 3 h at room temperature and rinsed in H2O. Cells were pre-embedded in 2% agarose in water, dehydrated in acetone and then embedded in epoxy resin (Electron Microscopy Sciences, EM-bed812). Ultrathin sections (60–80 nm) were cut on a Reichert OM-U3 ultramicrotome, collected on nickel grids and then stained with uranyl acetate and lead citrate. The specimens were observed with a JEM 1200 EX II (JEOL, Peabody, MA, United States) electron microscope operating at 100 kV and equipped with a MegaView G2 CCD camera (Olympus OSIS, Tokyo, Japan).

TABLE 2 | Primary antibodies.

Protein	Clonality/Code	Source/Isotype	Company	Dilution
TPCN1	Polyclonal, SAB2104213	Rabbit	Sigma-Aldrich	1:1,000
TPC2	Polyclonal, ab119915	Rabbit	Abcam	1:1,000
phospho-ERK1/2	Monoclonal, #4370	Rabbit IgG	Cell Signaling	1:1,000
ERK1/2	Polyclonal, #9102	Rabbit	Cell Signaling	1:1,000
phospho-AKT	Monoclonal, #4056	Rabbit IgG	Cell Signaling	1:1,000
AKT	Polyclonal, #9272	Rabbit	Cell Signaling	1:1,000
GAPDH	Polyclonal, sc-25778	Rabbit	Santa Cruz	1:1,000

2.8 Cell Proliferation

C-MSCs were plated in 6-well plates (100,000 cells/well) and serum starved for 4 h. Cells were then stimulated with 20% FBS in the absence (Ctrl) or presence of 100 μM of NED-19, a selective TPC blocker (Galione, 2015; Jin et al., 2020). 24 and 48 h after stimulation with FBS, the medium was removed, cells detached from the plates, and counted.

2.9 Flow Cytometry

To evaluate whether blocking TPCs with NED-19 was able to induce apoptosis in C-MSCs, Annexin V Alexa Fluor™ 488 Dye (Thermo Fisher Scientific, MA, United States) has been used, according to the manufacturer's instructions. Briefly, cells were detached using TrypLE™ Select Enzyme (Thermo Fisher Scientific, MA, United States) and incubated with Annexin V Alexa Fluor™ 488 Dye for 15 min at RT. The fluorescence emission at 530 nm corresponding to apoptotic cells has been measured using flow cytometry (Gallios, Beckman Coulter, Brea, CA, United States).

3 RESULTS

3.1 Nicotinic Acid Adenine Dinucleotide Phosphate Induces Intracellular Ca^{2+} Signals by Mobilizing Lysosomal Ca^{2+} in Cardiac Mesenchymal Stromal Cells

In order to assess whether they are endowed with a NAADP-sensitive Ca^{2+} store, C-MSCs were loaded with Fura-2/AM (2 μM), a Ca^{2+} sensitive fluorophore, as shown elsewhere (Maione et al., 2020a). Human MSCs may exhibit spontaneous oscillations in $[Ca^{2+}]_i$ (Kawano et al., 2002; Kawano et al., 2003; Kawano et al., 2006). Consistently, a fraction of C-MSCs (≈56.4%) exhibited a few (1-4) Ca^{2+} spikes in the absence of extracellular stimulation (**Supplementary Figure S1**). These cells were, therefore, discarded from subsequent analysis as shown elsewhere (Zuccolo et al., 2017; Zuccolo et al., 2019), since the spontaneous, unpredictable Ca^{2+} activity could mask or even prevent (in case of transient depletion of endogenous target organelle) the Ca^{2+} response to NAADP. We then assessed whether NAADP-AM, a membrane-permeable analogue of NAADP (Macgregor et al., 2007; Brailoiu et al., 2010), was able to increase the $[Ca^{2+}]_i$ in C-MSCs. NAADP-AM (1 μM) evoked a short train of intracellular Ca^{2+} oscillations that declined ≈25 min after their onset in the presence of extracellular Ca^{2+} in 88 out of 164 cells (53.6%) (**Figure 1A**). In 58 out of 164 cells (35.4%), NAADP-AM (1 μM) induced a transient increase in $[Ca^{2+}]_i$ that lasted ≈800 s returned to the baseline in the continuous presence of the agonist (**Figure 1A**). Eighteen cells (11%) were not responsive to NAADP-AM (1 μM). Under $0Ca^{2+}$ conditions, NAADP-AM (1 μM) induced only a transient increase in $[Ca^{2+}]_i$ that was not followed by additional Ca^{2+} spikes (**Figure 1B**). Intriguingly, the duration of the elevation in $[Ca^{2+}]_i$ was significantly shorter, i.e., ≈280 s, while the peak amplitude was higher (**Figure 1C**), as compared to the Ca^{2+} transient recorded in the presence of extracellular Ca^{2+}. The subsequent restitution of extracellular Ca^{2+} after the full recovery of $[Ca^{2+}]_i$ to the baseline resulted in a second Ca^{2+} signal that was due to extracellular Ca^{2+} entry (**Figure 1B**). NAADP-AM was removed from the perfusate 100 s before re-addition of extracellular Ca^{2+} (**Figure 1B**), which suggests that the Ca^{2+} entry pathway recruited downstream of NAADP-AM-induced Ca^{2+} release is provided by store-operated Ca^{2+} entry (SOCE), as more widely discussed below (Yamazaki et al., 2007; Sanchez-Hernandez et al., 2010; Negri et al., 2020). The statistical analysis of the two distinct components of the Ca^{2+} response to NAADP-AM (i.e., endogenous Ca^{2+} release and SOCE) is presented in **Figure 1D**. NAADP is recognized as a mobilizer of the lysosomal Ca^{2+} pool (Galione, 2015; Patel, 2015). Control experiments confirmed that adding back extracellular Ca^{2+} after 700 s exposure to $0Ca^{2+}$ conditions did not increase the in C-MSCs (**Supplementary Figure S2**). In accord, NAADP-AM-evoked intracellular Ca^{2+} release was significantly ($p < 0.001$) reduced by discharging the lysosomal Ca^{2+} store with the lysosomotropic compound, dipeptide glycyl-l-phenylalanine 2-naphthylamide (GPN; 200 μM, 30 min) (Kilpatrick et al., 2013; Yuan et al., 2021) (**Figures 1E,F**). Of note, GPN has recently been reaffirmed as a reliable pharmacological tool to mobilize lysosomal Ca^{2+} (Yuan et al., 2021). Furthermore, NAADP-AM-evoked endogenous Ca^{2+} mobilization was abolished by collapsing the lysosomal H^+ gradient that maintains lysosomal Ca^{2+} refilling with the H^+/K^+ ionophore, nigericin (50 μM, 30 min) (**Figures 1E,F**), or with the v-ATPase inhibitor, bafilomycin A1 (1 μM, 30 min) (**Figures 1E,F**) (Morgan et al., 2011; Ronco et al., 2015; Faris et al., 2019; Yuan et al., 2021). **Supplementary Figure S3** shows that GPN (200 μM), nigericin (50 μM), and bafilomycin A1 (1 μM) induced a remarkable reduction in Lysotracker Red fluorescence, thereby confirming that all of these drugs target

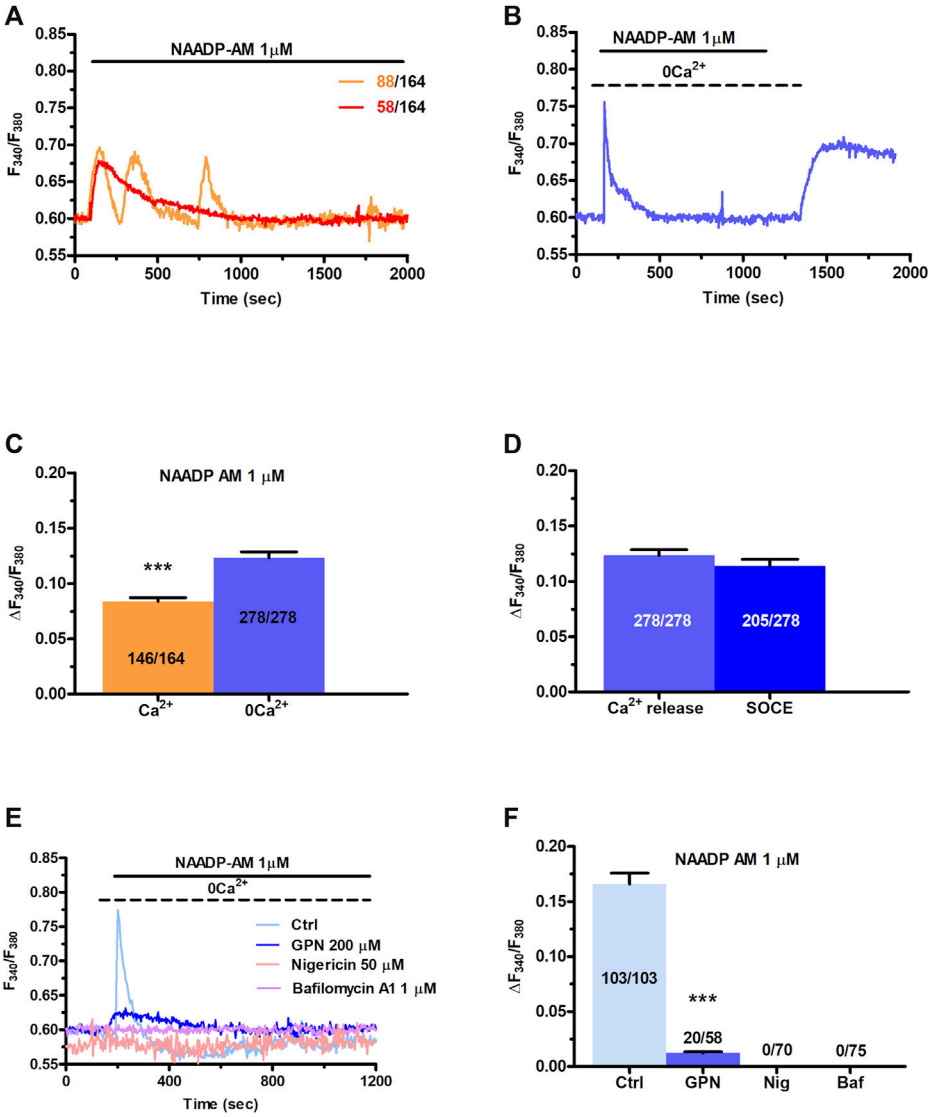

FIGURE 1 | NAADP induces intracellular Ca^{2+} signals by mobilizing lysosomal Ca^{2+} in C-MSCs. **(A)** Exogenous administration of NAADP-AM (1 μM) indues either intracellular Ca^{2+} oscillations or a transient increase in $[Ca^{2+}]_i$. **(B)** In absence of external Ca^{2+} ($0Ca^{2+}$), NAADP-AM (1 μM) induced only a transient increase in $[Ca^{2+}]_i$, whereas subsequent restitution of extracellular Ca^{2+} after the full recovery of $[Ca^{2+}]_i$ to the baseline resulted in a second Ca^{2+} signal that was due to extracellular Ca^{2+} entry. **(C)** Mean ± SE of the amplitude of the peak Ca^{2+} response to NAADP in the presence and absence of extracellular Ca^{2+}. Student's t-test: $^{***}p < 0.001$. **(D)** Mean ± SE of the amplitude of NAADP-induced intracellular Ca^{2+} release and SOCE. **(E)** Disrupting the lysosomal Ca^{2+} store with GPN (200 μM, 30 min), nigericin (50 μM, 30 min) or bafilomycin A1 (1 μM, 30 min) severely affected the intracellular Ca^{2+} response to NAADP-AM. **(F)** Mean ± SE of the amplitude of the peak Ca^{2+} response to NAADP-AM in the absence and in the presence of GPN, nigericin (Nig), or bafilomycin A1 (Baf). One-Way Anova followed by the post-hoc Dunnett's test: $^{***}p < 0.001$.

lysosomal Ca^{2+} (Pandey et al., 2009; Faris et al., 2019; Yuan et al., 2021). In accord with these observations, ammonium chloride (NH_4Cl), which disrupts the lysosomal Ca^{2+} pool by inducing intraluminal alkalinization (Christensen et al., 2002), also reduced Lysotracker Red Fluorescence and impaired NAADP-AM-evoked intracellular Ca^{2+} mobilization (**Supplementary Figure S4**).

Overall, these findings provide the first evidence that NAADP may induce lysosomal Ca^{2+} release followed by extracellular Ca^{2+} entry in C-MSCs.

3.2 Nicotinic Acid Adenine Dinucleotide Phosphate-Induced Intracellular Ca^{2+} Release is Mediated by TPCs in Cardiac Mesenchymal Stromal Cells

TPCs mediate NAADP-induced intracellular Ca^{2+} release throughout the phylogenetic tree (Patel, 2015; Galione, 2019; Jin et al., 2020), including the cardiovascular system (Moccia et al., 2021a; Negri et al., 2021b). In accord, qRT-PCR analysis showed that both TPC1 and TPC2 transcripts are expressed in

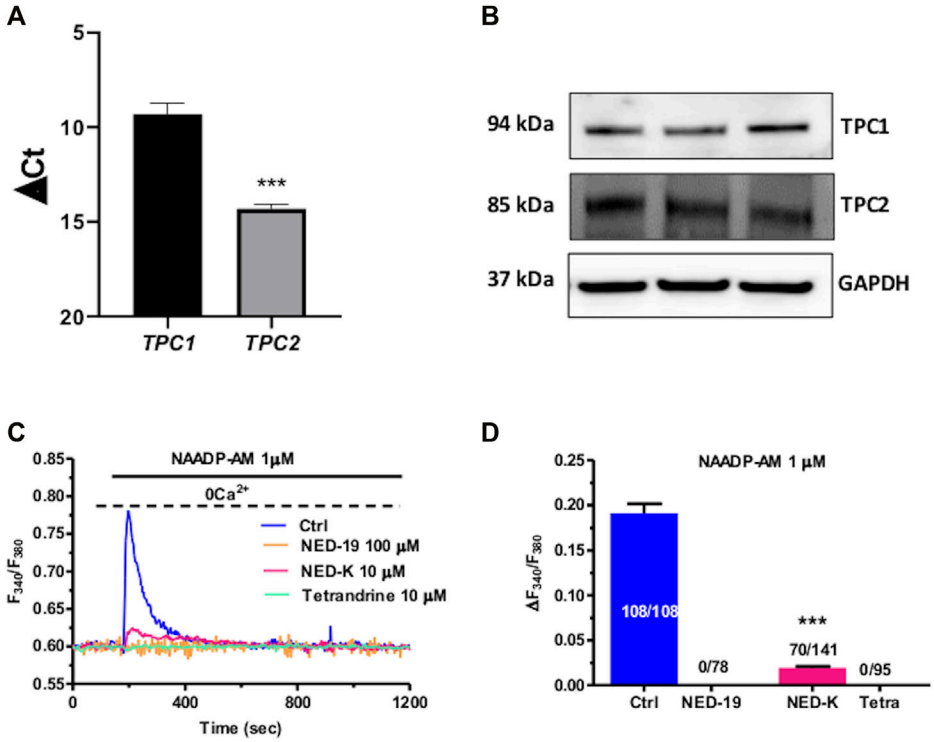

FIGURE 2 | Two-pore channels (TPCs) mediate NAADP-induced lysosomal Ca^{2+} release in C-MSCs. **(A)** TPC1 and TPC2 gene expression in total RNA extracts of C-MSCs. qRT-PCR data are shown as transcript abundance (genes threshold cycles [Ct] with respect to the house-keeping gene GAPDH). n = 4/group. Student's t-test: ***$p < 0.001$. **(B)** Western Blot analysis of TPC1 and TPC2 proteins in total cellular extracts. n = 3/group. **(C)** The Ca^{2+} response to NAADP-AM was suppressed by incubating the cells with the following TPC inhibitors: NED-19 (100 μM, 30 min), NED-K (10 μM, 30 min), and tetrandrine (10 μM, 30 min). **(D)** Mean ± SE of the amplitude of the peak Ca^{2+} response to NAADP in the absence (Ctrl) and in the presence of NED-19, NED-K and tetrandrine (Tetra). Student's t-test: ***$p < 0.001$.

C-MSCs, although TPC1 mRNA is slightly more abundant (**Figure 2A**). Negative controls were performed by omitting reverse transcriptase from the reaction (not shown) (Faris et al., 2019). Immunoblotting confirmed that TPC1 and TPC2 are also expressed at protein level. Two single bands of, respectively, 94 and 85 kDa were found for TPC1 and TPC2 proteins (**Figure 2B**). C-MSCs are not amenable for lipofectamine-mediated transfection of selective small interfering RNAs (Maione, Sommariva, and Pompilio, unpublished results), which is the strategy we have recently employed to downregulate TPC1 expression in different cellular models (Faris et al., 2019; Moccia et al., 2021b). Therefore, we probed the effect of NED-19, a selective TPC inhibitor (Galione, 2015; Jin et al., 2020), which has been widely employed to inhibit NAADP-dependent TPC activation throughout the cardiovascular system (Macgregor et al., 2007; Jiang et al., 2013; Hu et al., 2021; Moccia et al., 2021a; Negri et al., 2021a). As predicted, NED-19 (100 μM, 30 min) fully suppressed NAADP-AM-evoked intracellular Ca^{2+} mobilization (**Figures 2C,D**). Likewise, NED-K (10 μM, 30 min), a chemically modified analogue of NED-19 that has recently been shown to selectively inhibit TPC1 (Davidson et al., 2015), and tetrandrine (10 μM, 30 min), a traditional Chinese herbal remedy that block both TPC1 and TPC2 (Sakurai et al., 2015; Moccia et al., 2021a), respectively, inhibited ($p < 0.001$) and abrogated NAADP-AM-evoked intracellular Ca^{2+} release (**Figures 2C,D**). In aggregate, these data demonstrate that NAADP stimulates TPCs to mobilize lysosomal Ca^{2+} in c-MSCs.

3.3 $InsP_3Rs$ at MCSs are Activated Downstream of NAADP-AM-Induced Intracellular Ca^{2+} Release in Cardiac Mesenchymal Stromal Cells

The local release of lysosomal Ca^{2+} evoked by NAADP has long been known to be amplified into a global increase in $[Ca^{2+}]_i$ by the recruitment of juxtaposed $InsP_3Rs$ on the ER membrane (Churchill and Galione, 2001; Kinnear et al., 2004; Davis et al., 2012; Faris et al., 2019; Moccia et al., 2021b). To assess whether the ER Ca^{2+} store is required to maintain lysosomal Ca^{2+} release, we first exploited cyclopiazonic acid (CPA), an established inhibitor of Sarco-Endoplasmic reticulum Ca^{2+}-ATPase activity, as recently shown elsewhere (Kilpatrick et al., 2013; Faris et al., 2019; Moccia et al., 2021b). In the absence of extracellular Ca^{2+} ($0Ca^{2+}$), CPA (30 μM) induced a transient elevation in $[Ca^{2+}]_i$ due to Ca^{2+} efflux into the cytosol through ER leakage channels followed by Ca^{2+} extrusion across the plasma membrane (**Figure 3A**). While NAADP-AM (1 μM) was able to induce robust Ca^{2+} release in not-treated cells (**Figure 3B**), it failed to evoke endogenous Ca^{2+} mobilization upon

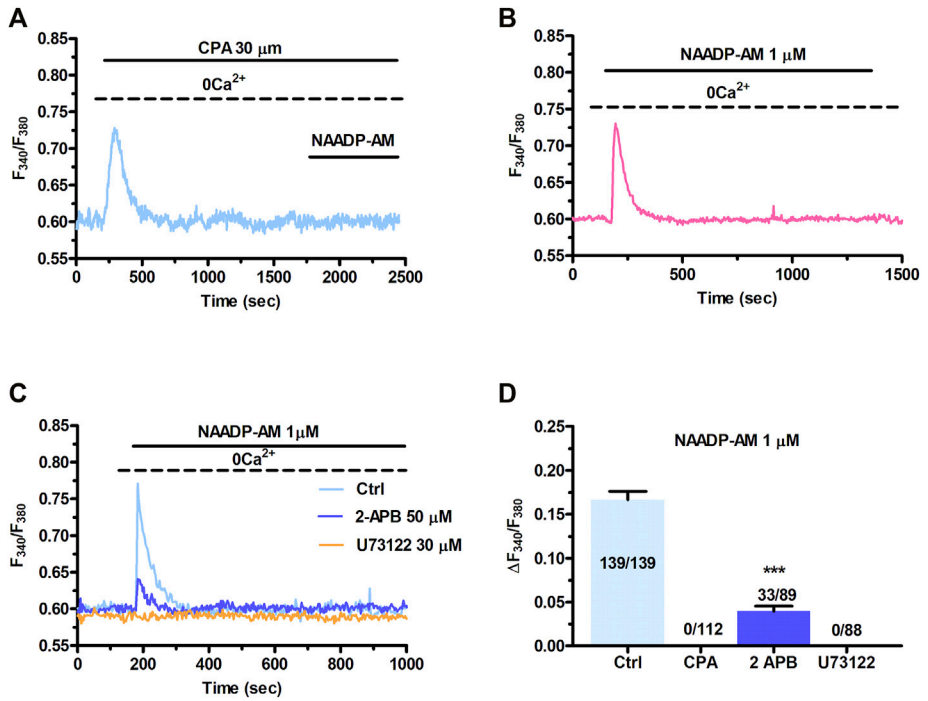

FIGURE 3 | $InsP_3Rs$ support the Ca^{2+} response to NAADP. **(A)** Administration of NAADP-AM (1 μM) after the pharmacological depletion of the ER Ca^{2+} pool with CPA (30 μm, 30 min) failed to induce intracellular Ca^{2+} release. CPA induced a transient increase in $[Ca^{2+}]_i$ that reflects passive ER Ca^{2+} leakage from the ER. **(B)** The intracellular Ca^{2+} transient evoked by NAADP-AM (1 μM) in the absence of extracellular Ca^{2+} ($0Ca^{2+}$) under control conditions. **(C)** The intracellular Ca^{2+} release evoked by NAADP-AM (1 μM) under control (Ctrl) conditions was severely affected by blocking $InsP_3Rs$ with 2-APB (50 μm, 30 min) or inhibiting PLC activity with U73122 (10 μm, 10 min). **(D)** Mean ± SE of the amplitude of the peak intracellular Ca^{2+} response to NAADP-AM under the designated treatments. Student's t-test: ***$p < 0.001$.

CPA-induced depletion of the ER Ca^{2+} store (**Figure 3A**). A preliminary characterization of the Ca^{2+} handling machinery revealed that C-MSCs express $InsP_3Rs$, but not RyRs, and that $InsP_3$-induced ER Ca^{2+} discharge activates SOCE (Maione et al., 2020a). To assess the contribution of $InsP_3Rs$ to NAADP-induced intracellular Ca^{2+} mobilization, we adopted a similar strategy to that described in (Kilpatrick et al., 2013; Kilpatrick et al., 2016; Faris et al., 2019; Moccia et al., 2021b). The transient increase in $[Ca^{2+}]_i$ evoked by NAADP-AM (1 μM) was significantly ($p < 0.001$) reduced by blocking $InsP_3Rs$ with 2-Aminoethoxydiphenyl borate (2-APB) (50 μM, 30 min) (**Figure 3C**) (Kilpatrick et al., 2013; Kilpatrick et al., 2016) and was suppressed by inhibiting the basal production of $InsP_3$ with U73122 (10 μM, 10 min) (**Figure 3C**), which selectively interferes with phospholipase C (PLC) activity (Moccia et al., 2006; Negri et al., 2021a). The statistical analysis of these data has been presented in **Figure 3D**. The lack of full inhibition of NAADP-AM-evoked intracellular Ca^{2+} mobilization could be due to the incomplete inhibition of $InsP_3Rs$, as also reported in ECFCs (Moccia et al., 2021b), rat gastric smooth muscle cells (Pereira et al., 2014), and MDA-MB-231 breast cancer cells (Vismara et al., 2021). Therefore, $InsP_3Rs$ provide a robust source of Ca^{2+} during lysosomal Ca^{2+} mobilization and, based upon previous observations (Davis et al., 2012; Kilpatrick et al., 2013; Ronco et al., 2015; Kilpatrick et al., 2016; Faris et al., 2019; Moccia et al., 2021b), it can be concluded that they can be recruited by CICR upon NAADP-induced lysosomal Ca^{2+} release. TEM was then exploited to assess whether MCSs between lysosomal vesicles and ER cisternae can also be detected and thereby sustain the Ca^{2+}-dependent cross-talk between the two organelles also in C-MSCs (Kilpatrick et al., 2013). For this purpose, after glutaraldehyde fixation cells have been post-fixed in aqueous OsO_4 in order to darkly stain lipids and membranes, as described in **Section 2**. TEM micrographs indicated extensive ER-lysosome MCSs (<20 nm, 14.3 ± 1.13, $n = 27$ from five cells) with ultrastructural resolution (**Figure 4**). As also reported in human fibroblasts, in the regions of close appositions (e.g., **Figure 4A**), fibres that appear to tether lysosomes and ER membranes were clearly discernible. In addition, we detected regions where the apposing membranes appeared to be physically coupled with no visible space between them (e.g., **Figures 4B,C**). Quantification in random sections showed that 60.5% of lysosomes established contact sites with the ER. As also discussed in Kilpatrick et al. (2013), this is likely to be an underestimate as lysosomal diameter spans between 200 and 500 nm and is, therefore, predicted to extend over several sections above and below the selected plane, where additional contact sites might have been established. Of note, lysosomes could establish extensive contact sites both with the smooth (**Figure 4D**) and the rough (**Figure 4E**) ER. We also found that ER cisternae could come in direct contacts with more than one lysosome (**Figure 4E**). Overall, these findings provide the ultrastructural evidence that the architecture of lysosomes and ER MCSs is fully consistent with the recruitment of ER-embedded $InsP_3Rs$ by NAADP-induced lysosomal Ca^{2+} release through TPCs.

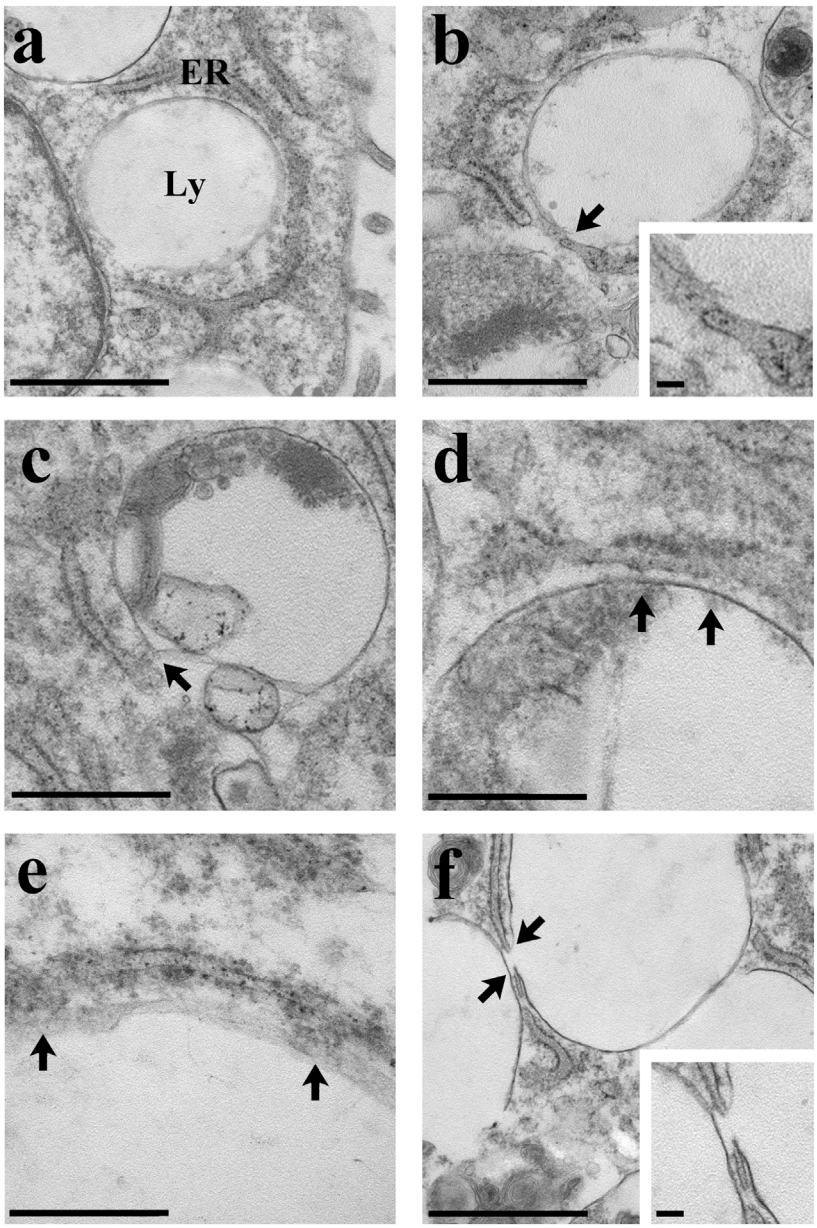

FIGURE 4 | Ultrastructural analysis of C-MSCs. Several examples of membrane contacts between lysosomes (Ly) and ER are shown. **(A)** Note the closeness of the lysosomes with the cell nucleus and ER. Scale bar: 1 μm. **(B)** The lysosome-ER contact site is indicated (arrow and inset). Scale bar: 1 μm; inset scale bar: 100 nm. **(C)** The arrow indicates the membrane contact site. Scale bar: 500 nm. **(D)** Extensive contact (arrows) between the lysosomal and the ER membranes. Scale bar: 500 nm. **(E)** Note the contact (arrows) between the ribosomes-rich ER and the lysosome. Scale bar: 200 nm. **(F)** Two close lysosomes; the one on the right is in tight contact with the ER (arrows and inset). Scale bar: 1 μm; inset scale bar: 100 nm.

3.4 SOCE Maintains NAADP-AM-Evoked Intracellular Ca^{2+} Signals in Cardiac Mesenchymal Stromal Cells

Figure 1B clearly shows that NAADP-AM-induced mobilization of intercellularly stored Ca^{2+} resulted in extracellular Ca^{2+} entry even after the agonist washout from the perfusate. This feature clearly hints at SOCE as the Ca^{2+} entry pathway sustaining the long-lasting increase in $[Ca^{2+}]_i$ evoked by NAADP in the presence of extracellular Ca^{2+}. Indeed, $InsP_3$-dependent ER Ca^{2+} mobilization results in SOCE activation virtually in all mammalian cells (Prakriya and Lewis, 2015; Emrich et al., 2021), including C-MSCs (Maione et al., 2020a). In order to assess whether NAADP-AM-induced lysosomal Ca^{2+} release can lead to SOCE *via* intermediate ER Ca^{2+} depletion, we repeated the "Ca^{2+} add-back" protocol described in **Figure 1** in the absence and presence of BTP-2 or Pyr6, two selective blockers of SOCE (Schleifer et al., 2012; Moccia et al., 2016). This strategy has long

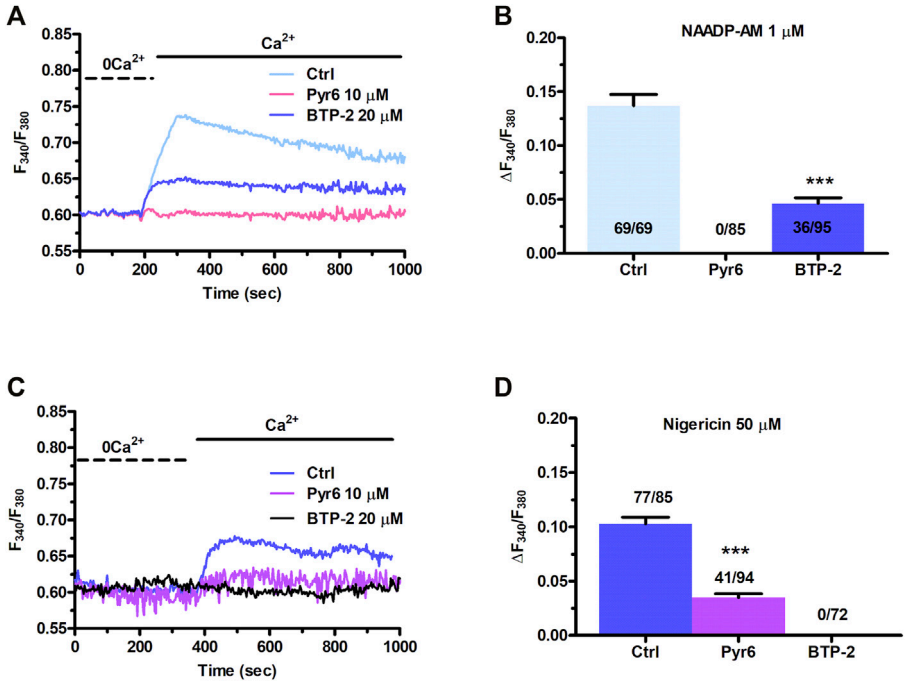

FIGURE 5 | NAADP-AM-induced lysosomal Ca^{2+} mobilization is functionally coupled to SOCE in C-MSCs. **(A)** The influx of extracellular Ca^{2+} evoked by NAADP-AM (1 μM) upon depletion of intracellular Ca^{2+} stores (Ctrl) was severely affected by inhibiting SOCE with Pyr6 (10 μM, 10 min) or BTP-2 (20 μm, 20 min). The previous NAADP-AM-evoked endogenous Ca^{2+} release has not been shown. **(B)** Mean ± SE of the amplitude of NAADP-AM-evoked Ca^{2+} entry evoked by nigericin in the absence (Ctrl) and presence of Pyr-6 and BTP-2. Student's t-test: ***$p < 0.001$. **(C)** Nigericin-evoked extracellular Ca^{2+} entry was attenuated or inhibited by, respectively, blocking SOCE with BTP-2 (20 μM, 20 min) or Pyr6 (10 μM, 10 min). **(D)** Mean ± SE of the amplitude of Ca^{2+} entry evoked by nigericin in the absence (Ctrl) and presence of Pyr-6 and BTP-2. Student's t-test: ***$p < 0.001$.

been exploited to selectively evaluate the blocking effect of SOCE-targeting drugs on agonist-evoked extracellular Ca^{2+} entry rather than on the previous phase of endogenous Ca^{2+} mobilization (Sanchez-Hernandez et al., 2010; Jairaman et al., 2015; Rahman and Rahman, 2017; Scarpellino et al., 2019; Negri et al., 2020; Schach et al., 2020). The influx of Ca^{2+} secondary to Ca^{2+} restitution to the perfusate after removal of NAADP-AM (**Figure 5A**) from the perfusate was significantly ($p < 0.001$) attenuated by BTP-2 (20 μM, 20 min) and abrogated by Pyr6 (10 μM, 10 min) (**Figure 5A**). The statistical analysis of these data has been presented in **Figure 5B**. These observations demonstrate that NAADP-induced lysosomal Ca^{2+} mobilization in C-MSCs is functionally coupled to SOCE *via* $InsP_3$-dependent ER Ca^{2+} release. Therefore, lysosomal Ca^{2+} release must induce depletion of ER Ca^{2+} *via* $InsP_3Rs$, thereby leading to SOCE recruitment on the plasma membrane. To further support this conclusion, **Supplementary Figure S5A** shows that also the pharmacological depletion of the lysosomal Ca^{2+} store with nigericin (50 μM) induced both intracellular Ca^{2+} release and extracellular Ca^{2+} entry. Furthermore, the intracellular Ca^{2+} response to nigericin (50 μM) was significantly ($p < 0.001$) reduced by blocking $InsP_3Rs$ with 2-APB (50 μM, 30 min) (**Supplementary Figures S5B,C**) and by interfering with basal $InsP_3$ production with U73122 (10 μM, 10 min) (**Supplementary Figures S5B,C**), as recently shown in primary cultures of colorectal cancer cells (Faris et al., 2019) and in circulating ECFCs (Moccia et al., 2021b). Finally, nigericin-evoked extracellular Ca^{2+} entry was significantly ($p < 0.001$) attenuated by blocking SOCE with either BTP-2 (20 μM, 20 min) or Pyr6 (10 μM, 10 min) (**Figures 5C,D**). This result is, therefore, consistent with the evidence reported above that NAADP-induced Ca^{2+} release through TPCs is able to induce ER Ca^{2+} depletion followed by SOCE activation.

3.5 Nicotinic Acid Adenine Dinucleotide Phosphate-Induced Lysosomal Ca^{2+} Release *via* TPCs Supports FBS-Induced Intracellular Ca^{2+} Oscillations in C-MSCs

FBS has been shown to induce intracellular Ca^{2+} signals to stimulate proliferation in primary MSCs harvested from rat bone marrow (Foreman et al., 2006). 20% FBS induced intracellular Ca^{2+} oscillations also in ≈26% of C-MSCs, whereas it promoted a transient increase elevation in $[Ca^{2+}]_i$ in the remaining 74% cells (**Figure 6A**). Intracellular Ca^{2+} oscillations lasted for at least 30 min, while the transient Ca^{2+} signal took approximately 13 min to decline to pre-stimulation levels (**Figure 6A**). In the absence of extracellular Ca^{2+} ($0Ca^{2+}$), 20% FBS induced a rapid (≈3 min) increase in $[Ca^{2+}]_i$ that

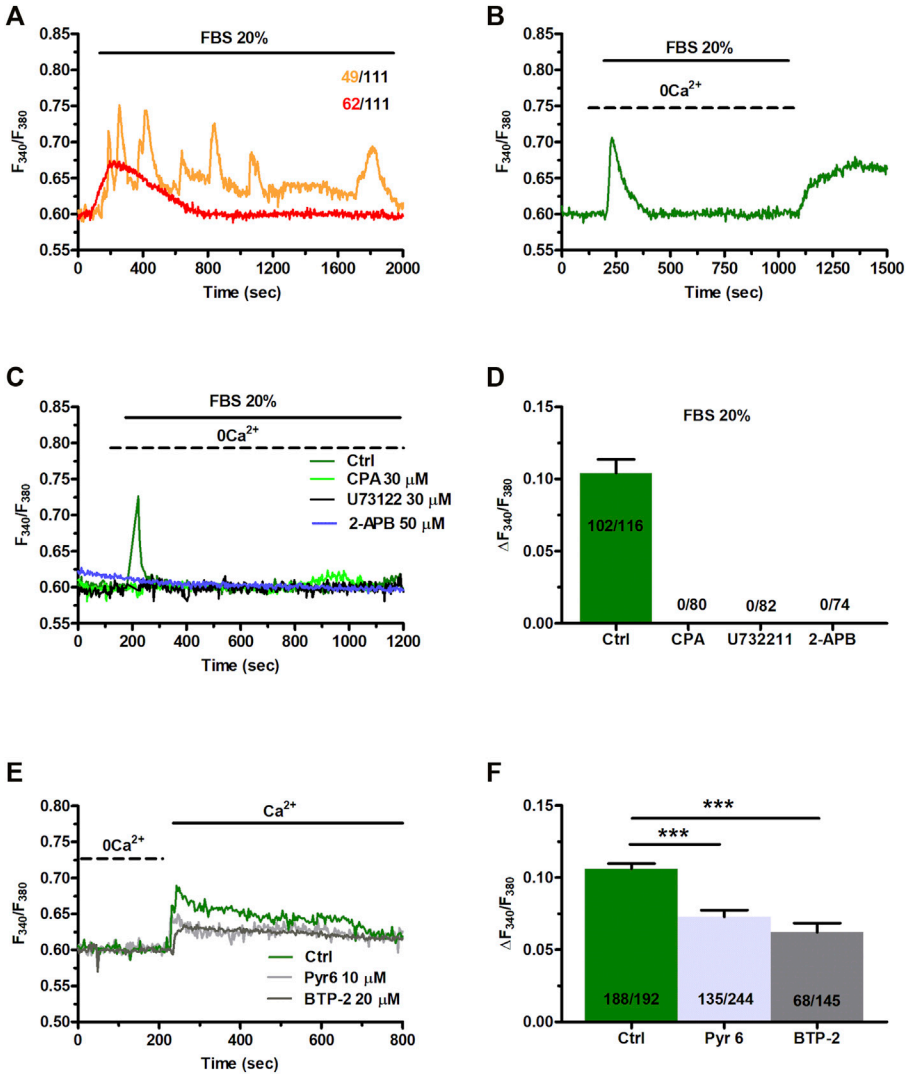

FIGURE 6 | Fetal bovine serum (FBS)-induces intracellular Ca^{2+} release from endogenous stores and enhance SOCE. **(A)** 20% FBS induced oscillatory or transient increases in $[Ca^{2+}]_i$. **(B)** Under $0Ca^{2+}$ conditions, 20% FBS induced a transient elevation in $[Ca^{2+}]_i$. Subsequent re-addition of extracellular Ca^{2+}, 100 s after agonist removal from the bath, resulted in a second bump in $[Ca^{2+}]_i$ that was indicative of SOCE. **(C)** The intracellular Ca^{2+} release evoked by 20% FBS (Ctrl) was inhibited by depleting the ER Ca^{2+} pool with CPA (30 µM, 30 min), by blocking $InsP_3Rs$ with 2-APB (50 µM, 30 min), or inhibiting PLC with U73122 (10 µM, 10 min). **(D)** Mean ± SE of the amplitude of the peak intracellular Ca^{2+} response to 20% FBS under the designated treatments. **(E)** Subsequent to store depletion by 20% of FBS application (data are not shown her**(E)**, FBS were washed out from bath, then extracellular Ca^{2+} added to the bath to bath in the presence and absence of SOCE inhibitors, Pyr6 (10 µm, 10 min) or BTP-2 (20 µm, 20 min). **(F)** Mean ± SE of the amplitude of Ca^{2+} entry evoked by 20% FBS in the absence (Ctrl) and presence of Pyr6 and BTP-2. The asterisk indicates $^{***}p < 0.001$.

reflected endogenous Ca^{2+} mobilization. The subsequent re-addition of extracellular Ca^{2+}, 100 s after FBS removal from the bath, resulted in a second bump in $[Ca^{2+}]_i$, which was due to extracellular Ca^{2+} entry and was likely to be mediated by SOCE (**Figure 6B**). FBS-induced intracellular Ca^{2+} signals are known to be triggered by $InsP_3$-induced ER Ca^{2+} mobilization and maintained over time by SOCE (Foreman et al., 2006; Hu et al., 2009; Zuccolo et al., 2018b). Preliminary experiments confirmed that 20% FBS-induced intracellular Ca^{2+} release was abrogated by depleting the ER Ca^{2+} store with CPA (30 µM, 30 min) (**Figures 6C,D**), inhibiting $InsP_3Rs$ with 2-APB (50 µM, 30 min) (**Figures 6C,D**), and blocking PLC with U73122 (10 µM, 10 min) (**Figures 6C,D**). Furthermore, 20% FBS-induced extracellular Ca^{2+} entry was significantly ($p < 0.001$) reduced by inhibiting SOCE with BTP-2 (20 µM, 20 min) or Pyr6 (10 µM, 10 min) (**Figures 6E,F**).

The evidence reported above clearly showed that NAADP-induced lysosomal Ca^{2+} release via TPCs was able to promote $InsP_3$-induced Ca^{2+} release from the ER, thereby resulting in SOCE activation on the plasma membrane. Therefore, we sought to assess the role of NAADP-induced lysosomal Ca^{2+} release in the Ca^{2+} response to 20% FBS (**Figure 7A**). The depletion of the

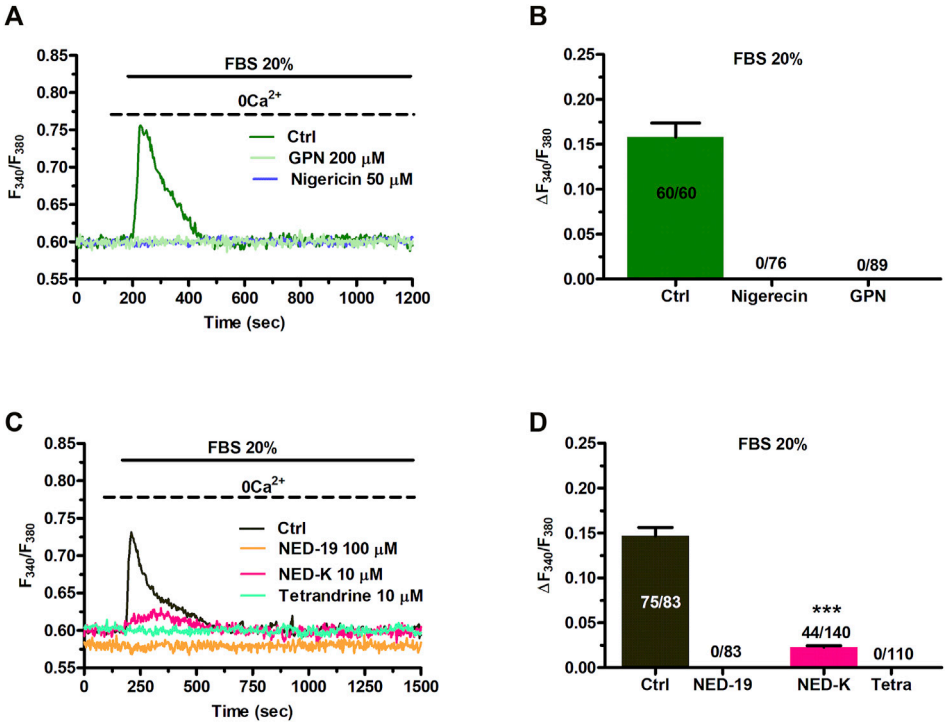

FIGURE 7 | TPCs mediate 20% FBS-induced intracellular Ca^{2+} release. **(A)** Intracellular Ca^{2+} release induced by 20% FBS was abolished upon depletion of the lysosomal Ca^{2+} pool with either GPN (200 μM, 30 min) or nigericin (50 μM, 30 min). **(B)** Mean ± SE of the amplitude of the intracellular Ca^{2+} peak evoked by 20% FBS under the designated treatments. **(C)** 20% FBS induced an intracellular Ca^{2+} transient that was significantly reduced or inhibited by blocking TPCs with, respectively, NED-K (10 μM, 30 min), tetrandrine (10 μM, 30 min) or NED-19 (100 μM, 30 min). **(D)** Mean ± SE of the amplitude of the intracellular Ca^{2+} peak evoked by 20% FBS in the absence (Ctrl) or presence of NED-19, NED-K or tetrandrine (Tetra). Student's t-test: ***$p < 0.001$.

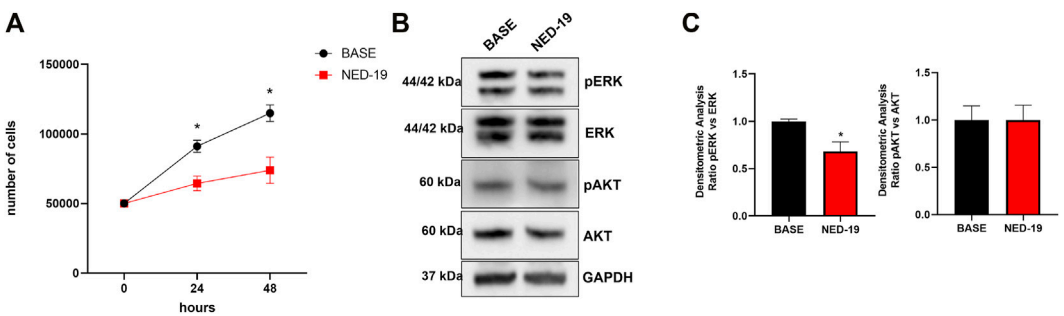

FIGURE 8 | TPCs mediate 20% FBS-induced proliferation and ERK phosphorylation in C-MSCs. Following 4 h of growth without serum, cells were treated with NED-19 (100 μM, 30 min) and subsequently stimulated with 20% FBS. **(A)** Following 24 and 48 h of FBS stimulation, the medium was removed, cells detached from the plates, and counted by hemocytometer ($n = 3$/group). Student's t-test: *$p < 0.05$. **(B)** The cells were lysate after 60 min of FBS stimulation. Total protein extract from treated cells was subjected to Western blot analysis to visualize active phosphorylated form and total of ERK and AKT using specific antibodies. Phospho-ERK1/2 and Phospho-AKT levels were corrected by total ERK1/2 and AKT densitometry respectively. **(C)** Western blot data are presented as the fold change of target protein expression. The results are expressed as mean ± SEM ($n = 3$/group). Student's t-test: *$p < 0.05$.

lysosomal Ca^{2+} store with either GPN (200 μM, 30 min) (**Figures 7A,B**) or nigericin (50 μM, 30 min) (**Figures 7A,B**) abrogated FBS-induced intracellular Ca^{2+} mobilization. The same effect was achieved upon pharmacological blockade of TPCs with NED-19 (100 μM, 30 min) (**Figures 7C,D**), NED-K (10 μM, 30 min) (**Figures 7C,D**), and tetrandrine (**Figures 7C,D**). Therefore, NAADP plays a crucial role in igniting the Ca^{2+} response to 20% FBS in C-MSCs.

3.6 TPCs Mediate 20% FBS-Induced Proliferation and ERK Phosphorylation in Cardiac Mesenchymal Stromal Cells

In order to assess the physiological role of NAADP-induced lysosomal Ca^{2+} release through TPCs, 20% FBS-induced C-MSC proliferation was evaluated in the absence (Ctrl) and presence of NED-19 (100 μM, 30 min). **Figure 8A** shows that the pharmacological blockade of TPCs significantly ($p < 0.05$) reduced the total cell number at 24 and 48 h, thereby showing the crucial role of TPCs in supporting C-MSC proliferation. Flow cytometric analysis of Annexin V fluorescence confirmed that pre-treating C-MSCs with NED-19 did not induce apoptosis (**Supplementary Figure S6**). In order to determine whether TPCs recruit mitogen-associated protein kinases (MAPKs), we evaluated the phosphorylated levels of the Ca^{2+}-dependent extracellular signal-regulated protein kinases 1 and 2 (ERK1/2) and of the survival kinase, Akt (Zuccolo et al., 2018a; Faris et al., 2019; Negri et al., 2021b). **Figures 8B,C** illustrate that 20% FBS-induced ERK1/2, but not Akt, phosphorylation was significantly ($p < 0.05$) inhibited by blocking TPCs with NED-19 (100 μM, 30 min). Overall, these findings demonstrate that NAADP-induced lysosomal Ca^{2+} release through TPCs stimulates C-MSC proliferation by engaging ERK1/2.

4 DISCUSSION

NAADP is emerging as a crucial regulator of intracellular Ca^{2+} signalling and Ca^{2+}-dependent processes in the cardiovascular system (Macgregor et al., 2007; Collins et al., 2011; Fameli et al., 2017; Moccia et al., 2021a). C-MSCs represent the large majority of supportive cells in the heart, are critical to normal cardiac function and contribute to maladaptive cardiac remodelling under multiple pathological conditions. Herein, we showed for the first time that NAADP mobilizes EL Ca^{2+} *via* TPCs also in C-MSCs. NAADP-evoked intracellular Ca^{2+} signals are amplified by $InsP_3$-sensitive ER Ca^{2+} release at lysosomes-ER C-MCSs followed by SOCE activation. The functional crosstalk between NAADP-evoked lysosomal Ca^{2+} release, $InsP_3$-induced ER Ca^{2+} mobilization and SOCE sustains FBS-induced intracellular Ca^{2+} signals and proliferation by promoting ERK phosphorylation.

4.1 Nicotinic Acid Adenine Dinucleotide Phosphate Evokes Complex Ca^{2+} Signals in Cardiac Mesenchymal Stromal Cells

Intracellular Ca^{2+} signals tightly control a plethora of crucial functions in human MSCs from multiple sources, as reviewed in Moccia et al. (2015), Forostyak et al. (2016), and Jiang et al. (2017). According to the canonical model, the Ca^{2+} response evoked by chemical stimulation in human MSCs is triggered by $InsP_3$-dependent ER Ca^{2+} and may be maintained over time by SOCE (Kawano et al., 2002; Peng et al., 2016; Kotova et al., 2018). Herein, we expanded our knowledge of the molecular mechanisms shaping intracellular Ca^{2+} signalling in these cells by focusing on the role played by NAADP in C-MSCs. The intracellular delivery of NAADP mobilizes acidic Ca^{2+} stores throughout the cardiovascular system (Moccia et al., 2021a), e.g., in guinea pig ventricular (Macgregor et al., 2007) and atrial (Collins et al., 2011) cardiomyocytes, rat pulmonary artery VSMCs (Kinnear et al., 2004), human aortic endothelial cells (Brailoiu et al., 2010), mouse brain endothelial cells (Zuccolo et al., 2019), and circulating ECFCs (Di Nezza et al., 2017; Moccia et al., 2021b). Likewise, NAADP-AM, a membrane-permeable analogue of NAADP, could induce either a transient elevation in $[Ca^{2+}]_i$ or a burst of intracellular Ca^{2+} oscillations. This latter observation is in accord with the evidence that: 1) intracellular delivery of NAADP may induce oscillatory Ca^{2+} signals in human Jurkat T-lymphocytes (Berg et al., 2000), cytotoxic T lymphocytes (Davis et al., 2012), and human pancreatic β-cells (Johnson and Misler, 2002); 2) NAADP contributes to agonist-induced repetitive Ca^{2+} spikes in several types of endothelial cells (Zuccolo et al., 2019; Berra-Romani et al., 2020; Balducci et al., 2021), and that 3) NAADP induces intracellular Ca^{2+} oscillations in mouse cardiomyocytes during reperfusion injury (Davidson et al., 2015). Early work conducted on echinoderms first suggested that NAADP was able to elicit repetitive Ca^{2+} oscillations by promoting a Ca^{2+}-dependent crosstalk between two different Ca^{2+} pools (Churchill and Galione, 2001), which were later shown to be located in acidic vesicles and ER (Churchill et al., 2002; Moccia et al., 2006).

4.2 Nicotinic Acid Adenine Dinucleotide Phosphate-Induced Intracellular Ca^{2+} Signals Are Triggered by Lysosomal Ca^{2+} Release *via* TPCs, Amplified by $InsP_3$-Evoked ER Ca^{2+} Release and Maintained by SOCE

The Ca^{2+} response to NAADP in C-MSCs comprised an early phase of intracellular Ca^{2+} mobilization followed by a later phase of extracellular Ca^{2+} entry, which required the previous depletion of the endogenous Ca^{2+} pool but not the NAADP-AM presence in the perfusate. First, we found that GPN, nigericin, and bafilomycin A1, which provide three established pharmacological tools to mobilize acidic Ca^{2+} stores (Kilpatrick et al., 2013; Ronco et al., 2015; Morgan and Galione, 2021; Yuan et al., 2021), prevent NAADP-induced intracellular Ca^{2+} mobilization. In agreement with the hypothesis that the lysosomal compartment represents the primary source of this increase in $[Ca^{2+}]_i$, all of these drugs, as well as NH_4Cl, induced a rapid reduction in Lysotracker Red fluorescence. Although a recent investigation questioned the documented GPN ability to release lysosomal Ca^{2+} (Atakpa et al., 2019), Patel's group provided the clear-cut evidence that this compound mobilizes Ca^{2+} from acidic organelles and may, therefore, be safely exploited to probe the endogenous store primarily targeted by NAADP (Morgan et al., 2020; Yuan et al., 2021). We further showed that C-MSCs express both TPC1 and TPC2 transcripts and proteins, and that the Ca^{2+} response to NAADP was inhibited by blocking TPCs with two selective antagonists, such as NED-19 (Macgregor et al., 2007; Di Nezza et al., 2017; Jin et al., 2020; Moccia et al., 2021a) and NED-

K (Davidson et al., 2015), and the traditional Chinese herbal remedy, tetrandrine, which can target both TPC1 and TPC2 (Sakurai et al., 2015; Moccia et al., 2021a). As recently reviewed in Moccia et al. (2021a) and Negri et al. (2021b), TPC1 and TPC2 are both present in mouse ventricular cardiomyocytes, but this is the first time that they were reported in any other cellular component of the human heart. As reviewed in Pitt et al. (2016), TPC1 presents a limited Ca^{2+} permeability, while TPC2 is predicted to release more Ca^{2+} upon activation. Nevertheless, it has been shown that even a small Ca^{2+} flux through TPC1 can generate a global increase in $[Ca^{2+}]_i$ when lysosomal vesicles are juxtaposed to ER cisternae (Galione, 2019). For instance, TPC1 alone supports NAADP-induced intracellular Ca^{2+} oscillations in circulating ECFCs (Di Nezza et al., 2017; Moccia et al., 2021b) and in mouse cardiac myocytes undergoing the ischemia-reperfusion injury (Davidson et al., 2015). Furthermore, TPC1 was sufficient to maintain the intracellular Ca^{2+} response to nutrients or incretins in mouse pancreatic β cells deficient for TPC2 (Cane et al., 2016). Three pieces of evidence suggest that $InsP_3Rs$ in ER cisternae contribute to amplify NAADP-induced lysosomal Ca^{2+} release. First, depletion of the ER Ca^{2+} pool with CPA suppressed or attenuated the intracellular Ca^{2+} release evoked by both NAADP and the H^+/K^+ antiporter, nigericin. Second, NAADP-induced endogenous Ca^{2+} mobilization was impaired by inhibiting $InsP_3Rs$ with 2-APB and by blocking basal $InsP_3$ production with U73122. Conversely, functional RyRs are absent in C-MSCs (Maione et al., 2020a). The requirement for $InsP_3Rs$ to sustain the increase in $[Ca^{2+}]_i$ resulting from NAADP-AM-evoked Ca^{2+} release from lysosomal vesicles is in full agreement with previous work carried out on human fibroblasts (Kilpatrick et al., 2013), human ECFCs (Moccia et al., 2021b), COS-7 cells (Morgan and Galione, 2021), HeLa cells (Ronco et al., 2015), and human metastatic colorectal cancer cells (Faris et al., 2019). Third, TEM revealed clearly discernible ER-lysosomes MCSs, which closely resemble those previously described in human fibroblasts (Kilpatrick et al., 2013) and could provide the subcellular framework to enable $InsP_3R$ recruitment by local Ca^{2+} release through TPCs (Penny et al., 2014). Likewise, the MCSs between lysosomal vesicles and ER cisternae in C-MSCs are similar to the cytoplasmic nanojunctions between lysosomes and sarcoplasmic reticulum (SR) recently reported in rat aortic VSMCs (Fameli et al., 2014).

The different extent of coupling between lysosomal TPCs and ER-embedded $InsP_3Rs$ (due to changes in either their distribution or density at MCSs) could explain the onset of a long-lasting elevation in $[Ca^{2+}]_i$ that replaces the intracellular Ca^{2+} oscillations in a fraction of C-MSCs. For instance, computational modelling indicated that TPC clustering within the microdomain could accelerate the frequency of $InsP_3Rs$-driven Ca^{2+} oscillations (Penny et al., 2014), which could ultimately lead to the fusion of the Ca^{2+} spikes and the occurrence of a single, broader increase in $[Ca^{2+}]_i$ (Bartlett et al., 2020).

Removal of extracellular Ca^{2+} shortened the duration of the Ca^{2+} response to NAADP-AM. Therefore, NAADP is predicted to gate a Ca^{2+}-permeable pathway on the plasma membrane. This observation is supported by the evidence that restitution of extracellular Ca^{2+} following exposure to NAADP (or nigericin) under $0Ca^{2+}$ conditions, results in a second bump in $[Ca^{2+}]_i$ that reflects extracellular Ca^{2+} entry. This influx of Ca^{2+} occurs after washout of the agonist from the bath and, therefore, it is exclusively coupled to the previous depletion of endogenous Ca^{2+} stores. As discussed elsewhere (Yamazaki et al., 2007; Sanchez-Hernandez et al., 2010; Negri et al., 2020), this feature hints at SOCE as being responsible for NAADP-induced extracellular Ca^{2+} entry. In agreement with this hypothesis, NAADP-evoked Ca^{2+} influx was remarkably reduced in the presence of either BTP-2 or Pyr6, two different inhibitors of Orai1 channels, which provide the pore-forming subunit of store-operated Ca^{2+} channels in non-excitable cells (Prakriya and Lewis, 2015; Emrich et al., 2021) and MSCs (Lee et al., 2016; Peng et al., 2016). SOCE activation ultimately results from the reduction of ER Ca^{2+} concentration (Emrich et al., 2021). As discussed elsewhere (Davis et al., 2012; Brailoiu and Brailoiu, 2016), the engagement of SOCE by NAADP (and nigericin) hints at the depletion of the ER Ca^{2+} content as the intermediate step between lysosomal Ca^{2+} release and extracellular Ca^{2+} entry. However, extracellular Ca^{2+} entry directly evoked by NAADP delivery was not always engaged during acidic Ca^{2+} signalling in the cell types where this functional interplay has been investigated (Faris et al., 2019; Moccia et al., 2021b). Therefore, it is conceivable that lysosomal Ca^{2+} release recruits ER subdomains that are functionally coupled to the SOCE machinery in C-MSCs, but not in other cell types, as widely discussed in Parekh and Putney (2005). These observations hint at NAADP as a Ca^{2+}-releasing second messenger that can trigger a functional crosstalk among multiple Ca^{2+} sources (lysosomes, ER, and plasma membrane) in C-MSCs. In these cells, NAADP may serve as a provider of the "trigger" Ca^{2+} response to extracellular stimulation that is subsequently amplified by $InsP_3Rs$ on the ER and maintained over time by SOCE activation on the plasma membrane, as previously reported in many mammalian cells, including human fibroblasts (Kilpatrick et al., 2013), human ECFCs (Moccia et al., 2021b) and brain microvascular endothelial cells (Zuccolo et al., 2019), human metastatic colorectal cancer cells (Faris et al., 2019), human primary CTL cells (Davis et al., 2012), and rat pulmonary artery VSMCs (Kinnear et al., 2004).

4.3 Lysosomal Ca^{2+} Release *via* TPCs is Crucial to FBS-Induced Intracellular Ca^{2+} Signalling and Proliferation in Cardiac Mesenchymal Stromal Cells

It has long been known that FBS stimulates proliferation through an increase in $[Ca^{2+}]_i$ that can adopt either a biphasic (Faris et al., 2019) or an oscillatory pattern (Tao et al., 2011) in a variety of cell types, including rat bone marrow MSCs (Foreman et al., 2006). FBS-induced intracellular Ca^{2+} signals are known to impinge on the interplay between $InsP_3$-induced Ca^{2+} release from the ER and SOCE (Foreman et al., 2006; Hu et al., 2009). Intriguingly, a recent investigation reported the first evidence that NAADP-evoked lysosomal Ca^{2+} release via TPC1 interacts with $InsP_3$-

dependent ER Ca^{2+} mobilization and SOCE to promote FBS-induced proliferation in human metastatic colorectal cancer cells (Faris et al., 2019). Unveiling the molecular mechanisms that drive C-MSC proliferation is crucial to improve the therapeutic outcome of regenerative strategies aiming at utilizing these cells to promote cardiac repair (Bagno et al., 2018; Braunwald, 2018). Preliminary analysis showed that FBS evoked a complex increase in $[Ca^{2+}]_i$ also in C-MSCs, which displayed either an oscillatory or a biphasic Ca^{2+} signal. Pharmacological manipulation confirmed that the Ca^{2+} response to FBS comprised $InsP_3$-induced ER Ca^{2+} mobilization followed by SOCE activation. Indeed, FBS-induced intracellular Ca^{2+} release was suppressed by inhibiting $InsP_3Rs$ with 2-APB, by blocking basal $InsP_3$ production with U73122 and by depleting the ER Ca^{2+} store with CPA, whereas FBS-induced extracellular Ca^{2+} entry was remarkably attenuated by blocking SOCE with BTP-2 and Pyr6. Next, we provided the evidence that the NAADP-sensitive acidic Ca^{2+} store is crucial to FBS-induced intracellular Ca^{2+} signals and proliferation in C-MSCs. Indeed, FBS-induced intracellular Ca^{2+} release was abrogated by depleting the lysosomal Ca^{2+} store with either GPN or nigericin, as previously shown in human metastatic colorectal cancer cells (Faris et al., 2019). In agreement with these observations, the selective blockade of TPCs with NED-19, NED-K or tetrandrine also abolished the intracellular Ca^{2+} response to FBS. Therefore, NAADP-induced lysosomal Ca^{2+} release is indispensable to trigger the cytosolic Ca^{2+} response to FBS and this requires the functional recruitment of $InsP_3Rs$ on the ER *via* CICR at lysosomal-ER MCSs. That the ER is depleted *via* $InsP_3Rs$-mediated ER Ca^{2+} release following NAADP-induced lysosomal Ca^{2+} mobilization in response to FBS is also suggested by FBS-induced SOCE activation, which requires a reduction in ER Ca^{2+} concentration (Brailoiu et al., 2009; Davis et al., 2012). The mechanism whereby FBS stimulation results to intracellular NAADP generation in C-MSCs, as well as in human metastatic cancer cells (Faris et al., 2019), remains to be elucidated. Nevertheless, FBS is likely to engage the multifunctional enzyme CD38, which catalyses the "base exchange" of the nicotinamide moiety of NADP with nicotinic acid, thereby resulting in NAADP production in most cell types (Galione, 2015), including cardiomyocytes (Negri et al., 2021b). A recent paper suggested that the dual NADPH oxidases, DUOX1 and DUOX2, contribute to NAADP biosynthesis in murine T lymphocytes (Gu et al., 2021), but their role in NAADP-dependent Ca^{2+} response to FBS is yet to be investigated.

The physiological role of NAADP-induced intracellular Ca^{2+} signals were further assessed by evaluating the effect of NED-19 on C-MSC proliferation. The pharmacological blockade of TPCs with NED-19 strongly reduced FBS-induced C-MSC proliferation at 24 and 48 h. Preliminary experiments indicated that the massive release of Ca^{2+} induced by nigericin *per se* resulted in C-MSC cell death already at 24 h from exposure to this lysosomotropic compound. While this observation is in accord with the reported effects of nigericin on various cell models (Murakami et al., 2012), it prevented us from probing its ability to interfere with FBS-induced proliferation. Previous work showed that NAADP-induced Ca^{2+} release may stimulate proliferation by recruiting the Ca^{2+}-dependent ERK1/2 and Akt signalling pathways (Faris et al., 2019; Negri et al., 2021b). Consistently, FBS-induced ERK1/2 phosphorylation was impaired by the pharmacological blockade of TPCs with NED-19, whereas Akt engagement was unaffected. Interestingly, ERK1/2, but not Akt, was harnessed by intracellular Ca^{2+} oscillations to drive FBS-induced proliferation also in human bone marrow MSCs (Tao et al., 2011). Additionally, NAADP-induced intracellular Ca^{2+} oscillations could underpin another crucial function of C-MSCs, i.e., the regulation of extracellular matrix (ECM) composition (Maione et al., 2020b). For instance, bone marrow-derived human MSCs exhibited repetitive Ca^{2+} spikes during aligned collagen matrix formation (Gilchrist et al., 2019), whereas extracellular Ca^{2+} entry in human airway epithelial cells drives the expression and secretion of matrix-degrading enzymes, such as matrix metalloprotease 1 (Li et al., 2011). Interestingly, an increase in $[Ca^{2+}]_i$ in cardiac fibroblasts may also regulate collagen remodelling in mouse hearts (Adapala et al., 2020). Therefore, future studies will have to assess the role of NAADP-induced Ca^{2+} signalling in the modulation of ECM composition by C-MSCs.

In conclusion, this study demonstrated that NAADP induces intracellular Ca^{2+} signals in C-MSCs by promoting lysosomal Ca^{2+} release *via* TPCs that is in turn amplified by ER-embedded $InsP_3Rs$ at lysosomal-ER MCSs. The following depletion of the ER Ca^{2+} pool activates SOCE, which prolongs the Ca^{2+} response to NAADP. FBS impinges on the NAADP-induced Ca^{2+}-dependent crosstalk between lysosomes and ER to stimulate proliferation through the Ca^{2+}-dependent ERK1/2 signalling pathway. These findings pave the way for future studies assessing whether NAADP signalling in C-MSCs could be targeted to favour cardiac repair upon an ischemic insult or to other pathologies associated to maladaptive cardiac remodelling, such as ACM, heart failure and cardiac fibrosis.

DATA AVAILABILITY STATEMENT

The raw data supporting the conclusion of this article will be made available by the authors, without undue reservation.

ETHICS STATEMENT

The studies involving human participants were reviewed and approved by the IEO-CCM IRCCS Ethic Committee (project CCM1072). The patients/participants provided their written informed consent to participate in this study.

AUTHOR CONTRIBUTIONS

FM conceived and directed the project in collaboration with AM. FM, MB, and AM conceived the experiments. PF, CC, AM, SN, and LI performed the experiments and analysed the data. All authors contributed to the article and approved the submitted version.

FUNDING

The authors gratefully acknowledge financial support from: Italian Ministry of Education, University and Research (MIUR): Dipartimenti di Eccellenza Program (2018–2022)—Department of Biology and Biotechnology "L. Spallanzani," University of Pavia (MB and FM); Fondo Ricerca Giovani from the University of Pavia (MB and FM); EU Horizon 2020 FETOPEN-2018-2020 Programme "LION-HEARTED," grant agreement No. 828984 (FM); Italian Ministry of Health—RCXXXXXX—(AM); "Fondazione di Comunità di Milano" and "Fondo Giacomo Ponzone" (AM).

ACKNOWLEDGMENTS

The authors gratefully acknowledge the Laboratory of Electron Transmission Microscopy, Centro Grandi Strumenti of the University Pavia, for excellent technical and scientific support.

SUPPLEMENTARY MATERIAL

The Supplementary Material for this article can be found online at: https://www.frontiersin.org/articles/10.3389/fcell.2022.874043/full#supplementary-material

REFERENCES

Adapala, R. K., Kanugula, A. K., Paruchuri, S., Chilian, W. M., and Thodeti, C. K. (2020). TRPV4 Deletion Protects Heart from Myocardial Infarction-Induced Adverse Remodeling via Modulation of Cardiac Fibroblast Differentiation. *Basic Res. Cardiol.* 115, 14. doi:10.1007/s00395-020-0775-5

Atakpa, P., Van Marrewijk, L. M., Apta-Smith, M., Chakraborty, S., and Taylor, C. W. (2019). GPN Does Not Release Lysosomal Ca2+ but Evokes Ca2+ Release from the ER by Increasing the Cytosolic pH Independently of Cathepsin C. *J. Cel Sci* 132. doi:10.1242/jcs.223883

Bagno, L., Hatzistergos, K. E., Balkan, W., and Hare, J. M. (2018). Mesenchymal Stem Cell-Based Therapy for Cardiovascular Disease: Progress and Challenges. *Mol. Ther.* 26, 1610–1623. doi:10.1016/j.ymthe.2018.05.009

Balducci, V., Faris, P., Balbi, C., Costa, A., Negri, S., Rosti, V., et al. (2021). The Human Amniotic Fluid Stem Cell Secretome Triggers Intracellular Ca2+ Oscillations, NF-κB Nuclear Translocation and Tube Formation in Human Endothelial colony-forming Cells. *J. Cel Mol Med* 25, 8074–8086. doi:10.1111/jcmm.16739

Bartlett, P. J., Cloete, I., Sneyd, J., and Thomas, A. P. (2020). IP3-Dependent Ca2+ Oscillations Switch into a Dual Oscillator Mechanism in the Presence of PLC-Linked Hormones. *iScience* 23, 101062. doi:10.1016/j.isci.2020.101062

Berg, I., Potter, B. V. L., Mayr, G. W., and Guse, A. H. (2000). Nicotinic Acid Adenine Dinucleotide Phosphate (Naadp+) Is an Essential Regulator of T-Lymphocyte Ca2+-Signaling. *J. Cel Biol* 150, 581–588. doi:10.1083/jcb.150.3.581

Berra-Romani, R., Faris, P., Pellavio, G., Orgiu, M., Negri, S., Forcaia, G., et al. (2020). Histamine Induces Intracellular Ca2+ Oscillations and Nitric Oxide Release in Endothelial Cells from Brain Microvascular Circulation. *J. Cel Physiol* 235, 1515–1530. doi:10.1002/jcp.29071

Brailoiu, G. C., Brailoiu, E., Parkesh, R., Galione, A., Churchill, G. C., Patel, S., et al. (2009). NAADP-mediated Channel 'chatter' in Neurons of the Rat Medulla Oblongata. *Biochem. J.* 419 (91-97), 91–97. doi:10.1042/BJ20081138

Brailoiu, G. C., and Brailoiu, E. (2016). Modulation of Calcium Entry by the Endo-Lysosomal System. *Adv. Exp. Med. Biol.* 898, 423–447. doi:10.1007/978-3-319-26974-0_18

Brailoiu, G. C., Gurzu, B., Gao, X., Parkesh, R., Aley, P. K., Trifa, D. I., et al. (2010). Acidic NAADP-Sensitive Calcium Stores in the Endothelium. *J. Biol. Chem.* 285, 37133–37137. doi:10.1074/jbc.c110.169763

Braunwald, E. (2018). Cell-Based Therapy in Cardiac Regeneration. *Circ. Res.* 123, 132–137. doi:10.1161/circresaha.118.313484

Brown, R. D., Ambler, S. K., Mitchell, M. D., and Long, C. S. (2005). The Cardiac Fibroblast: Therapeutic Target in Myocardial Remodeling and Failure. *Annu. Rev. Pharmacol. Toxicol.* 45, 657–687. doi:10.1146/annurev.pharmtox.45.120403.095802

Camelliti, P., Borg, T., and Kohl, P. (2005). Structural and Functional Characterisation of Cardiac Fibroblasts. *Cardiovasc. Res.* 65, 40–51. doi:10.1016/j.cardiores.2004.08.020

Cane, M. C., Parrington, J., Rorsman, P., Galione, A., and Rutter, G. A. (2016). The Two Pore Channel TPC2 Is Dispensable in Pancreatic β-cells for normal Ca2+ Dynamics and Insulin Secretion. *Cell Calcium* 59, 32–40. doi:10.1016/j.ceca.2015.12.004

Capel, R. A., Bolton, E. L., Lin, W. K., Aston, D., Wang, Y., Liu, W., et al. (2015). Two-pore Channels (TPC2s) and Nicotinic Acid Adenine Dinucleotide Phosphate (NAADP) at Lysosomal-Sarcoplasmic Reticular Junctions Contribute to Acute and Chronic β-Adrenoceptor Signaling in the Heart. *J. Biol. Chem.* 290, 30087–30098. doi:10.1074/jbc.m115.684076

Carriero, F., Martinelli, C., Gabriele, F., Barbieri, G., Zanoletti, L., Milanesi, G., et al. (2021). Berberine Photo-Activation Potentiates Cytotoxicity in Human Astrocytoma Cells through Apoptosis Induction. *J. Pers Med.* 11. doi:10.3390/jpm11100942

Christensen, K. A., Myers, J. T., and Swanson, J. A. (2002). pH-dependent Regulation of Lysosomal Calcium in Macrophages. *J. Cel Sci* 115, 599–607. doi:10.1242/jcs.115.3.599

Churchill, G. C., and Galione, A. (2001). NAADP Induces Ca2+ Oscillations via a Two-Pool Mechanism by Priming IP3- and cADPR-Sensitive Ca2+ Stores. *EMBO J.* 20, 2666–2671. doi:10.1093/emboj/20.11.2666

Churchill, G. C., Okada, Y., Thomas, J. M., Genazzani, A. A., Patel, S., and Galione, A. (2002). NAADP Mobilizes Ca2+ from Reserve Granules, Lysosome-Related Organelles, in Sea Urchin Eggs. *Cell* 111, 703–708. doi:10.1016/s0092-8674(02)01082-6

Collins, T. P., Bayliss, R., Churchill, G. C., Galione, A., and Terrar, D. A. (2011). NAADP Influences Excitation-Contraction Coupling by Releasing Calcium from Lysosomes in Atrial Myocytes. *Cell Calcium* 50, 449–458. doi:10.1016/j.ceca.2011.07.007

Czapla, J., Matuszczak, S., Wiśniewska, E., Jarosz-Biej, M., Smolarczyk, R., Cichoń, T., et al. (2016). Human Cardiac Mesenchymal Stromal Cells with CD105+CD34- Phenotype Enhance the Function of Post-Infarction Heart in Mice. *PLoS One* 11, e0158745. doi:10.1371/journal.pone.0158745

Davidson, S. M., Foote, K., Kunuthur, S., Gosain, R., Tan, N., Tyser, R., et al. (2015). Inhibition of NAADP Signalling on Reperfusion Protects the Heart by Preventing Lethal Calcium Oscillations via Two-Pore Channel 1 and Opening of the Mitochondrial Permeability Transition Pore. *Cardiovasc. Res.* 108, 357–366. doi:10.1093/cvr/cvv226

Davis, L. C., Morgan, A. J., Chen, J.-L., Snead, C. M., Bloor-Young, D., Shenderov, E., et al. (2012). NAADP Activates Two-Pore Channels on T Cell Cytolytic Granules to Stimulate Exocytosis and Killing. *Curr. Biol.* 22, 2331–2337. doi:10.1016/j.cub.2012.10.035

Di Nezza, F., Zuccolo, E., Poletto, V., Rosti, V., De Luca, A., Moccia, F., et al. (2017). Liposomes as a Putative Tool to Investigate NAADP Signaling in Vasculogenesis. *J. Cel. Biochem.* 118, 3722–3729. doi:10.1002/jcb.26019

Diedrichs, F., Stolk, M., Jürchott, K., Haag, M., Sittinger, M., and Seifert, M. (2019). Enhanced Immunomodulation in Inflammatory Environments Favors Human Cardiac Mesenchymal Stromal-like Cells for Allogeneic Cell Therapies. *Front. Immunol.* 10, 1716. doi:10.3389/fimmu.2019.01716

Emrich, S. M., Yoast, R. E., and Trebak, M. (2021). Physiological Functions of CRAC Channels. *Annu. Rev. Physiol.* 84:355. doi:10.1146/annurev-physiol-052521-013426

Fameli, N., Evans, A. M., and Van Breemen, C. (2017). Tissue Specificity: The Role of Organellar Membrane Nanojunctions in Smooth Muscle Ca2+ Signaling. *Adv. Exp. Med. Biol.* 993, 321–342. doi:10.1007/978-3-319-57732-6_17

Fameli, N., Ogunbayo, O. A., Van Breemen, C., and Evans, A. M. (2014). Cytoplasmic Nanojunctions between Lysosomes and Sarcoplasmic

Reticulum Are Required for Specific Calcium Signaling. *F1000Res* 3, 93. doi:10.12688/f1000research.3720.1

Faris, P., Pellavio, G., Ferulli, F., Di Nezza, F., Shekha, M., Lim, D., et al. (2019). Nicotinic Acid Adenine Dinucleotide Phosphate (NAADP) Induces Intracellular Ca2+ Release through the Two-Pore Channel TPC1 in Metastatic Colorectal Cancer Cells. *Cancers (Basel)* 11. E542. doi:10.3390/cancers11040542

Faris, P., Shekha, M., Montagna, D., Guerra, G., and Moccia, F. (2018). Endolysosomal Ca(2+) Signalling and Cancer Hallmarks: Two-Pore Channels on the Move. TRPML1 Lags behind!. *Cancers (Base1)* 11, 27. doi:10.3390/cancers11010027

Favia, A., Desideri, M., Gambara, G., D'alessio, A., Ruas, M., Esposito, B., et al. (2014). VEGF-induced Neoangiogenesis Is Mediated by NAADP and Two-Pore Channel-2-dependent Ca2+ Signaling. *Proc. Natl. Acad. Sci.* 111, E4706–E4715. doi:10.1073/pnas.1406029111

Ferrera, L., Barbieri, R., Picco, C., Zuccolini, P., Remigante, A., Bertelli, S., et al. (2021). TRPM2 Oxidation Activates Two Distinct Potassium Channels in Melanoma Cells through Intracellular Calcium Increase. *Int. J. Mol. Sci.* 22. doi:10.3390/ijms22168359

Foreman, M. A., Smith, J., and Publicover, S. J. (2006). Characterisation of Serum-Induced Intracellular Ca2+ Oscillations in Primary Bone Marrow Stromal Cells. *J. Cel. Physiol.* 206, 664–671. doi:10.1002/jcp.20521

Forostyak, O., Forostyak, S., Kortus, S., Sykova, E., Verkhratsky, A., and Dayanithi, G. (2016). Physiology of Ca2+ Signalling in Stem Cells of Different Origins and Differentiation Stages. *Cell Calcium* 59, 57–66. doi:10.1016/j.ceca.2016.02.001

Galione, A. (2019). NAADP Receptors. *Cold Spring Harb Perspect. Biol.* 11. doi:10.1101/cshperspect.a035071

Galione, A. (2015). A Primer of NAADP-Mediated Ca2+ Signalling: From Sea Urchin Eggs to Mammalian Cells. *Cell Calcium* 58, 27–47. doi:10.1016/j.ceca.2014.09.010

Garrity, A. G., Wang, W., Collier, C. M., Levey, S. A., Gao, Q., and Xu, H. (2016). The Endoplasmic Reticulum, Not the pH Gradient, Drives Calcium Refilling of Lysosomes. *Elife* 5. doi:10.7554/eLife.15887

Gilchrist, C. L., Leddy, H. A., Kaye, L., Case, N. D., Rothenberg, K. E., Little, D., et al. (2019). TRPV4-mediated Calcium Signaling in Mesenchymal Stem Cells Regulates Aligned Collagen Matrix Formation and Vinculin Tension. *Proc. Natl. Acad. Sci. USA* 116, 1992–1997. doi:10.1073/pnas.1811095116

Gu, F., Krüger, A., Roggenkamp, H. G., Alpers, R., Lodygin, D., Jaquet, V., et al. (2021). Dual NADPH Oxidases DUOX1 and DUOX2 Synthesize NAADP and Are Necessary for Ca2+ Signaling during T Cell Activation. *Sci. Signal.* 14, eabe3800. doi:10.1126/scisignal.abe3800

Gunaratne, G. S., Brailoiu, E., He, S., Unterwald, E. M., Patel, S., Slama, J. T., et al. (2021). Essential Requirement for JPT2 in NAADP-Evoked Ca2+ Signaling. *Sci. Signal.* 14. doi:10.1126/scisignal.abd5605

Hu, R., He, M.-l., Hu, H., Yuan, B.-X., Zang, W.-J., Lau, C.-P., et al. (2009). Characterization of Calcium Signaling Pathways in Human Preadipocytes. *J. Cel. Physiol.* 220, 765–770. doi:10.1002/jcp.21823

Hu, W., Zhao, F., Chen, L., Ni, J., and Jiang, Y. (2021). NAADP-induced Intracellular Calcium Ion Is Mediated by the TPCs (Two-pore Channels) in Hypoxia-induced Pulmonary Arterial Hypertension. *J. Cel Mol Med* 25, 7485–7499. doi:10.1111/jcmm.16783

Jairaman, A., Yamashita, M., Schleimer, R. P., and Prakriya, M. (2015). Store-Operated Ca2+ Release-Activated Ca2+ Channels Regulate PAR2-Activated Ca2+ Signaling and Cytokine Production in Airway Epithelial Cells. *J.I.* 195, 2122–2133. doi:10.4049/jimmunol.1500396

Jiang, L.-H., Mousawi, F., Yang, X., and Roger, S. (2017). ATP-induced Ca2+-Signalling Mechanisms in the Regulation of Mesenchymal Stem Cell Migration. *Cell. Mol. Life Sci.* 74, 3697–3710. doi:10.1007/s00018-017-2545-6

Jiang, Y.-L., Lin, A. H. Y., Xia, Y., Lee, S., Paudel, O., Sun, H., et al. (2013). Nicotinic Acid Adenine Dinucleotide Phosphate (NAADP) Activates Global and Heterogeneous Local Ca2+ Signals from NAADP- and Ryanodine Receptor-Gated Ca2+ Stores in Pulmonary Arterial Myocytes. *J. Biol. Chem.* 288, 10381–10394. doi:10.1074/jbc.m112.423053

Jiang, Y., Zhou, Y., Peng, G., Tian, H., Pan, D., Liu, L., et al. (2018). Two-pore Channels Mediated Receptor-Operated Ca2+ Entry in Pulmonary Artery Smooth Muscle Cells in Response to Hypoxia. *Int. J. Biochem. Cel Biol.* 97, 28–35. doi:10.1016/j.biocel.2018.01.012

Jin, X., Zhang, Y., Alharbi, A., Hanbashi, A., Alhoshani, A., and Parrington, J. (2020). Targeting Two-Pore Channels: Current Progress and Future Challenges. *Trends Pharmacol. Sci.* 41, 582–594. doi:10.1016/j.tips.2020.06.002

Johnson, J. D., and Misler, S. (2002). Nicotinic Acid-Adenine Dinucleotide Phosphate-Sensitive Calcium Stores Initiate Insulin Signaling in Human Beta Cells. *Proc. Natl. Acad. Sci.* 99, 14566–14571. doi:10.1073/pnas.222099799

Jugdutt, B. I. (2003). Ventricular Remodeling after Infarction and the Extracellular Collagen Matrix. *Circulation* 108, 1395–1403. doi:10.1161/01.cir.0000085658.98621.49

Kakkar, R., and Lee, R. T. (2010). Intramyocardial Fibroblast Myocyte Communication. *Circ. Res.* 106, 47–57. doi:10.1161/circresaha.109.207456

Kawano, S., Otsu, K., Kuruma, A., Shoji, S., Yanagida, E., Muto, Y., et al. (2006). ATP Autocrine/paracrine Signaling Induces Calcium Oscillations and NFAT Activation in Human Mesenchymal Stem Cells. *Cell Calcium* 39, 313–324. doi:10.1016/j.ceca.2005.11.008

Kawano, S., Otsu, K., Shoji, S., Yamagata, K., and Hiraoka, M. (2003). Ca2+ Oscillations Regulated by Na+ -Ca2+ Exchanger and Plasma Membrane Ca2+ Pump Induce Fluctuations of Membrane Currents and Potentials in Human Mesenchymal Stem Cells. *Cell Calcium* 34, 145–156. doi:10.1016/s0143-4160(03)00069-1

Kawano, S., Shoji, S., Ichinose, S., Yamagata, K., Tagami, M., and Hiraoka, M. (2002). Characterization of Ca2+ Signaling Pathways in Human Mesenchymal Stem Cells. *Cell Calcium* 32, 165–174. doi:10.1016/s0143416002001240

Kilpatrick, B. S., Yates, E., Grimm, C., Schapira, A. H., and Patel, S. (2016). Endo-lysosomal TRP Mucolipin-1 Channels Trigger Global ER Ca2+ Release and Ca2+ Influx. *J. Cel Sci* 129, 3859–3867. doi:10.1242/jcs.190322

Kilpatrick, B. S., Eden, E. R., Schapira, A. H., Futter, C. E., and Patel, S. (2013). Direct Mobilisation of Lysosomal Ca2+ Triggers Complex Ca2+ Signals. *J. Cel Sci* 126, 60–66. doi:10.1242/jcs.118836

Kinnear, N. P., Boittin, F.-X., Thomas, J. M., Galione, A., and Evans, A. M. (2004). Lysosome-Sarcoplasmic Reticulum Junctions. *J. Biol. Chem.* 279, 54319–54326. doi:10.1074/jbc.m406132200

Kotova, P. D., Bystrova, M. F., Rogachevskaja, O. A., Khokhlov, A. A., Sysoeva, V. Y., Tkachuk, V. A., et al. (2018). Coupling of P2Y Receptors to Ca2+ Mobilization in Mesenchymal Stromal Cells from the Human Adipose Tissue. *Cell Calcium* 71, 1–14. doi:10.1016/j.ceca.2017.11.001

Lee, S. H., Park, Y., Song, M., Srikanth, S., Kim, S., Kang, M. K., et al. (2016). Orai1 Mediates Osteogenic Differentiation via BMP Signaling Pathway in Bone Marrow Mesenchymal Stem Cells. *Biochem. Biophysical Res. Commun.* 473, 1309–1314. doi:10.1016/j.bbrc.2016.04.068

Lee, S., Paudel, O., Jiang, Y., Yang, X.-R., and Sham, J. S. K. (2015). CD38 Mediates Angiotensin II-Induced Intracellular Ca2+Release in Rat Pulmonary Arterial Smooth Muscle Cells. *Am. J. Respir. Cel Mol Biol* 52, 332–341. doi:10.1165/rcmb.2014-0141oc

Lewis, A. M., Aley, P. K., Roomi, A., Thomas, J. M., Masgrau, R., Garnham, C., et al. (2012). SS-Adrenergic Receptor Signaling Increases NAADP and cADPR Levels in the Heart. *Biochem. Biophysical Res. Commun.* 427, 326–329. doi:10.1016/j.bbrc.2012.09.054

Li, J., Kanju, P., Patterson, M., Chew, W.-L., Cho, S.-H., Gilmour, I., et al. (2011). TRPV4-mediated Calcium Influx into Human Bronchial Epithelia upon Exposure to Diesel Exhaust Particles. *Environ. Health Perspect.* 119, 784–793. doi:10.1289/ehp.1002807

Macgregor, A., Yamasaki, M., Rakovic, S., Sanders, L., Parkesh, R., Churchill, G. C., et al. (2007). NAADP Controls Cross-Talk between Distinct Ca2+ Stores in the Heart. *J. Biol. Chem.* 282, 15302–15311. doi:10.1074/jbc.m611167200

Maione, A. S., Faris, P. S., Bisonni, L., Lodola, F., Casella, M., Catto, V., et al. (2020a). Imbalance of Calcium-dependent Mechanisms in Cardiac Mesenchymal Stromal Cells from Arrhythmogenic Cardiomyopathy Patients. *Vasc. Pharmacol.* 132, 106732. doi:10.1016/j.vph.2020.106732

Maione, A. S., Pilato, C. A., Casella, M., Gasperetti, A., Stadiotti, I., Pompilio, G., et al. (2020b). Fibrosis in Arrhythmogenic Cardiomyopathy: The Phantom Thread in the Fibro-Adipose Tissue. *Front. Physiol.* 11, 279. doi:10.3389/fphys.2020.00279

Maione, A. S., Stadiotti, I., Pilato, C. A., Perrucci, G. L., Saverio, V., Catto, V., et al. (2021). Excess TGF-Beta1 Drives Cardiac Mesenchymal Stromal Cells to a Pro-fibrotic Commitment in Arrhythmogenic Cardiomyopathy. *Int. J. Mol. Sci.* 22. doi:10.3390/ijms22052673

Moccia, F., Lodola, F., Stadiotti, I., Pilato, C. A., Bellin, M., Carugo, S., et al. (2019). Calcium as a Key Player in Arrhythmogenic Cardiomyopathy: Adhesion Disorder or Intracellular Alteration? *Int. J. Mol. Sci.* 20. doi:10.3390/ijms20163986

Moccia, F., Negri, S., Faris, P., Perna, A., De Luca, A., Soda, T., et al. (2021a). Targeting Endolysosomal Two-Pore Channels to Treat Cardiovascular Disorders in the Novel COronaVIrus Disease 2019. *Front. Physiol.* 12, 629119. doi:10.3389/fphys.2021.629119

Moccia, F., Nusco, G. A., Lim, D., Kyozuka, K., and Santella, L. (2006). NAADP and InsP3 Play Distinct Roles at Fertilization in Starfish Oocytes. *Develop. Biol.* 294, 24–38. doi:10.1016/j.ydbio.2006.02.011

Moccia, F., Ruffinatti, F., and Zuccolo, E. (2015). Intracellular Ca2+ Signals to Reconstruct A Broken Heart: Still A Theoretical Approach? *Cdt* 16, 793–815. doi:10.2174/1389450116666141219121723

Moccia, F., Zuccolo, E., Di Nezza, F., Pellavio, G., Faris, P. S., Negri, S., et al. (2021b). Nicotinic Acid Adenine Dinucleotide Phosphate Activates Two-pore Channel TPC1 to Mediate Lysosomal Ca2+ Release in Endothelial colony-forming Cells. *J. Cel Physiol* 236, 688–705. doi:10.1002/jcp.29896

Moccia, F., Zuccolo, E., Poletto, V., Turin, I., Guerra, G., Pedrazzoli, P., et al. (2016). Targeting Stim and Orai Proteins as an Alternative Approach in Anticancer Therapy. *Cmc* 23, 3450–3480. doi:10.2174/0929867323666160607111220

Morgan, A. J., and Galione, A. (2021). Lysosomal Agents Inhibit Store-Operated Ca2+ Entry. *J. Cel Sci* 134. doi:10.1242/jcs.248658

Morgan, A. J., Platt, F. M., Lloyd-Evans, E., and Galione, A. (2011). Molecular Mechanisms of Endolysosomal Ca2+ Signalling in Health and Disease. *Biochem. J.* 439, 349–378. doi:10.1042/bj20110949

Morgan, A. J., Yuan, Y., Patel, S., and Galione, A. (2020). Does Lysosomal Rupture Evoke Ca2+ Release? A Question of Pores and Stores. *Cell Calcium* 86, 102139. doi:10.1016/j.ceca.2019.102139

Murakami, T., Ockinger, J., Yu, J., Byles, V., Mccoll, A., Hofer, A. M., et al. (2012). Critical Role for Calcium Mobilization in Activation of the NLRP3 Inflammasome. *Proc. Natl. Acad. Sci.* 109, 11282–11287. doi:10.1073/pnas.1117765109

Nebel, M., Schwoerer, A. P., Warszta, D., Siebrands, C. C., Limbrock, A.-C., Swarbrick, J. M., et al. (2013). Nicotinic Acid Adenine Dinucleotide Phosphate (NAADP)-mediated Calcium Signaling and Arrhythmias in the Heart Evoked by β-Adrenergic Stimulation. *J. Biol. Chem.* 288, 16017–16030. doi:10.1074/jbc.m112.441246

Negri, S., Faris, P., Maniezzi, C., Pellavio, G., Spaiardi, P., Botta, L., et al. (2021a). NMDA Receptors Elicit Flux-independent Intracellular Ca2+ Signals via Metabotropic Glutamate Receptors and Flux-dependent Nitric Oxide Release in Human Brain Microvascular Endothelial Cells. *Cell Calcium* 99, 102454. doi:10.1016/j.ceca.2021.102454

Negri, S., Faris, P., and Moccia, F. (2021b). Endolysosomal Ca2+ Signaling in Cardiovascular Health and Disease. *Int. Rev. Cel Mol Biol* 363, 203–269. doi:10.1016/bs.ircmb.2021.03.001

Negri, S., Faris, P., Pellavio, G., Botta, L., Orgiu, M., Forcaia, G., et al. (2020). Group 1 Metabotropic Glutamate Receptors Trigger Glutamate-Induced Intracellular Ca2+ Signals and Nitric Oxide Release in Human Brain Microvascular Endothelial Cells. *Cel. Mol. Life Sci.* 77, 2235–2253. doi:10.1007/s00018-019-03284-1

Pandey, V., Chuang, C.-C., Lewis, A. M., Aley, P. K., Brailoiu, E., Dun, N. J., et al. (2009). Recruitment of NAADP-Sensitive Acidic Ca2+ Stores by Glutamate. *Biochem. J.* 422, 503–512. doi:10.1042/bj20090194

Parekh, A. B., and Putney, J. W., Jr. (2005). Store-operated Calcium Channels. *Physiol. Rev.* 85, 757–810. doi:10.1152/physrev.00057.2003

Patel, S. (2015). Function and Dysfunction of Two-Pore Channels. *Sci. Signal.* 8, re7. doi:10.1126/scisignal.aab3314

Peng, H., Hao, Y., Mousawi, F., Roger, S., Li, J., Sim, J. A., et al. (2016). Purinergic and Store-Operated Ca2+ Signaling Mechanisms in Mesenchymal Stem Cells and Their Roles in ATP-Induced Stimulation of Cell Migration. *Stem Cells* 34, 2102–2114. doi:10.1002/stem.2370

Penny, C. J., Kilpatrick, B. S., Han, J. M., Sneyd, J., and Patel, S. (2014). A Computational Model of Lysosome-ER Ca2+ Microdomains. *J. Cel Sci* 127, 2934–2943. doi:10.1242/jcs.149047

Pereira, G. J. S., Hirata, H., Do Carmo, L. G., Stilhano, R. S., Ureshino, R. P., Medaglia, N. C., et al. (2014). NAADP-sensitive Two-Pore Channels Are Present and Functional in Gastric Smooth Muscle Cells. *Cell Calcium* 56, 51–58. doi:10.1016/j.ceca.2014.04.005

Pilato, C. A., Stadiotti, I., Maione, A. S., Saverio, V., Catto, V., Tundo, F., et al. (2018). Isolation and Characterization of Cardiac Mesenchymal Stromal Cells from Endomyocardial Bioptic Samples of Arrhythmogenic Cardiomyopathy Patients. *J. Vis. Exp.* 132, e57263. doi:10.3791/57263

Pitt, S. J., Reilly-O'donnell, B., and Sitsapesan, R. (2016). Exploring the Biophysical Evidence that Mammalian Two-Pore Channels Are NAADP-Activated Calcium-Permeable Channels. *J. Physiol.* 594, 4171–4179. doi:10.1113/jp270936

Prakriya, M., and Lewis, R. S. (2015). Store-Operated Calcium Channels. *Physiol. Rev.* 95, 1383–1436. doi:10.1152/physrev.00020.2014

Rahman, S., and Rahman, T. (2017). Unveiling Some FDA-Approved Drugs as Inhibitors of the Store-Operated Ca2+ Entry Pathway. *Sci. Rep.* 7, 12881. doi:10.1038/s41598-017-13343-x

Remigante, A., Zuccolini, P., Barbieri, R., Ferrera, L., Morabito, R., Gavazzo, P., et al. (2021). NS-11021 Modulates Cancer-Associated Processes Independently of BK Channels in Melanoma and Pancreatic Duct Adenocarcinoma Cell Lines. *Cancers (Basel)* 13. doi:10.3390/cancers13236144

Ronco, V., Potenza, D. M., Denti, F., Vullo, S., Gagliano, G., Tognolina, M., et al. (2015). A Novel Ca2+-Mediated Cross-Talk between Endoplasmic Reticulum and Acidic Organelles: Implications for NAADP-dependent Ca2+ Signalling. *Cell Calcium* 57, 89–100. doi:10.1016/j.ceca.2015.01.001

Ruas, M., Rietdorf, K., Arredouani, A., Davis, L. C., Lloyd-Evans, E., Koegel, H., et al. (2010). Purified TPC Isoforms Form NAADP Receptors with Distinct Roles for Ca2+ Signaling and Endolysosomal Trafficking. *Curr. Biol.* 20, 703–709. doi:10.1016/j.cub.2010.02.049

Sakurai, Y., Kolokoltsov, A. A., Chen, C.-C., Tidwell, M. W., Bauta, W. E., Klugbauer, N., et al. (2015). Two-pore Channels Control Ebola Virus Host Cell Entry and Are Drug Targets for Disease Treatment. *Science* 347, 995–998. doi:10.1126/science.1258758

Sánchez-Hernández, Y., Laforenza, U., Bonetti, E., Fontana, J., Dragoni, S., Russo, M., et al. (2010). Store-Operated Ca2+ Entry Is Expressed in Human Endothelial Progenitor Cells. *Stem Cell Develop.* 19, 1967–1981. doi:10.1089/scd.2010.0047

Scarpellino, G., Genova, T., Avanzato, D., Bernardini, M., Bianco, S., Petrillo, S., et al. (2019). Purinergic Calcium Signals in Tumor-Derived Endothelium. *Cancers (Basel)*. 11, 766. doi:10.3390/cancers11060766

Schach, C., Wester, M., Leibl, F., Redel, A., Gruber, M., Maier, L. S., et al. (2020). Reduced Store-operated Ca2+ Entry Impairs Mesenteric Artery Function in Response to High External Glucose in Type 2 Diabetic ZDF Rats. *Clin. Exp. Pharmacol. Physiol.* 47, 1145–1157. doi:10.1111/1440-1681.13300

Schleifer, H., Doleschal, B., Lichtenegger, M., Oppenrieder, R., Derler, I., Frischauf, I., et al. (2012). Novel Pyrazole Compounds for Pharmacological Discrimination between Receptor-operated and Store-operated Ca2+ Entry Pathways. *Br. J. Pharmacol.* 167, 1712–1722. doi:10.1111/j.1476-5381.2012.02126.x

Sommariva, E., Brambilla, S., Carbucicchio, C., Gambini, E., Meraviglia, V., Dello Russo, A., et al. (2016). Cardiac Mesenchymal Stromal Cells Are a Source of Adipocytes in Arrhythmogenic Cardiomyopathy. *Eur. Heart J.* 37, 1835–1846. doi:10.1093/eurheartj/ehv579

Stadiotti, I., Catto, V., Casella, M., Tondo, C., Pompilio, G., and Sommariva, E. (2017). Arrhythmogenic Cardiomyopathy: the Guilty Party in Adipogenesis. *J. Cardiovasc. Trans. Res.* 10, 446–454. doi:10.1007/s12265-017-9767-8

Tao, R., Sun, H.-Y., Lau, C.-P., Tse, H.-F., Lee, H.-C., and Li, G.-R. (2011). Cyclic ADP Ribose Is a Novel Regulator of Intracellular Ca2+ Oscillations in Human Bone Marrow Mesenchymal Stem Cells. *J. Cel Mol Med* 15, 2684–2696. doi:10.1111/j.1582-4934.2011.01263.x

Trufanov, S. K., Rybakova, E. Y., Avdonin, P. P., Tsitrina, A. A., Zharkikh, I. L., Goncharov, N. V., et al. (2019). The Role of Two-Pore Channels in Norepinephrine-Induced [Ca(2+)]i Rise in Rat Aortic Smooth Muscle Cells and Aorta Contraction. *Cells* 8. 1144. doi:10.3390/cells8101144

Vassileva, K., Marsh, M., and Patel, S. (2020). Two-pore Channels as Master Regulators of Membrane Trafficking and Endocytic Well-Being. *Curr. Opin. Physiol.* 17, 163–168. doi:10.1016/j.cophys.2020.08.002

Vismara, M., Zarà, M., Negri, S., Canino, J., Canobbio, I., Barbieri, S. S., et al. (2021). Platelet-derived Extracellular Vesicles Regulate Cell Cycle Progression

and Cell Migration in Breast Cancer Cells. *Biochim. Biophys. Acta (Bba) - Mol. Cel Res.* 1868, 118886. doi:10.1016/j.bbamcr.2020.118886

Yamazaki, D., Ohya, S., Asai, K., and Imaizumi, Y. (2007). Characteristics of the ATP-Induced Ca2+-Entry Pathway in the T-BBEC 117 Cell Line Derived from Bovine Brain Endothelial Cells. *J. Pharmacol. Sci.* 104, 103–107. doi:10.1254/jphs.sc0070080

Yuan, Y., Kilpatrick, B. S., Gerndt, S., Bracher, F., Grimm, C., Schapira, A. H., et al. (2021). The Lysosomotrope GPN Mobilises Ca2+ from Acidic Organelles. *J. Cel Sci* 134. doi:10.1242/jcs.256578

Zhang, J., Guan, X., Shah, K., and Yan, J. (2021). Lsm12 Is an NAADP Receptor and a Two-Pore Channel Regulatory Protein Required for Calcium Mobilization from Acidic Organelles. *Nat. Commun.* 12, 4739. doi:10.1038/s41467-021-24735-z

Zuccolini, P., Ferrera, L., Remigante, A., Picco, C., Barbieri, R., Bertelli, S., et al. (2022). The VRAC Blocker DCPIB Directly gates the BK Channels and Increases Intracellular Ca(2+) in Melanoma and Pancreatic Duct Adenocarcinoma (PDAC) Cell Lines. *Br. J. Pharmacol.*, 1–18. doi:10.1111/bph.15810

Zuccolo, E., Di Buduo, C., Lodola, F., Orecchioni, S., Scarpellino, G., Kheder, D. A., et al. (2018a). Stromal Cell-Derived Factor-1α Promotes Endothelial Colony-Forming Cell Migration through the Ca2+-dependent Activation of the Extracellular Signal-Regulated Kinase 1/2 and Phosphoinositide 3-Kinase/AKT Pathways. *Stem Cell Develop.* 27, 23–34. doi:10.1089/scd.2017.0114

Zuccolo, E., Kheder, D. A., Lim, D., Perna, A., Nezza, F. D., Botta, L., et al. (2019). Glutamate Triggers Intracellular Ca2+ Oscillations and Nitric Oxide Release by Inducing NAADP- and InsP 3 -dependent Ca2+ Release in Mouse Brain Endothelial Cells. *J. Cel Physiol* 234, 3538–3554. doi:10.1002/jcp.26953

Zuccolo, E., Laforenza, U., Ferulli, F., Pellavio, G., Scarpellino, G., Tanzi, M., et al. (2018b). Stim and Orai Mediate Constitutive Ca2+ Entry and Control Endoplasmic Reticulum Ca2+ Refilling in Primary Cultures of Colorectal Carcinoma Cells. *Oncotarget* 9, 31098–31119. doi:10.18632/oncotarget.25785

Zuccolo, E., Lim, D., Kheder, D. A., Perna, A., Catarsi, P., Botta, L., et al. (2017). Acetylcholine Induces Intracellular Ca2+ Oscillations and Nitric Oxide Release in Mouse Brain Endothelial Cells. *Cell Calcium* 66, 33–47. doi:10.1016/j.ceca.2017.06.003

Conflict of Interest: The authors declare that the research was conducted in the absence of any commercial or financial relationships that could be construed as a potential conflict of interest.

Publisher's Note: All claims expressed in this article are solely those of the authors and do not necessarily represent those of their affiliated organizations, or those of the publisher, the editors and the reviewers. Any product that may be evaluated in this article, or claim that may be made by its manufacturer, is not guaranteed or endorsed by the publisher.

frontiers | Frontiers in Cell and Developmental Biology

ORIGINAL RESEARCH
published: 04 April 2022
doi: 10.3389/fcell.2022.861644

Dysregulated Erythroid Mg^{2+} Efflux in Type 2 Diabetes

Ana Ferreira[1†], *Alicia Rivera*[2*†], *Jay G. Wohlgemuth*[3], *Jeffrey S. Dlott*[3], *L. Michael Snyder*[3], *Seth L. Alper*[2] *and Jose R. Romero*[4]

[1]Interdisciplinary Centre of Social Sciences (CICS.NOVA), Faculty of Social Sciences and Humanities (NOVA FCSH), Lisbon, Portugal, [2]Department of Medicine, Beth Israel Deaconess Medical Center and Harvard Medical School, Boston, MA, United States, [3]Quest Diagnostics, Secaucus, NJ, United States, [4]Division of Endocrinology, Diabetes and Hypertension, Department of Medicine, Brigham and Women's Hospital and Harvard Medical School, Boston, MA, United States

Hyperglycemia is associated with decreased Mg^{2+} content in red blood cells (RBC), but mechanisms remain unclear. We characterized the regulation of Mg^{2+} efflux by glucose in *ex vivo* human RBC. We observed that hemoglobin A_{1C} (HbA_{1C}) values correlated with Na^+-dependent Mg^{2+} efflux (Na^+/Mg^{2+} exchange) and inversely correlated with cellular Mg content. Treatment of cells with 50 mM D-glucose, but not with sorbitol, lowered total cellular Mg (2.2 ± 0.1 to 2.0 ± 0.1 mM, $p < 0.01$) and enhanced Na^+/Mg^{2+} exchange activity [0.60 ± 0.09 to 1.12 ± 0.09 mmol/10^{13} cell × h (flux units, FU), $p < 0.05$]. In contrast, incubation with selective Src family kinase inhibitors PP2 or SU6656 reduced glucose-stimulated exchange activation ($p < 0.01$). Na^+/Mg^{2+} exchange activity was also higher in RBC from individuals with type 2 diabetes (T2D, 1.19 ± 0.13 FU) than from non-diabetic individuals (0.58 ± 0.05 FU, $p < 0.01$). Increased Na^+/Mg^{2+} exchange activity in RBC from T2D subjects was associated with lower intracellular Mg content. Similarly increased exchange activity was evident in RBC from the diabetic *db/db* mouse model as compared to its non-diabetic control ($p < 0.03$). Extracellular exposure of intact RBC from T2D subjects to recombinant peptidyl-N-glycosidase F (PNGase F) reduced Na^+/Mg^{2+} exchange activity from 0.98 ± 0.14 to 0.59 ± 0.13 FU ($p < 0.05$) and increased baseline intracellular Mg content (1.8 ± 0.1 mM) to normal values (2.1 ± 0.1 mM, $p < 0.05$). These data suggest that the reduced RBC Mg content of T2D RBC reflects enhanced RBC Na^+/Mg^{2+} exchange subject to regulation by Src family kinases and by the N-glycosylation state of one or more membrane proteins. The data extend our understanding of dysregulated RBC Mg^{2+} homeostasis in T2D.

Keywords: red blood cells, ion transporter, ion flux, ion exchange, diabetes mellitus, cell magnesium

OPEN ACCESS

Edited by:
Silvia Dossena,
Paracelsus Medical University, Austria

Reviewed by:
Angela Marino,
University of Messina, Italy
Francesca Di Sole,
Des Moines University, United States

****Correspondence:***
Alicia Rivera
Arivera3@bidmc.harvard.edu

[†]These authors have contributed equally to this work

Specialty section:
This article was submitted to Cellular Biochemistry, a section of the journal Frontiers in Cell and Developmental Biology

Received: *24 January 2022*
Accepted: *09 March 2022*
Published: *04 April 2022*

Citation:
Ferreira A, Rivera A, Wohlgemuth JG, Dlott JS, Snyder LM, Alper SL and Romero JR (2022) Dysregulated Erythroid Mg^{2+} Efflux in Type 2 Diabetes. Front. Cell Dev. Biol. 10:861644. doi: 10.3389/fcell.2022.861644

INTRODUCTION

Cellular Mg^{2+} levels play a fundamental role in many critical processes, including regulation of cellular ionic composition, enzymatic activity, cell volume and initiation of protein synthesis (Raftos et al., 1999; Rubin, 2005; Vidair and Rubin, 2005). Small variations in cellular or serum Mg content or Mg^{2+} have been associated with various pathological conditions such as diabetes, hypertension, sickle cell anemia and cancer (Sartori et al., 1992; Resnick et al., 1993a; Picado et al., 1994; Barbagallo et al., 1996; Dewitte et al., 2004; Maltezos et al., 2004; Zehtabchi et al., 2004). Mammalian cells maintain cellular Mg^{2+} levels within a narrow range by the combined action of ion transporters and cellular Mg^{2+} buffering capacity. ATP, 2,3-bisphosphoglycerate, cellular phosphoproteins (including

phosphorylation-regulated protein kinases and phosphatases themselves) and other nucleic acids (including polynucleic acids) constitute the major cellular Mg^{2+} buffers (Laing et al., 1994; Raftos et al., 1999; Chiu and Dickerson, 2000; Waas and Dalby, 2003). Cellular Mg^{2+} transport encompasses both influx of extracellular Mg^{2+}, attributed to TRPM6/7 channels and (more controversially) to CNNM and MagT1 transporters (Nadler et al., 2001; Runnels et al., 2001; Monteilh-Zoller et al., 2003; Schmitz et al., 2003; Voets et al., 2004; Goytain and Quamme, 2008; Giménez-Mascarell et al., 2019), and efflux of intracellular Mg^{2+}, mediated by both Na^+-dependent and Na^+-independent mechanisms (Féray and Garay, 1986; Ferreira et al., 2004). Na^+-dependent Mg^{2+} efflux (Na^+/Mg^{2+} exchange) has been functionally described in various cell types including human RBC (Féray and Garay, 1986; Murphy et al., 1991; Günther and Vormann, 1992; Romani et al., 1993; Wolf et al., 1997; Touyz and Schiffrin, 1999a; Touyz et al., 2001; Standley and Standley, 2002; Ferreira et al., 2004). We and others have shown that Mg^{2+} transport across the RBC plasma membrane is regulated by insulin, norepinephrine, angiotensin II, and vasopressin through activation of Na^+/Mg^{2+} exchange (Romani et al., 1993; Touyz and Schiffrin, 1999b; Cefaratti and Romani, 2003; Ferreira et al., 2004; He et al., 2005; Rubin, 2005). The *SLC41A1* gene has been proposed to encode the erythroid Na^+/Mg^{2+} exchanger polypeptide (Schweigel et al., 2000; Sahni et al., 2007; Kolisek et al., 2008; Kolisek et al., 2012), a hypothesis strengthened by the demonstration that SLC41A3 mediates mitochondrial Na^+/Mg^{2+} exchange (Mastrototaro et al., 2016). However, more a more recent report has failed to detect extracellular Na^+-dependence of SLC41A1-mediated Mg^{2+} transport (Arjona et al., 2019).

Type 2 diabetes (T2D) affects nearly 500 million people worldwide, with a rapidly rising annual toll exceeding four million deaths (Palomino-Schätzlein et al., 2020). The multiple pathophysiological effects of hyperglycemia are not completely explained by glucose-induced changes in cellular energy stores or in red cell (Morabito et al., 2020) and mononuclear cell oxidative stress (Fortuño et al., 2006). In particular, the relationship between divalent cation metabolism and the pathogenesis and complications of hyperglycemic, often insulin-resistant conditions such as T2D is not fully understood. The hypomagnesemia observed in up to half of people with T2D (Gommers et al., 2016), as well as in many children with insulin-dependent diabetes (Rohn et al., 1993), has been traditionally attributed to urinary magnesium wasting secondary to the osmotic diuresis accompanying diabetic glycosuria (Gommers et al., 2016). In contrast, elevated glucose concentrations have been shown to lower RBC Mg content through as yet undefined mechanisms (Paolisso et al., 1986; Resnick et al., 1993b; John, 1997; Rodríguez-Morán et al., 2011; Chan et al., 2015). Serum glucose concentrations are associated with low Mg^{2+} levels in both serum and RBC (Resnick et al., 1993b; Guerrero-Romero and Rodríguez-Morán, 2002; Rodríguez-Morán and Guerrero-Romero, 2003). The mechanisms by which glucose induces reduction in cellular Mg content and contributes to development of diabetic complication are not completely understood. Elevated serum glucose levels lead to glycation of circulating and of membrane-bound proteins. Indeed, glycated HbA_{1c} is an excellent clinical marker of glycemic status over time (John, 1997; Pani et al., 2008). HbA_{1c} in T2D subjects is higher than in control subjects and negatively correlates with Mg levels in plasma, platelets, mononuclear cells, and muscle cells (Allegra et al., 1997).

We now present evidence that glucose modulates erythrocyte Mg levels by stimulating Mg^{2+} efflux through activation of Na^+/Mg^{2+} exchange in *ex vivo* RBC from humans with type 2 diabetes (T2D) and otherwise healthy individuals, as well as in a rodent model of T2D. We also show that RBC from T2D subjects have lower cellular Mg content and increased baseline Na^+/Mg^{2+} exchange activity as compared to cells from normal control subjects. Treatment of RBC from T2D subjects with extracellular N-glycosidase increased cellular Mg content and decreased Na^+/Mg^{2+} exchange activity to non-diabetic control levels. Thus, our results suggest that RBC protein glycation adducts and protein N-glycans directly or indirectly modulate Na^+/Mg^{2+} exchanger activity, contributing to dysregulation of Mg^{2+} homeostasis in T2D.

EXPERIMENTAL PROCEDURES

Materials: A23187, bovine serum albumin (BSA, fraction V), choline chloride (Choline Cl), PP2 and SU6656 were purchased from Calbiochem (San Diego, CA). Wortmannin (WT) was from Alexis Corp. (San Diego, CA). Dimethyl sulfoxide (DMSO) was from Fisher Scientific (Pittsburgh, PA). Acationox was from Baxter Scientific Products (McGaw Park, IL). All other reagents were purchased from Sigma Aldrich (St. Louis, MO).

Isolation of Red Cells: Human blood samples were obtained between 7:00 a.m. and 10:00 a.m. after overnight fast (>6 h) per approved clinical protocol and processed within 3 h of receipt, as previously described (Ferreira et al., 2004; Rivera et al., 2005). Briefly, freshly isolated blood was passed through cotton and eluted with choline wash solution (CWS-Mg free, containing (in mM) 150 choline chloride, 10 Tris MOPS pH 7.4 at 4°C) to remove the buffy coat (>85% of white blood cells and platelets). The red cells were washed 4× at 4°C with CWS-Mg free kept on ice until use. Hematological parameters were measured by ADVIA hemoanalyzer (Bayer, Terrytown, NY). Glycated hemoglobin (HbA_{1c}) was measured by Hitachi 917 autoanalyzer (Manheim/Boehringer). Total intracellular contents of Na, K, and Mg were measured by atomic absorption spectrophotometry (Perkin Elmer 800). To avoid changes in mean cellular volumes (MCV), mouse blood was prepared as specified for human RBC, but in solutions adjusted to the osmolarity of normal mouse plasma (330 mOsm).

Cellular Mg^{2+} efflux measurements: Cells were loaded with Mg^{2+} as we previously described (Ferreira et al., 2004; Rivera et al., 2005). Cells at 10% hematocrit were incubated with 6 μM Ca^{2+}/Mg^{2+} ionophore A23187 in Mg^{2+}-loading solution (MLS) containing (in mM) 140 KCl, 12 $MgCl_2$, 10 D-glucose, and 10 Tris MOPS (pH 7.4) for 30 min at 37°C. To obtain a range of different intracellular Mg concentrations in **Figure 5B**, MLS solutions contained 0–16 mM $MgCl_2$ concentrations between 0 and

16 mM, with corresponding KCl concentrations between 138 and 158 mM. A23187 was subsequently removed with four washes of 25 volumes of 0.1% BSA in MLS at 37°C at 15 min intervals. Mg^{2+}-loaded cells at 3% hematocrit were incubated at 37°C for periods of 5 or 45 min in NaCl or choline choline chloride flux media containing (in mM) 140 NaCl or 140 choline Cl, 10 D-glucose, 10 Tris MOPS (pH 7.4), 20 sucrose, 0.1 ouabain, and 0.01 bumetanide. Mg^{2+} efflux was calculated from the slope of linear regression analyses of Mg content (expressed as calculated concentration) in supernatant vs. time (5 and 45 min in triplicate determinations). Na^+/Mg^{2+} exchange activity was calculated as the difference between Mg^{2+} efflux in NaCl and in choline Cl flux media. Flux values were corrected for changes in mean corpuscular volume (MCV) and expressed as $mmol/10^{13}$ cells × h (flux units, FU), as previously described (Ferreira et al., 2004; Rivera et al., 2005). Mouse RBC assay osmolytes were adjusted to reflect the normal mouse plasma osmolarity of ~330 mOsm, to minimize cell volume changes and hemolysis during Mg^{2+} loading (Rivera et al., 2005).

Glucose-induced Mg^{2+} efflux: RBC were incubated up to 24 h at 37°C in isotonic saline solution containing (in mM): 140 NaCl, 0–100 D-glucose, 10 Tris MOPS (pH 7.4), 0–20 sucrose, 0.1 ouabain, and 0.01 bumetanide, with the indicated concentrations of D-glucose or sorbitol. Incubated RBC were centrifuged 5 min at 2,500 rpm at 37°C and suspended in Mg^{2+}-free choline wash solution as previously described (Acosta et al., 2000). Previous investigation (Viskupicova et al., 2015) revealed that 1 h exposure of RBC to >45 mM glucose at 37°C does not increase hemolysis, eryptosis or GSSG/GSH ratio (Viskupicova et al., 2015). Moreover, lipid peroxidation, superoxide production and intracellular (Ca^{2+}) remain unchanged under these conditions. We observed no hemolysis after 24 h incubation of RBC in the presence of 50 mM glucose. We noted trace hemolysis after 24 h incubation in the presence of 100 mM glucose, but no further hemolysis was evident in RBC after resuspension in flux medium. Aliquots of 50% suspension were taken for measurements of Mg^{2+} efflux and total cellular contents of Mg, K, and Na as described above. We also studied the effects of Peptidyl-N-Glycosidase F (PNGase F), an amidase that cleaves the GlcNAc-asparagine linkage of high mannose and complex oligosaccharides of N-linked glycoproteins (Maley et al., 1986). Intact RBC were incubated with 0.1 U/ml PNGase F (New England BioLabs, Ipswich, MA) for 1.5 h at 37°C in isotonic saline solution, then centrifuged 5 min at 2,500 rpm at 37°C and resuspended in Mg^{2+}-free choline wash solution as described (Tarentino and Plummer, 1994). Timed aliquots of 50% suspension were taken for measurement of total RBC Mg, K, and Na.

Study subjects: The study protocol was approved by the Institutional Review Board of the Brigham and Women's Hospital (Protocol #: 2003P001861). Normal (n = 33) and T2D individuals (n = 30) were recruited at the Brigham and Women's Hospital. Informed written consent was obtained from all subjects before participation. T2D was diagnosed according to accepted guidelines (National Diabetes Data Group: Classification and diagnosis of diabetes mellitus and other categories of glucose intolerance, 1979). Diabetic participants were not being treated with antihypertensive or any other medication except for medication related to their diabetes. Not all subjects were studied in all analyses, and subjects were not matched for clinical characteristics. Subjects varied in age between 22 and 62, with body mass index (BMI) <31 kg/m^2 for women or <33 kg/m^2 for men. Diabetic and control groups did not differ significantly in age.

db/db Mice: All mouse studies were conducted under protocols approved by the Institutional Animal Care and Use Committee of Brigham and Women's Hospital. *db/db* mice (The Jackson Laboratory; Bar Harbor, Maine; Catalog #000642) and heterozygote controls (Catalog #000662) were purchased at 6 weeks of age, fed *ad libitum* with rodent chow (LabDiet #5053; Richmond, IN) and water, then sacrificed and venisected by intracardiac puncture at 25 weeks of age. *db/db* mice are homozygous for a spontaneous mutation of the leptin receptor ($Lepr^{db}$) leading to unrestrained weight gain and eventual development of obesity-associated diabetes. *db/db* but not *db/+* mice exhibit hyperglycemia as early as 8 weeks of age and have been used to model human T2D (Shafrir and Sima, 2001; Joost and Schürmann, 2014). Although not measured in these experimental mouse groups, blood glucose levels in mice of the same age (25 weeks) from the same supplier and maintained in the same animal facility had blood glucose levels of 159 ± 21 mg/dl (*db/+*) and 769 ± 41 mg/dl (*db/db*) (Guo et al., 2008).

Statistical Analyses: The data are reported as means ± standard error of the mean (SEM), with statistical significance (p value as indicated) determined by non-parametric analysis t-test unless otherwise stated. The kinetic parameters of Na^+/Mg^{2+} exchange activation were analyzed with GraphPad Prism version 8.0.0 for Windows (GraphPad Software, San Diego, California United States). Pearson and Spearman coefficients of correlation were estimated using SPSS 10.0 software (SPSS, Chicago, IL).

RESULTS

Glycated Hemoglobin (HbA_{1C}) Correlates With Cellular Mg^{2+} and Na^+/Mg^{2+} Exchange Activity

We hypothesized that RBC membrane protein glycation (or another consequence of chronic hyperglycemia) may alter Mg^{2+} homeostasis. To investigate the relationship between glycemic status and red cell Mg^{2+} homeostasis, we examined the correlation between HbA_{1c} and erythrocyte Mg^{2+} levels in normal red cells. We observed a negative correlation between baseline levels of total cellular Mg^{2+} content and HbA_{1C} levels (Pearson r = −0.600, $p < 0.01$; Spearman σ = −0.491 and $p < 0.05$, n = 23) (**Figure 1A**). These results suggest a relationship between RBC glycation state and increased Mg^{2+} loss from RBC.

Cellular Mg^{2+} transport across the plasma membrane is mediated by Na^+-dependent and Na^+-independent mechanisms. We and others have shown that Na^+-dependent Mg^{2+} efflux (Na^+/Mg^{2+} exchange activity) contributes to RBC

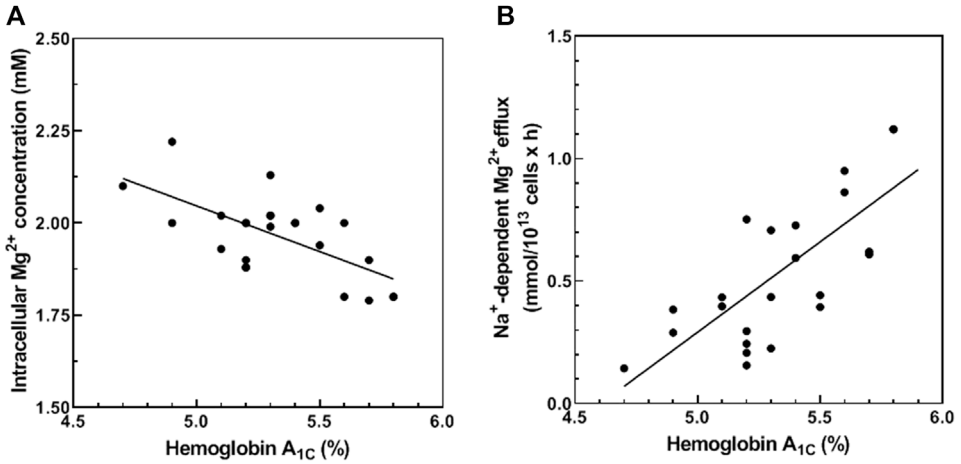

FIGURE 1 | Correlation between HbA_{1C} and total cellular Mg^{2+} content **(A)** and Na^+-dependent Mg^{2+} efflux. **(A)** Cells from 23 normal subjects were assayed for hemoglobin A_{1C} (HbA_{1C}) and total cellular Mg^{2+} content as described in Methods. The graph represents total cellular Mg^{2+} content vs. HbA_{1C} ($n = 23$, r = –0.600 and $p < 0.01$; $\sigma = -0.491$ and $p < 0.05$). **(B)** Cells from 23 normal subjects were assayed for HbA_{1C} and Na^+-dependent Mg^{2+} efflux (Na^+/Mg^{2+} exchanger activity) as described in Methods. The graph represents Na^+/Mg^{2+} exchanger activity vs. HbA_{1C} ($n = 23$, $p < 0.001$ and r = 0.716 and $p < 0.001$; $\sigma = 695$ and $p < 0.001$).

Mg^{2+} homeostasis (Féray and Garay, 1986; Touyz et al., 2001; Ferreira et al., 2004). In this study, we measured HbA_{1C} levels and Na^+/Mg^{2+} exchange activity in RBC from normal subjects. Normal RBC revealed a positive correlation between HbA_{1C} and Na^+/Mg^{2+} exchange activity (Pearson r = 0.716, $p < 0.001$; Spearman $\sigma = 0.695$, $p < 0.001$, $n = 23$) (**Figure 1B**). These results are consistent with a regulatory mechanism linking Mg^{2+} homeostasis and cell glycemic status. In contrast, HbA_{1C} levels correlated poorly with Na^+-independent Mg^{2+} efflux activity of normal RBC (Pearson r = 0.142, $p = 0.270$; Spearman $\sigma = 0.225$, $p = 0.163$, $n = 23$, data not shown). These data suggest that reduced Mg content of RBC in hyperglycemic individuals reflects, at least in part, modulation of Na^+/Mg^{2+} exchange activity.

Effect of Glucose on Red Blood Cells Mg^{2+} Levels and Na^+/Mg^{2+} Exchanger Activity *In Vitro*

To study the mechanisms involved in RBC Mg^{2+} regulation by high glycemic status, we assayed Na^+/Mg^{2+} exchange activity as a function of extracellular glucose concentration from 0 to 100 mM, as described in Methods. RBC exposure to up to 100 mM glucose for 24 h at 37°C is known not to increase hemolysis, eryptosis, or concentrations of HbA_{1C} or intracellular Ca^{2+} (Viskupicova et al., 2015). We observed that Mg^{2+}-loaded RBC exhibited a glucose concentration-dependent increase in Na^+/Mg^{2+} exchange activity (**Figure 2A**). Kinetic analyses of the hyperbolic curve (r = 0.998) indicated a maximal velocity (V_{max}) of 0.978 ± 0.01 mmol/10^{13} cell × h and EC_{50} of 18.1 ± 3.0 mM, representing a ~50% increase over basal exchange activity in the presence of 100 mM glucose. In contrast, Na^+-independent Mg^{2+} efflux was unaffected by changing extracellular glucose concentration (r = 0.620, data not shown). These results show that exposure of erythrocytes to high glucose media will modify cellular Mg^{2+} homeostasis.

To characterize the glucose-mediated activation of Na^+/Mg^{2+} exchange, we monitored time-dependent changes in exchange activity. RBC stimulated by 50 mM D-glucose were examined for Na^+/Mg^{2+} exchange activity at 0.5, 1.5, 4, 12, and 24 h. Significant change in Na^+/Mg^{2+} exchange activity was detected after 1.5 h, with peak response observed as early as 4 h (**Figure 2B**). We also measured Na^+/Mg^{2+} exchange activity at baseline conditions in Mg^{2+}-unloaded RBC after 4 h exposure to either 6 mM or 50 mM D-glucose. RBC incubation with 50 mM glucose increased Na^+/Mg^{2+} exchange activity from 0.006 ± 0.003 to 0.013 ± 0.005 mmol/10^{13} cells × h ($n = 3$, $p < 0.05$). Thus, high glucose stimulates Na^+/Mg^{2+} exchange activity in both Mg^{2+}-loaded and -unloaded cells.

We hypothesized that altering the glycation state of RBC surface proteins may change intracellular Mg^{2+} homeostasis. Protein glycation rate in RBC is time- and glucose concentration-dependent (Watala, 1988). At high glucose concentration, most membrane protein glycation occurs within 12 h (Watala, 1988). To examine whether glycation status would affect the exchanger activity, we first examined the effects on Na^+/Mg^{2+} exchange activity of the non-glycating sugar, sorbitol (Yan et al., 2003), and compared its effects to those of glucose. RBC were incubated with physiological concentrations of either D-glucose (6 mM), high D-glucose (50 mM) or 50 mM sorbitol for 24 h at 37°C. As previously observed, exchange activity was higher in RBC incubated with 50 mM D-glucose than in RBC incubated either at the physiological glucose level of 6 mM or in 50 mM sorbitol ($n = 3$, $p < 0.05$) (**Figure 2C**). These results are consistent with the possibility that RBC membrane glycation state alters Na^+/Mg^{2+} exchange activity. We also observed a significant decrease in total cell Mg content in RBC incubated with 50 mM glucose (1.55 ± 0.02 mM) as compared to cells incubated with 6 mM glucose (1.75 ± 0.03 mM, $n = 3$, $p < 0.01$). In contrast,

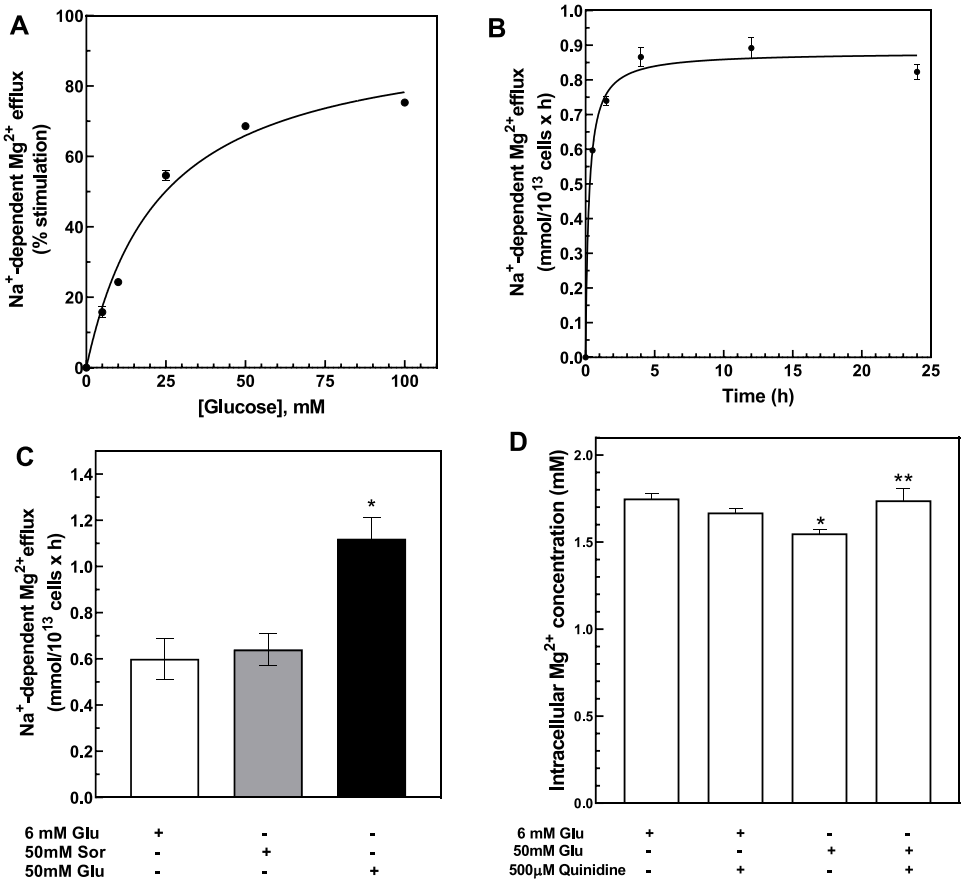

FIGURE 2 | Activation of Na^+-dependent Mg^{2+} efflux by glucose. **(A)** Glucose dose-dependent activation of Na^+-dependent Mg^{2+} efflux. Cells from normal subjects were incubated with 0–100 mM D-glucose for 24 h and assayed for Na^+-dependent Mg^{2+} efflux or Na^+/Mg^{2+} exchanger activity. Hyperbolic pattern curve best fit was used to derive V_{max} = 0.978 ± 0.01 FU, K_m = 3.2 ± 0.5 mM. Plot shows % of stimulation over 0 glucose present. Values are expressed as means ± SE of three experiments in triplicate determinations (r = 0.998). Plot shows % of stimulation over 0 glucose present. **(B)** Time course of glucose-dependent activation of the Na^+/Mg^{2+} exchanger. Cells from normal subjects were incubated with 50 mM D-glucose for 0–24 h and assayed for Na^+/Mg^{2+} exchanger activity as described in Methods. Hyperbolic pattern curve best fit was used to derive V_{max} = 0.98 ± 0.01 FU, reaching half-activity in 1.6 ± 0.0 h (r = 0.90). Values are expressed as means ± SEM of three experiments in triplicate determinations. **(C)** Activation of Na^+/Mg^{2+} exchanger by glucose but not sorbitol. Cells from normal subjects were incubated with 6 or 50 mM D-glucose or 50 mM sorbitol solutions for 24 h and assayed for Na^+/Mg^{2+} exchanger activity as described in Methods. Values represent the activity of the exchanger and are expressed as means ± SEM. (* paired non-parametric *t* test, $p < 0.005$, $n = 3$). **(D)** Effect of quinidine on glucose-induced cellular Mg^{2+} levels. Cells from normal subjects were incubated with 6 or 50 mM glucose and in the presence or absence of 500 µM quinidine for 1.5 h and assayed for total cellular Mg^{2+} content as described in Methods. Results are expressed as means ± SEM of four experiment in triplicates. (* unpaired non-parametric t test 6 vs. 50 mM glucose $p < 0.05$; ** paired non-parametric t test 50 mM glucose vs. 50 mM glucose plus 500 µM quinidine $p < 0.04$).

incubation of cells with 50 mM sorbitol failed to alter RBC Mg levels (1.8 ± 0.02 mM, $n = 3$, data not shown). These observations suggest that the possibility that increased RBC surface glycation might stimulate Na^+/Mg^{2+} exchange.

We and others have reported that quinidine inhibits red cell Na^+/Mg^{2+} exchange (Féray and Garay, 1986; Murphy et al., 1991; Günther and Vormann, 1992; Picado et al., 1994; Touyz and Schiffrin, 1999a; Touyz et al., 2001; Günther, 2006). We tested the effect of quinidine on glucose-induced loss of intracellular Mg from RBC. Quinidine (500 microM) prevented the intracellular loss of Mg^{2+} induced by 50 mM D-glucose (**Figure 2D**). These observations are consistent with a role for Na^+/Mg^{2+} exchange in mediating glucose-induced Mg^{2+} loss from RBC.

TABLE 1 | Hematological values of normal and diabetic subjects.

	Normal	Diabetic	*p* value
N	20	16	—
MCV, %	91.7 ± 1.3	94.3 ± 1.0	0.700
MCHC, g/dL	32.7 ± 0.4	32.4 ± 0.4	0.700
Reticulocytes, %	1.9 ± 0.1	1.6 ± 0.2	0.522
RDW	14.1 ± 0.2	14.0 ± 0.3	0.621
Na^+, mM	8.3 ± 0.8	6.9 ± 0.6	0.538
K^+, mM	84.3 ± 3.4	86.2 ± 2.6	0.700
Mg^{2+}, mM	2.3 ± 0.1	2.0 ± 0.1	<0.001

Mean cellular volume (MCV); mean corpuscular hemoglobin concentration (MCHC); red cell density width (RDW); total cellular Na^+; K^+ and Mg^{2+} were determined as described in Methods. p *values were determined by unpaired Mann-Whitney test.*

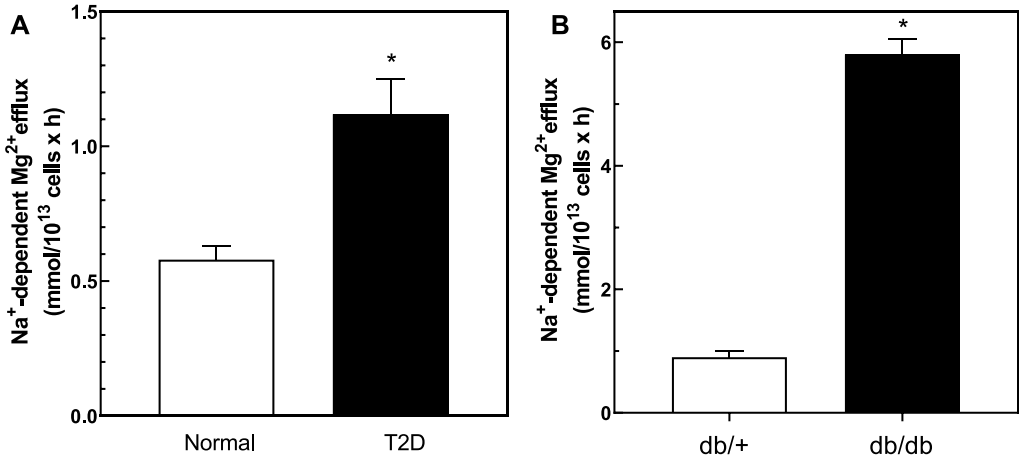

FIGURE 3 | Baseline Na^+/Mg^{2+} exchanger activity in cells from normal and type 2 diabetic human subjects and db/db and db/+ mice. Cells were used to determine the activity of the Na^+/Mg^{2+} exchanger as described in Methods. **(A)** Na^+/Mg^{2+} exchanger activity in cells from normal and T2D human subjects (n = 33 and n = 30 in normal and diabetic subjects, respectively; * unpaired t test, $p < 0.001$). **(B)** Na^+/Mg^{2+} exchanger activity in red cells from diabetic db/db and non-diabetic db/+ mice (n = 3); * unpaired t test nonparametric, $p < 0.01$). Results are expressed as means ± SEM of three experiments in triplicate determinations.

Cellular Mg^{2+} Regulation in Red Blood Cells From Type 2 Diabetic Subjects

Our model predicts that RBC from T2D subjects should exhibit increased Na^+/Mg^{2+} exchange activity. We first examined various red cell parameters in freshly isolated RBC from otherwise healthy normal and T2D subjects. We found no significant differences in total cellular Na and K content, mean corpuscular volume (MCV) or mean corpuscular hemoglobin concentration (MCHC). However, total cellular Mg^{2+} levels were significantly lower in RBC from T2D subjects than in those from control subjects (**Table 1**), as previously reported (Djurhuus et al., 1995; Eibl et al., 1995; Vidair and Rubin, 2005).

We measured Na^+/Mg^{2+} exchange activity in T2D and control RBC. We found that Na^+/Mg^{2+} exchange activity was higher in T2D RBC (1.19 ± 0.13 FU; n = 33) than in RBC from normal subjects (0.58 ± 0.05 FU; n = 30, p = 0.0011) (**Figure 3A**). In contrast, Na^+-independent Mg^{2+} efflux from T2D RBC (3.57 ± 0.53 FU; n = 30) did not differ statistically from that of normal RBC (2.51 ± 0.37 FU, n = 30; means ± SEM). These data are consistent with a major role for Na^+/Mg^{2+} exchange in Mg^{2+} loss from T2D RBC. Furthermore, exposure to quinidine (500 μM) decreased Na^+/Mg^{2+} exchange activity in RBC from T2D subjects by 0.44 ± 0.06 FU (n = 3) but only by 0.18 ± 0.07 FU (n = 4) in normal RBC (data not shown).

We also examined cellular Mg^{2+} levels and exchanger activity in *ex vivo* RBC from *db/db* mice, a well-described model of T2D, and in RBC from non-diabetic *db/+* mice (**Figure 3B**). Consistent with our observations in T2D subjects, RBC from 25 weeks old *db/db* mice exhibited lower cellular Mg^{2+} content (2.3 ± 0.2 mmol/kg Hb) than RBC of *db/+* control mice of similar age (4.4 ± 0.5, n = 3; $p < 0.03$). *db/db* diabetic mouse RBC also exhibited higher rates of Na^+/Mg^{2+} exchange activity than did RBC of nondiabetic *db/+* mice (**Figure 3B**).

Src-Kinase Inhibitors Regulate Glucose-Stimulated Na^+/Mg^{2+} Exchanger Activity

Hyperglycemia increases Src family tyrosine kinase activity that in turn increases production of reactive oxygen species (Schaeffer et al., 2003). To evaluate the role of Src kinases on Na^+/Mg^{2+} exchanger activity, normal RBC were treated with either 6 or 50 mM glucose in the presence or absence of the Src inhibitor, PP2 (**Figure 4A**). Incubation with PP2 did not alter Na^+/Mg^{2+} exchanger activity in the absence of glucose, but blocked the glucose-induced increase of exchanger activity. Similar results were observed in normal RBC using a structurally dissimilar Src inhibitor, SU6656 (300 nM) (n = 3, $p < 0.01$), and known "off-target" effects of SU6656 (Gao et al., 2013; Ross et al., 2017) and PP2 (Brandvold et al., 2012) do not overlap among red cell kinases or those of other cells. We also tested the effects of Src inhibitors in RBC from T2D subjects, under similar conditions. PP2 inhibited exchanger activity in T2D RBC stimulated either by 6 or 50 mM D-glucose (**Figure 4B**), suggesting that a Src kinase-regulated pathway mediates the glucose-induced increase in RBC Na^+/Mg^{2+} exchange activity.

Na^+/Mg^{2+} Exchange Activity as a Function of Extracellular Na^+ and Intracellular Mg^{2+}

We previously reported that V_{max} of Na^+/Mg^{2+} exchange activity in RBC from patients with sickle cell disease (HbSS) was higher than in cells from subjects with normal hemoglobin A expression (HbAA) (Rivera et al., 2005) due in part to changes in extracellular Na^+ affinity and not through changes in intracellular Mg^{2+} affinity. These results suggested possible cooperativity of extracellular Na^+ binding to the exchanger at basal state. To investigate whether similar mechanisms might apply to Na^+/Mg^{2+} exchange in T2D RBC, we assayed Na^+/Mg^{2+}

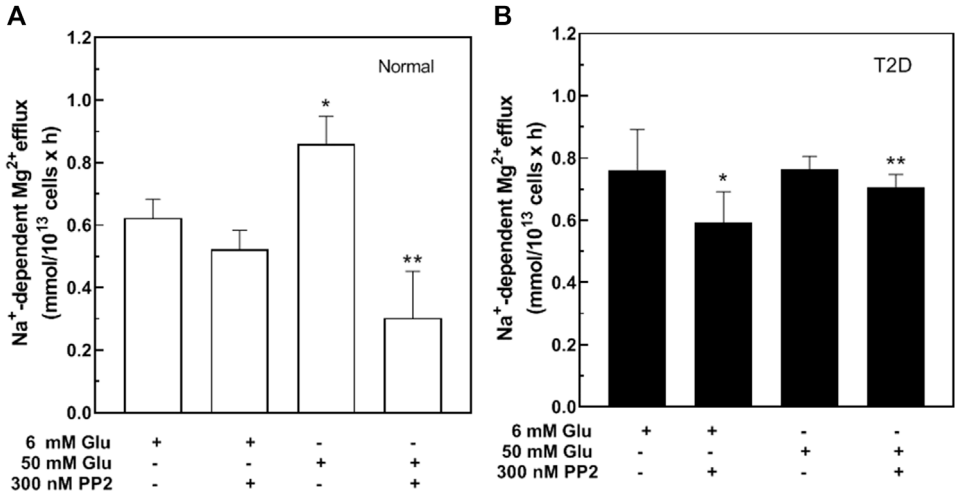

FIGURE 4 | Effect of Src inhibitors on Na^+/Mg^{2+} exchanger activity in cells from type 2 diabetic subjects. Cells were incubated in glucose solutions of 6 mM (106 mg/dl) or 50 mM (900 mg/dl), in the presence or absence of 300 nM PP2 as indicated, then assayed for Na^+/Mg^{2+} exchanger activity. **(A)** Values represent exchanger activity in cells from normal subjects and are expressed as means ± SEM of three experiments in triplicate determinations. Non-parametric paired t test, $*p < 0.003$ $**p < 0.002$ from basal activity of the exchanger; **(B)** Values represent exchanger activity in cells from diabetic subjects and are expressed as means ± SEM of three experiments in triplicates. Non-parametric paired t test $*p < 0.05$, $**p < 0.05$ from basal activity.

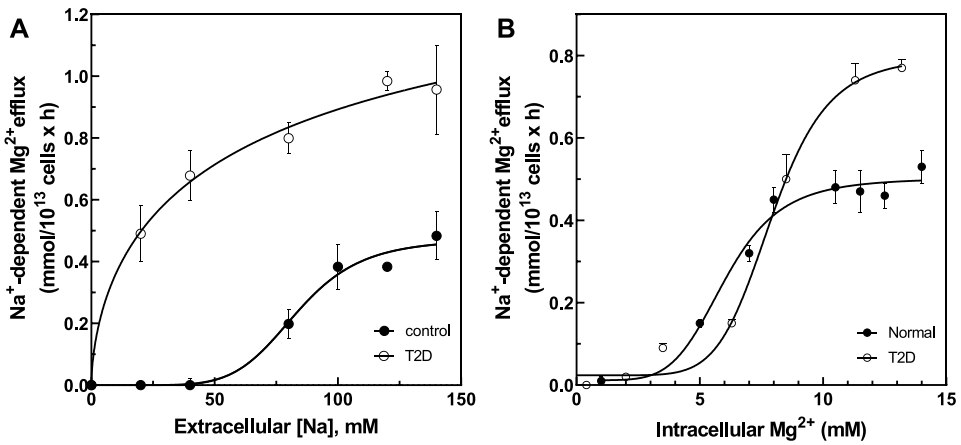

FIGURE 5 | Activation of Na^+/Mg^{2+} exchanger by extracellular Na^+ and intracellular Mg^{2+} in cells from normal and type 2 diabetic subjects. **(A)** Activation of Na^+/Mg^{2+} exchanger by extracellular Na^+ in normal (closed circles, $V_{max} = 0.472 \pm 0.01$ FU, hill = 6.4 ± 0.13, $K_{1/2} = 83.5$ mM, $n = 3$) and diabetic subjects (open circles, $V_{max} = 1.16 \pm 0.05$ FU, $K_m = 28.9 \pm$ mM, $n = 3$). **(B)** Activation of Na^+/Mg^{2+} exchanger by intracellular Mg^{2+} in normal (closed circles, $V_{max} = 0.50 \pm 0.02$ mmol/10^{13} cell × h, hill = 5.1 ± 0.1, $K_{1/2} = 5.97 \pm 0.2$ mM, $n = 3$) and diabetic subjects (open circles, $V_{max} = 0.81 \pm 0.032$ FU, hill = 6.3 ± 0.2, $K_{1/2} = 7.87 \pm 0.39$ mM, $n = 3$). Values represent the activity of the Na^+/Mg^{2+} exchanger and are expressed as means ± SEM of $n = 3$ in triplicates determinations.

exchange activity in RBC from normal and T2D subjects as a function of extracellular (Na^+) (**Figure 5A**). In T2D RBC the plot of exchange activity vs. extracellular (Na^+) was best fit by a hyperbolic Michaelis-Menten curve (r = 0.995) exhibiting a K_m of 28.9 ± 2.4 mM for external Na^+ and a V_{max} of 1.16 ± 0.05 FU ($n = 3$, r = 0.99). In contrast, the Na^+ -dependence of Na^+/Mg^{2+} exchange activity in normal RBC was best fit by a sigmoidal curve (n = 3, r = 0.99) with an affinity constant for external Na^+ of 83.5 ± 4 mM ($p < 0.0001$ vs. T2D) and a V_{max} of 0.472 ± 0.01 FU, ($p < 0.0001$ vs. T2D), with Hill coefficient (n) of 6.4 ± 0.13. These results suggest that increased Na^+/Mg^{2+} exchanger activity in T2D subjects may reflect increased affinity at extracellular Na^+ binding sites possibly attributable to chronic exposure to high glucose.

The affinity for intracellular Mg^{2+} was also examined (**Figure 5B**). Cells were Mg-loaded to estimated intracellular concentrations between ~0 and ~14 mM (**Figure 5B**). Increasing intracellular Mg^{2+} stimulated exchanger activity in a sigmoidal pattern in RBC of both normal (r = 0.993) and T2D subjects (r = 0.996). RBC from normal subjects exhibited an affinity constant for intracellular Mg^{2+} of 5.97 ± 0.2 mM with Hill coefficient of 5.1 ± 0.1, as compared to an affinity constant of

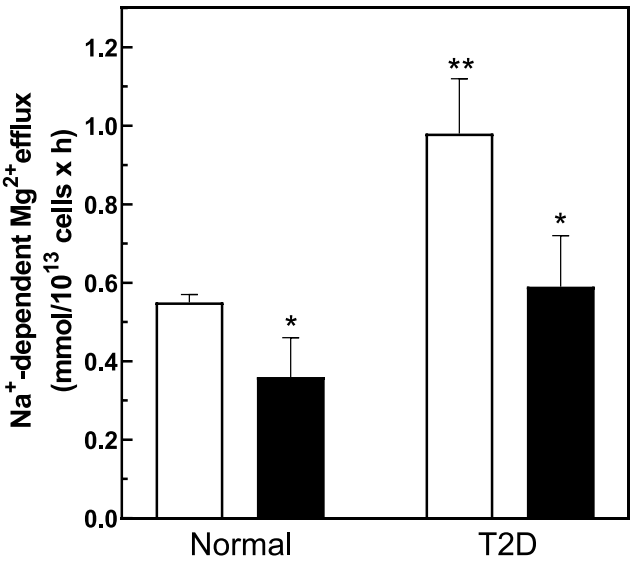

FIGURE 6 | Regulation of the Na^+/Mg^{2+} exchanger activity by PNGase treatment. Cells from normal and diabetic subjects were pre-incubated in the absence (white bar) or presence (black bars) of 0.1 U/mL PNGase F for 1.5 h and assayed for Na^+/Mg^{2+} exchanger activity as described in *Methods*. Values are expressed as means ± SEM of three and five experiments in triplicate determinations in normal and diabetic subjects, respectively. Non-parametric paired *t* test of control vs. de-glycation in both normal (*$p < 0.03$) and diabetic subjects (*$p < 0.001$). Unpaired t test nonparametric of control in normal vs. control in diabetic subjects (**$p < 0.0001$).

7.87 ± 0.39 mM (n.s.) with Hill coefficient of 6.3 ± 0.2 in T2D red cells (both $n = 3$). V_{max} in RBC from T2D subjects was 0.81 ± 0.032 FU vs. 0.50 ± 0.02 FU in RBC from normal subjects ($p = 0.003$). Since the affinity constants for intracellular Mg^{2+} were statistically indistinguishable in T2D and normal RBC, we propose that changes in external Na^+ binding affinity and V_{max} drive increased Na^+/Mg^{2+} exchange activity in T2D RBC.

Regulation of Mg^{2+} Levels and Na^+/Mg^{2+} Exchanger Activity *In Vitro* by Pre-Treatment With PNGase F

To investigate if changes in cell surface N-linked protein glycosylation state might regulate Na^+/Mg^{2+} exchange activity, we incubated intact RBC with peptidyl-N-Glycosidase F (PNGase F) to remove accessible N-linked glycans from RBC surface proteins (Watala, 1988; Tarentino and Plummer, 1994). PNGase F is an amidase that cleaves N-linked glycoproteins between the innermost GlcNAc and asparagine residues. In T-cells, pre-treatment with PNGase F *in vitro* reduced N-glycan content of cell surface proteins (Cabral et al., 2017) without significant loss of T cell regulatory function. To investigate if surface protein N-glycosylation contributes to Na^+/Mg^{2+} exchange activity, we preincubated RBC with PNGase F following similar experimental protocols. We found that 1 h pretreatment of intact RBC from T2D subjects with PNGase F significantly reduced Mg^{2+} efflux to values comparable to those of normal RBC (**Figure 6**). This reduced Na^+/Mg^{2+} exchange activity was also associated with a significant increase in cellular Mg content ($n = 5$, $p < 0.05$, **Table 2**). In RBC from healthy subjects, we further observed a decrease in Na^+/Mg^{2+} exchanger activity in RBC from healthy subjects following PNGase F pretreatment of the intact cells, similarly associated with changes in intracellular Mg^{2+} ($n = 3$, $p < 0.05$, **Table 2**). These results are consistent with the possibility that ecto-N-glycosylation state of the Na^+/Mg^{2+} exchanger polypeptide at the cell surface, or of an interacting regulatory protein, contributes to maintenance of erythrocyte Mg^{2+} homeostasis.

To assess reversibility of the effects of N-deglycosylation on Na^+/Mg^{2+} exchange activity, we measured high glucose-induced Na^+/Mg^{2+} exchange activity following PNGase F treatment. Interestingly, exposure of erythrocytes to high concentration of

TABLE 2 | Total cellular Mg^{2+} content in PNGase-treated red cells.

	Untreated cells	PNGase-treated cells	*p* values
Normal ($n = 3$)	2.0 ± 0.1	2.1 ± 0.06	<0.034
Diabetic ($n = 5$)	1.8 ± 0.1	2.1 ± 0.1	<0.031

Erythrocytes from normal and diabetic subjects were pre-incubated with with the N-glycanase (PNGase F), as described in Methods, and analyzed for total cellular Mg^{2+} as indicated. Values represent the means of triplicate determinations of three independent experiments. Mg^{2+} levels are expressed as mmol/Kg Hb. p *values were determined by paired Wilcoxon text.*

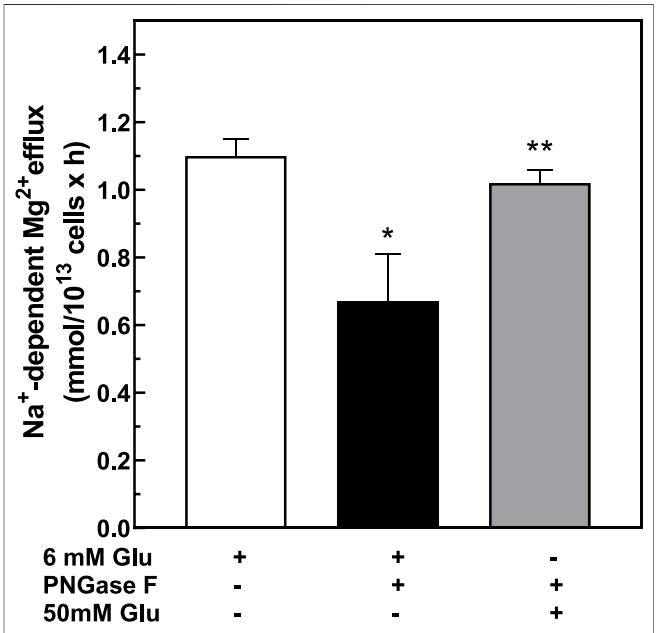

FIGURE 7 | Effect of PNGase-treatment on glucose-stimulated exchanger activity. Cells from T2D subjects were treated with 6 mM glucose or 50 mM glucose for 1.5 h after pre-treatment with 0.1 U/mL PNGase F and assayed for Na^+/Mg^{2+} exchanger activity as described in Methods. Values are expressed as means ± SEM of three experiments in triplicate determinations. * Non-parametric paired *t* test between 6 mM glucose (white bar) vs. PNGase-treated (black bar): *$p < 0.002$. Non-parametric paired t test between PNGase-treated vs. PNGase- and 50 mM glucose-treated (gray bar),**$p < 0.05$.

glucose after PNGase F treatment restored the higher levels of Na^+/Mg^{2+} exchange to pre-PNGase levels (**Figure 7**). The reversibility of PNGase-F-induced inhibition of Na^+/Mg^{2+} exchange by high extracellular glucose suggests that the stimulation of red cell Na^+/Mg^{2+} exchange by high glucose, reflecting either red cell protein glycation or another effect of glucose, can override the inhibitory effect of protein ecto-N-deglycosylation on Na^+/Mg^{2+} exchange. Thus, both RBC protein glycation state and RBC surface protein N-glycosylation state may contribute to RBC Mg^{2+} homeostasis through regulation of RBC Na^+/Mg^{2+} exchange.

DISCUSSION

We hypothesized that glucose modulates intracellular ionic composition of RBC, and that dysregulated ion metabolism characterizes the pathophysiology of T2D. We report our observation that HbA_{1c} levels correlate directly with Na^+/Mg^{2+} exchange activity and inversely with intracellular Mg levels in RBC from healthy subjects. The dysregulated erythroid Mg^{2+} homeostasis in T2D reflects enhanced glucose-regulated Na^+/Mg^{2+} exchange activity. These findings suggest that hemoglobin glycation state predicts intracellular Mg levels controlled by regulation of Mg^{2+} efflux pathways in RBC, and complement previous observations of the inverse association between RBC Mg levels and fasting blood glucose (Resnick et al., 1993b; Barbagallo et al., 1996; Barbagallo et al., 2001). Na^+/Mg^{2+} exchange thus joins the K_{ATP} channel, the L-type Ca^{2+} channel and GLUT4 of the pancreatic beta cell, K channel Kir4.1 of retina, and (*via* insulin) TRPM6 and the thiazide receptor NCC of kidney (Gommers et al., 2016) as a Mg^{2+}-regulated ion transport pathway.

The regulation by glucose of Na^+/Mg^{2+} exchange activity could in principle reflect the hyperglycemia-associated hypomagnesemia of diabetes, which has been attributed to diabetic glycosuria. Indeed, acute glucose infusion can promote magnesuria, and the SGLT2 knockout mouse exhibits hypermagnesemia. However, SGLT2 inhibitors used to treat T2DM do not promote magnesuria, but rather had been observed to lead to hypermagnesemia (Tang et al., 2016).

We also report pharmacological evidence that glucose-stimulated activation of Na^+/Mg^{2+} exchange requires Src family tyrosine kinase activity. Inhibition of Src family tyrosine kinase activity was sufficient to attenuate the increased Na^+/Mg^{2+} exchange activity or T2D RBC. Src tyrosine kinase functions in part as downstream signaling molecule for receptors without intrinsic kinase activity (Parsons and Parsons, 1997). While the mechanism by which RBC Src tyrosine kinase regulates Na^+/Mg^{2+} exchange remains to be determined, Src kinase and caveolin are known together to contribute to activation of the receptor for advanced glycation end-products (RAGE) in vascular tissues (Reddy et al., 2006). RAGE mediates inflammatory and white blood cell migration-associated signals associated with vascular complications of hyperglycemia (Igarashi et al., 1999; Schmidt, 2015; Hudson and Lippman, 2018). Thus, the Src family of tyrosine kinases may be potential targets for development of new therapeutic strategies to ameliorate glucose-mediated complications associated with T2D.

Nonenzymatic glycation affects not only hemoglobin, but extends to proteins of the RBC surface (Miller et al., 1980). Red cell glycation status has been correlated with cellular survival and with rheology that is modifiable by control of glycemic status (Peterson et al., 1977). Hyperglycemia has also been associated with decreased red cell membrane fluidity (Watala, 1988). However, a direct relationship between red cell surface glycation status and transport protein function remains to be established. Nonetheless, exposure to extracellular glucose modulates activities of the Na^+ pump (Garner et al., 1990; Umudum et al., 2002; Nandhini and Anuradha, 2003), Ca^{2+} pump (González Flecha et al., 1993), Na^+/H^+ exchanger (Williams and Howard, 1994), GLUT1 (Nandhini and Anuradha, 2003), as well as the non-erythroid Na^+/Glucose cotransporter of epithelia (Han et al., 2005). We have extended these studies to demonstrate that glucose regulates erythroid Mg^{2+} levels by modulating Na^+/Mg^{2+} exchange activity. Consistent with a role for deregulated cation metabolism in the pathogenesis of T2D, we found reduced cellular Mg^{2+} levels and increased Na^+/Mg^{2+} exchanger activity in *ex vivo* RBC from T2D subjects as compared to cells from otherwise healthy subjects. *ex vivo* RBC from *db/db* mice showed Mg^{2+} transport abnormalities resembling those of RBC from T2D subjects. Exposure of RBC to extracellular glucose abolished apparent cooperativity in the extracellular Na^+ -dependence of Na^+/Mg^{2+} exchange activity, accompanied by reduction in $K_{1/2}$ for extracellular Na^+ from 83 to 29 mM. This change may reflect a noncovalent effect of glucose or a direct or indirect effect of non-enzymatic glycation at or near the putative extracellular Na^+ binding site of the Na^+/Mg^{2+} exchanger, or of residues in one or more of the exchanger's hypothesized regulatory proteins.

Covalent reaction of the open form of glucose with proteins leads to protein glycation (Rabbani and Thornalley, 2012) occurs predominantly on N-terminal α-amino groups and ε-amino groups of Lys residues, as well as on side chains of Arg and Cys residues. Early glycation proceeds sequentially through glycosylamine formation and dehydration to Schiff bases in a process requiring hours. Subsequent Amadori rearrangement to fructosamine or non-Amadori rearrangement to α-oxo-aldehydes, both of which can then more slowly degrade over weeks *in vitro* (Valencia et al., 2004) to multiple advanced glycation end-products (AGEs). Protein susceptibility to glycation and the gradually increasing burden of protein glycation in circulation and in cells likely contributes to pathogenesis of hyperglycemic disorders (McAvan et al., 2020).

SLC41A1 has been often (Sponder et al., 2013), if controversially (Sahni and Scharenberg, 2013), modeled as 10 transmembrane spans with intracellular N- and C-termini. In this model, SLC41A1 has four ecto-Lys residues in two putative extracellular loops and multiple ecto-Arg residues in each of the five predicted extracellular loops, any of which might serve as glycation targets. As glucose-induced activation of Na^+/Mg^{2+} exchange occurs within 1.5 h, the observed effects of extracellular glucose on RBC Na^+/Mg^{2+} exchange activity do not likely reflect the action of AGE formation of binding to their receptors (RAGEs). The time- and concentration-dependence of Na^+/Mg^{2+} exchange activation by extracellular

glucose, is consistent with those previously reported by Watala et al. for red cell membrane glycation (Watala, 1988). Also consistent with our results, impaired Mg^{2+} uptake and homeostasis characterizes the streptozotocin-induced rat model of type 1 diabetes (T1D) (Cefaratti and Romani, 2003). Hepatic plasmalemmal vesicles from streptozotocin-treated rats, exhibited >2-fold higher rates of Na^+-dependent Mg^{2+} efflux than those from untreated rats (Cefaratti et al., 2004; Fagan et al., 2004). These data together demonstrate that hyperglycemia, as observed in T2D and in a model of T1D, induces changes in Mg^{2+} transport.

We found that RBC pre-treatment with extracellular PNGase F restores Na^+/Mg^{2+} exchange activity to normal levels, reversing its elevation by high glucose levels. PNGase F exposure at 37°C for 1 h has been used to partially remove surface N-linked glycans from intact T regulatory cells without compromising cellular function (Cabral et al., 2017). We showed that PNGase F treatment of RBC from T2D subjects increased glucose-mediated intracellular Mg levels and decreased Na^+/Mg^{2+} exchanger activity, suggesting that enzymatic removal of RBC surface protein-linked N-glycans can regulate Mg^{2+} homeostasis in T2D RBC. The 10-transmembrane span model of SLC41A1 predicts a single consensus site for ecto-N-linked glycosylation, but neither mutational nor enzymatic evidence for this site has yet been presented. Thus, the functionally important RBC surface polypeptide substrate(s) for extracellular PNGase regulation of erythroid Na^+/Mg^{2+} exchange remain to be defined.

Enhanced glycation of RBC and endothelial surface proteins can enhance vascular dysfunction, suggesting that attenuation of protein glycation might delay development of vascular complications in T2D. Our results suggest that RBC surface glycation and N-glycan state of the Na^+/Mg^{2+} exchange protein or of one or more interacting regulatory protein(s) can regulate intracellular Mg^{2+} and Mg^{2+} homeostasis in T2D RBC. Additional work is needed to identify the glycated and glycosylated proteins responsible for Na^+/Mg^{2+} exchange activation in RBC of T2D subjects. Also remaining to be investigated is the possible effect on Na^+/Mg^{2+} exchange of the recently reported deposition of amylin aggregates in or on T2D red cells (Verma et al., 2020). As regulation of RBC Mg^{2+} transport may have parallels in endothelial and vascular smooth muscle cells, we speculate that identification and modulation of Mg-regulatory glycation and N-deglycosylation targets may have therapeutic potential in treatment of the vascular complications of T2D.

DATA AVAILABILITY STATEMENT

The original contributions presented in the study are included in the article/Supplementary Material, further inquiries can be directed to the corresponding author.

ETHICS STATEMENT

The studies involving human participants were reviewed and approved by the Committee on Clinical Investigations, Brigham and Women's Hospital. Written informed consent for participation was not required for this study in accordance with the national legislation and the institutional requirements. The animal study was reviewed and approved by the Institutional Animal Care and Use Committee, Brigham and Women's Hospital.

AUTHOR CONTRIBUTIONS

AF performed and analyzed experiments and drafted manuscript. AR conceived, performed, analyzed and supervised experiments and drafted and revised manuscript. JW critiqued draft. JD critiqued draft. LS critiqued draft. SA drafted and revised manuscript. JR conceived and supervised experiments, and revised manuscript.

FUNDING

This work was supported by grants from the National Institutes of Health (5R01HL096518-04 and 5R03DK064841-03 to JR, HL067699 and DK069388 to AR), the Foundation for Science and Technology of the Portuguese Ministry of Science (CEECIND/01053/2017), and research funds from Quest Diagnostics to SA.

ACKNOWLEDGMENTS

We acknowledge the helpful comments of Michael McPhaul and Jeff Radcliff, both of Quest Diagnostics. AR is a Fellow of the Center of Excellence in Minority Health and Health Disparities at Harvard Medical School.

REFERENCES

Acosta, J., Hettinga, J., Fluckiger, R., Krumrei, N., Goldfine, A., Angarita, L., et al. (2000). Molecular Basis for a Link between Complement and the Vascular Complications of Diabetes. *Proc. Natl. Acad. Sci.* 97, 5450–5455. doi:10.1073/pnas.97.10.5450

Allegra, A., Corsonello, A., Buemi, M., D'Angelo, R., di Benedetto, A., Bonanzinga, S., et al. (1997). Plasma, Erythrocyte and Platelet Magnesium Levels in Type 1 Diabetic Patients with Microalbuminuria and Clinical Proteinuria. *J. Trace Elem. Med. Biol.* 11, 154–157. doi:10.1016/s0946-672x(97)80044-2

Arjona, F. J., Latta, F., Mohammed, S. G., Thomassen, M., van Wijk, E., Bindels, R. J. M., et al. (2019). SLC41A1 Is Essential for Magnesium Homeostasis *In Vivo*. *Pflugers Arch. - Eur. J. Physiol.* 471, 845–860. doi:10.1007/s00424-018-2234-9

Barbagallo, M., Dominguez, L. J., Bardicef, O., and Resnick, L. M. (2001). Altered Cellular Magnesium Responsiveness to Hyperglycemia in Hypertensive Subjects. *Hypertension* 38, 612–615. doi:10.1161/hy09t1.095764

Barbagallo, M., Gupta, R. K., and Resnick, L. M. (1996). Cellular Ions in NIDDM: Relation of Calcium to Hyperglycemia and Cardiac Mass. *Diabetes Care* 19, 1393–1398. doi:10.2337/diacare.19.12.1393

Brandvold, K. R., Steffey, M. E., Fox, C. C., and Soellner, M. B. (2012). Development of a Highly Selective C-Src Kinase Inhibitor. *ACS Chem. Biol.* 7, 1393–1398. doi:10.1021/cb300172e

Cabral, J., Hanley, S. A., Gerlach, J. Q., O'Leary, N., Cunningham, S., Ritter, T., et al. (2017). Distinctive Surface Glycosylation Patterns Associated with Mouse and Human CD4+ Regulatory T Cells and Their Suppressive Function. *Front. Immunol.* 8, 987. doi:10.3389/fimmu.2017.00987

Cefaratti, C., McKinnis, A., and Romani, A. (2004). Altered Mg2+transport across Liver Plasma Membrane from Streptozotocin-Treated Rats. *Mol. Cel Biochem* 262, 145–154. doi:10.1023/b:mcbi.0000038230.86485.52

Cefaratti, C., and Romani, A. (2003). Intravesicular Glucose Modulates Magnesium2+ Transport in Liver Plasma Membrane from Streptozotocin-Treated Rats. *Metabolism* 52, 1464–1470. doi:10.1016/s0026-0495(03)00283-x

Chan, K. H. K., Chacko, S. A., Song, Y., Cho, M., Eaton, C. B., Wu, W.-C. H., et al. (2015). Genetic Variations in Magnesium-Related Ion Channels May Affect Diabetes Risk Among African American and Hispanic American Women. *J. Nutr.* 145, 418–424. doi:10.3945/jn.114.203489

Chiu, T. K., and Dickerson, R. E. (2000). 1 Å crystal Structures of B -DNA Reveal Sequence-specific Binding and Groove-specific Bending of DNA by Magnesium and Calcium 1 1Edited by I. Tinoco. *J. Mol. Biol.* 301, 915–945. doi:10.1006/jmbi.2000.4012

Dewitte, K., Dhondt, A., Giri, M., Stöckl, D., Rottiers, R., Lameire, N., et al. (2004). Differences in Serum Ionized and Total Magnesium Values during Chronic Renal Failure between Nondiabetic and Diabetic Patients. *Diabetes Care* 27, 2503–2505. doi:10.2337/diacare.27.10.2503

Djurhuus, M. S., Skøtt, P., Hother-Nielsen, O., Klitgaard, N. A. H., and Beck-Nielsen, H. (1995). Insulin Increases Renal Magnesium Excretion: a Possible Cause of Magnesium Depletion in Hyperinsulinaemic States. *Diabet Med.* 12, 664–669. doi:10.1111/j.1464-5491.1995.tb00566.x

Eibl, N. L., Kopp, H.-P., Nowak, H. R., Schnack, C. J., Hopmeier, P. G., and Schernthaner, G. (1995). Hypomagnesemia in Type II Diabetes: Effect of a 3-month Replacement Therapy. *Diabetes Care* 18, 188–192. doi:10.2337/diacare.18.2.188

Fagan, T. E., Cefaratti, C., and Romani, A. (2004). Streptozotocin-induced Diabetes Impairs Mg2+homeostasis and Uptake in Rat Liver Cells. *Am. J. Physiology-Endocrinology Metab.* 286, E184–E193. doi:10.1152/ajpendo.00200.2003

Féray, J.-C., and Garay, R. (1986). An Na+-Stimulated Mg2+-Transport System in Human Red Blood Cells. *Biochim. Biophys. Acta (Bba) - Biomembranes* 856, 76–84. doi:10.1016/0005-2736(86)90012-x

Ferreira, A., Rivera, A., and Romero, J. R. (2004). Na+/Mg2+ Exchange Is Functionally Coupled to the Insulin Receptor. *J. Cel. Physiol.* 199, 434–440. doi:10.1002/jcp.10463

Fortuño, A., San José, G., Moreno, M. U., Beloqui, O., Díez, J., and Zalba, G. (2006). Phagocytic NADPH Oxidase Overactivity Underlies Oxidative Stress in Metabolic Syndrome. *Diabetes* 55, 209–215. doi:10.2337/diabetes.55.01.06.db05-0751

Gao, Y., Davies, S. P., Augustin, M., Woodward, A., Patel, U. A., Kovelman, R., et al. (2013). A Broad Activity Screen in Support of a Chemogenomic Map for Kinase Signalling Research and Drug Discovery. *Biochem. J.* 451, 313–328. doi:10.1042/bj20121418

Garner, M. H., Bahador, A., and Sachs, G. (1990). Nonenzymatic Glycation of Na,K-ATPase. Effects on ATP Hydrolysis and K+ Occlusion. *J. Biol. Chem.* 265, 15058–15066. doi:10.1016/s0021-9258(18)77223-2

Giménez-Mascarell, P., González-Recio, I., Fernández-Rodríguez, C., Oyenarte, I., Müller, D., Martínez-Chantar, M. L., et al. (2019). Current Structural Knowledge on the CNNM Family of Magnesium Transport Mediators. *Int. J. Mol. Sci.* 20. doi:10.3390/ijms20051135

Gommers, L. M. M., Hoenderop, J. G. J., Bindels, R. J. M., and de Baaij, J. H. F. (2016). Hypomagnesemia in Type 2 Diabetes: A Vicious Circle? *Diabetes* 65, 3–13. doi:10.2337/db15-1028

González Flecha, F. L., Castello, P. R., Caride, A. J., Gagliardino, J. J., and Rossi, J. P. (1993). The Erythrocyte Calcium Pump Is Inhibited by Non-enzymic Glycation: Studies *In Situ* and with the Purified Enzyme. *Biochem. J.* 293 (Pt 2), 369–375. doi:10.1042/bj2930369

Goytain, A., and Quamme, G. A. (2008). Identification and Characterization of a Novel Family of Membrane Magnesium Transporters, MMgT1 and MMgT2. *Am. J. Physiology-Cell Physiol.* 294, C495–C502. doi:10.1152/ajpcell.00238.2007

Guerrero-Romero, F., and Rodríguez-Morán, M. (2002). Low Serum Magnesium Levels and Metabolic Syndrome. *Acta Diabetol.* 39, 209–213. doi:10.1007/s005920200036

Günther, T. (2006). Mechanisms, Regulation and Pathologic Significance of Mg2+ Efflux from Erythrocytes. *Magnes Res.* 19, 190–198.

Günther, T., and Vormann, J. (1992). Activation of Na+/Mg2+antiport in Thymocytes by cAMP. *FEBS Lett.* 297, 132–134. doi:10.1016/0014-5793(92)80343-f

Guo, C., Ricchiuti, V., Lian, B. Q., Yao, T. M., Coutinho, P., Romero, J. R., et al. (2008). Mineralocorticoid Receptor Blockade Reverses Obesity-Related Changes in Expression of Adiponectin, Peroxisome Proliferator-Activated Receptor-γ, and Proinflammatory Adipokines. *Circulation* 117, 2253–2261. doi:10.1161/circulationaha.107.748640

Han, H. J., Lee, Y. J., Park, S. H., Lee, J. H., and Taub, M. (2005). High Glucose-Induced Oxidative Stress Inhibits Na+/glucose Cotransporter Activity in Renal Proximal Tubule Cells. *Am. J. Physiology-Renal Physiol.* 288, F988–F996. doi:10.1152/ajprenal.00327.2004

He, Y., Yao, G., Savoia, C., and Touyz, R. M. (2005). Transient Receptor Potential Melastatin 7 Ion Channels Regulate Magnesium Homeostasis in Vascular Smooth Muscle Cells. *Circ. Res.* 96, 207–215. doi:10.1161/01.res.0000152967.88472.3e

Hudson, B. I., and Lippman, M. E. (2018). Targeting RAGE Signaling in Inflammatory Disease. *Annu. Rev. Med.* 69, 349–364. doi:10.1146/annurev-med-041316-085215

Igarashi, M., Wakasaki, H., Takahara, N., Ishii, H., Jiang, Z.-Y., Yamauchi, T., et al. (1999). Glucose or Diabetes Activates P38 Mitogen-Activated Protein Kinase via Different Pathways. *J. Clin. Invest.* 103, 185–195. doi:10.1172/jci3326

John, W. G. (1997). Glycated Haemoglobin Analysis. *Ann. Clin. Biochem.* 34 (Pt 1), 17–31. doi:10.1177/000456329703400105

Joost, H.-G., and Schürmann, A. (2014). The Genetic Basis of Obesity-Associated Type 2 Diabetes (Diabesity) in Polygenic Mouse Models. *Mamm. Genome* 25, 401–412. doi:10.1007/s00335-014-9514-2

Kolisek, M., Launay, P., Beck, A., Sponder, G., Serafini, N., Brenkus, M., et al. (2008). SLC41A1 Is a Novel Mammalian Mg2+ Carrier. *J. Biol. Chem.* 283, 16235–16247. doi:10.1074/jbc.m707276200

Kolisek, M., Nestler, A., Vormann, J., and Schweigel-Röntgen, M. (2012). Human geneSLC41A1encodes for the Na+/Mg2+exchanger. *Am. J. Physiology-Cell Physiol.* 302, C318–C326. doi:10.1152/ajpcell.00289.2011

Laing, L. G., Gluick, T. C., and Draper, D. E. (1994). Stabilization of RNA Structure by Mg Ions. *J. Mol. Biol.* 237, 577–587. doi:10.1006/jmbi.1994.1256

Maley, F., Maley, G. F., West, D. K., Belfort, M., and Chu, F. K. (1986). RNA Processing in a Structural Gene from Bacteriophage T4. *Biochem. Soc. Trans.* 14, 813–815. doi:10.1042/bst0140813

Maltezos, E., Papazoglou, D., Exiara, T., Kambouromiti, G., and Antonoglou, C. (2004). Serum Magnesium Levels in Non-diabetic Offspring of Patients with Type 2 Diabetes Mellitus. *Diabetes Nutr. Metab.* 17, 12–16.

Mastrototaro, L., Smorodchenko, A., Aschenbach, J. R., Kolisek, M., and Sponder, G. (2016). Solute Carrier 41A3 Encodes for a Mitochondrial Mg2+ Efflux System. *Sci. Rep.* 6, 27999. doi:10.1038/srep27999

McAvan, B. S., France, A. P., Bellina, B., Barran, P. E., Goodacre, R., and Doig, A. J. (2020). Quantification of Protein Glycation Using Vibrational Spectroscopy. *Analyst* 145, 3686–3696. doi:10.1039/c9an02318f

Miller, J. A., Gravallese, E., and Bunn, H. F. (1980). Nonenzymatic Glycosylation of Erythrocyte Membrane Proteins. Relevance to Diabetes. *J. Clin. Invest.* 65, 896–901. doi:10.1172/jci109743

Monteilh-Zoller, M. K., Hermosura, M. C., Nadler, M. J. S., Scharenberg, A. M., Penner, R., and Fleig, A. (2003). TRPM7 Provides an Ion Channel Mechanism for Cellular Entry of Trace Metal Ions. *J. Gen. Physiol.* 121, 49–60. doi:10.1085/jgp.20028740

Morabito, R., Remigante, A., Spinelli, S., Vitale, G., Trichilo, V., Loddo, S., et al. (2020). High Glucose Concentrations Affect Band 3 Protein in Human Erythrocytes. *Antioxidants (Basel)* 9. doi:10.3390/antiox9050365

Murphy, E., Freudenrich, C. C., and Lieberman, M. (1991). Cellular Magnesium and Na/Mg Exchange in Heart Cells. *Annu. Rev. Physiol.* 53, 273–287. doi:10.1146/annurev.ph.53.030191.001421

Nadler, M. J. S., Hermosura, M. C., Inabe, K., Perraud, A.-L., Zhu, Q., Stokes, A. J., et al. (2001). LTRPC7 Is a Mg·ATP-Regulated Divalent Cation Channel Required for Cell Viability. *Nature* 411, 590–595. doi:10.1038/35079092

Nandhini, T. A., and Anuradha, C. V. (2003). Inhibition of Lipid Peroxidation, Protein Glycation and Elevation of Membrane Ion Pump Activity by Taurine in

RBC Exposed to High Glucose. *Clinica Chim. Acta* 336, 129–135. doi:10.1016/s0009-8981(03)00337-1

Palomino-Schätzlein, M., Lamas-Domingo, R., Ciudin, A., Gutiérrez-Carcedo, P., Marés, R., Aparicio-Gómez, C., et al. (2020). A Translational *In Vivo* and *In Vitro* Metabolomic Study Reveals Altered Metabolic Pathways in Red Blood Cells of Type 2 Diabetes. *J. Clin. Med.* 9, 2020. doi:10.3390/jcm9061619

Pani, L. N., Nathan, D. M., and Grant, R. W. (2008). Clinical Predictors of Disease Progression and Medication Initiation in Untreated Patients with Type 2 Diabetes and A1C Less Than 7%. *Diabetes Care* 31, 386–390. doi:10.2337/dc07-1934

Paolisso, G., Sgambato, S., Passariello, N., Giughano, D., Scheen, A., 'Onofrio, F. D., et al. (1986). Insulin Induces Opposite Changes in Plasma and Erythrocyte Magnesium Concentrations in normal Man. *Diabetologia* 29, 644–647. doi:10.1007/bf00869264

Parsons, J. T., and Parsons, S. J. (1997). Src Family Protein Tyrosine Kinases: Cooperating with Growth Factor and Adhesion Signaling Pathways. *Curr. Opin. Cel Biol.* 9, 187–192. doi:10.1016/s0955-0674(97)80062-2

Peterson, C. M., Jones, R. L., Koenig, R. J., Melvin, E. T., and Lehrman, M. L. (1977). Reversible Hematologic Sequelae of Diabetes Mellitus. *Ann. Intern. Med.* 86, 425–429. doi:10.7326/0003-4819-86-4-425

Picado, M. J., de la Sierra, A., Aguilera, M. T., Coca, A., and Urbano-Márquez, A. (1994). Increased Activity of the Mg2+/Na+ Exchanger in Red Blood Cells from Essential Hypertensive Patients. *Hypertension* 23, 987–991. doi:10.1161/01.hyp.23.6.987

Rabbani, N., and Thornalley, P. J. (2012). Amino Acids Glycation Section. *Amino Acids* 42, 1085–1086. doi:10.1007/s00726-011-0956-5

Raftos, J. E., Lew, V. L., and Flatman, P. W. (1999). Refinement and Evaluation of a Model of Mg2+ Buffering in Human Red Cells. *Eur. J. Biochem.* 263, 635–645. doi:10.1046/j.1432-1327.1999.00506.x

Reddy, M. A., Li, S.-L., Sahar, S., Kim, Y.-S., Xu, Z.-G., Lanting, L., et al. (2006). Key Role of Src Kinase in S100B-Induced Activation of the Receptor for Advanced Glycation End Products in Vascular Smooth Muscle Cells. *J. Biol. Chem.* 281, 13685–13693. doi:10.1074/jbc.m511425200

Resnick, L. M., Altura, B. T., Gupta, R. K., Laragh, J. H., Alderman, M. H., and Altura, B. M. (1993a). Intracellular and Extracellular Magnesium Depletion in Type 2 (Non-insulin-dependent) Diabetes Mellitus. *Diabetologia* 36, 767–770. doi:10.1007/bf00401149

Resnick, L. M., Barbagallo, M., Gupta, R. K., and Laragh, J. H. (1993b). Ionic Basis of Hypertension in Diabetes Mellitus. *Am. J. Hypertens.* 6, 413–417. doi:10.1093/ajh/6.5.413

Rivera, A., Ferreira, A., Bertoni, D., Romero, J. R., and Brugnara, C. (2005). Abnormal Regulation of Mg2+ Transport via Na/Mg Exchanger in Sickle Erythrocytes. *Blood* 105, 382–386. doi:10.1182/blood-2003-11-3755

Rodríguez-Morán, M., and Guerrero-Romero, F. (2003). Oral Magnesium Supplementation Improves Insulin Sensitivity and Metabolic Control in Type 2 Diabetic Subjects: a Randomized Double-Blind Controlled Trial. *Diabetes Care* 26, 1147–1152. doi:10.2337/diacare.26.4.1147

Rodríguez-Morán, M., Simental Mendía, L. E., Zambrano Galván, G., and Guerrero-Romero, F. (2011). The Role of Magnesium in Type 2 Diabetes: a Brief Based-Clinical Review. *Magnes Res.* 24, 156–162. doi:10.1684/mrh.2011.0299

Rohn, R. D., Pleban, P., and Jenkins, L. L. (1993). Magnesium, Zinc and Copper in Plasma and Blood Cellular Components in Children with IDDM. *Clinica Chim. Acta* 215, 21–28. doi:10.1016/0009-8981(93)90245-y

Romani, A., Marfella, C., and Scarpa, A. (1993). Hormonal Stimulation of Mg2+ Uptake in Hepatocytes. Regulation by Plasma Membrane and Intracellular Organelles. *J. Biol. Chem.* 268, 15489–15495. doi:10.1016/s0021-9258(18)82283-9

Ross, F. A., Hawley, S. A., Auciello, F. R., Gowans, G. J., Atrih, A., Lamont, D. J., et al. (2017). Mechanisms of Paradoxical Activation of AMPK by the Kinase Inhibitors SU6656 and Sorafenib. *Cel Chem. Biol.* 24, 813–824. doi:10.1016/j.chembiol.2017.05.021

Rubin, H. (2005). Central Roles of Mg2+ and MgATP2− in the Regulation of Protein Synthesis and Cell Proliferation: Significance for Neoplastic Transformation. *Adv. Cancer Res.* 93, 1–58. doi:10.1016/s0065-230x(05)93001-7

Runnels, L. W., Yue, L., and ClaphamTRP-Plik, D. E. (2001). TRP-PLIK, a Bifunctional Protein with Kinase and Ion Channel Activities. *Science* 291, 1043–1047. doi:10.1126/science.1058519

Sahni, J., Nelson, B., and Scharenberg, A. M. (2007). SLC41A2 Encodes a Plasma-Membrane Mg2+ Transporter. *Biochem. J.* 401, 505–513. doi:10.1042/bj20060673

Sahni, J., and Scharenberg, A. M. (2013). The SLC41 Family of MgtE-like Magnesium Transporters. *Mol. Aspects Med.* 34, 620–628. doi:10.1016/j.mam.2012.05.012

Sartori, S., Nielsen, I., Tassinari, D., Mazzotta, D., Vecchiatti, G., Sero, A., et al. (1992). Serum and Erythrocyte Magnesium Concentrations in Solid Tumours: Relationship with Stage of Malignancy. *Magnes Res.* 5, 189–192.

Schaeffer, G., Levak-Frank, S., Spitaler, M. M., Fleischhacker, E., Esenabhalu, V. E., Wagner, A. H., et al. (2003). Intercellular Signalling within Vascular Cells under High D-Glucose Involves Free Radical-Triggered Tyrosine Kinase Activation. *Diabetologia* 46, 773–783. doi:10.1007/s00125-003-1091-y

Schmidt, A. M. (2015). Soluble RAGEs - Prospects for Treating & Tracking Metabolic and Inflammatory Disease. *Vasc. Pharmacol.* 72, 1–8. doi:10.1016/j.vph.2015.06.011

Schmitz, C., Perraud, A.-L., Johnson, C. O., Inabe, K., Smith, M. K., Penner, R., et al. (2003). Regulation of Vertebrate Cellular Mg2+ Homeostasis by TRPM7. *Cell* 114, 191–200. doi:10.1016/s0092-8674(03)00556-7

Schweigel, M., Vormann, J., and Martens, H. (2000). Mechanisms of Mg2+ Transport in Cultured Ruminal Epithelial Cells. *Am. J. Physiology-Gastrointestinal Liver Physiol.* 278, G400–G408. doi:10.1152/ajpgi.2000.278.3.g400

Shafrir, E., and Sima, A. A. F. (2001). *Animal Models in Diabetes: A Primer*. Amsterdam, Netherlands: Harwood Academia Publishers.

Sponder, G., Rutschmann, K., and Kolisek, M. (2013). "Inside-in" or "Inside-Out"? the Membrane Topology of SLC41A1. *Magnes Res.* 26, 176–181. doi:10.1684/mrh.2014.0351

Standley, P. R., and Standley, C. A. (2002). Identification of a Functional Na+/Mg2+ Exchanger in Human Trophoblast Cells. *Am. J. Hypertens.* 15, 565–570. doi:10.1016/s0895-7061(02)02272-0

Tang, H., Zhang, X., Zhang, J., Li, Y., Del Gobbo, L. C., Zhai, S., et al. (2016). Elevated Serum Magnesium Associated with SGLT2 Inhibitor Use in Type 2 Diabetes Patients: a Meta-Analysis of Randomised Controlled Trials. *Diabetologia* 59, 2546–2551. doi:10.1007/s00125-016-4101-6

Tarentino, A. L., and Plummer, T. H., Jr. (1994). [4] Enzymatic Deglycosylation of Asparagine-Linked Glycans: Purification, Properties, and Specificity of Oligosaccharide-Cleaving Enzymes from Flavobacterium Meningosepticum. *Methods Enzymol.* 230, 44–57. doi:10.1016/0076-6879(94)30006-2

Touyz, R. M., Mercure, C., and Reudelhuber, T. L. (2001). Angiotensin II Type I Receptor Modulates Intracellular Free Mg2+ in Renally Derived Cells via Na+-dependent Ca2+-independent Mechanisms. *J. Biol. Chem.* 276, 13657–13663. doi:10.1074/jbc.m008101200

Touyz, R. M., and Schiffrin, E. L. (1999). Activation of the Na + -H + Exchanger Modulates Angiotensin II-Stimulated Na + -Dependent Mg 2+ Transport in Vascular Smooth Muscle Cells in Genetic Hypertension. *Hypertension* 34, 442–449. doi:10.1161/01.hyp.34.3.442

Touyz, R. M., and Schiffrin, E. L. (1999). Ang II-Stimulated Superoxide Production Is Mediated via Phospholipase D in Human Vascular Smooth Muscle Cells. *Hypertension* 34, 976–982. doi:10.1161/01.hyp.34.4.976

Umudum, F. Z., Yücel, O., Şahin, Y. N., and Bakan, E. (2002). Erythrocyte Membrane Glycation and NA+-K+ Levels in NIDDM. *J. Diabetes its Complications* 16, 359–362. doi:10.1016/s1056-8727(01)00223-9

Valencia, J. V., Weldon, S. C., Quinn, D., Kiers, G. H., DeGroot, J., TeKoppele, J. M., et al. (2004). Advanced Glycation End Product Ligands for the Receptor for Advanced Glycation End Products: Biochemical Characterization and Formation Kinetics. *Anal. Biochem.* 324, 68–78. doi:10.1016/j.ab.2003.09.013

Verma, N., Liu, M., Ly, H., Loria, A., Campbell, K. S., Bush, H., et al. (2020). Diabetic Microcirculatory Disturbances and Pathologic Erythropoiesis Are Provoked by Deposition of Amyloid-Forming Amylin in Red Blood Cells and Capillaries. *Kidney Int.* 97, 143–155. doi:10.1016/j.kint.2019.07.028

Vidair, C., and Rubin, H. (2005). Mg 2+ as Activator of Uridine Phosphorylation in Coordination with Other Cellular Responses to Growth Factors. *Proc. Natl. Acad. Sci. U.S.A.* 102, 662–666. doi:10.1073/pnas.0409082102

Viskupicova, J., Blaskovic, D., Galiniak, S., Soszyński, M., Bartosz, G., Horakova, L., et al. (2015). Effect of High Glucose Concentrations on Human Erythrocytes *In Vitro*. *Redox Biol.* 5, 381–387. doi:10.1016/j.redox.2015.06.011

Voets, T., Nilius, B., Hoefs, S., van der Kemp, A. W. C. M., Droogmans, G., Bindels, R. J. M., et al. (2004). TRPM6 Forms the Mg2+ Influx Channel Involved in Intestinal and Renal Mg2+ Absorption. *J. Biol. Chem.* 279, 19–25. doi:10.1074/jbc.m311201200

Waas, W. F., and Dalby, K. N. (2003). Physiological Concentrations of Divalent Magnesium Ion Activate the Serine/threonine Specific Protein Kinase ERK2. *Biochemistry* 42, 2960–2970. doi:10.1021/bi027171w

Watala, C. (1988). *In Vitro* glycation of Red Blood Cell Proteins: High Levels of Glucose Lower Lipid Fluidity of Erythrocyte Membranes. *Exp. Pathol.* 33, 233–238.

Williams, B., and Howard, R. L. (1994). Glucose-induced Changes in Na+/H+ Antiport Activity and Gene Expression in Cultured Vascular Smooth Muscle Cells. Role of Protein Kinase C. *J. Clin. Invest.* 93, 2623–2631. doi:10.1172/jci117275

Wolf, F. I., Di Francesco, A., Covacci, V., and Cittadini, A. (1997). Regulation of Magnesium Efflux from Rat Spleen Lymphocytes. *Arch. Biochem. Biophys.* 344, 397–403. doi:10.1006/abbi.1997.0199

Yan, S. F., Ramasamy, R., Naka, Y., and Schmidt, A. M. (2003). Glycation, Inflammation, and RAGE. *Circ. Res.* 93, 1159–1169. doi:10.1161/01.res.0000103862.26506.3d

Zehtabchi, S., Sinert, R., Rinnert, S., Chang, B., Heinis, C., Altura, R. A., et al. (2004). Serum Ionized Magnesium Levels and Ionized Calcium-To-Magnesium Ratios in Adult Patients with Sickle Cell Anemia. *Am. J. Hematol.* 77, 215–222. doi:10.1002/ajh.20187

Conflict of Interest: Authors JW and JD were employed by the company Quest Diagnostics. Authors LS and SA were consultants to Quest Diagnostics.

The remaining authors declare that the research was conducted in the absence of any commercial or financial relationships that could be construed as a potential conflict of interest.

Publisher's Note: All claims expressed in this article are solely those of the authors and do not necessarily represent those of their affiliated organizations, or those of the publisher, the editors and the reviewers. Any product that may be evaluated in this article, or claim that may be made by its manufacturer, is not guaranteed or endorsed by the publisher.

frontiers | Frontiers in Molecular Biosciences

ORIGINAL RESEARCH
published: 05 May 2022
doi: 10.3389/fmolb.2022.874186

Identification of IQGAP1 as a SLC26A4 (Pendrin)-Binding Protein in the Kidney

Jie Xu[1,2], *Sharon Barone*[1,2,3], *Mujan Varasteh Kia*[2], *L. Shannon Holliday*[4], *Kamyar Zahedi*[1,2,3] *and Manoocher Soleimani*[1,2,3]*

[1]Research Services, VA Medical Center, Albuquerque, NM, United States, [2]Department of Medicine, University of Cincinnati, Cincinnati, OH, United States, [3]Department of Medicine, University of New Mexico, Albuquerque, NM, United States, [4]Department of Orthodontics, University of Florida, Gainesville, FL, United States

Background: Several members of the SLC26A family of transporters, including SLC26A3 (DRA), SLC26A5 (prestin), SLC26A6 (PAT-1; CFEX) and SLC26A9, form multi-protein complexes with a number of molecules (e.g., cytoskeletal proteins, anchoring or adaptor proteins, cystic fibrosis transmembrane conductance regulator, and protein kinases). These interactions provide regulatory signals for these molecules. However, the identity of proteins that interact with the Cl^-/HCO_3^- exchanger, SLC26A4 (pendrin), have yet to be determined. The purpose of this study is to identify the protein(s) that interact with pendrin.

Methods: A yeast two hybrid (Y2H) system was employed to screen a mouse kidney cDNA library using the C-terminal fragment of SLC26A4 as bait. Immunofluorescence microscopic examination of kidney sections, as well as co-immunoprecipitation assays, were performed using affinity purified antibodies and kidney protein extracts to confirm the co-localization and interaction of pendrin and the identified binding partners. Co-expression studies were carried out in cultured cells to examine the effect of binding partners on pendrin trafficking and activity.

Results: The Y2H studies identified IQ motif-containing GTPase-activating protein 1 (IQGAP1) as a protein that binds to SLC26A4's C-terminus. Co-immunoprecipitation experiments using affinity purified anti-IQGAP1 antibodies followed by western blot analysis of kidney protein eluates using pendrin-specific antibodies confirmed the interaction of pendrin and IQGAP1. Immunofluorescence microscopy studies demonstrated that IQGAP1 co-localizes with pendrin on the apical membrane of B-intercalated cells, whereas it shows basolateral expression in A-intercalated cells in the cortical collecting duct (CCD). Functional and confocal studies in HEK-293 cells, as well as confocal studies in MDCK cells, demonstrated that the co-transfection of pendrin and IQGAP1 shows strong co-localization of the two molecules on the plasma membrane along with enhanced Cl^-/HCO_3^- exchanger activity.

Conclusion: IQGAP1 was identified as a protein that binds to the C-terminus of pendrin in B-intercalated cells. IQGAP1 co-localized with pendrin on the apical membrane of B-intercalated cells. Co-expression of IQGAP1 with pendrin resulted in strong co-localization of the two molecules and increased the activity of pendrin in the plasma membrane in cultured cells. We propose that pendrin's interaction with IQGAP1 may play

OPEN ACCESS

Edited by:
Silvia Dossena,
Paracelsus Medical University, Austria

Reviewed by:
Eleanor DeLand Lederer,
University of Texas Southwestern Medical Center, United States
Grazia Tamma,
University of Bari Aldo Moro, Italy

***Correspondence:**
Manoocher Soleimani
MSoleimani@salud.unm.edu

Specialty section:
This article was submitted to Cellular Biochemistry, a section of the journal Frontiers in Molecular Biosciences

Received: *17 February 2022*
Accepted: *22 March 2022*
Published: *05 May 2022*

Citation:
Xu J, Barone S, Varasteh Kia M, Holliday LS, Zahedi K and Soleimani M (2022) Identification of IQGAP1 as a SLC26A4 (Pendrin)-Binding Protein in the Kidney. Front. Mol. Biosci. 9:874186. doi: 10.3389/fmolb.2022.874186

a critical role in the regulation of CCD function and physiology, and that disruption of this interaction could contribute to altered pendrin trafficking and/or activity in pathophysiologic states.

Keywords: kidney tubules, collecting duct, bicarbonate secretion, chloride absorption, intercalated cells

1 INTRODUCTION

Complex biological systems are composed of networks of interacting proteins, which are crucial for all levels of cellular function, including signaling, metabolism and communication. Several members of the Slc26 family of anion transporters form multi-protein complexes with the cytoskeleton, anchoring proteins, PDZ adaptor proteins and certain protein kinases (Lohi et al., 2003; Ko et al., 2004; Rossmann et al., 2005; Thomson et al., 2005; Bertrand et al., 2009; Lee et al., 2012; Kim et al., 2012; Zheng et al., 2010; Hillesheim et al., 2007; Dossena et al., 2011). The formations of these complexes impart regulatory signals on ion transport by members of the SLC26 transporter family. While several studies have identified binding partners for SLC26A3 (DRA), SLC26A5 (prestin), SLC26A6 (PAT-1; CFEX) and SLC26A9 (Lohi et al., 2003; Ko et al., 2004; Thomson et al., 2005; Rossmann et al., 2005; Hillesheim et al., 2007; Bertrand et al., 2009; Kim et al., 2012; Lee et al., 2012; Zheng et al., 2010; Dossena et al., 2011), little information is available about the proteins that interact with SLC26A4/pendrin.

SLC26A4 is a Cl^-/HCO_3^- exchanger located on the apical membrane of non-A intercalated cells and plays an important role in bicarbonate secretion and chloride absorption in the kidney CCD (Soleimani et al., 2001; Royaux et al., 2001; Wall et al., 2003; Vallet et al., 2006; Bonar and Casey, 2008; Sindić et al., 2007; Amlal et al., 2010; Soleimani, 2013; Alper and Sharma, 2013; Wall and Weinstein, 2013; Mohebbi et al., 2013). The purpose of the current studies was to identify the binding partners of SLC26A4 in the kidney. Toward this end, yeast two hybrid (Y2H) screening was utilized to identify the proteins that bind to the C-terminal end of pendrin. The C-terminus was chosen as bait for these studies because it contains the Sulfate Transporter and anti-Sigma factor antagonist (STAS) domain, as well as residues that are important in pendrin function (Dossena et al., 2011; Alper and Sharma, 2013; Soleimani, 2013). Results were further confirmed by immunoprecipitation experiments and functional and confocal image analysis in cultured cells, kidney sections, and proteins. We identify IQGAP1 as a binding partner of pendrin in the kidney. The significance of the results will be discussed.

2 MATERIALS AND METHODS

2.1 Yeast Two Hybrid Screening

In order to identify binding partners of mouse *Slc26a4* in the kidney, the Y2H screening (Joung, et al., 2000; Gietz et al., 1997) was employed. The intracellular portion of the c-terminal fragment of SLC26A4 (amino acids 508–780) was used as bait (**Figure 1A**). Briefly, the pBD-*Slc26a4* yeast two hybrid expression vector was constructed by PCR amplification of the cDNA fragment that codes for the SLC26A4 c-terminal fragment using the following primers: KUP2Hyb, 5′-GAC TGTGGTCCTGAGAGTTCAG-3′, and KLOW2Hyb, 5′ TCA GGAAGCAAGTCTACGCATG-3′. The sequence of the PCR amplified pendrin fragment was confirmed prior to initiation of the yeast two hybrid studies. The fragment was ligated into the *Sal*I restriction endonuclease site of pBD-GAL4 (Stratagene, La Jolla, CA, United States). A mouse kidney cDNA library (HybriZapTM two hybrid library, Stratagene) was co-transformed with pBD-*Slc26a4* into YRG-2-competent yeast cells. A total of 6×10^3 interacting clones were identified by growth in selective media (Leu−, Trp−, His−), out of which 14 clones were determined to be positive when screened for β-gal expression. Plasmids from these clones were purified and co-transformed again with pBD-*Slc26a4* and with control plasmids in order to confirm the interaction. Cloned fragments were sequenced to confirm that they were in frame and without mutations.

2.2 Cloning of Full Length Human *SL26A4* and *IQGAP1*

For expression studies in HEK293 cells, the open reading frames of both *SLC26A4* (NM_000441) encompassing nucleotides 225–2,567 and *IQGAP1* (NM_003870) encompassing nucleotides 102–5,075 were amplified by PCR. Purified PCR products were sub-cloned into a pTarget ex-pression vector (Promega, Madison, WI, United States). Sequences and directionality of both sub-cloned fragments were confirmed.

2.3 Immunofluorescent Microscopic Analysis of Pendrin and IQGAP1 in the Kidney

The expression and localization of IQGAP1, SLC26A4 (pendrin), and H^+-ATPase were characterized by immunofluorescence microscopic examination (Petrovic et al., 2006; Xu et al., 2011; Xu, et al., 2006) on paraffin-embedded mouse kidney sections using specific antibodies to SLC26A4, H^+-ATPase B subunit, and IQGAP1.

2.4 Co-Immunoprecipitation and Western Analysis

For immunoprecipitation, 2 μg of mouse IQGAP1 antibody (SCBT, Dallas, TX, United States) was diluted in 200 μl of PBS with Tween-20 (PBS-T), and added to 50 μl of Dynabead Protein-G slurry (Invitrogen, Waltham, MA, United States). The mixture

A

^{508}TVVLRVQFPSWNGLGSVPS**T**DI**Y**KSITHYKNLEEPEGV

KILRFS**S**PIF**Y**GNVDGFKK**C**INST**V**GF**D**AIRVYNKRK**A**LR

RIQKLIKKGQ**L**RATKNGIISDIG**S**SNNAFEPDEDVEEP**E**EL

NIPTKE**I**EIQVDWNSELPVKVNVPKVPIH**S**L**V**LDCGAV**SF**

LDVV**G**VRS**L**RMIVKE**F**QRI**D**VNVYFALL**Q**DDVLEKMEQ

CGFFD**D**N**I**R**K**DRF**F**L**TVHD**AILHLQNQVKSR**E**GQDSLLE

TVARIRDCKDPLDLMEAEMNAEELDVQDEAM**R**RLAS^{780}

B

Type Seq	Gene Name (Best Match)	Global PBS	Frame	Sense/Antisense	%Id 5p/3p
5p 3p	Mus musculus - 9530068E07Rik	N/A	??	AntiSense	100.0 / 98.5
5p 3p	Mus musculus - 9530068E07Rik	N/A	??	AntiSense	100.0 / 98.9
5p 3p	Mus musculus - Actn4	N/A	OOF2	Sense	98.6 / 95.9
5p 3p	Mus musculus - Actn4	N/A	OOF2	Sense	97.8 / 94.0
5p 3p	Mus musculus - Cd97	B	IF	Sense	100.0 / 99.3
5p 3p	Mus musculus - Cd97	B	IF	Sense	100.0 / 99.6
5p 3p	Mus musculus - Cd97	B	IF	Sense	93.6 / 93.0
5p 3p	Mus musculus - Cd97	B	IF	Sense	100.0 / 100.0
5p 3p	Mus musculus - Cd97	B	IF	Sense	100.0 / 100.0
5p 3p	Mus musculus - Cd97	B	IF	Sense	100.0 / 100.0
5p 3p	Mus musculus - Cd97	B	IF	Sense	98.7 / 98.7
5p 3p	Mus musculus - Cd97	B	IF	Sense	98.0 / 97.0
5p	Mus musculus - Gusb	D	IF	Sense	96
5p	Mus musculus - Gusb	D	IF	Sense	97.4
5p	Mus musculus - Gusb	D	IF	Sense	93.7
5p 3p	**Mus musculus - Iqgap1**	**A**	**IF**	**Sense**	**91.0 / 91.0**
5p 3p	**Mus musculus - Iqgap1**	**A**	**IF**	**Sense**	**94.1 / 93.5**
5p 3p	**Mus musculus - Iqgap1**	**A**	**IF**	**Sense**	**98.3 / 98.2**
5p 3p	**Mus musculus - Iqgap1**	**A**	**IF**	**Sense**	**98.6 / 97.3**
5p 3p	**Mus musculus - Iqgap1**	**A**	**IF**	**Sense**	**91.0 / 93.7**
5p 3p	**Mus musculus - Iqgap1**	**A**	**IF**	**Sense**	**90.6 / 92.3**
5p 3p	**Mus musculus - Iqgap1**	**A**	**IF**	**Sense**	**95.4 / 99.3**
5p 3p	**Mus musculus - Iqgap1**	**A**	**IF**	**Sense**	**99.5 / 98.8**
5p 3p	**Mus musculus - Iqgap1**	**A**	**IF**	**Sense**	**99.6 / 95.8**
5p 3p	**Mus musculus - Iqgap1**	**A**	**IF**	**Sense**	**98.4 / 95.5**
5p 3p	**Mus musculus - Iqgap1**	**A**	**IF**	**Sense**	**99.5 / 97.1**
3p	**Mus musculus - Iqgap1**	**A**	**??**	**Sense**	**97**
5p 3p	**Mus musculus - Iqgap1**	**A**	**IF**	**Sense**	**99.7 / 98.8**
5p 3p	**Mus musculus - Iqgap1**	**A**	**IF**	**Sense**	**100.0 / 98.5**
5p 3p	Mus musculus - Isca1	N/A	OOF1	Sense	99.6 / 98.6
5p 3p	Mus musculus - Pdhx	D	IF	Sense	99.0 / 96.4
5p 3p	Mus musculus - Pdhx	D	IF	Sense	96.4 / 97.9
5p 3p	Mus musculus - Ranbp9	F	IF	Sense	97.3 / 95.9

FIGURE 1 | Identification of IQGAP1 as a pendrin binding partner. **(A)** The C-terminus of pendrin was used as bait in Y2H in order to identify the protein(s) that interact with pendrin. The C-terminus of mouse pendrin protein spanning amino acids 508–780 was used in Y2H studies in order to identify the proteins that interact with pendrin. This region was used because it contains the STAS domain. The missense mutations (highlighted, bolded and underlined) correspond to those of that affect the function of the human pendrin protein and are associated with Pendred Syndrome and DFNB4. **(B)** Our studies identified a total of 33 interactions between pendrin and prey sequences. Of these only 22 interactions were shown to be specific while others we excluded due to out of frame translation, reversed direction of the cloned sequence, or low affinity of the bait/prey interaction. The interaction with IQGAP1 represented 14 of the 22 significant interactions. Based on the Global PBS score, IQGAP/pendrin interaction had a very high degree of confidence. The Global PBS score is automatically computed through algorithms with the following scoring system: A) Very high confidence in the interaction; B) High confidence in the interaction; C) Good confidence in the interaction; D) Moderate confidence in the interaction; E) Interactions highly connected prey domains, warning of non-specific interaction; and F) Experimentally proven technical artifacts. In addition to IQGAP1, the Y2H system also identified CD97 as a protein with a "high confidence of interaction" giving it a Global PBS score of B. The relationship between pendrin and CD97 as a binding partner needs further examination. The % Id 5p/3p indicates the degree of identity to the putative binding protein.

was subjected to rotation for 10 min at room temperature. The Dynabead-antibody complex was washed with PBS-T. Kidney lysates (200 µg in 100 µl of PBS-T) from wild-type (WT) and pendrin knockout (KO) (Amlal et al., 2010) were precleared by incubation with Dyna- bead Protein-G slurry for 30 min. The precleared lysates were added to the Dynabead-Ab complex. The mixture was subjected to rotation for 10 min at room temperature. The Dynabead-Ab-antigen complex was washed 3 times using 200 µl of PBS-T. The bound proteins were eluted by addition of 40 µl of 1:1 mixture of reducing laemmli and elution buffers and heating the samples for 10 min at 70 degrees C. The eluted proteins were subjected to western blot analysis using a mouse monoclonal anti-SLC26A4 antibody (LS Bio, Seattle, WA, United States).

2.5 Co-Expression of Pendrin and IQGAP1 in HEK293 and MDCK Cells

SLC26A4 (pendrin) and *IQGAP1* expression vectors were used for transient transfection of HEK293 or MDCK cells. Briefly, cells were grown in 60 mm tissue culture plates or on coverslips. Monolayers (~70% confluent) were transfected with 8 µg of the full-length SLC26A4 (pendrin), IQGAP1 or both expression vectors using Lipofectamine 2000, according to an established protocol (Li et al., 2004; Li et al., 2007). Cells were maintained at 37°C in a 5% CO_2 atmosphere and were examined 48 h after transfection.

2.6 Confocal Microscopy

For confocal microscopy experiments, HEK293 or MDCK cells were grown on glass coverslips and transiently transfected with *Iqgap1*, *Slc26a4* (pendrin), or both expression vectors. The coverslips were fixed 48 h later with 4% paraformaldehyde 48 h after transfection. Fixed cells were labeled with IQGAP1 and SLC26A4 antibodies. The slides were observed using a Zeiss confocal 710. Z-stack images were obtained with LSM 5 Image software.

2.7 Intracellular pH Measurement

The intracellular pH (pH_i) in HEK293 cells was determined by microfluorometry using the pH-sensitive fluoroprobe BCECF (Xu, et al., 2011; Petrovic, et al., 2003; Rahmati, et al., 2013). The cells were first perfused with a Cl^-- and HCO_3^--containing solution of the following composition (in mM): 115 NaCl, 25 Na-HCO_3, 3 KCl, 1.8 $CaCl_2$, 1 $MgCl_2$, and 5 HEPES, pH 7.4, gassed with 5% CO_2-95% O_2. Once the baseline pH_i was established, the perfusate was then switched to a Cl^--free medium of the following composition

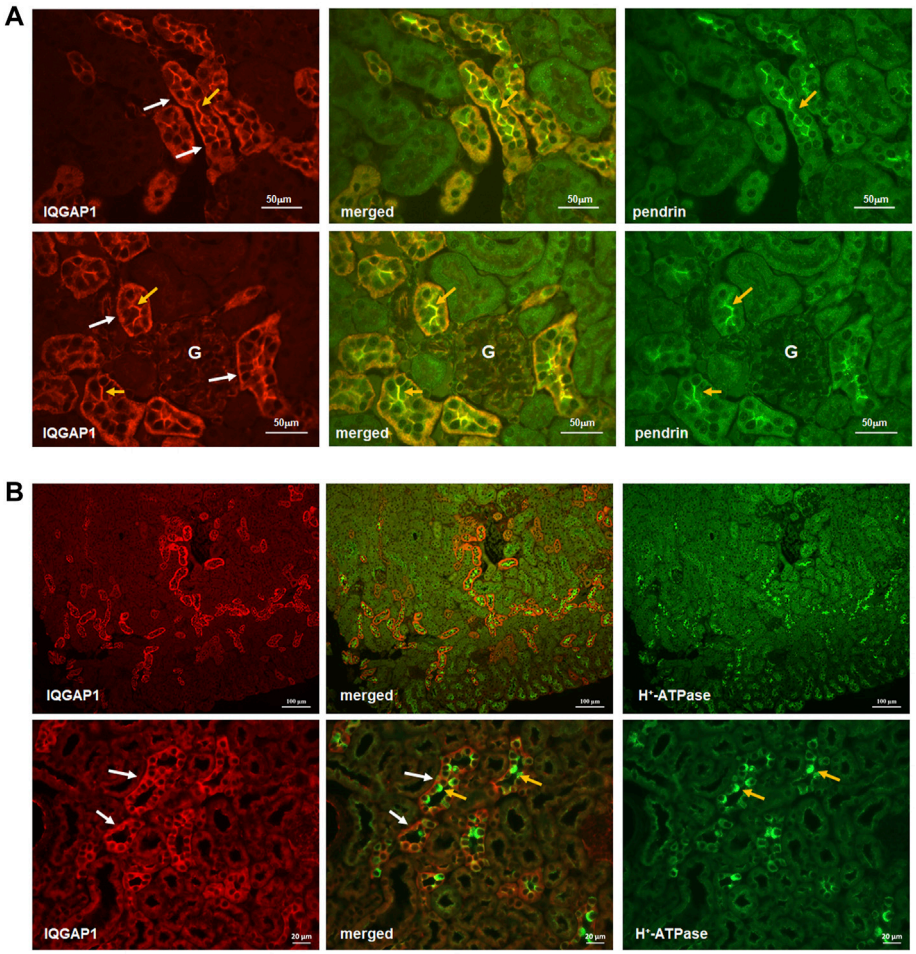

FIGURE 2 | Co-localization IQGAP1, pendrin, and H^+-ATPase in the kidney by immunofluorescence microscopy. **(A)** Top and bottom panels are immunofluorescence double labeling of mouse kidney sections with anti-IQGAP1 and anti-pendrin antibodies (×40 magnification). The expression of IQGAP1 is detected on the basolateral membrane in the of majority of cells in the CCD (Left Panels, top and bottom rows; white arrows). In addition, IQGAP1 shows apical localization in a subset of cells in CCD (Left Panels, top and bottom rows; orange arrows). The expression of pendrin is shown in right panels (orange arrows). Merged images (middle panels) demonstrates a remarkable co-localization of IQGAP1 and pendrin on the apical membrane of pendrin-expressing cells (orange arrows). "G" signifies glomerulus. **(B)** To determine the identity of tubular cells expressing IQGAP1, double immunofluorescence labeling with IQGAP1 and H^+-ATPase antibodies was performed. As shown, IQGAP1 was detected in several cortical collecting duct and connecting tubules based on the presence of H^+-ATPase, tubular morphology, and when the merged images were acquired (middle images in both top and bottom panels). There was occasional and faint expression of IQGAP1 on the basolateral membrane of the proximal tubule cells. In cortical collecting duct (CCD), IQGAP1 shows predominant localization on the basolateral membrane of most cells (bottom panels; white arrows). However, IQGAP1 also shows distinct localization on the apical membrane of a subset of intercalated cells (bottom panels; yellow arrows).

(in mM): 115 Na^+-gluconate, 25 $NaHCO_3$, 3 KCl, 1.8 Ca^{2+}-gluconate, 1 Mg^{2+}-gluconate, and 5 HEPES, pH 7.4, and gassed with 5% CO_2-95% O_2. Upon pH_i stabilization in Cl^--free medium, cells were returned to the Cl^--containing solution. Values of pH_i were calculated from the fluorescence ratio (F480/F430) measured at 530 nm. The system was calibrated by the high-K^+/nigericin technique.

2.8 Antibodies and Other Reagents

Polyclonal pendrin and H^+-ATPase B1 subunit antibodies were generated in our laboratory as described (Petrovic, et al., 2006; Xu, et al., 2011; Xu, et al., 2006). Monoclonal H^+-ATPase E subunit was a generous gift from Dr. Shannon Holliday. Monoclonal pendrin antibody was from LS Bio (Seattle, WA, United States). IQGAP1 antibody was purchased from Santa Cruz Biotechnology (Dallas, TX, United States). HRP-labeled goat anti-rabbit Ig was from PharMingen (San Diego, CA, United States). Dynabead protein-G immunoprecipitation kit was purchased from Thermo Fisher Scientific (Waltham, MA, United States). Western blot densitometry measurements were performed using Image-J software (National Institutes of Health, United States).

2.9 Statistical Analysis

The results for cell pH experiments are presented as means ± SE. Statistical significance between two experimental groups was determined by unpaired Student's t-test. The statistical significance of results comparing multiple experimental groups

was determined by ANOVA. A $p < 0.05$ was considered to be statistically significant.

3 RESULTS

3.1 Identification of SLC26A4 Binding Partners

Figure 1A shows the amino acid sequence of the C-terminus of pendrin. This fragment encompasses the Sulfate Transporter and anti-Sigma factor antagonist (STAS) domain (amino acids 515–734), the intervening sequence (amino acids 574–652), and includes a number of disease-associated mutations (Bonar and Casey, 2008; Sindić et al., 2007; Soleimani, 2013; Alper and Sharma, 2013; Dossena, et al., 2011). The pendrin mutations included in **Figure 1A** are responsible for a variety of sensorineural hearing loss, including those found in patients with Pendred syndrome, as well as patients afflicted with non-syndromic hearing loss caused by enlarged vestibular aqueducts (EVA) (Dossena, et al., 2011; Roesch, et al., 2021). Y2H studies were used to identify the binding partners that interacted with the C-terminus of SLC26A4 (amino acids 508–780). These studies identified a total of 33 interactions, of these only 22 interactions were shown to be specific while others we excluded due to out of frame translation, reversed direction of the cloned sequence, or low affinity of the bait/prey interaction. The interaction with IQGAP1 represented 14 of the 22 significant interactions (**Figure 1B**). Our studies identified IQGAP1 as a protein that binds to the intracellular c-terminal portion of pendrin with a very strong degree of confidence (**Figure 1B**). There were two other proteins (Cluster of differentiation 97; Cd97 and beta-glucuronidase; Gusb) that were identified; however, their binding affinity was significantly less than IQGAP1.

IQGAP1 is a scaffolding protein with five identified protein binding domains (White, et al., 2012; Nammalwar, et al., 2015; Nauert, et al., 2003; Jacquemet, et al., 2013; Johnson, et al., 2013; Hedman, et al., 2015). It binds and/or stabilizes ezrin, CDC42 and RAC1, and interacts with a number of cytoskeletal and cell adhesion molecules (e.g., mDia and Cadherin) (White, et al., 2012; Nammalwar, et al., 2015; Nauert, et al., 2003; Jacquemet, et al., 2013; Johnson, et al., 2013; Hedman, et al., 2015). As such, IQGAP1 plays a role in the regulation of signal transduction, cytoskeleton, cell adhesion and cell cycle (White, et al., 2012; Hedman, et al., 2015).

3.2 Co-Localization of SLC26A4 (Pendrin) and IQGAP1 in the Kidney

Given the results of Y2H system identifying IQGAP1 as a SLC26A4 binding protein, we sought to examine the localization of IQGAP1 vis-à-vis SLC26A4. Toward this end, double immunolocalization studies with SLC26A4 and IQGAP1 antibodies were performed in the kidney. IQGAP1 shows a predominant basolateral localization in various CCD cells (**Figure 2A**, left panels, top and bottom rows, white arrows). Certain cells also express IQGAP1 on their apical membrane (left panels, top and bottom rows, orange arrows). Merged images demonstrate a remarkable co-localization of SLC26A4 (pendrin)

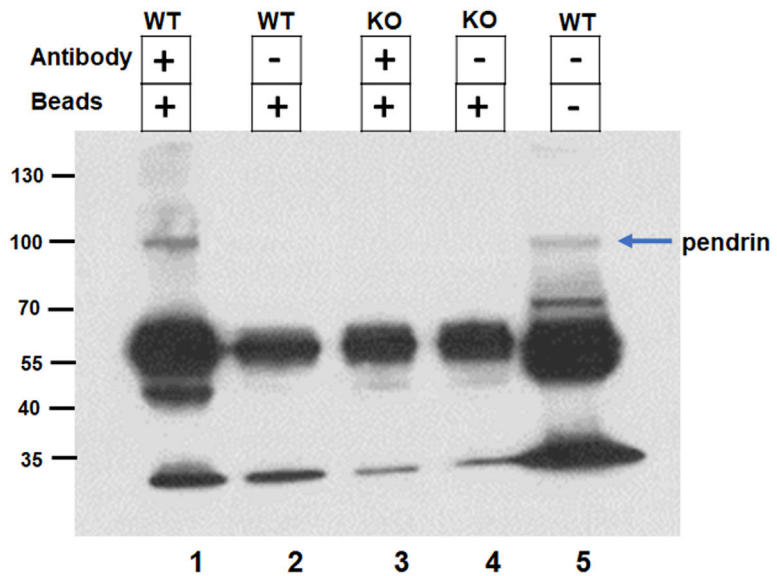

FIGURE 3 | Confirmation of IQGAP1 and pendrin interaction by co-immunoprecipitation. The interaction of pendrin with IQGAP1 was confirmed by co-immunoprecipitation. Kidney extracts from wildtype and pendrin knockout animals were incubated with IQGAP1 antibody coated beads, the bound proteins were eluted, size fractionated and subjected to western blot analysis using anti-pendrin antibody. Lane 1) Binding of WT kidney extract with IQGAP1 antibody coated beads; Lane 2) Binding of WT kidney extract with G-protein coated beads; Lane 3) Binding of pendrin KO kidney extract with IQGAP1 coated beads; Lane 4) Binding of pendrin KO kidney extract with G-protein coated beads; and Lane 5) WT whole kidney extract. Blue arrow designates the 110 kDa band recognized by anti-pendrin antibody.

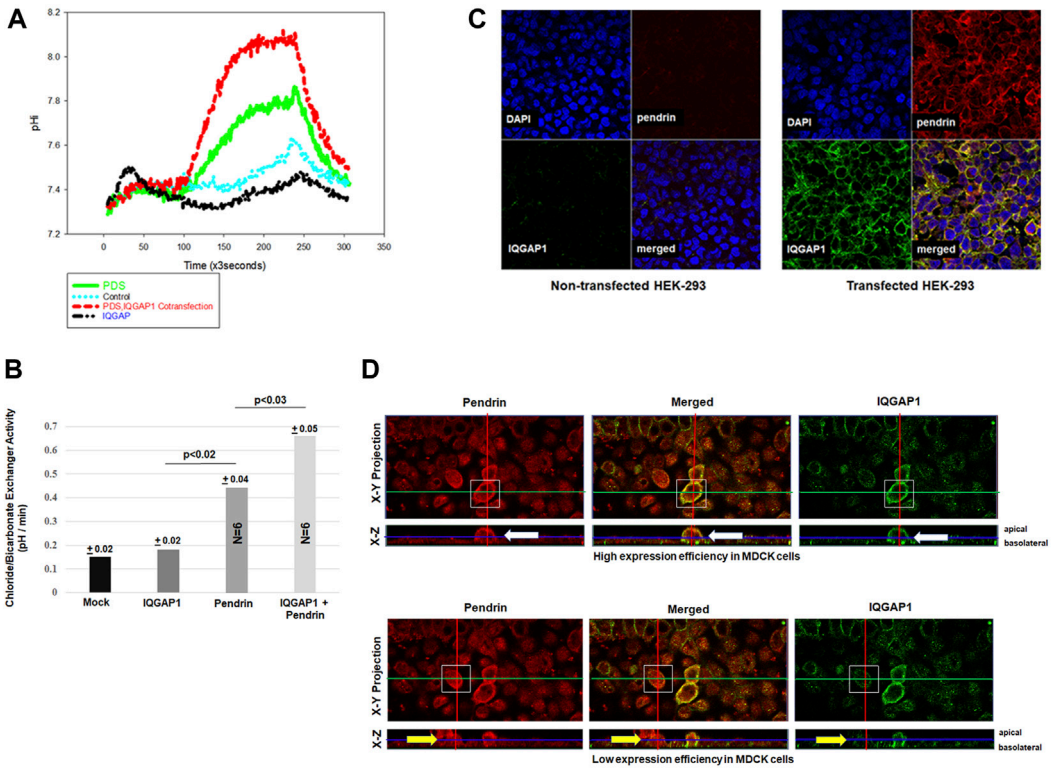

FIGURE 4 | Effect of IQGAP1 on pendrin activity and expression in cultured cells. **(A)** Representative tracing demonstrating the Cl^-/HCO_3^- exchanger activity in transfected HEK293 cells. The mock transfected HEK293 cells were not significantly different vs. IQGAP1 transfected cells. The pH_i tracings in HEK293 cells transfected with pendrin alone show significant Cl^-/HCO_3^- exchanger activity compared to mock or IQGAP1 only transfected cells. HEK293 cells co-transfected with pendrin and IQGAP1 show significant enhancement in Cl^-/HCO_3^- exchanger activity vs. pendrin-transfected cells. **(B)** The summary of six separate experiments show significant enhancement in pendrin-mediated Cl^-/HCO_3^- exchanger activity in cells co-transfected with pendrin and IQGAP1 vs. pendrin alone transfected cells. IQGAP1 transfection in cells did not elicit any Cl^-/HCO_3^- exchanger activity when compared to mock transfected. **(C)** Representative confocal images of HEK293 cells transfected with IQGAP1, pendrin or IQGAP1 plus pendrin construct. Non-transfected cells (**C**; left top and bottom panels of non-transfected groups) did not show any expression of either pendrin or IQGAP1. HEK293 cells co-transfected with SLC26A4 and IQGAP1 (**C**; right top and bottom panels of transfected groups) show sharp co-localization of the two molecules on the plasma membrane of transfected cells (**C**; merged panel of transfected groups). **(D)** Representative confocal images of pendrin localization in high (**D**; upper panels) and low (**D**; bottom panels) IQGAP1-expressing MDCK cells. Both X-Y and X-Z projections are provided. White boxes highlight the cells that were analyzed. Cells with an elevated expression of IQGAP1 (**D**; top right and left panels, white arrow) have increased pendrin localization to the cell membrane. Whereas, low expression of IQGAP1 is associated with reduced membrane and increased intracellular localization of pendrin (**D**; bottom right and left panels, yellow arrow).

and IQGAP1 on the apical membrane of pendrin-expressing cells in the CCD (**Figure 2A**, merged images in the middle panel; top and bottom rows, orange arrows), consistent with the apical localization of IQGAP1 in B-intercalated cells.

Additional images depicting the localization of H^+-ATPase vis-à-vis IQGAP1 are shown in the **Figure 2B**. In addition to confirming the predominant localization of IQGAP1 on the basolateral membrane of majority of CCD cells (**Figure 2B**; left bottom and middle panels, white arrows), these images clearly indicate the absence of IQGAP1 localization on the apical membrane of A-intercalated cells (**Figure 2B**; middle bottom panel, orange arrows). The images also show the apical localization of IQGAP1 in a subset of cells distinct from A-intercalated cells. Taken together with images in **Figure 2**, these studies indicate the apical localization of IQGAP1 in B-, but not A-, intercalated cells.

3.3 Co-Immunoprecipitation Studies

The interaction of SLC26A4 (pendrin) with IQGAP1 was further confirmed by co-immunoprecipitation. Kidney extracts from wildtype and pendrin knockout animals were incubated with IQGAP1 antibody coated beads, the bound proteins were eluted, size fractionated and subjected to western blot analysis using anti-pendrin antibodies. Our western blot results (**Figure 3**) show the presence of a band that corresponds in size (MW~110 kDa) and reacts with anti-pendrin antibody in the whole kidney extract of WT mice (Lane 5), as well as kidney extracts of WT mice subjected to co-immunoprecipitation with anti-IQGAP1 antibody (Lane 1). This band was absent in the kidney extracts of pendrin KO mice that were subjected to co-immunoprecipitation using anti-IQGAP antibody (Lane 3). Non-specific binding of extract proteins to the matrix in the absence of anti-IQGAP antibody was minimal (Lanes 2 and 4).

3.4 Effect of IQGAP1 on Pendrin Activity and Localization in Cultured Cells

3.4.1 Intracellular pH Studies

To determine if the interaction of IQGAP1 and SLC26A4 affects the activity of the latter, cultured HEK293 cells were co-transfected with *IQGAP1* and *SLC26A4* expression vectors and assayed for SLC26A4-mediated Cl^-/HCO_3^- exchanger activity. For comparison, cells transfected with pendrin or IQGAP1 expression vector alone were examined. The results in **Figure 4** depict a representative intracellular pH (pH_i) tracings (**Figure 4A**) and summary of multiple experiments (**Figure 4B**). These results indicate that the Cl^-/HCO_3^- exchanger activity in HEK293 cells transfected with the *IQGAP1* vector were not different than the mock transfected cells (background activity). HEK293 cells transfected with *SLC26A4* cDNA alone displayed significant Cl^-/HCO_3^- exchanger activity (**Figures 4A,B**). However, when HEK293 cells were co-transfected with both *SLC26A4* and *IQGAP1* expression constructs there was a significant enhancement in their Cl^-/HCO_3^- exchanger activity when compared to pendrin-transfected cells alone (**Figures 4A,B**).

3.4.2 Pendrin Expression in Cultured Cells

Confocal microscopy was performed to examine the impact of IQGAP1 expression on SLC26A4 (pendrin) distribution in cultured cells. As indicated, the non-transfected cells (**Figure 4C**; left top and bottom panels of non-transfected groups) did not show any expression of either pendrin or IQGAP1 as verified by confocal microscopy. The results further indicate that HEK293 cells co-transfected with pendrin and IQGAP1 (**Figure 4C**; left top and bottom panels of transfected groups) show sharp co-localization of IQGAP1 and pendrin in the merged image of the transfected panel (**Figure 4C**; merged panel of transfected groups). Additional experiments were conducted to verify the interaction between pendrin and IQGAP1 in a polarized cell model and the role of this interaction in the localization of pendrin. Towards this end, confocal images of MDCK cells transiently transfected with both pendrin and IQGAP1 expression vectors are shown in **Figure 4D**. One limitation with expression studies in MDCK cells is a low or variable transfection efficiency. Therefore, we examined cells showing either high or low IQGAP1 expression. Our results indicate that cells with high expression levels of IQGAP1 (**Figure 4D**; top right panel, white arrow) have increased pendrin membrane localization (**Figure 4D**; top left panel, white arrow). As indicated, cells showing a strong abundance of IQGAP1 demonstrate discrete apical co-localization of IQGAP1 and pendrin. In contrast, cells expressing low levels of IQGAP1 show reduced membrane and increased intracellular localization of pendrin (**Figure 4D**; bottom right and left panels, yellow arrow).

4 DISCUSSION

In the current studies Y2H screening, co-immunoprecipitation, double immunofluorescence labeling and functional studies were performed to identify pendrin binding proteins in the kidney. Our studies demonstrated that IQGAP1, a known scaffolding protein, binds to pendrin in the kidney with strong affinity (**Figure 1**). Immunofluorescence labeling studies demonstrated co-localization of pendrin and IQGAP1 on the apical membrane of B-intercalated cells (**Figure 2A**). In addition to the apical membrane, IQGAP1 also shows basolateral distribution pattern in B-intercalated cells (**Figure 2A**). Co-immunoprecipitation studies revealed that pendrin binds and co-precipitates with IQGAP1 (**Figure 3**). IQGAP1 shows a strong basolateral expression in a majority of cells in the CCD. The co-localization studies with H^+-ATPase and IQGAP1 antibodies suggest that these cells are predominantly A-intercalated cells (**Figure 2B**).

Previous immunohistochemical staining studies localized IQGAP1 to the basolateral membrane of cells in the CCD and several other nephron segments (Lai, et al., 2008). Our studies clearly confirm this finding with IQGAP1 exhibiting abundant expression in the CCD (**Figure 2**). There were 2 distinct patterns of expression for IQGAP1 in the collecting duct. IQGAP1 is predominantly localized to the basolateral membrane of intercalated cells, and also on the apical membrane of B-intercalated cells (**Figure 2**). The localization of IQGAP1 in principal cells remains conflicting, with previous studies showing a cytoplasmic pattern and our studies indicating a mixture of cytoplasmic and basolateral labeling (personal observation on AQP-2 and IQGAP1 double-labeling). The specific expression pattern of IQGAP1 in CCD cells suggest that this scaffolding protein, through its differential localization in specific cell populations, may play important roles in determining the cell specific localization of transporters and tubular functions.

Published reports indicate that as a scaffolding protein, IQGAP1 is important in cell differentiation, proliferation, cell polarity and cell-cell adhesion (White et al., 2012; Hedman et al., 2015). Through its IQ motifs, IQGAP1 binds to epidermal growth factor receptor (EGFR), which is responsible for maintaining IQGAP1 in the basolateral membrane domain (White, et al., 2012; Nammalwar, et al., 2015; Nauert, et al., 2003; Jacquemet, et al., 2013; Johnson, et al., 2013; Hedman, et al., 2015). EGFR is known to play an important role in salt and water reabsorption through the epithelial sodium channel (ENaC) and AQP-2 in principal cells, where IQGAP1 is detected on their basolateral membrane domain (Kwakkenbos, et al., 2004; Cheung, et al., 2016). How much of these EGFR regulatory functions require its interaction with IQGAP1 remains speculative. Further, the role of apical IQGAP1 and its binding with pendrin in bicarbonate secretion and chloride absorption in B-intercalated cells requires further investigation.

The cytoplasmic C-terminus of pendrin and the other nine members of SLC26 members is largely comprised of a STAS domain (Bonar and Casey, 2008; Sindić, et al., 2007; Soleimani, 2013; Alper and Sharma, 2013). Mutations in some of the SLC26 genes cause hereditary recessive disorders, including chondrodysplasia (SLC26A2/DTD), chloride-losing diarrhea (SLC26A3/DRA), and Pendred Syndrome (SLC26A4/pendrin) (Bonar and Casey, 2008; Sindić, et al., 2007; Soleimani, 2013; Alper and Sharma, 2013). Many of these mutations involve the respective STAS domains. The C-terminus fragment used for

our Y2H expression studies encompasses a number of mutations that are associated with Pendred syndrome and EVA/DFNB4 (Dossena, et al., 2011; Roesch, et al., 2021). This fragment includes the entire STAS domain, strongly suggesting that IQGAP1 is binding to the pendrin STAS domain.

Functional studies in cultured cells indicated that co-expression of IQGAP1 with SLC26A4 enhanced Cl^-/HCO_3^- exchanger activity mediated *via* SLC26A4, and confocal microscopy showed increased membrane expression of pendrin in the presence of IQGAP1, consistent with enhanced trafficking to the membrane (**Figure 4D**). While the membrane localization of pendrin is enhanced by co-expression of IQGAP1 and may lead to increased transport function, the possibility that other signaling pathways may contribute to enhanced pendrin activity could not be excluded. Our studies suggest that the interaction of pendrin and IQGAP1 may play an important role in the cell surface localization of pendrin (**Figure 4D**). Previous studies have shown that IQGAP1 is associated with the actin cytoskeleton and enhances the cross-linking of actin (Bashour et al., 1997; Fukata, et al., 1997). IQGAP1 interaction and crosslinking of the actin cytoskeleton depends on its multimerization mediated *via* binding with the RHO-GTPase family proteins, RAC1 and CDC2 (Fukata et al., 1997). IQGAP1 interacts with other proteins such as ezrin, a membrane F-actin linker protein, and nephrin, a component of slit diaphragm of podocytes, both of which bind to the actin cytoskeleton in polarized cells and may act as nucleation hubs for the formation of signaling complexes (Liu et al., 2015; Nammalwar et al., 2015). Studies by Russo et al. (2017) also demonstrated the RhoA dependent interaction of pendrin with F-actin in cultured bronchiolar cells. The above studies indicate that both pendrin and IQGAP1 interact with the actin cytoskeleton. The latter observations, as well as the direct binding of pendrin and IQGAP1 (documented in this manuscript), support a view that IQGAP1 may play an important role in the regulation of localization and function of SLC26A4.

In conclusion, IQGAP1 co-localizes with SLC26A4 (pendrin) on the apical membrane of B-intercalated cells. IQGAP1 enhances the membrane expression and activity of SLC26A4 in cultured cells. We propose that SLC26A4 interaction with IQGAP1 could play an important role in the regulation of CCD function and physiology, and that disruption of this interaction may contribute to altered SLC26A4 trafficking and/or activity in pathophysiologic states.

DATA AVAILABILITY STATEMENT

The original contributions presented in the study are included in the article/**Supplementary Material**, further inquiries can be directed to the corresponding author.

ETHICS STATEMENT

The animal study was reviewed and approved by IACUC University of Cincinnati, IACUC University of New Mexico, and IACUC VA Health Services.

AUTHOR CONTRIBUTIONS

JX-conducted experiments, acquired confocal images, analyzed results. SB-conducted experiments, analyzed results, created figures, wrote/edited manuscript. MK-conducted experiments and analyzed results. SH-provided antibody and consulted on manuscript. KZ-designed Y2H bait sequence, conducted experiments, analyzed results, created figures, wrote/edited manuscript. MS-conceptualized experiments, directed studies, analyzed results, wrote/edited manuscript.

FUNDING

The studies in this manuscript were supported by a Merit Review Award 5 I01 BX001000-10 from the Department of Veterans Health Administration, and an award from the Dialysis Clinic Inc. (C-4149). MS is a Senior Clinician Scientist Investigator with the Department of Veterans Health Administration. This research made use of the Fluorescence Microscopy and Cell Imaging Shared Resource, which is supported partially by University of New Mexico (UNM) Comprehensive Cancer Center Support Grant NCI P30CA118100. This study received funding from the Dialysis Clinic, Inc. The funder was not involved in the study design, collection, analysis, interpretation of data, the writing of this article or the decision to submit it for publication.

SUPPLEMENTARY MATERIAL

The Supplementary Material for this article can be found online at: https://www.frontiersin.org/articles/10.3389/fmolb.2022.874186/full#supplementary-material

REFERENCES

Alper, S. L., and Sharma, A. K. (2013). The SLC26 Gene Family of Anion Transporters and Channels. *Mol. Aspects Med.* 34 (2-3), 494–515. doi:10.1016/j.mam.2012.07.009

Amlal, H., Petrovic, S., Xu, J., Wang, Z., Sun, X., Barone, S., et al. (2010). Deletion of the Anion Exchanger Slc26a4 (Pendrin) Decreases Apical Cl−/HCO3−exchanger Activity and Impairs Bicarbonate Secretion in Kidney Collecting Duct. *Am. J. Physiology-Cell Physiol.* 299 (1), C33–C41. doi:10.1152/ajpcell.00033.2010

Bashour, A.-M., Fullerton, A. T., Hart, M. J., and Bloom, G. S. (1997). IQGAP1, a Rac- and CDC42-Binding Protein, Directly Binds and Cross-Links Microfilaments. *J. Cel Biol* 137 (7), 1555–1566. doi:10.1083/jcb.137.7.1555

Bertrand, C. A., Zhang, R., Pilewski, J. M., and Frizzell, R. A. (2009). SLC26A9 Is a Constitutively Active, CFTR-Regulated Anion Conductance in Human Bronchial Epithelia. *J. Gen. Physiol.* 133 (4), 421–438. doi:10.1085/jgp.200810097

Bonar, P. T., and Casey, J. R. (2008). Plasma Membrane Cl-/hco3-Exchangers: Structure, Mechanism and Physiology. *Channels* 2 (5), 337–345. doi:10.4161/chan.2.5.6899

Cheung, P. W., Nomura, N., Nair, A. V., Pathomthongtaweechai, N., Ueberdiek, L., Lu, H. A. J., et al. (2016). EGF Receptor Inhibition by Erlotinib Increases Aquaporin 2-Mediated Renal Water Reabsorption. *Jasn* 27 (10), 3105–3116. doi:10.1681/ASN.2015080903

Dossena, S., Nofziger, C., Tamma, G., Bernardinelli, E., Vanoni, S., Nowak, C., et al. (2011). Molecular and Functional Characterization of Human Pendrin and its Allelic Variants. *Cell Physiol Biochem* 28 (3), 451–466. doi:10.1159/000335107

Fukata, M., Kuroda, S., Fujii, K., Nakamura, T., Shoji, I., Matsuura, Y., et al. (1997). Regulation of Cross-Linking of Actin Filament by IQGAP1, a Target for Cdc42. *J. Biol. Chem.* 272 (47), 29579–29583. doi:10.1074/jbc.272.47.29579

Gietz, R. D., Robbins, A., Graham, K. C., Triggs-Raine, B., and Woods, R. A. (1997). Identification of Proteins that Interact with a Protein of Interest: Applications of the Yeast Two-Hybrid System. *Mol. Cel Biochem.* 172 (1–2), 67–79. doi:10.1007/978-1-4615-6353-2_7

Gordon, S., Lin, H.-H., Hamann, J. r., Kwakkenbos, M. J., Kop, E. N., Stacey, M., et al. (2004). The EGF-TM7 Family: a Postgenomic View. *Immunogenetics* 55 (10), 655–666. doi:10.1007/s00251-003-0625-2

Hedman, A. C., Smith, J. M., and Sacks, D. B. (2015). The Biology of IQGAP Proteins: beyond the Cytoskeleton. *EMBO Rep.* 16 (4), 427–446. doi:10.15252/embr.201439834

Hillesheim, J., Riederer, B., Tuo, B., Chen, M., Manns, M., Biber, J., et al. (2007). Down Regulation of Small Intestinal Ion Transport in PDZK1- (CAP70/NHERF3) Deficient Mice. *Pflugers Arch. - Eur. J. Physiol.* 454 (4), 575–586. doi:10.1007/s00424-007-0239-x

Jacquemet, G., Morgan, M. R., Byron, A., Humphries, J. D., Choi, C. K., Chen, C. S., et al. (2013). Rac1 Is Deactivated at Integrin Activation Sites *via* an IQGAP1/filamin-A/RacGAP1 Pathway. *J. Cel Sci* 126 (Pt 18), 4121–4135. doi:10.1242/jcs.121988

Johnson, M. A., Sharma, M., Mok, M. T. S., and Henderson, B. R. (2013). Stimulation of *In Vivo* Nuclear Transport Dynamics of Actin and its Co-factors IQGAP1 and Rac1 in Response to DNA Replication Stress. *Biochim. Biophys. Acta (Bba) - Mol. Cel Res.* 1833 (10), 2334–2347. doi:10.1016/j.bbamcr.2013.06.002

Joung, J. K., Ramm, E. I., and Pabo, C. O. (2000). A Bacterial Two-Hybrid Selection System for Studying Protein-DNA and Protein-Protein Interactions. *Proc. Natl. Acad. Sci. U.S.A.* 97 (13), 7382–7387. doi:10.1073/pnas.110149297

Kim, N.-H., Cheong, K. A., Lee, T. R., and Lee, A.-Y. (2012). PDZK1 Upregulation in Estrogen-Related Hyperpigmentation in Melasma. *J. Invest. Dermatol.* 132 (11), 2622–2631. doi:10.1038/jid.2012.175

Ko, S. B. H., Zeng, W., Dorwart, M. R., Luo, X., Kim, K. H., Millen, L., et al. (2004). Gating of CFTR by the STAS Domain of SLC26 Transporters. *Nat. Cel Biol* 6 (4), 343–350. doi:10.1038/ncb1115

Lai, L.-W., Yong, K.-C., and Lien, Y.-H. H. (2008). Site-specific Expression of IQGAP1, a Key Mediator of Cytoskeleton, in Mouse Renal Tubules. *J. Histochem. Cytochem.* 56 (7), 659–666. doi:10.1369/jhc.2008.950113

Lee, J. H., Nam, J. H., Park, J., Kang, D.-W., Kim, J. Y., Lee, M. G., et al. (2012). Regulation of SLC26A3 Activity by NHERF4 PDZ-Mediated Interaction. *Cell Signal.* 24 (9), 1821–1830. doi:10.1016/j.cellsig.2012.05.010

Li, H. C., Li, E. Y., Neumeier, L., Conforti, L., and Soleimani, M. (2007). Identification of a Novel Signal in the Cytoplasmic Tail of the Na+:HCO3−cotransporter NBC1 that Mediates Basolateral Targeting. *Am. J. Physiology-Renal Physiol.* 292 (4), F1245–F1255. doi:10.1152/ajprenal.00410.2006

Li, H. C., Worrell, R. T., Matthews, J. B., Husseinzadeh, H., Neumeier, L., Petrovic, S., et al. (2004). Identification of a Carboxyl-Terminal Motif Essential for the Targeting of Na+-HCO3- Cotransporter NBC1 to the Basolateral Membrane. *J. Biol. Chem.* 279 (41), 43190–43197. doi:10.1074/jbc.M405780200

Liu, Y., Liang, W., Yang, Y., Pan, Y., Yang, Q., Chen, X., et al. (2015). IQGAP1 Regulates Actin Cytoskeleton Organization in Podocytes through Interaction with Nephrin. *Cell Signal.* 27 (4), 867–877. doi:10.1016/j.cellsig.2015.01.015

Lohi, H., Lamprecht, G., Markovich, D., Heil, A., Kujala, M., Seidler, U., et al. (2003). Isoforms of SLC26A6 Mediate Anion Transport and Have Functional PDZ Interaction Domains. *Am. J. Physiology-Cell Physiol.* 284 (3), C769–C779. doi:10.1152/ajpcell.00270.2002

Mohebbi, N., Perna, A., van der Wijst, J., Becker, H. M., Capasso, G., and Wagner, C. A. (2013). Regulation of Two Renal Chloride Transporters, AE1 and Pendrin, by Electrolytes and Aldosterone. *PLoS One* 8 (1), e55286. doi:10.1371/journal.pone.0055286

Nammalwar, R. C., Heil, A., and Gerke, V. (2015). Ezrin Interacts with the Scaffold Protein IQGAP1 and Affects its Cortical Localization. *Biochim. Biophys. Acta (Bba) - Mol. Cel Res.* 1853 (9), 2086–2094. doi:10.1016/j.bbamcr.2014.12.026

Nauert, J. B., Rigas, J. D., and Lester, L. B. (2003). Identification of an IQGAP1/AKAP79 Complex in ?-cells. *J. Cel. Biochem.* 90 (1), 97–108. doi:10.1002/jcb.10604

Petrovic, S., Amlal, H., Sun, X., Karet, F., Barone, S., and Soleimani, M. (2006). Vasopressin Induces Expression of the Cl−/HCO3− Exchanger SLC26A7 in Kidney Medullary Collecting Ducts of Brattleboro Rats. *Am. J. Physiology-Renal Physiol.* 290 (5), F1194–F1201. doi:10.1152/ajprenal.00247.2005

Petrovic, S., Ju, X., Barone, S., Seidler, U., Alper, S. L., Lohi, H., et al. (2003). Identification of a Basolateral Cl−/HCO 3 − Exchanger Specific to Gastric Parietal Cells. *Am. J. Physiology-Gastrointestinal Liver Physiol.* 284 (6), G1093–G1103. doi:10.1152/ajpgi.00454.2002

Rahmati, N., Kunzelmann, K., Xu, J., Barone, S., Sirianant, L., De Zeeuw, C. I., et al. (2013). Slc26a11 Is Prominently Expressed in the Brain and Functions as a Chloride Channel: Expression in Purkinje Cells and Stimulation of V H+-ATPase. *Pflugers Arch. - Eur. J. Physiol.* 465 (11), 1583–1597. doi:10.1007/s00424-013-1300-6

Roesch, S., Rasp, G., Sarikas, A., and Dossena, S. (2021). Genetic Determinants of Non-syndromic Enlarged Vestibular Aqueduct: A Review. *Audiol. Res.* 11 (3), 423–442. doi:10.3390/audiolres11030040

Rossmann, H., Jacob, P., Baisch, S., Hassoun, R., Meier, J., Natour, D., et al. (2005). The CFTR Associated Protein CAP70 Interacts with the Apical Cl-/HCO3- Exchanger DRA in Rabbit Small Intestinal Mucosa. *Biochemistry* 44, 4477–4487. doi:10.1021/bi048828b

Royaux, I. E., Wall, S. M., Karniski, L. P., Everett, L. A., Suzuki, K., Knepper, M. A., et al. (2001). Pendrin, Encoded by the Pendred Syndrome Gene, Resides in the Apical Region of Renal Intercalated Cells and Mediates Bicarbonate Secretion. *Proc. Natl. Acad. Sci. U.S.A.* 98 (7), 4221–4226. doi:10.1073/pnas.071516798

Russo, A., Ranieri, M., Di Mise, A., Dossena, S., Pellegrino, T., Furia, E., et al. (2017). Interleukin-13 Increases Pendrin Abundance to the Cell Surface in Bronchial NCI-H292 Cells *via* Rho/actin Signaling. *Pflugers Arch. - Eur. J. Physiol.* 469 (9), 1163–1176. doi:10.1007/s00424-017-1970-6

Sinđić, A., Chang, M.-H., Mount, D. B., and Romero, M. F. (2007). Renal Physiology of SLC26 Anion Exchangers. *Curr. Opin. Nephrol. Hypertens.* 16 (5), 484–490. doi:10.1097/MNH.0b013e3282e7d7d0

Soleimani, M., Greeley, T., Petrovic, S., Wang, Z., Amlal, H., Kopp, P., et al. (2001). Pendrin: an Apical Cl−/OH−/HCO3 −exchanger in the Kidney Cortex. *Am. J. Physiology-Renal Physiol.* 280 (2), F356–F364. doi:10.1152/ajprenal.2001.280.2.F356

Soleimani, M. (2013). SLC26 Cl -/HCO 3 - Exchangers in the Kidney: Roles in Health and Disease. *Kidney Int.* 84 (4), 657–666. doi:10.1038/ki.2013.138

Thomson, R. B., Wang, T., Thomson, B. R., Tarrats, L., Girardi, A., Mentone, S., et al. (2005). Role of PDZK1 in Membrane Expression of Renal brush Border Ion Exchangers. *Proc. Natl. Acad. Sci. U.S.A.* 102 (37), 13331–13336. doi:10.1073/pnas.0506578102

Vallet, M., Picard, N., Loffing-Cueni, D., Fysekidis, M., Bloch-Faure, M., Deschênes, G., et al. (2006). Pendrin Regulation in Mouse Kidney Primarily Is Chloride-dependent. *Jasn* 17 (8), 2153–2163. doi:10.1681/ASN.2005101054

Wall, S. M., Hassell, K. A., Royaux, I. E., Green, E. D., Chang, J. Y., Shipley, G. L., et al. (2003). Localization of Pendrin in Mouse Kidney. *Am. J. Physiology-Renal Physiol.* 284 (1), F229–F241. doi:10.1152/ajprenal.00147.2002

Wall, S. M., and Weinstein, A. M. (2013). Cortical Distal Nephron Cl−transport in Volume Homeostasis and Blood Pressure Regulation. *Am. J. Physiology-Renal Physiol.* 305 (4), F427–F438. doi:10.1152/ajprenal.00022.2013

White, C. D., Erdemir, H. H., and Sacks, D. B. (2012). IQGAP1 and its Binding Proteins Control Diverse Biological Functions. *Cell Signal.* 24 (4), 826–834. doi:10.1016/j.cellsig.2011.12.005

Xu, J., Barone, S., Li, H., Holiday, S., Zahedi, K., and Soleimani, M. (2011). Slc26a11, a Chloride Transporter, Localizes with the Vacuolar H + -ATPase of A-Intercalated Cells of the Kidney. *Kidney Int.* 80 (9), 926–937. doi:10.1038/ki.2011.196

Xu, J., Worrell, R. T., Li, H. C., Barone, S. L., Petrovic, S., Amlal, H., et al. (2006). Chloride/bicarbonate Exchanger SLC26A7 Is Localized in Endosomes in Medullary Collecting Duct Cells and Is Targeted to the Basolateral Membrane in Hypertonicity and Potassium Depletion. *Jasn* 17 (4), 956–967. doi:10.1681/ASN.2005111174

Zheng, L., Zheng, J., Whitlon, D. S., Garcia-Anoveros, J., and Bartles, J. R. (2010). Targeting of the Hair Cell Proteins Cadherin 23, Harmonin, Myosin XVa, Espin, and Prestin in an Epithelial Cell Model. *J. Neurosci.* 30 (21), 7187–7201. doi:10.1523/JNEUROSCI.0852-10.2010

Conflict of Interest: The authors declare that the research was conducted in the absence of any commercial or financial relationships that could be construed as a potential conflict of interest.

Publisher's Note: All claims expressed in this article are solely those of the authors and do not necessarily represent those of their affiliated organizations, or those of the publisher, the editors and the reviewers. Any product that may be evaluated in this article, or claim that may be made by its manufacturer, is not guaranteed or endorsed by the publisher.

frontiers | Frontiers in Cell and Developmental Biology

ORIGINAL RESEARCH
published: 03 June 2022
doi: 10.3389/fcell.2022.891996

Carbamazepine Increases the Risk of Sudden Cardiac Arrest by a Reduction of the Cardiac Sodium Current

Lixia Jia[1†], *Talip E. Eroglu*[2,3†], *Ronald Wilders*[4], *Arie O. Verkerk*[1,4] *and Hanno L. Tan*[1,5*]

[1]Department of Clinical and Experimental Cardiology, Heart Center, Amsterdam UMC, University of Amsterdam, Amsterdam, Netherlands, [2]Division of Pharmacoepidemiology and Clinical Pharmacology, Utrecht Institute for Pharmaceutical Sciences, Utrecht University, Utrecht, Netherlands, [3]Department of Cardiology, Herlev and Gentofte Hospital, University of Copenhagen, Gentofte, Denmark, [4]Department of Medical Biology, Amsterdam Cardiovascular Sciences, Amsterdam UMC, University of Amsterdam, Amsterdam, Netherlands, [5]Netherlands Heart Institute, Utrecht, Netherlands

OPEN ACCESS

Edited by:
Alessia Remigante,
University of Messina, Italy

Reviewed by:
Michael Pusch,
National Research Council (CNR), Italy
Roberta De Zio,
University of Bari Aldo Moro, Italy

***Correspondence:**
Hanno L. Tan
h.l.tan@amsterdamumc.nl

[†]*These authors have contributed equally to this work and share first authorship*

Specialty section:
This article was submitted to Cellular Biochemistry, a section of the journal Frontiers in Cell and Developmental Biology

Received: *08 March 2022*
Accepted: *09 May 2022*
Published: *03 June 2022*

Citation:
Jia L, Eroglu TE, Wilders R, Verkerk AO and Tan HL (2022) Carbamazepine Increases the Risk of Sudden Cardiac Arrest by a Reduction of the Cardiac Sodium Current. Front. Cell Dev. Biol. 10:891996. doi: 10.3389/fcell.2022.891996

Aim: To assess the risk of sudden cardiac arrest (SCA) associated with the use of carbamazepine (CBZ) and establish the possible underlying cellular electrophysiological mechanisms.

Methods: The SCA risk association with CBZ was studied in general population cohorts using a case–control design (n = 5,473 SCA cases, 21,866 non-SCA controls). Effects of 1–100 μM CBZ on action potentials (APs) and individual membrane currents were determined in isolated rabbit and human cardiomyocytes using the patch clamp technique.

Results: CBZ use was associated with increased risk of SCA compared with no use (adjusted odds ratio 1.90 [95% confidence interval: 1.12–3.24]). CBZ reduced the AP upstroke velocity of rabbit and human cardiomyocytes, without prominent changes in other AP parameters. The reduction occurred at ≥30 μM and was frequency-dependent with a more pronounced reduction at high stimulus frequencies. The cardiac sodium current (I_{Na}) was reduced at ≥30 μM; this was accompanied by a hyperpolarizing shift in the voltage-dependency of inactivation. The recovery from inactivation was slower, which is consistent with the more pronounced AP upstroke velocity reduction at high stimulus frequencies. The main cardiac K^+ and Ca^{2+} currents were unaffected, except reduction of L-type Ca^{2+} current by 100 μM CBZ.

Conclusion: CBZ use is associated with an increased risk of SCA in the general population. At concentrations of 30 μM and above, CBZ reduces AP upstroke velocity and I_{Na} in cardiomyocytes. Since the concentration of 30 μM is well within the therapeutic range (20–40 μM), we conclude that CBZ increases the risk of SCA by a reduction of the cardiac I_{Na}.

Keywords: anti-epileptic drugs, sudden cardiac arrest, risk association, cardiomyocytes, sodium current, action potentials

1 INTRODUCTION

Sudden cardiac arrest (SCA) is a global public health problem with an annual incidence of 40–100 per 100,000 individuals (Fishman et al., 2010; Hayashi et al., 2015). SCA accounts for 50% of deaths from cardiovascular disease and 15–20% of all deaths in industrialized societies (Zipes and Wellens 1998; Wong et al., 2019). Most cases of SCA are caused by cardiac arrhythmias (ventricular fibrillation (VF) or ventricular tachycardia (VT)). Such arrhythmias may arise from functional changes in the ion channels that underlie the cardiac action potential (AP) (Antzelevitch and Burashnikov 2011). These functional changes may be evoked by various drugs used for the treatment of cardiac or non-cardiac conditions. This is best known for drugs that affect cardiac repolarization (QT prolonging drugs) (Haverkamp et al., 2000). However, there is increasing recognition that it also applies to drugs that affect cardiac depolarization (Bardai et al., 2013). An example of such drugs are anti-epileptic drugs (AEDs) (Bardai et al., 2015). Some AEDs are primarily developed for blocking neuronal ion channels, e.g., voltage-gated Na^+, Ca^{2+} or K^+ channels, while other AEDs act by impacting on neurotransmitters such as γ-aminobutyric acid (Davies 1995; Sills and Rogawski 2020). Importantly, neuronal and cardiac ion channel isoforms are highly homologous (Heinemann et al., 1994; Fozzard and Hanck 1996). Thus, AEDs may not only affect neuronal electrical activity but may also act on cardiac ion channels, thereby causing cardiac arrhythmias (Danielsson et al., 2005). Accordingly, the increased SCA risk of epilepsy patients may be partly explained by AED use (Bardai et al., 2015).

Carbamazepine (CBZ) is a prime example of such drugs, because it has high efficacy in the treatment of epilepsy (Pellock 2000) through various mechanism, including block of neuronal Na^+ channels (Ragsdale and Avoli 1998; Catterall 1999; Sun et al., 2006; Lasoń et al., 2013). CBZ may also impact on cardiac electrophysiology as suggested by several CBZ-related case reports and retrospective studies, which report bradycardia, sinoatrial and atrioventricular block, QRS interval prolongation, cardiac arrhythmias, and cardiac arrest, as summarized in **Table 1** (Beermann et al., 1975; Hamilton 1978; Herzberg 1978; Boesen et al., 1983; Leslie et al., 1983; Benassi et al., 1987; Kasarskis et al., 1992; Hojer et al., 1993; Schmidt and Schmitz-Buhl 1995; Koutsampasopoulos et al., 2014). Still, the underlying electrophysiological mechanism is not completely understood. Our current study has two aims: 1) to establish whether CBZ is associated with increased SCA risk in a large dataset from a cohort that was specifically designed to study SCA in the general population; 2) to establish the effects of CBZ on cardiac APs and individual membrane currents of rabbit and human cardiomyocytes using patch clamp methodology.

2 METHODS AND MATERIALS

2.1 Epidemiological Studies

We studied the SCA risk associated with CBZ use in a case–control design. Cases were patients who suffered out-of-hospital SCA with presumed cardiac causes in the Amsterdam Resuscitation Studies (ARREST) registry. ARREST is an ongoing, prospective, population-based registry that we designed to study the occurrence and outcome of out-of-hospital SCA in the general population. Patients are collected in collaboration with dispatch centers, ambulance personnel, pharmacies and hospitals in one contiguous study region in the Netherlands (2.6 million inhabitants, urban and rural areas), thereby assuring collection of >95% of all out-of-hospital SCA patients in the study region and minimizing inclusion bias (Blom et al., 2014). Each out-of-hospital SCA case was matched with up to five non-SCA controls based on age, sex and index-date (SCA-date). Non-SCA controls were randomly drawn from the general population using the PHARMO Database Network (Kuiper et al., 2020), which contains, among other things, complete medication data from the community pharmacists across the Netherlands.

TABLE 1 | Cardiac arrhythmias observed in patients using CBZ.

Source	Sex/Age (years) of Patient	Cardiac Arrhythmia Reported	CBZ Dose (Daily) or Serum/Plasma Level
Beermann et al. (1975)	F/66	3rd degree AV block	1,200 mg
Herzberg (1978)	F/85	sinus bradycardia	1,000 mg
Hamilton (1978)	F/77	sinus bradycardia	1,200 mg
Leslie et al. (1983)	M/50	sinus arrest	overdose (20 g), plasma level 62 mg/L (261 μM)
Boesen et al. (1983)	F/72	3rd degree AV block	400 mg
	F/82	SA block	600 mg
	F/86	SA block	400 mg
Benassi et al. (1987)	F/55	3rd degree AV block	800 mg, plasma level 8.5 μg/mL
	F/59	3rd degree AV block	800 mg, plasma level 4.7 μg/mL
Kasarskis et al. (1992)	F/58	bradycardia, AV block, sinus arrest	peak serum level 79.4 μM
Hojer et al. (1993)	M/34	ventricular fibrillation	peak serum level 218 μM
	M/54	AV block	peak serum level 285 μM
	M/83	3rd degree AV block	peak serum level 220 μM
	F/20	QRS widening	peak serum level 176 μM
Schmidt and Schmitz-Buhl (1995)	not reported	bradycardia/AV block (n = 2), cardiac arrest (n = 2)	overdose (dose not reported)
Koutsampasopoulos et al. (2014)	F/82	3rd degree AV block	1,200 mg

AV, atrioventricular; F, female; M, male; SA, sinoatrial.

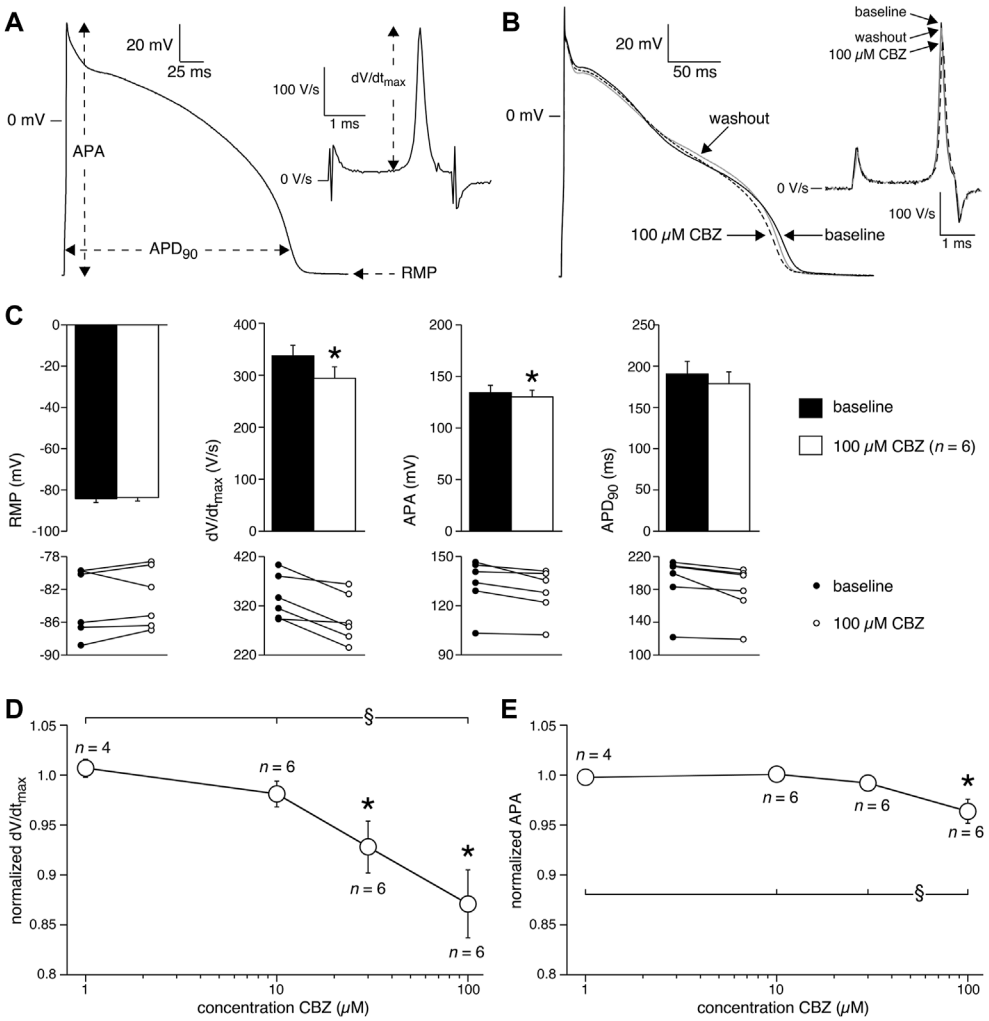

FIGURE 1 | Carbamazepine (CBZ) reduces the action potential (AP) upstroke velocity and AP amplitude of rabbit ventricular cardiomyocytes. **(A)** AP recording illustrating the analyzed AP parameters. Inset: time derivative (dV/dt) of the AP upstroke on an expanded time scale. RMP, resting membrane potential; APA, AP amplitude; APD_{90}, AP duration at 90% of repolarization; dV/dt_{max}, maximal AP upstroke velocity. **(B)** Superimposed representative APs at 1 Hz under baseline conditions, in presence of 100 μM CBZ, and upon washout of the drug. Inset: time derivatives of the AP upstrokes. **(C)** Average AP characteristics at 1 Hz (top panels) and individual (paired) data points (bottom panels). *$p < 0.05$ CBZ versus baseline (One-Way RM ANOVA). **(D,E)** Average normalized dV/dt_{max} **(D)** and APA **(E)** at 1 Hz in response to 1, 10, 30, and 100 μM CBZ. Values are normalized to the values measured under baseline conditions. Numbers near symbols indicate the number of cells (*n*) measured at a given concentration. *$p < 0.05$ CBZ versus baseline (One-Way RM ANOVA); §$p < 0.05$ CBZ 100 μM versus lower concentrations (One-Way ANOVA).

Drug dispensing records for drugs prescription were obtained from computerized databases of pharmacists. Use of CBZ was defined as having a drug-dispensing record within 90 days prior to index-date. We chose a period of 90 days, since, in the Netherlands, prescription length for drugs used for chronic disease is 90 days.

For all cases and controls, we included cardiovascular disease and diabetes mellitus in our analyses because these are known risk factors for SCA. We derived cardiovascular disease and diabetes mellitus by using medication use as proxies as we did previously (Eroglu et al., 2020). Cardiovascular disease was defined by use of β-adrenoceptor blockers, calcium channel blockers, diuretics, renin-angiotensin system inhibitors, diuretics, antithrombotics, nitrates and statins. Diabetes mellitus was defined by use of antidiabetics. Patients were considered users of cardiovascular drugs and antidiabetics if there was any drug-dispensing record within 6 months prior to index-date.

2.2 Cellular Electrophysiological Studies

2.2.1 Cell Preparations

Full details of rabbit ventricular and human atrial cell isolation procedures are provided in the **Supplementary Material**. The investigation using rabbits conformed to the Guide for the Care and Use of Laboratory Animals (NIH Publication 85–23, 1996) and was approved by the institutional animal experiments committee. The human atrial cardiomyocytes were isolated

from explanted hearts of male patients with end-stage heart failure caused by ischemic cardiomyopathy. All patients were in New York Heart Association functional class IV and received standard therapy for chronic heart failure (**Supplementary Table S1**). Informed consent was obtained before heart transplantation, and the protocol complied with institutional guidelines.

2.2.2 Action Potentials

APs were measured at 36 ± 0.2°C in modified Tyrode's solution containing (in mM): NaCl 140, KCl 5.4, $CaCl_2$ 1.8, $MgCl_2$ 1.0, glucose 5.5, HEPES 5.0; pH 7.4 (NaOH). Patch pipettes were filled with solution composed of (in mM): K-gluconate 125, KCl 20, NaCl 5.0, K_2ATP 2.0, HEPES 10; pH 7.2 (KOH). Detailed recording procedures are provided in the **Supplementary Material**. APs were evoked at stimulation rates of 0.2–4 Hz using square 3-ms current pulses through the patch pipette. To reduce variability in the moment of AP upstroke, stimulus amplitude was chosen such that the AP upstroke originated just before the end of the stimulus, as we described previously (Remme et al., 2006). The maximal AP upstroke velocity (dV/dt_{max}) was determined from the first derivative of the AP upstroke from which the approximately constant initial dV/dt in response to the stimulus pulse was subtracted (**Figure 1A**, inset). In addition, we analyzed resting membrane potential (RMP), AP amplitude (APA), and AP duration at 90% repolarization (APD_{90}), as also shown in **Figure 1A**. AP parameters from 10 consecutive APs were averaged.

2.2.3 Membrane Current Measurements

The L-type Ca^{2+} current ($I_{Ca,L}$), inward rectifier K^+ current (I_{K1}), delayed rectifier K^+ current (I_K), and transient outward K^+ current (I_{to1}) were all measured at 36 ± 0.2°C with the same solutions as used for the AP measurements. However, I_{to1} was measured in the presence of $CdCl_2$ (0.25 mM) to block I_{Na} and $I_{Ca,L}$, thereby also preventing activation of the outward Ca^{2+}-activated Cl^- current (Verkerk et al., 2011). Suppression of these inward and outward currents allows accurate determination of I_{to1}. The whole-cell sodium current (I_{Na}) in freshly isolated cardiomyocytes is an extremely large and fast activating and inactivating membrane current, which for technical reasons cannot be reliably measured at a close-to-physiological temperature and normal Na^+ gradients over the cell membrane (see Berecki et al. (2010) and primary references cited therein). Therefore, we measured I_{Na} at room temperature with modified bath and pipette solutions (including an identical Na^+ concentration in pipette and bath solution), which allowed specific measurements of Na^+ currents only. Bath solution for I_{Na} measurements contained (in mM): NaCl 7.0, CsCl 133, $CaCl_2$ 1.8, $MgCl_2$ 1.2, glucose 11.0, HEPES 5.0, and nifedipine 0.05; pH 7.4 (CsOH). Patch pipettes for I_{Na} measurements were filled with (in mM): NaCl 3.0, CsCl 133, $MgCl_2$ 2.0, Na_2ATP 2.0, TEA-Cl 2.0, EGTA 10, HEPES 5.0; pH 7.3 (CsOH). The membrane currents were measured with specific voltage clamp protocols as depicted in the insets to **Figures 3–5** and described in detail in the **Supplementary Material**. Recording procedures and data analysis are also described in detail in the **Supplementary Material**.

2.2.4 Preparation of Carbamazepine

CBZ obtained from Sigma-Aldrich (St. Louis, MO, US) was freshly dissolved every day in dimethyl sulfoxide (DMSO) as 100 mM stock and diluted in the bath solution to the desired concentration just before use. APs and membrane currents were measured in the presence of the vehicle DMSO and after wash-in of CBZ (1, 10, 30, or 100 μM) in the same cardiomyocytes. In order to obtain steady-state conditions, signals were recorded after a 5 min stimulation period, i.e. under baseline conditions, and 5 min after application of CBZ.

2.3 Statistics

Data are presented as mean ± SEM. The association between CBZ and SCA was estimated by calculating the adjusted odds ratio with 95% confidence interval using conditional logistic regression by adjusting for the use of cardiovascular drugs and antidiabetics. For the patch-clamp study, comparisons were made using One-Way ANOVA, One-Way Repeated Measures (RM) ANOVA, or Two-Way RM ANOVA, followed by pairwise comparison using the Student-Newman-Keuls *post hoc* test. For the epidemiological study, differences in baseline values for binary variables between cases and controls were tested using a chi-square test. Differences in baseline values for continuous variables between cases and controls were tested using an independent *t*-test. $p < 0.05$ defined statistical significance.

3 RESULTS

3.1 Carbamazepine Use and the Risk of Sudden Cardiac Arrest

We first conducted a systematic study to establish whether CBZ use is associated with increased risk of SCA in the general population. We identified 5,473 SCA cases, and matched them to 21,866 non-SCA controls. The mean age of the cases was 68.8 years and 69.9% were male. As expected, the prevalence of cardiovascular drugs and antidiabetics was higher among the cases than controls (**Table 2**). We observed that the proportion of CBZ users was significantly higher among cases ($n = 24$, 0.44%) than among controls ($n = 41$, 0.19%) (**Table 3**). After adjusting for cardiovascular drugs and antidiabetics, we found that use of CBZ was associated with increased risk of SCA compared with no use of CBZ, with an adjusted odds ratio of 1.90 (95% confidence interval: 1.12–3.24; **Table 3**).

3.2 Effects of Carbamazepine on Action Potentials of Rabbit Ventricular Cardiomyocytes

Next, we characterized the effects of 1, 10, 30, and 100 μM CBZ on APs elicited at 1 Hz in rabbit ventricular cardiomyocytes. **Figure 1B** shows typical APs under baseline conditions (solid line), in the presence of 100 μM CBZ (dashed line), and upon washout of the drug (gray line). Exposure to 100 μM CBZ resulted in substantial alterations in AP morphology in comparison to baseline conditions, particularly a decrease in dV/dt_{max} and APA

TABLE 2 | Characteristics of cases and controls.

	Cases (*n* = 5,473)	Controls (*n* = 21,866)
Age, years (mean ± SD)	68.8 ± 14.0	68.8 ± 14.0
Male sex	3,823 (69.9%)	15,263 (69.8%)
Cardiovascular pharmacotherapy[a]		
Beta blockers	1,998 (36.5%)	3,839 (17.6%)
Digoxin	295 (5.4%)	334 (1.5%)
Renin-angiotensin system inhibitors	2,073 (37.9%)	4,802 (22.0%)
Calcium channel blockers	902 (16.5%)	2,016 (9.2%)
Antithrombotics	2,299 (42.0%)	4,853 (22.2%)
Diuretics	1,590 (29.1%)	2,712 (12.4%)
Nitrates	574 (10.5%)	841 (3.9%)
Antiarrhythmic drugs class 1 or 3[b]	114 (2.1%)	183 (0.8%)
Antidiabetics	936 (17.1%)	2,145 (9.8%)

[a]*Defined as use within 6 months before index date.*
[b]*Defined as use within 90 days before index date.*

TABLE 3 | Carbamazepine (CBZ) and risk of out-of-hospital cardiac arrest.

	Cases (*n* = 5,473)	Controls (*n* = 21,866)	Crude Odds Ratio	Adjusted Odds Ratio
No use of CBZ	5,438 (99.4%)	21,807 (99.7%)	1.0 (reference)	1.0 (reference)
Use of CBZ	24 (0.44%)[a]	41 (0.19%)[a]	2.34 (1.42–3.89[b])	1.90 (1.12–3.24[b])

[a]*Not included are 11 cases (0.20%) and 18 control (0.08%) who used CBZ in combination with other antiepileptic drugs.*
[b]*95% confidence interval.*

(as measures of cardiac depolarization) and a slight decrease of APD_{90} (as a measure of cardiac repolarization). The effects were partially reversible upon washout of the drug. Average data are shown in the top panels of **Figure 1C**, with the individual (paired) data of the 6 cells tested shown in the bottom panels. These data indicate that dV/dt_{max} and APA were significantly decreased by 12.9 ± 3.3% (294 ± 22 (CBZ) vs. 337 ± 20 V/s (baseline)) and 3.6 ± 1.2% (128 ± 6.5 (CBZ) vs. 133 ± 7.2 mV (baseline)), respectively. The effects of CBZ on dV/dt_{max} and APA were concentration dependent (**Figures 1D,E**). At 100 μM CBZ, RMP was unaffected (–83.0 ± 1.7 (CBZ) vs. –83.5 ± 1.8 mV (baseline)) and the small effect on APD_{90} (177 ± 14 (CBZ) vs. 189 ± 15 ms (baseline)) did not reach the level of statistical significance (**Figure 1C**). Similarly, no statistically significant effects on RMP and APD_{90} were observed at other stimulus frequencies or at lower CBZ concentrations (**Supplementary Figure S1**).

The upstroke of APs in working cardiomyocytes is mainly due to I_{Na} (see Berecki et al. (2010) and primary references cited therein), which suggests that the CBZ-induced decrease in dV/dt_{max} is due to blockade of I_{Na}. It is well-known that drugs may block I_{Na} in a voltage- and use-dependent manner (Bagal et al., 2015). The latter means that the amount of block may increase upon higher stimulus frequencies. **Figure 2A** shows typical AP time derivatives under baseline and 100 μM CBZ conditions at stimulus frequencies ranging from 0.2 to 4 Hz, while **Figure 2B** summarizes the average effects on dV/dt_{max} at 100 μM CBZ as well as lower concentrations. An increase in stimulus frequency resulted in a significantly lower dV/dt_{max} at every concentration tested (**Figure 2B**, filled squares; see also **Supplementary Figure S2**), consistent with a reduced I_{Na} recovery from inactivation at fast pacing rates (Berecki et al., 2010). In addition, the CBZ-induced decrease in dV/dt_{max} is more pronounced at higher stimulus frequencies (**Figure 2B**, open circles). For example, 100 μM CBZ decreased dV/dt_{max} by 14.1 ± 3.4% (294 ± 20 (CBZ) vs. 342 ± 18 V/s (baseline)) at 0.2 Hz, but by as much as 41.5 ± 12% (143 ± 21 (CBZ) vs. 264 ± 33 V/s (baseline)) at 4 Hz. Because APA and dV/dt_{max} are both importantly determined by I_{Na} (Krishnan and Antzelevitch 1991; Berecki et al., 2010), it is not surprising that the APA shows a largely similar concentration and frequency dependency as dV/dt_{max} (**Figures 2B,C**).

3.3 Effects of Carbamazepine on Membrane Currents of Rabbit Ventricular Cardiomyocytes

We next studied the effects of CBZ on the main membrane currents underlying cardiac APs in rabbit ventricular cardiomyocytes. First, we focused on the main current underlying the AP depolarization, i.e., I_{Na}. **Figure 3A** shows typical I_{Na} recordings (at −80 to 0 mV) and **Figure 3B** shows the average current-voltage (I-V) relationships of I_{Na} under baseline conditions and in the presence of 100 μM CBZ. CBZ significantly decreased I_{Na} in the voltage range from −45 to +10 mV, e.g., by 30.3 ± 6.7% at −30 mV (67.8 ± 6.7% (CBZ) vs. 97.3 ± 2.0% (baseline) of the maximal peak amplitude under baseline conditions). **Figure 3C** shows the dose-dependency of the CBZ effects on I_{Na} and demonstrates that I_{Na} was also significantly reduced by 30 μM CBZ. **Figure 3D** shows the steady-state activation and inactivation curves for I_{Na} under

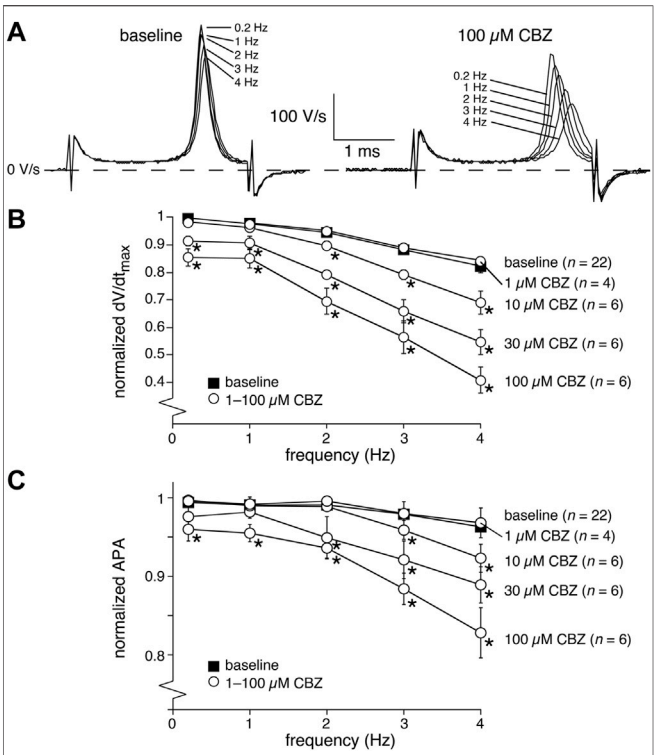

FIGURE 2 | Carbamazepine (CBZ) reduces the AP upstroke velocity and amplitude of rabbit ventricular cardiomyocytes in a frequency dependent manner. **(A)** Superimposed typical time derivatives (dV/dt) during the AP upstroke phase at stimulus frequencies ranging from 0.2 to 4 Hz under baseline conditions (left) and in presence of 100 μM CBZ (right). **(B)** Average dV/dt_{max} under baseline conditions (filled squares) and in response to 1–100 μM CBZ (open circles) at stimulus frequencies ranging from 0.2 to 4 Hz. Values are normalized to the highest dV/dt_{max} measured at 0.2–4 Hz under baseline conditions. *$p < 0.05$ CBZ versus baseline (Two-Way RM ANOVA). See **Supplementary Figure S2** for statistical significance of the frequency dependent effects. **(C)** Average APA under baseline conditions (filled squares) and in response to 1–100 μM CBZ (open circles) at stimulus frequencies ranging from 0.2 to 4 Hz. Values are normalized to the highest APA measured at 0.2–4 Hz under baseline conditions. *$p < 0.05$ CBZ versus baseline (Two-Way RM ANOVA).

baseline conditions and in the presence of 100 μM CBZ. While CBZ did not affect the voltage dependency of activation, the voltage dependency of inactivation was significantly shifted to more negative membrane potentials. On average, the negative shift in $V_{1/2}$ was 6.2 ± 1.3 mV (−90.4 ± 1.8 (CBZ) vs. −84.3 ± 1.0 mV (baseline)), while the slope of the inactivation curve was not significantly different between baseline (−5.0 ± 0.9 mV) and CBZ (−5.4 ± 0.7 mV). **Figures 3E,F**, show the recovery from inactivation of I_{Na}, with in **Figure 3E** typical I_{Na} recordings (bottom) obtained in response to a double-pulse protocol (top) with an interpulse interval of 100 ms, and in **Figure 3F** the average data with all interpulse intervals tested. CBZ results in a severe delay in the recovery from inactivation. For example, with an interpulse interval of 100 ms, recovery from inactivation was as large as 78.1 ± 4.5% at baseline, but only 15.4 ± 3.1% in the presence of CBZ.

Second, we studied the main currents underlying the AP repolarization. Although APD_{90} was not significantly affected by CBZ, a potential increase (or decrease) in outward currents can be balanced by a similar increase (or decrease) in inward currents, or vice versa. **Figure 4A** shows typical recordings (at 0 mV) and **Figure 4B** shows the average I-V relationships of the inward $I_{Ca,L}$ under baseline conditions and in the presence of 100 μM CBZ. CBZ significantly decreased the $I_{Ca,L}$ density in the voltage range from −20 to +20 mV (**Figure 4B**). **Figure 4C** shows that $I_{Ca,L}$ was only significantly reduced at the highest concentration of CBZ tested, i.e., 100 μM. The reduction in peak $I_{Ca,L}$ at 0 mV was 10.3 ± 3.7% (86.0 ± 3.0% (CBZ) vs. 96.2 ± 3.2% (baseline) of the maximal peak amplitude under baseline conditions). **Figure 4D** shows typical recordings and **Figure 4E** shows the average I-V relationships of the steady-state outward K^+ currents, I_K and I_{K1}, under baseline conditions and in the presence of 100 μM CBZ. **Figure 4F** shows the concentration dependency of I_K and I_{K1}. Neither I_K nor I_{K1} were significantly affected by CBZ. **Figure 4G** shows typical recordings and **Figure 4H** shows the average I-V relationships of I_{to1} under baseline and 100 μM CBZ conditions. **Figure 4I** shows the concentration dependency of I_{to1}. We observed no significant changes in the amplitude of I_{to1} at any voltage and concentration tested.

3.4 Effects of Carbamazepine on Action Potentials of Human Atrial Cardiomyocytes

Having established the effects of CBZ on AP properties and membrane current of rabbit cardiomyocytes, we measured the effects of 100 μM CBZ on APs and I_{Na} density of freshly isolated human atrial cardiomyocytes to study whether these effects may also occur in the human heart. In patch clamp experiments on single isolated human atrial cardiomyocytes, the amount of quiescent, Ca^{2+}-tolerant cells is typically low and non-depolarized cells are scarce (Verkerk et al., 2021). Here, we selected cardiomyocytes with an RMP of −75 mV or more negative, which generated stable APs after an initial 8–10 min period of continuous pacing at 1 Hz. **Figure 5A** shows typical APs at 1 Hz under baseline conditions and in the presence of 100 μM CBZ. Average AP parameters are summarized in the top panels of **Figure 5B**, with the individual (paired) data of the 5 cells tested shown in the bottom panels. Under baseline conditions, the pre-selected human atrial cardiomyocytes had an RMP of −81.9 ± 1.3 mV and a high maximum AP upstroke velocity, and the APs largely overshot the zero potential value. CBZ (100 μM) significantly reduced the AP upstroke velocity and significantly shortened AP duration, without affecting RMP or APA (**Figure 5B**). These effects are largely comparable to those in rabbit ventricular cardiomyocytes. For example, the AP upstroke velocity decreased significantly by 23.4 ± 6.5% (from 435 ± 58 (baseline) to 328 ± 30 V/s (CBZ)), while the APD_{90} was significantly decreased by 11.8 ± 3.5% (from 187 ± 49 (control) to 169 ± 51 ms (CBZ)). Furthermore, human APs showed a frequency dependency in maximum AP upstroke velocity with a decrease at higher frequencies (**Figure 5C**, filled circles). The frequency dependency in the presence of CBZ was more pronounced, indicating a similar use-

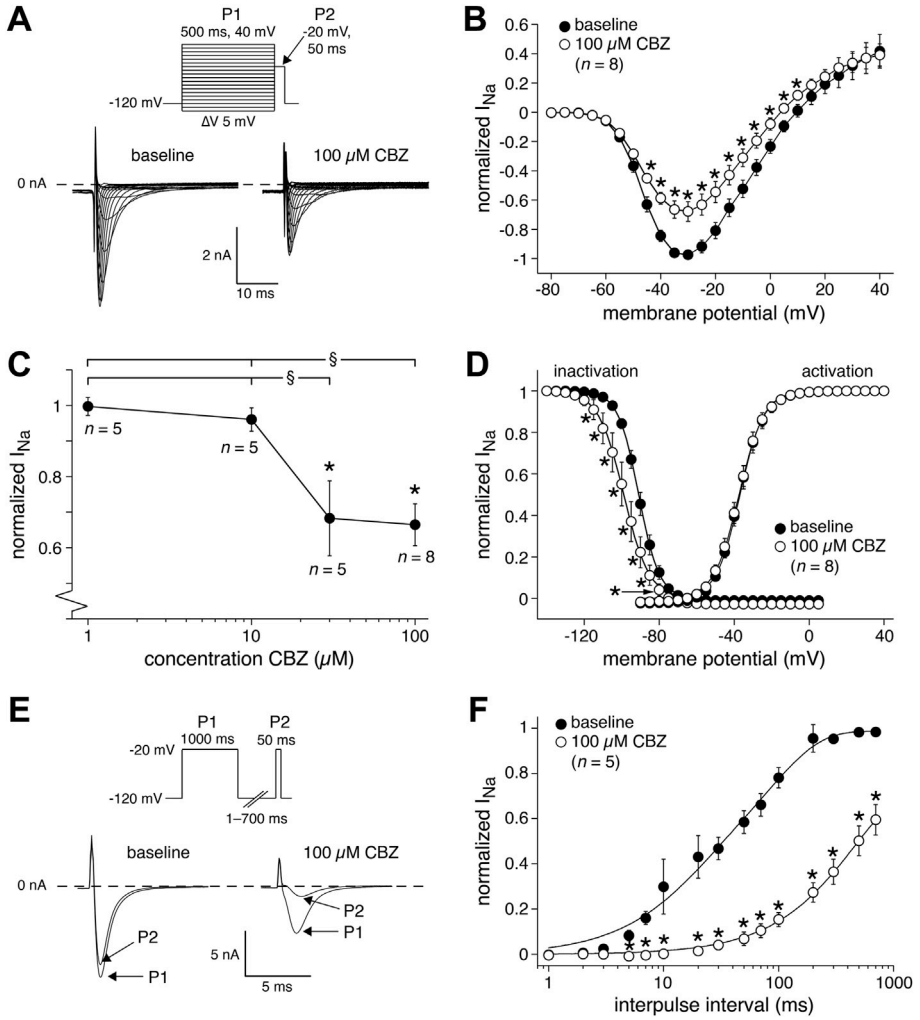

FIGURE 3 | Carbamazepine (CBZ) reduces the sodium current (I_{Na}) of rabbit ventricular cardiomyocytes in a use-dependent manner. **(A)** Typical I_{Na} recordings between –80 and 0 mV under baseline conditions and in presence of 100 μM CBZ. Inset: double-pulse voltage clamp protocol used to measure current-voltage (I–V) relationships **(B)** as well as the voltage dependency of (in)activation **(D)**. Cycle length was 5 s. **(B)** Average I-V relationship of I_{Na} under baseline conditions and in presence of 100 μM CBZ. I_{Na} was normalized to the maximal peak amplitude under baseline conditions, but peak current was set to –1 to retain the well-known inward direction of I_{Na}. $^{*}p < 0.05$ CBZ versus baseline (Two-Way RM ANOVA). **(C)** Concentration dependency of the CBZ effects on I_{Na} amplitude at –35 mV $^{*}p < 0.05$ CBZ versus baseline (One-Way RM ANOVA); $^{§}p < 0.05$ higher versus lower CBZ concentrations (One-Way ANOVA). **(D)** Voltage dependency of (in)activation. Solid lines are Boltzmann fits to the average data. $^{*}p < 0.05$ CBZ versus baseline (Two-Way RM ANOVA). **(E,F)** Recovery from I_{Na} inactivation measured with a double-pulse protocol (E, inset). **(E)** Typical I_{Na} recordings under baseline conditions and in presence of 100 μM CBZ with an interpulse interval of 100 ms. **(F)** Average data. Solid lines are double-exponential fits to the average data. $^{*}p < 0.05$ CBZ versus baseline (Two-Way RM ANOVA).

dependent reduction of I_{Na} by CBZ (**Figure 5C**, open circles) as found in rabbit cardiomyocytes. **Figure 5D** (top panel), shows the I-V relationships of I_{Na} in human atrial cardiomyocytes under baseline conditions and in presence of 100 μM CBZ. CBZ significantly reduced I_{Na} density, without changes in $V_{1/2}$ and k of activation (**Figure 5D**, bottom panels).

4 DISCUSSION

The main findings of the present study are: 1) CBZ use is associated with increased SCA risk in the general population; 2) CBZ reduces cardiac AP upstroke velocity and I_{Na} in human and rabbit cardiomyocytes; 3) CBZ results in a tendency to (in rabbit) and significant (in human) cardiac AP shortening and reduces $I_{Ca,L}$, while leaving sarcolemmal potassium currents unaltered. All of the observed effects are consistent with each other: reduction in cardiac AP upstroke velocity is well explained by reduction in I_{Na} (Berecki et al., 2010), and may, in turn, lead to reduction in cardiac excitability and conduction velocity of the excitation wavefront in the heart, as represented by CBZ-induced QRS interval prolongation (Leslie et al., 1983). It also facilitates reentrant excitation, VF/VT, and SCA, as shown for the use of class IC antiarrhythmic drugs (potent I_{Na} blockers) (Rogers et al., 1989), and in Brugada syndrome (where 20% of patients have an identifiable loss-of-function mutation in *SCN5A*, the gene that

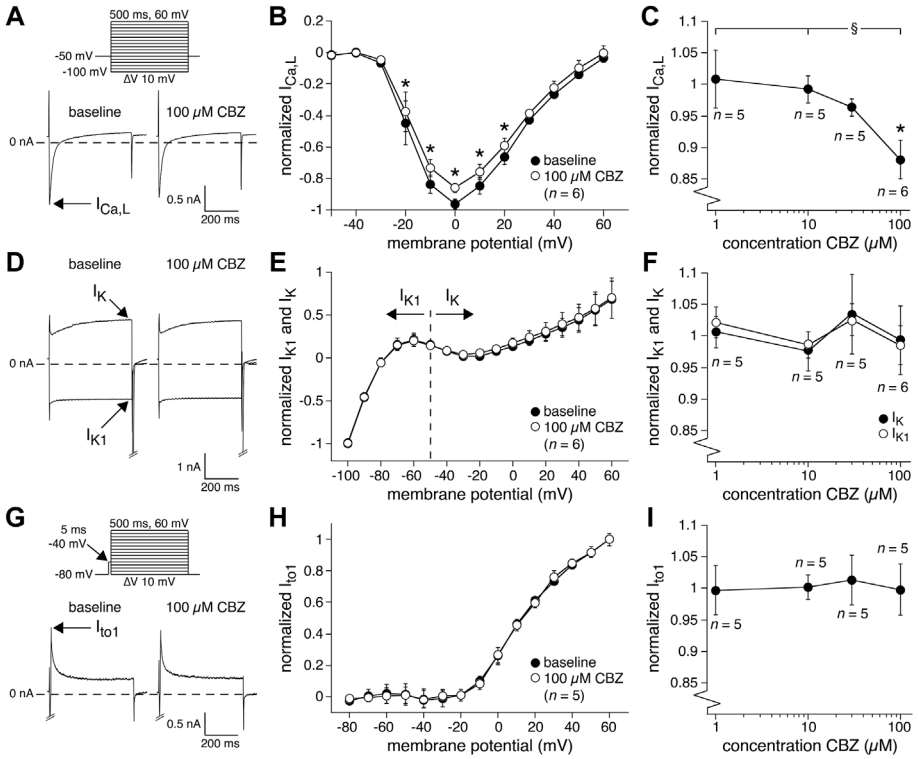

FIGURE 4 | Carbamazepine (CBZ) reduces the L-type Ca^{2+} current of rabbit ventricular cardiomyocytes without affecting K^+ currents. **(A)** Typical recordings of the L-type Ca^{2+} current ($I_{Ca,L}$) at 0 mV under baseline conditions and in presence of 100 μM CBZ. Inset: voltage clamp protocol used. Cycle length was 2 s. **(B)** Average I-V relationship of $I_{Ca,L}$ under baseline conditions and in presence of 100 μM CBZ. $I_{Ca,L}$ was normalized to the maximal peak amplitude under baseline conditions, but peak current was set to −1 to retain the well-known inward direction of $I_{Ca,L}$. $^*p < 0.05$ CBZ versus baseline (Two-Way RM ANOVA). **(C)** Concentration dependency of the CBZ effect on $I_{Ca,L}$ amplitude measured at 0 mV. $^*p < 0.05$ CBZ versus baseline (One-Way RM ANOVA); $^§p < 0.05$ CBZ 100 μM versus lower concentrations (One-Way ANOVA). **(D)** Typical recordings of the delayed rectifier K^+ current (I_K; at +60 mV) and inward rectifier K^+ current (I_{K1}; at −100 mV) under baseline conditions and in presence of 100 μM CBZ. Voltage clamp protocol as in panel **(A). (E)** Average I-V relationships of I_K and I_{K1} under baseline conditions and in presence of 100 μM CBZ. The currents were normalized to the current measured at −100 mV (and set to −1) under baseline conditions. **(F)** Concentration dependency of the CBZ effect on I_{K1} and I_K amplitude measured at −100 mV and +60 mV, respectively. **(G)** Typical recordings of the transient outward K^+ current (I_{to1}) at +60 mV under baseline conditions and in presence of 100 μM CBZ. Inset: voltage clamp protocol used. Cycle length was 5 s. **(H)** Average I-V relationships of I_{to1} under baseline conditions and in presence of 100 μM CBZ. I_{to1} was normalized to the current at +60 mV under baseline conditions. **(I)** Concentration dependency of the CBZ effect on I_{to1} amplitude at +60 mV.

encodes the $Na_V1.5$ α-subunit of the cardiac Na^+ channel) (Meregalli et al., 2005). Previous case reports (**Table 1**) have reported findings that are consistent with these electrophysiological effects of CBZ. Accordingly, we found that CBZ use is associated with a 90% increase in the risk of SCA in the general population. These epidemiological findings are consistent with a previous study by Bardai et al. (2015) on the association of SCA with epilepsy and with the use of CBZ, which was conducted in a smaller patient set (10 cases used CBZ and 26 controls were included) and with less certain SCA ascertainment (no ECG documentation). In our study, we had no information regarding the epilepsy status. Hence, we could not adjust for epilepsy in the epidemiological analysis. This is an important limitation considering that epilepsy is associated with increased SCA risk (Surges et al., 2009). Therefore, our findings from the epidemiological analysis should be interpreted with caution. However, Bardai et al. (2015) found that the AEDs with putative cardiac I_{Na} blocking properties such as CBZ are similarly associated with an increased SCA risk. This was not only observed among patients with epilepsy, but also among patients who had no epilepsy (but used AEDs for other indications, e.g., neuralgia). Moreover, the observed association between CBZ and SCA remained unchanged after correction for epilepsy (Bardai et al., 2015). This suggested that the SCA risk associated with CBZ use resulted from the drug effect rather than from suffering epilepsy *per se*.

Of note, we measured the effects of different concentrations of CBZ (1–100 μM) *in vitro*, including concentrations corresponding to plasma levels that provide anticonvulsant effects (20–40 μM) (Bertilsson 1978). CBZ displays a high distribution volume, entering the bloodstream from tissue reserves (Charlier et al., 2021), which, together with the fine end-branches of the vasculature of the heart, would make sure that all cardiomyocytes (not only the cells on the surface) are exposed to the compounds in the blood and the extracellular fluid. Thus, the plasma CBZ concentration is a good measure of the concentration of free CBZ "seen" by the cardiomyocytes in the intact heart and in our *in vitro* experiments. Kennebäck et al.

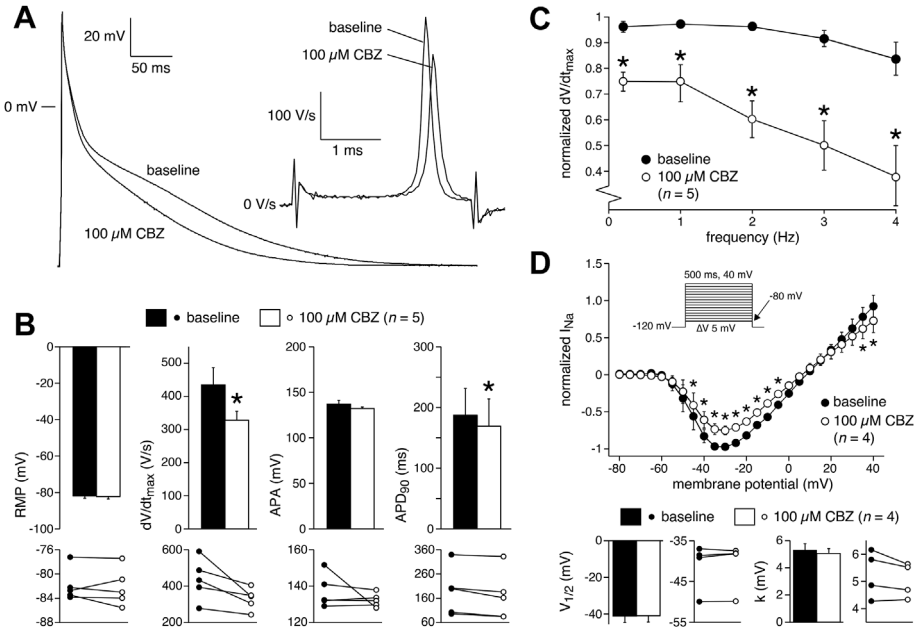

FIGURE 5 | Carbamazepine (CBZ) affects human atrial electrophysiology. **(A)** Superimposed representative human atrial APs at a stimulus frequency of 1 Hz in control conditions and in presence of 100 μM CBZ. Inset: time derivatives during the AP upstroke phase. **(B)** Average AP characteristics at a stimulus frequency of 1 Hz under baseline conditions and in presence of 100 μM CBZ (top panels) and individual (paired) data points (bottom panels). *$p < 0.05$ CBZ versus baseline (One-Way RM ANOVA). **(C)** Average dV/dt_{max} in response to 100 μM CBZ at stimulus frequencies ranging from 0.2 to 4 Hz. Values are normalized to the highest dV/dt_{max} measured under baseline conditions. *$p < 0.05$ CBZ versus baseline (Two-Way RM ANOVA). **(D)** Average I-V relationship of I_{Na} under baseline conditions and in presence of 100 μM CBZ (top panel) and $V_{1/2}$ and k of activation (bottom panels). Inset: voltage clamp protocol used. Cycle length was 5 s. I_{Na} was normalized to the maximal peak amplitude under baseline conditions, but peak current was set to −1 to retain the well-known inward direction of I_{Na}. *$p < 0.05$ CBZ versus baseline (Two-Way RM ANOVA).

(1995) reported a CBZ plasma concentration of 26.1 ± 5.5 μM (mean ± SD) at a dose of 400 mg/day and 35.6 ± 5.9 μM at 800 mg/day in healthy volunteers. Correspondingly, our study showed that the CBZ-induced reduction of upstroke velocity was present at 10 μM at 2 Hz and faster, and at 30 μM at all pacing frequencies, which is thus within the range of therapeutic concentrations. Our observed reduction of upstroke velocity is consistent with findings in guinea-pig ventricular cardiomyocytes where 75 μM CBZ significantly reduced dV/dt_{max} at 1 Hz frequency stimulation by ≈ 13% (Delaunois et al., 2015).

We here compared our used CBZ concentrations to plasma concentrations in healthy volunteers. However, as reviewed by Bertilsson (1978), a poor correlation between the prescribed dose and the actual plasma concentration of CBZ is found in epileptic patients. Furthermore, CBZ plasma levels may be affected by several factors, among which age, pregnancy, and pharmacokinetic drug interactions, including interactions with both central nervous system and cardiovascular drugs (Bertilsson 1978; Panday et al., 2017). Consequently, CBZ plasma levels show a considerable inter-individual variability (Bertilsson 1978; Panday et al., 2017). On the one hand, plasma levels can be so low that therapeutic efficacy is lost, while on the other hand the therapeutic range of 4–10 or 4–12 μg/mL (17–42 or 17–51 μM, respectively) is exceeded in a substantial percentage of patients treated with CBZ (Shakya et al., 2008; Al-Balawi et al., 2020; Eroğlu et al., 2021; Grześk et al., 2021), which may have contributed to the observed cardiac arrhythmias of **Table 1**. Supratherapeutic CBZ plasma levels were found in 4.9% of their patients by Shakya et al. (2008), in 8.6% by Al-Balawi et al. (2020), in 16% by Eroğlu et al. (2021), and in 2.1% by Grześk et al. (2021).

The CBZ-induced changes in upstroke velocity support our epidemiological findings, and suggest that CBZ affects I_{Na} (Berecki et al., 2010). Indeed, we found that ≥30 μM CBZ reduced cardiac I_{Na} and that it affected various gating properties (hyperpolarizing shift in voltage dependency of inactivation and slower recovery from inactivation). Our finding is supported by previous studies on CBZ's effects on cardiac and neuronal I_{Na} (Kuo et al., 1997; Sun et al., 2007; Sheets et al., 2008; Harmer et al., 2011; Theile and Cummins 2011). For example, Harmer et al. (2011) found an IC_{50} of 152 μM for $Na_V1.5$ channels expressed in CHO cells, while IC_{50} values for "brain-type" Na^+ channels expressed in HEK293 cells were 2.5 and 1.6 mM for $Na_V1.3$ and $Na_V1.7$ channels in resting state, respectively (Sheets et al., 2008). In resting state, tetrodotoxin-resistant (TTX-R) $Na_V1.8$ channels had an IC_{50} of 840 μM in dorsal root ganglion cells (Sheets et al., 2008). CBZ-induced shift in voltage dependency of inactivation and slowed recovery of inactivation were also observed for $Na_V1.3$, $Na_V1.7$ and $Na_V1.8$ channels (Sheets et al., 2008; Theile and Cummins 2011). This strengthens the notion that I_{Na} block is a plausible contributing mechanism of increased SCA risk associated with CBZ and likely other AEDs with similar cardiac electrophysiological effects. This

notion may serve as a basis to adapt clinical procedures for prescription of CBZ with the aim of reducing SCA risk (Benassi et al., 1987). This may be achieved by identifying individuals who are vulnerable to this risk when prescription of I_{Na} blocking CBZ is considered. This may be based on identification of the clinical conditions that increase SCA risk in the context of I_{Na} block, similar to guidelines regarding the prescription of I_{Na} blocking (class IC) antiarrhythmic drugs in case of ischemic heart disease and heart failure (Greenberg et al., 1995). Also, procedures to screen for genetic vulnerability (pharmacogenetics) may be developed (Surges et al., 2009). Finally, at set out above, CBZ levels are affected by several factors and supratherapeutic CBZ levels have been found in a substantial percentage of CBZ users. Therefore, CBZ concentrations need to be closely evaluated (Panday et al., 2017; Charlier et al., 2021).

While I_{Na} block is a plausible mechanism underlying the higher SCA risk observed during CBZ use, there is less compelling evidence to support the notion that increased SCA risk results from changes in AP repolarization. We found mild effects of CBZ on AP repolarization as indicated by the tendency to (in rabbit cardiomyocytes) and significant (in human cardiomyocytes) APD_{90} shortening at 100 μM CBZ, which is above the reported plasma concentrations (Kennebäck et al., 1995). An AP shortening was also observed at 75 μM CBZ in guinea-pig ventricular myocytes at 1 Hz stimulation frequency (Delaunois et al., 2015), but QT intervals, ECG measures of the ventricular AP durations, were not affected by therapeutic doses of CBZ (Arhan et al., 2009; Amin et al., 2010; Dogan et al., 2010; Sathyaprabha et al., 2018). The mild extent of CBZ effects on AP repolarization fits with our voltage clamp experiments. We observed a lack of CBZ effects on the main cardiac repolarizing currents, I_{K1}, I_K and I_{to1}, consistent with previous findings in other tissues and expression systems (Wooltorton and Mathie 1993; Rundfeldt 1997; Kobayashi et al., 2009). CBZ (10–50 μM) had no effect on I_K in rat isolated sympathetic neurons (Wooltorton and Mathie 1993) and NG108-15 neuronal cells (Rundfeldt 1997), while it did not affect Kir2.1 currents (Kobayashi et al., 2009), with Kir2.1 as the major Kir isoform of I_{K1} channels in cardiac myocytes. Although one study reported that CBZ inhibited the I_{Kr} tail current, the CBZ dosages used in that study (250–500 μM) were much higher than recommended therapeutic concentrations (Danielsson et al., 2003). We found a mild reduction of the depolarizing current $I_{Ca,L}$ at 100 μM. Although it agrees with findings in cultured rat hippocampus neurons (Ambrósio et al., 1999) and rat sensory spinal ganglion cells (Schirrmacher et al., 1995), it is unlikely that such a decrease contributes to the SCA increase and relates to CBZ-induced changes in whole heart parameters, because the reduction is rather small and only observed at 100 μM, which is above the therapeutic plasma concentrations (Kennebäck et al., 1995). It has been demonstrated that CBZ reduced connexin43 expression in cultured cardiomyocytes (Schirrmacher et al., 1995), but more studies are required to determine the exact role of cardiac connexins in the altered ECG parameters and arrhythmias by CBZ use, and our observation of increased SCA.

The effects of CBZ on APs and I_{Na} density of freshly isolated human atrial cardiomyocytes were only tested at 100 μM due to the limited availability of Ca^{2+}-tolerant, non-depolarized cells (Verkerk et al., 2021). We used human atrial cardiomyocytes isolated from explanted hearts of patients (with various medications) with end-stage heart failure caused by ischemic cardiomyopathy. Although such cells may be in a diseased state, the main effects of CBZ on those human atrial cardiomyocytes were largely similar to those on ventricular cardiomyocytes of control rabbits, indicating that the effects of CBZ are also present in human conditions. The K^+ currents and $I_{Ca,L}$ were measured with very general voltage clamp protocols without specific solutions and/or blockers. Although such measurements might also involve small contributions of other membrane currents, the CBZ effects were assessed in paired experiments. In addition, our findings match with CBZ findings on membrane currents in non-cardiomyocytes (Wooltorton and Mathie 1993; Rundfeldt 1997; Ambrósio et al., 1999; Danielsson et al., 2003; Sheets et al., 2008; Kobayashi et al., 2009; Theile and Cummins 2011), indicating that the CBZ effects on these (net) currents were reliably characterized.

5 CONCLUSION

CBZ reduces cardiac depolarization by reducing I_{Na}, and inducing an associated reduction of the AP upstroke velocity, in cardiomyocytes at therapeutic plasma concentrations. CBZ also affects cardiac repolarization, by reducing $I_{Ca,L}$, and an associated reduction of AP duration, but only at relatively high concentrations. These electrophysiological effects may contribute to the found increased SCA risk upon CBZ use in the general population.

DATA AVAILABILITY STATEMENT

The original contributions presented in the study are included in the article/**Supplementary Material**, further inquiries can be directed to the corresponding author.

ETHICS STATEMENT

The studies involving human participants were reviewed and approved by The Medical Ethics Committee of Academic Medical Center Amsterdam. The patients/participants provided their written informed consent to participate in this study. The animal study was reviewed and approved by Institutional Animal Care and Use Committee of the University of Amsterdam.

AUTHOR CONTRIBUTIONS

HT conceived and designed the study. TE structured and carried out the epidemiological studies. AV structured and designed the patch-clamp studies. LJ and AV carried out the patch-clamp experiments. RW carried out the statistical analysis of the patch-clamp data. LJ

and TE drafted the first version of the manuscript. All authors contributed to manuscript revision and approved the final version.

FUNDING

This work has received funding from the European Union's Horizon 2020 research and innovation program under acronym ESCAPE-NET, registered under grant agreement No. 733381, and the COST Action PARQ (grant agreement No. CA19137) supported by COST (European Co-operation in Science and Technology), and Chinese Scholarship Council.

ACKNOWLEDGMENTS

The authors thank Berend de Jonge for his excellent technical assistance.

SUPPLEMENTARY MATERIAL

The Supplementary Material for this article can be found online at: https://www.frontiersin.org/articles/10.3389/fcell.2022.891996/full#supplementary-material

REFERENCES

Al-Balawi, R. S., Alshehri, M. A., Alatawi, A. S., Al Shehri, A. M., Alshehry, M. A., and Al-Gayyar, M. M. H. (2020). Measuring the Appropriateness of Carbamazepine and Valproic Acid Prescribing and Utilization Using a Newly Implemented Online System in the Tabuk Region of Saudi Arabia. *Saudi Pharm. J.* 28, 844–849. doi:10.1016/j.jsps.2020.06.008

Ambrósio, A. F., Silva, A. P., Malva, J. O., Soares-da-Silva, P., Carvalho, A. P., and Carvalho, C. M. (1999). Carbamazepine Inhibits L-type Ca^{2+} Channels in Cultured Rat Hippocampal Neurons Stimulated with Glutamate Receptor Agonists. *Neuropharmacology* 38, 1349–1359. doi:10.1016/s0028-3908(99)00058-1

Amin, O. S. M., Shwanni, S. S., Noori, S. F., and Hasan, A. M. (2010). Carbamazepine and the QTc Interval: Any Association? *Neurol. Asia* 15, 119–123. Available at: https://www.neurology-asia.org/. http://www.neurology-asia.org/articles/20102_119.pdf

Antzelevitch, C., and Burashnikov, A. (2011). Overview of Basic Mechanisms of Cardiac Arrhythmia. *Card. Electrophysiol. Clin.* 3, 23–45. doi:10.1016/j.ccep.2010.10.012

Arhan, E., Ayçiçek, Ş., Akaln, N., Güven, A., and Köse, G. (2009). Cardiac Effects of Carbamazepine Treatment in Childhood Epilepsy. *Neurologist* 15, 268–273. doi:10.1097/NRL.0b013e31818600a4

Bagal, S. K., Marron, B. E., Owen, R. M., Storer, R. I., and Swain, N. A. (2015). Voltage Gated Sodium Channels as Drug Discovery Targets. *Channels* 9, 360–366. doi:10.1080/19336950.2015.1079674

Bardai, A., Amin, A. S., Blom, M. T., Bezzina, C. R., Berdowski, J., Langendijk, P. N. J., et al. (2013). Sudden Cardiac Arrest Associated with Use of a Non-Cardiac Drug that Reduces Cardiac Excitability: Evidence from Bench, Bedside, and Community. *Eur. Heart J.* 34, 1506–1516. doi:10.1093/eurheartj/eht054

Bardai, A., Blom, M. T., Van Noord, C., Verhamme, K. M., Sturkenboom, M. C. J. M., and Tan, H. L. (2015). Sudden Cardiac Death Is Associated Both with Epilepsy and with Use of Antiepileptic Medications. *Heart* 101, 17–22. doi:10.1136/heartjnl-2014-305664

Beermann, B., Edhag, O., and Vallin, H. (1975). Advanced Heart Block Aggravated by Carbamazepine. *Br. Heart J.* 37, 668–671. doi:10.1136/hrt.37.6.668

Benassi, E., Bo, G.-P., Cocito, L., Maffini, M., and Loeb, C. (1987). Carbamazepine and Cardiac Conduction Disturbances. *Ann. Neurol.* 22, 280–281. doi:10.1002/ana.410220217

Berecki, G., Wilders, R., De Jonge, B., Van Ginneken, A. C. G., and Verkerk, A. O. (2010). Re-Evaluation of the Action Potential Upstroke Velocity as a Measure of the Na^+ Current in Cardiac Myocytes at Physiological Conditions. *PLoS One* 5, e15772. doi:10.1371/journal.pone.0015772

Bertilsson, L. (1978). Clinical Pharmacokinetics of Carbamazepine. *Clin. Pharmacokinet.* 3, 128–143. doi:10.2165/00003088-197803020-00003

Blom, M. T., Van Hoeijen, D. A., Bardai, A., Berdowski, J., Souverein, P. C., De Bruin, M. L., et al. (2014). Genetic, Clinical and Pharmacological Determinants of Out-of-Hospital Cardiac Arrest: Rationale and Outline of the AmsteRdam Resuscitation Studies (ARREST) Registry. *Open Heart* 1, e000112. doi:10.1136/openhrt-2014-000112

Boesen, F., Andersen, E. B., Jensen, E. K., and Ladefoged, S. D. (1983). Cardiac Conduction Disturbances During Carbamazepine Therapy. *Acta Neurol. Scand.* 68, 49–52. doi:10.1111/j.1600-0404.1983.tb04814.x

Catterall, W. A. (1999). Molecular Properties of Brain Sodium Channels: An Important Target for Anticonvulsant Drugs. *Adv. Neurol.* 79, 441–456.

Charlier, B., Coglianese, A., De Rosa, F., De Grazia, U., Operto, F. F., Coppola, G., et al. (2021). The Effect of Plasma Protein Binding on the Therapeutic Monitoring of Antiseizure Medications. *Pharmaceutics* 13, 1208. doi:10.3390/pharmaceutics13081208

Danielsson, B. R., Lansdell, K., Patmore, L., and Tomson, T. (2005). Effects of the Antiepileptic Drugs Lamotrigine, Topiramate and Gabapentin on hERG Potassium Currents. *Epilepsy Res.* 63, 17–25. doi:10.1016/j.eplepsyres.2004.10.002

Danielsson, B. R., Lansdell, K., Patmore, L., and Tomson, T. (2003). Phenytoin and Phenobarbital Inhibit Human HERG Potassium Channels. *Epilepsy Res.* 55, 147–157. doi:10.1016/s0920-1211(03)00119-0

Davies, J. A. (1995). Mechanisms of Action of Antiepileptic Drugs. *Seizure* 4, 267–271. doi:10.1016/s1059-1311(95)80003-4

Delaunois, A., Colomar, A., Depelchin, B. O., and Cornet, M. (2015). Cardiac Safety of Lacosamide: The Non-Clinical Perspective. *Acta Neurol. Scand.* 132, 337–345. doi:10.1111/ane.12413

Dogan, E. A., Dogan, U., Yıldız, G. U., Akıllı, H., Genc, E., Genc, B. O., et al. (2010). Evaluation of Cardiac Repolarization Indices in Well-Controlled Partial Epilepsy: 12-Lead ECG Findings. *Epilepsy Res.* 90, 157–163. doi:10.1016/j.eplepsyres.2010.04.008

Eroğlu, E., Harmanci, N., Yildirim, E., and Sirmagül, B. (2021). Therapeutic Drug Monitoring of Antiepileptic Drugs in Turkey: Five Years' Experiences. *Osman. J. Med.* 43, 36–41. doi:10.20515/otd.767494

Eroglu, T. E., Mohr, G. H., Blom, M. T., Verkerk, A. O., Souverein, P. C., Torp-Pedersen, C., et al. (2020). Differential Effects on Out-of-Hospital Cardiac Arrest of Dihydropyridines: Real-World Data from Population-Based Cohorts Across Two European Countries. *Eur. Heart J. Cardiovasc. Pharmacother.* 6, 347–355. doi:10.1093/ehjcvp/pvz038

Fishman, G. I., Chugh, S. S., Dimarco, J. P., Albert, C. M., Anderson, M. E., Bonow, R. O., et al. (2010). Sudden Cardiac Death Prediction and Prevention. *Circulation* 122, 2335–2348. doi:10.1161/CIRCULATIONAHA.110.976092

Fozzard, H. A., and Hanck, D. A. (1996). Structure and Function of Voltage-Dependent Sodium Channels: Comparison of Brain II and Cardiac Isoforms. *Physiol. Rev.* 76, 887–926. doi:10.1152/physrev.1996.76.3.887

Greenberg, H. M., Dwyer, E. M., Jr., Hochman, J. S., Steinberg, J. S., Echt, D. S., and Peters, R. W. (1995). Interaction of Ischaemia and Encainide/Flecainide Treatment: A Proposed Mechanism for the Increased Mortality in CAST I. *Br. Heart J.* 74, 631–635. doi:10.1136/hrt.74.6.631

Grześk, G., Stolarek, W., Kasprzak, M., Grześk, E., Rogowicz, D., Wiciński, M., et al. (2021). Therapeutic Drug Monitoring of Carbamazepine: A 20-Year Observational Study. *J. Clin. Med.* 10, 5396. doi:10.3390/jcm10225396

Hamilton, D. V. (1978). Carbamazepine and Heart Block. *Lancet* 311, 1365. doi:10.1016/s0140-6736(78)92442-x

Harmer, A., Valentin, J.-P., and Pollard, C. (2011). On the Relationship Between Block of the Cardiac Na^+ Channel and Drug-Induced Prolongation of the QRS Complex. *Br. J. Pharmacol.* 164, 260–273. doi:10.1111/j.1476-5381.2011.01415.x

Haverkamp, W., Breithardt, G., Camm, A. J., Janse, M. J., Rosen, M. R., Antzelevitch, C., et al. (2000). The Potential for QT Prolongation and Proarrhythmia by Non-Antiarrhythmic Drugs: Clinical and Regulatory Implications. Report on a Policy Conference of the European Society of Cardiology. *Eur. Heart J.* 21, 1216–1231. doi:10.1053/euhj.2000.2249

Hayashi, M., Shimizu, W., and Albert, C. M. (2015). The Spectrum of Epidemiology Underlying Sudden Cardiac Death. *Circ. Res.* 116, 1887–1906. doi:10.1161/CIRCRESAHA.116.304521

Heinemann, S. H., Schlief, T., Mori, Y., and Imoto, K. (1994). Molecular Pore Structure of Voltage-Gated Sodium and Calcium Channels. *Braz. J. Med. Biol. Res.* 27, 2781–2802. Available at: https://www.bjournal.org/

Herzberg, L. (1978). Carbamazepine and Bradycardia. *Lancet* 311, 1097–1098. doi:10.1016/s0140-6736(78)90940-6

Hojer, J., Malmlund, H.-O., and Berg, A. (1993). Clinical Features in 28 Consecutive Cases of Laboratory Confirmed Massive Poisoning with Carbamazepine Alone. *J. Toxicol. Clin. Toxicol.* 31, 449–458. doi:10.3109/15563659309000412

Kasarskis, E. J., Kuo, C.-S., Berger, R., and Nelson, K. R. (1992). Carbamazepine-lnduced Cardiac Dysfunction: Characterization of Two Distinct Clinical Syndromes. *Arch. Intern. Med.* 152, 186–191. doi:10.1001/archinte.1992.00400130184025

Kennebäck, G., Bergfeldt, L., and Tomson, T. (1995). Electrophysiological Evaluation of the Sodium-Channel Blocker Carbamazepine in Healthy Human Subjects. *Cardiovasc. Drugs Ther.* 9, 709–714. doi:10.1007/BF00878554

Kobayashi, T., Hirai, H., Iino, M., Fuse, I., Mitsumura, K., Washiyama, K., et al. (2009). Inhibitory Effects of the Antiepileptic Drug Ethosuximide on G Protein-Activated Inwardly Rectifying K^+ Channels. *Neuropharmacology* 56, 499–506. doi:10.1016/j.neuropharm.2008.10.003

Koutsampasopoulos, K., Zotos, A., Papamichalis, M., and Papaioannou, K. (2014). Carbamazepine Induced Atrial Tachycardia with Complete AV Block. *Hippokratia* 18, 185–186. Available at: https://www.hippokratia.gr/ or more specifically. https://www.hippokratia.gr/category/volume-18-2014-issue-2/

Krishnan, S. C., and Antzelevitch, C. (1991). Sodium Channel Block Produces Opposite Electrophysiological Effects in Canine Ventricular Epicardium and Endocardium. *Circ. Res.* 69, 277–291. doi:10.1161/01.res.69.2.277

Kuiper, J. G., Bakker, M., Penning-Van Beest, F. J. A., and Herings, R. M. C. (2020). Existing Data Sources for Clinical Epidemiology: The PHARMO Database Network. *Clin. Epidemiol. 12* 12, 415–422. doi:10.2147/CLEP.S247575

Kuo, C.-C., Chen, R.-S., Lu, L., and Chen, R.-C. (1997). Carbamazepine Inhibition of Neuronal Na^+ Currents: Quantitative Distinction from Phenytoin and Possible Therapeutic Implications. *Mol. Pharmacol.* 51, 1077–1083. doi:10.1124/mol.51.6.1077

Lasoń, W., Chlebicka, M., and Rejdak, K. (2013). Research Advances in Basic Mechanisms of Seizures and Antiepileptic Drug Action. *Pharmacol. Rep.* 65, 787–801. doi:10.1016/s1734-1140(13)71060-0

Leslie, P. J., Heyworth, R., and Prescott, L. F. (1983). Cardiac Complications of Carbamazepine Intoxication: Treatment by Haemoperfusion. *Br. Med. J. (Clin. Res. Ed.)* 286, 1018. doi:10.1136/bmj.286.6370.1018

Meregalli, P., Wilde, A. A. M., and Tan, H. L. (2005). Pathophysiological Mechanisms of Brugada Syndrome: Depolarization Disorder, Repolarization Disorder, or More? *Cardiovasc. Res.* 67, 367–378. doi:10.1016/j.cardiores.2005.03.005

Panday, D. R., Panday, K. R., Basnet, M., Kafle, S., Shah, B., and Rauniar, G. P. (2017). Therapeutic Drug Monitoring of Carbamazepine. *Int. J. Neurorehabilitation Eng.* 4, 245. doi:10.4172/2376-0281.1000245

Pellock, J. M. (2000). Treatment of Epilepsy in the New Millennium. *Pharmacotherapy* 20, 129S–138S. doi:10.1592/phco.20.12.129s.35252

Ragsdale, D. S., and Avoli, M. (1998). Sodium Channels as Molecular Targets for Antiepileptic Drugs. *Brain Res. Rev.* 26, 16–28. doi:10.1016/s0165-0173(97)00054-4

Remme, C. A., Verkerk, A. O., Nuyens, D., Van Ginneken, A. C. G., Van Brunschot, S., Belterman, C. N. W., et al. (2006). Overlap Syndrome of Cardiac Sodium Channel Disease in Mice Carrying the Equivalent Mutation of Human *SCN5A* -1795insD. *Circulation* 114, 2584–2594. doi:10.1161/CIRCULATIONAHA.106.653949

Rogers, W. J., Epstein, A. E., Arciniegas, J. G., Dailey, S. M., Kay, G. N., Little, R. E., et al. (1989). Preliminary Report: Effect of Encainide and Flecainide on Mortality in a Randomized Trial of Arrhythmia Suppression after Myocardial Infarction. *N. Engl. J. Med.* 321, 406–412. doi:10.1056/NEJM198908103210629

Rundfeldt, C. (1997). The New Anticonvulsant Retigabine (D-23129) Acts as an Opener of K^+ Channels in Neuronal Cells. *Eur. J. Pharmacol.* 336, 243–249. doi:10.1016/s0014-2999(97)01249-1

Sathyaprabha, T. N., Koot, L. A. M., Hermans, B. H. M., Adoor, M., Sinha, S., Kramer, B. W., et al. (2018). Effects of Chronic Carbamazepine Treatment on the ECG in Patients with Focal Seizures. *Clin. Drug Investig.* 38, 845–851. doi:10.1007/s40261-018-0677-6

Schirrmacher, K., Mayer, A., Walden, J., Düsing, R., and Bingmann, D. (1995). Effects of Carbamazepine on Membrane Properties of Rat Sensory Spinal Ganglion Cells In Vitro. *Eur. Neuropsychopharmacol.* 5, 501–507. doi:10.1016/0924-977x(95)80010-y

Schmidt, S., and Schmitz-Buhl, M. (1995). Signs and Symptoms of Carbamazepine Overdose. *J. Neurol.* 242, 169–173. doi:10.1007/BF00936891

Shakya, G., Malla, S., Shakya, K. N., and Shrestha, R. (2008). Therapeutic Drug Monitoring of Antiepileptic Drugs. *J. Nepal Med. Assoc.* 47, 94–97. doi:10.31729/jnma.294 Available at: https://www.jnma.com.np/jnma/index.php/jnma/issue/view/41. https://www.chemguide.co.uk/analysis/masspec/howitworks.html

Sheets, P. L., Heers, C., Stoehr, T., and Cummins, T. R. (2008). Differential Block of Sensory Neuronal Voltage-Gated Sodium Channels by Lacosamide [(2R)-2-(acetylamino)-N-Benzyl-3-Methoxypropanamide], Lidocaine, and Carbamazepine. *J. Pharmacol. Exp. Ther.* 326, 89–99. doi:10.1124/jpet.107.133413

Sills, G. J., and Rogawski, M. A. (2020). Mechanisms of Action of Currently Used Antiseizure Drugs. *Neuropharmacology* 168, 107966. doi:10.1016/j.neuropharm.2020.107966

Sun, G.-C., Werkman, T. R., Battefeld, A., Clare, J. J., and Wadman, W. J. (2007). Carbamazepine and Topiramate Modulation of Transient and Persistent Sodium Currents Studied in HEK293 Cells Expressing the $Na^v1.3$ α-Subunit. *Epilepsia* 48, 774–782. doi:10.1111/j.1528-1167.2007.01001.x

Sun, G.-C., Werkman, T. R., and Wadman, W. J. (2006). Kinetic Changes and Modulation by Carbamazepine on Voltage-Gated Sodium Channels in Rat CA1 Neurons after Epilepsy. *Acta Pharmacol. Sin.* 27, 1537–1546. doi:10.1111/j.1745-7254.2006.00452.x

Surges, R., Thijs, R. D., Tan, H. L., and Sander, J. W. (2009). Sudden Unexpected Death in Epilepsy: Risk Factors and Potential Pathomechanisms. *Nat. Rev. Neurol.* 5, 492–504. doi:10.1038/nrneurol.2009.118

Theile, J. W., and Cummins, T. R. (2011). Inhibition of Navβ4 Peptide-Mediated Resurgent Sodium Currents in Nav1.7 Channels by Carbamazepine, Riluzole, and Anandamide. *Mol. Pharmacol.* 80, 724–734. doi:10.1124/mol.111.072751

Verkerk, A. O., Baartscheer, A., De Groot, J. R., Wilders, R., and Coronel, R. (2011). Etiology-Dependency of Ionic Remodeling in Cardiomyopathic Rabbits. *Int. J. Cardiol.* 148, 154–160. doi:10.1016/j.ijcard.2009.10.047

Verkerk, A. O., Marchal, G. A., Zegers, J. G., Kawasaki, M., Driessen, A. H. G., Remme, C. A., et al. (2021). Patch-Clamp Recordings of Action Potentials from Human Atrial Myocytes: Optimization Through Dynamic Clamp. *Front. Pharmacol.* 12, 649414. doi:10.3389/fphar.2021.649414

Wong, C. X., Brown, A., Lau, D. H., Chugh, S. S., Albert, C. M., Kalman, J. M., et al. (2019). Epidemiology of Sudden Cardiac Death: Global and Regional Perspectives. *Heart Lung Circ.* 28, 6–14. doi:10.1016/j.hlc.2018.08.026

Wooltorton, J. R. A., and Mathie, A. (1993). Block of Potassium Currents in Rat Isolated Sympathetic Neurones by Tricyclic Antidepressants and Structurally Related Compounds. *Br. J. Pharmacol.* 110, 1126–1132. doi:10.1111/j.1476-5381.1993.tb13931.x

Zipes, D. P., and Wellens, H. J. J. (1998). Sudden Cardiac Death. *Circulation* 98, 2334–2351. doi:10.1161/01.cir.98.21.2334

Conflict of Interest: The authors declare that the research was conducted in the absence of any commercial or financial relationships that could be construed as a potential conflict of interest.

Publisher's Note: All claims expressed in this article are solely those of the authors and do not necessarily represent those of their affiliated organizations, or those of the publisher, the editors and the reviewers. Any product that may be evaluated in this article, or claim that may be made by its manufacturer, is not guaranteed or endorsed by the publisher.

frontiers | Frontiers in Cell and Developmental Biology

ORIGINAL RESEARCH
published: 09 June 2022
doi: 10.3389/fcell.2022.930235

Mfsd8 Modulates Growth and the Early Stages of Multicellular Development in *Dictyostelium discoideum*

Shyong Quan Yap[1], *William D. Kim*[1] *and Robert J. Huber*[1,2]*

[1]*Environmental and Life Sciences Graduate Program, Trent University, Peterborough, ON, Canada,* [2]*Department of Biology, Trent University, Peterborough, ON, Canada*

MFSD8 is a transmembrane protein that has been reported to transport chloride ions across the lysosomal membrane. Mutations in *MFSD8* are associated with a subtype of Batten disease called CLN7 disease. Batten disease encompasses a family of 13 inherited neurodegenerative lysosomal storage diseases collectively referred to as the neuronal ceroid lipofuscinoses (NCLs). Previous work identified an ortholog of human MFSD8 in the social amoeba *D. discoideum* (gene: *mfsd8*, protein: Mfsd8), reported its localization to endocytic compartments, and demonstrated its involvement in protein secretion. In this study, we further characterized the effects of *mfsd8* loss during *D. discoideum* growth and early stages of multicellular development. During growth, *mfsd8*$^-$ cells displayed increased rates of proliferation, pinocytosis, and expansion on bacterial lawns. Loss of *mfsd8* also increased cell size, inhibited cytokinesis, affected the intracellular and extracellular levels of the quorum-sensing protein autocrine proliferation repressor A, and altered lysosomal enzyme activity. During the early stages of development, loss of *mfsd8* delayed aggregation, which we determined was at least partly due to impaired cell-substrate adhesion, defects in protein secretion, and alterations in lysosomal enzyme activity. Overall, these results show that Mfsd8 plays an important role in modulating a variety of processes during the growth and early development of *D. discoideum*.

Keywords: Batten disease, CLN7, *Dictyostelium discoideum*, growth, development, lysosome, MFSD8, neuronal ceroid lipofuscinoses

OPEN ACCESS

Edited by:
Paola Gavazzo,
National Research Council (CNR), Italy

Reviewed by:
Satoshi Sawai,
The University of Tokyo, Japan
Ritva Tikkanen,
University of Giessen, Germany

***Correspondence:**
Robert J. Huber
roberthuber@trentu.ca

Specialty section:
This article was submitted to Cellular Biochemistry, a section of the journal Frontiers in Cell and Developmental Biology

Received: *27 April 2022*
Accepted: *23 May 2022*
Published: *09 June 2022*

Citation:
Yap SQ, Kim WD and Huber RJ (2022) Mfsd8 Modulates Growth and the Early Stages of Multicellular Development in Dictyostelium discoideum. Front. Cell Dev. Biol. 10:930235. doi: 10.3389/fcell.2022.930235

Abbreviations: AprA, autocrine proliferation repressor A; CadA, calcium-dependent cell adhesion protein A; cAMP, 3′,5′-cyclic adenosine monophosphate; CB, conditioned starvation buffer; CLN, ceroid lipofuscinosis neuronal; CM, conditioned growth media; CtnA, countin; CTSB, cathepsin B; CTSD, cathepsin D; CTSF, cathepsin F; DscA, discoidin A; FITC, fluoroscein isothiocyanate; HRP, horseradish peroxidase; MEF, mouse embryonic fibroblast; MES, 2-N-morpholinoethanesulfonic acid; MFSD8, major facilitator superfamily domain-containing 8; NAG, N-acetylglucosaminidase; NCL, neuronal ceroid lipofuscinosis; PPT1, palmitoyl-protein thioesterase 1; TPP1, tripeptidyl peptidase 1; WC, whole cell; WT, wild type.

INTRODUCTION

Batten disease, clinically known as the neuronal ceroid lipofuscinoses (NCLs), is a family of neurodegenerative disorders that affect people of all ages and ethnicities (Mole and Cotman, 2015). Clinical symptoms of the disease include vision loss leading to blindness, seizures, deterioration in motor and cognitive function, and premature death (Schulz et al., 2013). There are 13 different subtypes of NCL, each one resulting from a mutation in a distinct ceroid lipofuscinosis neuronal (*CLN*) gene (*CLN1-8*, *CLN10-14*) (Mole and Cotman, 2015). *CLN* genes encode soluble lysosomal proteins (PPT1/CLN1, TPP1/CLN2, CLN5, CTSD/CLN10 and CTSF/CLN13), lysosomal membrane proteins (CLN3, MFSD8/CLN7, and ATP13A2/CLN12), membrane proteins localizing to the endoplasmic reticulum (CLN6 and CLN8), cytoplasmic proteins (GRN/CLN11 and KCTD7/CLN14), and a protein that localizes to synaptic vesicles (DNAJC5/CLN4) (Cárcel-Trullols et al., 2015). While these proteins have a wide range of localizations and functions, it has been suggested that they function in shared or convergent cellular pathways (Persaud-Sawin et al., 2007; Huber, 2020).

Mutations in major facilitator superfamily domain-containing 8 (*MFSD8*) cause a late-infantile form of NCL called CLN7 disease (Aiello et al., 2009). In mammalian cells, MFSD8 is proteolytically cleaved and has been reported to transport chloride ions across the lysosomal membrane (Siintola et al., 2007; Sharifi et al., 2010; Steenhuis et al., 2010; Steenhuis et al., 2012; Wang et al., 2021). However, how MFSD8 influences cellular processes related to NCL pathology is not fully understood. Previous work using *Mfsd8*-deficient mouse embryonic fibroblasts (MEFs) showed that loss of *Mfsd8* alters the amounts of several soluble lysosomal proteins (Danyukova et al., 2018). In addition, loss of *Mfsd8* in mice affects autophagy, neuronal cell survival, and the size and trafficking of lysosomes (Brandenstein et al., 2016; von Kleist et al., 2019; Wang et al., 2021). Further work in human *MFSD8* knockout HEK293T cells revealed the role of MFSD8 in regulating lysosomal chloride conductance, luminal calcium content, lysosomal membrane potential, and lysosomal pH (Wang et al., 2021).

The social amoeba *D. discoideum* is a eukaryotic microbe that is used as a biomedical model organism for studying a variety of human diseases, including the NCLs (Huber, 2021; Kirolos et al., 2021; Mathavarajah et al., 2021; Pain et al., 2021). During the growth phase of the life cycle, haploid amoebae feed on nutrients and divide by mitosis (Mathavarajah et al., 2017). Removal or depletion of the food source triggers a 24-h multicellular developmental program that begins with the chemotactic aggregation of cells into multicellular mounds and ends with the formation of fruiting bodies that are composed of terminally differentiated spores held atop slender stalks of terminally differentiated stalk cells (Mathavarajah et al., 2017). As a result, *D. discoideum* can be used to study a variety of fundamental cellular and developmental processes. The *D. discoideum* genome encodes homologs of 11 of the 13 CLN proteins (Huber, 2016). Recent work on the *D. discoideum* homologs of human tripeptidyl peptidase 1 (TPP1)/CLN2 (Tpp1), CLN3 (Cln3), and CLN5 (Cln5) has provided valuable new insight into the localizations and functions of these proteins in human cells (Huber and Mathavarajah, 2019; McLaren et al., 2019; Smith et al., 2019; Huber, 2020; Huber et al., 2020a; Huber, 2021; McLaren et al., 2021). The *D. discoideum* homolog of human MFSD8 (gene: *mfsd8*, protein: Mfsd8) is expressed throughout the life cycle and a proteomic analysis revealed that Mfsd8 is present in the macropinocytic pathway (Rot et al., 2009; Journet et al., 2012). Recent work in *D. discoideum* showed that Mfsd8 localizes to endocytic compartments, including acidic intracellular vesicles and late endosomes, influences the secretion of two other CLN protein homologs, Cln5 and cathepsin D (CtsD), and interacts with a diversity of proteins during growth and the early stages of multicellular development (Huber et al., 2020b).

In this study, we further characterized the function of Mfsd8 in *D. discoideum* by assessing the effects of *mfsd8* loss on growth and the early stages of multicellular development. Results presented here support a function for Mfsd8 in cell proliferation, pinocytosis, cytokinesis, protein secretion, lysosomal enzyme activity, aggregation, and cell-substrate adhesion. We then integrated these findings into an emerging model summarizing the known roles of Mfsd8 in *D. discoideum*.

MATERIALS AND METHODS

Cell Lines, Antibodies, and Chemicals

Cell lines were grown and maintained on SM/2 agar with *Klebsiella aerogenes* at 21°C (Fey et al., 2007). Cells were also grown axenically in HL5 medium at 21°C and 150 rpm. For all experiments, cells were harvested in the mid-log phase of growth (1–5 × 10^6 cells/ml). Cultures were supplemented with 100 μg/ml ampicillin and 300 μg/ml streptomycin sulfate to prevent bacterial growth. AX4, hereafter referred to as WT, was the parental cell line for *mfsd8*$^-$, which was purchased from the Genome Wide *Dictyostelium* Insertion (GWDI) bank *via* the Dicty Stock Center (https://remi-seq.org) (Fey et al., 2019; Gruenheit et al., 2021). Blasticidin S hydrochloride (10 μg/ml) was used to select *mfsd8*$^-$ cells. HL5 and low-fluorescence HL5 were purchased from Formedium (Hunstanton, Norfolk, United Kingdom). 2-N-morpholinoethanesulfonic acid (MES) was purchased from Fisher Scientific Company (Ottawa, ON, Canada). Rabbit polyclonal antibodies against autocrine proliferation repressor (AprA) and countin (CtnA) were provided as gifts by Dr. Richard Gomer (Brock and Gomer, 1999; Brock and Gomer, 2005). Rabbit polyclonal antibody against calcium dependent cell adhesion protein (CadA) was generated and validated in a previous study (McLaren et al., 2021). Mouse monoclonal anti-α-actinin (47-18-9) and mouse monoclonal anti-discoidin (DscA) (80-52-13) were purchased from the Developmental Studies Hybridoma Bank (University of Iowa, Iowa City, IA, United States) (Stadler et al., 1984). Mouse monoclonal anti-β-actin was purchased from Santa Cruz Biotechnology Incorporated (Dallas, TX, United States). Horseradish peroxidase (HRP)-conjugated secondary antibodies were purchased from New England

Biolabs (Whitby, ON, Canada). p-Nitrophenyl-β-D-glucopyranoside (487507) (substrate for β-glucosidase), p-Nitrophenyl-a-D-glucopyranoside (487506) (substrate for α-glucosidase), 4-Nitrophenyl-α-D-mannopyranoside (N2127) (substrate for α-mannosidase), *o*-Nitrophenyl-β-D-galactopyranoside (48712-M) (substrate for β-galactosidase), 4-Nitrophenyl-α-D-galactopyranoside (N0877) (substrate for α-galactosidase), 4-Nitrophenyl N-acetyl-β-D-glucosaminide (N9376) (substrate for N-acetylglucosaminidase, NAG), Ala-Ala-Phe-7-amido-4-methylcoumarin (A3401) (substrate for TPP1), Fluorogenic Cathepsin B Substrate III (219392) (substrate for cathepsin B, CTSB), and β-glucosidase (49290) were purchased from Sigma Aldrich Canada (Oakville, ON, Canada). 4-Methylumbelliferyl 6-thio-Palmitate-β-D-Glucopyranoside (19524) (substrate for palmitoyl-protein thioesterase 1, PPT1) and Fluorogenic Cathepsin F Substrate (80350-BP) (substrate for cathepsin F, CTSF) were purchased from Cedarlane Laboratories (Burlington, ON, Canada). The Cathepsin D Activity Assay Kit (10013-596) was purchased from VWR International (Mississauga, ON, Canada).

Cell Proliferation, Pinocytosis, Cell Size, and Cytokinesis Assays

To assess cell proliferation, cells in the mid-log phase of growth were washed thrice with fresh HL5. Cells were then diluted to 1–2 $\times 10^5$ cells/ml in HL5 and incubated at 21°C and 150 rpm. Cell concentrations were measured every 24 h over a 96-h growth period using a hemocytometer. The pinocytosis assay was conducted using a method described elsewhere (Rivero and Maniak, 2006; Huber et al., 2014). Briefly, cells in the mid-log phase of growth were placed in 5 ml of HL5 at a density of 5×10^6 cells/ml. 100 µl of a 20 mg/ml fluorescein isothiocyanate (FITC)-dextran (70,000 M_r) stock solution was added to the 5 ml suspension, which was then incubated for 120 min at 21°C and 150 rpm. 500 µl were collected every 15 min, washed twice with ice-cold Sorenson's buffer (2 mM Na_2HPO_4, 14.6 mM KH_2PO_4, pH 6.0) and lysed with 1 ml of buffer containing 50 mM Na_2HPO_4 (pH 9.3) and 0.2% Triton-X. Lysates were added to separate wells of black bottom 96-well plates and fluorescence was measured using a BioTek Synergy HTX plate reader and the following filters (460/40 nm for excitation, 528/20 nm for emission) (BioTek Instruments Incorporated, Winooski, VT, United States). To measure cell area, cells in the mid-log phase of growth were deposited onto a hemocytometer. Cells were imaged with a Nikon Ts2R-FL inverted microscope equipped with a Nikon Digital Sight Qi2 monochrome camera (Nikon Canada Incorporated Instruments Division, Mississauga, ON, Canada). The area of each individual cell was quantified using Fiji/ImageJ (Schindelin et al., 2012). To assess cytokinesis, cells (5×10^5 total) in the mid-log phase of growth were collected and deposited onto coverslips placed inside separate wells of a 12-well dish. Coverslips were then submerged in low-fluorescence HL5 and incubated overnight at 21°C. The following day, cells were fixed in −80°C methanol for 45 min and mounted onto slides with Prolong Gold Anti-Fade Reagent containing DAPI (Fisher Scientific Company, Ottawa, ON, Canada). Cells were then imaged using a Nikon Ts2R-FL inverted microscope equipped with a Nikon Digital Sight Qi2 monochrome camera. For each independent experiment, the number of nuclei within each cell (at least 100) was scored and expressed as a percentage of the total number of cells analyzed.

Plaque Expansion on Bacterial Lawns

Three full inoculation loops of *K. aerogenes* were collected and resuspended in KK2 buffer (0.7 g/L K_2HPO_4 and 2.2 g/L KH_2PO_4, pH 6.5). 25 µl of the suspension were then deposited onto SM/2 agar and incubated at 21°C. Two days later, *D. discoideum* cells in the mid-log phase of growth were harvested, washed thrice with KK2 buffer, and resuspended in KK2 buffer to obtain a final concentration of 0.4×10^6 cells/ml. Cells (1×10^2 total) were deposited onto the center of the *K. aerogenes* lawns. Plaques were captured at the indicated time points using a Leica EZ4W stereomicroscope equipped with an internal 5MP CMOS camera (Leica Microsystems Incorporated, Concord, ON, Canada). Plaque diameters were quantified using Fiji/ImageJ.

Autocrine Proliferation Repressor Protein Levels During Growth

Cells from the proliferation assay described above were harvested after 24, 48, and 72 h of growth (Huber et al., 2014). Cells were lysed with buffer containing 50 mM Tris–HCl (pH 8.0), 150 mM NaCl, 0.5% NP40, and a protease inhibitor tablet (PIA32965) (Fisher Scientific Company, Ottawa, ON, Canada). Samples of conditioned media (CM) were collected and standardized based on cell number (1×10^6 total). Whole cell (WC) lysates and equal volumes of CM were separated by SDS-PAGE and analyzed by western blotting. The following primary and secondary antibodies were used: anti-AprA (1:1000), anti-β-actin (1:1000), and HRP-conjugated secondary antibodies (1:2000). Protein bands were imaged using the ChemiDoc Imaging System (Bio-Rad Laboratories Limited, Mississauga, ON, Canada) and quantified using Fiji/ImageJ.

Aggregation Assay

Aggregation was examined using a method described previously with minor modifications (Huber, 2017). Briefly, cells (6×10^6 total) harvested from the mid-log phase of growth were deposited into separate wells of a 6-well dish. Cells were allowed to adhere to the surface of the dish for 1 h after which time they were washed two times with KK2 buffer, and then starved in 1 ml of KK2 buffer. Cells were imaged at the indicated times with a Nikon Ts2R-FL inverted microscope equipped with a Nikon 10 Digital Sight Qi2 monochrome camera. A conditioned buffer (CB) swap experiment was conducted to test the effect of proteins secreted by WT cells on the aggregation of *mfsd8*$^-$ cells (Huber et al., 2017). Briefly, the CB from WT cells starved for 2 h in 1.5 ml of KK2 buffer was collected and spun down to remove any cells present in the buffer. *mfsd8*$^-$ cells were submerged in either 1 ml of KK2 buffer (control) or CB collected from starving WT cells. Cells were imaged at the indicated times with a Nikon Ts2R-FL inverted microscope equipped with a Nikon 10 Digital Sight Qi2 monochrome camera. Aggregation was also examined on 0.5%

agar/KK2 (Huber and Mathavarajah, 2018). Briefly, cells in the mid-log phase of growth were harvested from HL5, washed two times with KK2 buffer, and plated (1.5×10^8 cells/ml) in 0.5 µl volumes on 0.5% agar/KK2. Cell spots were imaged at 0 and 5 h using a Nikon Ts2R-FL inverted microscope equipped with a Nikon Digital Sight Qi2 monochrome camera. Images were viewed using NIS Elements Basic Research and analyzed using Fiji/ImageJ. The area after 5 h was expressed as a percentage of the area at 0 h to provide a measure of the amount of aggregation.

Protein Secretion During Aggregation

Cells (8×10^6 total) in the mid-log phase of growth were deposited into 60 mm × 15 mm Petri dishes and allowed to adhere for 1 h, after which time the HL5 was removed. Adherent cells were washed two times with KK2 buffer and then submerged in 4 ml of KK2 buffer for 4 h, after which time the CB was collected and concentrated using an Amicon Ultra-4 centrifugal filter unit (UFC801024) (Fisher Scientific Company, Ottawa, ON, Canada) according to the manufacturer's instructions. Adherent cells were lysed with NP40 lysis buffer (recipe noted above). SDS-PAGE and western blotting were then used to determine the effect of *mfsd8* loss on the intracellular and extracellular amounts of CtnA, CadA, and DscA. The following primary and secondary antibodies were used: anti-CtnA (1:1000), anti-CadA (1:1000), anti-DscA (1:1000), anti-β-actin (1:1000), anti-α-actinin (1:1000), and HRP-conjugated secondary antibodies (1:2000). Protein bands were imaged using the ChemiDoc Imaging System (Bio-Rad Laboratories Limited, Mississauga, ON, Canada) and quantified using Fiji/ImageJ.

Cell-Substrate Adhesion Assay

Cell-substrate adhesion was assessed using a previously described method with minor modifications (Huber et al., 2017; Huber and Mathavarajah, 2018). Briefly, cells (6×10^6 total) were deposited into separate wells of a 6-well dish and allowed to adhere for 1 h after which time they were washed twice with KK2 buffer and starved in 1.5 ml of KK2 buffer for 4 h. After 4 h, cells were shaken at 150 rpm for 30 min. Samples of CB were collected and cells in CB were counted using a hemocytometer to determine cell dissociation. Cells remaining on the dish were also lysed with NP40 lysis buffer (recipe noted above) and protein concentrations of the lysates were quantified using the Qubit Protein Assay Kit (Q33211) and a Qubit 2.0 Fluorometer (Fisher Scientific Company, Ottawa, ON, Canada).

Enzyme Activity Assays

To assess various enzyme activities, cells were grown in HL5 overnight to confluency in 60 mm × 15 mm Petri dishes (8×10^6 total). Growth-phase cells and cells starved for 4 h in KK2 buffer were then lysed with buffer containing 50 mM MES pH 6.53 and 0.1% NP40, unless stated otherwise (Phillips and Gomer, 2015). Protein concentrations of lysates were quantified using the Qubit Protein Assay Kit and a Qubit 2.0 Fluorometer, and 150 µg of protein was used for the enzyme assays described below. For all enzyme assays, the absorbance and fluorescence values for the experimental samples were corrected using a lysis buffer control.

Lysosomal hydrolases: To assay α-galactosidase activity, lysates were added to 18 µl of 2 mM of 4-Nitrophenyl-α-D-galactopyranoside in sodium citrate/phosphate buffer (pH 4.5) (Kilpatrick and Stirling, 1976). Samples were then incubated for 45 min at 37°C and quenched with equal volume of 1 M sodium glycinate buffer (pH 10.4). The reactions were then deposited into 96-well black clear bottom plates and the absorbance (405 nm) was measured using a BioTek Synergy HTX plate reader. To assay β-galactosidase activity, lysates were added to 36 µl of 25 mM of *o*-Nitrophenyl-β-D-galactopyranoside in 100 mM citrate buffer (pH 4.0) (Maruhn, 1976). The reaction mixtures were incubated for 45 min at 37°C, after which time an equal volume of 2-amino-2-methyl-1-propnanol/HCl solution was added. The reactions were then deposited into 96-well black clear bottom plates and the absorbance (405 nm) was measured using a BioTek Synergy HTX plate reader. To assay α-glucosidase activity, WC lysates were incubated in 2 mM p-Nitrophenyl-a-D-glucopyranoside within 0.1 M sodium succinate (pH 6.0) in a total volume of 150 µl (Wimmer et al., 1997). The reaction solution was incubated for 1 h at 65°C followed by the addition of 300 µl of 1 M sodium carbonate to quench the reaction. The quenched reactions were then deposited into 96-well black clear bottom plates and the absorbance (395 nm) was measured using a BioTek Synergy HTX plate reader. To assay β-glucosidase activity, lysates were added to 18 µl of 10 mM of p-Nitrophenyl-β-D-glucopyranoside in 50 mM acetate buffer (pH 5.0) (Coston and Loomis, 1969). The reactions were incubated at 35°C for 45 min. The reactions were then quenched with an equal volume of 1 M sodium carbonate and deposited into 96-well black clear bottom plates and the absorbance (405 nm) was measured using a BioTek Synergy HTX plate reader. To assay α-mannosidase activity, lysates were added to 18 µl of 5 mM of 4-Nitrophenyl-α-D-mannopyranoside in 5 mM acetate buffer (pH 5.0) (Loomis, 1970). Samples were incubated for 45 min at 35°C after which time an equal volume of 1 M Na_2CO_3 was added to quench the reactions. The quenched reactions were then deposited into 96-well black clear bottom plates and the absorbance (405 nm) was measured using a BioTek Synergy HTX plate reader. To assay NAG activity, WC lysates were added to 75 µl of 7 mM of 4-Nitrophenyl N-acetyl-β-D-glucosaminide in 100 mM acetate buffer (pH 5.0). Samples were then incubated for 5 min at 35°C, after which time an equal volume of 1 M Na_2CO_3 was added to quench the reactions (Loomis, 1969; Huber and Mathavarajah, 2018). The quenched reactions were then deposited into 96-well black clear bottom plates and the absorbance (405 nm) was measured using a BioTek Synergy HTX plate reader.

Ppt1 and Tpp1: To assay Ppt1 activity, lysates were added to 5 µl of 9 mM of 4-Methylumbelliferyl 6-thio-Palmitate-β-D-Glucopyranoside dissolved in McIlvaine phosphate/citric-acid buffer (pH 4) supplemented with 15 mM dithiothreitol and 0.375% Triton X-100. The reactions were incubated at 37°C for 1 h after which time they were boiled for 3 min at 95°C (van Diggelen et al., 1999; Brand et al., 2018). Once the reactions were cooled, 2.75 µl of 2.5 M NaOH and 4 µl of 0.025 U/µl β-glucosidase were added to the reactions and incubated for another hour at 37°C. The reaction was quenched by

adding 0.5 M sodium carbonate-bicarbonate buffer containing 0.025% Triton X-100 (pH 10.7). The quenched reactions were then deposited into 96-well opaque black bottom plates and the fluorescence was measured using a BioTek Synergy HTX plate reader and the following filters (360/40 nm for excitation, 460/40 nm for emission). To assay Tpp1 activity, cells were lysed with buffer containing 50 mM sodium phosphate (pH 6.5) and 0.5% NP40, and then added to 80 µl of 200 µM Ala-Ala-Phe-7-amido-4-methylcoumarin dissolved in reaction buffer (150 mM NaCl, 100 mM sodium acetate, pH 4.5, 0.1% Triton X-100) (Stumpf et al., 2017). Reactions were incubated in the dark at 37°C for 1 h and then quenched by adding stop solution (150 mM NaCl, 100 mM sodium acetate, pH 4.3). The quenched reactions were then deposited into 96-well opaque black bottom plates and the fluorescence was measured using a BioTek Synergy HTX plate reader and the following filters (360/40 nm for excitation, 460/40 nm for emission).

Cathepsins: To assay CtsB activity, methods were adapted with minor revisions (Barrett, 1980). Briefly, WC lysates were incubated in reaction buffer (352 mM KH_2PO_4, 48 mM Na_2HPO_4, 4 mM EDTA, pH 6.0) with 8 mM cysteine in a total volume of 150 µl and incubated at 40°C for 5 min. A final concentration of 5 µM of substrate was added to the reaction solution, which was then incubated at 40°C for 30 min. The reaction solutions were quenched with 200 µl of 100 mM sodium chloroacetate (30 mM $NaC_2H_3O_2$, 70 mM $HC_2H_3O_2$, pH 4.3). The quenched reactions were then deposited into 96-well opaque black bottom plates and the fluorescence was measured using a BioTek Synergy HTX plate reader and the following filters (360/40 nm for excitation, 460/40 nm for emission). CtsD activity was measured following the manufacturer's instructions specified in the Cathepsin D Activity Assay Kit. Briefly, cells were lysed with 100 µl of chilled cell lysis buffer (provided in kit) and incubated on ice for 10 min. The solution was then centrifuged for 5 min. Following centrifugation, 27.5 µg of clear cell lysate was added to 100 µl of reaction buffer (provided in kit) mixed with 2 µl of substrate. Reactions were incubated at 37°C for 1 h and 30 min. The reactions were then deposited into 96-well opaque black bottom plates and the fluorescence was measured using a BioTek Synergy HTX plate reader and the following filters (360/40 nm for excitation, 460/40 nm for emission). To assay CtsF activity, WC lysates were added to 0.5 µl of 25% HCl and 1 µl of 250 µg/ml pepsin. 50 µl reactions were incubated for 1 h at 37°C after which time 0.24 µl of 0.5 mM Fluorogenic Cathepsin F Substrate followed by 5.76 µl dimethyl sulfoxide and 70 µl of 0.1 M sodium phosphate buffer containing 1 mM EDTA and 0.1% (v/v) PEG 6000 (pH 6.5) were added to the reaction mixture (total volume of 120 µl). Reactions were incubated at 27°C for 1 h (Fonovic et al., 2004). The reactions were then deposited into 96-well opaque black bottom plates and the fluorescence was measured using a BioTek Synergy HTX plate reader and the following filters (360/40 nm for excitation, 460/40 nm for emission).

Statistical Analyses

Numeric data are reported as the means ± SEM. Statistical analyses for all experiments were performed using GraphPad Prism 8 (GraphPad Software Incorporated, La Jolla, CA, United States). A one-sample *t*-test was used for evaluating data where the raw data between biological replicates was inherently variable (e.g., quantifying pixel intensity from a western blot). A p-value < 0.05 was considered significant for all analyses and n represents the number of independent experiments that were performed. Details on the specific statistical analyses performed are found in the figure captions.

RESULTS

Expression Profile of *mfsd8* During the *D. discoideum* Life Cycle

A previous study in *D. discoideum* showed that Mfsd8 localizes to endocytic compartments, linked the function of Mfsd8 to protein secretion, and revealed the Mfsd8 interactome during growth and starvation (Huber et al., 2020b). To gain further insight into the function of Mfsd8 in *D. discoideum*, here, we performed an in-depth characterization of an *mfsd8*$^-$ cell line. The expression of *mfsd8* increases during the early stages of development, which involves the chemotactic aggregation of cells into multicellular mounds (Rot et al., 2009; Mathavarajah et al., 2017). Following mound formation, *mfsd8* expression decreases dramatically reaching its lowest level just prior to terminal differentiation of pre-spore and pre-stalk cells. Expression then rises slightly during fruiting body formation. This expression profile suggested to us that Mfsd8 primarily functions during growth and the early stages of development. As a result, we focused our analysis on the effects of *mfsd8*-deficiency on processes that occur during these stages of the life cycle.

mfsd8$^-$ Cells Display Increased Proliferation and Accumulation of Fluorescein Isothiocyanate-Dextran During Growth

When cultured in liquid growth medium, *mfsd8*$^-$ cells proliferated at a significantly increased rate compared to WT cells (**Figure 1A**). Since *D. discoideum* cells ingest extracellular liquid nutrients through macropinocytosis, we assessed whether the rate of pinocytosis was affected by *mfsd8*-deficiency (Hacker et al., 1997). Cells were incubated in liquid growth medium containing FITC-dextran for a 120-min period and the amount of intracellular fluorescence was measured every 15 min. Like proliferation, the rate of FITC-dextran accumulation was significantly increased in *mfsd8*$^-$ cells relative to WT cells (**Figure 1B**).

Since loss of *mfsd8* impacted cell proliferation and the accumulation of FITC-dextran in liquid growth medium, we tested whether *mfsd8*$^-$ cells would display the same phenotype when grown on bacteria lawns. Cell lines were plated on lawns of *K. aerogenes* and plaque formation was monitored. In general, we observed that *mfsd8*$^-$ cells formed plaques earlier than WT cells and the plaques were larger than WT plaques at all time points examined (**Figure 1C**). Of note, 32 h after depositing cells onto lawns, *mfsd8*$^-$ plaques were translucent, while WT plaques were semi-translucent, indicating that *mfsd8*$^-$ cells cleared bacterial lawns earlier than WT cells. When feeding

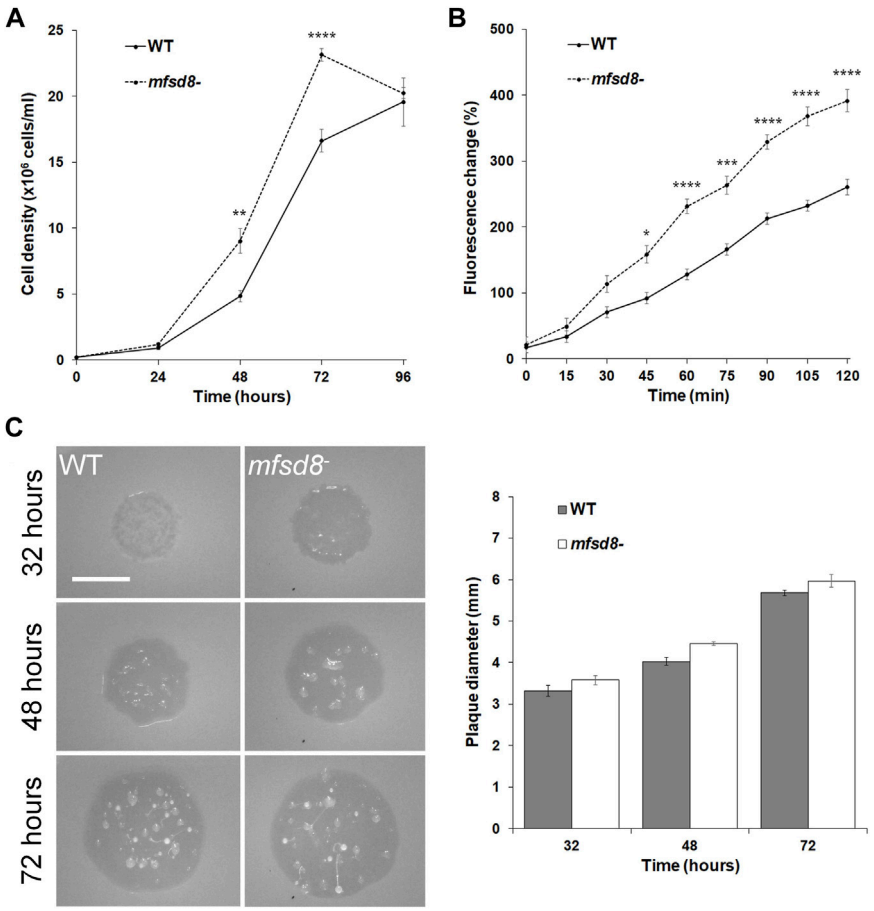

FIGURE 1 | Effect of *mfsd8*-deficiency on cell proliferation, pinocytosis, and plaque expansion. **(A)** Effect of *mfsd8*-deficiency on cell proliferation. WT and *mfsd8*$^{-}$ cells were grown axenically in HL5 medium. Cell densities were measured every 24 h over a 96-h period. Data presented as mean concentration (×10^6 cells/ml) ± SEM ($n = 5$). Statistical significance was assessed using two-way ANOVA followed by Bonferroni post-hoc analysis. $^{**}p < 0.05$ and $^{****}p < 0.0001$ vs. WT at the indicated time points. **(B)** Effect of *mfsd8*-deficiency on pinocytosis. WT and *mfsd8*$^{-}$ cells were incubated in HL5 containing FITC-dextran for 120 min. Cells were collected, washed, and lysed every 15 min. The fluorescence of the lysates was then measured using a plate reader. The data were corrected for background signals and expressed as the mean fluorescence change (%) relative to the 0-min time point. Data presented as mean fluorescence change (%) ± SEM ($n = 3$). Statistical significance was assessed using two-way ANOVA followed by Bonferroni post-hoc analysis. $^{*}p < 0.05$, $^{***}p < 0.001$, and $^{****}p < 0.0001$ vs. WT at the indicated time points. **(C)** Effect of *mfsd8*-deficiency on plaque expansion on bacterial lawns. WT and *mfsd8*$^{-}$ cells grown axenically in HL5 were harvested, washed with KK2 buffer, and deposited onto lawns of *K. aerogenes*. Plaques were imaged at the indicated time points and their diameters were quantified using Fiji/ImageJ. Scale bar = 20 μm. Data presented as mean plaque diameter (mm) ± SEM ($n = 4$).

on bacterial lawns, *D. discoideum* amoebae chemotactically respond to folic acid that is secreted by bacteria (Pan et al., 1972). However, we observed no significant effect of *mfsd8*-deficiency on folic acid-mediated chemotaxis (**Supplementary Figure S1**). Together, these results suggest that Mfsd8 regulates cell proliferation, pinocytosis, and growth on bacterial lawns in *D. discoideum*.

Loss of *mfsd8* Increases Cell Size and Inhibits Cytokinesis During Growth

When examining the proliferation of *mfsd8*$^{-}$ cells, we observed that *mfsd8*$^{-}$ cells appeared larger than WT cells. Indeed, when we quantified the area of cells cultured in liquid growth medium, we found that *mfsd8*$^{-}$ cultures contained a significantly higher proportion of cells > 200 μm^2 compared to WT cultures, and a correlated lower proportion of cells 100–200 μm^2 (**Figure 2A**).

When cultured in liquid growth medium, the majority of *D. discoideum* cells are mononucleated. However, it is well established that axenically grown cultures of *D. discoideum* can also contain polynucleated cells, which form due to defects in cytokinesis and tend to be larger than mononucleated cells (Waddell et al., 1987). Based on these findings, we examined the proportions of mononucleated and polynucleated cells in *mfsd8*$^{-}$ cultures. We observed that loss of *mfsd8* significantly decreased the proportion of mononucleated cells in culture and increased the proportion of polynucleated cells (**Figure 2B**). Together, these findings showed that *mfsd8*-deficiency increases cell size and reduces cytokinesis during the growth phase of the *D. discoideum* life cycle.

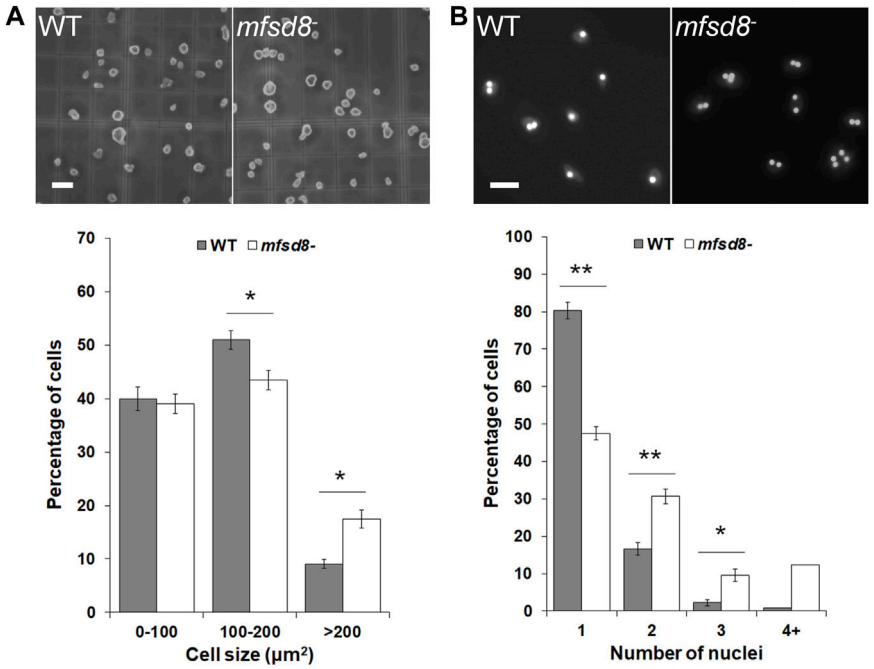

FIGURE 2 | Effect of *mfsd8*-deficiency on cell size and cytokinesis. **(A)** Effect of *mfsd8*-deficiency on cell size. WT and *mfsd8*$^{-}$ cells grown axenically in HL5 were deposited onto a hemocytometer and imaged. Scale bar = 20 µm. The area of each individual cell was quantified using Fiji/ImageJ. Data was placed into different cell area bins and expressed as a mean percentage of total cells analyzed ± SEM (n = 5). Statistical significance was assessed using two-way ANOVA followed by Bonferroni post-hoc analysis. *p < 0.05 vs. WT. **(B)** Effect of *mfsd8*-deficiency on cytokinesis. WT and *mfsd8*$^{-}$ cells grown axenically in HL5 were collected and deposited onto coverslips placed inside separate wells of a 12-well dish. Cells on coverslips were then submerged in low-fluorescence HL5 overnight at 21°C. The following day, cells were fixed in –80°C methanol mounted onto slides with Prolong Gold Anti-Fade Reagent containing DAPI. Scale bar = 20 µm. The number of nuclei within each cell was scored. For each experiment, 10 random images, each containing at least 10 cells, were obtained from each coverslip. Data presented as mean percentage of total cells analyzed ±SEM (n = 7). Statistical significance was assessed using two-way ANOVA followed by Bonferroni post-hoc analysis. *p < 0.05 and **p < 0.01 vs. WT.

Loss of *mfsd8* Alters the Levels of Autocrine Proliferation Repressor During Growth

To gain insight into the possible mechanisms underlying the increased proliferation of *mfsd8*$^{-}$ cells, the intracellular and extracellular levels of AprA were examined. AprA functions extracellularly to repress cell proliferation in *D. discoideum* and has previously been shown to be aberrantly secreted by *cln3*$^{-}$ cells, which like *mfsd8*$^{-}$ cells, also display increased rates of proliferation (Brock and Gomer, 2005; Huber et al., 2014). WC lysates and CM from WT and *mfsd8*$^{-}$ cells were collected after 24, 48, and 72 h of axenic growth (**Figure 1A**). When analyzed by western blotting, anti-AprA detected two protein bands; one at 60 kDa and the other at 55 kDa, which is consistent with the banding pattern reported in previous studies (Brock and Gomer, 2005; Huber et al., 2014) (**Figure 3**). Intracellularly, the amounts of 60 kDa AprA remained constant during all stages of axenic growth for both WT and *mfsd8*$^{-}$ cultures (**Figure 3A**). However, the amounts of 60 kDa AprA in *mfsd8*$^{-}$ cells were lower at all time points analyzed compared to WT cells. The amounts of intracellular 55 kDa AprA decreased in WT and *mfsd8*$^{-}$ cells during axenic growth but there were no differences between cell lines. In samples of CM, loss of *mfsd8* reduced the extracellular amount of 60 kDa AprA after 24 and 48 h of axenic growth, compared to WT cells, but there was no effect at the 72-h time point (**Figure 3B**). In addition, CM collected from *mfsd8*$^{-}$ cells after 72 h of axenic growth contained more 55 kDa AprA than CM collected from WT cells. Blots containing samples of CM were also probed with anti-β-actin to validate that CM did not contain intracellular proteins due to cell lysis (data not shown). Since AprA functions as a proliferation repressor, these findings suggest that altered levels of intracellular and extracellular AprA may have contributed to the increased rate of proliferation of *mfsd8*$^{-}$ cells.

mfsd8-Deficiency Increases the Intracellular Activities of Several Lysosomal Enzymes During Growth

Lysosomal enzymes play an essential role in degrading material internalized by amoebae during the growth phase of the *D. discoideum* life cycle to provide cells with nutrients (Ashworth and Quance, 1972). Interestingly, in mice, loss of *Mfsd8* has been shown to affect the levels of several lysosomal enzymes (Danyukova et al., 2018). Thus, we were interested in assessing lysosomal enzyme activity in *mfsd8*$^{-}$ cells during growth. Loss of *mfsd8* significantly increased the intracellular activities of α-galactosidase, α-glucosidase, β-glucosidase, α-mannosidase, and N-acetylglucosaminidase (**Figure 4**). The activity of β-galactosidase was also slightly elevated but not statistically significant (p = 0.08). *mfsd8*-

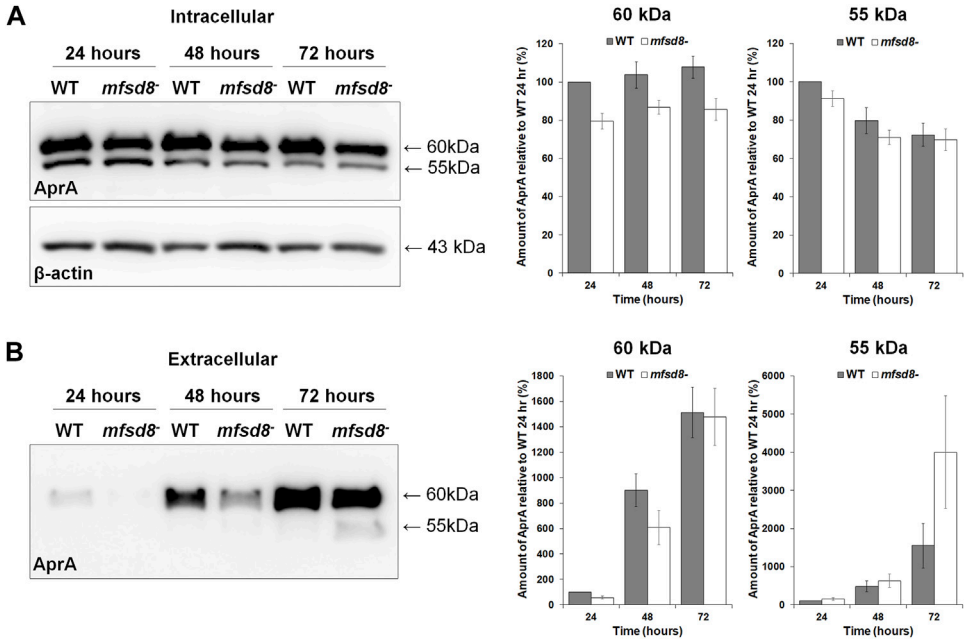

FIGURE 3 | Effect of *mfsd8*-deficiency on the intracellular and extracellular levels of AprA during growth. WT and *mfsd8*$^{-}$ cells were grown in HL5, harvested after 24, 48, and 72 h of growth, and lysed. Conditioned media (CM) was also harvested at each time point. **(A)** Whole cell lysates (15 μg) were separated by SDS-PAGE and analyzed by western blotting with anti-AprA and anti-β-actin (loading control). Molecular weight markers (in kDa) are shown to the right of each blot. Protein bands were quantified using Fiji/ImageJ. The amounts of AprA were normalized against the amounts of β-actin. Data presented as mean amount of AprA relative to WT 24 h (%) ± SEM (n = 7). **(B)** Samples of CM were harvested at each time point and standardized against cell number. Equal volumes of CM (15 μl) were separated by SDS-PAGE and analyzed by western blotting with anti-AprA. Molecular weight markers (in kDa) are shown to the right of each blot. Protein bands were quantified using Fiji/ImageJ. Data presented as mean amount of AprA relative to WT 24 h (%) ± SEM (n = 7).

deficiency also elevated the activities of Ppt1 and CtsF. In humans, mutations in *PPT1* and *CTSF* cause the CLN1 and CLN13 subtypes of NCL, respectively (Mole and Cotman, 2015). Finally, there was no effect of *mfsd8* loss on the activities of Tpp1, CtsB, or CtsD. In humans, mutations in *TPP1* and *CTSD* cause the CLN2 and CLN10 subtypes of NCL, respectively, and CTSB has been identified as a potential biomarker for CLN6 disease (Huber, 2021). Together, these data suggest that *mfsd8*$^{-}$ cells increase the activities of some, but not all, lysosomal enzymes to support their increased rates of proliferation and pinocytosis.

Loss of *mfsd8* Delays Aggregation During the Early Stages of Multicellular Development

Based on the increased expression of *mfsd8* during the early stages of development (Rot et al., 2009), we suspected that loss of *mfsd8* would affect cellular processes during this stage of the life cycle. Therefore, we performed two assays to examine the impact of *mfsd8*-deficiency on aggregation. In the first assay, cells adhered to Petri dishes were submerged in KK2 buffer to initiate the developmental program. After 8 h, there was a noticeable delay in the aggregation of *mfsd8*$^{-}$ cells compared to WT cells (**Figure 5A**). A delay in *mfsd8*$^{-}$ aggregation was also observed when cells were deposited on KK2-buffered agar (**Figure 5B**). In *D. discoideum*, mound formation occurs through the chemotactic aggregation of cells towards 3′,5′-cyclic adenosine monophosphate (cAMP) (Konijn et al., 1967). However, we did not observe a significant effect of *mfsd8*-deficiency on cAMP-mediated chemotaxis (**Supplementary Figure S1**).

A previous study showed that *mfsd8*-deficiency alters the secretion of two other CLN protein homologs in *D. discoideum*, Cln5 and CtsD, during the early stages of development (Huber et al., 2020b). Thus, we performed a CB swap experiment to examine the possible role of altered secretion in the delayed aggregation of *mfsd8*$^{-}$ cells. For this assay, we starved WT cells for 2 h and then collected the CB. In nine independent experiments, we observed that incubating *mfsd8*$^{-}$ cells in CB collected from WT cells partially restored the delayed aggregation of *mfsd8*$^{-}$ cells relative to WT cells (**Figure 6**). We also examined the effect of *mfsd8*-deficiency on cell-substrate adhesion, which plays an essential role in aggregation (Tarantola et al., 2014). During the early stages of development, loss of *mfsd8* caused more cells to de-adhere from Petri dishes relative to WT cells (**Figure 7**). Combined, these data suggest that reduced cell-substrate adhesion along with aberrant protein secretion likely contribute to the delayed aggregation of *mfsd8*$^{-}$ cells during the early stages of *D. discoideum* development.

mfsd8-Deficiency Affects the Intracellular and Extracellular Amounts of Proteins Involved in Aggregation and Cell Adhesion

To gain further insight into the cellular mechanisms affected by *mfsd8*-deficiency, we starved WT and *mfsd8*$^{-}$ cells for 4 h and

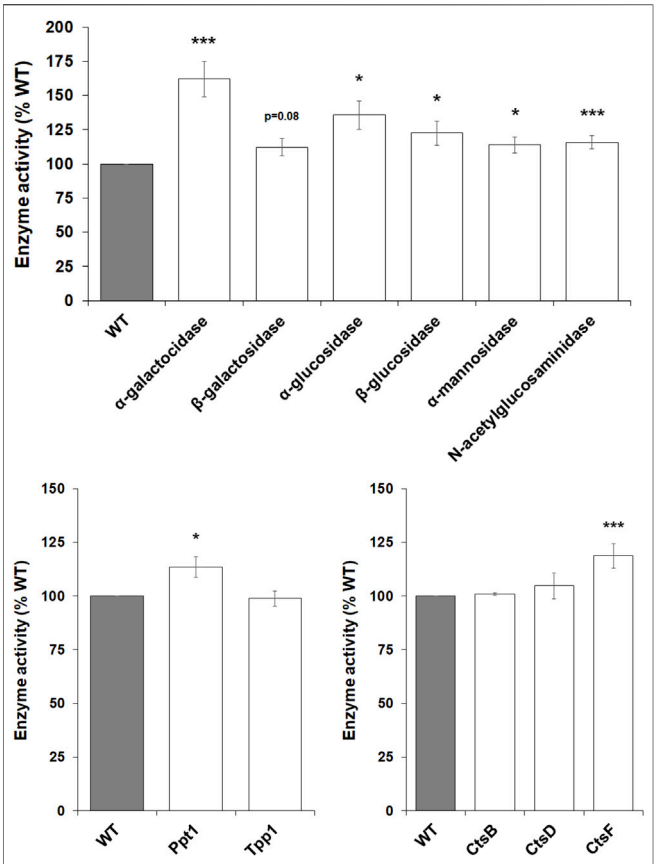

FIGURE 4 | Effect of *mfsd8*-deficiency on enzyme activity during growth. WT and *mfsd8*$^{-}$ cells grown axenically in HL5 were collected and lysed. The activities of α-galactosidase, β-galactosidase, α-glucosidase, β-glucosidase, α-mannosidase, N-acetylglucosaminidase, palmitoyl-protein thioesterase 1 (Ppt1), tripeptidyl peptidase 1 (Tpp1), cathepsin B (CtsB), cathepsin D (CtsD), and cathepsin F (CtsF) were assessed as described in the Materials and Methods. Data presented as mean enzyme activity (% WT) ± SEM ($n > 4$). Statistical significance was determined using the one-sample *t*-test (mean, 100; two-tailed) vs. WT. *$p < 0.05$ and ***$p < 0.001$ vs. WT.

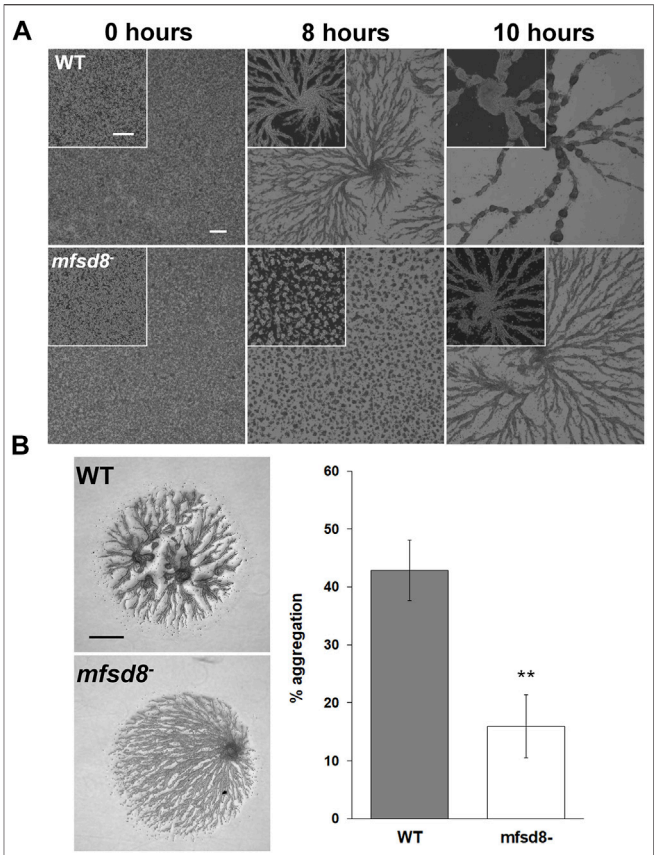

FIGURE 5 | Effect of *mfsd8*-deficiency on aggregation. **(A)** WT and *mfsd8*$^{-}$ cells grown axenically in HL5 were submerged in KK2 buffer and imaged at the indicated time points. Scale bars = 250 μm. Images are representative of six independent experiments. **(B)** WT and *mfsd8*$^{-}$ cells grown axenically in HL5 were harvested, washed with KK2 buffer, and deposited onto 0.5% agar/KK2. Images were taken once cells were deposited and after 5 h. Scale bar = 250 μm. The amount of aggregation of each cell line was quantified by measuring the area of the cell spot that remained after 5 h of starvation, subtracting it from the initial area, and then expressing the difference as a percentage of the area of the cell spot at 0 h. Data presented as mean % aggregation ± SEM ($n = 9$). Statistical significance was assessed using the Kruskal-Wallis test followed by the Dunn's multiple comparisons test. **$p < 0.01$.

analyzed the intracellular and extracellular amounts of CtnA, CadA, and DscA. CtnA is a component of a secreted 450 kDa protein complex that regulates group size during aggregation by repressing cell-cell adhesion (Roisin-Bouffay et al., 2000). CadA and DscA, which were previously shown to interact with Mfsd8 (Huber et al., 2020b), both play important roles in regulating cell adhesion during the early stages of development (Cano and Pestaña, 1984; Springer et al., 1984; Knecht et al., 1987; Brar and Siu, 1993). In addition, loss of *dscA* impairs cell-substrate adhesion during aggregation (Springer et al., 1984; Bastounis et al., 2016). In this study, loss of *mfsd8* significantly reduced the intracellular level of CtnA but increased the amount of the protein in CB, suggesting that secretion of CtnA was increased due to *mfsd8*-deficiency (**Figure 8**). Loss of *mfsd8* had no effect on the amount of CadA inside cells but significantly increased its level extracellularly. Finally, loss of *mfsd8* reduced the intracellular and extracellular levels of DscA. Combined, these data indicate that *mfsd8*-deficiency affects the intracellular and extracellular amounts of proteins involved in aggregation and cell adhesion, which could explain the delayed aggregation and reduced adhesion of *mfsd8*$^{-}$ cells during the early stages of development.

Loss of *mfsd8*$^{-}$ Alters Lysosomal Enzyme Activities During the Early Stages of Development

During multicellular development, *D. discoideum* amoebae rely on autophagy and the actions of several lysosomal enzymes to provide cells with energy and building blocks required for fueling aggregation and fruiting body formation (Loomis, 1969; Loomis, 1970; Dimond et al., 1973; Kilpatrick and Stirling, 1976; Knecht et al., 1985; Otto et al., 2003; Kiel, 2010). As noted above, previous

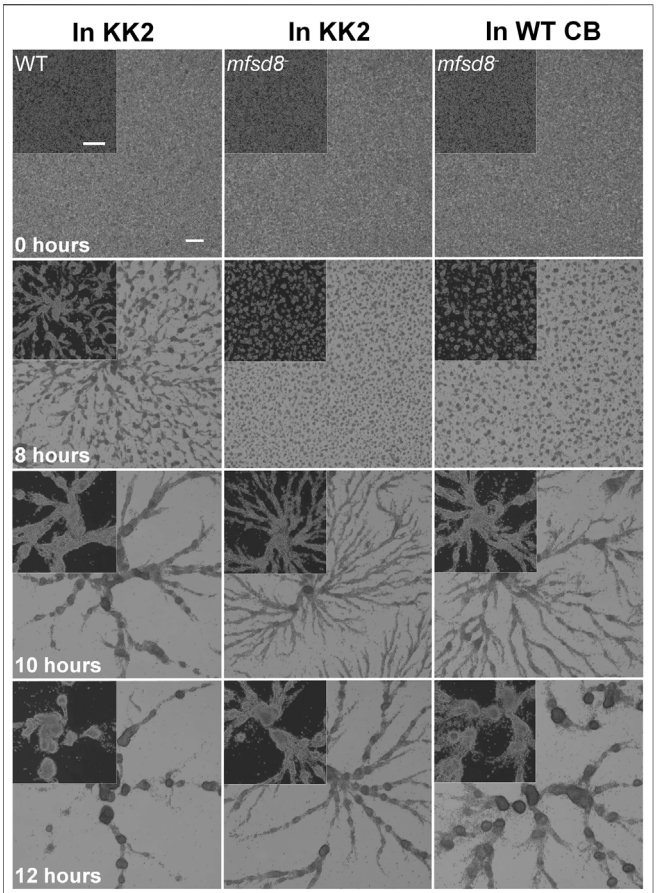

FIGURE 6 | Effect of conditioned buffer on the aggregation of *mfsd8*⁻ cells. WT cells were submerged in KK2 buffer for 2 h, after which time, the conditioned buffer (CB) of starving WT cells was collected and added to *mfsd8*⁻ cells at the onset of starvation. Images are representative of nine independent experiments. Scale bar = 250 μm.

work in mice showed that loss of *Mfsd8* affects the levels of several lysosomal enzymes (Danyukova et al., 2018). Thus, we assessed the effect of *mfsd8*-deficiency on lysosomal enzyme activity during the early stages of *D. discoideum* development. After 4 h of starvation, we observed increased intracellular activity of α-mannosidase and decreased activity of Ppt1 and CtsF (**Figure 9**). There was no significant effect of *mfsd8*-deficiency on the activities of α-galactosidase, β-galactosidase, α-glucosidase, β-glucosidase, N-acetylglucosaminidase, Tpp1, CtsB, or CtsD. Combined, these findings show that loss of *mfsd8* alters the activities of some, but not all, lysosomal enzymes during aggregation.

DISCUSSION

In this study, we examined the cellular roles of Mfsd8 during the growth and early development of *D. discoideum* (**Figure 10**). During growth, *mfsd8*-deficiency enhanced cell proliferation, FITC-dextran accumulation, and growth on bacterial lawns. The increased proliferation of *mfsd8*⁻ cells correlated with altered levels of the proliferation repressor AprA and increased activity of several lysosomal enzymes. We also showed that Mfsd8 functions during the early stages of development to regulate cell adhesion, protein secretion, lysosomal enzyme activity, and aggregation. Together, this study provides new insights into the multifaceted roles of MFSD8 in the eukaryotic cell.

The enhanced proliferation and accumulation of FITC-dextran observed in *mfsd8*⁻ cells suggests that the increased proliferation was at least partly due to increased nutrient uptake. When grown on bacterial lawns, *mfsd8*⁻ cells form plaques earlier than WT cells, further supporting their increased rate of growth. However, we showed that loss of *mfsd8* has no effect on folic acid-mediated chemotaxis, which drives bacterial acquisition during feeding (Pan et al., 1972), suggesting that Mfsd8 influences mechanisms other than folic acid signalling during bacterial uptake.

Mfsd8 localizes to the macropinocytosis pathway in *D. discoideum* (Journet et al., 2012). In addition, previous work has shown that Mfsd8 interacts with proteins that negatively regulate endocytosis such as the Ras GTPase RapA and the nucleoside diphosphate kinase NdkC-1 (Seastone et al., 1999; Annesley et al., 2011). As a result, the loss of *mfsd8* could have impacted the ability of these proteins to limit the rate of endocytosis in *mfsd8*⁻ cells. Mfsd8-interactors also include transport proteins as well as proteins that localize to endocytic vesicles and the cytoskeleton (e.g., actin-10, myosin-2 heavy chain, tubulin alpha chain, and V-ATPase subunit B) (Huber et al., 2020b). Since endocytic processes are highly dependent on cytoskeletal elements for membrane invagination and vesicle transport (Kumari et al., 2010; Mooren et al., 2012), these observations provide insight into the mechanisms underlying the role of Mfsd8 in pinocytosis.

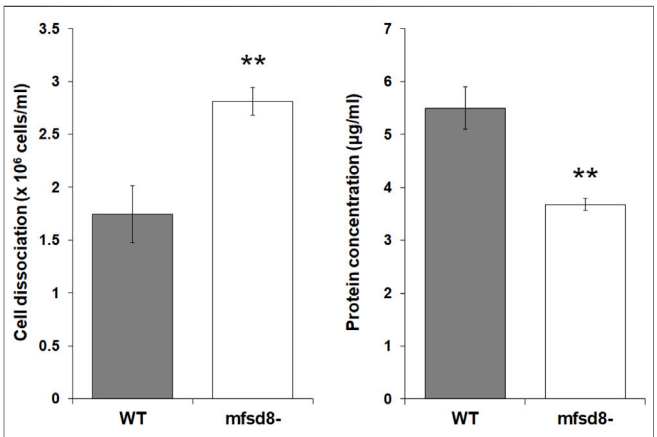

FIGURE 7 | Effect of *mfsd8*-deficiency on cell-substrate adhesion. WT and *mfsd8*⁻ cells were submerged in KK2 buffer for 4 h, after which time they were shaken at 150 rpm for 30 min. Samples of conditioned buffer were collected to measure cell dissociation, while cells remaining on the dish were lysed to assess protein concentration. Data presented as mean cell dissociation ($\times 10^6$ cells/ml) and protein concentration (μg/ml) ± SEM ($n = 9$). Statistical significance was assessed using one-way ANOVA followed by Bonferroni post-hoc analysis. $^{**}p < 0.01$ vs. WT.

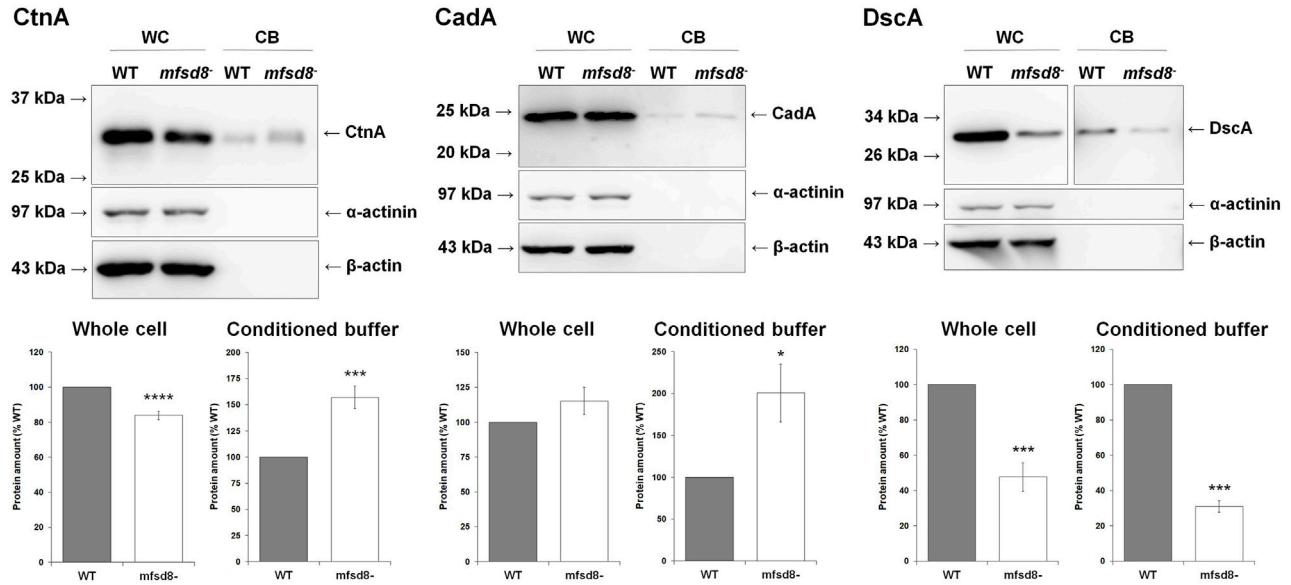

FIGURE 8 | Effect of *mfsd8*-deficiency on the intracellular and extracellular levels of CtnA, CadA, and DscA. Cells grown axenically in HL5 were starved for 4 h in KK2 buffer, after which time whole cell (WC) lysates and conditioned buffer (CB) were collected. WC lysates (15 μg) and concentrated CB (0.25 μg) were separated by SDS-PAGE and analyzed by western blotting with anti-CtnA, anti-CadA, anti-DscA, anti-α-actinin (loading and fractionation control), and anti-β-actin (loading and fractionation control). Protein bands from WC lysates were standardized against the levels of α-actinin and β-actin. Data presented as mean protein amount (% WT) ± SEM (n = 8). Statistical significance was assessed using the one sample t-test. *p < 0.05, ***p < 0.001, and ****p < 0.0001 vs. WT.

Loss of *mfsd8* increases cell size, which like proliferation, could be explained by increased liquid nutrient uptake. However, we also observed that *mfsd8*-deficiency reduces cytokinesis, which is consistent with previous work in *D. discoideum* that correlated reduced cytokinesis and enhanced pinocytosis to increased cell size (Adachi, 2001; Winckler et al., 2001; Lim et al., 2005). In addition, enhanced proliferation and reduced cytokinesis have been observed in other *D. discoideum* mutants (Brock and Gomer, 2005; Bakthavatsalam et al., 2008; Huber et al., 2014; Mathavarajah et al., 2018). In this study, we observed reduced cytokinesis of *mfsd8*$^{-}$ cells submerged in growth medium on dishes. We suspect the cytokinesis defect could be due to aberrant adhesion, which is consistent with our observations of reduced adhesion of *mfsd8*$^{-}$ cells and previous work in *D. discoideum* linking aberrant cytokinesis to defects in adhesion (Nagasaki et al., 2009; Tsujioka et al., 2012). Finally, Mfsd8 was previously shown to interact with several proteins involved in cytokinesis, including actin-10, RapA, myosin-2 heavy chain, and Ras-like protein RasG (Tuxworth et al., 1997; Huber et al., 2020b). Together, these findings support a role for Mfsd8 in cytokinesis.

In *D. discoideum,* AprA is a secreted factor that represses cell proliferation and shares structural and functional similarity with human dipeptidyl peptidase 4 (Brock and Gomer, 2005; Herlihy et al., 2013; Herlihy et al., 2017). In addition to repressing cell proliferation, AprA also coordinates cytokinesis following mitosis and helps to reduce the formation of multinucleated cells (Brock and Gomer, 2005). In this study, extracellular AprA accumulated in parallel with cell density, which aligns with observations in previous studies (Brock and Gomer, 2005; Huber et al., 2014). However, loss of *mfsd8* reduced the intracellular and extracellular levels of 60 kDa AprA suggesting that Mfsd8 may regulate proliferation by modulating both the synthesis and secretion of AprA. Contrary to the levels of 60 kDa AprA, loss of *mfsd8* dramatically increased the extracellular levels of 55 kDa AprA as cells approached the stationary phase of axenic growth. While the identity of the 55 kDa band is not known, it has been proposed to be a AprA cleavage product (Huber et al., 2014). Therefore, its increased presence in *mfsd8*$^{-}$ CM during the later stages of axenic growth could be due to AprA degradation once cells reach the stationary phase of growth, which is consistent with our observation of *mfsd8*$^{-}$ cells reaching stationary phase earlier than WT cells. Combined, these observations suggest that loss of *mfsd8* affects the synthesis and secretion of AprA, which may have played a role in the aberrant proliferation and cytokinesis observed in *mfsd8*$^{-}$ cells.

Lysosomes play an essential role in degrading endocytosed material to simple metabolites (Tjelle et al., 1996; Pillay et al., 2002). A recent study using MEFs derived from a *Mfsd8*$^{-/-}$ mouse showed that loss of *Mfsd8* alters the amounts of soluble lysosomal proteins (Danyukova et al., 2018). In addition, our previous work showed that 61% of Mfsd8-interactors during growth have catalytic activity (Huber et al., 2020b). In this study, we observed that loss of *mfsd8* increases the intracellular activities of several lysosomal enzymes, including α-galactosidase, α-glucosidase, β-glucosidase, α-mannosidase, N-acetylglucosaminidase, Ppt1, and CtsF. While these observations suggest that Mfsd8 plays a role in regulating lysosomal enzyme activity, the increased activities of these and potentially other lysosomal enzymes could also be explained by *mfsd8*$^{-}$ cells ingesting material at an increased rate. The increased

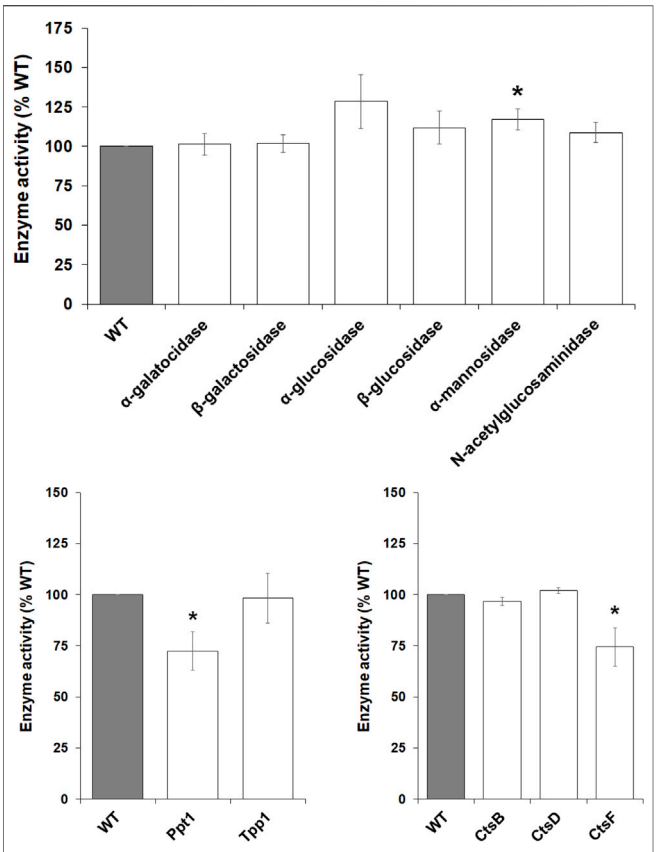

FIGURE 9 | Effect of *mfsd8*-deficiency on enzyme activity during starvation. WT and *mfsd8*$^{-}$ cells grown axenically in HL5 were starved in KK2 buffer for 4 h, after which time cells were lysed. The activities of α-galactosidase, β-galactosidase, α-glucosidase, β-glucosidase, α-mannosidase, N-acetylglucosaminidase, palmitoyl-protein thioesterase 1 (Ppt1), tripeptidyl peptidase 1 (Tpp1), cathepsin B (CtsB), cathepsin D (CtsD), and cathepsin F (CtsF) were assessed as described in the Materials and Methods. Data presented as mean enzyme activity (% WT) ± SEM ($n > 4$). Statistical significance was determined using the one-sample *t*-test (mean, 100; two-tailed) vs. WT. *$p < 0.05$ and ***$p < 0.001$ vs. WT.

lysosomal enzyme activity would allow material to be digested at an enhanced rate to prevent its accumulation and/or provide macromolecules required to fuel the increased rate of proliferation. Although one could argue that the increased intracellular fluorescence in *mfsd8*$^{-}$ cells could be due to reduced degradation of the internalized material, this seems unlikely since the increased lysosomal enzyme activity suggests that degradation of internalized material is normal in *mfsd8*$^{-}$ cells. Finally, while loss of *mfsd8* affected CtsF activity, there are several proteins in *D. discoideum* that share sequence similarity with human CTSF (Huber et al., 2020a). Therefore, it is currently not known which CTSF-like protein(s) in *D. discoideum* is/are affected by *mfsd8*-deficiency.

Here, we showed that loss of *mfsd8* delays aggregation but has no effect on cAMP-mediated chemotaxis. In addition, submerging *mfsd8*$^{-}$ cells in CB harvested from starving WT cells partially restored the timing of aggregation to WT levels. These findings support a regulatory role for Mfsd8 in processes involved in aggregation and suggest that Mfsd8 may regulate protein secretion. In a previous study, we showed that *mfsd8*-deficiency alters the secretion of Cln5 and CtsD (Huber et al., 2020b). Here, we showed that loss of *mfsd8* also modulates the secretion of CtnA. However, we did not observe any obvious effects of *mfsd8*-deficiency on global protein secretion during growth or starvation (data not shown). Thus, it seems that Mfsd8 may regulate the secretion of selected proteins *via* an undetermined pathway to regulate aggregation.

mfsd8-deficiency also affected cell adhesion during the early stages of development. Consistent with this phenotype, we observed increased extracellular amounts of CadA in *mfsd8*$^{-}$ CB and reduced intracellular and extracellular amounts of DscA. Thus, it appears that altered levels of these two cell adhesion proteins likely contributed to the reduced adhesion of *mfsd8*$^{-}$ cells. This is further supported by work that has reported impaired cell-substrate adhesion for cells lacking *dscA* (Springer et al., 1984; Bastounis et al., 2016). Intriguingly, both CadA and DscA were identified in the Mfsd8-interactome (Huber et al., 2020b). In addition, the increased secretion of CtnA also likely contributed to the reduced adhesion of *mfsd8*$^{-}$ cells, since increased extracellular CtnA has been shown to reduce adhesion (Roisin-Bouffay et al., 2000).

During multicellular development, *D. discoideum* amoebae utilize autophagy and lysosomal enzymes to provide cells with energy required for fruiting body formation (Loomis, 1969; Loomis, 1970; Dimond et al., 1973; Kilpatrick and Stirling, 1976; Knecht et al., 1985; Otto et al., 2003; Kiel, 2010). In this study, we observed increased activity of α-mannosidase in *mfsd8*$^{-}$ cells and reduced activity of Ppt1 and CtsF. Intriguingly, α-mannosidase activity is also increased in *Mfsd8*$^{-/-}$ MEFs suggesting that the regulation of α-mannosidase may be an evolutionarily conserved function of MFSD8 (Danyukova et al., 2018). However, this effect may be cell type-dependent since Damme et al. (2014) reported unaltered activity of α-mannosidase in protein extracts generated from the cerebral cortex and liver of aged *Mfsd8*-depleted mice. In addition, a reduced amount of intracellular PPT1 was reported in human *MFSD8* knockout HAP1 cells (Danyukova et al., 2018). Finally, Danyokova et al. (2018) reported reduced amounts of intracellular CLN5 and CTSD, which is supported by our findings in *D. discoideum* of reduced intracellular levels of Cln5 and CtsD in *mfsd8*$^{-}$ cells due to increased secretion (Danyukova et al., 2018; Huber et al., 2020b). Combined, these findings support a role for MFSD8 in regulating lysosomal enzyme activity. However, at present, we are unable to determine if the altered activities of α-mannosidase, Ppt1, and CtsF in *mfsd8*$^{-}$ cells contributed to the delayed aggregation or if the delayed aggregation altered the activities of those enzymes.

Collectively, our data shows that Mfsd8 plays a pleiotropic role in regulating *D. discoideum* growth and the early stages of multicellular development. While the molecular function of Mfsd8 in *D. discoideum* is not known, several of the phenotypes we uncovered could be explained by Mfsd8 functioning as a chloride channel, as has been reported in

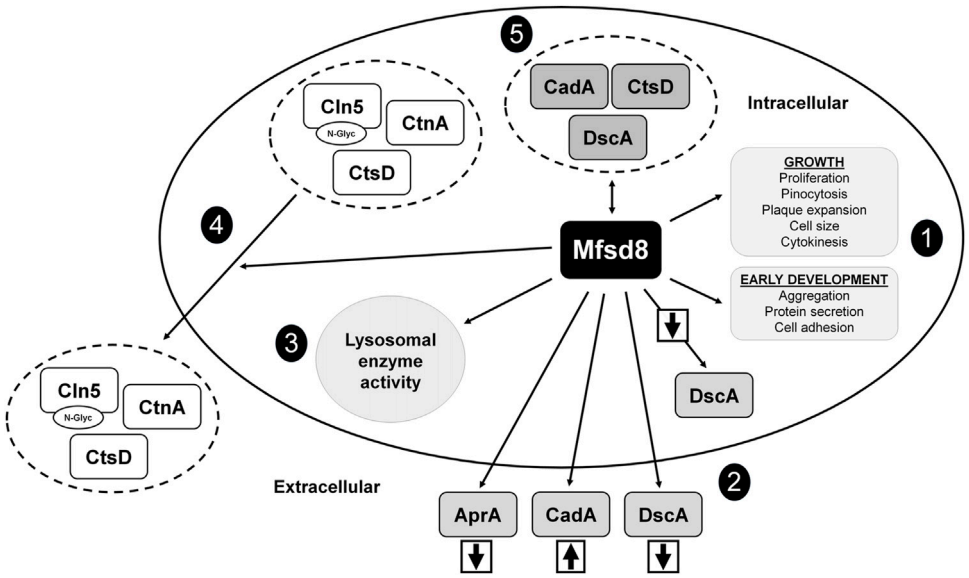

FIGURE 10 | Current model depicting the functions of Mfsd8 in *D. discoideum*. (1) Loss of *mfsd8* affects cell proliferation, pinocytosis, plaque expansion, cell size, and cytokinesis during growth, and aggregation, protein secretion, and cell adhesion during the early stages of development. (2) Loss of *mfsd8* reduces the intracellular and extracellular amounts of DscA during the early stages of development and increases the extracellular amount of CadA. Loss of *mfsd8* decreases the extracellular amount of AprA during growth. (3) Loss of *mfsd8* affects lysosomal enzyme activity during growth and the early stages of development. (4) Mfsd8 regulates the secretion of Cln5, CtsD, and CtnA during the early stages of development. (5) Mfsd8 interacts with CadA, CtsD, and DscA during growth and the early stages of development.

mammalian models (Wang et al., 2021). Future research to resolve the molecular function of Mfsd8 in *D. discoideum* should provide clarity on how loss of *mfsd8* affects the diversity of processes we uncovered in this study. Intriguingly, aberrant phenotypes observed in cells lacking *mfsd8* are also seen in other *D. discoideum* NCL models, further suggesting that CLN proteins function in shared or convergent biological pathways (Journet et al., 1999; Huber et al., 2014; Huber, 2017; Huber et al., 2017; Huber and Mathavarajah, 2018; Mathavarajah et al., 2018; Smith et al., 2019; Huber, 2020; McLaren et al., 2021). Overall, the findings of this study have provided novel insight into the roles of Mfsd8 in *D. discoideum*, which could be used to inform research in mammalian models of CLN7 disease.

DATA AVAILABILITY STATEMENT

The original contributions presented in the study are included in the article/**Supplementary Material**, further inquiries can be directed to the corresponding author.

AUTHOR CONTRIBUTIONS

SQY data acquisition and analysis, writing-original draft, review and editing; WK: data acquisition and analysis, writing-review and editing; RH: conceptualization, data acquisition and analysis, writing–review and editing, funding acquisition, supervision. All authors read and approved the final draft of the manuscript.

FUNDING

This work was supported by a Discovery Grant from the Natural Sciences and Engineering Research Council of Canada (RGPIN-2018-04855 to RH). SQY was supported by an Ontario Graduate Scholarship. WK was supported by a Canada Graduate Scholarship from the Natural Sciences and Engineering Research Council of Canada and a Queen Elizabeth II Graduate Scholarship in Science and Technology.

ACKNOWLEDGMENTS

We would like to thank Sabateeshan Mathavarajah for providing technical assistance during the early stages of this work and Dr. Richard Gomer for providing antibodies against AprA and CtnA.

SUPPLEMENTARY MATERIAL

The Supplementary Material for this article can be found online at: https://www.frontiersin.org/articles/10.3389/fcell.2022.930235/full#supplementary-material

REFERENCES

Adachi, H. (2001). Identification of Proteins Involved in Cytokinesis of *Dictyostelium*. *Cell Struct. Funct.* 26, 571–575. doi:10.1247/csf.26.571

Aiello, C., Terracciano, A., Simonati, A., Discepoli, G., Cannelli, N., Claps, D., et al. (2009). Mutations in MFSD8/CLN7 are a Frequent Cause of Variant-Late Infantile Neuronal Ceroid Lipofuscinosis. *Hum. Mutat.* 30, E530–E540. doi:10.1002/humu.20975

Annesley, S. J., Bago, R., Bosnar, M. H., Filic, V., Marinović, M., Weber, I., et al. (2011). *Dictyostelium discoideum* Nucleoside Diphosphate Kinase C Plays a Negative Regulatory Role in Phagocytosis, Macropinocytosis and Exocytosis. *PLoS One* 6, e26024. doi:10.1371/journal.pone.0026024

Ashworth, J. M., and Quance, J. (1972). Enzyme Synthesis in Myxamoebae of the Cellular Slime Mould *Dictyostelium discoideum* during Growth in Axenic Culture. *Biochem. J.* 126, 601–608. doi:10.1042/bj1260601

Bakthavatsalam, D., Brock, D. A., Nikravan, N. N., Houston, K. D., Hatton, R. D., and Gomer, R. H. (2008). The Secreted *Dictyostelium* Protein CfaD is a Chalone. *J. Cell Sci.* 121, 2473–2480. doi:10.1242/jcs.026682

Barrett, A. J. (1980). Fluorimetric Assays for Cathepsin B and Cathepsin H with Methylcoumarylamide Substrates. *Biochem. J.* 187, 909–912. doi:10.1042/bj1870909

Bastounis, E., Álvarez-González, B., del Álamo, J. C., Lasheras, J. C., and Firtel, R. A. (2016). Cooperative Cell Motility during Tandem Locomotion of Amoeboid Cells. *MBoC* 27, 1262–1271. doi:10.1091/mbc.e15-12-0836

Brand, S., Roy, S., Schröder, P., Rathmer, B., Roos, J., Kapoor, S., et al. (2018). Combined Proteomic and *In Silico* Target Identification Reveal a Role for 5-Lipoxygenase in Developmental Signaling Pathways. *Cell Chem. Biol.* 25, 1095–1106. doi:10.1016/j.chembiol.2018.05.016

Brandenstein, L., Schweizer, M., Sedlacik, J., Fiehler, J., and Storch, S. (2016). Lysosomal Dysfunction and Impaired Autophagy in a Novel Mouse Model Deficient for the Lysosomal Membrane Protein Cln7. *Hum. Mol. Genet.* 25, 777–791. doi:10.1093/hmg/ddv615

Brar, S. K., and Siu, C. H. (1993). Characterization of the Cell Adhesion Molecule Gp24 in *Dictyostelium discoideum*. Mediation of Cell-Cell Adhesion via a Ca(2+)-dependent Mechanism. *J. Biol. Chem.* 268, 24902–24909. doi:10.1016/s0021-9258(19)74550-5

Brock, D. A., and Gomer, R. H. (1999). A Cell-Counting Factor Regulating Structure Size in *Dictyostelium*. *Genes & Dev.* 13, 1960–1969. doi:10.1101/gad.13.15.1960

Brock, D. A., and Gomer, R. H. (2005). A Secreted Factor Represses Cell Proliferation in Dictyostelium. *Development* 132, 4553–4562. doi:10.1242/dev.02032

Cárcel-Trullols, J., Kovács, A. D., and Pearce, D. A. (2015). Cell Biology of the NCL Proteins: What They Do and Don't Do. *Biochim. Biophys. Acta* 1852, 2242–2255. doi:10.1016/j.bbadis.2015.04.027

Cano, A., and Pestaña, A. (1984). The Role of Membrane Lectins in *Dictyostelium discoideum* Aggregation as Ascertained by Specific Univalent Antibodies against Discoidin I. *J. Cell. Biochem.* 25, 31–43. doi:10.1002/jcb.240250104

Coston, M. B., and Loomis, W. F. (1969). Isozymes of β-Glucosidase in *Dictyostelium discoideum*. *J. Bacteriol.* 100, 1208–1217. doi:10.1128/jb.100.3.1208-1217.1969

Damme, M., Brandenstein, L., Fehr, S., Jankowiak, W., Bartsch, U., Schweizer, M., et al. (2014). Gene Disruption of Mfsd8 in Mice Provides the First Animal Model for CLN7 Disease. *Neurobiol. Dis.* 65, 12–24. doi:10.1016/j.nbd.2014.01.003

Danyukova, T., Ariunbat, K., Thelen, M., Brocke-Ahmadinejad, N., Mole, S. E., and Storch, S. (2018). Loss of CLN7 Results in Depletion of Soluble Lysosomal Proteins and Impaired mTOR Reactivation. *Hum. Mol. Genet.* 27, 1711–1722. doi:10.1093/hmg/ddy076

Dimond, R. L., Brenner, M., and Loomis, W. F. (1973). Mutations Affecting N -Acetylglucosaminidase in *Dictyostelium discoideum*. *Proc. Natl. Acad. Sci. U.S.A.* 70, 3356–3360. doi:10.1073/pnas.70.12.3356

Fey, P., Kowal, A. S., Gaudet, P., Pilcher, K. E., and Chisholm, R. L. (2007). Protocols for Growth and Development of *Dictyostelium discoideum*. *Nat. Protoc.* 2, 1307–1316. doi:10.1038/nprot.2007.178

Fey, P., Dodson, R. J., Basu, S., Hartline, E. C., and Chisholm, R. L. (2019). dictyBase and the Dicty Stock Center (Version 2.0) - A Progress Report. *Int. J. Dev. Biol.* 63, 563–572. doi:10.1387/ijdb.190226pf

Fonovic, M., Brömme, D., Turk, V., and Turk, B. (2004). Human Cathepsin F: Expression in Baculovirus System, Characterization and Inhibition by Protein Inhibitors. *Biol. Chem.* 385, 505–509. doi:10.1515/BC.2004.059

Gruenheit, N., Baldwin, A., Stewart, B., Jaques, S., Keller, T., Parkinson, K., et al. (2021). Mutant Resources for Functional Genomics in *Dictyostelium discoideum* Using REMI-Seq Technology. *BMC Biol.* 19, 172. doi:10.1186/s12915-021-01108-y

Hacker, U., Albrecht, R., and Maniak, M. (1997). Fluid-phase Uptake by Macropinocytosis in *Dictyostelium*. *J. Cell Sci.* 110, 105–112. doi:10.1242/jcs.110.2.105

Herlihy, S. E., Pilling, D., Maharjan, A. S., and Gomer, R. H. (2013). Dipeptidyl Peptidase IV is a Human and Murine Neutrophil Chemorepellent. *J. Immunol.* 190, 6468–6477. doi:10.4049/jimmunol.1202583

Herlihy, S. E., Tang, Y., Phillips, J. E., and Gomer, R. H. (2017). Functional Similarities between the dictyostelium Protein AprA and the Human Protein Dipeptidyl-Peptidase IV. *Protein Sci.* 26, 578–585. doi:10.1002/pro.3107

Huber, R. J., and Mathavarajah, S. (2018). Secretion and Function of Cln5 during the Early Stages of *Dictyostelium* Development. *Biochim. Biophys. Acta Mol. Cell Res.* 1865, 1437–1450. doi:10.1016/j.bbamcr.2018.07.017

Huber, R. J., and Mathavarajah, S. (2019). Comparative Transcriptomics Reveals Mechanisms Underlying Cln3-Deficiency Phenotypes in *Dictyostelium*. *Cell. Signal.* 58, 79–90. doi:10.1016/j.cellsig.2019.02.004

Huber, R. J., Myre, M. A., and Cotman, S. L. (2014). Loss of Cln3 Function in the Social Amoeba *Dictyostelium discoideum* Causes Pleiotropic Effects that are Rescued by Human CLN3. *PLoS One* 9, e110544. doi:10.1371/journal.pone.0110544

Huber, R. J., Myre, M. A., and Cotman, S. L. (2017). Aberrant Adhesion Impacts Early Development in a *Dictyostelium* Model for Juvenile Neuronal Ceroid Lipofuscinosis. *Cell Adhesion Migr.* 11, 399–418. doi:10.1080/19336918.2016.1236179

Huber, R. J., Hughes, S. M., Liu, W., Morgan, A., Tuxworth, R. I., and Russell, C. (2020a). The Contribution of Multicellular Model Organisms to Neuronal Ceroid Lipofuscinosis Research. *Biochim. Biophys. Acta Mol. Basis Dis.* 1866, 165614. doi:10.1016/j.bbadis.2019.165614

Huber, R. J., Mathavarajah, S., and Yap, S. Q. (2020b). Mfsd8 Localizes to Endocytic Compartments and Influences the Secretion of Cln5 and Cathepsin D in *Dictyostelium*. *Cell. Signal.* 70, 109572. doi:10.1016/j.cellsig.2020.109572

Huber, R. J. (2016). Using the Social Amoeba *Dictyostelium* to Study the Functions of Proteins Linked to Neuronal Ceroid Lipofuscinosis. *J. Biomed. Sci.* 23, 83. doi:10.1186/s12929-016-0301-0

Huber, R. J. (2017). Loss of Cln3 Impacts Protein Secretion in the Social Amoeba *Dictyostelium*. *Cell. Signal.* 35, 61–72. doi:10.1016/j.cellsig.2017.03.022

Huber, R. J. (2020). Molecular Networking in the Neuronal Ceroid Lipofuscinoses: Insights from Mammalian Models and the Social Amoeba *Dictyostelium discoideum*. *J. Biomed. Sci.* 27, 64. doi:10.1186/s12929-020-00653-y

Huber, R. J. (2021). Altered Protein Secretion in Batten Disease. *Dis. Model Mech.* 14, dmm049152. doi:10.1242/dmm.049152

Journet, A., Chapel, A., Jehan, S., Adessi, C., Freeze, H., Klein, G., et al. (1999). Characterization of *Dictyostelium discoideum* Cathepsin D. *J. Cell Sci.* 112, 3833–3843. doi:10.1242/jcs.112.21.3833

Journet, A., Klein, G., Brugière, S., Vandenbrouck, Y., Chapel, A., Kieffer, S., et al. (2012). Investigating the Macropinocytic Proteome of Dictyostelium Amoebae by High-Resolution Mass Spectrometry. *Proteomics* 12, 241–245. doi:10.1002/pmic.201100313

Kiel, J. A. K. W. (2010). Autophagy in Unicellular Eukaryotes. *Phil. Trans. R. Soc. B* 365, 819–830. doi:10.1098/rstb.2009.0237

Kilpatrick, D. C., and Stirling, J. L. (1976). Properties and Developmental Regulation of an α-d-galactosidase from *Dictyostelium discoideum*. *Biochem. J.* 158, 409–417. doi:10.1042/bj1580409

Kirolos, S. A., Rijal, R., Consalvo, K. M., and Gomer, R. H. (2021). Using *Dictyostelium* to Develop Therapeutics for Acute Respiratory Distress Syndrome. *Front. Cell Dev. Biol.* 9, 710005. doi:10.3389/fcell.2021.710005

Knecht, D. A., Green, E. D., Loomis, W. F., and Dimond, R. L. (1985). Developmental Changes in the Modification of Lysosomal Enzymes in

Dictyostelium discoideum. *Dev. Biol.* 107, 490–502. doi:10.1016/0012-1606(85)90330-6

Knecht, D. A., Fuller, D. L., and Loomis, W. F. (1987). Surface Glycoprotein, Gp24, Involved in Early Adhesion of *Dictyostelium discoideum*. *Dev. Biol.* 121, 277–283. doi:10.1016/0012-1606(87)90160-6

Konijn, T. M., Van De Meene, J. G., Bonner, J. T., and Barkley, D. S. (1967). The Acrasin Activity of Adenosine-3',5'-Cyclic Phosphate. *Proc. Natl. Acad. Sci. U.S.A.* 58, 1152–1154. doi:10.1073/pnas.58.3.1152

Kumari, S., Mg, S., and Mayor, S. (2010). Endocytosis Unplugged: Multiple Ways to Enter the Cell. *Cell Res.* 20, 256–275. doi:10.1038/cr.2010.19

Lim, C. J., Zawadzki, K. A., Khosla, M., Secko, D. M., Spiegelman, G. B., and Weeks, G. (2005). Loss of the *Dictyostelium* RasC Protein Alters Vegetative Cell Size, Motility and Endocytosis. *Exp. Cell Res.* 306, 47–55. doi:10.1016/j.yexcr.2005.02.002

Loomis, W. F. (1969). Acetylglucosaminidase, an Early Enzyme in the Development of *Dictyostelium discoideum*. *J. Bacteriol.* 97, 1149–1154. doi:10.1128/jb.97.3.1149-1154.1969

Loomis, W. F. (1970). Developmental Regulation of α-Mannosidase in *Dictyostelium discoideum*. *J. Bacteriol.* 103, 375–381. doi:10.1128/jb.103.2.375-381.1970

Maruhn, D. (1976). Rapid Colorimetric Assay of β-galactosidase and N-Acetyl-β-Glucosaminidase in Human Urine. *Clin. Chim. Acta* 73, 453–461. doi:10.1016/0009-8981(76)90147-9

Mathavarajah, S., Flores, A., and Huber, R. J. (2017). *Dictyostelium discoideum*: A Model System for Cell and Developmental Biology. *Curr. Protoc. Essent. Lab. Tech.* 15, 14.1.1–14.1.19. doi:10.1002/cpet.15

Mathavarajah, S., McLaren, M. D., and Huber, R. J. (2018). Cln3 Function Is Linked to Osmoregulation in a *Dictyostelium* Model of Batten Disease. *Biochim. Biophys. Acta Mol. Basis Dis.* 1864, 3559–3573. doi:10.1016/j.bbadis.2018.08.013

Mathavarajah, S., VanIderstine, C., Dellaire, G., and Huber, R. J. (2021). Cancer and the Breakdown of Multicellularity: What *Dictyostelium discoideum*, a Social Amoeba, Can Teach Us. *Bioessays* 43, e2000156. doi:10.1002/bies.202000156

McLaren, M., Mathavarajah, S., and Huber, R. (2019). Recent Insights into NCL Protein Function Using the Model Organism *Dictyostelium discoideum*. *Cells* 8, 115. doi:10.3390/cells8020115

McLaren, M. D., Mathavarajah, S., Kim, W. D., Yap, S. Q., and Huber, R. J. (2021). Aberrant Autophagy Impacts Growth and Multicellular Development in a *Dictyostelium* Knockout Model of CLN5 Disease. *Front. Cell Dev. Biol.* 9, 657406. doi:10.3389/fcell.2021.657406

Mole, S. E., and Cotman, S. L. (2015). Genetics of the Neuronal Ceroid Lipofuscinoses (Batten Disease). *Biochim. Biophys. Acta Mol. Basis Dis.* 1852, 2237–2241. doi:10.1016/j.bbadis.2015.05.011

Mooren, O. L., Galletta, B. J., and Cooper, J. A. (2012). Roles for Actin Assembly in Endocytosis. *Annu. Rev. Biochem.* 81, 661–686. doi:10.1146/annurev-biochem-060910-094416

Nagasaki, A., Kanada, M., and Uyeda, T. Q. (2009). Cell Adhesion Molecules Regulate Contractile Ring-independent Cytokinesis in *Dictyostelium discoideum*. *Cell Res.* 19, 236–246. doi:10.1038/cr.2008.318

Otto, G. P., Wu, M. Y., Kazgan, N., Anderson, O. R., and Kessin, R. H. (2003). Macroautophagy is Required for Multicellular Development of the Social Amoeba *Dictyostelium discoideum*. *J. Biol. Chem.* 278, 17636–17645. doi:10.1074/jbc.m212467200

Pain, E., Shinhmar, S., and Williams, R. S. B. (2021). Using *Dictyostelium* to Advance Our Understanding of the Role of Medium Chain Fatty Acids in Health and Disease. *Front. Cell Dev. Biol.* 9, 722066. doi:10.3389/fcell.2021.722066

Pan, P., Hall, E. M., and Bonner, J. T. (1972). Folic Acid as Second Chemotactic Substance in the Cellular Slime Moulds. *Nat. New Biol.* 237, 181–182. doi:10.1038/newbio237181a0

Persaud-Sawin, D.-A., Mousallem, T., Wang, C., Zucker, A., Kominami, E., and Boustany, R.-M. N. (2007). Neuronal Ceroid Lipofuscinosis: A Common Pathway? *Pediatr. Res.* 61, 146–152. doi:10.1203/pdr.0b013e31802d8a4a

Phillips, J. E., and Gomer, R. H. (2015). Partial Genetic Suppression of a Loss-Of-Function Mutant of the Neuronal Ceroid Lipofuscinosis-Associated Protease TPP1 in *Dictyostelium discoideum*. *Dis. Model Mech.* 8, 147–156. doi:10.1242/dmm.018820

Pillay, C. S., Elliott, E., and Dennison, C. (2002). Endolysosomal Proteolysis and its Regulation. *Biochem. J.* 363, 417–429. doi:10.1042/bj3630417

Rivero, F., and Maniak, M. (2006). Quantitative and Microscopic Methods for Studying the Endocytic Pathway. *Methods Mol. Biol.* 346, 423–438. doi:10.1385/1-59745-144-4:423

Roisin-Bouffay, C., Jang, W., Caprette, D. R., and Gomer, R. H. (2000). A Precise Group Size in *Dictyostelium* is Generated by a Cell-Counting Factor Modulating Cell-Cell Adhesion. *Mol. Cell* 6, 953–959. doi:10.1016/s1097-2765(05)00082-1

Rot, G., Parikh, A., Curk, T., Kuspa, A., Shaulsky, G., and Zupan, B. (2009). Dictyexpress: A *Dictyostelium discoideum* Gene Expression Database with an Explorative Data Analysis Web-Based Interface. *BMC Bioinform.* 10, 265. doi:10.1186/1471-2105-10-265

Schindelin, J., Arganda-Carreras, I., Frise, E., Kaynig, V., Longair, M., Pietzsch, T., et al. (2012). Fiji: An Open-Source Platform for Biological-Image Analysis. *Nat. Methods* 9, 676–682. doi:10.1038/nmeth.2019

Schulz, A., Kohlschütter, A., Mink, J., Simonati, A., and Williams, R. (2013). NCL Diseases - Clinical Perspectives. *Biochim. Biophys. Acta Mol. Basis Dis.* 1832, 1801–1806. doi:10.1016/j.bbadis.2013.04.008

Seastone, D. J., Zhang, L., Buczynski, G., Rebstein, P., Weeks, G., Spiegelman, G., et al. (1999). The Small MrRas-like GTPase Rap1 and the Phospholipase C Pathway Act to Regulate Phagocytosis inDictyostelium Discoideum. *MBoC* 10, 393–406. doi:10.1091/mbc.10.2.393

Sharifi, A., Kousi, M., Sagné, C., Bellenchi, G. C., Morel, L., Darmon, M., et al. (2010). Expression and Lysosomal Targeting of CLN7, a Major Facilitator Superfamily Transporter Associated with Variant Late-Infantile Neuronal Ceroid Lipofuscinosis. *Hum. Mol. Genet.* 19, 4497–4514. doi:10.1093/hmg/ddq381

Siintola, E., Topcu, M., Aula, N., Lohi, H., Minassian, B. A., Paterson, A. D., et al. (2007). The Novel Neuronal Ceroid Lipofuscinosis Gene MFSD8 Encodes a Putative Lysosomal Transporter. *Am. J. Hum. Genet.* 81, 136–146. doi:10.1086/518902

Smith, P. K., Sen, M. G., Fisher, P. R., and Annesley, S. J. (2019). Modelling of Neuronal Ceroid Lipofuscinosis Type 2 in *Dictyostelium discoideum* Suggests that Cytopathological Outcomes Result from Altered TOR Signalling. *Cells* 8, 469. doi:10.3390/cells8050469

Springer, W. R., Cooper, D. N. W., and Barondes, S. H. (1984). Discoidin I is Implicated in Cell-Substratum Attachment and Ordered Cell Migration of *Dictyostelium discoideum* and Resembles Fibronectin. *Cell* 39, 557–564. doi:10.1016/0092-8674(84)90462-8

Stadler, J., Bauer, G., Westphal, M., and Gerisch, G. (1984). Monoclonal Antibody against Cytoplasmic Lectins of *Dictyostelium discoideum*: Cross-Reactivity with a Membrane Glycoprotein, Contact Site A, and with *E. coli* β-galactosidase and *Lac* Repressor. *Hoppe Seylers Z Physiol. Chem.* 365, 283–288. doi:10.1515/bchm2.1984.365.1.283

Steenhuis, P., Herder, S., Gelis, S., Braulke, T., and Storch, S. (2010). Lysosomal Targeting of the CLN7 Membrane Glycoprotein and Transport via the Plasma Membrane Require a Dileucine Motif. *Traffic* 11, 987–1000. doi:10.1111/j.1600-0854.2010.01073.x

Steenhuis, P., Froemming, J., Reinheckel, T., and Storch, S. (2012). Proteolytic Cleavage of the Disease-Related Lysosomal Membrane Glycoprotein CLN7. *Biochim. Biophys. Acta Mol. Basis Dis.* 1822, 1617–1628. doi:10.1016/j.bbadis.2012.05.015

Stumpf, M., Müller, R., Gaßen, B., Wehrstedt, R., Fey, P., Karow, M. A., et al. (2017). A Tripeptidyl Peptidase 1 is a Binding Partner of the Golgi pH Regulator (GPHR) in *Dictyostelium*. *Dis. Model Mech.* 10, 897–907. doi:10.1242/dmm.029280

Tarantola, M., Bae, A., Fuller, D., Bodenschatz, E., Rappel, W.-J., and Loomis, W. F. (2014). Cell Substratum Adhesion during Early Development of *Dictyostelium discoideum*. *PloS One* 9, e106574. doi:10.1371/journal.pone.0106574

Tjelle, T. E., Brech, A., Juvet, L. K., Griffiths, G., and Berg, T. (1996). Isolation and Characterization of Early Endosomes, Late Endosomes and Terminal Lysosomes: Their Role in Protein Degradation. *J. Cell Sci.* 109, 2905–2914. doi:10.1242/jcs.109.12.2905

Tsujioka, M., Yumura, S., Inouye, K., Patel, H., Ueda, M., and Yonemura, S. (2012). Talin Couples the Actomyosin Cortex to the Plasma Membrane during Rear Retraction and Cytokinesis. *Proc. Natl. Acad. Sci. U.S.A.* 109, 12992–12997. doi:10.1073/pnas.1208296109

Tuxworth, R. I., Cheetham, J. L., Machesky, L. M., Spiegelmann, G. B., Weeks, G., and Insall, R. H. (1997). *Dictyostelium* RasG is Required for Normal Motility and Cytokinesis, but Not Growth. *J. Cell Biol.* 138, 605–614. doi:10.1083/jcb.138.3.605

van Diggelen, O. P., Keulemans, J. L. M., Winchester, B., Hofman, I. L., Vanhanen, S. L., Santavuori, P., et al. (1999). A Rapid Fluorogenic Palmitoyl-Protein Thioesterase Assay: Pre- and Postnatal Diagnosis of INCL. *Mol. Genet. Metabolism* 66, 240–244. doi:10.1006/mgme.1999.2809

von Kleist, L., Ariunbat, K., Braren, I., Stauber, T., Storch, S., and Danyukova, T. (2019). A Newly Generated Neuronal Cell Model of CLN7 Disease Reveals Aberrant Lysosome Motility and Impaired Cell Survival. *Mol. Genet. Metabolism* 126, 196–205. doi:10.1016/j.ymgme.2018.09.009

Waddell, D. R., Duffy, K., and Vogel, G. (1987). Cytokinesis is Defective in *Dictyostelium* Mutants with Altered Phagocytic Recognition, Adhesion, and Vegetative Cell Cohesion Properties. *J. Cell Biol.* 105, 2293–2300. doi:10.1083/jcb.105.5.2293

Wang, Y., Zeng, W., Lin, B., Yao, Y., Li, C., Hu, W., et al. (2021). CLN7 is an Organellar Chloride Channel Regulating Lysosomal Function. *Sci. Adv.* 7, eabj9608. doi:10.1126/sciadv.abj9608

Wimmer, B., Lottspeich, F., Ritter, J., and Bronnenmeier, K. (1997). A Novel Type of Thermostable α-D-glucosidase from Thermoanaerobacter Thermohydrosulfuricus Exhibiting Maltodextrinohydrolase Activity. *Biochem. J.* 328, 581–586. doi:10.1042/bj3280581

Winckler, T., Trautwein, C., Tschepke, C., Neuhäuser, C., Zündorf, I., Beck, P., et al. (2001). Gene Function Analysis by Amber Stop Codon Suppression: CMBF Is a Nuclear Protein that Supports Growth and Development of *Dictyostelium* Amoebae. *J. Mol. Biol.* 305, 703–714. doi:10.1006/jmbi.2000.4341

Conflict of Interest: The authors declare that the research was conducted in the absence of any commercial or financial relationships that could be construed as a potential conflict of interest.

Publisher's Note: All claims expressed in this article are solely those of the authors and do not necessarily represent those of their affiliated organizations, or those of the publisher, the editors and the reviewers. Any product that may be evaluated in this article, or claim that may be made by its manufacturer, is not guaranteed or endorsed by the publisher.

frontiers | Frontiers in Cell and Developmental Biology

ORIGINAL RESEARCH
published: 24 June 2022
doi: 10.3389/fcell.2022.912812

Discovery of Small Molecule KCC2 Potentiators Which Attenuate *In Vitro* Seizure-Like Activity in Cultured Neurons

Francis J. Prael III[1,2], *Kwangho Kim*[2,3], *Yu Du*[1], *Brittany D. Spitznagel*[1], *Gary A. Sulikowski*[1,2,3], *Eric Delpire*[4] *and C. David Weaver*[*,1,2,3]

[1]Department of Pharmacology, Vanderbilt University, Nashville, TN, United States, [2]Vanderbilt Institute of Chemical Biology, Vanderbilt University, Nashville, TN, United States, [3]Department of Chemistry, Vanderbilt University, Nashville, TN, United States, [4]Department of Anesthesiology, Vanderbilt University School of Medicine, Nashville, TN, United States

KCC2 is a K^+-Cl^- cotransporter that is expressed in neurons throughout the central nervous system. Deficits in KCC2 activity have been implicated in a variety of neurological disorders, including epilepsy, chronic pain, autism spectrum disorders, and Rett syndrome. Therefore, it has been hypothesized that pharmacological potentiation of KCC2 activity could provide a treatment for these disorders. To evaluate the therapeutic potential of pharmacological KCC2 potentiation, drug-like, selective KCC2 potentiators are required. Unfortunately, the lack of such tools has greatly hampered the investigation of the KCC2 potentiation hypothesis. Herein, we describe the discovery and characterization of a new class of small-molecule KCC2 potentiator. This newly discovered class exhibits KCC2-dependent activity and a unique mechanistic profile relative to previously reported small molecules. Furthermore, we demonstrate that KCC2 potentiation by this new class of KCC2 potentiator attenuates seizure-like activity in neuronal-glial co-cultures. Together, our results provide evidence that pharmacological KCC2 potentiation, by itself, is sufficient to attenuate neuronal excitability in an *in vitro* model that is sensitive to anti-epileptic drugs. Our findings and chemical tools are important for evaluating the promise of KCC2 as a therapeutic target and could lay a foundation for the development of KCC2-directed therapeutics for multiple neurological disorders.

Keywords: KCC, small molecule, potentiator, HTS, epilepsy

OPEN ACCESS

Edited by:
Silvia Dossena, Paracelsus Medical University, Austria

Reviewed by:
David Harden, Janssen Pharmaceuticals, Inc., United States
Simona Rodighiero, European Institute of Oncology (IEO), Italy

***Correspondence:**
C. David Weaver
david.weaver@vanderbilt.edu

Specialty section:
This article was submitted to Cellular Biochemistry, a section of the journal Frontiers in Cell and Developmental Biology

Received: *04 April 2022*
Accepted: *02 June 2022*
Published: *24 June 2022*

Citation:
Prael III FJ, Kim K, Du Y, Spitznagel BD, Sulikowski GA, Delpire E and Weaver CD (2022) Discovery of Small Molecule KCC2 Potentiators Which Attenuate In Vitro Seizure-Like Activity in Cultured Neurons. Front. Cell Dev. Biol. 10:912812. doi: 10.3389/fcell.2022.912812

INTRODUCTION

KCC2 (*SLC12A5*) is a K^+-Cl^- cotransporter that utilizes the electrochemical K^+ gradient to drive the efflux of Cl^- from cells (Payne, 1997). This activity is critical for establishing and maintaining low intracellular Cl^- [$(Cl^-)_i$] in neurons of the mature nervous system (Williams et al., 1999; Schulte et al., 2018). It is the resulting Cl^- gradient that underlies the ability of $GABA_A$ and glycine receptors to mediate inhibitory neurotransmission and a healthy excitatory/inhibitory balance.

Pathologically elevated levels of $[Cl^-]_i$ in neurons are implicated in a variety of neurological disorders, including: epilepsy (Duy et al., 2019; Fukuda and Watanabe, 2019) neuropathic pain (Kahle et al., 2014a), autism spectrum disorders (Tyzio et al., 2014), and Rett syndrome (Tang et al.,

2019). These pathologically high levels of neuronal $[Cl^-]_i$ are thought to cause excessive neural excitability that is a hallmark of these disorders (Schulte et al., 2018; Akita and Fukuda, 2020). During pathological states, elevated $[Cl^-]_i$ is thought to cause excess neuronal excitability through decreasing the efficacy of Cl^- channel effectors of fast inhibitory neurotransmission, namely $GABA_A$ and glycine receptors, which use the Cl^- gradient generated by low neuronal $[Cl^-]_i$ to exert their inhibitory effects. Diminished fast inhibitory neurotransmission leads to pathological increases in excitatory neuronal activity (Raimondo et al., 2017). Therefore, restoring a normal $[Cl^-]_i$ through potentiation of KCC2-mediated Cl^- transport could counteract pathologically elevated levels of neuronal $[Cl^-]_i$ in the epilepsies and other diseases, and thus produce a therapeutic effect.

There is consistency between 1) clinical and 2) preclinical evidence supporting KCC2 potentiation as a viable therapeutic strategy in epilepsy. 1) Clinically, over a dozen loss-of-function KCC2 mutations in humans have been linked to epilepsies (Kahle et al., 2014b; Puskarjov et al., 2014; Stödberg et al., 2015; Saitsu et al., 2016; Saito et al., 2017), and resected tissue from epileptic patients has shown electrophysiological and protein expression-level abnormalities consistent with diminished KCC2 function (Huberfeld et al., 2007; Munakata et al., 2007). 2) preclinically, pharmacological (Sivakumaran et al., 2015; Kelley et al., 2016; Dzhala and Staley, 2020) or genetic (Woo et al., 2002; Silayeva et al., 2015; Chen et al., 2017; Kelley et al., 2018) inhibition of KCC2 activity exacerbates seizure-like activity across multiple epilepsy models. In contrast, genetically increasing KCC2 activity attenuates seizure-like activity in the same model systems, without overt side effects (Chen et al., 2017; Moore et al., 2018; Magloire et al., 2019). Furthermore, TrkB modulators that indirectly increase KCC2 activity restore the efficacy of phenobarbital (PB), a $GABA_A$ positive allosteric modulator and antiepileptic drug, in PB-resistant seizure models (Carter et al., 2018; Kang et al., 2020; Kipnis et al., 2020). While some preliminary evidence exists linking pharmacological KCC2 potentiation to antiepileptic efficacy (Carter et al., 2018; Dzhala and Staley, 2020; Kang et al., 2020; Kipnis et al., 2020), further validation of the efficacy of KCC2 potentiation is warranted, owing to limitations with current small-molecule KCC2 potentiators.

To further evaluate if pharmacological KCC2 potentiation is antiepileptic, small molecule KCC2 potentiators with adequate potency, efficacy, and selectivity are required. Recently described KCC2 potentiators have increased the field's understanding of KCC2 in neurological disease (Tang et al., 2019). However, these compounds have critical limitations because they 1) either act by modulating signaling pathways that have pleiotropic effects on cells (Lee et al., 2007; Yamada et al., 2016; Tang et al., 2019; Zhang et al., 2020), thereby complicating the interpretation of their effects, or 2) have some controversy surrounding their ability to potentiate KCC2 (Gagnon et al., 2013; Cardarelli et al., 2017; Gagnon et al., 2017). Therefore, discovery of new, selective KCC2 potentiators would greatly benefit the field.

Herein we describe the discovery of a new class of small-molecule KCC2 potentiator with a unique mechanism-of-action. We demonstrate that the compounds in this class attenuate seizure-like neuronal hyperactivity in cortical neuronal-glial co-cultures providing supporting the hypothesis that pharmacological KCC2 potentiation alone is sufficient to attenuate neuronal hyper-excitability.

MATERIALS AND METHODS

HEK-293 Cell Culture

HEK-293 cells were cultured up to 80%–90% confluence in T75 flasks (TPP) containing HEK-293 medium [α-MEM (Corning) supplemented with 10% (v/v) fetal bovine serum (FBS) (Gibco), 1x glutagro (Corning)] and appropriate antibiotics for selection (vide infra) at 37°C and 5% CO_2. Cells were passaged every 3–4 days using TrypLE (Gibco) up to a maximum of 20 passages.

Rat Husbandry

Timed-pregnant Sprague Dawley dams were purchased from Taconic Biosciences. Experiments involving animals were approved by and adhered to the guidelines of the Vanderbilt Institutional Animal Care and Use Committee.

Antibodies for Western Blotting and Immunofluorescence

Primary antibodies used for Western blotting were: 1:1,000 rabbit Anti-K^+-Cl^- cotransporter (KCC2) Antibody (MilliporeSigma 07-432) and 1:500 mouse Transferrin Receptor Monoclonal Antibody (H68.4) (ThermoFisher Scientific 13-6800). Secondary antibodies used for Western blotting were: 1:15,000 goat anti-Rabbit IRDye 800CW (LI-COR 926-32211) and 1: 10,000 goat anti-Mouse IgG IRDye 680RD (LI-COR 926-68070). Primary antibodies used for immunofluorescence were: 1:100 mouse anti-KCC2/SLC12A5 Antibody (S1-12) (Novus Biologicals NBP2-59337) and 1:50 rabbit anti-GAD65/GAD67 (Thermo Fisher Scientific PA5-36080). Secondary antibodies used for immunofluorescence were: 1:500 goat anti-Mouse IgG IRDye 680RD (LI-COR 926-68070) and 1:500 Goat anti-Rabbit Alexa Fluor 555 Secondary Antibody (ThermoFisher A-21428). Cell nuclei were labeled using Hoechst 33,342 at 1 μg/ml.

Molecular Cloning

The most widely expressed KCC2 isoform in the adult mammalian brain (KCC2b) was subcloned from the pCITF-KCC2 vector (Addgene plasmid #61404) into pcDNA4/TO (ThermoFisher Scientific) between the AflII and NotI restriction sites using Gibson Assembly (New England Biolabs) for inducible expression of KCC2b. SuperClomeleon (Grimley et al., 2013) was subcloned into the pENTR1A no ccDB (w48-1) (Addgene #17398) Entry Vector (Campeau et al., 2009) using Gibson Assembly. The SuperClomeleon ORF was subsequently recombined into the pLenti CMV Puro DEST (w118-1) (Addgene #17452) destination vector for lentiviral transduction and constitutive SuperClomeleon expression using LR Clonase II Enzyme Mix (ThermoFisher Scientific). The SuperClomeleon-pLenti-CMV-puro vector was propagated in NEB® Stable Competent *E. coli* (New England Biolabs) to prevent

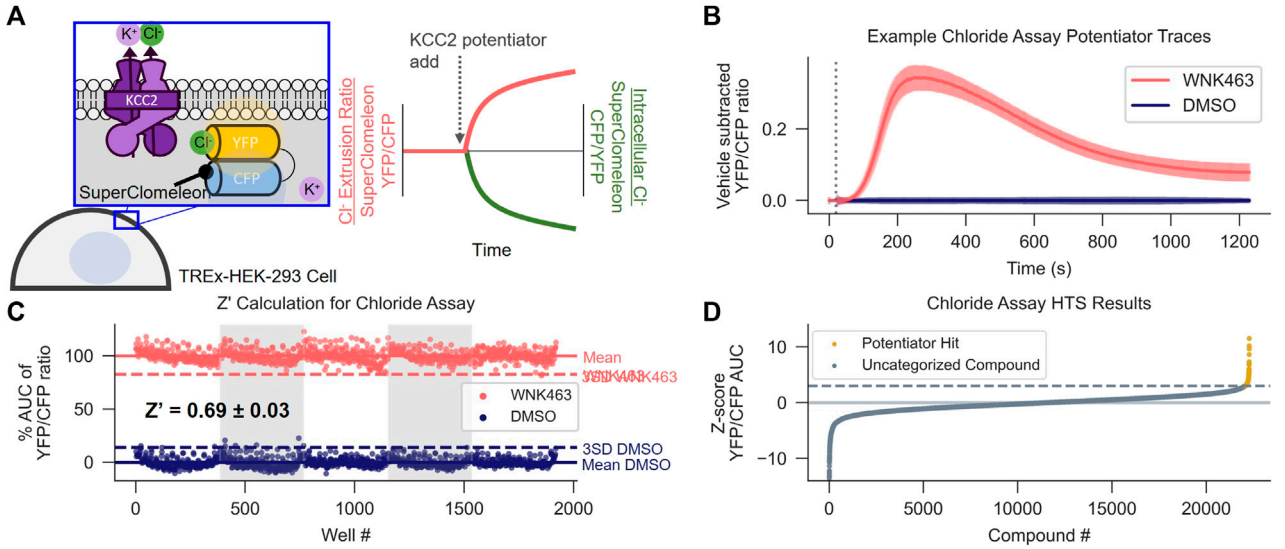

FIGURE 1 | Discovery of KCC2 Potentiators by High-throughput Screening. **(A)** Cl^- flux assay schematic and data normalization. KCC2 activity is approximated by measuring intracellular Cl^- using HEK-293 cells overexpressing KCC2 and the Cl^- sensor SuperClomeleon. Data are normalized as a YFP/CFP ratio, such that an increase in KCC2 activity registers as an increase in value. **(B,C)** Calculation of Z′ for the Cl^- flux assay. **(B)** Vehicle control subtracted and averaged traces from the Cl^- flux assay used for Z′ calculation. Cells were treated with either the indirect KCC2 potentiator WNK463 or DMSO control. Error bars represent standard deviation of the mean (SD). **(C)** Percent Area Under the Curve (AUC) of Cl^- flux assay traces in **(B)**. The mean AUC (solid line) and three x SD away from mean AUC (dotted line) are displayed for each treatment (n = 192). **(D)** Results of screening approximately 23,000 unique compounds at a concentration of 10 μM in the Cl^- flux assay. Data are presented as Z-scores relative to vehicle control values on each plate. A Z-score of 3 (dotted line) was used as a cut off for separating potentiator hits (gold) from uncategorized compounds (gray). All experiments were performed at 37°C.

homologous recombination of long terminal repeats. All sequences were verified by Sanger Sequencing (GenHunter) before cell line generation.

Polyclonal Cell Line Generation for the Cl^- Flux Assay

Two polyclonal cell lines were created for use with the Cl^- flux assay 1) one expressing KCC2 and 2) one lacking KCC2 expression. 1) Generation of a KCC2-expressing polyclonal cell line: to allow for inducible expression of KCC2, T-REx-293 cells (ThermoFisher Scientific) seeded at 40% confluence in a T75 flask were transfected with the pcDNA4/TO-KCC2 construct using FuGENE6 (Promega), according to the manufacturer's instructions. One day after transfection, the cells were treated with 5 μg/ml blasticidin, to select for the tetracycline repressor protein in T-REx-293 cells, and 250 μg/ml zeocin, to select for KCC2. Cells remained under selection for 2 weeks to ensure stable KCC2 expression. To generate a stable T-REx-293-KCC2-SuperClomeleon cell line, SuperClomeleon-containing lentivirus was produced in HEK-293T cells through transfection of the pLenti-CMV-puro-SuperClomeleon transfer vector, the pCMV-VSV-G (Addgene #8454) envelope plasmid, and the pMDLg/pRRE (Addgene #12251) and pRSV-Rev (Addgene #12253) packaging plasmids using FuGENE6. The T-REx-293-KCC2 polyclonal cell line was then seeded at 40% confluence in a T75 flask and transduced with SuperClomeleon-containing lentivirus as described in (Campeau et al., 2009). One day after transduction, the virus-containing medium was removed, and the cells were washed with fresh HEK-293 medium. Cells were treated with 5 μg/ml blasticidin, 250 μg/ml zeocin, and 3 μg/ml puromycin roughly 24 h after removal of the virus to generate the polyclonal T-REx-293-KCC2-SuperClomeleon cell line. 2) Generation of a control cell line lacking KCC2 expression: The T-REx-293-SuperClomeleon polyclonal cell line was generated by transducing T-REx-293 with SuperClomeleon-bearing lentivirus as described above. A clone was selected whose YFP and CFP fluorescence levels matched those of uninduced 4p2.F7 cells used for screening (see below) to control for baseline SuperClomelon expression.

Monoclonal Cell Line Generation for HTS

The T-REx-293-KCC2-SuperClomeleon polyclonal cell line was cell-sorted based on highest YFP and CFP fluorescence into individual wells of a 96-well, TC-treated plate (Corning) using a BD FACSAria IIIu. After allowing the cells to proliferate to near confluence in the presence of antibiotic selection, the ~200 resulting monoclonal cell lines were screened using the Cl^- flux assay (described below) ± 100 μM KCC2 potentiator N-Ethylmaleimide (NEM) (MilliporeSigma) and ± KCC2 induction with 1 μM tetracycline (MilliporeSigma). The six cell lines having the highest KCC2 induction-dependent NEM activity, as determined by the highest Area Under the Curve (AUC) of the YFP/CFP ratio in treated vs. untreated cells, were then tested for 1) suitability for HTS by Z′ value calculation (see below), and 2) for predicted KCC2 pharmacology by testing a

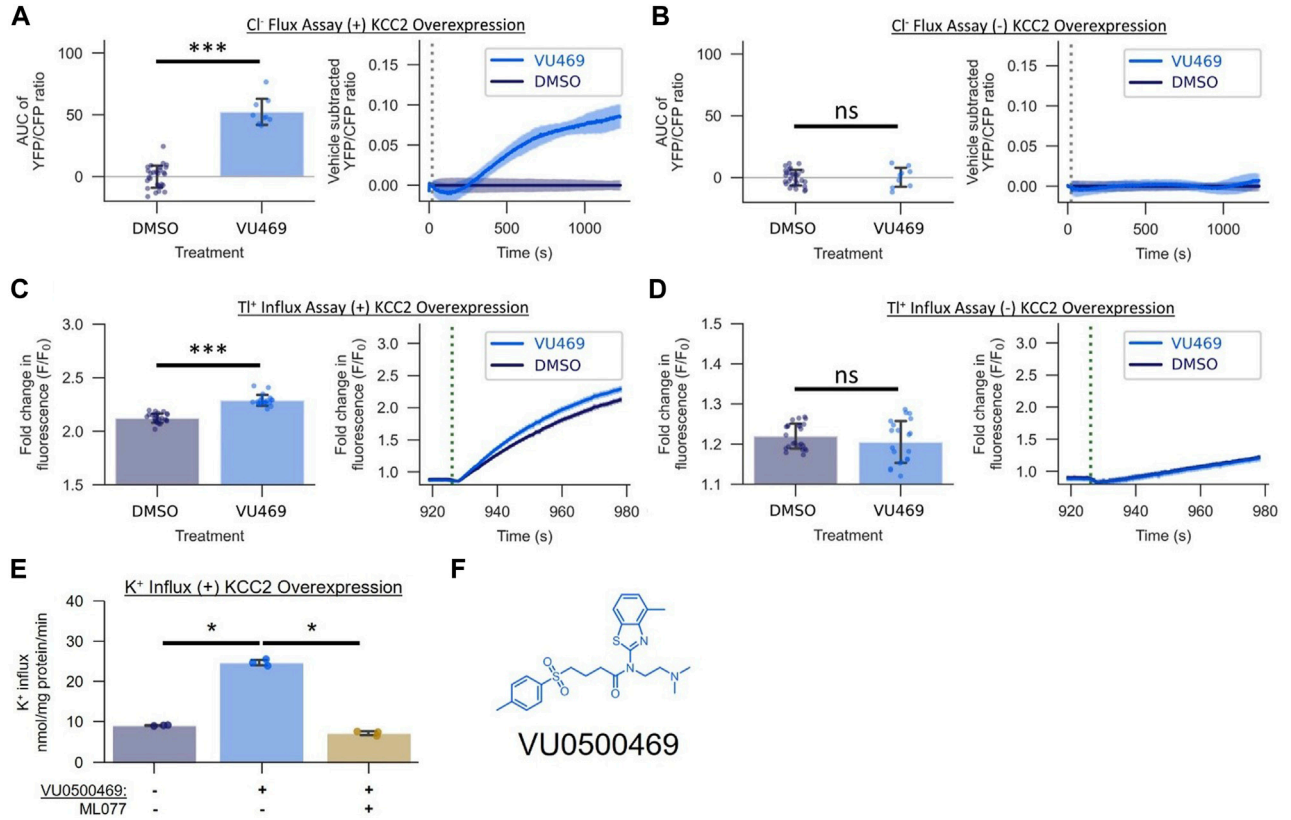

FIGURE 2 | VU0500469 (VU469) potentiates KCC2-mediated Cl^- transport across mechanistically distinct assays of KCC2 activity in HEK-293 cells. **(A,B)** Effect of 15 μM VU0500469 on Cl^- flux in the presence or absence of KCC2 overexpression ($n > 9$). **(A)** Cl^- Flux Assay in cells overexpressing KCC2. Left: AUC of the YFP/CFP Cl^- efflux ratio. Right: Vehicle control subtracted and averaged traces of the YFP/CFP Cl^- efflux ratio. Dotted line represents time of compound addition. **(B)** Cl^- flux assay in cells lacking KCC2 overexpression. **(C,D)** Effect of 15 μM VU0500469 on Tl^+ influx in the presence or absence of KCC2 overexpression ($n > 20$). **(C)** Tl^+ influx in cells overexpressing KCC2. Left: maximum fold increase in Tl^+-sensitive dye fluorescence. Right: fold increase in Tl^+-sensitive dye fluorescence over time. Dotted line represents time point of Tl^+ addition. **(D)** Tl^+ influx in cells lacking KCC2 overexpression. **(E)** Effect of 30 μM VU0500469 on K^+ influx in cells overexpressing KCC2 in the absence or presence of KCC2 inhibitor ML077 ($n = 3$). **(F)** VU0500469 structure. All experiments conducted at 37°C. Error bars represent SD. Statistical significance calculated by Welch's t-test **(E)** and Mann–Whitney U test **(A–D)**: * = $p < 0.05$, *** = $p < 0.001$, ns = $p > 0.05$.

panel of known KCC2 modulators (**Supplementary Figure S1A**). The cell line, 4p2.F7, which had the highest Z' value and exhibited pharmacology consistent with KCC2 expression was subsequently used for HTS.

Cl^- Flux Assay

The Cl^- flux assay functioned by monitoring $[Cl^-]_i$ levels via a the genetically encoded Cl^- sensor, SuperClomeleon (Grimley et al., 2013), and, after compound treatment, using the reported changes in $[Cl^-]_i$ as a surrogate for changes in KCC2 Cl^- transport activity. The SuperClomeleon Cl^- sensor functions by FRET between a Cl^--sensitive YFP, which is quenched upon Cl^- binding, and a Cl^--insensitive CFP, which is used as a control for SuperClomeleon expression. The corresponding changes in FRET ratio are then used to quantify changes in $[Cl^-]_i$. The day before the experiment, HEK-293 cells were counted and plated at 20,000 cells/well in black-walled, amine-coated, 384-well plates (Corning) at 20 μl/well in HEK-293 medium supplemented with 10 ng/ml tetracycline to induce KCC2 expression. After incubation for approximately 24 h at 37°C and 5% CO_2, cell culture medium was removed by centrifugation in the Blue Washer (BlueCatBio) under the GentleSpin setting, and 20 μl/well Assay Buffer [1x Hank's Buffered Salt Solution (ThermoFisher) + 20 mM HEPES (Corning) (pH 7.3)] was added to each well. Compound plates were made in polypropylene, v-bottom, 384-well plates (Greiner) with compounds dissolved at 2x relative to the desired concentration in Assay Buffer; dimethyl sulfoxide (DMSO) concentrations were kept below 0.8% (v/v) final. Cell plates were incubated at 37°C within the Panoptic plate reader (WaveFront Biosciences) for at least 30 min prior to the beginning of the run to allow for temperature equilibration to 37°C. To measure Cl^- flux, fluorescence was recorded at 1 Hz [excitation at 440/40 nm and emission alternating between 480/17 nm (CFP) and 536/40 nm [YFP FRET]) for 20 s, then 20 μl/well of the 2x compound solution was added and fluorescence was recorded for an additional 20 min. For data analysis, a YFP/CFP FRET ratio was calculated by taking the YFP fluorescence intensity value and, to account for the temporal offset between CFP and YFP recordings, interpolating CFP values to match the

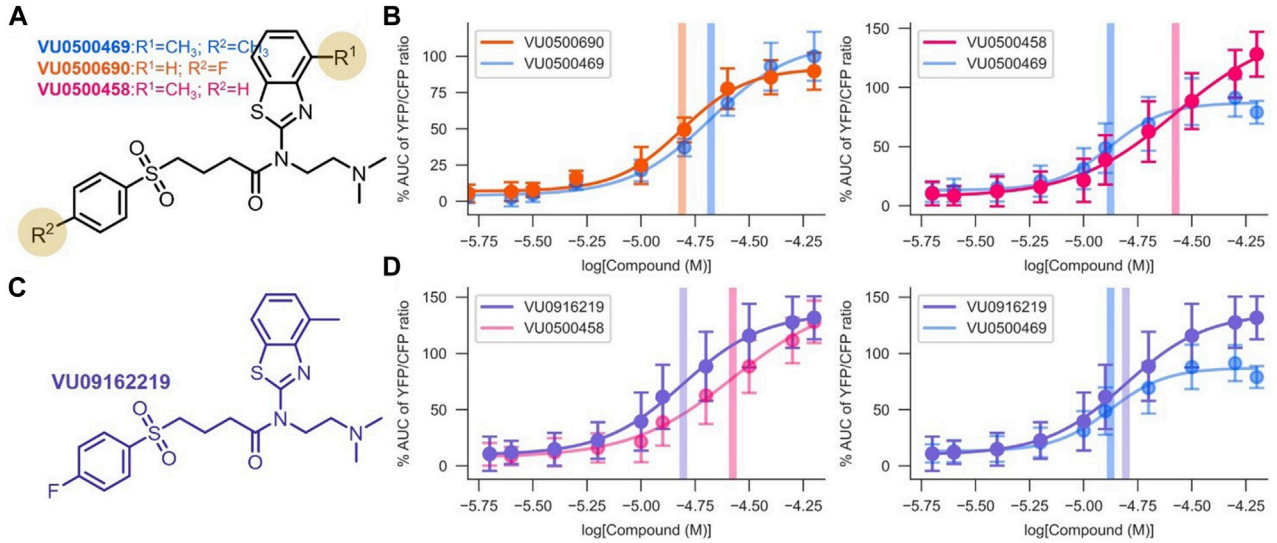

FIGURE 3 | Development of VU0916219, a KCC2 potentiator with improved activity. Experiments conducted at 37°C, using the Cl^- Flux Assay in HEK-293 cells overexpressing KCC2. Data are normalized to maximum VU0500469 activity being 100%. **(A)** Structures of the most potent and efficacious VU0500469 analogs. **(B)** Comparison of VU0500469 dose-response curve to the most potent (left panel) and efficacious (right panel) compounds. **(C)** Structure of VU0916219. **(D)** Comparison of VU0916219 to the most efficacious compound (left panel), and VU0500469 (right panel). (n ≥ 6), error bars represent SD.

YFP timepoints. The YFP values were then divided by the interpolated CFP values to generate a YFP/CFP FRET ratio to quantify Cl^- extrusion (**Figure 1A**). The FRET ratio traces were subsequently normalized by dividing each fluorescence trace by the trace's average FRET ratio before compound addition. To quantify Cl^- flux over the course of the run, average vehicle control-treated traces were subtracted from each trace to reveal the signal dependent on presence of an active test compound, and AUC for each FRET trace was calculated using the trapezoidal rule. For cotreatment experiments, compounds were sourced from the following distributors: Go6983 (Tocris), WNK463 (Selleckchem), Bumetanide (MilliporeSigma), and VU0463271 (Tocris). All other compounds were either synthesized in house (see Synthesis sections below) or purchased from Life Chemicals Inc.

Z' Calculation

Z' values were calculated as in (Zhang et al., 1999) using the following formula:

$$Z' = 1 - \left((3\sigma\_(c+)) + (3\sigma\_(c-)) \Big/ \left(\left| \mu\_(c+) - \mu\_(c-) \right| \right) \right)$$

Where $\sigma\_(c+)$ is the standard deviation (SD) of positive control (KCC2 potentiator)-treated wells, $3\sigma\_(c-)$ is the SD of the vehicle-treated wells, $\mu\_(c+)$ is the mean of positive control-treated wells, and $\mu\_(c-)$ is the mean of the positive control-treated wells.

Thallium (Tl^+) Influx Assay

The day before the experiment, HEK-293 derived cell lines were resuspended in HEK-293 medium supplemented with 100 ng/ml tetracycline to induce KCC2 expression, counted, and were plated at 20,000 cells/well in black-walled, amine-coated, 384-well plates at 20 µl/well. On the day of the experiment, a 5x Tl^+ stimulus solution [125 mM sodium bicarbonate, 12 mM thallium sulfate, 1 mM magnesium sulfate, 1.8 mM calcium sulfate, 5 mM glucose, and 10 mM HEPES (pH 7.3)] was prepared and pipetted into a polypropylene, v-bottom, 384-well plate. Compounds were prepared at a 2x concentration in Assay Buffer in a separate polypropylene, v-bottom, 384-well plate, with a final DMSO concentration below 0.8% (v/v). The stimulus and 2x compound plates were sealed and incubated for at least 30 min at 37°C within the Panoptic plate reader before assaying. After approximately 24 h of induction, the cells were loaded with the Tl^+-sensitive dye, Thallos (ION Biosciences): the cell culture medium in the cell plate was removed and replaced with 20 µl/well Assay Buffer containing 2.5 µg/ml Thallos-AM, and cells were dye-loaded for 45 min at 37°C. After dye loading, the dye-loading solution was removed and replaced with 20 µl/well Assay Buffer pre-warmed to 37°C. The cell plate was then incubated for 10 additional minutes at 37°C in the Panoptic before assaying. After incubation, fluorescence intensity values were recorded at 1 Hz (482/35 nm excitation and 536/40 nm emission) for 10 s prior to compound addition. 20 µl/well of 2x compound solution was added to the cells and incubated for 10 min followed by the addition of 10 µl/well of the 5x Tl^+ stimulus solution and an additional 1 min of data collection. Data for each well were normalized by dividing data at each time point for a given well by the average of its own pre-compound addition baseline fluorescence (F/F_0) and Tl^+ influx was quantified by the maximum fluorescence after Tl^+ stimulus addition. The T-REx-293-KCC2 monoclonal cell line, TK2D2, and untransfected T-REx-293 cells were used for all Tl^+ influx experiments. The TK2D2 cell line was generated from the T-REx-293-KCC2

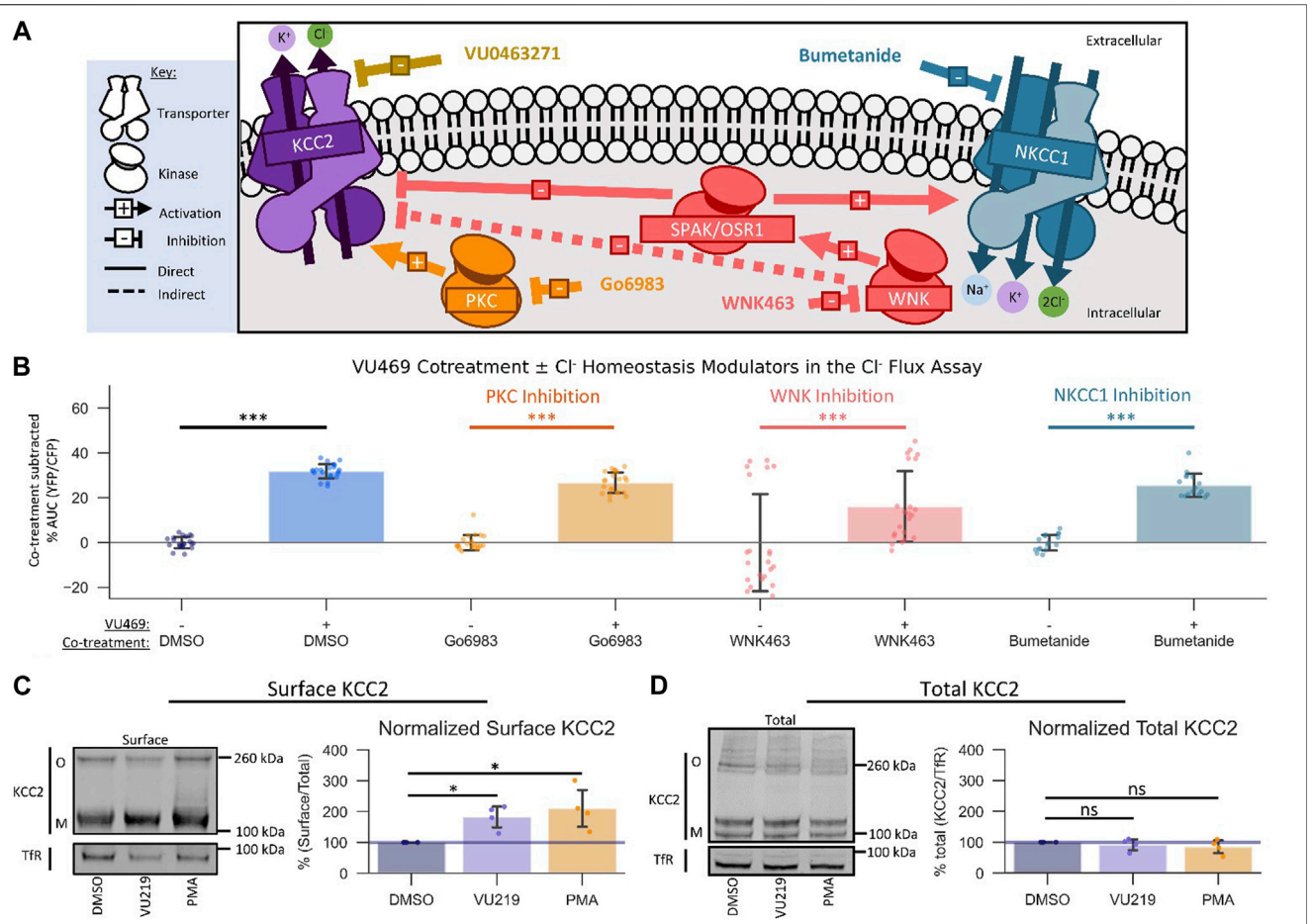

FIGURE 4 | VU0500469 potentiates KCC2 by a unique mechanism. All experiments conducted using the Cl^- flux assay in HEK-293 cells overexpressing KCC2 at 37°C, unless otherwise noted. **(A)** Schematic depicting investigated small molecule targets known to regulate Cl^- homeostasis. **(B)** Co-treatment of modulators of Cl^- homeostasis from **(A)** with or without VU0500469 ($n \geq 16$). **(C)** Left: representative Western blot of biotinylated surface fraction from cells treated with vehicle (DMSO), VU0916219 (VU219), or the positive control phorbol 12-myristate 13-acetate (PMA). Band intensity was normalized to Transferrin Receptor (TfR) levels. O, oligomeric KCC2, M, monomeric KCC2. Right: quantification of Surface KCC2/Total KCC2 normalized to TfR levels. **(D)** Left: representative Western blot of total protein fraction from cells treated as in **(C)**. Right: quantification of total KCC2 normalized to TfR levels. ($n = 4$) Error bars represent SD. Statistical significance calculated by Mann–Whitney U test **(B)** or paired t-test **(C,D)**: * = $p < 0.05$, *** = $p < 0.001$.

polyclonal cell line described in the "Polyclonal Cell Line Generation for the Cl^- Flux Assay" section by serial dilution and subsequent clonal selection based on maximum Tl^+ influx that was sensitive to the KCC2 inhibitor VU0463271.

High-Throughput Screening

Eighty nanoliters of 10 mM (nominal) test compound dissolved in DMSO was transferred from the Vanderbilt Institute of Chemical Biology (VICB) Discovery Collection to 384-well, v-bottomed, polypropylene plates (Greiner) using an Echo 555 Acoustic Liquid Handler (Labcyte) and diluted to a concentration of 20 µM by addition of 40 µl/well Assay Buffer using a Multidrop Combi Reagent Dispenser (ThermoFisher Scientific). The compound plates were mixed on a plate shaker (ThermoFisher Scientific) for at least 2 min, sealed and bath sonicated (Branson) for approximately 1 min. Compound plates and cell plates were incubated at 37°C for at least 30 min before assaying. The 4p2.F7 T-REx-293-KCC2-SuperClomeleon cell line was prepared and assayed at 37°C, at final compound concentration of 10 µM (nominal), as described in the Cl^- flux assay section. Z-scores were calculated relative to the YFP/CFP ratio AUCs of vehicle-treated wells on a plate-by-plate basis. Potentiator Hits were defined as compounds with a Z-score > 3. The first 9,000 compounds were screened at random from the VICB Discovery Collection. The final 14,000 compounds were iteratively screened, in batches of approximately 3,000 compounds, to enrich for compound classes which could accommodate chemical variation while still potentiating KCC2-dependent Cl^- extrusion in four steps. First, hits were selected and re-tested in the Cl^- flux assay, with or without KCC2 expression, to gauge reproducibility and KCC2-dependence. Second, hits were tested in the Tl^+ influx assay to test if their activity was consistent across disparate assays of KCC2 ion transport. Third, hits that exhibited reproducible and consistent activity at KCC2 were enriched in the next round of screening by selecting plates from the compound library

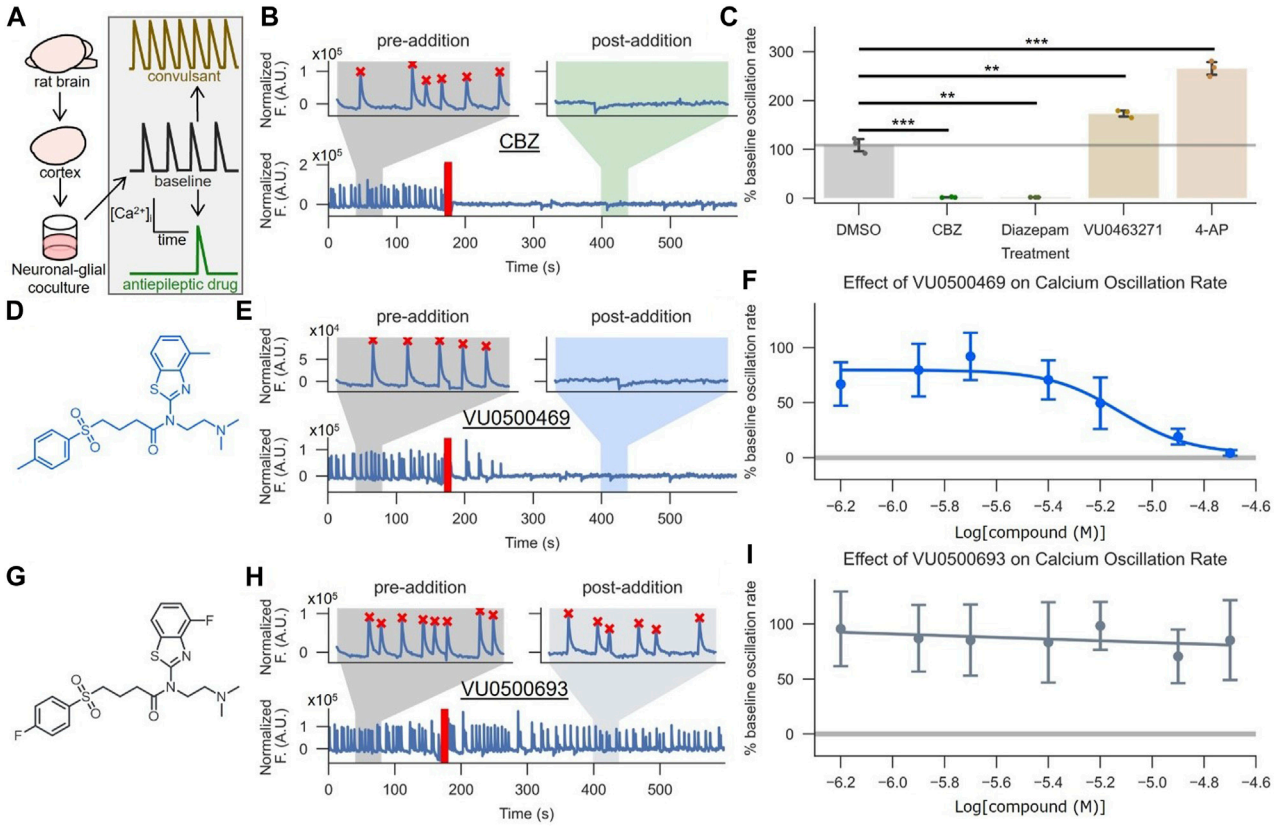

FIGURE 5 | VU0500469 inhibits seizure-like, synchronous Ca^{2+} oscillations in cultured rat cortical neurons. **(A)** Cartoon description of the synchronous Ca^{2+} oscillation assay, which uses neuronal Ca^{2+} oscillations from high density neuronal-glial cocultures to model epileptiform activity. **(B,C)** Validation of the synchronous neuronal Ca^{2+} oscillation assay's ability to report anti-epileptic and KCC2-dependent activity. **(B)** Example Ca^{2+} oscillation trace treated with the antiepileptic drug carbamazepine (CBZ). Segments before and after compound addition are highlighted to better show neuronal Ca^{2+} oscillations in the absence and presence of compound, respectively. The time point of compound addition denoted by the red line. Oscillations recognized by a spike counting algorithm are marked by a red "X." **(C)** Quantified % pre-addition oscillation rate for CBZ, the $GABA_A$ positive allosteric modulator diazepam, vehicle control, the convulsant 4-AP, and the KCC2 inhibitor VU0463271 (n = 3). **(D–F)** VU500469 dose-dependently prevents seizure-like Ca^{2+} oscillations. **(D)** VU0500469 structure. **(E)** Example trace treated with 20 μM VU0500469, annotated as in **(B)**. **(F)** Dose-dependent effect of VU0500469 on Ca^{2+} oscillation rate (n = 10). **(G–I)** VU0500469, a structurally related analog of VU0500469 without significant activity in the Cl^- flux assay, does not affect seizure-like Ca^{2+} oscillations. **(G)** VU0500469 structure. **(H)** Example trace treated with 20 μM VU0500469, presented as in **(B)**. **(I)** Dose-dependent effect of VU0500469 on % pre-addition oscillation rate. Error bars represent SD. (n = 10). Statistical significance calculated by one sample t-test (6B, DMSO v. diazepam) and Welch's t-test for all other samples: ** = $p < 0.01$, *** = $p < 0.001$.

containing structurally similar compounds, together with random compounds to continue a broad sampling of the chemical library throughout the screen. Compounds of similar structure were selected using chemical similarity searching in Python, using the RDKit Library (RDKit.org): chemical fingerprints for the entire compound library were generated using RDKit fingerprints, and similarity was quantified between hits and the rest of the VICB Discovery Collection by Tanimoto coefficient calculation. The highest Tanimoto coefficients were interpreted as the most chemically similar compounds. Fourth, compound plates containing the enriched compound set was then screened, and the process repeated after hit determination.

Potassium ($^{83}Rb^+$ Tracer) Influx Assay

Wild-type or KCC2-expressing HEK-293 cells were grown in 10-cm dishes in DMEM/F12 medium supplemented with 5% (v/v) fetal bovine serum and 1% (v/v) penicillin/streptomycin. For K^+ influx experiments, cells were plated (2 ml/dish) for 2 h in 35-mm, poly-L-Lysine (0.1 mg/ml, Sigma)-coated dishes. Medium was then aspirated and replaced with 1 ml of the appropriate buffer (below) for a 10 min preincubation period. For KCC2-mediated $^{83}Rb^+$ influx measurements, cells were rinsed and incubated with a Na^+-free solution containing 132 mM N-methylglucamine (NMDG)-Cl, 5 mM KCl, 2 mM $CaCl_2$, 0.8 mM $MgSO_4$, 1 mM glucose, 5 mM HEPES, pH 7.4 with NMDG. For NKCC1-mediated K^+ influx measurements, the solution contained 132 mM NaCl, 5 mM KCl, 1 mM $CaCl_2$, 0.8 mM $MgSO_4$, 1 mM glucose, 60 mM sucrose, 5 mM HEPES, pH 7.4 with NaOH. Following the preincubation period, the medium was aspirated and replaced with identical solutions containing 200 μM ouabain and 0.25 μCi/ml $^{83}Rb^+$. After three rapid washes in ice-cold solution, the cells were lysed with 0.5 ml 0.5 N NaOH for 1 h then neutralized by adding 0.25 ml glacial acetic acid. Aliquots were then collected for protein assay (Biorad) and

β-scintillation counting. K^+-influx were calculated based on $^{83}Rb^+$ uptake and expressed in pmole K^+/mg protein/min.

Surface Biotinylation

The surface biotinylation protocol was based on previously published work by Friedel et al. (2017), with modifications to accommodate compound treatment. The day before the experiment, 4p2.F7 T-REx-293-KCC2-SuperClomeleon cells were plated in 10 cm, TC-treated, cell-culture dishes containing HEK-293 medium supplemented with 1 μg/ml tetracycline to achieve 90% confluence during surface biotinylation. After approximately 24 h, cells were washed in Assay Buffer and treated with test compounds dissolved in Assay Buffer that had been warmed to 37°C. After 15 min at 37°C, the cells were washed once in Assay Buffer, and incubated with the compound-containing Assay Buffer solution supplemented with 0.4 mg/ml EZ-link Sulfo-NHS-SS Biotin (Pierce 89,881) at 20°C for 30 min. The biotinylation reaction was subsequently quenched using Phosphate-Buffered Saline (PBS)/Ca/Mg [PBS containing 0.1 mM $CaCl_2$ and 1 mM $MgCl_2$ (pH 7.3)] that had been supplemented with 100 mM lysine and adjusted to final osmolality of 300 mOsm with H_2O. Cells were then washed three times in ice-cold PBS/Ca/Mg and harvested by cell scraping. Cell pellets were generated by centrifugation at 500x g for 2 min, the supernatant solution was removed by aspiration, and the cells were transferred in ice-cold Lysis Buffer [50 mM NaCl, 1% (v/v) Triton X-100, 0.5% (v/v) deoxycholate, 0.1% (v/v) SDS, 50 mm Tris-HCl, 10 mM iodoacetamide, and protease inhibitors (ThermoFisher Scientific 78430) (pH 8)] to a microcentrifuge tube, and lysed with gentle agitation at 4°C for 30 min. Lysates were centrifuged at 1,200x g at 4°C for 5 min, and the clarified lysates were transferred to a new microcentrifuge tube. Protein concentrations were determined by BCA assay (Pierce) using BSA (MilliporeSigma) as a standard. Lysate containing 20 μg of protein were set aside at 4°C overnight, for use as a control of total protein levels, and lysate containing 400 μg of protein was incubated with streptavidin-conjugated agarose (Pierce 89,881) overnight at 4°C with gentle agitation. The next day, the agarose beads with bound biotinylated proteins were washed 3 times in ice-cold lysis buffer, and one time in ice-cold PBS/Ca/Mg supplemented with 10 mM iodoacetamide. Protein was eluted from agarose beads in 40 μl of Loading Buffer [65.8 mM Tris-HCl, 26.3% (w/v) glycerol, 2.1% (w/v) SDS, 5% (v/v) β-mercaptoethanol (pH 7)] pre-heated to 95°C. The 20 μg total protein sample (above) and 40 μl of the eluted protein from the streptavidin beads were then loaded onto an SDS-PAGE gel for Western blotting and quantification as described below.

SDS-PAGE and Western Blot

HEK-293 cells were lysed and protein concentrations quantified as described in the Surface Biotyinlation section. 20 μg of lysate, unless otherwise specified, was diluted 1:1 in Loading Buffer that was preheated to 95°C, immediately loaded onto a NuPAGE Bis-Tris 4%–12% (w/v) SDS-PAGE gel (ThermoFisher Scientific) and separated using the XCell SureLock Mini-Cell system (ThermoFisher Scientific). Proteins were transferred to a PVDF membrane using the iBlot2 transfer system (ThermoFisher Scientific), incubated in Intercept Blocking Buffer (LI-COR) for 1 h at room temperature to inhibit non-selective antibody binding, and incubated in primary antibody overnight. The blots were washed 3 times in Tris-Buffered Saline-Tween (TBS-T) [150 mM NaCl, 25 mM Tris base, 0.05% (v/v) Tween 20 (pH 7.4)] for 5 min each time, incubated with secondary antibody for 1 h at room temperature, washed 3 times in TBS-T, and rinsed in TBS. All blots were imaged using the Odyssey CLx system (LI-COR) and quantified using the Image Studio acquisition software (LI-COR). Consistent with previous reports, KCC2 had a multiband pattern (6). We interpreted the lower band at approximately 120 kDa, the predicted molecular weight for full length KCC2, as monomeric KCC2. We interpreted the bands at approximately 240 kDa and above as dimeric- and higher-order oligomers of KCC2. For quantification of the amount of KCC2 in each sample, values for monomeric and oligomeric bands were pooled. For surface biotinylation experiments, the amount of endogenous transferrin receptor (TfR) expression was used to normalize for loading differences in the total- and surface-fractions of KCC2. For surface/total protein quantification, the KCC2 signal from surface and total fractions were normalized to their respective TfR levels, and then the normalized KCC2 surface values were divided by normalized KCC2 total values.

Neuronal-Glial Co-Culture

Brain cortices were isolated from E18 Sprague Dawley rat embryos and placed in ice-cold PBS and prepared as described in (Pacico and Mingorance-Le Meur, 2014). Cortices were dissociated in 0.25% (w/v) Trypsin (Gibco) at 37°C for 20 min. The trypsin reaction was quenched by addition of neurobasal complete medium (NbC)[1x Neurobasal (Gibco), 1x B-27 supplement (Gibco), 1x glutamax (Gibco), 100 U/ml penicillin-streptomycin (Gibco)] supplemented with 10% (v/v) horse serum (NbC + HS) (Gibco). The tissue was then pelleted at 100x g for 5 min, the supernatant solution was removed by aspiration, and a single-cell suspension was generated by trituration in NbC + HS medium. The cells were then counted, diluted to 500 cells/μl in NbC + HS, and 100 μl of this suspension was plated in black-walled, poly-L-lysine-coated, 96-well plates (Greiner) for a final density of 50,000 cells/well. The neuronal-glial cocultures were then incubated at 37°C and 5% CO_2 for 4 h, and the serum-containing NbC + HS medium was then replaced with serum-free NbC medium. The neuronal-glial co-cultures were maintained until at least 14 days *in vitro* (DIV) at 37°C and 5% CO_2 before assaying. Half of the medium was exchanged with fresh NbC medium every 3–4 days.

Synchronized Neuronal Ca^{2+} Oscillation Assay

Neuronal-glial co-cultures were assayed between 14 DIV and 18 DIV using a protocol adapted from (Pacico and Mingorance-Le Meur, 2014). The medium was removed from the co-cultures and the co-cultures were loaded with Fluo-8 (AAT Bioquest) by incubation in 90 μl/well dye-loading solution [1x HBSS (Corning), 20 mM HEPES (MilliporeSigma), 1 μg/ml Fluo-8 AM, 1 mM probenecid, 3 mg/ml BSA (MilliporeSigma) (pH 7.3)] for 30 min at 37°C. The dye-loading solution was then removed and replaced with 180 μl/well Neuronal Assay Buffer

[1x Ca^{2+}- and Mg^{2+}-free HBSS (Corning) + 2 mM $CaCl_2$ + 3 mM $MgCl_2$ + 20 mM HEPES (pH 7.3)] that was pre-warmed to 37°C. The co-cultures were then immediately loaded into the Panoptic plate reader and assayed. Cultures were continuously imaged at 5 Hz (482/35 nm excitation and 536/40 nm emission) at 37°C throughout the run. After a 3-min reading to establish a Ca^{2+} oscillation baseline, 20 µl of a 100x compound solution was added to the co-cultures using the Panoptic. Co-cultures were subsequently imaged for 12 min to quantify the effect of compounds on the Ca^{2+} oscillation rate. Ca^{2+} oscillation rates were quantified using Python. Our data analysis workflow consisted of: 1) correction for baseline drift, 2) peak counting, and 3) oscillation rate normalization. 1) correction for baseline drift: fluorescent traces were corrected by calculating a smoothened version of each trace and then subtracting the smoothened trace from the original trace. Traces were smoothened by a mean filter generated by iterative convolutions of a 100-frame and a 200-frame averaging kernel over the timeseries data; afterward, the smoothened trace was subtracted from the overlapping region of the original trace. 2) peak counting: peaks were counted separately in the pre-compound addition and post-compound addition segments by counting peak-to-peak local maxima using a manually set threshold value and minimum distance between peaks to prevent over/under counting of peaks. 3) oscillation rate normalization: oscillation rates were calculated by dividing Ca^{2+} oscillation counts by time. Lastly, post-compound addition oscillation rates were normalized as a percentage of the baseline oscillation rate to yield a "% baseline oscillation rate." All edge wells in the 96-well plate (Rows A and H, together with columns 1 and 12) were omitted from data analysis owing to differences in signal observed in those wells relative to the rest of the plate.

Immunofluorescence

Immunofluorescence staining of cortical cocultures was performed after 14 DIV as described above for Ca^{2+}-imaging experiments. NbC medium was removed and cells were washed 3 times with PBS and fixed with 4% (w/v) paraformaldehyde in 1x HBSS for 20 min at room temperature. Cells were then washed with PBS and subsequently permeabilized with 0.3% (v/v) Triton X-100 (MilliporeSigma) in PBS for 15 min. Permeabilized cells were blocked in 10% (v/v) bovine serum albumin (BSA) (MilliporeSigma) in PBS for 45 min cells were washed 3 times with PBS. Cells were treated with mouse anti-KCC2/SLC12A5 antibody (S1-12) and rabbit anti-GAD65/GAD67 in 1% BSA in PBS at 4°C overnight. Cells were washed 3 times with PBS prior to being incubated with goat anti-mouse and goat anti-rabbit AF555 secondary antibodies for 45 min at room temperature. Cells were washed 3 times with PBS and stained with Hoechst (1:5,000, ThermoFisher Scientific, H3570). Images were recorded using the ImageXpress Micro XLS system (Molecular Devices).

Statistical Analyses

All reported data were drawn from at least three independent experimental replicates. Statistical analyses were conducted in R and Python. All tests with a two-sided $p < 0.05$ were considered statistically significant. Assumptions of normality were tested using the Shapiro-Wilk test. For two samples of normally distributed data, the Welch's unequal variances t-test was used for hypothesis tests using independent data, and the paired t-test was used for dependent data. To test if one, normally distributed sample was statistically significant from a single value, a one sample t-test was used. For two samples of data that were not necessarily normally distributed, the Mann-Whitney U test was used. For hypothesis testing of linear regression models containing normally distributed inputs, the Wald test was used with a t-distribution of the test statistic.

Compound Synthesis General Procedure

All non-aqueous reactions were performed in flame-dried or oven-dried round-bottomed flasks under an atmosphere of argon. Stainless steel syringes or cannula were used to transfer air- and moisture-sensitive liquids. Reaction temperatures were controlled using a thermocouple thermometer and analog hotplate stirrer and monitored using liquid-in-glass thermometers. Reactions were conducted at room temperature (approximately 21°C–23°C) unless otherwise noted. Flash column chromatography was conducted using silica gel 230–400 mesh. Reactions were monitored by analytical thin-layer chromatography, using Silica Gel 60 F254 glass-backed pre-coated silica gel plates (MilliporeSigma). The plates were visualized with UV light (254 nm) and stained with potassium permanganate or p- anisaldehyde-sulfuric acid followed by charring. Yields were determined by weight of isolated, spectroscopically pure compounds.

Materials for Compound Synthesis

Solvents and chemicals were purchased from Sigma-Aldrich, Acros Organics, TCI and/or Alfa Aesar and used without further purification. Solvents were purchased from Fisher Scientific. Dry dichloromethane (DCM) was collected from an MBraun MB-SPS solvent system. Dichloroethane (DCE) was distilled from calcium hydride and stored over 4 Å molecular sieves. Triethylamine, N,N-dimethylformamide (DMF) and DMSO were used as received in a bottle with a Sure/Seal. N,N-diisopropylethylamine was distilled from calcium hydride and stored over KOH. BF_3·diethyl ether was distilled prior to use from calcium hydride. Deuterated solvents were purchased from Cambridge Isotope Laboratories.

Instrumentation for Compound Synthesis

Preparative reverse-phase HPLC (Gilson) was performed using a Phenomenex Gemini column (5 micron, 110 Å, 50 mm × 21.20 mm, flow rate 30 ml/min) with UV/Vis detection. Low-resolution mass spectra were obtained on an Agilent 1200 series system with UV detection at 214 and 254 low-resolution mass spectra were obtained on an Agilent 6130 single quad mass spectrometer with electrospray ionization (ESI) in positive mode. LC-MS experiments were performed with the following parameters: Accucore C18 column 2.6 µm, 2.1 mm × 30 mm column) at 40°C; an acetonitrile (ACN)/water with 0.1% (v/v) trifluoroacetic acid gradient 7%–90% (v/v) ACN (method 1) for 1.5 min and 40%–90% (v/v) ACN (method 2) for 1.5 min; flow rate of 1.5 ml min-1. 1H NMR spectra were recorded on Bruker 400 or 600 MHz spectrometers and are reported relative to

internal chloroform (1H, δ 7.26), methanol (1H, δ 3.31), and DMSO (1H, δ 2.50). Data for 1H NMR spectra are reported as follows: chemical shift (δ ppm), multiplicity (s, singlet, d, doublet, t, triplet, dd, doublet of doublet, ddd, doublet of doublet of doublet, m, multiplet, br, broad), coupling constants (Hz), and integration. 13C NMR were recorded on Bruker 100 or 150 MHz spectrometers and are reported relative to internal chloroform (13C, δ 77.1), methanol (MeOH) (13C, δ 49.2), and DMSO (13C, δ 40.3).

Methyl 4-(P-Tolylthio)Butanoate 3

A mixture of methyl 4-bromobutanoate (2.19 g, 12.07 mmol), 4-methylbenzenethiol (1.0 g, 8.05 mmol), and K_2CO_3 (2.22 g, 16.10 mmol) in ACN (24 ml) was stirred for 3 h and solvent was removed in vacuo. The crude residue was dissolved in ethylacetate (EtOAc) (30 ml), washed with saturated NH_4Cl solution (30 ml), extracted with EtOAc (3 ml × 30 ml), and dried over $MgSO_4$. The solvent was removed under reduced pressure and the residue was purified by column chromatography (0%–30% (v/v) hexane/EtOAc gradient) to afford sulfide 3 as a yellow oil (2.46 mg, 95%). LCMS (ESI) Rt 1.14 min, m/z: 225.2 [M + H]+.

Methyl 4-Tosylbutanoate 4

To a solution of ester 3 (1.0 g, 4.46 mmol) in MeOH/tetrahydrofuran (THF) (22 ml/66 ml) was added a solution of Oxone (31.2 ml, 1.0 M in water). The reaction mixture was stirred for 20 h and concentrated in vacuo. The crude mixture was diluted with water (50 ml), extracted with EtOAc (3 ml × 50 ml), and dried over $MgSO_4$. The solvent was removed under reduced pressure and the residue was purified by column chromatography (0%–50% (v/v) hexane/EtOAc gradient) to afford sulfone 4 as a yellow oil (0.66 g, 58%). LCMS (ESI) Rt 0.86 min, m/z: 257.1 [M + H]+.

4-Tosylbutanoic Acid 5

To a solution of sulfone 4 (0.66 g, 2.57 mmol) in dioxane/methanol (10 ml/5 ml) was added NaOH (6.43 ml, 1.0 M solution). The reaction mixture was stirred for 3 h at 40°C, acidified to pH 2 with HCl (1.0 N solution), extracted with EtOAc (3 ml × 20 ml), and dried over MgSO4. The crude product was used without further purification. 1H NMR (DMSO-d6, 400 MHz) δ 7.76 (d, J = 8.0 Hz, 2H), 7.48 (d, J = 8.0 Hz, 2H), 3.32–3.27 (m, 2H), 2.43 (s, 3H), 2.33 (t, J = 7.2 Hz, 2H), 1.75–1.67 (m, 2H); LCMS (ESI) Rt: 0.72 min, m/z: 243.1 [M + H]+.

N-(4-Methylbenzo[d] Thiazol-2-yl)-4-Tosylbutanamide 6

To a solution of 4-tosylbutanoic acid 5 (100 mg, 0.61 mmol) in DMF (3 ml) was added N,N-Diisopropylethylamine (DIPEA) (0.43 ml, 2.44 mmol), followed by 1-[Bis(dimethylamino)methylene]-1H-1,2,3-triazolo[4,5-b]pyridinium 3-oxide hexafluorophosphate (HATU, 0.35 g, 0.92 mmol). After stirring for 30 min at 0°C, 4-methylbenzo[d]thiazol-2-amine (148 mg, 0.61 mmol) was added to reaction mixture. The reaction mixture was stirred 12 h, diluted with water (5 ml), and resulting precipitate collected and washed with water (3 ml × 10 ml). Amide 6 was obtained as a white solid product (174 mg, 73%) by filtration. 1H NMR (DMSO-d6, 400 MHz) δ 7.78 (dd, J = 8.8, 8.4 Hz, 3H), 7.48 (d, J = 8.0 Hz, 2H), 7.24 (d, J = 8.0 Hz, 1H), 7.19 (t, J = 8.4 Hz, 1H), 3.37–3.33 (m, 2H), 2.60 (t, J = 7.2 Hz, 2H), 2.56 (s, 3H), 2.42 (s, 3H), 1.86 (q, J = 7.2 Hz, 2H); LCMS (ESI) Rt 1.09 min, m/z: 389.3 [M + H]+.

N-(2-(Dimethylamino) Ethyl)-N-(4-Methylbenzo[d] Thiazol-2-yl)-4-Tosylbutanamide (VU0500469)

To a solution of N-(4-methylbenzo[d]thiazol-2-yl)-4-tosylbutanamide (50 mg, 0.128 mmol) in THF (3 ml) was added sodium bis(trimethylsilyl)amide (0.384 ml, 1 M solution in THF) at 0°C. After stirring for 10 min a solution of 2-bromo-N,N-dimethylethan-1-amine (60 mg, 0.26 mmol) in THF (0.8 ml) was added, the mixture was allowed come to room temperature, stirred for 12 h, and quenched with saturated NH_4Cl solution (10 ml). The quenched reaction was extracted with EtOAc (3 ml × 10 ml), and dried over $MgSO_4$. The solvent was removed under reduced pressure and the residue was purified by column chromatography (0%–10 % (v/v) DCM/MeOH gradient) to afford VU0500469 as a white solid (33 mg, 46%). 1H NMR (MeOH-d4, 400 MHz) δ 7.83 (d, J = 8.0 Hz, 2H), 7.64 (d, J = 8.0 Hz, 1H), 7.46 (d, J = 8.0 Hz, 2H), 7.24–7.18 (m, 2H), 4.37 (t, J = 7.2 Hz, 2H), 3.37 (t, J = 7.2 Hz, 2H), 3.00 (t, J = 8.0 Hz, 2H), 2.95 (t, J = 6.8 Hz, 2H), 2.78 (t, J = 8.0 Hz, 2H), 2.62 (s, 3H), 2.46 (s, 3H), 2.42 (s, 6H), 2.10 (t, J = 7.2 Hz, 2H); LCMS (ESI) tR: 1.01 min, m/z: 460.4 [M + H]+.

N-(4-Methylbenzo[d] Thiazol-2-yl)-4-(Phenylsulfonyl) Butanamide (1)

To a solution of 4-(phenylsulfonyl) butanoic acid (68 mg, 0.3 mmol) in DMF (2 ml) was added DIPEA (0.21 ml, 1.2 mmol), followed by 1-[Bis(dimethylamino)methylene]-1H-1,2,3-triazolo[4,5-b]pyridinium 3-oxide hexafluorophosphate (HATU, 171 mg, 0.45 mmol). After stirring for 30 min at 0°C, 4-methylbenzo[d]thiazol-2-amine (49 mg, 0.3 mmol) was added to reaction mixture. The reaction mixture was stirred 12 h, diluted with water (3 ml), and the resulting precipitate collected and washed with water (3 ml × 10 ml). The crude amide 1) was obtained as a white solid (82 mg, 73%) and used for the next step without further purification. LCMS (ESI) tR: 1.06 min, m/z: 375.3 [M + H]+.

4-((4-Fluorophenyl) Sulfonyl)-N-(4-Methylbenzo[d]Thiazol-2-yl) Butanamide (2)

Amide 2 was obtained as a white solid (82 mg, 70%) following the procedure described above except using 4-((4-fluorophenyl)

sulfonyl)butanoic acid (74 mg, 0.3 mmol) as the coupling partner. LCMS (ESI) tR: 1.07 min, m/z: 393.2 [M + H]+.

N-(2-(Dimethylamino) Ethyl)-N-(4-Methylbenzo[d] Thiazol-2-yl)-4-(Phenylsulfonyl)Butanamide (VU0500458)

To a solution of N-(4-methylbenzo[d]thiazol-2-yl)-4-(phenylsulfonyl)butanamide (33 mg, 0.088 mmol) in THF (2 ml) at 0°C was added a solution of sodium bis(trimethylsilyl)amide (0.26 ml, 1 M solution in THF). After maintaining the reaction mixture at 0°C for 10 min, 2-bromo-N,N-dimethylethan-1-amine (41 mg, 0.18 mmol) in THF (0.5 ml) was added. The reaction mixture was allowed to warm to room temperature, maintained for 12 h, and quenched with saturated NH_4Cl solution (5 ml). The quenched reaction was extracted with EtOAc (3 ml × 10 ml), and dried over $MgSO_4$. The solvent was removed under reduced pressure and the residue was purified by column chromatography (0%–10 % (v/v) DCM/MeOH gradient) to afford VU0500458 as a yellow solid (16 mg, 41 %). 1H NMR (MeOH-d4, 400 MHz) δ 7.97 (d, J = 9.2 Hz, 2H), 7.75 (t, J = 8.4 Hz, 1H), 7.67 (d, J = 8.4 Hz, 2H), 7.65–7.63 (m, 1H), 7.25–7.18 (m, 2H), 4.42 (t, J = 7.2 Hz, 2H), 3.40 (t, J = 7.2 Hz, 2H), 2.98 (t, J = 6.8 Hz, 2H), 2.86 (t, J = 7.6 Hz, 2H), 2.63 (s, 3H), 2.48 (s, 6H), 2.14 (q, J = 7.6 Hz, 2H); LCMS (ESI) Rt 0.97 min, m/z: 446.4 [M + H]+.

N-(2-(Dimethylamino) Ethyl)-4-((4-Fluorophenyl) Sulfonyl)-N-(4-Methylbenzo[d]Thiazol-2-yl) Butanamide (VU0916219)

VU0916219 was prepared using same method with VU0500458. 1H NMR (MeOH-D4, 400 MHz) δ 8.01 (dd, J = 8.8, 5.2 Hz, 2H), 7.65 (d, J = 7.2 Hz, 1H), 7.38 (t, J = 8.4 Hz, 2H), 7.27–7.19 (m, 2H), 4.4 (t, J = 7.2 Hz, 2H), 3.40 (t, J = 7.2 Hz, 2H), 3.00 (t, J = 6.0 Hz, 2H), 2.88 (t, J = 7.6 Hz, 2H), 2.63 (s, 3H), 2.50 (s, 6H), 2.15 (t, J = 7.6 Hz, 2H); LCMS (ESI) Rt 0.98 min, m/z: 464.3 [M + H]+.

RESULTS AND DISCUSSION

Discovery of KCC2 Potentiators by High-Throughput Screening

To identify small-molecule KCC2 potentiators, we developed a high-throughput screening (HTS)-compatible KCC2 activity assay using a monoclonal HEK-293 cell line inducibly expressing KCC2 and constitutively expressing the Cl^- sensor SuperClomeleon (Grimley et al., 2013). In this assay, changes in SuperClomeleon fluorescence, reflective of changes in $[Cl^-]_i$, were used as a surrogate for measuring KCC2 activity (**Figure 1A**). Note that our Cl^- efflux assay measures the effect of the compounds immediately following their addition to the cell, enabling detection of fast-acting modulators. Throughout this manuscript, data are normalized to the Förster resonance energy transfer (FRET) ratio between the Cl^--sensitive YFP and Cl^- insensitive CFP (YFP/CFP ratio) of SuperClomeleon, where an increase in this ratio is interpreted as an increase in KCC2 activity. All of the activity assay data in HEK-293 cells reported in the manuscript were obtained at 37°C due to our observation that many of the compounds tested, in particular those from the class we focus on in the present studies, exhibit strong temperature dependence within this cell line.

To establish that the Cl^- flux assay was suitable for HTS, first we determined that the Cl^- flux assay reports KCC2 activity by demonstrating that the assay responds to known KCC2 modulators including indirect-acting KCC2 potentiators as well as a direct-acting KCC2 inhibitor (**Supplementary Figure S1A**), and that the observed responses to these modulators are dependent on KCC2 expression (**Supplementary Figures S1B,C**). Further, none of the compounds affected Cl^- flux in SuperClomeleon-expressing cells that had not be transfected with KCC2. After establishing that the Cl^- flux assay is capable of measuring KCC2 activity, we established that the assay was suitable for HTS by demonstrating highly reproducible separation between assay signal in vehicle-treated and KCC2 potentiator-treated wells. Our results show highly reproducible separation between potentiator- and control-treated cells on a plate-by-plate and day-by-day basis as quantified using the Z′ method (Zhang et al., 1999). For Z′ value calculation, we treated every other well on the 384-well plate with either vehicle or WNK463 (Yamada et al., 2016), a With-No-Lysine (WNK) kinase inhibitor that indirectly potentiates KCC2. These experiments yielded a mean Z' value of 0.69 ± 0.03 (**Figures 1B,C**), consistent with a well-to-well and experiment-to-experiment separation of vehicle and KCC2 potentiator-treated wells suitable for HTS.

Having demonstrated that the Cl^- flux assay was suitable for HTS, we used it to screen ~23,000 small molecules from the Vanderbilt Discovery Collection (**Figure 1D**, **Supplementary Figure S1D**). Compounds that promoted an apparent decrease in $[Cl^-]_i$ with a Z-score > 3 compared to vehicle-treated controls were selected for further testing. The compounds that displayed activity in cells expressing KCC2 but not cells lacking KCC2 expression were considered verified hits. Of the verified hits we discovered, VU0500469 (**Figure 2F**) stood out based on its unique pharmacological profile which is described in detail below (**Figure 2**).

The Activity of VU0500469 Depends on the Expression of KCC2 and is Consistent Across Mechanistically Distinct Assays of KCC2-mediated Ion Transport

To establish that the activity of VU0500469 in the Cl^- efflux assay was dependent on the expression of KCC2, we tested it in HEK-293 cells in the presence and absence of KCC2 expression. VU0500469 enhanced Cl^- efflux compared to DMSO vehicle alone in cells expressing the cotransporter but not in cells lacking KCC2 expression (**Figures 2A,B**). To further evaluate VU0500469, we tested its activity in two mechanistically distinct KCC2 assays. We used the Tl^+ influx assay which utilizes Tl^+, a K^+ congener, and a Tl^+-sensitive fluorescent

indicator (Weaver et al., 2004; Delpire et al., 2009) to report KCC2-mediated Tl^+ influx. As seen in **Figures 2C,D**, cells expressing KCC2 demonstrate a significantly larger ($p < 0.001$) Tl^+ uptake than cells lacking KCC2, and VU0500469 further enhanced this Tl^+ influx in cells expressing the cotransporter. We also used radioactive $^{83}Rb^+$ uptake to measure KCC2-mediated K^+ influx (Xie et al., 2020) in KCC2 expressing HEK-293 cells. As seen in **Figure 2E**, 30 μM VU0500469 markedly stimulated K^+ influx ($p < 0.05$), an effect that was abolished by the addition of a maximally effective concentration of ML077, a selective KCC2 inhibitor (Delpire et al., 2012).

Improvement of the Pharmacological Properties of VU0500469 to Yield VU0916219

While we were encouraged by the first-in-class KCC2 potentiator activity of VU0500469, the compound exhibited lower potency (EC_{50}, 14.2 ± 0.7 μM; **Figure 3B**) than desired. Starting with VU0500469, we sought to improve potency by further screening our in-house compound library and through direct synthetic modification of the VU0500469 scaffold (**Figure 3**, **Supplementary Figure S2**). We began by screening 200 compounds from the Vanderbilt Discovery Collection with structural similarity to VU500469 to develop a preliminary structure-activity relationship (**Supplementary Figure S2A**). Structural similarity to VU0500469 was quantified by Tanimoto coefficient (Tc) calculation after chemical fingerprinting (Peltason and Bajorath, 2008) of the Vanderbilt Discovery Collection. Compounds with the highest Tc were screened using the Cl^- flux assay in the presence and absence of KCC2 expression. From this screen, we discovered inactive analogs with high structural similarity to VU0500469, e.g., VU0500693 (Tc = 0.82) and VU0500849 (Tc = 0.79), which were utilized as inactive control compounds (**Supplementary Figures S2B,C**). The data demonstrate that changes to the structure of compounds closely related to VU0500469 can result in considerable changes in activity. Importantly, we discovered multiple KCC2-dependent Cl^- efflux potentiators with either improved potency, e.g. VU0500690 (Tc = 0.87), or improved efficacy, e.g. VU0500458 (Tc = 0.99) relative to VU0500469 (**Figures 3A,B**). We also discovered VU0500469 analogs that, while sharing the central benzothiazole moiety and retaining KCC2 potentiator activity, had appreciable differences in structure through the rest of the molecule. This is the case for VU0500789 (Tc = 0.73) and VU0496374 (Tc = 0.55) (**Supplementary Figures S2D,E**). From these data, we conclude that VU0500469 analogs can tolerate structural changes while maintaining an ability to potentiate KCC2 activity.

To confirm that the activities of VU0500469 and VU0500458 were in fact due to compounds with the structures as drawn, we resynthesized VU0500469 (**Supplementary Scheme S1**) and VU0500458 (**Supplementary Scheme S2**), and demonstrated that these resynthesized compounds (**Figures 3B,D**) retained the same activity in the Cl^- flux assay as the stocks from the Vanderbilt Discovery Collection (**Figure 2A**).

To improve upon the pharmacological properties of VU0500469, we sought to combine the fluorophenyl group of VU0500690 (the most potent compound discovered, **Figures 3A,B**) with the 4 methyl-benzthiazole from VU0500458 (the most efficacious compound. **Figures 3A,B**). We synthesized VU0916219 using a similar synthetic route to VU0500458 (**Supplementary Scheme S2**). As seen in **Figure 3D**, VU0916219 matched the efficacy of VU0500458 and increased in potency (EC_{50}, 17.1 ± 1.2 μM vs. 28.8 ± 4.2 μM). While the potency of VU0916219 was still slightly lower than VU0500469 (EC_{50}, 17.1 ± 1.2 μM vs. 14.2 ± 0.7 μM), the >40% increase in efficacy relative to VU0500469 resulted in an overall increase in KCC2 activity. These data establish a preliminary SAR for VU0500469-like compounds and indicate that the VU0500469 structural class is a suitable starting point for future medicinal chemistry efforts.

VU0500469 Exhibits a Unique Pharmacological Profile Relative to Known KCC2 Potentiators

Confident that the activity of VU0500469 was KCC2-dependent, we next sought to evaluate whether VU0500469-like compounds act through an established KCC2 regulatory mechanism, or a novel one (**Figure 4**, **Supplementary Figure S3**).

There are many signaling pathways that indirectly influence the activity of KCC2 (Medina et al., 2014). Based on the rapid onset of VU0500469's ability to potentiate Cl^- efflux, we reasoned that VU0500469 might act through one of three Cl^- homeostasis effectors known to be expressed in HEK-293 cells: PKC (Lee et al., 2007), WNK-SPAK/OSR1 (Friedel et al., 2015), and NKCC1 (Delpire et al., 2009) (**Figure 4A**). To test if VU0500469 affected these regulatory pathways, we first used a pharmacological co-treatment approach, together with the Cl^- flux assay, in KCC2-expressing HEK-293 cells. We observed that 20 μM VU0500469 retained its ability to potentiate Cl^- efflux (**Figure 4B**, **Supplementary Figure S3A**; $p < 0.001$) despite treating cells with saturating inhibitory concentrations of either PKC (Go6983) or WNK (WNK463) (**Supplementary Figures S3B,C**), suggesting that VU0500469 acts independently of these regulatory mechanisms. In addition, VU0500469 did not affect the flux of K^+ in native HEK-293 cells with or without addition of bumetanide, indicating that the compound does not affect NKCC1 activity. Furthermore, we reasoned that VU0500469 acts by a distinct mechanism relative to compounds which increase KCC2 activity on the timescale of hours to days, such as CLP257 (Gagnon et al., 2013), owing to its rapid onset on the scale of minutes, and that VU0500469 works independent of pathways that increase KCC2 expression, such as KCC2 expression enhancing compounds (KEECs) (Tang et al., 2019), because VU0916219, our most active analog of VU0500469, does not alter total KCC2 protein expression (**Figure 4D**).

An established mechanism to increase the amount of KCC2 ion transport activity is by increasing the surface expression of KCC2 (Lee et al., 2007). To determine if VU0500469-like compounds were acting via this mechanism, we quantified KCC2 surface levels using surface biotinylation (Friedel et al., 2017) in response to compound treatment. We isolated surface fractions using streptavidin affinity purification from HEK-293 cells expressing KCC2, and we

subsequently quantified surface and total KCC2 expression levels by immunoblot. Treatment with either 100 nM phorbol 12-myristate 13-acetate (PMA), a PKC agonist previously shown to increase KCC2 surface expression (Lee et al., 2007), or 60 μM VU0916219, our most active analog of VU0500469 (**Figure 3C**, Tc = 0.82), caused a statistically significant increase in KCC2 surface levels relative to vehicle-treated controls (**Figure 4C**; $p < 0.05$). In contrast, total KCC2 levels were statistically indistinguishable from vehicle-treated controls for both PMA and VU0916219 (**Figure 4D**; $p > 0.05$). Taken together, these data are consistent with the conclusion that the VU0500469-like compounds increase KCC2 surface expression without affecting total KCC2 expression.

VU0500469 Prevents Synchronized Ca^{2+} Oscillations in Neuronal-Glial Co-Cultures

To assess the activity of VU0500469 on KCC2 in a more native system and investigate if this chemical class had activity on a seizure-like process, we utilized a neuronal-glial co-culture 'seizure' model (Pacico and Mingorance-Le Meur, 2014) (**Figure 5A**). This model is based on the observation that high-density neuronal-glial rat cortical cultures undergo synchronous Ca^{2+} oscillations that mirror synchronous electrical activity during seizure events. The rate of these Ca^{2+} oscillations is reduced when the cultures are treated with antiepileptic drugs, such as carbamazepine (CBZ) (**Figures 5B,C**; $p < 0.01$), and elevated when treated with convulsants, such as 4-aminopyridine (4-AP) (**Figure 5C**; $p < 0.001$).

To validate the suitability of this system for modeling KCC2 activity during seizure-like events, we demonstrated that 1) KCC2 was expressed in neuronal populations using immunofluorescence (**Supplementary Figure S4A**), and 2) KCC2 was functional in these neurons by demonstrating that selective pharmacological inhibition of KCC2 increased Ca^{2+} oscillation rates (**Figure 5C**; $p < 0.01$), while pharmacological potentiation of $GABA_A$ receptors, which relies on the Cl^- gradient established by KCC2, decreased Ca^{2+} oscillation rates (**Figure 5C**; $p < 0.01$) (Schulte et al., 2018).

Treatment of these neuronal-glial co-cultures with VU0500469 caused a dose-dependent decrease in Ca^{2+} oscillations (**Figures 5D–F**) while a closely related analog, VU0500693, that showed negligible activity in the Cl^- flux assay (**Supplementary Figure S2B**) failed to decrease Ca^{2+} oscillation rate (**Figures 5G–I**). Moreover, there was a statistically significant correlation between increased KCC2 activity in the HEK-293 cell-based Cl^- flux assay and a decrease in neuronal Ca^{2+} oscillation rate (**Supplementary Figure S4B**, $p < 0.05$). Collectively, these results support the conclusion that VU0500469 potentiates KCC2 activity in neurons and in doing so, decreases seizure-like activity.

CONCLUSION

We have discovered and performed preliminary characterization of a new class of small-molecule KCC2 potentiator, and we have determined that this class can decrease seizure-like events in an *in vitro* model of epilepsy. The discovery of a new KCC2 potentiator class is significant because these compounds provide a new set of tools to further the investigation of KCC2's therapeutic potential in a host of neurological disorders with tremendous unmet medical need. Our discovery that the VU0500469 class prevents *in vitro* seizure-like events further validates the antiepileptic promise of KCC2 potentiation, and provides preliminary evidence that pharmacological KCC2 potentiation, alone, is sufficient to produce an antiepileptic effect. These findings could help lay the foundation for the development of new treatments for epilepsy. While promising, our current best compounds do have limitations, most notably in terms of their potency for potentiating KCC2. Future work will focus on improving the potency of compounds in the VU0500469 class, more fully evaluating the selectivity of VU0500469-like compounds across a broad range of targets and establishing a more complete understanding of the mechanism by which VU0500469-like compounds potentiate KCC2 activity.

DATA AVAILABILITY STATEMENT

The raw data supporting the conclusion of this article will be made available by the authors, without undue reservation.

ETHICS STATEMENT

The animal study was reviewed and approved by the Vanderbilt Institutional Animal Care and Use Committee, Vanderbilt University, Nashville, TN United States.

AUTHOR CONTRIBUTIONS

FP, ED, KK, GS, and DW designed research, FP, KK, YD, BS, and ED performed research, FP, DW, and ED analysed data, FP, ED, and DW wrote the manuscript.

FUNDING

This work was supported by funding from the Vanderbilt Institute for Clinical and Translational Research (VR52556 and VR55033) and the National Institutes of Health 5T32GM065086-15 to FP and R01DK093501 to ED. BS, DW, FP, and YD received funding from the Vanderbilt Department of Pharmacology. The HTS Core Facility receives support from the Vanderbilt Institute of Chemical Biology and the Vanderbilt Ingram Cancer Center (P30CA68485). The Panoptic kinetic imaging plate reader was purchased with funds provided by provided by the Office of The Director (OD) of the National Institutes of Health under the award number 1S10OD021734.

ACKNOWLEDGMENTS

We thank the Vanderbilt High-Throughput Screening Facility for their assistance with instrumentation and compound management, especially C. Whitwell, D. Mi, J. Bauer, P. N.

Vinson, and D. Baughman, and the Vanderbilt Flow Cytometry Shared Resource for technical support. We thank S. Berndt, I. Perez, and S. Short for guidance on molecular biology, and G. A. Kaas and K. A. Zavalin for guidance on primary neuronal cell culture.

SUPPLEMENTARY MATERIAL

The Supplementary Material for this article can be found online at: https://www.frontiersin.org/articles/10.3389/fcell.2022.912812/full#supplementary-material

REFERENCES

Akita, T., and Fukuda, A. (2020). Intracellular Cl^- Dysregulation Causing and Caused by Pathogenic Neuronal Activity. *Pflugers Arch. - Eur. J. Physiol.* 472 (7), 977–987. doi:10.1007/s00424-020-02375-4

Campeau, E., Ruhl, V. E., Rodier, F., Smith, C. L., Rahmberg, B. L., Fuss, J. O., et al. (2009). A Versatile Viral System for Expression and Depletion of Proteins in Mammalian Cells. *PLoS One* 4 (8), e6529. doi:10.1371/journal.pone.0006529

Cardarelli, R. A., Jones, K., Pisella, L. I., Wobst, H. J., Mcwilliams, L. J., Sharpe, P. M., et al. (2017). The Small Molecule CLP257 Does Not Modify Activity of the K^+/Cl^- Co–Transporter KCC2 but it Does Potentiate GABAA Receptor Activity. *Nat. Med.* 23, 1394–1396. doi:10.1038/nm.4442

Carter, B. M., Sullivan, B. J., Landers, J. R., and Kadam, S. D. (2018). Dose-Dependent Reversal of KCC2 Hypofunction and Phenobarbital-Resistant Neonatal Seizures by ANA12. *Sci. Rep.* 8, 11987. doi:10.1038/s41598-018-30486-7

Chen, L., Wan, L., Wu, Z., Ren, W., Huang, Y., Qian, B., et al. (2017). KCC2 Downregulation Facilitates Epileptic Seizures. *Sci. Rep.* 7, 156. doi:10.1038/s41598-017-00196-7

Delpire, E., Days, E., Lewis, L. M., Mi, D., Kim, K., Lindsley, C. W., et al. (2009). Small-molecule Screen Identifies Inhibitors of the Neuronal K-Cl Cotransporter KCC2. *Proc. Natl. Acad. Sci. U.S.A.* 106, 5383–5388. doi:10.1073/pnas.0812756106

Delpire, E., Baranczak, A., Waterson, A. G., Kim, K., Kett, N., Morrison, R. D., et al. (2012). Further Optimization of the K-Cl Cotransporter KCC2 Antagonist ML077: Development of a Highly Selective and More Potent *In Vitro* Probe. *Bioorg. Med. Chem. Lett.* 22, 4532–4535. doi:10.1016/j.bmcl.2012.05.126

Duy, P. Q., David, W. B., and Kahle, K. T. (2019). Identification of KCC2 Mutations in Human Epilepsy Suggests Strategies for Therapeutic Transporter Modulation. *Front. Cell. Neurosci.* 13, 515. doi:10.3389/fncel.2019.00515

Dzhala, V. I., and Staley, K. J. (2020). KCC2 Chloride Transport Contributes to the Termination of Ictal Epileptiform Activity. *eNeuro* 8, ENEURO.0208-20.2020. doi:10.1523/ENEURO.0208-20.2020

Friedel, P., Kahle, K. T., Zhang, J., Hertz, N., Pisella, L. I., Buhler, E., et al. (2015). WNK1-regulated Inhibitory Phosphorylation of the KCC2 Cotransporter Maintains the Depolarizing Action of GABA in Immature Neurons. *Sci. Signal.* 8, ra65. doi:10.1126/scisignal.aaa0354

Friedel, P., Ludwig, A., Pellegrino, C., Agez, M., Jawhari, A., Rivera, C., et al. (2017). A Novel View on the Role of Intracellular Tails in Surface Delivery of the Potassium-Chloride Cotransporter KCC2. *eNeuro* 4, ENEURO.0055-17.2017. doi:10.1523/ENEURO.0055-17.2017

Fukuda, A., and Watanabe, M. (2019). Pathogenic Potential of Human SLC12A5 Variants Causing KCC2 Dysfunction. *Brain Res.* 1710, 1–7. Elsevier B.V. doi:10.1016/j.brainres.2018.12.025

Gagnon, M., Bergeron, M. J., Lavertu, G., Castonguay, A., Tripathy, S., Bonin, R. P., et al. (2013). Chloride Extrusion Enhancers as Novel Therapeutics for Neurological Diseases. *Nat. Med.* 19, 1524–1528. doi:10.1038/nm.3356

Gagnon, M., Bergeron, M. J., Perez-Sanchez, J., Plasencia-Fernandez, I., Godin, A. G., Castonguay, A., et al. (2017). Gagnon et al. Reply: The Small Molecule CLP257 Does Not Modify Activity of the K^+/Cl^- Co–Transporter KCC2 but it does Potentiate $GABA_A$ Receptor Activity. *Nat. Med.* 23 (12), 1394–1396. doi:10.1038/nm.4449

Grimley, J. S., Li, L., Wang, W., Wen, L., Beese, L. S., Hellinga, H. W., et al. (2013). Visualization of Synaptic Inhibition with an Optogenetic Sensor Developed by Cell-Free Protein Engineering Automation. *J. Neurosci.* 33, 16297–16309. doi:10.1523/jneurosci.4616-11.2013

Huberfeld, G., Wittner, L., Clemenceau, S., Baulac, M., Kaila, K., Miles, R., et al. (2007). Perturbed Chloride Homeostasis and GABAergic Signaling in Human Temporal Lobe Epilepsy. *J. Neurosci.* 27, 9866–9873. doi:10.1523/jneurosci.2761-07.2007

Kahle, K. T., Khanna, A., Clapham, D. E., and Woolf, C. J. (2014a). Therapeutic Restoration of Spinal Inhibition via Druggable Enhancement of Potassium-Chloride Cotransporter Kcc2-Mediated Chloride Extrusion in Peripheral Neuropathic Pain. *JAMA Neurol.* 71, 640–645. doi:10.1001/jamaneurol.2014.21

Kahle, K. T., Merner, N. D., Friedel, P., Silayeva, L., Liang, B., Khanna, A., et al. (2014b). Genetically Encoded Impairment of Neuronal KCC2 Cotransporter Function in Human Idiopathic Generalized Epilepsy. *EMBO Rep.* 15, 766–774. doi:10.15252/embr.201438840

Kang, S. K., Ammanuel, S., Adler, D. A., and Kadam, S. D. (2020). Rescue of PB-Resistant Neonatal Seizures with Single-Dose of Small-Molecule TrkB Antagonist Show Long-Term Benefits. *Epilepsy Res.* 159, 106249. doi:10.1016/j.eplepsyres.2019.106249

Kelley, M. R., Deeb, T. Z., Brandon, N. J., Dunlop, J., Davies, P. A., and Moss, S. J. (2016). Compromising KCC2 Transporter Activity Enhances the Development of Continuous Seizure Activity. *Neuropharmacology* 108, 103–110. doi:10.1016/j.neuropharm.2016.04.029

Kelley, M. R., Cardarelli, R. A., Smalley, J. L., Ollerhead, T. A., Andrew, P. M., Brandon, N. J., et al. (2018). Locally Reducing KCC2 Activity in the Hippocampus Is Sufficient to Induce Temporal Lobe Epilepsy. *EBioMedicine* 32, 62–71. doi:10.1016/j.ebiom.2018.05.029

Kipnis, P. A., Sullivan, B. J., Carter, B. M., and Kadam, S. D. (2020). TrkB-agonists Prevent Postischemic Emergence of Refractory Neonatal Seizures in Mice. *JCI Insight* 5 (12), e136007. doi:10.1172/jci.insight.136007

Lee, H. H. C., Walker, J. A., Williams, J. R., Goodier, R. J., Payne, J. A., and Moss, S. J. (2007). Direct Protein Kinase C-dependent Phosphorylation Regulates the Cell Surface Stability and Activity of the Potassium Chloride Cotransporter KCC2. *J. Biol. Chem.* 282, 29777–29784. doi:10.1074/jbc.m705053200

Magloire, V., Cornford, J., Lieb, A., Kullmann, D. M., and Pavlov, I. (2019). KCC2 Overexpression Prevents the Paradoxical Seizure-Promoting Action of Somatic Inhibition. *Nat. Commun.* 10 (1), 1225. doi:10.1038/s41467-019-08933-4

Medina, I., Friedel, P., Rivera, C., Kahle, K. T., Kourdougli, N., Uvarov, P., et al. (2014). Current View on the Functional Regulation of the Neuronal K(+)-Cl(-) Cotransporter KCC2. *Front. Cell. Neurosci.* 8, 27. doi:10.3389/fncel.2014.00027

Moore, Y. E., Deeb, T. Z., Chadchankar, H., Brandon, N. J., and Moss, S. J. (2018). Potentiating KCC2 Activity Is Sufficient to Limit the Onset and Severity of Seizures. *Proc. Natl. Acad. Sci. U. S. A.* 115, 10166–10171. doi:10.1073/pnas.1810134115

Munakata, M., Watanabe, M., Otsuki, T., Nakama, H., Arima, K., Itoh, M., et al. (2007). Altered Distribution of KCC2 in Cortical Dysplasia in Patients with Intractable Epilepsy. *Epilepsia* 48, 837–844. doi:10.1111/j.1528-1167.2006.00954.x

Pacico, N., and Mingorance-Le Meur, A. (2014). New *In Vitro* Phenotypic Assay for Epilepsy: Fluorescent Measurement of Synchronized Neuronal Calcium Oscillations. *PLoS ONE* 9, e84755. doi:10.1371/journal.pone.0084755

Payne, J. A. (1997). Functional Characterization of the Neuronal-specific K-Cl Cotransporter : Implications for [K+]o Regulation. *Am. J. Physiol.* 273, C1516–C1525. doi:10.1152/ajpcell.1997.273.5.C1516

Peltason, L., and Bajorath, J. (2008). "Chapter 4. Molecular Similarity Analysis in Virtual Screening," in *In Silico Medicinal Chemistry: Computational Methods to Support Drug Design*, 120–149. doi:10.1039/9781847558879-00120

Puskarjov, M., Seja, P., Heron, S. E., Williams, T. C., Ahmad, F., Iona, X., et al. (2014). A Variant of KCC2 from Patients with Febrile Seizures Impairs Neuronal Cl- Extrusion and Dendritic Spine Formation. *EMBO Rep.* 15, 723–729. doi:10.1002/embr.201438749

Raimondo, J. V., Richards, B. A., and Woodin, M. A. (2017). Neuronal Chloride and Excitability — the Big Impact of Small Changes. *Curr. Opin. Neurobiol.* 43, 35–42. doi:10.1016/j.conb.2016.11.012

Saito, T., Ishii, A., Sugai, K., Sasaki, M., and Hirose, S. (2017). A de novo Missense Mutation in SLC12A5 Found in a Compound Heterozygote Patient with Epilepsy of Infancy with Migrating Focal Seizures. *Clin. Genet.* 92, 654–658. doi:10.1111/cge.13049

Saitsu, H., Watanabe, M., Akita, T., Ohba, C., Sugai, K., Ong, W. P., et al. (2016). Impaired Neuronal KCC2 Function by Biallelic SLC12A5 Mutations in Migrating Focal Seizures and Severe Developmental Delay. *Sci. Rep.* 6, 30072. doi:10.1038/srep30072

Schulte, J. T., Wierenga, C. J., and Bruining, H. (2018). Chloride Transporters and GABA Polarity in Developmental, Neurological and Psychiatric Conditions. *Neurosci. Biobehav. Rev.* 90, 260–271. doi:10.1016/j.neubiorev.2018.05.001

Silayeva, L., Deeb, T. Z., Hines, R. M., Kelley, M. R., Munoz, M. B., Lee, H. H. C., et al. (2015). KCC2 Activity Is Critical in Limiting the Onset and Severity of Status Epilepticus. *Proc. Natl. Acad. Sci. U.S.A.* 112, 3523–3528. doi:10.1073/pnas.1415126112

Sivakumaran, S., Cardarelli, R. A., Maguire, J., Kelley, M. R., Silayeva, L., Morrow, D. H., et al. (2015). Selective Inhibition of KCC2 Leads to Hyperexcitability and Epileptiform Discharges in Hippocampal Slices and *In Vivo*. *J. Neurosci.* 35, 8291–8296. doi:10.1523/jneurosci.5205-14.2015

Stödberg, T., McTague, A., Ruiz, A. J., Hirata, H., Zhen, J., Long, P., et al. (2015). Mutations in SLC12A5 in Epilepsy of Infancy with Migrating Focal Seizures. *Nat. Commun.* 6, 8038. doi:10.1038/ncomms9038

Tang, X., Drotar, J., Li, K., Clairmont, C. D., Brumm, A. S., Sullins, A. J., et al. (2019). Pharmacological Enhancement of KCC2 Gene Expression Exerts Therapeutic Effects on Human Rett Syndrome Neurons and Mecp2 Mutant Mice. *Sci. Transl. Med.* 11, eaau0164. doi:10.1126/scitranslmed.aau0164

Tyzio, R., Nardou, R., Ferrari, D. C., Tsintsadze, T., Shahrokhi, A., Eftekhari, S., et al. (2014). Oxytocin-mediated GABA Inhibition during Delivery Attenuates Autism Pathogenesis in Rodent Offspring. *Science* 343, 675–679. doi:10.1126/science.1247190

Weaver, C. D., Harden, D., Dworetzky, S. I., Robertson, B., and Knox, R. J. (2004). A Thallium-Sensitive, Fluorescence-Based Assay for Detecting and Characterizing Potassium Channel Modulators in Mammalian Cells. *J. Biomol. Screen* 9, 671–677. doi:10.1177/1087057104268749

Williams, J. R., Sharp, J. W., Kumari, V. G., Wilson, M., and Payne, J. A. (1999). The Neuron-specific K-Cl Cotransporter, KCC2. Antibody Development and Initial Characterization of the Protein. *J. Biol. Chem.* 274 (18), 12656–12664. doi:10.1074/jbc.274.18.12656

Woo, N.-S., Lu, J., England, R., McClellan, R., Dufour, S., Mount, D. B., et al. (2002). Hyperexcitability and Epilepsy Associated with Disruption of the Mouse Neuronal-specific K-Cl Cotransporter Gene. *Hippocampus* 12, 258–268. doi:10.1002/hipo.10014

Xie, Y., Chang, S., Zhao, C., Wang, F., Liu, S., Wang, J., et al. (2020). Structures and an Activation Mechanism of Human Potassium-Chloride Cotransporters. *Sci. Adv.* 6 (50), eabc5883. doi:10.1126/sciadv.abc5883

Yamada, K., Park, H.-M., Rigel, D. F., DiPetrillo, K., Whalen, E. J., Anisowicz, A., et al. (2016). Small-molecule WNK Inhibition Regulates Cardiovascular and Renal Function. *Nat. Chem. Biol.* 12, 896–898. doi:10.1038/nchembio.2168

Zhang, J.-H., Chung, T. D. Y., and Oldenburg, K. R. (1999). A Simple Statistical Parameter for Use in Evaluation and Validation of High Throughput Screening Assays. *SLAS Discov.* 4, 67–73. doi:10.1177/108705719900400206

Zhang, J., Cordshagen, A., Medina, I., Nothwang, H. G., Wisniewski, J. R., Winklhofer, M., et al. (2020). Staurosporine and NEM Mainly Impair WNK-SPAK/OSR1 Mediated Phosphorylation of KCC2 and NKCC1. *PLoS ONE* 15, e0232967. doi:10.1371/journal.pone.0232967

Conflict of Interest: DW is an owner of WaveFront Biosciences and ION Biosciences who manufacture the Panoptic plate reader and Thallos thallium-sensitive fluorescent indicator, respectively.

The remaining authors declare that the research was conducted in the absence of any commercial or financial relationships that could be construed as a potential conflict of interest.

Publisher's Note: All claims expressed in this article are solely those of the authors and do not necessarily represent those of their affiliated organizations, or those of the publisher, the editors and the reviewers. Any product that may be evaluated in this article, or claim that may be made by its manufacturer, is not guaranteed or endorsed by the publisher.

frontiers | Frontiers in Cell and Developmental Biology

ORIGINAL RESEARCH
published: 29 June 2022
doi: 10.3389/fcell.2022.918760

Role of Nuclear Lamin A/C in the Regulation of Nav1.5 Channel and Microtubules: Lesson From the Pathogenic Lamin A/C Variant Q517X

Roberta De Zio[1], Giusy Pietrafesa[2], Serena Milano[1], Giuseppe Procino[1], Manuela Bramerio[3], Martino Pepe[4], Cinzia Forleo[4], Stefano Favale[4], Maria Svelto[1], Andrea Gerbino[1†] and Monica Carmosino[2†]*

[1]Department of Biosciences, Biotechnologies and Biopharmaceutics, University of Bari, Bari, Italy, [2]Department of Sciences, University of Basilicata, Potenza, Italy, [3]ASST Grande Ospedale Metropolitano Niguarda Pathological Anatomy Center, Milano, Italy, [4]Department of Emergency and Organ Transplantation, Cardiology Unit, University of Bari Aldo Moro, Bari, Italy

OPEN ACCESS

Edited by:
Alessia Remigante,
University of Messina, Italy

Reviewed by:
Tommaso Angelone,
University of Calabria, Italy
Francesco Moccia,
University of Pavia, Italy

***Correspondence:**
Monica Carmosino
monica.carmosino@unibas.it

[†]These authors have contributed equally to this work and share last authorship

Specialty section:
This article was submitted to Cellular Biochemistry, a section of the journal Frontiers in Cell and Developmental Biology

Received: 12 April 2022
Accepted: 23 May 2022
Published: 29 June 2022

Citation:
De Zio R, Pietrafesa G, Milano S, Procino G, Bramerio M, Pepe M, Forleo C, Favale S, Svelto M, Gerbino A and Carmosino M (2022) Role of Nuclear Lamin A/C in the Regulation of Nav1.5 Channel and Microtubules: Lesson From the Pathogenic Lamin A/C Variant Q517X. Front. Cell Dev. Biol. 10:918760. doi: 10.3389/fcell.2022.918760

In this work, we studied an *lmna* nonsense mutation encoding for the C-terminally truncated Lamin A/C (LMNA) variant Q517X, which was described in patients affected by a severe arrhythmogenic cardiomyopathy with history of sudden death. We found that LMNA Q517X stably expressed in HL-1 cardiomyocytes abnormally aggregates at the nuclear envelope and within the nucleoplasm. Whole-cell patch clamp experiments showed that LMNA Q517X-expressing cardiomyocytes generated action potentials with reduced amplitude, overshoot, upstroke velocity and diastolic potential compared with LMNA WT-expressing cardiomyocytes. Moreover, the unique features of these cardiomyocytes were 1) hyper-polymerized tubulin network, 2) upregulated acetylated α-tubulin, and 3) cell surface Nav1.5 downregulation. These findings pointed the light on the role of tubulin and Nav1.5 channel in the abnormal electrical properties of LMNA Q517X-expressing cardiomyocytes. When expressed in HEK293 with Nav1.5 and its β1 subunit, LMNA Q517X reduced the peak Na^+ current (I_{Na}) up to 63% with a shift toward positive potentials in the activation curve of the channel. Of note, both AP properties in cardiomyocytes and Nav1.5 kinetics in HEK293 cells were rescued in LMNA Q517X-expressing cells upon treatment with colchicine, an FDA-approved inhibitor of tubulin assembly. In conclusion, LMNA Q517X expression is associated with hyper-polymerization and hyper-acetylation of tubulin network with concomitant downregulation of Nav1.5 cell expression and activity, thus revealing 1) new mechanisms by which LMNA may regulate channels at the cell surface in cardiomyocytes and 2) new pathomechanisms and therapeutic targets in cardiac laminopathies.

Keywords: lamin A/C, arrhythmias, sodium channel, tubulin, electrophysiology

INTRODUCTION

Lamin A/C (LMNA) are type-V intermediate filament proteins expressed by the majority of differentiated somatic cells. Both proteins are encoded by the same gene on chromosome 1q22 through alternative splicing events and targeted to the nucleus where they polymerize to form the nuclear lamina, which is a scaffold that underlies the inner nuclear membrane. This mesh of proteins plays multifunctional roles in cell biology. Nuclear lamins are pivotal for the maintenance of cellular and nuclear integrity and for correct intranuclear mechanotransduction, spatial organization of chromatin, regulation of signaling, and gene expression (Carmosino et al., 2014; Gerbino et al., 2018).

Hundreds of different mutations in the *lmna* gene segregate with largely autosomal-dominant conditions identified as laminopathies. Mostly, these diseases affect specifically the striated muscle with a recurrent involvement of the heart. Notably, almost half of the LMNA cardiomyopathy patients succumb to sudden cardiac death as a result of a fatal arrhythmia, and conduction defects associated with LMNA mutations can substantially precede the onset of structural heart modification, meaning that subtle but fatal arrhythmias may occur before any noticeable change in the function (Hasselberg et al., 2018).

Several hypotheses have been postulated to underlying the electrical abnormalities in the heart of laminopathy patients.

We demonstrated that either nuclear fragility or ER stress may increase the rate of apoptosis in cells expressing pathogenic LMNA variants (Forleo et al., 2015; Carmosino et al., 2016). Recently, we also found proinflammatory cytokines deregulation in different LMNA mutant carriers with arrhythmogenic cardiomyopathies (Gerbino et al., 2021). Of note, either apoptosis or inflammation may in turn induce deposition of fibrotic tissue acting as an arrhythmic substrate.

Moreover, the expression and the function of the connexin 43 have been found altered in cardiomyocyte *syncytia* (Gerbino et al., 2017; Borin et al., 2020) and mouse heart (Macquart et al., 2019) expressing pathogenic variants of LMNA, thus accounting for conduction defects associated with those variants.

Electrical disturbance in the heart may also result from the defective electrical impulse generation due to ion channels remodeling of atrial and ventricular myocytes.

Some LMNA variants have been associated with changes in sodium currents. Olaopa and collaborators showed that variants R545H and A287Lfs*193 reduced the peak Na^+ current when coexpressed with Nav1.5 channel in HEK293 cells (Olaopa et al., 2018). The LMNA V445E mutant also reduced the peak current of I_{Na+} when coexpressed with Nav1.5 channel in HEK293 cells (Liu et al., 2016). Similarly, the expression of LMNA R399C mutant decreases the density of cardiac sodium current in Nav1.5-expressing HEK293 cells (Han et al., 2019). Recently, Savarini et al. showed that iPSC-derived cardiomyocytes expressing LMNA K219T pathogenic variant have altered action potentials, reduced peak sodium current, and diminished conduction velocity (Salvarani et al., 2019).

On the other hand, both peak and late I_{Na+} were significantly increased in cardiomyocytes from $Lmna^{N195K/N195K}$ transgenic mice (Markandeya et al., 2016) with concomitant prolongation of Action Potential (AP) duration.

Of note, the mechanisms through which LMNA mutants may affect Nav1.5 trafficking and activity have not been always elucidated. Interestingly, an epigenetic effect of LMNA K219T variant acting through the *scn5a* gene silencing has been reported (Salvarani et al., 2019).

Overall, regardless of which theory better explains the etiology of cardiac arrhythmia in laminopathies, dissecting the pathogenic mechanisms at the cellular level would offer information on the mechanism by which this nuclear protein may regulate the electrical properties of cardiomyocytes and personalized therapeutic approaches in the field of laminopathies.

Here, we characterized a truncated LMNA variant, Q517X, a pathogenic LMNA variant shown to be associated with dilated cardiomyopathy with conduction abnormalities and neuromuscular disorders (Stallmeyer et al., 2012). In the family involved in our study, however, LMNA Q517X segregates with a severe cardiac phenotype and history of sudden death without any neuromuscular involvement, most likely because of the genetic background of the mutation carriers and environmental influences. The LMNA haploinsufficiency due to the non-sense-mediated decay of the messengers encoding for truncated LMNA variants has been proposed as one of the pathogenic mechanisms in carriers of *lmna* nonsense gene mutations. However, we and others demonstrated the expression of the truncated LMNA variant in the tissues of the carriers (Arbustini et al., 2002; Carmosino et al., 2016). Accordingly, several studies performed on genotype–phenotype correlations in cardiac laminopathy demonstrated that truncation mutations are associated with more severe phenotypes and poor prognosis in LMNA mutation carriers because of the early onset of conduction disturbance, atrial fibrillation, malignant ventricular arrhythmias, and sudden death (van Rijsingen et al., 2012; Nishiuchi et al., 2017). Thus, unmasking the pathogenic mechanisms associated with the expression of C-terminal truncated LMNA variants in cardiomyocytes has high clinical relevance.

At the onset of the cardiomyopathy LMNA Q517X carriers presented sinus node dysfunction, first-, second-, and third-degree atrioventricular block and persistent atrial fibrillation. Years later DCM developed with ventricular arrhythmias and heart failure finally occurred. Since the key pathogenetic mechanism in this cardiomyopathy seems to be the electrical disturbance in the atria, we analyzed the possible effect of LMNA Q517X expression in HL-1 cardiomyocytes. These cardiomyocytes possess a mixed phenotype between an atrial cardiomyocyte and a pacemaker cell, as evident by the ion channels expressed at the plasma membrane of these cells (Claycomb et al., 1998; Yang and Murray, 2011). Consequently, these cells can beat spontaneously in culture for the presence of I_f current, but the AP generation is due to Na^+ inward current through Nav1.5 channel as in adult atrial cardiomyocytes (Strege et al., 2012), thus providing a unique model to investigate the effect of this LMNA mutant in atrial automaticity.

MATERIALS AND METHODS

Patients

The heterozygous nucleotide substitution c.1549C > T in exon 9 of the *lmna* gene, introducing a premature stop codon (*p*.Q517X), was detected in a 36-year-old man referred to our Cardiomyopathy Unit, Cardiology Unit, Department of Emergency and Organ Transplantation, University of Bari Aldo Moro, Bari (Italy). He presented conduction system disorders, premature ventricular complexes, and left ventricle dilatation. Clinical evaluations and molecular analysis were proposed in all first-degree relatives of our index patient. The participants underwent a clinical workup including medical history, physical examination, 12-lead electrocardiogram (ECG), transthoracic echocardiography, and 24-h ECG monitoring. Written informed consent was provided by all participating subjects and was obtained by parents of the minor included in the study. This project was consistent with the principles of the Declaration of Helsinki and was approved by the Ethics Committee of the University Hospital Consortium, Policlinico of Bari, Italy.

Cell Culture

HL1 cardiomyocytes were cultured in Claycomb Medium (51800C, Sigma-Aldrich) supplemented with 10% fetal bovine serum (F2442, Sigma-Aldrich), Penicillin/Streptomycin 100 U/mL: 100 µg/ml (P4333, Sigma-Aldrich), 2 mM L-Glutamine (G7513, Sigma-Aldrich), and 0.1 mM Norepinephrine [(±)-Arterenol] (A0937, Sigma-Aldrich) in a humidified 5% CO2, 95% O2 incubator at 37°C.

HEK293 cells and HEK293T packaging cells were cultured in Gibco™ DMEM, high glucose, GlutaMAX™ (31966-021, Life Technologies™) supplemented with 10% Gibco™ Fetal Bovine Serum (10270-106, Life Technologies™) and 1% Penicillin-Streptomycin (10,000 U/mL,15140122, Gibco™, Life Technologies™) in a humidified 5% CO_2, 95% O_2 incubator at 37 °C.

Cell concentration and viability were assessed using Trypan Blue Stain, 0.4% with LUNA-II™ Automated Cell Counter (Logos Biosystems).

Generation of LMNA-Expressing HL-1 Stable Clones

HL-1 cells stably expressing LMNA WT or LMNA Q517X were obtained using Lentiviral transduction.

For viral particles production HEK293T packaging cells were plated at 30% confluence on 60-mm Petri dishes coated with Poly-L-lysine hydrobromide (2,636, Sigma-Aldrich). After 24 h, cells were co-transfected, using Invitrogen™ Lipofectamine™ 2000 Transfection Reagent (Invitrogen Corporation), with the plasmid encoding the protein of interest (either Lamin WT mCherry-tagged pLV [Exp]-Neo-CMV > mCherry (ns): hLMNA [NM_170707.4] or LMNA Q517X mCherry-tagged pLV [Exp]-Neo-CMV > mCherry (ns):hLMNA [NM_170707.4]*, Vector Builder, CA), two additional plasmids such as an envelope protein VSV-G-expressing plasmid pMD2G and a packaging plasmid pSPAX2-expressing Gag-pol and Tat viral proteins (Addgene) in OPTIMEM (Gibco™ Opti-MEM™). The day after the transfection the medium was replaced by 3 ml of fresh supplemented DMEM with penicillin–streptomycin. 24-h after, the virus-containing medium was harvested, clarified with 0.45-µm filter, and stored at −80°C, and 3 ml of fresh medium was re-added to the cells. After additional 24-h of incubation, the virus-containing medium was harvested again and pooled with that collected the day before.

For viral transduction, the HL-1 cells were plated in a 6-well plate at 30–50% of confluency, and after adhesion, they were incubated with 500 µl of virus-containing medium at 37°C in a humidified 5% CO_2 incubator for 18h. The cells were then incubated with 400 µg/ml Geneticin (G418, Gibco, Life Technologies) for 1 week to select stable clones.

Generation of Transfected HEK293 Cells for Patch Clamp Studies

HEK293 cells were transiently co-transfected with plasmids encoding LMNA WT or LMNA Q517X, the voltage sodium channel Nav1.5, and the Nav1.5 accessory β1 subunit using lipofection following the manufacturer's instructions (Invitrogen Corporation), 24 h before patch clamp experiments.Where described, HEK293 were transiently co-transfected with plasmids encoding LMNA WT or LMNA Q517X and the voltage K^+ channel KCNH2 (**Supplementary Figure S4**).

The generation of the LMNA WT mCherry-tagged construct was previously described (Carmosino et al., 2016). The generation of the LMNA Q517X mCherry-tagged construct was performed by the mutagenesis of the LMNA WT mCherry construct using the "Stratagene's Quik Change II XL site-directed mutagenesis kit" KIT (Agilent Technologies, United States). The mutagenic primers were designed using the Quick Change Primer Design Program available online at www.agilent.com/genomics/qcpd/$. The mutation was verified by sequencing. Nav1.5 GFP-tagged and β_1 subunit constructs were kindly provided by Paola Imbrici from Department of Pharmacy-Drug Sciences, University of Bari, Italy. GFP-tagged KCNH2 encoding plasmid was previously characterized by us (De Zio et al., 2019).

Electrophysiological Recordings

Electrophysiological recordings were performed with the Patch Clamp technique in a whole-cell configuration using the Multiclamp 700B (Axon CNS-Molecular Devices, Sunnyvale, CA, United States) amplifier interfaced with the Axon Digidata 1,500 (Axon Instrument-Molecular Devices, Sunnyvale, CA, United States). Currents were sampled at 10 k Hz and low-pass filtered at 5 kHz. AxoScope 10.4 (Molecular Devices, Sunnyvale, CA, United States) and pClamp 10.4 (Molecular Devices, Sunnyvale, CA, United States) were used to acquire and analyze the data. After gigaseal formation and whole-cell access, pipette capacitance (Cp) and the membrane capacitance (Cm) were compensated adjusting the Cp fast and the Cp slow setting on the MultiClamp 700B. A Rs stable for the

entire experiment and lower than 20 MΩ was considered acceptable. All recordings were performed at room temperature (26 °C) on HL-1 cardiomyocytes stably expressing either LMNA Q517X or LMNA WT and on HEK293 cells transiently co-transfected with the GFP-tagged Nav1.5 channel, its associated β1 subunit, and LMNA Q517X or WT-expression plasmids. Where described HEK293 cells were transiently co-transfected with GFP-tagged KCNH2 and LMNA Q517X or WT-expression plasmids. Fluorescent tags were used for selecting the transfected cells. Borosilicate patch pipettes were pulled to obtain tip resistances of 2–4 MΩ with the P-1000 Pipette puller (SUTTER INSTRUMENT, Novato, CA 94949, United States).

For the electrophysiological recordings on HL-1 cardiomyocytes, cells stably expressing either LMNA WT or LMNA Q517X were plated at low confluence, on 35-mm Petri dishes coated with gelatin-fibronectin (5 μg/ml Fibronectin, F1141, Sigma-Aldrich, in 0.02% Gelatin from bovine skin, G9391, Sigma-Aldrich), the day before the experiments. After complete cell adhesion, 10-μM Colchicine (C-9754 Sigma) was added to the complete Claycomb media for an overnight treatment in a humidified 5% CO_2, 95% O_2 incubator at 37 °C, when required. HL-1 spontaneous action potentials were recorded using an extracellular solution contained (in mM): 138 NaCl, 4 KCl, 1 $MgCl_2$, 1,8 $CaCl_2$, 10 Hepes, 10 Glucose (pH of 7.4, adjusted with NaOH, and osmolarity of 290 ± 10 mmol/kg, adjusted with mannitol) and an internal pipette solution contained (in mM): 144 KCl, 2 $MgCl_2$, 10 Hepes, 5 EGTA (pH of 7.2 adjusted with KOH and osmolarity of 280 ± 10 mmol/kg, adjusted with mannitol). Spontaneous action potentials (APs) were recorded in current clamp mode without current injection and analyzed for the following parameters: amplitude (expressed in mV), overshoot (expressed in mV), upstroke (expressed as $\Delta V/\Delta t$), maximum diastolic potential (MDP, expressed in mV), and threshold (expressed in mV).

For the electrophysiological recordings on HEK293 cells transiently expressing either LMNA WT or LMNA Q517X, Nav1.5 channel and its β1 subunit were plated at low confluence the day before the experiments on 35-mm Petri dishes coated with Poly-L-lysine hydrobromide for 20 min at room temperature (2636 Sigma-Aldrich). After complete adhesion, 10-μM Colchicine (C-9754 Sigma) was added to the complete Glutamax media for an overnight treatment in a humidified 5% CO_2, 95% O_2 incubator at 37°C, when needed.

The whole-cell Na^+ current (I_{Na}) in the HEK293 cells was recorded using a bath solution contained (in mM): 140 NaCl, 5 KCl, 1 $CaCl_2$, 1 $MgCl_2$, 10 HEPES, 5 Glucose (pH of 7.4, adjusted with NaOH, and osmolarity of 290 ± 10 mmol/kg, adjusted with mannitol) and an internal pipette solution contained (in mM): 140 CsCl, 10 NaCl, 10 HEPES, 1 EGTA, pH 7.4, adjusted with CsOH. The I_{Na} current was measured by 20 ms depolarizing voltage steps ranging from −90 to +60 mV in 5 mV increments after a holding potential of −120 mV to remove the possible inactivation.

The peak values of I_{Na} recorded at each voltage step were normalized to the cell capacitance and reported (as current density, in pA/pF) plotted against the membrane potential (Vm). Additionally, a scatter plot was used to show the distribution of the maximum I_{Na} peaks of each experiment (expressed as current density, in pA/pF).

The conductance (G) was determined using the modified Ohm's law equation:

$$G = I/(Vm - V_{rev}),$$

where I is the peak current Na^+ evoked at the membrane potential Vm and V_{rev} the reversal potential for the Na^+ in our experimental condition. The conductance values were normalized with respect to the maximum conductance value (G/G_{max}) and plotted against the voltage. The conductance voltage curves were fitted with the Boltzmann function

$$G_{Na} = G_{Na,\,max}/\{1 + \exp[(V1/2 - Vm)/K]\}$$

to yield the membrane potentials at half-maximal conductance (V1⁄2), and the slope factors (K). Additionally, the scatter plots were used to show the distribution of V1/2 and the K of each experiment for both experimental conditions.

Electrophysiology on KCNH2-expressing HEK293 cells was conducted as previously described (De Zio et al., 2019).

Laser Confocal Immunofluorescence Analysis

For the immunofluorescence analysis HL-1 cardiomyocytes were plated on 12-mm diameter glass coverslips coated with gelatin-fibronectin (5 μg/ml Fibronectin, F1141 Sigma-Aldrich, in 0.02% Gelatin from bovine skin, G9391 Sigma-Aldrich). After complete cell adhesion, 10 μM Colchicine (C-9754 Sigma) was added to the complete Claycomb media for an overnight treatment in a humidified 5% CO_2, 95% O_2 incubator at 37°C, when needed. Cells were subjected to immunofluorescence analysis as previously described (Gerbino et al., 2016). Primary antibodies used were: anti-β-Tubulin antibody produced in mouse (1:1,000 in PBS-BSA 1%, T5293 Sigma-Aldrich), the anti-mCherry antibody (1:500 in PBS-BSA 1%, ab167453 Abcam), the anti-γ-tubulin antibody (1:200 in PBS-BSA 1%, T6557 Sigma-Aldrich). After 3 washes in PBS the cells were incubated with the appropriate Alexafluor-conjugated secondary antibodies (Life Technologies™) for 1 h at RT. The confocal images were obtained with a laser scanning fluorescence microscope Leica TSC-SP2 (HCX PL APO, ×63/1.32–0.60 oil objective); 8-bit images were saved at 1,024 × 256 and acquired using the Leica Confocal Software®. Fluorescence was quantified in a selected region of interest (ROI) using Fiji (https://imagej.net/Fiji).

For immunofluorescence analysis on cardiac biopsies, 10-μm-thick paraffine-embedded sections of heart biopsies were deparaffinized by incubation at room temperature with histolemon for 10 min and rehydrated with a graded series of ethanol. Sections were then subjected to antigen retrieval by boiling in citrate buffer (10 mM sodium citrate, pH 6) and incubated with PBS-1% SDS for 10'. After blocking with 1% bovine serum albumin in PBS for 30', the sections were incubated with anti-LAMIN A/C (1:100 in PBS-BSA 1%, #2032 Cell Signaling) and then with Alexa Fluor-conjugated secondary

antibodies (Life Technologies). The images were acquired as described for HL-1 cells.

Cell Surface Biotinylation

For biotinylation experiments, HL-1 cardiomyocytes were plated in wells of a 6-multiwell cell culture support coated with gelatin-fibronectin (5 μg/ml Fibronectin, F1141, Sigma-Aldrich, in 0.02% Gelatin from bovine skin, G9391 Sigma-Aldrich), at a density to be 100% at the time of biotinylation. When necessary cells were incubated with 10 μM colchicine overnight before biotinylation. The procedure was previously described with some modification (Carmosino et al., 2008). Briefly, the HL-1 cells were washed twice in cold phosphate buffer saline (PBS, pH 8) containing 1 mM Ca^{2+} and 0.5 mM Mg^{2+} (PBS-CM) and incubated for 30 min at 4 °C in 2 mg/ml Biotin 3-sulfo-N-hydroxysuccinimide ester sodium salt (B5161 Sigma-Aldrich) in PBS-CM. After three washes in PBS-CM the exceeding biotin was removed washing the cells twice, 10 min at 4 °C, with a quenching solution (50 mM NH_4 Cl in PBS). After biotin binding cells were lysed in Lysis buffer (in mM: 20 Tris-HCl pH 8, 150 NaCl, 5 EGTA, and 1% triton X-100) supplemented with 1X protease inhibitor mixture (Roche), and phosphatase inhibitor (in mM: 10 NaF, 100 orthovanadate, 15 pyrophosphate), for 30 min on ice and sonicated at 60 amplitude with Vibra-cell® (Sonics and Materials Inc.) 3 times for 15 s. After sonication, membranes were pelleted at 13000 rpm for 30 min at 4 °C and the supernatant was collected. Protein concentrations were determined by Bradford protein assay. An equal amount of total protein from each group was incubated with streptavidin-agarose beads (69203 Novogen) overnight at 4 °C in a rotating device. Beads were then washed with Lysis buffer supplemented with protease and phosphatase inhibitors, and proteins were eluted by incubation with Laemmli buffer and freshly added 100 mM DTT, for 20 min at 95 °C and 1,000 rpm. The protein samples were subjected to SDS-Page and western blot analysis as described below.

Cell and Tissue Lysates

HL-1 cells, 100% confluent, plated in the wells of a 6-multiwell cell culture support coated with gelatin-fibronectin (5 μg/ml Fibronectin, F1141 Sigma-Aldrich, in 0.02% Gelatin from bovine skin, G9391 Sigma-Aldrich) were placed on ice, washed in PBS, and exposed to RIPA buffer (in mM: 150 NaCl, 10 Tris/HCl, 1% Triton X-100, 0.1% SDS, 1% deoxycholate-Na, 5 EDTA; pH 7.2) supplemented with protease and phosphatase inhibitors (in mM: 10 NaF, 100 orthovanadate, 15 pyrophosphate). Cells were then sonicated at 60 amplitude with Vibra-cell® (Sonics and Materials Inc.) and membranes pelleted at 13000 rpm for 30 min at 4°C. Protein concentrations were determined by Bradford protein assay. Proteins were de-natured in 1 × Laemmli Sample Buffer (Bio-Rad), 50 mM DTT and subjected to SDS-PAGE and western blotting as described below.

Lysates were also prepared from cardiac biopsies from the index patient' transplanted heart. These biopsies were kindly provided by Niguarda Pathological Anatomy Center, Milano, Italy, where the index patient underwent heart transplantation. Twenty μm-thick paraffine-embedded sections of heart biopsies were deparaffinized by incubation at room temperature with histolemon for 10 min and rehydrated with a graded series of ethanol. The sections were then pelleted at 16000 × g for 5 min and homogenized in 500 mM Tris-HCl pH 8 and 2% SDS at 90°C for 3 h. The samples were centrifugated for 30 min at 16000 × g at 4°C and the supernatants were subjected to SDS-PAGE and western blotting as described below. Lysates from an explanted heart of a patient with heart disease not related to LMNA mutations were used as control, as previously described (Carmosino et al., 2016).

Western Blot

Protein samples were electrophoresed on 7.5% or 10% polyacrylamide SDS gel (Mini-PROTEAN TGX Stain-Free Precast Gels; Bio-Rad) and transferred on 0.2-μm PVDF membrane (Trans-Blot Turbo Mini 0.2 μm PVDF Transfer Packs #1704156; Bio-Rad) using the Trans-Blot Turbo Transfer System (Bio-Rad). After blocking at room temperature for 1 h in TBST-5% milk or in TBST-BSA 3% (TBST in mM: 50 Tris, 150 NaCl, 0.1% Tween-20; pH 7.4), blots were incubated overnight at 4°C with the following antibodies in blocking buffer: anti-Lamin A/C (1:1000 in TBST-1% BSA; 2032 Cell Signaling); anti-mCherry antibody (1:1000 in TBST-BSA 1%; ab167453 Abcam); anti-Nav1.5 (1:700 in TBST-1% BSA; S8809 Sigma-Aldrich), anti-acetylated α-tubulin antibody (1:1000 in TBST-1% BSA; T7451 Sigma-Aldrich), anti-β-tubulin antibody (1:1000 in TBST-1% BSA; T5293 Sigma-Aldrich), anti-AKT (1:2000 in TBST-1% BSA; 4691 Cell Signaling), anti-phospho-AKT (Ser473) XP® (1:4000 in TBST-1% BSA; 4060 Cell Signaling), anti-ERK1/2 p44/42 MAPK (ERK1/2) (1:1000 in Milk-5% BSA; 4695 Cell signaling), anti-phospho ERK1/2 p44/42 MAPK (ERK1/2) (1:2000 in Milk-5% BSA; 4695 Cell signaling); the anti-mCherry antibody (1:500 in PBS-BSA 1%, ab167453 Abcam. As secondary antibodies were used the goat anti-mouse IgG-HPR conjugate (1:5000 in TBST-3% BSA; Bio-Rad) and an anti-rabbit IgG-peroxidase antibody produced in goat (1:5000 in TBST- BSA 3%; Sigma-Aldrich) depending on the primary antibodies' species. The immunoreactive bands were detected with a ChemiDoc™ System (Bio-Rad). Densitometric analysis was performed by Image Lab 6.0 software. For protein load controls, the stain-free technology from Bio-Rad was used.

Statistical Analysis

GraphPad Prism 6 was used for the statistical analysis and graph representation of the data. Data are given as mean ± standard error of the mean. Statistical analysis was performed using one- or two-way ANOVA test or with Student's t-test for unpaired data depending on the data set analyzed.

RESULTS

Clinical Findings

The heterozygous nucleotide substitution c.1549C > T in exon 9 of the *lmna* gene introduced a premature stop codon producing a truncated version of the Lamin A/C (LMNA) protein after amino acid 517 (Q517X). This mutation was detected in a 36-year-old man referred to our Cardiomyopathy Unit, Cardiology Unit, Department of Emergency and Organ Transplantation,

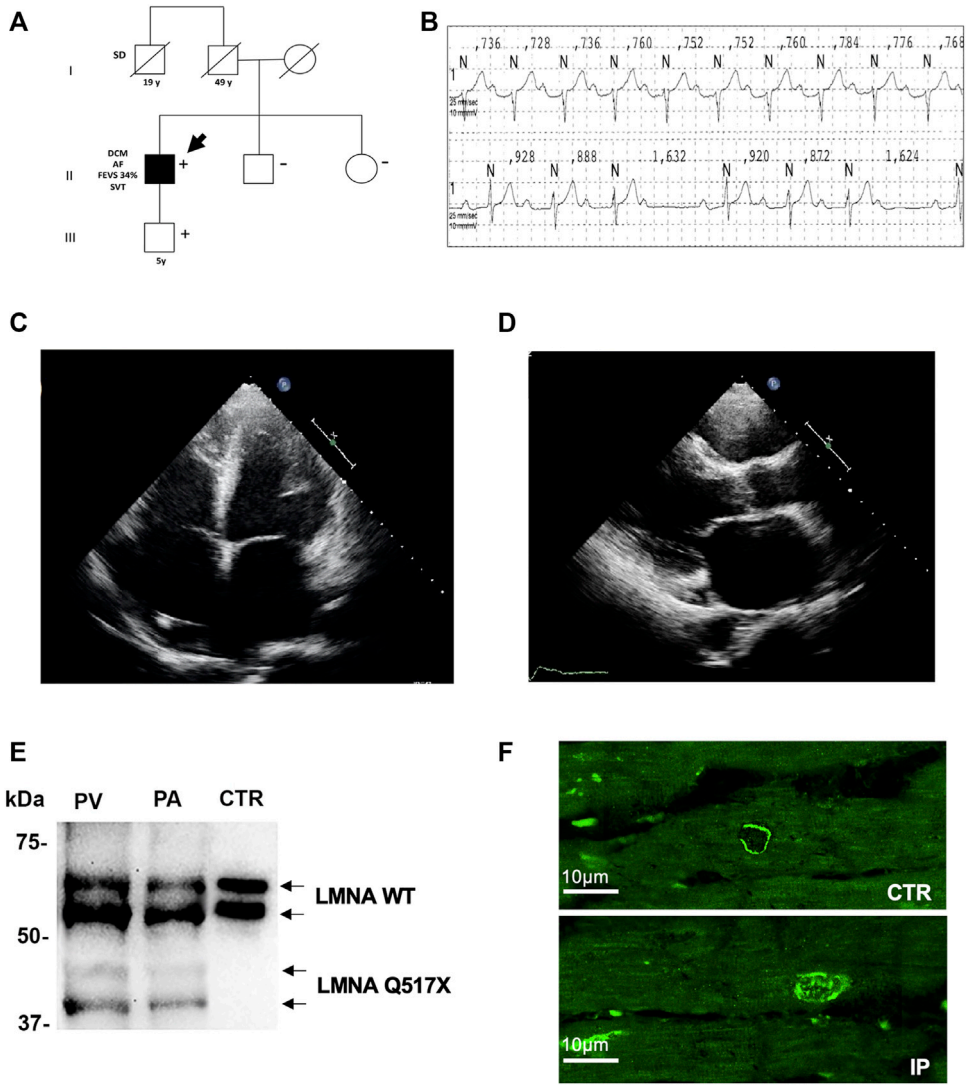

FIGURE 1 | (A) Pedigree of the family carrying the LMNA Q517X pathogenic variant. The filled symbols indicate clinically affected individuals, the diagonal slashes indicate deceased individuals; +/− indicate positive/negative for the mutation; the arrow indicates the index patient. **(B)** ECG data from index patient showing sinus rhythm, first-degree atrioventricular block (upper trace), and type 1 second-degree atrioventricular block (lower trace) recorded during a 24-h ECG monitoring. **(C)** Apical 4C views of echocardiographic imaging from index patient showing a spherical, severely dilated, and markedly hypocontractile left ventricle. **(D)** In the PLAX view of echocardiographic imaging from index patient, showing a highly dilated left atrium. **(E)** Western blot analysis of whole lysate of left atrium (PA) and (PV) ventricular myocardial tissue from the mutant carrier (black arrow in A) and control (CTR) heart biopsies. **(F)** Representative confocal immunofluorescence images of LMNA in heart biopsies from a control patient (CTR) and from the index patient (IP). ECG, electrocardiogram; PLAX view, parasternal long-axis view.

University of Bari Aldo Moro, Bari (Italy). The index patient had a family history of sudden death (father's brother died suddenly at the age of 19 during his sleep). The family members available for clinical evaluations and molecular analysis were the index patient's son and sister. The 5-year-old son carried the LMNA Q517X mutant and was asymptomatic, free of arrhythmias, and showed normal cardiac function, thus suggesting incomplete and age-related penetrance of the mutation. The 43-year-old sister was LMNA mutation-negative, clinically asymptomatic, and had no arrhythmias or structural cardiac abnormalities (**Figure 1A**, 5 years). The index patient (the arrow in the family three) presented with conduction system disturbances such as sinus node dysfunction, first-, second-, and third-degree atrioventricular block (**Figure 1B**), numerous repetitive premature ventricular complexes (PVCs), recurrence of persistent atrial fibrillation (**Supplementary Figure S1A**), and biatrial and biventricular dilation. Based on the electrocardiographic and echocardiographic findings, in combination with a positive family history of sudden death, he received a dual chamber implantable cardioverter-defibrillator (ICD) in primary prevention. Years later, 24-h Holter and ICD remote monitoring showed ventricular fibrillation (VF) discontinued by appropriate ICD shocks, after ineffective anti-tachycardia pacing (**Supplementary Figure S1B**). Moreover,

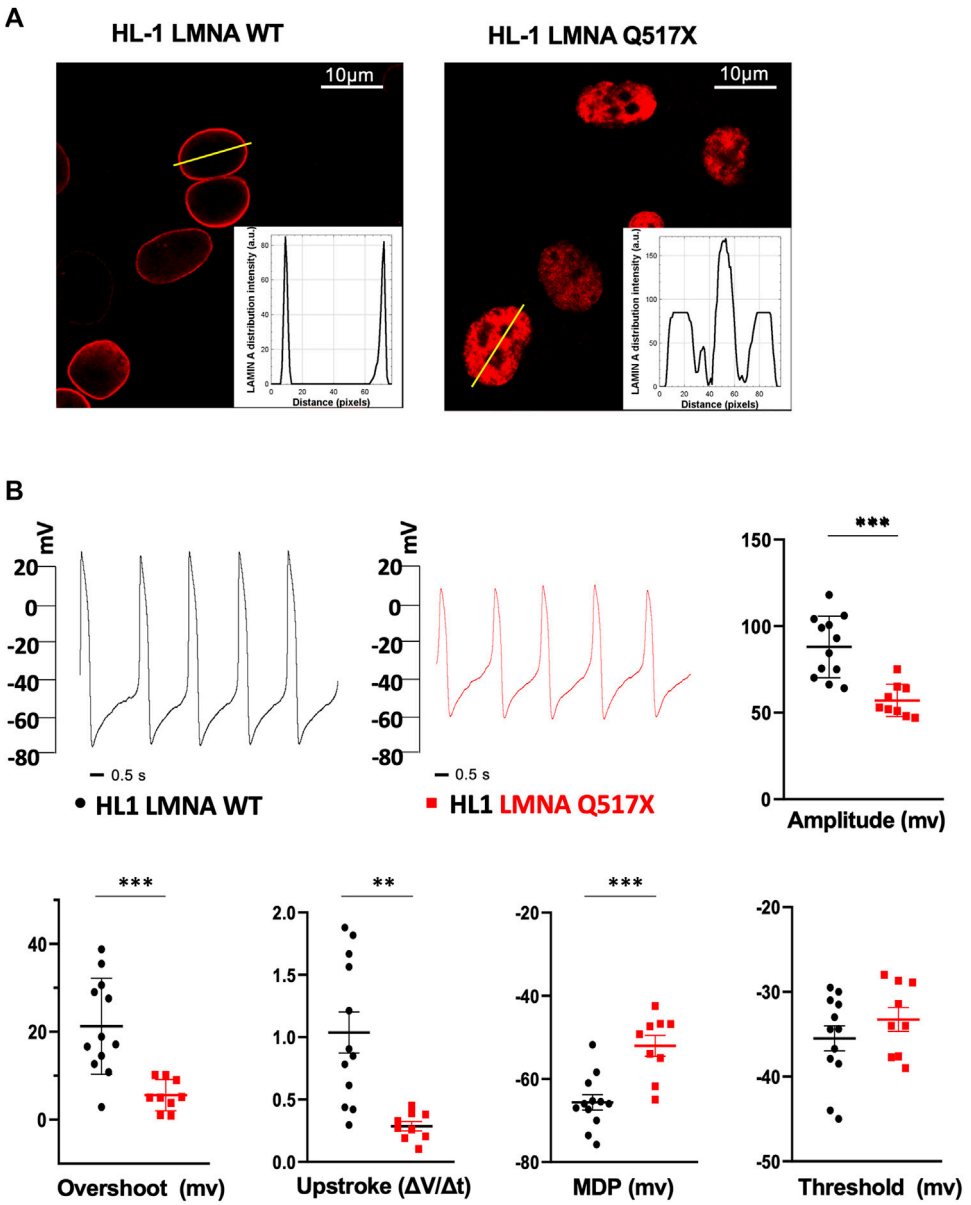

FIGURE 2 | (A) Representative confocal immunofluorescence images of LMNA WT and Q517X in stably transfected HL-1 cardiomyocytes. The insets report the fluorescence distribution along the line (yellow line) crossing nuclei in each cell line. **(B)** Representative AP recordings by whole-cell patch clamp in the current clamp configuration in LMNA WT (black trace) and LMNA Q517X-expressing HL-1 cells (red trace) and scatter plots for the analysis of AP parameters in LMNA WT (black dots, N = 12) and LMNA Q517X-expressing HL-1 cells (red squares, N = 9); ***$p < 0.001$; **$p < 0.01$; Student's t-test for unpaired data.

echocardiogram showed spherical, severely dilated (LVEDVi 92 ml/m2 and LVESVi 69 ml/m2) and markedly hypocontractile (LVEF 25%) left ventricle (**Figure 1C**) as well as highly dilated left atrium (**Figure 1D**). At the age of 49, the patient underwent heart transplant for both sustained VT/VF recurrences as a storm and severe impairment of left ventricular function. Western blot experiments on samples of ventricular and atrial myocardium obtained from the index patient at the time of cardiac transplantation confirmed the expression of the truncated LMNA variant in index patient's heart. As control, we used cardiac muscle tissues from a patient who experienced heart transplantation due to an ischemic heart disease not related to LMNA mutations (**Figure 1E**). The immunofluorescence confocal analysis using anti-LMNA antibodies on heart biopsies showed LMNA results expressed in protein aggregates in the nuclei of LMNA Q517X carrier's heart (**Figure 1F**, IP).

LMNA Q517X Alters Action Potential Properties in HL-1 Cardiomyocytes

When stably expressed in HL-1 cardiomyocytes, LMNA Q517X abnormally aggregated at the nuclear envelope and accumulated

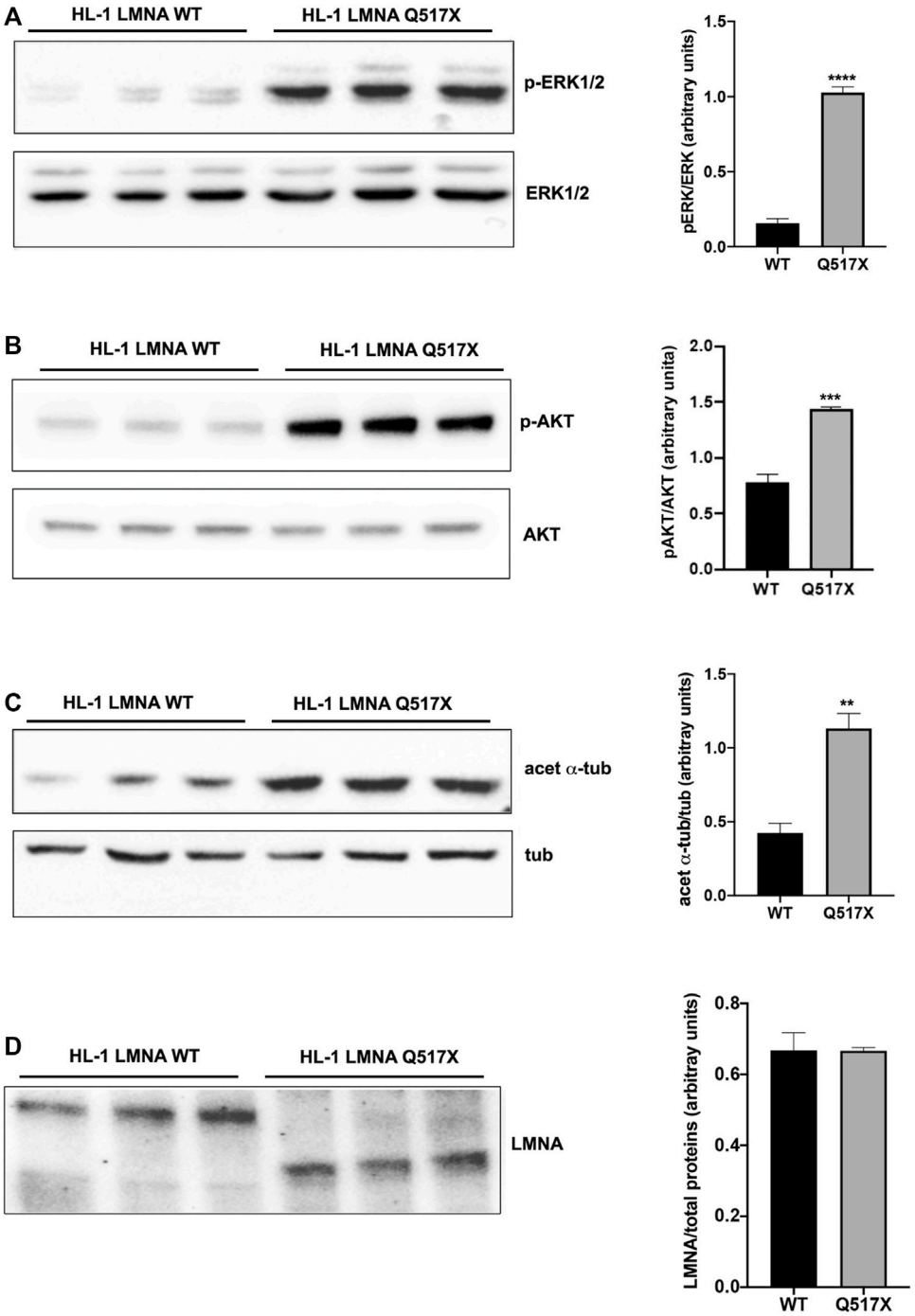

FIGURE 3 | (A) Left panel: representative western blot of p-ERK1/2 and ERK1/2 in lysates from LMNA WT and LMNA Q517X-expressing HL-1 cells; right panel: normalized densitometric analysis of p-ERK1/2 immunoreactive bands in LMNA WT and Q517X-expressing HL-1 cells. **(B)** Left panel: representative western blot of p-AKT and AKT in lysates from LMNA WT and LMNA Q517X-expressing HL-1 cells; right panel: normalized densitometric analysis of p-AKT immunoreactive bands in LMNA WT and Q517X-expressing HL-1 cells. **(C)** Left panel: representative western blot of acetylated α-tubulin (acet α-tub) and α-tubulin (tub) in lysates from LMNA WT and LMNA Q517X-expressing HL-1 cells; right panel: normalized densitometric analysis of acetylated α-tubulin immunoreactive bands in LMNA WT and Q517X-expressing HL-1 cells. **(D)** Left panel: representative western blot of mCherry-tagged LMNA in lysates from LMNA WT and LMNA Q517X-expressing HL-1 cells; right panel: normalized densitometric analysis of m-Cherry tagged LMNA immunoreactive bands. The data are means of 3 independent experiments. ****$p < 0.0001$ ***$p <= 0.001$; **$p < 0.01$; Student's t test for unpaired data.

within the nucleoplasm as clearly shown by the fluorescence distribution profile (**Figure 2A**, HL-1 LMNA WT, HL-1 LMNA Q517X, insets). This peculiar nuclear distribution is consistent with that of LMNA observed *in vivo* in the index patient's heart (**Figure 1E**).

To evaluate the effect of LMNA Q517X expression on the membrane electrical properties in cardiomyocytes, we analyzed the biophysical properties of spontaneous action potentials in HL-1 cardiomyocytes expressing either LMNA WT (**Figure 2B**, HL-1 LMNA WT, black trace) or Q517X (**Figure 2B**, HL-1 LMNA Q517X, red trace) by whole-cell patch clamp recordings in current clamp. The shape of the spontaneous action potential generated by cardiomyocytes expressing the LMNA mutant variant exhibited significant reduction in Action Potentials (APs) amplitude (**Figure 2B**, Amplitude in mV: black dots 88.04 ± 5.13 vs red squares 57.11 ± 3.11), APs overshoots (**Figure 2B**, Overshoot in mV: black dots 21.25 ± 3.14 vs red squares 5.58 ± 1.17), maximum upstroke velocity (**Figure 2B**, Upstroke in $\Delta V/\Delta t$: black dots 1.03 ± 0.16 vs red squares 0.28 ± 0.03), and maximum diastolic potential (MDP) (**Figure 2B**, MDP in mV: black dots 65.63 ± 1.86 vs red squares −52.03 ± 2.50) when compared to control cells; while no significant changes were detected in the APs' threshold between the two experimental conditions (**Figure 2B**, threshold in mV: black dots −35.49 ± 1.48 *vs* red squares −33.25 ± 1.41).

LMNA Q517X Alters Tubulin State and Decreased the Expression of Nav1.5 at the Plasma Membrane in HL-1 Cardiomyocytes

In LMNA WT and Q517X-expressing cardiomyocytes we studied the profile of key signaling molecules, already found to be dysregulated in lamin cardiomyopathies. Specifically, enhanced phosphorylation of ERK1/2 and AKT and decreased α-tubulin acetylation have been reported in the heart of Lmna $^{H222P/H222P}$ mice (Muchir et al., 2007; Choi et al., 2012). Here, we found that the activation profiles of ERK1/2 and AKT, quantified as the expression of their phosphorylated forms, were significantly increased in Q517X cardiomyocytes when compared with their control in accordance with the previous findings (**Figures 3A,B**). However, acetylated α-tubulin significantly increased in Q517X cardiomyocytes as unique feature of this mutant variant (**Figure 3C**). The expression of LMNA variants is comparable in the HL-1 clones used in the study (**Figure 3D**). It has been accepted that acetyl transferase has major affinity for polymerized tubulin (Janke and Chloë Bulinski, 2011); thus, we looked at the polymerization state of tubulin meshwork by fluorescence confocal analysis and found that it underwent hyper-polymerization in Q517X-expressing cardiomyocytes compared with their controls (**Figure 4A**). Quantitative analysis of fluorescence intensity showed that tubulin density significantly increased by approximately 50% in LMNA Q517X-expressing cardiomyocytes compared with their controls (**Figure 4A**, right panel). The perinuclear positioning of microtubule-organizing center (MTOC) was not affected by the expression of LMNA Q517X variant in these cells (**Supplementary Figure S2**), thus suggesting that the physical connection between the nucleus and microtubules is preserved upon LMNA Q517X expression.

It has been previously reported that the treatment with the anticancer drug Taxol, which polymerizes the cytoskeleton protein tubulin, may evoke cardiac arrhythmias reducing both the Nav1.5 expression at the plasma membrane and the Nav1.5 activation rate (Casini et al., 2010).

We indeed semi-quantified membrane Nav1.5 expression using cell surface biotinylation experiments in cardiomyocytes expressing either LMNA Q517X or WT. We found that the cells surface expression of Nav1.5 was significantly downregulated by approximately 40% in LMNA Q517X-expressing cardiomyocytes at the plasma membrane but not in the total lysate (**Figure 4B**).

Currents in HL-1 cardiomyocytes have been previously shown to have genotypic, phenotypic, and electrophysiologic properties similar to adult atrial cardiomyocytes, with the upstroke phase of the AP due to I_{Na} through Nav1.5 channel (Strege et al., 2012). Accordingly, we measured a significant decrease in tetrodotoxin-sensitive inward currents in LMNA Q517X-expressing cardiomyocytes (**Supplementary Figure S3**). Of note, outward currents were not affected by the expression of LMNA Q517X in HL-1 cardiomyocytes (**Supplementary Figure S3**). Indeed, the altered AP parameters registered in LMNA Q517X-expressing cardiomyocytes (**Figure 3B**) may be actually explained by a decreased density of Nav1.5 at the plasma membrane in these cells.

LMNA Q517X Significantly Alters Nav1.5 Function in HEK293 Cells

To better analyze Nav1.5 biophysics in the presence of LMNA Q517X we moved in HEK293 cells. **Figure 5A** shows representative Na^+ currents measured in HEK293 cells coexpressing Nav1.5, its β1 subunits (Nav1.5 + β1) and either LMNA WT or Q517X. As shown by the current–voltage curve (**Figure 5B**; black line for Nav1.5 + β1 + LMNA WT, red line for Nav1.5 + β1 + LMNA Q517X), the peak sodium current density evoked by depolarizing steps of currents was significantly decreased in cells expressing LMNA Q517X when compared with control cells expressing LMNA WT. The scatter plot of the maximum peak sodium currents clearly showed an up to 63% decrease in current density upon LMNA Q517X expression (peak current in pA/pF: black dots −504.46 ± 56.72 *vs* red squares −213.59 ± 32.380). This is consistent with the reduced expression of Nav1.5 at the plasma membrane shown above (**Figure 4A**). The voltage dependency of the steady-state activation for LMNA Q517X was shifted toward positive potentials with respect to WT (**Figure 5C**). The scatter plot of V1/2 showed a slight but significative shift of approximately 6 mV toward positive values for this parameter upon LMNA Q517X expression (**Figure 5C**, V1/2: black dots −51 ± 4.8 mV vs red squares −45.25 ± 2.060 mV), thus indicating the need of a more intense depolarization for the activation of Nav1.5 in these cells. The slope factor of activation (K) was significantly increased upon LMNA Q517X expression (**Figure 5C**, slope factor in mV: black dots 1.019 ± 0.22 vs red squares 2.635 ±

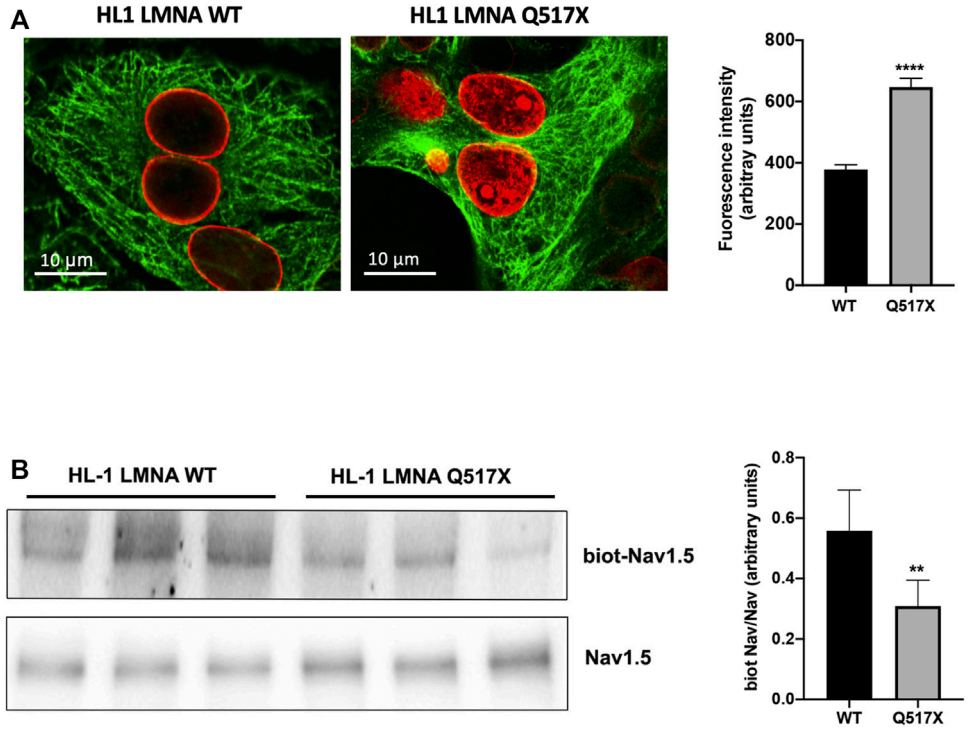

FIGURE 4 | (A) Left panel: representative confocal laser immunofluorescence images in LMNA WT and LMNA Q517X-expressing HL-1 cells (in red LMNA, in green β-tubulin); right panel: region of interest (ROI) for tubulin fluorescence quantification in LMNA WT and Q517X-expressing HL-1 cells. N = 15 for each experimental condition. **(B)** Left panel: representative western blots of Nav1.5 α subunit in cell surface biotinylated proteins (biot-Nav1.5) and in cell lysates (Nav1.5) from LMNA WT and Q517X-expressing HL-1 cells; right panel: normalized densitometric analysis of biot-Nav 1.5 immunoreactive bands in LMNA WT and Q517X-expressing HL-1 cells. The data are means of 3 independent experiments. ****$p < 0.0001$; **$p < 0.01$; Student's t test for unpaired data.

0.546), suggesting an alteration in voltage dependence of Nav1.5 activation in LMNA-Q517X-expressing HEK293 cells.

Interestingly, it has been also proved that a high prevalence of variants in K^+ channel encoding genes such as KCNH2 might control atrial repolarization and predispose carriers to atrial fibrillation (10.1161/circep.114.002519; 10.1093/eurheartj/ehm619). Indeed, outward K^+ currents through KCNH2 channel were analyzed in HEK293 cells transiently expressing KCNH2 together with WT or Q517X LMNA. This K^+ channel is highly expressed in HL-1 cells where it is involved in the repolarization phase of AP (Stimers et al., 2015). We found that the biophysics of this channel was not affected by the expression of LMNA Q517X variant (**Supplementary Figure S4**).

Tubulin State Manipulation Recovers AP Parameters in LMNA Q517X-Expressing HL-1 Cardiomyocytes and Nav1.5 Biophysics in HEK293 Cells

Alpha tubulin hyper-polymerization and hyper-acetylation are the unique features of LMNA Q517X-expressing HL-1 cardiomyocytes, likely accounting for the AP abnormalities in these cells.

An FDA-approved alkaloid, colchicine, inhibits tubulin polymerization in heart (Deftereos et al., 2013) and depolymerizes the tubulin network of LMNA Q517X-expressing cardiomyocytes to the same extent of control cells (**Figure 6A**, LMNA Q517X + colchi).

Concomitantly, colchicine treatment reduced the levels of acetylated α-tubulin (**Figure 6B**) and increased the cell surface expression of Nav1.5 in LMNA Q517X-expressing cardiomyocytes (**Figure 6C**) toward the levels of those found in LMNA WT-expressing cardiomyocytes.

Interestingly, **Figure 7** shows that the treatment of HL-1 cardiomyocytes expressing LMNA Q517X with colchicine leads to a WT-like shape of AP when compared with untreated cardiac cells (red traces for LMNA Q517X, gray traces for LMNA Q517X + colchicine). Moreover, colchicine treatment induced a significant recovery of all AP's parameters measured in LMNA Q517X cardiomyocytes toward those found in LMNA WT-expressing cardiomyocytes. Specifically, as shown in the scatter plots (**Figure 7**, scatter plots) AP amplitude (amplitude in mV: red squares 57.11 ± 3.11, vs gray squares 80.32 ± 7.45), AP overshoot (overshoots in mV: red squares 5.58 ± 1.17, vs gray squares 19.88 ± 4.07), maximum upstroke velocity (upstroke in mV/ms: red squares 0.28 ± 0.03, *vs* gray squares 0.90 ± 0.24), and the maximum diastolic potential (MDP in mV: red squares −52.03 ± 2.50, *vs* gray squares -61.6 ± 2.675) were all significantly increased in LMNA Q517X-treated cardiomyocytes compared with their controls. No significant

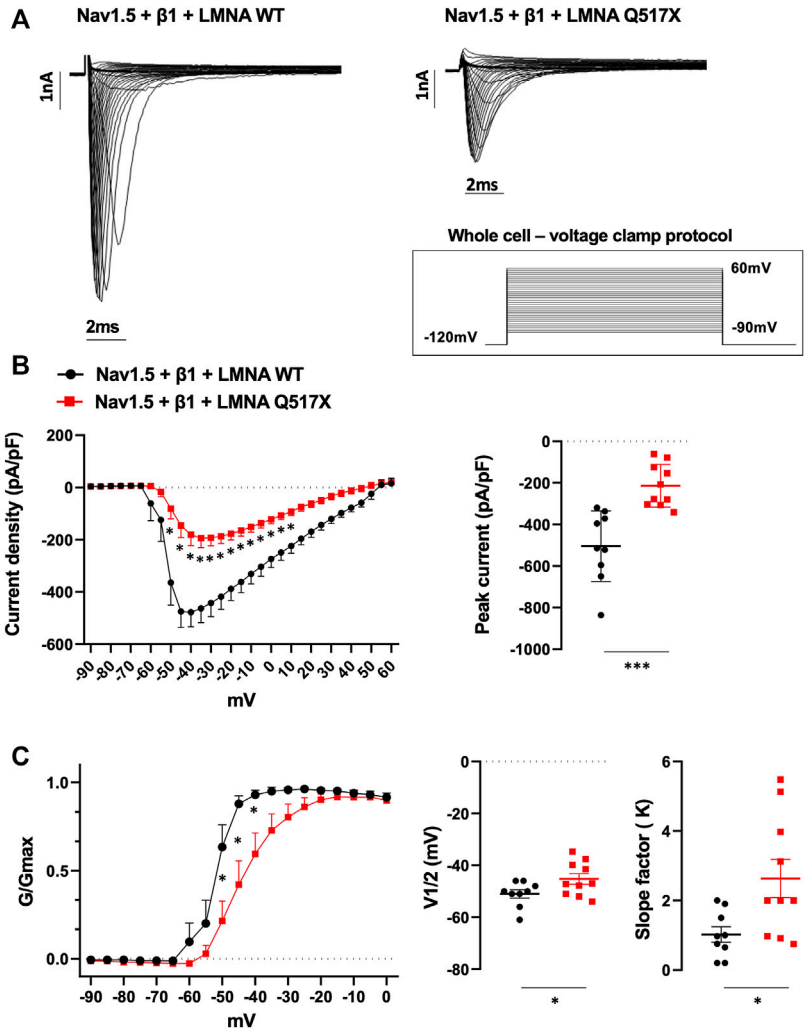

FIGURE 5 | (A) Representative traces of inward Na^+ currents evoked in HEK293 cells expressing either LMNA WT or LMNA Q517X, under 20s depolarizing steps from −90mV to +60 mV (with 5-mV increments) starting from an holding potential of −120 mV. **(B)** Left panel: current density (pA/pF)–voltage relationships (I–V curve) of the Na^+ currents recorded for LMNA WT (black trace, *N* = 9), and LMNA Q517X-expressing HEK293 cells (red trace, *N* = 10); *p* < 0,0001 from −50 mV to −20 mV; *p*-value< 0.001 at F02D15 mV an −10 mV; *p*-value < 0,01 at −5 mV and *p*-value < 0,05 at 0 mV and 5 mV, two-way Anova. Right panel: scatter plot of the maximum peak sodium currents (pA/pF) for LMNA WT (black dots) and LMNA Q517X-expressing HEK293 cells (red squares); ***$p < 0.001$, Student's *t* test for unpaired data). **(C)** Left panel: conductance voltage (G/Gmax) relationships of Na^+ currents (G–V curve) obtained for LMNA WT (black trace, N = 9) and LMNA Q517X-expressing HEK293 cells (red trace, N = 10); *p*-value < 0,0001 at −50 mV and −45 mV; < 0.001 at −40 mV, two-way Anova. Right panel: scatter plots of the half-maximal conductance (V1⁄2) and the slope factors (K) in LMNA WT (black dots) or LMNA Q517X-expressing HEK293 cells (red squares), respectively; *$p < 0.01$ Student's *t* test for unpaired data.

changes were observed in APs' threshold between the two experimental conditions (thresholds in mV: red squares −33.25 ± 1.41, *vs* gray squares −33.96 ± 1.57).

Similarly, colchicine treatment reversed the Nav1.5 biophysical parameters measured in LMNA Q517X-expressing HEK293 cells toward those measured in LMNA WT-expressing HEK293 cells. As shown in **Figure 8A** (representative current traces) and 8B (current density plots: red line for Nav1.5 + β1 + LMNA Q517X, gray line for Nav1.5 + β1 + LMNA Q517X + colchicine), Na^+ currents recorded in HEK293 cells expressing LMNA Q517X significantly increased upon colchicine treatment. The peak current of Na^+ returned to that observed in LMNA WT-expressing-HEK293 cells (**Figure 8B**, peak current in pA/pF: red squares −170.5 ± 32,942 *vs* gray squares −437,166 ± 33,843). Upon colchicine treatment the steady-state activation curve of Nav1.5 in LMNA Q517X-expressing cells returned to that observed in LMNA WT-expressing cells (**Figure 8C**, G/Gmax: red line for Nav1.5 + β1 + LMNA Q517X, gray line for Nav1.5 + β1 + LMNA Q517X + colchicine). Finally, upon colchicine treatment both V1/2 and slope factor values measured in LMNA Q517X-expressing HEK293 returned to those observed in LMNA WT-expressing cells (**Figure 8C**; V1/2 in mV: red squares −42.68 ± 2.235 *vs* gray squares −49.93 ± 2.034; slope factor in mV: red squares 2.886 ± 0.650 *vs* gray squares 1.141 ± 0.422).

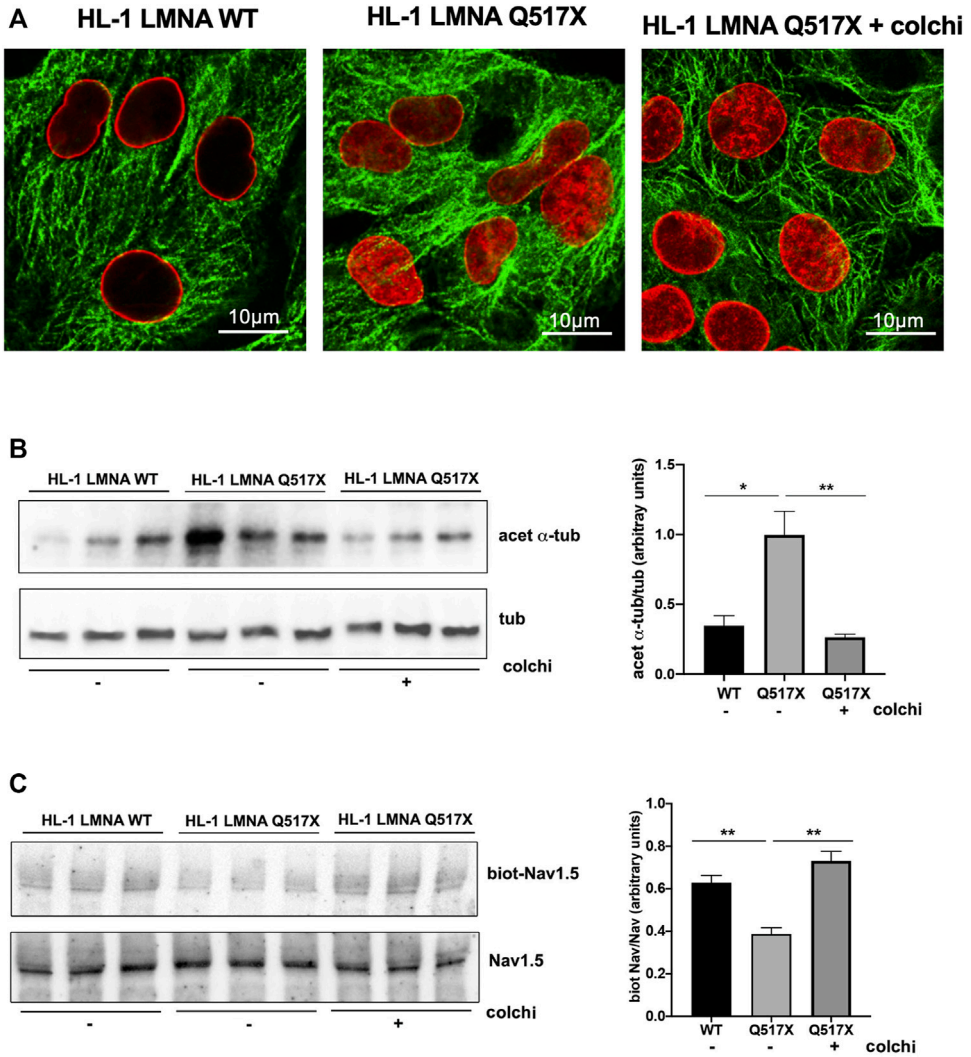

FIGURE 6 | (A) Representative immunofluorescence confocal images of HL-1 cells expressing either LMNA WT or LMNA Q517X, the latter treated or not with colchicine (+colchi). **(B)** Left panel: representative western blot of acetylated α tubulin (acet α-tub) and total α tubulin (tub) in the absence (–) or the presence (+) of colchicine (colchi) in LMNA WT and LMNA Q517X-expressing HL-1 cells; right panel: normalized densitometric analysis of acetylated α-tubulin immunoreactive bands in all the experimental conditions shown in the left panel. **(C)** Left panel: representative western blot of cells surface biotinylated Nav1.5 (biot-Nav1.5) and Nav1.5 in cell lysates (Nav1.5) in the absence (–) or presence (+) of colchicine (colchi) in LMNA WT and LMNA Q517X-expressing HL-1 cells; right panel: normalized densitometric analysis of biot-Nav1.5 immunoreactive bands in all the experimental conditions shown in the left panel. The data are means of 3 independent experiments $^{*}p < 0.01$, $^{**}p < 0.001$, one-way Anova.

DISCUSSION

In this work, we found that the pathogenetic LMNA Q517X variant, through a modulation of the microtubule meshwork state, impairs Nav1.5 expression and function at the plasma membrane in the murine atrial cell line HL-1, thus proving new insights into both the way how LMNA may regulate cardiac function in physiopathological conditions and the possible therapeutic approaches in the field of cardiac laminopathies.

As a consequence of the reduced Nav1.5 activity at the plasma membrane, APs have reduced amplitude, overshoot, upstroke velocity, and increased diastolic potential in LMNA Q517X-expressing cardiomyocytes compared with their controls. These AP features may decrease conduction velocity in atrial cardiomyocytes and autorhythmic cells inducing atrial fibrillation, sick sinus syndrome, and AV-block, all clinical findings of the index family carrying LMNA Q517X mutant (**Figure 1A**, results). Atrial fibrillation is one of the most common causes for cardiac function deterioration in the setting of DCM (Middlekauff et al., 1991; Mamas et al., 2009), which also occurred in LMNA Q517X carriers. Accordingly, loss-of-function mutations in Nav1.5 encoding gene, *scn5a*, have been found associated with atrial fibrillation and conduction defects (Olson et al., 2005; Darbar et al., 2008). Of note, loss of function in the Nav1.5 channel can be also associated with DCM and

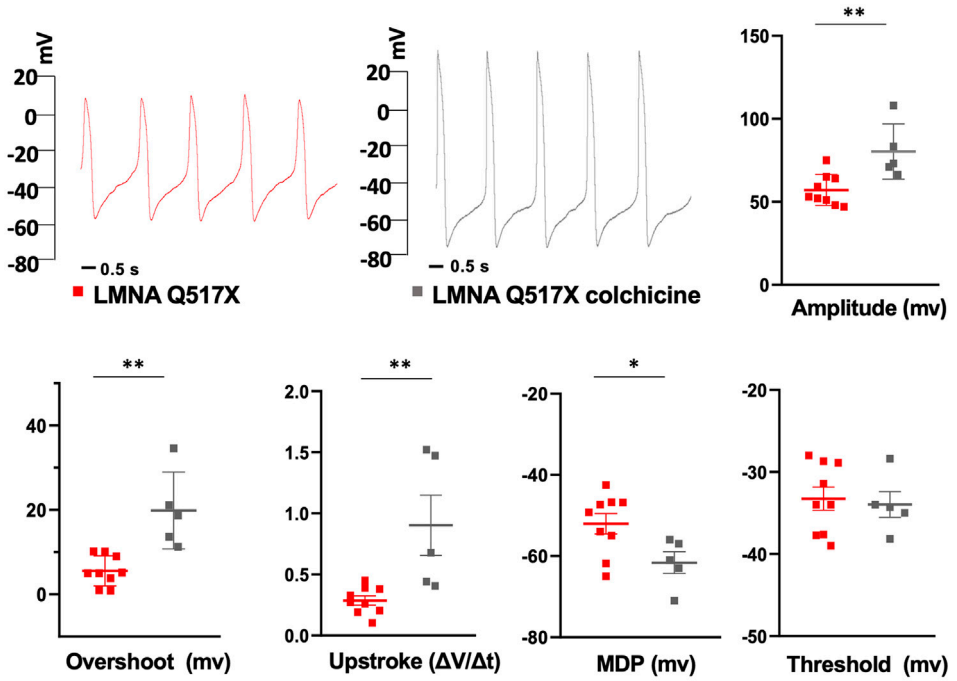

FIGURE 7 | Representative AP recordings by whole-cell patch clamp in current clamp configuration in untreated (red traces) and colchicine-treated LMNA Q517X-expressing HL-1 cells (gray traces) and scatter plots for the analysis of AP parameters in untreated (red squares, $N = 9$) and colchicine-treated LMNA Q517X-expressing HL-1 cells (gray squares, $N = 5$). $^{*}p < 0.01$, $^{**}p < 0.001$, Student's t test for unpaired data.

ventricular arrhythmias, regardless of whether the atrial fibrillation occurred, suggesting that reduction in the inward Na^+ current may affect directly electrical properties and fates of ventricular cardiomyocytes (McNair et al., 2004). Indeed, we cannot exclude that LMNA Q517X variant expressed in the whole heart of carriers may affect directly ventricular function.

The clinical history of the index family carrying LMNA Q517X mutant, however, puts the permanent atrial fibrillation and conduction defects showed at the onset of the cardiomyopathy as key events for the following heart failure.

We found that LMNA Q517X expression induced both microtubules hyper-polymerization and Nav1.5 downregulation at the plasma membrane in atrial HL-1 cardiomyocytes and significant reduction in the peak I_{Na} amplitude in Nav1.5-expressing HEK293 cells. These results are in agreement with the findings of Casini et al., showing that treatment with the anticancer drug Taxol, which polymerizes tubulin, reduces sarcolemmal Nav1.5 in neonatal cardiomyocytes, and I_{Na} amplitude in Na1.5-expressing HEK293 cells of about two-fold (Casini et al., 2010).

The density of the microtubule alters microtubule interactome not only affecting channel delivery/turnover (Steele and Fedida, 2014), but also E-C coupling, myofilament contractility, and proteostasis (Chinnakkannu et al., 2010), thus accounting also for structural cardiac abnormality.

Interestingly, the increase in α tubulin density is paralleled by a significant increase in the acetylation level of α tubulin at 40 lisine (K40) in the amino acidic sequence on α tubulin (**Figure 3C**), as expected by the known higher affinity of the tubulin acetyltransferase (aTAT1) for polymerized tubulin (Janke and Chloë Bulinski, 2011). It was demonstrated that K40 acetylation weakens lateral interactions between protofilaments, thus softening the microtubules (Portran et al., 2017). As microtubules in living cells are frequently exposed to mechanical forces, an acetylation-induced increase in their flexibility would allow microtubules to better resist mechanical stress consequently making acetylated microtubules more long-lived. At the same time, longer-lived microtubules are still more likely to experience mechanical stress, thus further accumulating acetylation marks, which could reflect the notion that acetylation is a marker of microtubule age.

Indeed, it can be hypothesized that LMNA Q517X mutant impairing the mechanical nuclear–cytoskeletal coupling induces an adaptive cellular response such as microtubules polymerization and acetylation mimicking aged microtubules, with consequences on dis-regulated trafficking of Nav1.5 channel at the cell surface and the creation of pro-arrhythmic substrate.

The increasing in the α-tubulin acetylation may also account for the upregulation of AKT pathway we also found in LMNA Q517X-expressing cardiomyocytes. Interestingly, Giustignani et al. found that tubulin acetylation recruits the chaperon protein Hsp90 to microtubules stimulating the signaling pathways of its client kinase AKT (Giustiniani et al., 2009).

Of note, microtubules polymerization and stabilization obtained by either Taxol or Discodermolide two known chemotherapies, significantly increased ERK1/2 phosphorylation in different cell lines (Seidman et al., 2001; Klein et al., 2005). Accordingly, we cannot exclude that the

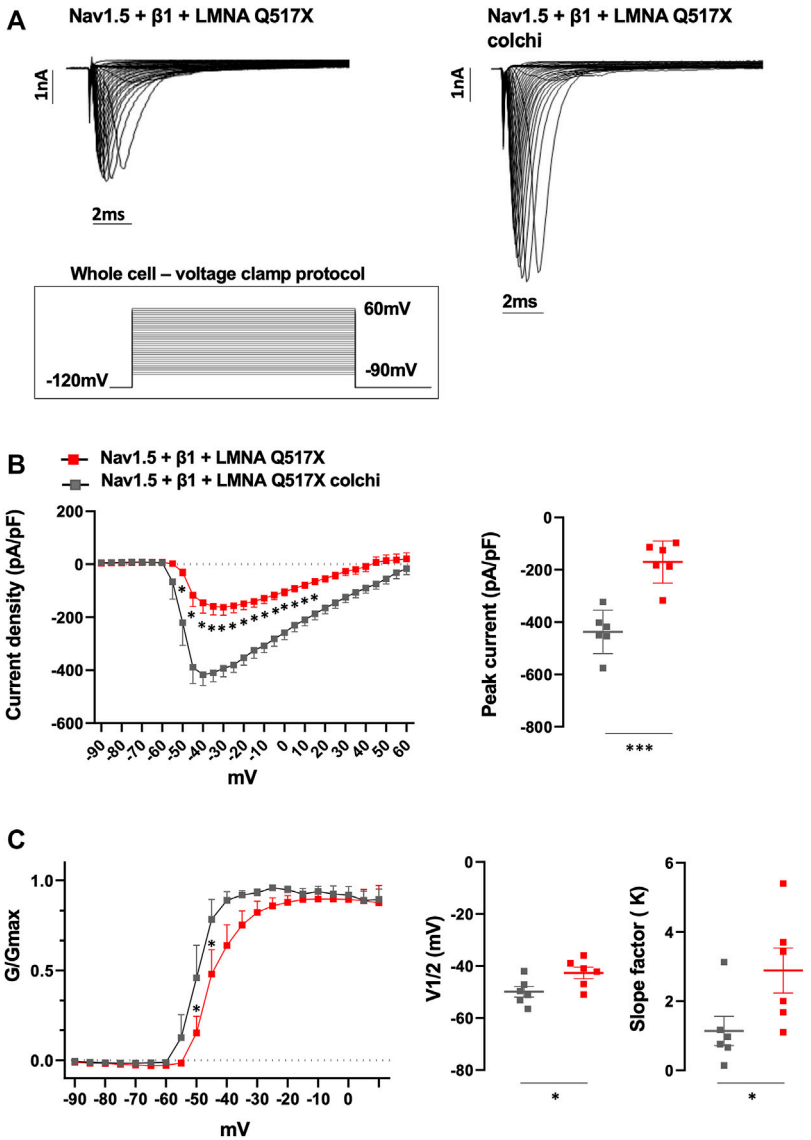

FIGURE 8 | (A) Representative traces of inward Na^+ currents evoked in untreated (Nav1.5 + β1 + LMNA Q517X) or colchicine-treated LMNA Q517X-expressing HEK293 cells (Nav1.5 + β1 + LMNA Q517X colchi). **(B)** Left panel: current density (pA/pF)–voltage relationships (I–V curve) of the Na^+ currents recorded in untreated (red trace, $N = 6$), and colchicine-treated LMNA Q517X-expressing HEK293 cells (gray trace, $N = 6$); p-value < 0,0001 from –50 mV to –10 mV; p-value< 0.001 at –5 mV and at 0 mV; p-value < 0.01 at 5 mV and p-value < 0,05 at 10 mV and 15 mV, two-way Anova. Right panel: scatter plot of the maximum peak sodium currents (pA/pF) in untreated (red squares) and in colchicine-treated LMNA Q517X-expressing HEK293 cells (gray squares). **(C)** Left panel: conductance voltage (G/Gmax) relationships of Na^+ currents (G–V curve) obtained for untreated (red trace, $N = 6$), and colchicine-treated LMNA Q517X-expressing HEK293 cells (gray trace, $N = 6$); p-value < 0.001 at –50 mV and at –45 mV, two-way Anova. Right panel: scatter plot of the half-maximal conductance (V1/2) and slope factors (K) in untreated (red squares) and in colchicine-treated LMNA Q517X-expressing HEK293 cells (gray squares); *p < 0.01; **p < 0.001, Student's t test for unpaired data.

activation of ERK1/2 pathway we found in LMNA Q517X-expressing cardiomyocytes may be a downstream process to microtubules hyper-polymerization we found associated with this LMNA variant.

The altered tubulin state has already been found associated with some LMNA pathogenic variants. Instable microtubule network with a decrease in the acetylation of α tubulin triggered abnormal CX43 localization and consequent electrical communication between cardiomyocytes in $Lmna^{H222P/H222P}$ and $Lmna^{N195K/N195K}$ mice (Macquart et al., 2019; Borin et al., 2020). Accordingly, stabilization of microtubules using paclitaxel, a microtubule-stabilization agent commonly used in chemotherapy, repositioned CX43 in cardiomyocytes of $Lmna^{N195K/N195K}$ mice and improved intraventricular conduction defects in these mice (Macquart et al., 2019). Recently, instable microtubules meshwork was also found in cardiomyocytes expressing E161K and D192G pathogenic LMNA variants with again a displacement of CX43 (Borin et al., 2020), demonstrating a different pathogenic mechanism by which LMNA may displace a sarcolemmal

protein through the microtubule network thus impairing heart electrical physiology.

To the best of our knowledge, we reported for the first time that an LMNA pathogenic variant is associated with an excess of microtubule polymerization and stabilization, which impairs Nav1.5 sarcolemmal expression and biophysics generating abnormalities in AP generation and propagation in cardiomyocytes.

Interestingly, we showed that a well-known FDA-approved alkaloid, colchicine, which depolymerizes the tubulin meshwork, reverted the altered AP properties of LMNA Q517X-expressing cardiomyocytes recapitulating those of the LMNA WT-expressing cardiomyocytes.

Similarly, when colchicine was tested on HEK293 cells expressing Nav1.5 and LMNA Q517X, I_{Na} currents and kinetics returned to those measured in control cells. The effect of colchicine non only provided evidence that the altered state of tubulin we observed is actually the key event in the electrical features of mutant expressing cardiomyocytes but also suggested a therapeutic intervention for this LMNA cardiomyopathy.

Interestingly, *in vivo* colchicine treatment significantly reduced microtubule density in cardiomyocytes of different rat models (Prins et al., 2017; Scarborough et al., 2021). Moreover, in the last 15 years colchicine was introduced in the field of cardiology for the treatment and prevention of different cardiovascular diseases (Fiolet et al., 2021), thus suggesting colchicine as a possible ready-to-use treatment for LMNA Q517X carriers.

In conclusion, our results confirm that LMNA protein at the nuclear envelope controls a chain of events involved not only in the mechanical but also in the electrical signaling transfer from the nucleus to the cell membrane in cardiomyocytes. Moreover, our findings suggest that every LMNA mutant may act with different pathogenic mechanisms in generating a common clinical phenotype in heart such as arrythmias and conduction defects. Indeed, it is very important to characterize each LMNA pathogenic variant in cardiomyocytes to gain insights on both the complexity of the cardiac cell biology, the mechanisms leading to cardiac dysfunction in laminopathies and the possible therapeutic approaches.

DATA AVAILABILITY STATEMENT

The raw data supporting the conclusion of this article will be made available by the authors, without undue reservation.

ETHICS STATEMENT

The studies involving human participants were reviewed and approved by the Ethics Committee of the University Hospital Consortium, Policlinico of Bari, Italy. Written informed consent to participate in this study was provided by the participants' legal guardian/next of kin. Written informed consent was obtained from the individual(s) for the publication of any potentially identifiable images or data included in this article.

AUTHOR CONTRIBUTIONS

RD: design of the work and acquisition, analysis, and interpretation of data from electrophysiology; GPi and SM: western blotting experiments and analysis; GPr and MS: analysis and interpretation of data and revising them critically for important intellectual content; MB: clinical data acquisition; CF, MP, and SF: clinical data acquisition and analysis; AG: design of the work, analysis and interpretation of data from electrophysiology, and drafting and revising the work critically for important intellectual content; and MC: conception and design of the work, analysis and interpretation of data for the work, drafting the work and revising it critically for important intellectual content, final approval of the version to be published, and agreement to be accountable for all aspects of the work.

FUNDING

This work was supported by funding from "Carmosino19LAMINOPATIE" and "Carmosino20RIL" to MC and to 2020-PON 2014-2020 Innovative and Industrial PhD programs identification code # DOT208JXBA to GPi.

SUPPLEMENTARY MATERIAL

The Supplementary Material for this article can be found online at: https://www.frontiersin.org/articles/10.3389/fcell.2022.918760/full#supplementary-material

REFERENCES

Arbustini, E., Pilotto, A., Repetto, A., Grasso, M., Negri, A., Diegoli, M., et al. (2002). Autosomal Dominant Dilated Cardiomyopathy with Atrioventricular Block: A Lamin A/C Defect-Related Disease. *J. Am. Coll. Cardiol.* 39, 981–990. doi:10.1016/s0735-1097(02)01724-2

Borin, D., Peña, B., Chen, S. N., Long, C. S., Taylor, M. R. G., Mestroni, L., et al. (2020). Altered Microtubule Structure, Hemichannel Localization and Beating Activity in Cardiomyocytes Expressing Pathologic Nuclear Lamin A/C. *Heliyon* 6, e03175. doi:10.1016/j.heliyon.2020.e03175

Carmosino, M., Giménez, I., Caplan, M., and Forbush, B. (2008). Exon Loss Accounts for Differential Sorting of Na-K-Cl Cotransporters in Polarized Epithelial Cells. *MBoC* 19, 4341–4351. doi:10.1091/mbc.e08-05-0478

Carmosino, M., Torretta, S., Procino, G., Gerbino, A., Forleo, C., Favale, S., et al. (2014). Role of Nuclear Lamin A/C in Cardiomyocyte Functions. *Biol. Cell* 106, 346–358. doi:10.1111/boc.201400033

Carmosino, M., Gerbino, A., Schena, G., Procino, G., Miglionico, R., Forleo, C., et al. (2016). The Expression of Lamin A Mutant R321X Leads to Endoplasmic Reticulum Stress with Aberrant Ca^{2+} Handling. *J. Cell. Mol. Med.* 20, 2194–2207. doi:10.1111/jcmm.12926

Casini, S., Tan, H. L., Demirayak, I., Remme, C. A., Amin, A. S., Scicluna, B. P., et al. (2010). Tubulin Polymerization Modifies Cardiac Sodium Channel Expression and Gating. *Cardiovasc. Res.* 85, 691–700. doi:10.1093/cvr/cvp352

Chinnakkannu, P., Samanna, V., Cheng, G., Ablonczy, Z., Baicu, C. F., Bethard, J. R., et al. (2010). Site-specific Microtubule-Associated Protein 4 Dephosphorylation Causes Microtubule Network Densification in Pressure Overload Cardiac Hypertrophy. *J. Biol. Chem.* 285, 21837–21848. doi:10.1074/jbc.m110.120709

Choi, J. C., Wu, W., Muchir, A., Iwata, S., Homma, S., and Worman, H. J. (2012). Dual Specificity Phosphatase 4 Mediates Cardiomyopathy Caused by Lamin A/C (LMNA) Gene Mutation. *J. Biol. Chem.* 287, 40513–40524. doi:10.1074/jbc.m112.404541

Claycomb, W. C., Lanson, N. A., Jr., Stallworth, B. S., Egeland, D. B., Delcarpio, J. B., Bahinski, A., et al. (1998). HL-1 Cells: A Cardiac Muscle Cell Line that Contracts and Retains Phenotypic Characteristics of the Adult Cardiomyocyte. *Proc. Natl. Acad. Sci. U.S.A.* 95, 2979–2984. doi:10.1073/pnas.95.6.2979

Darbar, D., Kannankeril, P. J., Donahue, B. S., Kucera, G., Stubblefield, T., Haines, J. L., et al. (2008). Cardiac Sodium Channel (SCN5A) Variants Associated with Atrial Fibrillation. *Circulation* 117, 1927–1935. doi:10.1161/circulationaha.107.757955

De Zio, R., Gerbino, A., Forleo, C., Pepe, M., Milano, S., Favale, S., et al. (2019). Functional Study of a KCNH2 Mutant: Novel Insights on the Pathogenesis of the LQT2 Syndrome. *J. Cell Mol. Med.* 23, 6331–6342. doi:10.1111/jcmm.14521

Deftereos, S., Giannopoulos, G., Papoutsidakis, N., Panagopoulou, V., Kossyvakis, C., Raisakis, K., et al. (2013). Colchicine and the Heart: Pushing the Envelope. *J. Am. Coll. Cardiol.* 62, 1817–1825. doi:10.1016/j.jacc.2013.08.726

Fiolet, A. T. L., Opstal, T. S. J., Mosterd, A., Eikelboom, J. W., Jolly, S. S., Keech, A. C., et al. (2021). Efficacy and Safety of Low-Dose Colchicine in Patients with Coronary Disease: a Systematic Review and Meta-Analysis of Randomized Trials. *Eur. Heart J.* 42, 2765–2775. doi:10.1093/eurheartj/ehab115

Forleo, C., Carmosino, M., Resta, N., Rampazzo, A., Valecce, R., Sorrentino, S., et al. (2015). Clinical and Functional Characterization of a Novel Mutation in Lamin A/c Gene in a Multigenerational Family with Arrhythmogenic Cardiac Laminopathy. *PLoS One* 10, e0121723. doi:10.1371/journal.pone.0121723

Gerbino, A., Schena, G., Milano, S., Milella, L., Barbosa, A. F., Armentano, F., et al. (2016). Spilanthol from Acmella Oleracea Lowers the Intracellular Levels of cAMP Impairing NKCC2 Phosphorylation and Water Channel AQP2 Membrane Expression in Mouse Kidney. *PLoS One* 11, e0156021. doi:10.1371/journal.pone.0156021

Gerbino, A., Bottillo, I., Milano, S., Lipari, M., Zio, R. D., Morlino, S., et al. (2017). Functional Characterization of a Novel Truncating Mutation in Lamin A/C Gene in a Family with a Severe Cardiomyopathy with Conduction Defects. *Cell Physiol. Biochem.* 44, 1559–1577. doi:10.1159/000485651

Gerbino, A., Procino, G., Svelto, M., and Carmosino, M. (2018). Role of Lamin A/C Gene Mutations in the Signaling Defects Leading to Cardiomyopathies. *Front. Physiol.* 9, 1356. doi:10.3389/fphys.2018.01356

Gerbino, A., Forleo, C., Milano, S., Piccapane, F., Procino, G., Pepe, M., et al. (2021). Pro-inflammatory Cytokines as Emerging Molecular Determinants in Cardiolaminopathies. *J. Cell Mol. Med.* 25, 10902–10915. doi:10.1111/jcmm.16975

Giustiniani, J., Daire, V., Cantaloube, I., Durand, G., Poüs, C., Perdiz, D., et al. (2009). Tubulin Acetylation Favors Hsp90 Recruitment to Microtubules and Stimulates the Signaling Function of the Hsp90 Clients Akt/PKB and P53. *Cell. Signal.* 21, 529–539. doi:10.1016/j.cellsig.2008.12.004

Han, M., Zhao, M., Cheng, C., Huang, Y., Han, S., Li, W., et al. (2019). Lamin A Mutation Impairs Interaction with Nucleoporin NUP155 and Disrupts Nucleocytoplasmic Transport in Atrial Fibrillation. *Hum. Mutat.* 40, 310–325. doi:10.1002/humu.23691

Hasselberg, N. E., Haland, T. F., Saberniak, J., Brekke, P. H., Berge, K. E., Leren, T. P., et al. (2018). Lamin A/C Cardiomyopathy: Young Onset, High Penetrance, and Frequent Need for Heart Transplantation. *Eur. Heart J.* 39, 853–860. doi:10.1093/eurheartj/ehx596

Janke, C., and Chloë Bulinski, J. (2011). Post-translational Regulation of the Microtubule Cytoskeleton: Mechanisms and Functions. *Nat. Rev. Mol. Cell Biol.* 12, 773–786. doi:10.1038/nrm3227

Klein, L. E., Freeze, B. S., Smith, A. B., 3rd, and Horwitz, S. B. (2005). The Microtubule Stabilizing Agent Discodermolide Is a Potent Inducer of Accelerated Cell Senescence. *Cell Cycle* 4, 501–507. doi:10.4161/cc.4.3.1550

Liu, Z., Shan, H., Huang, J., Li, N., Hou, C., and Pu, J. (2016). A Novel Lamin A/C Gene Missense Mutation (445 V > E) in Immunoglobulin-like Fold Associated with Left Ventricular Non-compaction. *Europace* 18, 617–622. doi:10.1093/europace/euv044

Macquart, C., Jüttner, R., Morales Rodriguez, B., Le Dour, C., Lefebvre, F., Chatzifrangkeskou, M., et al. (2019). Microtubule Cytoskeleton Regulates Connexin 43 Localization and Cardiac Conduction in Cardiomyopathy Caused by Mutation in A-type Lamins Gene. *Hum. Mol. Genet.* 28, 4043–4052. doi:10.1093/hmg/ddy227

Mamas, M. A., Caldwell, J. C., Chacko, S., Garratt, C. J., Fath-Ordoubadi, F., and Neyses, L. (2009). A Meta-Analysis of the Prognostic Significance of Atrial Fibrillation in Chronic Heart Failure. *Eur. J. Heart Fail.* 11, 676–683. doi:10.1093/eurjhf/hfp085

Markandeya, Y. S., Tsubouchi, T., Hacker, T. A., Wolff, M. R., Belardinelli, L., and Balijepalli, R. C. (2016). Inhibition of Late Sodium Current Attenuates Ionic Arrhythmia Mechanism in Ventricular Myocytes Expressing LaminA-N195k Mutation. *Heart Rhythm* 13, 2228–2236. doi:10.1016/j.hrthm.2016.08.007

McNair, W. P., Ku, L., Taylor, M. R. G., Fain, P. R., Dao, D., Wolfel, E., et al. (2004). SCN5A Mutation Associated with Dilated Cardiomyopathy, Conduction Disorder, and Arrhythmia. *Circulation* 110, 2163–2167. doi:10.1161/01.cir.0000144458.58660.bb

Middlekauff, H. R., Stevenson, W. G., and Stevenson, L. W. (1991). Prognostic Significance of Atrial Fibrillation in Advanced Heart Failure. A Study of 390 Patients. *Circulation* 84, 40–48. doi:10.1161/01.cir.84.1.40

Muchir, A., Pavlidis, P., Decostre, V., Herron, A. J., Arimura, T., Bonne, G., et al. (2007). Activation of MAPK Pathways Links LMNA Mutations to Cardiomyopathy in Emery-Dreifuss Muscular Dystrophy. *J. Clin. Invest.* 117, 1282–1293. doi:10.1172/jci29042

Nishiuchi, S., Makiyama, T., Aiba, T., Nakajima, K., Hirose, S., Kohjitani, H., et al. (2017). Gene-Based Risk Stratification for Cardiac Disorders in LMNA Mutation Carriers. *Circ. Cardiovasc Genet.* 10, e001603. doi:10.1161/CIRCGENETICS.116.001603

Olaopa, M. A., Spoonamore, K. G., Bhakta, D., Chen, Z., Celestino-Soper, P. B. S., Chen, P.-S., et al. (2018). Lamin-A/C Variants Found in Patients with Cardiac Conduction Disease Reduce Sodium Currents. *Cardiogenetics* 8, 7127. doi:10.4081/cardiogenetics.2018.7127

Olson, T. M., Michels, V. V., Ballew, J. D., Reyna, S. P., Karst, M. L., Herron, K. J., et al. (2005). Sodium Channel Mutations and Susceptibility to Heart Failure and Atrial Fibrillation. *JAMA* 293, 447–454. doi:10.1001/jama.293.4.447

Portran, D., Schaedel, L., Xu, Z., Théry, M., and Nachury, M. V. (2017). Tubulin Acetylation Protects Long-Lived Microtubules against Mechanical Ageing. *Nat. Cell Biol.* 19, 391–398. doi:10.1038/ncb3481

Prins, K. W., Tian, L., Wu, D., Thenappan, T., Metzger, J. M., and Archer, S. L. (2017). Colchicine Depolymerizes Microtubules, Increases Junctophilin-2, and Improves Right Ventricular Function in Experimental Pulmonary Arterial Hypertension. *J. Am. Heart Assoc.* 6, e006195. doi:10.1161/JAHA.117.006195

Salvarani, N., Crasto, S., Miragoli, M., Bertero, A., Paulis, M., Kunderfranco, P., et al. (2019). The K219T-Lamin Mutation Induces Conduction Defects through Epigenetic Inhibition of SCN5A in Human Cardiac Laminopathy. *Nat. Commun.* 10, 2267. doi:10.1038/s41467-019-09929-w

Scarborough, E. A., Uchida, K., Vogel, M., Erlitzki, N., Iyer, M., Phyo, S. A., et al. (2021). Microtubules Orchestrate Local Translation to Enable Cardiac Growth. *Nat. Commun.* 12, 1547. doi:10.1038/s41467-021-21685-4

Seidman, R., Gitelman, I., Sagi, O., Horwitz, S. B., and Wolfson, M. (2001). The Role of ERK 1/2 and P38 MAP-Kinase Pathways in Taxol-Induced Apoptosis in Human Ovarian Carcinoma Cells. *Exp. Cell Res.* 268, 84–92. doi:10.1006/excr.2001.5262

Stallmeyer, B., Koopmann, M., and Schulze-Bahr, E. (2012). Identification of Novel Mutations in LMNA Associated with Familial Forms of Dilated Cardiomyopathy. *Genet. Test. Mol. Biomarkers* 16, 543–549. doi:10.1089/gtmb.2011.0214

Steele, D. F., and Fedida, D. (2014). Cytoskeletal Roles in Cardiac Ion Channel Expression. *Biochim. Biophys. Acta Biomembr.* 1838, 665–673. doi:10.1016/j.bbamem.2013.05.001

Stimers, J. R., Song, L., Rusch, N. J., and Rhee, S. W. (2015). Overexpression of the Large-Conductance, Ca2+-Activated K+ (BK) Channel Shortens Action Potential Duration in HL-1 Cardiomyocytes. *PLoS One* 10, e0130588. doi:10.1371/journal.pone.0130588

Strege, P., Beyder, A., Bernard, C., Crespo-Diaz, R., Behfar, A., Terzic, A., et al. (2012). Ranolazine Inhibits Shear Sensitivity of Endogenous Na+ Current and Spontaneous Action Potentials in HL-1 Cells. *Channels* 6, 457–462. doi:10.4161/chan.22017

van Rijsingen, I. A. W., Arbustini, E., Elliott, P. M., Mogensen, J., Hermans-van Ast, J. F., van der Kooi, A. J., et al. (2012). Risk Factors for Malignant Ventricular Arrhythmias in Lamin A/c Mutation Carriers a European Cohort Study. *J. Am. Coll. Cardiol.* 59, 493–500. doi:10.1016/j.jacc.2011.08.078

Yang, Z., and Murray, K. T. (2011). Ionic Mechanisms of Pacemaker Activity in Spontaneously Contracting Atrial HL-1 Cells. *J. Cardiovasc Pharmacol.* 57, 28–36. doi:10.1097/fjc.0b013e3181fda7c4

Conflict of Interest: The authors declare that the research was conducted in the absence of any commercial or financial relationships that could be construed as a potential conflict of interest.

Publisher's Note: All claims expressed in this article are solely those of the authors and do not necessarily represent those of their affiliated organizations, or those of the publisher, the editors, and the reviewers. Any product that may be evaluated in this article, or claim that may be made by its manufacturer, is not guaranteed or endorsed by the publisher.

frontiers | Frontiers in Cell and Developmental Biology

ORIGINAL RESEARCH
published: 07 July 2022
doi: 10.3389/fcell.2022.931326

KCC3a, a Strong Candidate Pathway for K^+ Loss in Alkalemia

Mohammed Zubaerul Ferdaus[1], *Andrew Scott Terker*[2], *Rainelli Koumangoye*[1] *and Eric Delpire*[1]*

[1]Department of Anesthesiology, Vanderbilt University School of Medicine, Nashville, TN, United States, [2]Division of Nephrology, Department of Medicine, Vanderbilt University School of Medicine, Nashville, TN, United States

Loss-of-function mutations in the human potassium chloride cotransporter-3 (KCC3) cause a hereditary motor sensory neuropathy associated with agenesis of the corpus callosum. While recapitulating the neuropathy, KCC3-knockout mice also exhibit high blood pressure. This phenotype is believed to have neurogenic and/or vascular origins. The role of KCC3 in the kidney is poorly understood. KCC3 is encoded by two major isoforms originating from alternative promoters: KCC3a and KCC3b, with KCC3b being the predominant transcript in the kidney. Although the transporter has previously been localized to the proximal tubule, we show here the unique expression of the KCC3a isoform in the connecting tubule. Using a KCC3a-specific polyclonal antibody validated for both immunofluorescence and immunoblotting, we showed an intense KCC3a signal restricted to cortical intercalated cells. No overlap is detected between KCC3a and sodium chloride cotransporter (NCC), a distal convoluted tubule (DCT) marker; or between KCC3a and ENaC or calbindin, which are both principal cell markers. KCC3a signal was observed in cells expressing the apical V-ATPase and pendrin, establishing a unique expression pattern characteristic of intercalated cells of type-B or type-nonA/nonB. We further show that treatment of wild-type mice with hydrochlorothiazide, amiloride, or fed a K^+-deficient diet up-regulates KCC3a level, suggesting that volume depletion increases KCC3a abundance. This hypothesis was confirmed by showing a higher abundance of KCC3a protein after 23-h water restriction or after placing the mice on a low-salt diet. More importantly, abundance of the Cl^-/HCO_3^- exchanger, pendrin, which is known to secrete bicarbonate in alkalotic conditions, was significantly diminished in KCC3-knockout mice. In addition, KCC3a abundance increased significantly alongside pendrin abundance in bicarbonate-treated alkalotic mice, providing a credible mechanism for K^+ loss in metabolic alkalosis.

Keywords: K–Cl cotransport, intercalated cells, bicarbonate, metabolic alkalosis, K^+ loss

OPEN ACCESS

Edited by:
Silvia Dossena, Paracelsus Medical University, Austria

Reviewed by:
Arohan Subramanya, University of Pittsburgh, United States
Seth Leo Alper, Beth Israel Deaconess Medical Center and Harvard Medical School, United States

***Correspondence:**
Eric Delpire
eric.delpire@vanderbilt.edu

Specialty section:
This article was submitted to Cellular Biochemistry, a section of the journal Frontiers in Cell and Developmental Biology

Received: *28 April 2022*
Accepted: *24 May 2022*
Published: *07 July 2022*

Citation:
Ferdaus MZ, Terker AS, Koumangoye R and Delpire E (2022) KCC3a, a Strong Candidate Pathway for K^+ Loss in Alkalemia. Front. Cell Dev. Biol. 10:931326. doi: 10.3389/fcell.2022.931326

INTRODUCTION

Alkalemia is defined as an arterial blood pH exceeding a value of 7.45. It can be caused by the accumulation of alkali (HCO_3^-) or the loss of acids (H^+) (Foy and De Morais, 2017; Emmett, 2020; Brinkman and Sharma, 2022). Different physiological conditions resulting in an increased intracellular shift of H^+, gastrointestinal loss, or renal H^+ waste lead to metabolic alkalosis. The consumption of alkali, the uses of diuretics, repeated vomiting, severe dehydration, and certain endocrine disorders also cause metabolic alkalosis (Berend, 2018; Emmett, 2020). The kidney plays a key role to neutralize metabolic

alkalosis by rapidly excreting excess HCO_3^- in the urine. One key mechanism for abating alkalosis is the secretion of bicarbonate by type-B intercalated cells in the distal nephron (Wall et al., 2020). This is achieved by pendrin, an exchanger located at the apical membrane of intercalated cells which secrete HCO_3^- in exchange for Cl^- (Royaux et al., 2001). Loss of blood K^+ is often associated with metabolic alkalosis. Hypokalemia and metabolic alkalosis are, for instance, observed in conditions like Bartter and Gitelman syndromes (Bhandari and Turney, 1998). In these cases, an increased Na^+ delivery to the aldosterone-sensitive distal nephron results in the activation of the renal outer medullary potassium channel (ROMK), and subsequent loss of K^+. Low blood K^+ has also been linked to a reduction in pendrin level, which could contribute to the maintenance of alkalosis in hypokalemia (Xu et al., 2017). Pendrin's ability to secrete HCO_3^- in the urine depends on Cl^- recycling between the tubular lumen and the intracellular compartment. Different transport systems have been implicated in coupling Cl^- recycling to pendrin function along the distal nephron. The sodium-driven chloride/bicarbonate exchanger (NDCBE) and the cystic fibrosis transmembrane conductance regulator (CFTR) are two hypothesized examples of distal nephron transport systems that have been linked to pendrin activity (Wall, 2022).

KCC3, a K–Cl cotransporter mediating the tightly coupled efflux of K^+ and Cl^-, is expressed in the kidney (Pearson et al., 2001). KCC3 is involved in the pathogenesis of a human disease called HSMN/ACC (hereditary sensory-motor neuropathy associated with agenesis of corpus callosum) (Howard et al., 2002). The disorder was first reported in the medical literature by Dr. Frederick Andermann, a Canadian neurologist whose name is often associated with the syndrome (Andermann et al., 1972). A relatively high incidence of HSMN/ACC cases exists in parts of Quebec, Canada, due to a founder effect dating back to the 17th century (Andermann and Andermann, 1994). In addition, there are additional sporadic cases described in the literature (Boettger et al., 2003; Uyanik et al., 2006). While mouse models of inactive KCC3 recapitulate the neuropathy phenotype, the mice also display high blood pressure (Boettger et al., 2003; Adragna et al., 2004; Garneau et al., 2016). Studies have attributed this high blood pressure to neurogenic (Rust et al., 2006) and vascular effects (Adragna et al., 2004). The possibility that renal KCC3 might also be involved in the blood pressure phenotype has yet to be addressed.

The human protein atlas reveals low RNA tissue specificity for KCC3 with relatively high expression levels in the retina, bone marrow, testis, vagina, esophagus, kidney, and lower levels in all other tissues (Uhlén et al., 2015; Sjöstedt et al., 2020). In 2001, we reported two distinct transcripts of KCC3 starting with alternative first exons: KCC3a starting with exon 1a (encoding 90 amino acids) and KCC3b, initiated from exon 1b (encoding 39 distinct amino acids). The KCC3a transcript is more abundant in the brain, whereas KCC3b is more abundant in the kidney (Pearson et al., 2001). RNA-seq analyses of microdissected rat kidney tubule segments reveal a low expression level of KCC3 along the nephron (Lee et al., 2015). The analysis, however, does not distinguish between the two major isoforms. Information about KCC3 expression and function in the kidney is rather limited. Using an antibody made to an exon 3–specific peptide, we showed KCC3 at the basolateral membrane of the proximal tubule S1 segment (Mercado et al., 2005), a signal later shown to increase in hyperglycemia (Melo et al., 2013). Another study examining renal function in the KCC3-knockout mouse revealed increased diuresis (Garneau et al., 2016). Interestingly, aldosterone was unchanged despite a significant increase in mean arterial pressure and blood K^+, indicating possible renal involvement in the observed phenotype.

Here, we show abundant expression of KCC3a in intercalated cells type-B or type-nonA/nonB. The signal was most abundant in the cortex, indicating expression in connecting tubule (CNT), the aldosterone-sensitive segment that links the distal convoluted tubule to the collecting duct. Furthermore, we discovered that KCC3a and pendrin are expressed in the same cells and are functionally connected in terms of HCO_3^- secretion. We propose that coupling of pendrin function with KCC3a function results in $KHCO_3$ secretion and that KCC3a might be a key pathway for K^+ loss in metabolic alkalosis.

MATERIALS AND METHODS

Animal Experiments

C57BL/6J male and female mice aged 2–3 months were used in this study. All animals had been maintained in a temperature-controlled and pathogen-free barrier facility in ventilated cages with a 12-h light/12-h dark cycle. KCC3-knockout (KCC3-KO) mice were generated by disrupting exon 3 using targeted homologous recombination in the embryonic stem cells as described before (Howard et al., 2002). Homozygous KCC3-KO ($KCC3^{-/-}$) and controls ($KCC3^{+/+}$) were generated by breeding heterozygous KCC3 ($KCC3^{+/-}$) mice. For diet manipulation, mice were maintained on control diet (Envigo Teklad custom diet, TD.88238; 1.05% K^+, 0.29% Na^+, 0.9% Cl^-), potassium-deficient diet (Envigo Teklad custom diet, TD.88239; 0% K^+, 0.29% Na^+, 0.45% Cl^-), high-sodium diet (Envigo Teklad custom diet, TD.190009; 1.05% K^+, 1.57% Na^+, 3.38% Cl^-), or sodium-deficient diet (Envigo Teklad custom diet, TD.190152; 1.05% K^+, 0 Na^+, 0.95% Cl^-) for 4–5 days with free access to water. For the water deprivation study, C57BL/6J mice were randomly assigned to 23-h water deprivation with free access to food, while control mice had free access to both water and food. For tissue collection, mice were sacrificed by isoflurane administration (inhalation), followed by cervical dislocation. All studies using mice were approved by the Vanderbilt Animal Care and Use Committee.

PCR Genotyping

Mice were genotyped at age ~postnatal day 21 by collecting tail snips under isoflurane anesthesia. The 3–5 mm tail samples were digested in 200 μL lysis buffer (25 mM NaOH, 0.2 mM EDTA, pH ~12.0) at 95°C for 1 h and then neutralized with 200 μL Tris buffer (40 mM, pH ~5.0). PCR reactions were set up to identify the mutant gene (forward: 5′ GAACTTTGTGTTGATTCCTTTGG 3′; reverse: 5′ TACAACACACACTCCAACCTCCG 3′) and a control gene (forward: 5′ GAACTTTGTGTTGATTCCTTTGG 3′; reverse: 5′ TCTCCTAACTCCA TCTCCAGGG 3’). PCR reactions were run on 1.5% agarose gel.

TABLE 1 | Antibodies.

Antibody	Host/Type	Dilution (use)	Source	References/Catalogue
KCC3a	Rabbit polyclonal	1:500 (WB), 1:100 (IF)	Eric Delpire	Ding and Delpire, (2014)
Pendrin	Rabbit	1:5000 (WB), 1:1000 (IF)	Susan Wall	(Knauf et al., 2001; Pham et al., 2020)
pNCC	Rabbit polyclonal	1:2000 (WB)	PhosphoSolutions	p1311-53
GFP	Alpaca	1:40 (IP)	ChromoTek	Gta-20
GFP	Mouse monoclonal	1:1000 (WB)	VAPR	Clone 1C9A5
pNCC-T46	Sheep polyclonal	1:50 (IF)	MRC Dundee	S241C
V-ATPase	Mouse monoclonal	1:100 (IF)	Santa Cruz	sc-55544
Calbindin-28	Mouse monoclonal	1:100 (IF)	Abcam	ab82812
ENaC (γ)	Rabbit polyclonal	1:50 (IF)	StressMarq	SPC-405D
β-actin	Rabbit monoclonal	1:3000 (WB)	Abcam	ab8227
anti-rabbit	HRP-conjugated	1:2000	Promega	W401B
anti-mouse	HRP-conjugated	1:2000	Promega	W402B

KCC3a, K^+–Cl^- cotransporter isoform a; pNCC, phosphorylated NCC (Thr53); ENaC, epithelial sodium channel; V-ATPase, vacuolar-type ATPase; HRP-conjugated, horseradish peroxidase-conjugated; WB, Western blot; IF, immunofluorescence; VAPR, Vanderbilt Antibody and Protein Resource.

Kidney Western Blot

Kidneys were snap-frozen in liquid nitrogen immediately after harvesting and utilized directly or stored at −80°C. Single kidneys were homogenized using a Potter homogenizer in 1 mL ice-cold homogenization buffer containing 300 mM sucrose, 50 mM Tris-HCl (pH 7.4), 1 mM EDTA, 1 mM EGTA, 1 mM dithiothreitol, 1 mM phenylmethylsulphonyl fluoride, Halt protease and phosphatase cocktail (Thermo Fisher Scientific, catalog#: 78442), and PhosSTOP phosphatase inhibitor cocktail tablet (Roche, catalog#: 04906837001). Homogenate was centrifuged at 6,000 rpm for 15 min at 4°C, and the supernatant was transferred to a new tube and stored at −80°C. Protein assay was done using Bio-Rad protein assay dye reagent (Bio-Rad, catalog#: 5000006). Then, 40 μg protein was separated on a 4–20% Mini-PROTEAN TGX Precast protein gel (Bio-Rad, catalog#: 4561095). Proteins were transferred to a polyvinylidene fluoride membrane using the Trans-Blot Turbo Transfer System (Bio-Rad, catalog#: 1704150). The membrane was blocked with 5% nonfat milk in TBS-Tween, followed by incubation with primary antibody for either 1 h at room temperature or overnight at 4°C. The membrane was then washed in TBS-Tween, incubated with horseradish peroxidase-conjugated anti-rabbit IgG (Promega, catalog#: W401B) at room temperature, and washed again in TBS-Tween. Proteins on the membrane were visualized by incubating them in luminol/enhancer solution (Bio-Rad Clarity Western ECL Substrate, catalog#: 1705061). The signal was detected with a ChemiDoc MP Imaging System (Bio-Rad, catalog#: 12003154). Protein signal quantification was performed with ImageJ (http://rsbweb.nih.gov/ij/) with all data normalized to actin.

Immunofluorescence

Kidneys were fixed in 10% neutral buffered formalin and slides with paraffin-embedded sections were prepared. The tissues on slides were de-paraffinized and rehydrated in decreasing strengths of ethanol and then washed with PBS at room temperature. After antigen retrieval in citra plus solution (BioGenex, Catalog#: HK080-9K), tissue sections were incubated overnight at 4°C with primary antibodies (**Table 1**), followed by poly-HRP–conjugated secondary antibody (**Table 1**) for 30 min, washed in PBS and incubated with tyramide solution for 2 min at room temperature. After washing in PBS, tissue sections were mounted on microscope slides with ProLong Gold antifade reagent with DAPI (Invitrogen, catalog#: P36931). Images were captured with a Zeiss LSM 880 laser scanning confocal microscope.

TABLE 2 | Blood $[K^+]$.

Vehicle mean ± SEM, mmol/L	HCTZ mean ± SEM, mmol/L	Amiloride mean ± SEM, mmol/L
3.4 ± 0.03	3.4 ± 0.16	6.4 ± 0.42**

*HCTZ, hydrochlorothiazide; **p = 0.001 vehicle versus amiloride.*

KCC3a-Specific Antibody

The KCC3 antibody utilized in this study was raised in rabbits against the first 132 amino acids of mouse KCC3a. This fragment is encoded by exon 1a, exon 2, and the majority (84%) of exon 3. The KCC3a-specific antibody was then purified using a fusion protein that included only the first 44 residues of the transporter, encoded by part of exon 1a. To establish the specificity of the antibody, we created proteins with exon 1a and exons 2–3 fused to EGFP. Exons were PCR amplified from mouse cDNA and inserted into a pCDNA5 vector that contains the entire open reading frame of EGFP. After verification of proper sequence by sequencing, the DNA was purified with a Qiagen Medi prep kit and transfected into HEK293-T cells for expression.

Cell Culture and Transfection

HEK293-T cells were maintained in the DMEM:F12 medium (Gibco, catalog#:11320-033), supplemented with 10% fetal bovine serum (R&D Systems, catalog#: S111110) and 2% penicillin/streptomycin (Gibco, catalog#: 15140-122). Cells in 10-cm dishes at 60–80% confluency were transfected with 15 μg DNA and 45 μL Fugene 6 transfection reagent (Promega, catalog#: 11 814 443 001). Briefly, 15 μg DNA was added to 400 μL Opti-MEM (Gibco, catalog#: 31985-070), followed by 45 μL Fugene 6. After vigorous mixing with a pipet, the mixture was incubated at room temperature for 20 min prior to dropwise

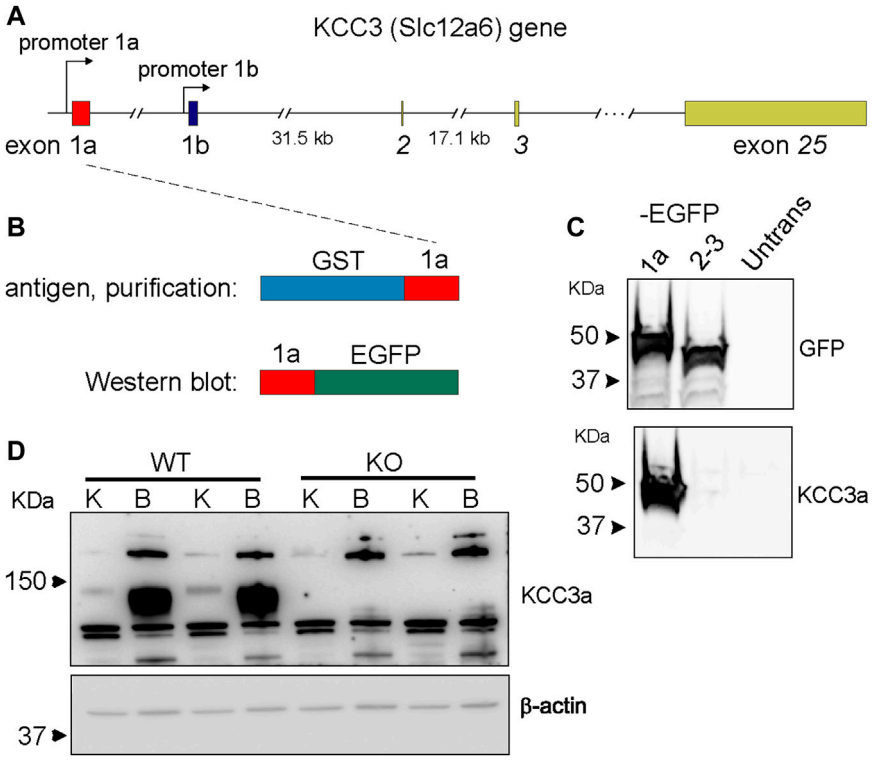

FIGURE 1 | Generation of a potassium chloride cotransporter 3a (KCC3a)–specific antibody. **(A)** Structure of the mouse *Slc12a6* (KCC3) gene showing alternative promoters and exons 1a and 1b, as well as exons 2, 3, and 25. **(B)** Glutathione-S-transferases (GST)–exon 1a fusion protein used to purify the rabbit immune serum and fusion protein exon 1a–enhanced green fluorescent protein (EGFP) purified from transfected HEK293 cells used to assess antibody specificity. **(C)** Immunoblot showing EGFP expression in HEK293 cells transfected with 1a-EGFP or 2-3-EGFP but not untransfected cells. KCC3 signal in cells transfected with 1a-EGFP, but not 2-3-EGFP or untransfected cells. **(D)** Immunoblot shows the band at ~130 kDa with kidney (K) and brain (B) samples from wild-type mice, but not from KCC3-knockout (KO) mice. Notably, there is an abundance of KCC3a in brain tissue, compared to the kidney.

addition to a 10-cm culture dish. Cells were then returned to the 37°C air with a 5% CO_2 incubator for 36–48 h. Cells were then washed once with 10 mL Hank's saline with calcium and magnesium (Gibco, catalog#: 14175-095), scraped with 700 µL RIPA buffer (Sigma, catalog#: R0278) containing protease inhibitors, incubated on ice for 20 min, briefly sonicated, incubated on ice for an additional 10 min, and centrifuged at 21.1 g for 20 min.

Immunoprecipitation

Cell lysate (500 µg) was mixed with 25 µL GFP-Trap Agarose beads (ChromoTek, Planegg-Martinsried, Germany) in a 1.5-mL Eppendorf tube by rotating end-over-end for 2 h at 4°C. The bead–protein complex was washed three times in RIPA buffer and sedimented by centrifugation at 2,500 × g for 5 min at 4°C. Immunoprecipitates were resuspended in 80 µL of 4x Laemmli-sample buffer with dithiothreitol and incubated at 65°C for 15 min to dissociate immunocomplexes from beads. The beads were sedimented by centrifugation at 2,500 x g for 2 min at 4°C. Precipitated proteins in the supernatant were separated by SDS-PAGE and blotted on PVDF membranes. Membranes were probed with the primary antibody followed by HRP-conjugated secondary antibody. Proteins on the membrane were visualized by incubating them in the luminol/enhancer solution (Bio-Rad). The signal was detected with a ChemiDoc MP Imaging System.

Diuretic Test

C57BL/6J mice were randomly assigned to a vehicle (glycol:water = 300:100), hydrochlorothiazide (37.5 mg/kg body weight) or amiloride (9.375 mg/kg body weight) treatment, administered once a day for 7 days by oral gavage. Blood and kidneys were collected after 7 days of treatment.

Urine Analysis

Urine K^+ was analyzed using the Diamond Diagnostics CareLyte Plus electrolyte analyzer. For urinary K^+ measurement, a 100 µL urine sample was employed.

Blood Analysis

Blood was collected *via* cardiac puncture and transferred into heparinized tubes. Immediately after collection, 80 µL of blood was loaded into a Chem8+ cartridge for electrolyte measurement using an i-STAT analyzer (Abbot Point of Care).

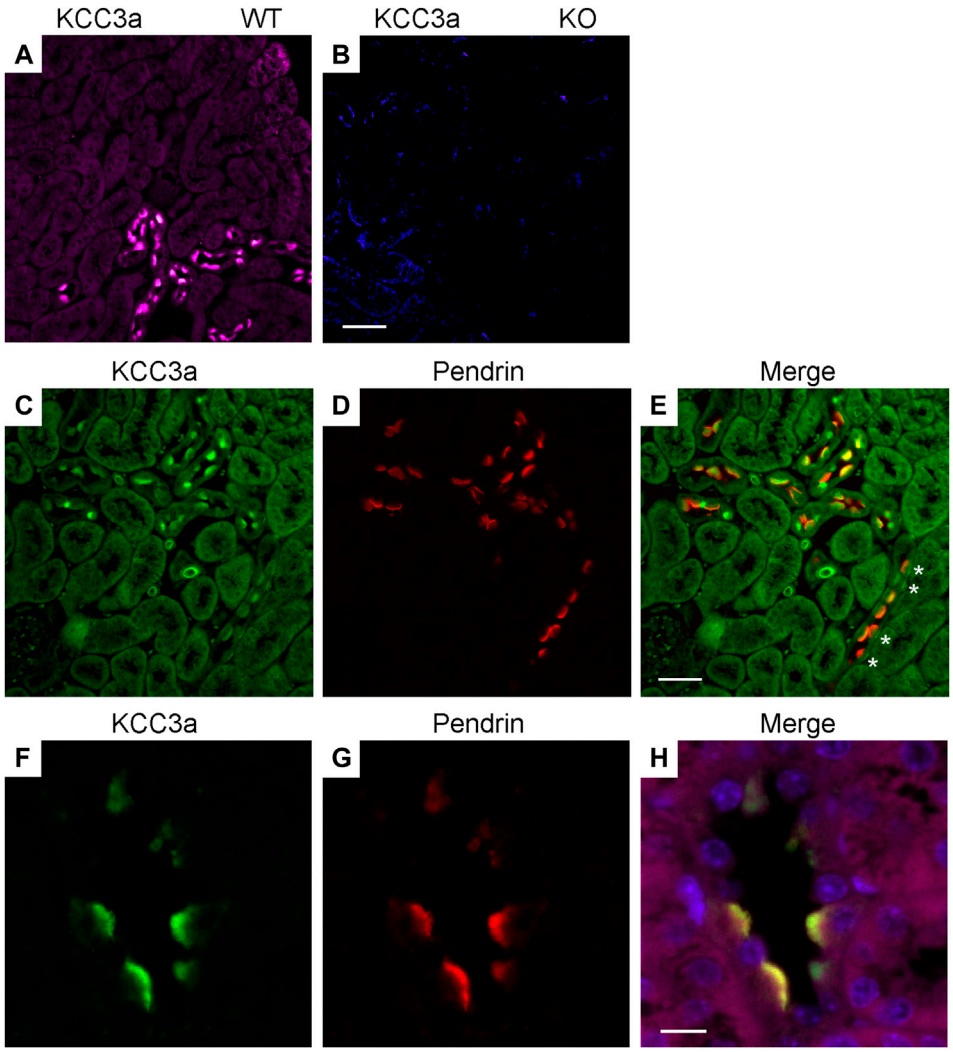

FIGURE 2 | Potassium chloride cotransporter 3a (KCC3a) expression in pendrin-expressing cells. KCC3a signal (purple) in the kidney cortex of wild-type mice **(A)**, but not KCC3-knockout mice **(B)**. KCC3a expression [green, **(C)**] and pendrin expression [red, **(D)**] with an overlap of signal [yellow, **(E)**] in the kidney cortex at 40X. Notably, there is a presence of cells with faint basolateral KCC3a staining (white stars). Similarly, KCC3a expression [green, **(F)**] and pendrin expression [red, **(G)**] with overlap [yellow, **(H)**] at 63X. The absence of KCC3 expression in most tubule segments surrounding the positive cells is also noted. Scale bars = 50 μm for panels **(A–E)** and 10 μm for panels **(F–H)**.

Statistics

The null hypothesis was tested using 2-tailed unpaired t-tests or paired *t*-test by using GraphPad Prism 9 as indicated in the figure legends. All data are plotted as means ± SEM. $p < 0.05$ was considered significant.

RESULTS

KCC3a Antibody Validation

The KCC3a antibody was generated by immunizing rabbits with a peptide fragment encoded by exon 1a–3 (**Figure 1A**) fused to glutathione-S-transferase (Ding and Delpire, 2014). The antibody was then purified from serum using a shorter GST fusion protein, *specific to exon 1a*, and validated by Western blot analysis using exon 1a-EGFP, a fusion protein expressed in HEK293-T cells (**Figures 1B,C**), as well as brain and kidney lysates isolated from wild-type mice and KCC3-knockout littermates (**Figure 1D**). In mouse tissues, the specific signal for KCC3a was observed at ~130 kDa and absent from the KCC3-knockout mice. Notably, there was a relatively low abundance of the protein in kidney samples compared to brain samples.

Localization of KCC3a Along the Nephron

Immunofluorescence (IF) was performed to determine the localization of KCC3a along the nephron and the antibody was validated for IF using KCC3-knockout mice. In kidney sections from wild-type mice, the KCC3a signal was generally low, except in distinct cells in the cortex. This signal was absent in KCC3-

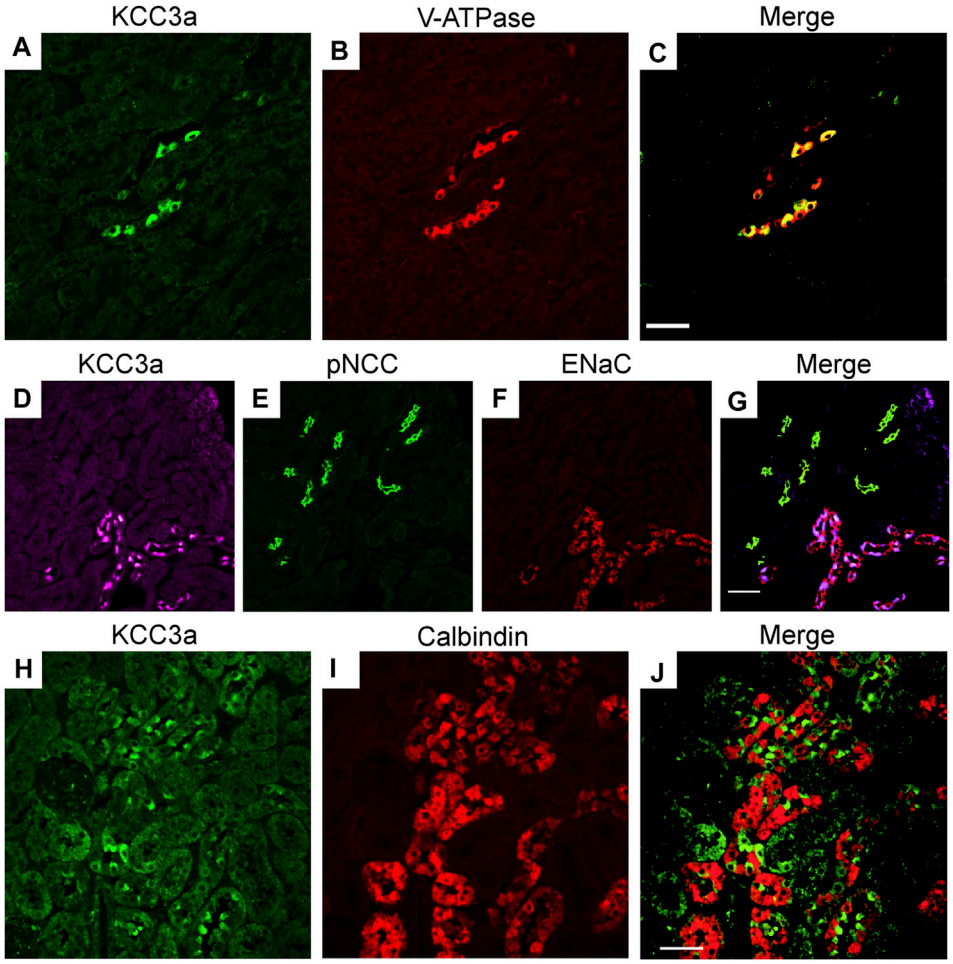

FIGURE 3 | Potassium chloride cotransporter 3a (KCC3a) expression along the connecting tubule. KCC3a expression [green, **(A)**] and vacuolar-type ATPase (V-ATPase) expression [red, **(B)**] with overlap of signal [yellow, **(C)**] in kidney cortex. KCC3a expression [purple, **(D)**], phosphorylated sodium chloride cotransporter (pNCC) [green, **(E)**], epithelial sodium channels (ENaC) [red, **(F)**], and merged signal **(G)** in the kidney cortex. Expression of KCC3a [green, **(H)**], connecting tubule-specific principal cell marker—Calbindin-28 [red, **(I)**] and merged image **(J)** in the renal cortex. The signal for KCC3a is interspersed among the calbindin-positive cells. Scale bar = 50 μm.

knockout mice (**Figures 2A,B**). The discontinuous pattern of expression indicated the presence of KCC3a in the CNT. Using co-staining with pendrin antibody (**Figures 2C–E**), an intercalated cell marker, we localized KCC3a in intercalated cells of type-B or type-nonA/nonB. While a faint signal could be seen in a few cells on the basolateral membrane (white stars, **Figure 2E**), most of the signal was apical. **Figures 2F–H** show higher magnification images with KCC3a and pendrin clearly overlapping at the apical pole. Further co-labeling experiments showed that the KCC3a signal was present in V-ATPase–positive cells (**Figures 3A–C**) and distinct from phosphorylated sodium chloride cotransporter (pNCC) (**Figures 3D,E,G**), ENaC (**Figures 3D,F,G**), and calbindin-28 signals (**Figures 3H–J**), indicating the absence of KCC3a expression in distal convoluted tubule (DCT, identified with pNCC) and CNT principal cells (identified with ENaC and calbindin-28). Notably, we did not confirm the absence of KCC3a expression in type-A intercalated cells.

Changes in KCC3a Abundance in Response to Blood K^+

Blood K^+ is known to exert a strong effect on the distal nephron (Terker et al., 2015; Ferdaus et al., 2016; Terker et al., 2016). As KCC3a transports both K^+ and Cl^-, we investigated whether a change in blood K^+ affects KCC3a expression. Mice were fed with a K^+-deficient diet for 4–5 days to decrease their blood K^+ concentration (López-Cayuqueo et al., 2018). KCC3a abundance was significantly increased after 4–5 days of dietary K^+ deficiency, compared with mice maintained on a matched control diet (**Figure 4A**). Signal quantitation showed 100% ± 29.10 for control K^+ diet *vs* 207.3% ± 28.01 for K^+ free diet (values are mean ± SEM, $p = 0.03$). To confirm the effectiveness of the K^+-deficient diet, we analyzed pNCC abundance (**Figure 4B**), which showed a significant increase in pNCC signal in the K^+-free diet group (100% ± 37.98 for control K^+ diet *vs.* 3035% ± 169.3 for K^+-free diet, $p < 0.0001$).

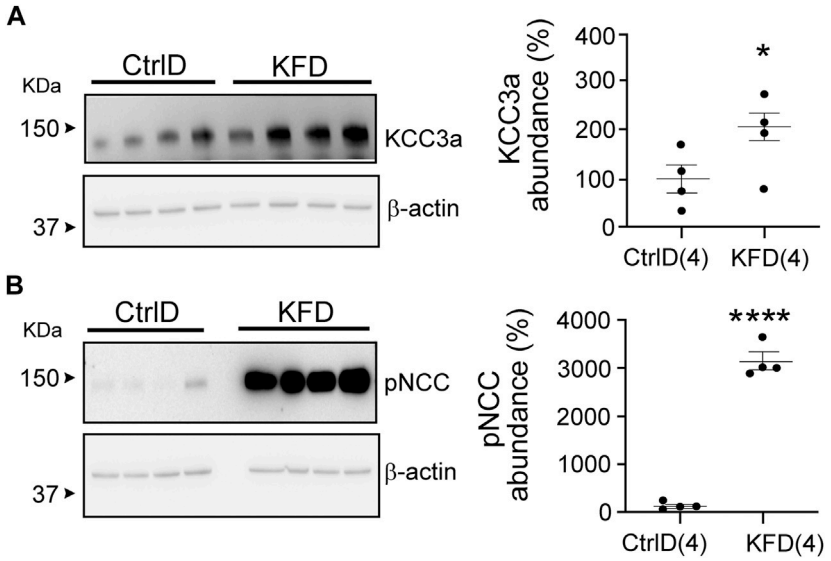

FIGURE 4 | Change in potassium chloride cotransporter 3a (KCC3a) abundance in the kidney in mice on K^+-deficient diet. **(A)** KCC3a abundance increased on K^+-free diet (KFD) than in the control (Ctrl) diet (two-tailed unpaired *t*-test). **(B)** The phosphorylated sodium chloride cotransporter (pNCC) abundance was higher on the KFD than on the control diet (two-tailed unpaired *t*-test), indicating the diet's efficiency. For blot quantification, densitometric values were normalized to β-actin. Values are means ± SEM; values in parentheses indicate n values. *$p < 0.05$; ****$p < 0.0001$.

Hydrochlorothiazide and amiloride treatments are known to cause opposite effects on blood K^+ (**Table 2**), with a decrease in K^+ associated with NCC inhibition (Gamba et al., 1993; Monroy et al., 2000; Terker et al., 2015). Interestingly, KCC3a abundance increased in mice treated for seven days with either hydrochlorothiazide or amiloride (**Figures 5A,C**). Indeed, KCC3a signal was 100% ± 54.73 in mice treated with vehicle *vs.* 467.6% ± 100.5 for mice treated with hydrochlorothiazide (p = 0.02) and 100% ± 60.38 for vehicle *vs.* 367.4% ± 85.97 for mice treated with amiloride (p = 0.04). Again, the effect of the diuretic treatments was assessed using pNCC abundance. Increased pNCC was observed in hydrochlorothiazide-treated mice (**Figure 5B**, 100% ± 34.0 for vehicle *vs.* 710.7% ± 96.65 for hydrochlorothiazide, p = 0.001). Conversely, decreased pNCC abundance was observed in mice treated with amiloride (**Figure 5D**, 100% ± 12.91 for vehicle *vs.* 2.87% ± 2.05 for amiloride, p = 0.0003).

Effect of Volume Depletion on KCC3a

Our data with hydrochlorothiazide and amiloride treatments indicate that KCC3a abundance might not be following blood K^+, but rather water loss and volume contraction. Indeed, both diuretics reduce the reabsorption of Na^+ and water, leading to volume contraction. To address this possibility, we subjected mice to a 23-h water deprivation protocol and to salt restriction. As seen in **Figure 6A**, KCC3a abundance increased significantly in mice after 23 h of water deprivation compared to mice with free access to drinking water [100% ± 42.48 (control) vs. 1466% ± 171.1 (water deprivation), mean ± SEM, p = 0.0002]. Na^+-deficient diet is known to cause volume depletion (Bagshaw et al., 2009; Bie, 2009). Again, as observed in **Figure 6B**, KCC3a abundance was significantly higher after four days on a low-Na^+ diet compared to mice fed for four days on a high-Na^+ diet [100% ± 12.25 (high-salt diet) *vs* 156.9% ± 13.57 (low-salt diet), p = 0.02].

KCC3a Responds to Alkalosis

Our observations suggest that maneuvers causing loss of water or volume depletion increased the abundance of the KCC3a protein. KCC3a localizes on the apical membrane of pendrin-expressing intercalated cells in the kidney cortex. To determine if KCC3a tracks with pendrin, we fed mice for 24 h with 280 mM bicarbonate in drinking water and observed a marked increase in both KCC3a and pendrin abundance (**Figures 7A,B**). For KCC3a, the increase was 2-fold [100% ± 24.03 (sucrose) *vs* 195.73% ± 11.22 (sucrose + bicarbonate), p = 0.006]; pendrin was also higher [100% ± 50.90 (sucrose) *vs* 326.03% ± 75.74 (sucrose + bicarbonate), p = 0.03]. Alkalosis-triggered K^+ loss was confirmed in wild-type mice treated with vehicle (2% sucrose drinking water) or 0.28 M $NaHCO_3$ (with 2% sucrose in drinking water) for 24 h (Genini et al., 2020) with 11.09 ± 4.62 μmol/body weight (BW) (g)/24 h for vehicle *vs* 22.93 ± 4.80 μmol/body weight (BW) (g)/24 h for $NaHCO_3$, p = 0.008 (**Figure 7C**).

Downregulation of Pendrin in KCC3-Knockout Mice

We evaluated pendrin abundance in KCC3-KO mice to confirm the functional linkage of KCC3a to pendrin and found that pendrin abundance was downregulated in KCC3-KO mice, implying that KCC3a is required for pendrin. Pendrin abundance was 100% ± 6.58 in control mice and 59.23% ± 11.92 in KCC3-KO mice, p = 0.006 (**Figure 8**).

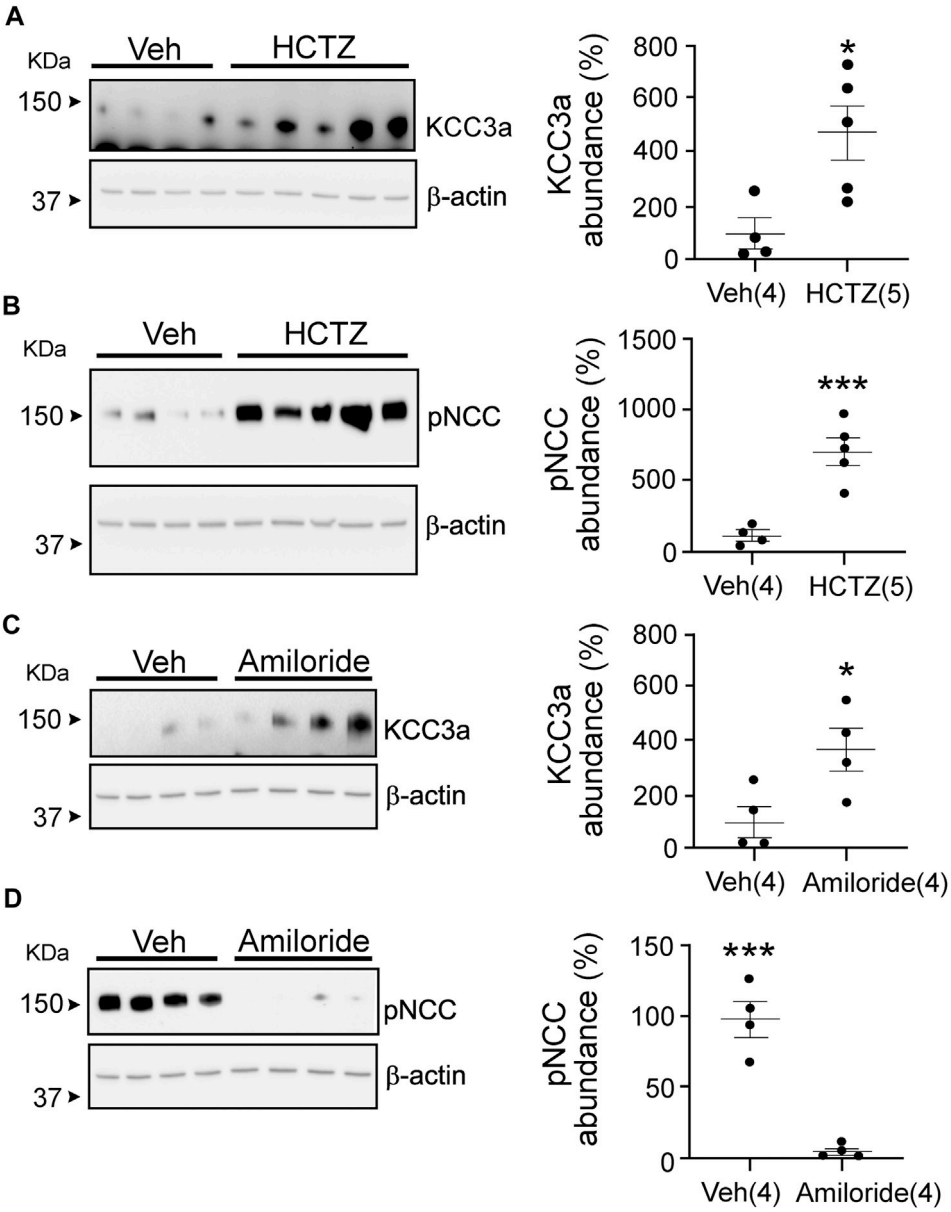

FIGURE 5 | Potassium chloride cotransporter 3a (KCC3a) abundance changes in response to hydrochlorothiazide (HCTZ) treatment. **(A)** KCC3a abundance increases after HCTZ (37.5 mg/kg body weight) treatment compared with the vehicle (Veh, glycol:water = 300:100)-treated group (two-tailed unpaired *t*-test). **(B)** After HCTZ treatment, compared with the Veh-treated mice, the abundance of phosphorylated sodium chloride cotransporter (pNCC) increases (two-tailed unpaired *t*-test), demonstrating the drug's effectiveness. **(C)** The abundance of KCC3a in amiloride-treated mice was higher than in vehicle-treated mice (two-tailed unpaired *t*-test). **(D)** In mice treated with vehicle, the abundance of pNCC was lower than in mice treated with amiloride (two-tailed unpaired *t*-test). For blot quantification, densitometric values were normalized to β-actin. Values are means ± SEM; values in parentheses indicate n values. $^{*}p < 0.05$; $^{***}p < 0.001$.

DISCUSSION

Limited information exists on the expression and role of K–Cl cotransporters in the kidney. Immunofluorescence studies have localized KCC3 on the basolateral membrane of murine proximal tubule epithelial cells (Mercado et al., 2005) and KCC4 on the basolateral membrane of rabbit DCT (Velázquez and Silva, 2003) and mouse intercalated cells type-A (Boettger et al., 2002). A mathematical model of rat distal convoluted tubule addressed the presence of a K–Cl cotransporter along the basolateral membrane of the distal convoluted tubule and viewed it necessary for luminal Cl^- reabsorption and cell volume maintenance (Weinstein, 2005). The nature of the K–Cl cotransporter in mouse DCT is still unknown. In the Mercado study, the proximal tubule KCC3 expression was demonstrated using an exon 3–specific antibody (Mercado et al., 2005) which cannot discriminate between the two main isoforms, KCC3a and KCC3b. Since we demonstrated in 2001 that KCC3b was the major

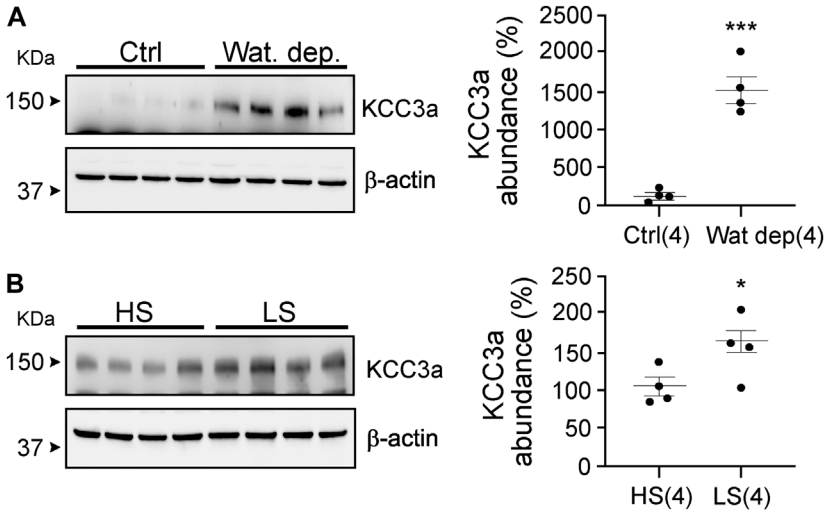

FIGURE 6 | Potassium chloride cotransporter 3a (KCC3a) abundance changes in response to water deprivation and high-salt versus low-salt diets. **(A)** Mice were water restricted for 23 h, (Wat. Dep.) and KCC3a abundance was compared to mice maintained on water during the same period Ctrl, (two-tailed unpaired *t*-test). **(B)** Mice were fed for 4 days on a high-salt or low-salt diet and analyzed for KCC3a expression (two-tailed unpaired *t*-test). For blot quantification, densitometric values were normalized to β-actin. Values are means ± SEM; values in parentheses indicate n values. $^{*}p < 0.05$; $^{***}p < 0.001$.

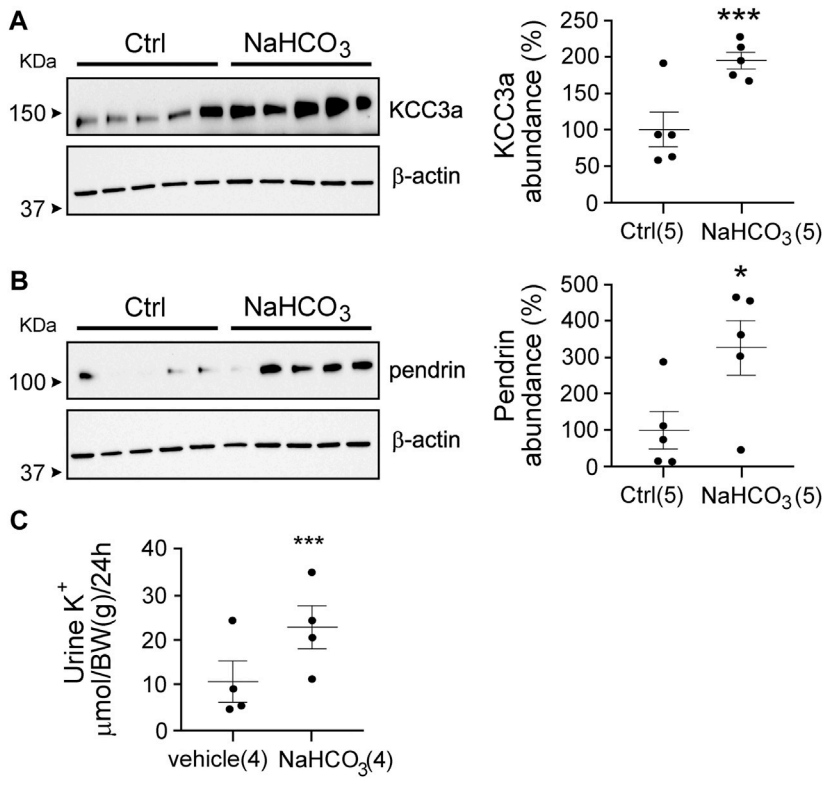

FIGURE 7 | Link between pendrin and KCC3a. **(A,B)** $NaHCO_3$ treatment for 24 h increased KCC3a and pendrin abundances compared to control (Ctrl), (two-tailed unpaired *t*-test). **(C)** Urinary K^+ excretion was higher in $NaHCO_3$-induced alkalotic condition (two-tailed paired *t*-test). For blot quantification, densitometric values were normalized to β-actin. Values are means ± SEM; values in parentheses indicate n values. $^{*}p < 0.05$; $^{***}p < 0.001$.

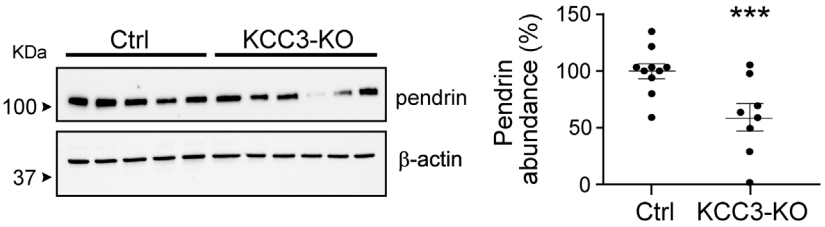

FIGURE 8 | KCC3 deletion in KCC3-knockout (KCC3-KO) mice downregulated pendrin abundance compared to control (Ctrl), (two-tailed unpaired *t*-test). For blot quantification, densitometric values were normalized to β-actin. Values are means ± SEM; values in parentheses indicate n values. ***$p < 0.001$.

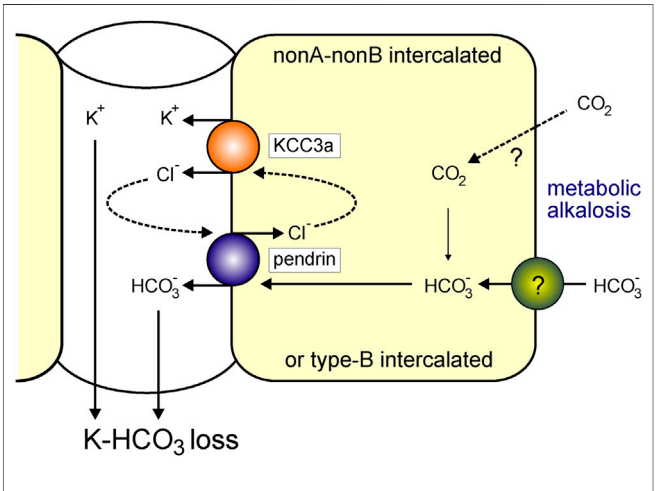

FIGURE 9 | KCC3a participates in K^+ loss in isolated alkalemia caused by metabolic alkalosis. Increased HCO_3^- with a consequent increase in blood pH is known as alkalemia. NonA/nonB and/or type-B intercalated cells express pendrin and KCC3a at the apical membrane. Pendrin and KCC3a are upregulated during base loading or metabolic alkalosis. As KCC3a secretes K^+ and Cl^- and pendrin recycles Cl^- in exchange for HCO_3^-, this leads to a net loss of $KHCO_3$.

isoform in the kidney, whereas KCC3a was the predominant isoform in the brain (Pearson et al., 2001), it was likely that proximal tubule cells were expressing KCC3b. This is further evidenced in this study where we used a KCC3a-specific antibody and observed signal only in the distal tubule.

We provide here the first report of a K–Cl cotransporter expressed on the luminal membrane of renal epithelial cells. Indeed, we observed intense KCC3a-specific staining at the apical membrane of cells expressing the V-ATPase and pendrin, thus localizing KCC3a in type-B or type-nonA/nonB intercalated cells. Furthermore, the KCC3a-expressing cells were surrounded by calbindin-positive cells, restricting KCC3a expression to the CNT and cortical collecting duct (CCD), the aldosterone-sensitive distal nephron, which performs many key renal functions. In mice and rats, connecting tubules and cortical collecting ducts are composed of ~40% intercalated cells and ~60% principal cells. Pendrin-positive nonA/nonB cells are found in abundance in the CNT of the mouse kidney, while pendrin-positive type-B cells predominate in the CCD (Kim et al., 1999; Song et al., 2007).

Net transport through KCC3 is driven by the combined gradients of K^+ and Cl^- across the membrane, and possibly the need for cell volume (swelling) activation. Microperfusion studies in the distal nephron provide luminal concentration values for K^+ and Cl^- of ~2 mM and 30–60 mM, respectively [summarized in Weinstein (2005)]. This means that the product of $[K^+]$ x $[Cl^-]$ on the outside is 20–25 times smaller than the product on the inside, and it would take an excess of 40–50 mM luminal K^+ to start reversing the gradients. Thus, due to the high intracellular and low luminal concentration of K^+ and Cl^-, transport through apical KCC3 should be poised in the direction of secretion, that is, K^+ loss.

Hydrochlorothiazide and amiloride are used as diuretics. Though both drugs trigger diuresis and a reduction in blood volume, they are known to have opposite effects on blood K^+. The fact that both diuretics led to an increase in KCC3a abundance indicates that volume contraction rather than blood K^+ was the factor that influenced the expression of the cotransporter. Similarly, long-term K^+ depletion is known to result in nephrogenic diabetes insipidus and the production of a large amount of urine (Marples et al., 1996; Oksche and Rosenthal, 1998; Boyd-Shiwarski et al., 2020). In mice, a long-term K^+-free diet also causes an increase in water excretion (Boyd-Shiwarski et al., 2020; Al-Qusairi et al., 2021 #4628). Plasma osmolarity, plasma Na^+, and electrolyte-free water clearance are higher on K^+-free diet than on a control K^+ diet. Furthermore, the vasopressin surrogate marker, copeptin, was also increased on K^+-free diet compared to the control diet (Al-Qusairi et al., 2021). As desmopressin treatment could not reverse the water diuresis in mice maintained on K^+-free diet, the data suggested that low blood K^+ is associated with nephrogenic diabetes insipidus. Diuresis and the fall in blood K^+ occurred concomitantly after four days on K^+-free diet. In our study, although the effect of the K^+-free diet at the cellular level was not investigated, in line with the observation of hydrochlorothiazide and amiloride treatments, we observed increased KCC3a abundance in mice on K^+-deficient diet.

Dehydration, imposed by water restriction, implies a reduction in total body water leading to hypertonicity. Dehydration is known to cause a reduction in body weight and mean arterial pressure, along with an increase in hematocrit, plasma osmolality, and vasopressin levels. To investigate the effect of total body water reduction on KCC3a, we performed a 23-h water deprivation study and observed that water-deprived mice also displayed a higher abundance of

KCC3a. Na^+ depletion leads to a reduction of the extracellular fluid compartment that is associated with a reduction in total body fluid (Hurley and Johnson, 2015). Consistently, we observed an increased abundance of KCC3a in mice exposed to a low-Na^+ diet compared with a high-Na^+ diet.

Contraction alkalosis is another possible reason of KCC3a upregulation caused by water loss. The extracellular fluid (ECF) volume reduces in contraction alkalosis with constant level of HCO_3^-. The ECF volume contraction causes alkalosis when stomach HCl is lost through vomiting or thiazide and/or loop diuretic treatment (Emmett, 2020). In our investigation, $NaHCO_3$ treatment increased both pendrin and KCC3a abundance, whereas deleting KCC3 decreased pendrin abundance, suggesting that KCC3a and pendrin are functionally linked. Notably, other transporters have been associated with pendrin function. Alterations in the amount of pendrin have been linked to changes in the cystic fibrosis transmembrane conductance regulator, CFTR (Ko et al., 2002). CFTR likely aids in the recycling of Cl^- during pendrin activity. Although CFTR is also known to secrete HCO_3^- (Kunzelmann et al., 2017; Berg et al., 2021), it is unknown whether CFTR mediates renal HCO_3^- secretion, independent of pendrin. Alkalosis-induced upregulation of renal CFTR may result in direct HCO_3^- secretion by CFTR channels along the distal nephron.

Acute metabolic alkalosis prevents the proximal tubule from reabsorbing $NaHCO_3$ and fluid, resulting in increased distal delivery of Na^+ and HCO_3^-, which promotes K^+ secretion by the distal nephron (Malnic et al., 1972). Greater distal Na^+ and fluid supply, as well as a luminal or systemic increase in HCO_3^- level and pH, stimulate ENaC, ROMK, and BK, resulting in increased distal K^+ secretion (Khuri et al., 1975; Palmer et al., 1998; Satlin et al., 2006; Pech et al., 2010). Increased K^+ secretion *via* ROMK would ultimately lessen the driving force for K^+ secretion by hyperpolarizing the membrane potential (Huang and Kuo, 2007). This would ultimately restrict overall K^+ secretion. Given the foregoing, KCC3a appears to be a likely candidate for the K^+ secretion observed during metabolic alkalosis. KCC3a most likely acts as a recycling mechanism for the Cl^- ions that pendrin needs to secrete HCO_3^- into the filtrate. A similar role has been assigned to the sodium-driven chloride/bicarbonate exchanger (NDCBE), which facilitates the recycling of Cl^- and HCO_3^-. However, NDCBE is required to maintain sodium balance and intravascular volume during salt depletion (Sinning et al., 2017). Moreover, pendrin is also more abundant and active in nonA and nonB intercalated cells (Kim et al., 2002) that do not express NDCBE (Roy et al., 2015). As KCC3a expression overlaps with pendrin expression, the cotransporter could potentially play an important role in Cl^- recycling in nonA/nonB intercalated cells, allowing pendrin to secrete HCO_3^- into the tubular lumen. This function would result in net $KHCO_3$ secretion (**Figure 9**). In metabolic alkalosis, the kidney seems then to prioritize bicarbonate secretion over K^+ loss. In a recent study, Wall et al. reported that pendrin-KO mice excreted more K^+ than wild-type mice on a combined NaCl- and K^+-deficient diet (Pham et al., 2022). While pendrin-KO mice have normal acid/base balance under basal conditions (Kim et al., 2005), they develop severe metabolic alkalosis due to combining NaCl- and K^+-deficient diet. We found that KCC3a was upregulated in response to metabolic alkalosis produced by $NaHCO_3$ administration and on both NaCl- and K^+-deficient diets. Based on our current findings, the observed increased K^+ excretion in pendrin-KO mice on a combined NaCl- and K^+-deficient diet could be attributable to the upregulation of KCC3a in pendrin-KO mice.

DATA AVAILABILITY STATEMENT

The raw data supporting the conclusion of this article will be made available by the authors, without undue reservation.

ETHICS STATEMENT

The animal study was reviewed and approved by Vanderbilt University Medical Center Institutional Animal Care and Use Committee (IACUC).

AUTHOR CONTRIBUTIONS

All authors listed have made a substantial, direct, and intellectual contribution to the work and approved it for publication.

FUNDING

This work was funded by NIH grants: R01DK093501 and R01DK110375, and by International Network of Excellence Leducq Foundation grant: 17CVD05. AST was the recipient of a postdoctoral fellowship from the American Heart Association. The Imaging Core is supported by NIH grants CA68485, DK20593, DK58404, DK59637, and EY08126.

ACKNOWLEDGMENTS

We are highly appreciative of Dr. Susan Wall for sharing her anti-pendrin antibody. We would like to acknowledge the Vanderbilt University Cell Imaging Shared Resource for providing state-of-the-art imaging equipment. We would also like to acknowledge the Vanderbilt Mouse Metabolic Phenotyping Center for providing space and equipment for mouse metabolic cage studies.

REFERENCES

Adragna, N. C., Chen, Y., Delpire, E., Lauf, P. K., and Morris, M. (2004). Hypertension in K-Cl Cotransporter-3 Knockout Mice. *Adv. Exp. Med. Biol.* 559, 379–385. doi:10.1007/0-387-23752-6_35

Al-Qusairi, L., Grimm, P. R., Zapf, A. M., and Welling, P. A. (2021). Rapid Development of Vasopressin Resistance in Dietary K^+ Deficiency. *Am. J. Physiology-Renal Physiology* 320, F748–F760. doi:10.1152/ajprenal.00655.2020

Andermann, E., Andermann, F., Nagy, R., Bergeron, D., Mathieu, J., and Langevin, P. (1994). "Genetic Studies of the Andermann Syndrome," in *Callosal Agenesis: A Natural Split Brain?* (Montreal: Springer), 31–38. doi:10.1007/978-1-4613-0487-6_5

Andermann, F., Andermann, E., Joubert, M., Karpati, G., Carpenter, S., and Melancon, D. (1972). Familial Agenesis of the Corpus Callosum with Anterior Horn Cell Disease: a Syndrome of Mental Retardation, Areflexia and Paraparesis. *Trans. Am. Neurol. Assoc.* 97, 242–244.

Bagshaw, S. M., Townsend, D. R., and Mcdermid, R. C. (2009). Disorders of Sodium and Water Balance in Hospitalized Patients. *Can. J. Anesth/J Can. Anesth.* 56, 151–167. doi:10.1007/s12630-008-9017-2

Berend, K. (2018). Diagnostic Use of Base Excess in Acid-Base Disorders. *N. Engl. J. Med.* 378, 1419–1428. doi:10.1056/nejmra1711860

Berg, P., Svendsen, S. L., Hoang, T. T. L., Praetorius, H. A., Sorensen, M. V., and Leipziger, J. (2021). Impaired Renal HCO_3^- Secretion in CFTR Deficient Mice Causes Metabolic Alkalosis during Chronic Base-Loading. *Acta Physiol. (Oxf)* 231, e13591. doi:10.1111/apha.13591

Bhandari, S., and Turney, J. H. (1998). The Molecular Basis of Hypokalaemic Alkalosis: Bartter's and Gitelman's Syndromes. *Nephron* 80, 373–379. doi:10.1159/000045209

Bie, P. (2009). Blood Volume, Blood Pressure and Total Body Sodium: Internal Signalling and Output Control. *Acta Physiol. (Oxf)* 195, 187–196. doi:10.1111/j.1748-1716.2008.01932.x

Boettger, T., Hübner, C. A., Maier, H., Rust, M. B., Beck, F. X., and Jentsch, T. J. (2002). Deafness and Renal Tubular Acidosis in Mice Lacking the K-Cl Co-transporter Kcc4. *Nature* 416, 874–878. doi:10.1038/416874a

Boettger, T., Rust, M. B., Maier, H., Seidenbecher, T., Schweizer, M., Keating, D. J., et al. (2003). Loss of K-Cl Co-transporter KCC3 Causes Deafness, Neurodegeneration and Reduced Seizure Threshold. *EMBO J.* 22, 5422–5434. doi:10.1093/emboj/cdg519

Boyd-Shiwarski, C. R., Weaver, C. J., Beacham, R. T., Shiwarski, D. J., Connolly, K. A., Nkashama, L. J., et al. (2020). Effects of Extreme Potassium Stress on Blood Pressure and Renal Tubular Sodium Transport. *Am. J. Physiology-Renal Physiology* 318, F1341–f1356. doi:10.1152/ajprenal.00527.2019

Brinkman, J. E., and Sharma, S. (2022). "Physiology, Metabolic Alkalosis," in StatPearls. *(Treasure Island (FL)* (Treasure Island, Fl: StatPearls Publishing).

Ding, J., and Delpire, E. (2014). Deletion of KCC3 in Parvalbumin Neurons Leads to Locomotor Deficit in a Conditional Mouse Model of Peripheral Neuropathy Associated with Agenesis of the Corpus Callosum. *Behav. Brain Res.* 274, 128–136. doi:10.1016/j.bbr.2014.08.005

Emmett, M. (2020). Metabolic Alkalosis: A Brief Pathophysiologic Review. *Clin. J. Am. Soc. Nephrol.* 15, 1848–1856. doi:10.2215/cjn.16041219

Ferdaus, M. Z., Barber, K. W., López-Cayuqueo, K. I., Terker, A. S., Argaiz, E. R., Gassaway, B. M., et al. (2016). SPAK and OSR1 Play Essential Roles in Potassium Homeostasis through Actions on the Distal Convoluted Tubule. *J. Physiol.* 594, 4945–4966. doi:10.1113/jp272311

Foy, D. S., and De Morais, H. A. (2017). A Quick Reference on Metabolic Alkalosis. *Veterinary Clin. N. Am. Small Animal Pract.* 47, 197–200. doi:10.1016/j.cvsm.2016.10.007

Gamba, G., Saltzberg, S. N., Lombardi, M., Miyanoshita, A., Lytton, J., Hediger, M. A., et al. (1993). Primary Structure and Functional Expression of a cDNA Encoding the Thiazide-Sensitive, Electroneutral Sodium-Chloride Cotransporter. *Proc. Natl. Acad. Sci. U.S.A.* 90, 2749–2753. doi:10.1073/pnas.90.7.2749

Garneau, A. P., Marcoux, A.-A., Noël, M., Frenette-Cotton, R., Drolet, M.-C., Couet, J., et al. (2016). Ablation of Potassium-Chloride Cotransporter Type 3 (Kcc3) in Mouse Causes Multiple Cardiovascular Defects and Isosmotic Polyuria. *PLoS One* 11, e0154398. doi:10.1371/journal.pone.0154398

Genini, A., Mohebbi, N., Daryadel, A., Bettoni, C., and Wagner, C. A. (2020). Adaptive Response of the Murine Collecting Duct to Alkali Loading. *Pflugers Arch. Eur. J. Physiol.* 472, 1079–1092. doi:10.1007/s00424-020-02423-z

Howard, H. C., Mount, D. B., Rochefort, D., Byun, N., Dupré, N., Lu, J., et al. (2002). The K-Cl Cotransporter KCC3 Is Mutant in a Severe Peripheral Neuropathy Associated with Agenesis of the Corpus Callosum. *Nat. Genet.* 32, 384–392. doi:10.1038/ng1002

Huang, C.-L., and Kuo, E. (2007). Mechanism of Hypokalemia in Magnesium Deficiency. *J. Am. Soc. Nephrol.* 18, 2649–2652. doi:10.1681/asn.2007070792

Hurley, S. W., and Johnson, A. K. (2015). The Biopsychology of Salt Hunger and Sodium Deficiency. *Pflugers Arch. Eur. J. Physiol.* 467, 445–456. doi:10.1007/s00424-014-1676-y

Khuri, R., Strieder, W., and Giebisch, G. (1975). Effects of Flow Rate and Potassium Intake on Distal Tubular Potassium Transfer. *Am. J. Physiology-Legacy Content* 228, 1249–1261. doi:10.1152/ajplegacy.1975.228.4.1249

Kim, J., Kim, Y.-H., Cha, J.-H., Tisher, C. C., and Madsen, K. M. (1999). Intercalated Cell Subtypes in Connecting Tubule and Cortical Collecting Duct of Rat and Mouse. *J. Am. Soc. Nephrol.* 10, 1–12. doi:10.1681/asn.v1011

Kim, Y.-H., Kwon, T.-H., Frische, S., Kim, J., Tisher, C. C., Madsen, K. M., et al. (2002). Immunocytochemical Localization of Pendrin in Intercalated Cell Subtypes in Rat and Mouse Kidney. *Am. J. Physiology-Renal Physiology* 283, F744–F754. doi:10.1152/ajprenal.00037.2002

Kim, Y.-H., Verlander, J. W., Matthews, S. W., Kurtz, I., Shin, W., Weiner, I. D., et al. (2005). Intercalated Cell H^+/OH^- transporter Expression Is Reduced inSlc26a4null Mice. *Am. J. Physiology-Renal Physiology* 289, F1262–F1272. doi:10.1152/ajprenal.00206.2005

Knauf, F., Yang, C.-L., Thomson, R. B., Mentone, S. A., Giebisch, G., and Aronson, P. S. (2001). Identification of a Chloride-Formate Exchanger Expressed on the Brush Border Membrane of Renal Proximal Tubule Cells. *Proc. Natl. Acad. Sci. U.S.A.* 98, 9425–9430. doi:10.1073/pnas.141241098

Ko, S. B. H., Shcheynikov, N., Choi, J. Y., Luo, X., Ishibashi, K., Thomas, P. J., et al. (2002). A Molecular Mechanism for aberrantCFTR-dependent HCO_3^- Transport in Cystic Fibrosis. *Embo. J.* 21, 5662–5672. doi:10.1093/emboj/cdf580

Kunzelmann, K., Schreiber, R., and Hadorn, H. B. (2017). Bicarbonate in Cystic Fibrosis. *J. Cyst. Fibros.* 16, 653–662. doi:10.1016/j.jcf.2017.06.005

Lee, J. W., Chou, C.-L., and Knepper, M. A. (2015). Deep Sequencing in Microdissected Renal Tubules Identifies Nephron Segment-specific Transcriptomes. *J. Am. Soc. Nephrol.* 26, 2669–2677. doi:10.1681/asn.2014111067

López-Cayuqueo, K. I., Chavez-Canales, M., Pillot, A., Houillier, P., Jayat, M., Baraka-Vidot, J., et al. (2018). A Mouse Model of Pseudohypoaldosteronism Type II Reveals a Novel Mechanism of Renal Tubular Acidosis. *Kidney Int.* 94, 514–523. doi:10.1016/j.kint.2018.05.001

Malnic, G., De Mello Aires, M., and Giebisch, G. (1972). Micropuncture Study of Renal Tubular Hydrogen Ion Transport in the Rat. *Am. J. Physiology-Legacy Content* 222, 147–158. doi:10.1152/ajplegacy.1972.222.1.147

Marples, D., Frøkiaer, J., Dørup, J., Knepper, M. A., and Nielsen, S. (1996). Hypokalemia-induced Downregulation of Aquaporin-2 Water Channel Expression in Rat Kidney Medulla and Cortex. *J. Clin. Invest.* 97, 1960–1968. doi:10.1172/jci118628

Melo, Z., Cruz-Rangel, S., Bautista, R., Vázquez, N., Castañeda-Bueno, M., Mount, D. B., et al. (2013). Molecular Evidence for a Role for K^+-Cl^- Cotransporters in the Kidney. *Am. J. Physiology-Renal Physiology* 305, F1402–F1411. doi:10.1152/ajprenal.00390.2013

Mercado, A., Vázquez, N., Song, L., Cortés, R., Enck, A. H., Welch, R., et al. (2005). NH2-terminal Heterogeneity in the KCC3 K^+-Cl^- Cotransporter. *Am. J. Physiology-Renal Physiology* 289, F1246–F1261. doi:10.1152/ajprenal.00464.2004

Monroy, A., Plata, C., Hebert, S. C., and Gamba, G. (2000). Characterization of the Thiazide-Sensitive Na^+-Cl^- Cotransporter: a New Model for Ions and Diuretics Interaction. *Am. J. Physiology-Renal Physiology* 279, F161–F169. doi:10.1152/ajprenal.2000.279.1.f161

Oksche, A., and Rosenthal, W. (1998). The Molecular Basis of Nephrogenic Diabetes Insipidus. *J. Mol. Med.* 76, 326–337. doi:10.1007/s001090050224

Palmer, L. G., Sackin, H., and Frindt, G. (1998). Regulation of Na^+ Channels by Luminal Na^+ in Rat Cortical Collecting Tubule. *J. Physiol.* 509 (Pt 1), 151–162. doi:10.1111/j.1469-7793.1998.151bo.x

Pearson, M. M., Lu, J., Mount, D. B., and Delpire, E. (2001). Localization of the K(+)-Cl(-) Cotransporter, KCC3, in the Central and Peripheral Nervous Systems: Expression in the Choroid Plexus, Large Neurons and White Matter Tracts. *Neuroscience* 103, 481–491. doi:10.1016/s0306-4522(00)00567-4

Pech, V., Pham, T. D., Hong, S., Weinstein, A. M., Spencer, K. B., Duke, B. J., et al. (2010). Pendrin Modulates ENaC Function by Changing Luminal HCO_3^-. *J. Am. Soc. Nephrol.* 21, 1928–1941. doi:10.1681/asn.2009121257

Pham, T. D., Elengickal, A. J., Verlander, J. W., Al-Qusairi, L., Chen, C., Abood, D. C., et al. (2022). Pendrin-null Mice Develop Severe Hypokalemia Following Dietary Na^+ and K^+ Restriction: Role of ENaC. *Am. J. Physiology-Renal Physiology* 322, F486–F497. doi:10.1152/ajprenal.00378.2021

Pham, T. D., Verlander, J. W., Wang, Y., Romero, C. A., Yue, Q., Chen, C., et al. (2020). Aldosterone Regulates Pendrin and Epithelial Sodium Channel Activity through Intercalated Cell Mineralocorticoid Receptor-dependent and -Independent Mechanisms over a Wide Range in Serum Potassium. *J. Am. Soc. Nephrol.* 31, 483–499. doi:10.1681/asn.2019050551

Roy, A., Al-Bataineh, M. M., and Pastor-Soler, N. M. (2015). Collecting Duct Intercalated Cell Function and Regulation. *Clin. J. Am. Soc. Nephrol.* 10, 305–324. doi:10.2215/cjn.08880914

Royaux, I. E., Wall, S. M., Karniski, L. P., Everett, L. A., Suzuki, K., Knepper, M. A., et al. (2001). Pendrin, Encoded by the Pendred Syndrome Gene, Resides in the Apical Region of Renal Intercalated Cells and Mediates Bicarbonate Secretion. *Proc. Natl. Acad. Sci. U.S.A.* 98, 4221–4226. doi:10.1073/pnas.071516798

Rust, M. B., Faulhaber, J., Budack, M. K., Pfeffer, C., Maritzen, T., Didie´, M., et al. (2006). Neurogenic Mechanisms Contribute to Hypertension in Mice with Disruption of the K-Cl Cotransporter KCC3. *Circulation Res.* 98, 549–556. doi:10.1161/01.res.0000204449.83861.22

Satlin, L. M., Carattino, M. D., Liu, W., and Kleyman, T. R. (2006). Regulation of Cation Transport in the Distal Nephron by Mechanical Forces. *Am. J. Physiology-Renal Physiology* 291, F923–F931. doi:10.1152/ajprenal.00192.2006

Sinning, A., Radionov, N., Trepiccione, F., López-Cayuqueo, K. I., Jayat, M., Baron, S., et al. (2017). Double Knockout of the Na^+-Driven Cl^-/HCO_3^- Exchanger and Na^+/Cl^- Cotransporter Induces Hypokalemia and Volume Depletion. *J. Am. Soc. Nephrol.* 28, 130–139. doi:10.1681/asn.2015070734

Sjöstedt, E., Zhong, W., Fagerberg, L., Karlsson, M., Mitsios, N., Adori, C., et al. (2020). An Atlas of the Protein-Coding Genes in the Human, Pig, and Mouse Brain. *Science* 367, eaay5947. doi:10.1126/science.aay5947

Song, H.-K., Kim, W.-Y., Lee, H.-W., Park, E.-Y., Han, K.-H., Nielsen, S., et al. (2007). Origin and Fate of Pendrin-Positive Intercalated Cells in Developing Mouse Kidney. *J. Am. Soc. Nephrol.* 18, 2672–2682. doi:10.1681/asn.2006101076

Terker, A. S., Zhang, C., Erspamer, K. J., Gamba, G., Yang, C.-L., and Ellison, D. H. (2016). Unique Chloride-Sensing Properties of WNK4 Permit the Distal Nephron to Modulate Potassium Homeostasis. *Kidney Int.* 89, 127–134. doi:10.1038/ki.2015.289

Terker, A. S., Zhang, C., Mccormick, J. A., Lazelle, R. A., Zhang, C., Meermeier, N. P., et al. (2015). Potassium Modulates Electrolyte Balance and Blood Pressure through Effects on Distal Cell Voltage and Chloride. *Cell. Metab.* 21, 39–50. doi:10.1016/j.cmet.2014.12.006

Uhlén, M., Fagerberg, L., Hallström, B. M., Lindskog, C., Oksvold, P., Mardinoglu, A., et al. (2015). Proteomics. Tissue-Based Map of the Human Proteome. *Science* 347, 1260419. doi:10.1126/science.1260419

Uyanik, G., Elcioglu, N., Penzien, J., Gross, C., Yilmaz, Y., Olmez, A., et al. (2006). Novel Truncating and Missense Mutations of the KCC3 Gene Associated with Andermann Syndrome. *Neurology* 66, 1044–1048. doi:10.1212/01.wnl.0000204181.31175.8b

Velázquez, H., and Silva, T. (2003). Cloning and Localization of KCC4 in Rabbit Kidney: Expression in Distal Convoluted Tubule. *Am. J. Physiol. Ren. Physiol.* 285, F49–F58. doi:10.1152/ajprenal.00389.2002

Wall, S. M. (2022). Regulation of Blood Pressure and Salt Balance by Pendrin-Positive Intercalated Cells: Donald Seldin Lecture 2020. *Hypertension* 79, 706–716. doi:10.1161/hypertensionaha.121.16492

Wall, S. M., Verlander, J. W., and Romero, C. A. (2020). The Renal Physiology of Pendrin-Positive Intercalated Cells. *Physiol. Rev.* 100, 1119–1147. doi:10.1152/physrev.00011.2019

Weinstein, A. M. (2005). A Mathematical Model of Rat Distal Convoluted Tubule. I. Cotransporter Function in Early DCT. *Am. J. Physiology-Renal Physiology* 289, F699–F720. doi:10.1152/ajprenal.00043.2005

Xu, N., Hirohama, D., Ishizawa, K., Chang, W. X., Shimosawa, T., Fujita, T., et al. (2017). Hypokalemia and Pendrin Induction by Aldosterone. *Hypertension* 69, 855–862. doi:10.1161/hypertensionaha.116.08519

Conflict of Interest: The authors declare that the research was conducted in the absence of any commercial or financial relationships that could be construed as a potential conflict of interest.

Publisher's Note: All claims expressed in this article are solely those of the authors and do not necessarily represent those of their affiliated organizations, or those of the publisher, the editors, and the reviewers. Any product that may be evaluated in this article, or claim that may be made by its manufacturer, is not guaranteed or endorsed by the publisher.

frontiers | Frontiers in Cell and Developmental Biology

ORIGINAL RESEARCH
published: 08 July 2022
doi: 10.3389/fcell.2022.919438

dDAVP Downregulates the AQP3-Mediated Glycerol Transport *via* V1aR in Human Colon HCT8 Cells

Mariangela Centrone[1†], *Mariagrazia D'Agostino*[1†], *Marianna Ranieri*[1], *Maria Grazia Mola*[1], *Pinuccia Faviana*[2], *Piero Vincenzo Lippolis*[3], *Domenico Alessandro Silvestris*[4], *Maria Venneri*[1], *Annarita Di Mise*[1], *Giovanna Valenti*[1] *and Grazia Tamma*[1*]

[1]*Department of Biosciences, Biotechnologies and Biopharmaceutics, University of Bari Aldo Moro, Bari, Italy,* [2]*Department of Surgical, Medical, Molecular Pathology, and Critical Area, University of Pisa, Pisa, Italy,* [3]*Department of Surgery, University of Pisa, Pisa, Italy,* [4]*Department of Onco-haematology, IRCCS Ospedale Pediatrico Bambino Gesù, Rome, Italy*

Vasopressin (AVP) plays a key function in controlling body water and salt balance through the activation of the vasopressin receptors V1aR and V2R. Abnormal secretion of AVP can cause the syndrome of inappropriate antidiuresis that leads to hyponatremia, which is an electrolyte disorder often observed in the elderly hospitalized and oncologic patients. Beyond kidneys, the colonic epithelium modulates water and salt homeostasis. The water channel AQP3, expressed in villus epithelial cells is implicated in water absorption across human colonic surface cells. Here, the action of dDAVP, a stable vasopressin analog, was evaluated on the AQP3 expression and function using human colon HCT8 cells as an experimental model. Confocal and Western Blotting analysis revealed that HCT8 cells express both V1aR and V2R. Long-term (72 h) treatment with dDAVP reduced glycerol uptake and cell viability. These effects were prevented by SR49059, a synthetic antagonist of V1aR, but not by tolvaptan, a specific V2R antagonist. Of note, the SR49059 action was impaired by DFP00173, a selective inhibitor of AQP3. Interestingly, compared to the normal colonic mucosa, in the colon of patients with adenocarcinoma, the expression of V1aR was significantly decreased. These findings were confirmed by gene expression analysis with RNA-Seq data. Overall, data suggest that dDAVP, through the V1aR dependent pathway, reduces AQP3 mediated glycerol uptake, a process that is reversed in adenocarcinoma, suggesting that the AVP-dependent AQP3 pathway may represent a novel target in colon diseases associated with abnormal cell growth.

Keywords: vasopressin, V1aR, V2R, AQP3, glycerol, tolvaptan, SR49059, DFP00173

OPEN ACCESS

Edited by:
Silvia Dossena,
Paracelsus Medical University, Austria

Reviewed by:
Tae-Hwan Kwon,
Kyungpook National University, South Korea
Nazih Nakhoul,
Tulane University, United States

****Correspondence:***
Grazia Tamma
grazia.tamma@uniba.it

[†]These authors have contributed equally to this work and share first authorship

Specialty section:
This article was submitted to Cellular Biochemistry, a section of the journal Frontiers in Cell and Developmental Biology

Received: *13 April 2022*
Accepted: *15 June 2022*
Published: *08 July 2022*

Citation:
Centrone M, D'Agostino M, Ranieri M, Mola MG, Faviana P, Lippolis PV, Silvestris DA, Venneri M, Di Mise A, Valenti G and Tamma G (2022) dDAVP Downregulates the AQP3-Mediated Glycerol Transport via V1aR in Human Colon HCT8 Cells. Front. Cell Dev. Biol. 10:919438. doi: 10.3389/fcell.2022.919438

INTRODUCTION

The hormone vasopressin (AVP) controls numerous functions under physiological and pathophysiological conditions. The actions evoked by AVP are mediated by three G protein-coupled receptors (V1aR, V1bR, and V2R). Stimulation of V1Rs causes the activation of PLC/PKC signaling and the mobilization of intracellular calcium (Thibonnier, 1992; Briley et al., 1994). The major role of AVP is to modulate the sodium and water body's homeostasis. In the kidney, AVP binds V2R and stimulates the cAMP/PKA signal transduction pathway leading to AQP2 phosphorylation and trafficking to the plasma membrane where water reabsorption takes place (Boone and Deen, 2008; Ranieri et al., 2019). In long term, stimulation with AVP or thirsting

increases the expression of AQP2 and AQP3 which have a cAMP response element CRE in their promoters (Yasui et al., 1997; Okahira et al., 2008). Beyond its endocrine roles (i.e., vasoconstriction and antidiuretic action), AVP also controls apoptosis, mitogenesis, cell growth, and death (Carter et al., 1993; Forti and Armelin, 2011; Miller et al., 2013). Abnormal release of AVP from the pituitary gland or non-pituitary sources causes the syndrome of inappropriate antidiuretic hormone secretion (SIADH), a condition characterized by water body deregulation and hyponatremia. SIADH has been associated with some forms of cancers including head and neck cancers, olfactory neuroblastomas, pancreatic neuroendocrine tumors, lymphoma, breast and colon cancers (Cabrijan et al., 1985; Gupta et al., 1986; Jayadeep et al., 2020; Navarro-Almenzar and Perianes, 2020; Li et al., 2021; Yasir and Mechanic, 2022). Importantly, several types of cancers express vasopressin receptors (VRs) that cause contrasting responses depending on receptor subtypes, their relative expression, and signaling (North et al., 1999; North, 2000; Heasley, 2001). Besides normal VRs, neoplastic tissue can express abnormal receptors concerning the sequence and signaling. Different subtypes of small cell lung cancer (SCLC) cells (NCI-H345; NCI-H82) express normal V1aR displaying, however, differential sensitivity to the action of vasopressin. In NCI-H82, stimulation with vasopressin increases the total level of inositol phosphate without a relevant rise of intracellular calcium compared to "classical" SCLC (North et al., 1997). On another hand, MCF7 cells express normal V2R and a C-terminally truncated V2R receptor (Rosenthal et al., 1994) which is mainly located intracellularly (Robben et al., 2005).

V1R stimulation is often associated with increased cell growth (Thibonnier et al., 2000) whereas V2R activation is correlated with cytostatic effects (Pifano et al., 2017).

Aquaporins are known targets of vasopressin action in health and disease (Yasui et al., 1997; Okahira et al., 2008; Valenti and Tamma, 2021).

Interestingly aquaporins have been found expressed in several tumor cells possibly playing a role in cell proliferation, invasion, and migration (Levin and Verkman, 2006; Jung et al., 2011; Di Giusto et al., 2012) but their regulatory actions remain still unclear. Aquaporins may promote water flux through the plasma membrane protrusion of migrating cells (Papadopoulos et al., 2008). In this respect, it has been nicely hypothesized that the compartmentalized cytoplasm, closed to the leading edge of migrating cells, may be subjected to changes in osmolality, secondary to actin depolymerization and ion flux. On the other hand, aquaporins may modulate cell proliferation being involved in mechanisms controlling cell volume, transport of glycerol, and other small molecules (Jung et al., 2021). Glycerol is a pivotal metabolite involved in the synthesis of triacylglycerols and glucose. Glycerol constitutes a substrate for ATP generation that is crucial for cell growth and proliferation (Méndez-Giménez et al., 2014). AQP3 is an aquaglyceroporin permeable to water, glycerol, urea, and hydrogen peroxide (H_2O_2) (Marlar et al., 2017). Importantly, it has been demonstrated that water and glycerol transport in AQP3 is gated by H^+ (Zeuthen and Klaerke, 1999). Conversely, the permeability of other AQPs, such as AQP1, AQP4, and AQP5, occurs in pH independent manner (Zeuthen and Klaerke, 1999). AQP3 is expressed in several human epithelia including kidney, skin, airways, breast, liver, and gastrointestinal tract. Moreover, AQP3 is expressed in gastric mucosa, in the ileum and colon where it is involved in water and glycerol transport (Kreda et al., 2001; Yamamoto et al., 2001; Mobasheri et al., 2005; Aburada et al., 2011; Gregoire et al., 2015; Yde et al., 2016; Marlar et al., 2017). Abnormal expression of AQP3 may be associated with different diseases including cancer. Physiologically, AQP1 and AQP3 are expressed in the colon, however, their expression profile is altered in colorectal cancer (CRC). Compared to adjacent normal colon epithelia, the abundance of AQP1 and AQP3 increased significantly in CRC tissue (Mobasheri and Marples, 2004; Pei et al., 2011). Numerous studies have demonstrated abnormal expression of AQP3 in various types of diseases. However, the molecular mechanisms controlling the AQP3 expression and function are poorly shown. In this study, we provide novel evidence that AVP controls the expression and the function of AQP3 in human colon carcinoma HCT8 cells. The obtained results suggest that the AVP-dependent AQP3 pathway might represent a possible target in colon diseases associated with abnormal cell growth.

MATERIALS AND METHODS

Chemicals and Reagents

Cell culture media and FBS (fetal bovine serum) were obtained from GIBCO (Thermo Fisher Scientific, Waltham, MA, United States). Desmopressin (dDAVP) was purchased from Merck (Merck KGaA, Darmstadt, Germany). Calcein-AM and Fluo-4 were bought from Molecular Probes (Thermo Fisher Scientific, Waltham, MA, United States). Tolvaptan was kindly gifted from Otsuka (Otsuka Pharmaceutical Co., Ltd, Tokyo Japan), SR49059 was from Merck (Merck KGaA, Darmstadt, Germany) and DFP00173 was purchased from Axon MedChem (S.I.A.L. s.r.l., Rome, Italy). TransFectin™ Lipid Reagent and Clarity Western ECL Substrates were bought from Bio-Rad (Bio-Rad Laboratories, Inc., Hercules, CA, United States).

Antibodies

A goat polyclonal antibody against Aquaporin-3 (C-18) was purchased from Santa Cruz Biotechnology (S.I.A.L. s.r.l., Rome, Italy). Recombinant rabbit monoclonal antibody against AVPR1A (7H23L17) was obtained from Invitrogen (Thermo Fisher Scientific, Waltham, MA, United States). Rabbit polyclonal antibody against AVPR2 (MBS8242744) was from MyBioSource (S.I.A.L. s.r.l., Rome, Italy). Secondary goat anti-rabbit and donkey anti-goat antibodies conjugated to horseradish peroxidase (HRP) were obtained respectively from Merck (Merck KGaA, Darmstadt, Germany) and Santa Cruz Biotechnology (S.I.A.L. s.r.l., Rome, Italy). Secondary donkey anti-goat and donkey anti-rabbit antibodies coupled to Alexa-488 were purchased from Thermo Fisher Scientific (Thermo Fisher Scientific, Waltham, MA, United States).

Cell Culture and Treatment

HCT8, human ileocecal adenocarcinoma cell line were cultured as previously described (Centrone et al., 2020a). Briefly, cells were

grown in Advanced RPMI-1640 supplemented with 10% FBS, 100 i.u. ml^{-1} penicillin, 100 μg·ml^{-1} streptomycin at 37°C in 5% CO_2. Cells were left under basal condition (untreated), treated with 100 nM desmopressin (dDAVP) for 72 h and/or treated with 100 nM tolvaptan or 100 nM SR49059 for 72 h or 2.5 μM DFP00173 for 48 h. As an internal control, cells were treated with 100 nM DMSO for 72 h.

Fluorescence Resonance Energy Transfer Measurements

To evaluate intracellular cAMP levels, fluorescence resonance energy transfer (FRET) experiments were performed. Briefly, HCT8 cells were seeded onto 12 mm diameter glass coverslips at 37°C, 5% CO_2, and transiently transfected with a plasmid encoding the H96 sensor (Klarenbeek et al., 2011) (a gift from Dr. K. Jalink) containing the cAMP-binding sequence of Epac1 sandwiched between ECFP (donor) and EYFP (acceptor). In detail, cells were transfected with 0.5 μg of DNA/cm^2 using TransFectin™ Lipid Reagent (1.5 μL/cm^2) according to the protocol provided by the manufacturer (Bio-Rad Laboratories, Inc., Hercules, CA, United States) and left under basal condition or treated as mentioned before. Experiments were performed 48 h after transfection. Visualization of ECFP- and/or EYFP-expressing cells and detection of FRET was performed on an inverted microscope (Nikon Eclipse TE2000-S) controlled by Metamorph® Microscopy Automation and Image Analysis Software (Molecular Devices, LLC, San Jose, CA, United States). Each image was corrected and analyzed as previously shown (Di Mise et al., 2019).

Intracellular Calcium Measurements

HCT8 cells were grown on 40-mm glass coverslips and then loaded with 4 μM Fluo-4 for 15 min at 37°C in Advanced RPMI 1640. Ringer's solution was used to perfuse cells during the experiment and containing 137 mM NaCl, 5.4 mM KCl, 0.5 mM $MgCl_2$, 1.3 mM $CaCl_2$, 4.2 mM $NaHCO_3$, 0.4 mM KH_2PO_4, 3 mM Na_2HPO_4, 10 mM Hepes sulfonic acid, 10 mM glucose, pH 7.4. In fluorescence measurements, the coverslips with dye-loaded cells were mounted in a perfusion chamber (FCS2 Closed Chamber System, BIOPTECHS, Butler, United States). Measurements were performed using an inverted TE2000-S microscope (Nikon Eclipse microscope, Tokyo, Japan). The Fluo-4 loaded sample was excited at 490 nm. Fluorescence signals were captured by a cooled ECCD camera (CoolSNAP HQ, Photometrics, Tucson, AZ, United States) and measured with Metafluor software (Molecular Devices, MDS Analytical Technologies, Toronto, ON, Canada). Responses were analyzed as changes in fluorescence intensity normalized to the initial value of Fluo-4 intensity (F_0) and compared with changes induced by ATP as a control stimulus, using GraphPad Prism (GraphPad Software, San Diego, CA, United States). Data are reported as mean values ± S.E.M. with *n* equal to the number of cells.

Human Cancer Specimens

Patients (3 females and 1 male) with colon mucinous adenocarcinoma provided written informed consent for sample collection and analysis. Fresh frozen samples of normal or neoplastic mucosa isolated from the same patient were used for Real-Time PCR and immunoblotting analysis.

Real-Time PCR Analysis of AQP3, V1aR, and V2R mRNA in HCT8 Cells and Human Colon Adenocarcinoma Biopsies

Real-Time PCR experiments were performed as previously described (Ranieri et al., 2021). Briefly, HCT8 cells were grown on 60-mm dishes and lysates in Trizol (Thermo Fisher Scientific, Waltham, MA, United States). Alternatively, human biopsies were equilibrated for 10 min in a buffer containing 118 mM NaCl, 16 mM HEPES, 17 mM Na-Hepes, 14 mM glucose, 3.2 mM KCl, 2.5 mM $CaCl_2$, 1.8 mM $MgSO_4$, and 1.8 mM KH_2PO_4 (pH 7.4). Specimens were then minced with a scissor directly in Trizol. Reverse transcription was performed on 2.5 μg of total RNA using SuperScript Vilo Master Mix (Thermo Fisher Scientific, Waltham, MA, United States), according to the manufacturer's suggestions (25°C for 10 min; 42°C for 60 min; 85°C for 5 min). Real-Time PCR amplification was performed by using TaqMan Fast Advanced Master Mix with AQP3 (Assay ID: Hs00185020_m1), V1aR (Assay ID: Hs00176122_m1), V2R (Assay ID: Hs04195588_s1), and 18S assays (Assay ID: Hs99999901_s1) (Thermo Fisher Scientific, Waltham, MA, United States) in StepOne Real-Time PCR System (Thermo Fisher Scientific, Waltham, MA, United States), setting the thermal cycling conditions as specified by the manufacturer (95°C for 20 s; 40 cycles alternatively at 95°C for 1 s and 60°C for 20 s). Results were expressed as $2^{-\Delta\Delta Ct}$ values (relative quantification) with ΔΔCt = (Ct target—Ct 18S) treated—(Ct target—Ct 18S) untreated.

Immunofluorescence

HCT8 cells were grown on 12 mm diameter glass coverslips and left untreated or stimulated as mentioned before. At 80% confluence, HCT8 cells were fixed in 4% paraformaldehyde solution for 20 min and permeabilized with 0.1% Triton X-100 in PBS for 5 min. Alternatively, cells were fixed using ice-cold methanol for 5 min. After blocking with 1% bovine serum albumin in PBS, cells were incubated overnight at 4°C with primary antibodies. After three washing in PBS, cells were incubated for 1 h with the appropriated Alexa Fluor-conjugated secondary antibodies. After washings, samples were mounted onto glass slides with Mowiol. Images were obtained with a confocal laser-scanning fluorescence microscope Leica TCS SP2 (Leica Microsystems, Heerbrugg, Switzerland).

Glycerol Permeability Assay

Glycerol permeability in HCT8 cells was measured using a calcein-quenching method (Mola et al., 2009; Mola et al., 2021). Nearly 80% of confluent cells were grown on 40-mm glass coverslips. After exposure to each treatment, cells were loaded with 12 μM membrane-permeable Calcein-AM in Advanced RPMI 1640 for 45 min at 37°C. Cytosolic calcein fluorophore exhibits concentration-dependent quenching by proteins or salts so that measured changes in fluorescence were directly proportional to changes in cell volume. The coverslips were mounted in a perfusion chamber (FCS2 Closed Chamber System, BIOPTECHS, Butler, United States) and single-

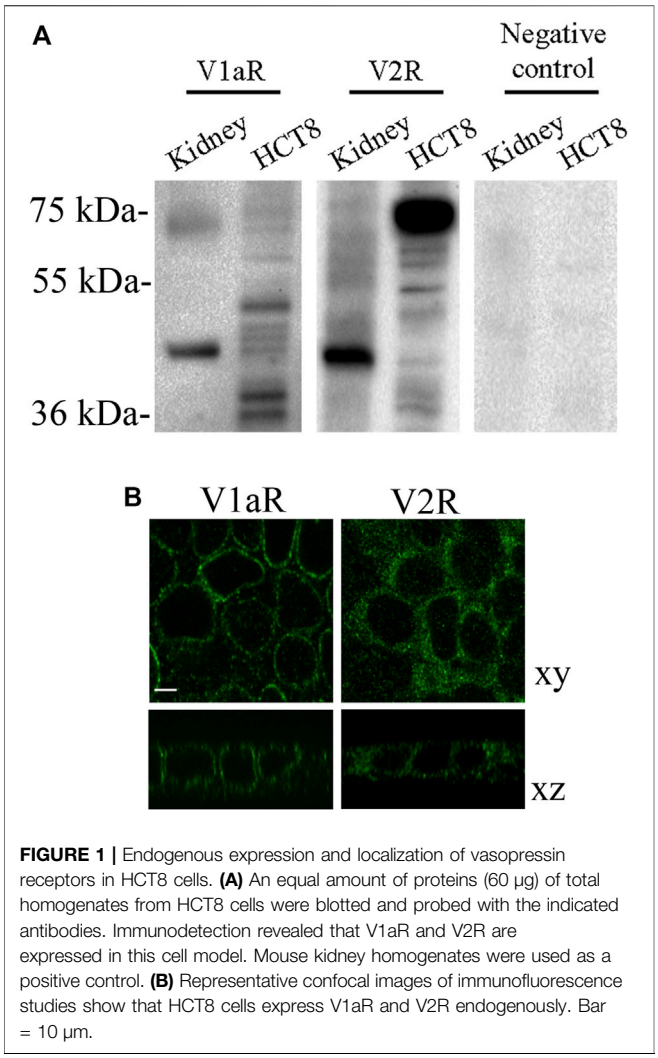

FIGURE 1 | Endogenous expression and localization of vasopressin receptors in HCT8 cells. **(A)** An equal amount of proteins (60 µg) of total homogenates from HCT8 cells were blotted and probed with the indicated antibodies. Immunodetection revealed that V1aR and V2R are expressed in this cell model. Mouse kidney homogenates were used as a positive control. **(B)** Representative confocal images of immunofluorescence studies show that HCT8 cells express V1aR and V2R endogenously. Bar = 10 µm.

cell measurements were performed using an inverted fluorescence microscope (Nikon ECLIPSE TE2000-S, Tokyo, Japan) equipped with a cooled CCD camera controlled by the Metafluor 4.6 software (Molecular Devices, MDS Analytical Technologies, Toronto, Canada). Calcein fluorescence was excited at 490 nm and detected at 520 nm. Cells in isotonic buffer (137 mM NaCl, 5.4 mM KCl, 0.5 mM $MgCl_2$, 1.3 mM $CaCl_2$, 4.2 mM $NaHCO_3$, 0.4 mM KH_2PO_4, 3 mM Na_2HPO_4, 10 mM Hepes sulfonic acid, 10 mM glucose, pH 7.4) were exposed to 100 mOsm/L inwardly directed glycerol osmotic gradient. Time course fluorescence data were acquired over the indicated period to record both the shrinking phase, induced by the osmotic water efflux, and the subsequent swelling phase indicative of the osmotic influx of water following glycerol entry along its gradient. The time constant (expressed as $1/\tau$, sec^{-1}) of the cell swelling, promoted by glycerol entry into the cells, was obtained by fitting the data with an exponential function using GraphPad Software (San Diego, CA, United States). Under such conditions, the calculated $1/\tau$ value is considered an index reflecting the membrane glycerol permeability. Solution osmolarities were measured using a vapor pressure osmometer (Wescor, United States).

Cell Viability Assay

As a measurement of cell viability, the crystal violet assay and the cell growth assay were performed. Crystal violet assay was performed as previously described (Centrone et al., 2020b). Briefly, cells were grown in a 96-well plate and left under basal conditions or treated as previously described. Cells were fixed with 4% paraformaldehyde for 20 min, washed in PBS, and stained with a solution containing 0.1% crystal violet in 20% methanol for 20 min. After washing, cells were lysed with 10% acetic acid. The optical density at 595 nm (DO595) of each well was measured with a Microplate Reader (Bio-Rad Laboratories, Inc., Hercules, CA, United States) and was used as a measurement of cell viability.

Alternatively, 3.000 cells per condition, were seeded on 12-mm glass coverslips and treated as mentioned above. Cells were fixed in 4% paraformaldehyde solution for 20 min, washed in PBS, and stained for 20 min with 0.2% Coomassie blue solution in 10% acetic acid and 45% methanol. Cells were then washed in destaining solution (10% acetic acid, 45% methanol) for 5 min and with dH_2O. After washing, digital pictures for each experimental condition were taken using the ChemiDoc System and the captured images were analyzed using Metamorph® software.

Human Colon Biopsies Homogenates

Biopsies sections were prepared and equilibrated for 10 min in a buffer containing 118 mM NaCl, 16 mM HEPES, 17 mM Na-Hepes, 14 mM glucose, 3.2 mM KCl, 2.5 mM $CaCl_2$, 1.8 mM $MgSO_4$, and 1.8 mM KH_2PO_4 (pH 7.4). Biopsies were minced with scissors in the same buffer in the presence of proteases and phosphatases inhibitors, sonicated (80 kHz for 20 s) and centrifuged at 12,000 g for 10 min at 4°C. Supernatants were collected and 15 µg of protein sample were separated by SDS-PAGE, transferred onto PVDF, and probed by Western blot analysis.

Gel Electrophoresis and Immunoblotting

Proteins were separated by SDS-PAGE (Corciulo et al., 2019) using 12% stain-free polyacrylamide gels (Bio-Rad Laboratories, Inc., Hercules, CA, United States). Protein bands were electrophoretically transferred onto PVDF Transfer membrane (Thermo Fisher Scientific, Waltham, MA, United States) and analyzed by Western blotting as previously described (Centrone et al., 2020b). Membranes were developed using Clarity Western ECL Substrate with the ChemiDoc System gels (Bio-Rad Laboratories, Milan, Italy). Obtained bands were normalized to total protein using the stain-free technology gels. Densitometry was performed using Image Lab software (Bio-Rad Laboratories, Milan, Italy).

RNA-Seq Analysis

Gene expression data relating to the AVPR1a, AVPR2, and AQP3 genes, from the TCGA (https://www.cancer.gov) for 288 colon tumors and the GTEx project (https://gtexportal.org) for 308 normal controls, were downloaded using the UCSC Xena browser (https://xena.ucsc.edu). The TPM (Transcripts Per Million) values for each gene obtained by bioinformatic analysis of

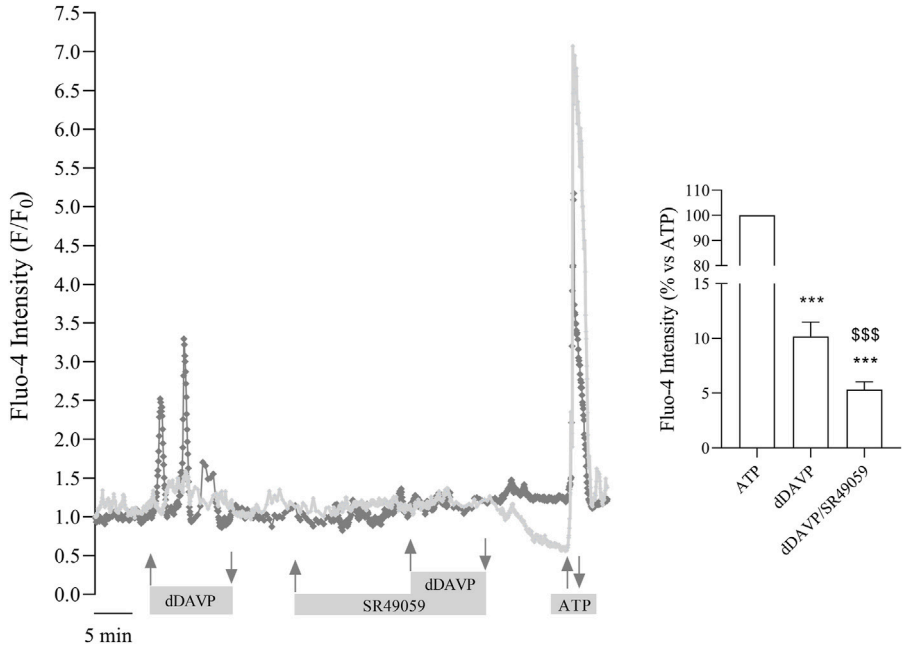

FIGURE 2 | Functional characterization of endogenous V1aR receptors in HCT8 cells. Cells were stimulated with 1 μM dDAVP or with 1 μM dDAVP and 100 nM SR49059, a V1aR antagonist. ATP (100 μM) stimulation was used as a positive control. dDAVP significantly increased cytosolic calcium. Stimulation with dDAVP in the presence of 100 nM SR49059 prevented the effect of dDAVP raising cytosolic calcium. Data are expressed as means ± S.E.M. and analyzed by one-way ANOVA followed by Tukey's multiple Comparisons test (***$p < 0.001$ vs. ATP; $^{\$\$\$}p < 0.001$ vs. dDAVP).

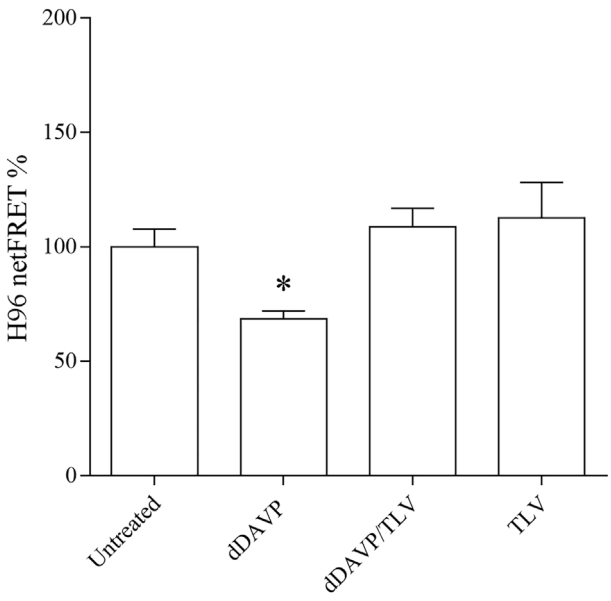

FIGURE 3 | Functional characterization of endogenous V2R receptor in HCT8 cells. cAMP levels were evaluated by FRET experiments in HCT8 cells transiently transfected with H96, as described in the Methods section. 5 min of stimulation with 100 nM dDAVP significantly reduced the netFRET signals consistent with a significant increase in the cAMP levels compared with untreated cells. Data are expressed as means ± S.E.M. and analyzed by one-way ANOVA followed by Dunnett's Multiple Comparison test (*$p < 0.05$ vs. untreated).

RNA-Seq were compared by Mann-Whitney test and plotted on logarithmic scale in base 2.

Statistical Analysis

All values are reported as means ± S.E.M. Statistical analysis was performed by one-way ANOVA followed by Dunnett's multiple comparisons test. When applicable, the Student *t*-test was also applied. A difference of $p < 0.05$ was considered statistically significant.

Supplementary Data

Antibodies

A goat polyclonal antibody against Aquaporin-1 (L-19), a monoclonal antibody against PCNA (PC10), and a monoclonal antibody against AQP2 (E-2) were purchased from Santa Cruz Biotechnology (S.I.A.L. s.r.l., Rome, Italy). Rabbit polyclonal antibodies against Aquaporin-4 (PA5-85767) and Aquaporin-5 (PA5-36529) were obtained from Invitrogen (Thermo Fisher Scientific, Waltham, MA, United States).

Water Permeability Video Imaging Measurements

Osmotic water permeability was measured by video imaging experiments. HCT8 cells were grown on 40 mm glass coverslips and exposed to specific treatments. Cells were loaded with 12 μM Calcein-AM in culture medium for 45 min at 37°C and then rinsed in isotonic solution (137 mM NaCl, 5.4 mM KCl, 0.5 mM $MgCl_2$, 1.3 mM $CaCl_2$, 4.2 mM $NaHCO_3$, 0.4 mM KH_2PO_4, 3 mM Na_2HPO_4, 10 mM Hepes sulfonic acid, 10 mM glucose, pH 7.4). The coverslips were mounted in a

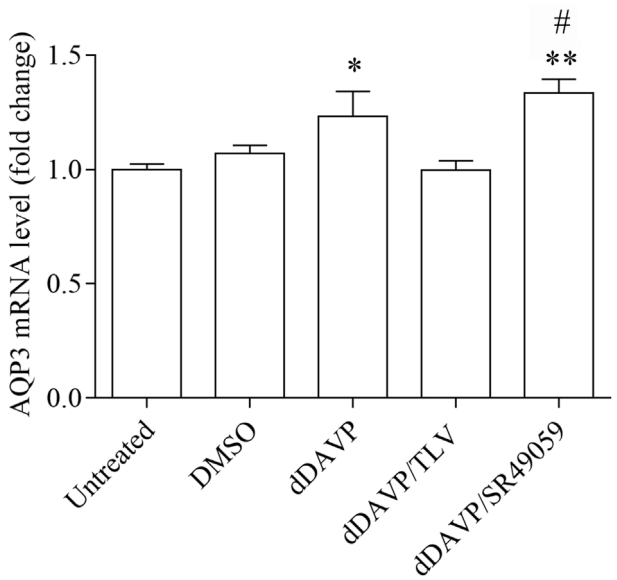

FIGURE 4 | AQP3 gene expression in HCT8 cells. Real-Time PCR was performed as described in the Methods. Treatment with dDAVP significantly increased AQP3 mRNA level compared with untreated cells. Cotreatment with dDAVP and SR49059 significantly increased AQP3 mRNA compared to untreated cells. By contrast, cotreatment with dDAVP and tolvaptan did not alter the AQP3 mRNA level. Data are shown as mean ± S.E.M. of 6 independent experiments and analyzed by one-way ANOVA followed by Dunnett's Multiple Comparison test (*$p < 0.05$ and **$p < 0.01$ vs. untreated; $^{\#}p < 0.05$ vs. DMSO).

perfusion chamber (FCS2 Closed Chamber System, BIOPTECHS, Butler, United States). Fluorescence signal changes in dye-loaded cells after 100 mOsm/L hypertonic gradient were recorded continuously using a Nikon inverted epifluorescence microscope (Nikon Eclipse TE2000-S) equipped with a ×40 objective lens [oil immersion, numerical aperture (NA) 1.3]. Calcein fluorescence was excited at 490 nm and the emitted fluorescence at 520 nm was captured by a cooled ECCD camera (CoolSNAP HQ, Photometrics). The changes in fluorescence intensity were directly proportional to changes in cell volume. The signal decreased upon the addition of hypertonic solution as a consequence of water efflux and cell shrinkage. Data acquisition was performed by Metafluor software (Molecular Devices, MDS Analytical Technologies, Toronto, ON, Canada) and the data were analyzed with GraphPad Prism software (La Jolla, CA, United States). The time constant ($1/\tau$, s^{-1}) of cell volume change upon hypertonic stimulus was obtained by fitting the experimental kinetic with an exponential function.

RESULTS

Expression of Vasopressin Receptors in HCT8 Cells

Normal and abnormal VRs are expressed in different tissues and several types of tumor cells including lung, breast, prostate and colon (North, 2000; Moon et al., 2003). To investigate the possible function of vasopressin in the colon, human colon carcinoma

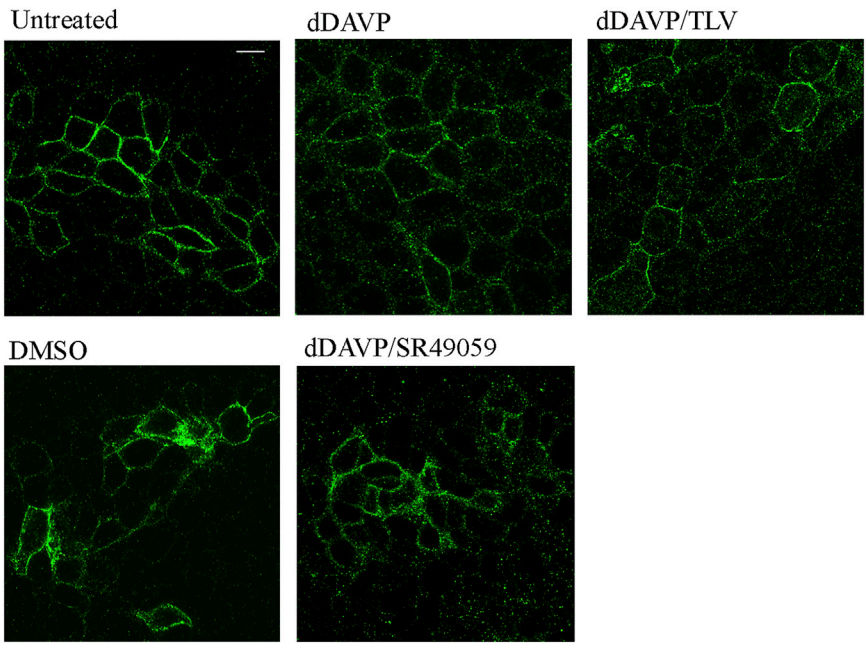

FIGURE 5 | Immunofluorescence localization of AQP3 in HCT8 cells. HCT8 cells were treated (as described in the methods section), stained for AQP3, and subjected to confocal laser scanning microscopy. Under basal conditions, AQP3 staining was mainly in the plasma membrane. Treatment with dDAVP or with dDAVP and tolvaptan caused a slight reduction of the AQP3 membrane localization. Bar = 10 μm.

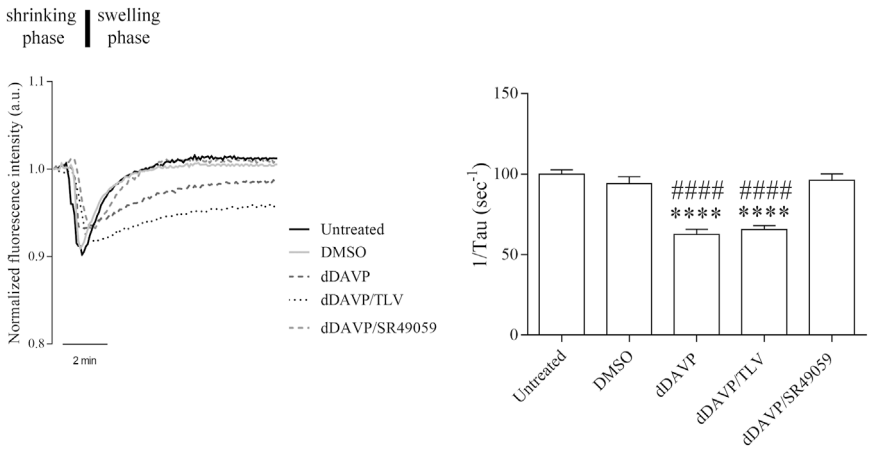

FIGURE 6 | Effect of Vasopressin receptors on glycerol permeability. Osmotically induced volume changes recorded by the calcein-quenching method in HCT8 cells exposed to dDAVP stimulation or cotreated with V1aR antagonist (dDAVP/TLV) or VR2 antagonist (dDAVP/SR49059) compared to control conditions (untreated, DMSO). On the left, a representative time course of cell shrinking (water exit) followed by cell swelling indicative of the osmotic influx of water promoted by glycerol entry along its gradient (Δ 100 mOsm/L). On the right, a bar plot showing the mean ± S.E.M. values of the cell swelling time constants ($1/\tau$, s^{-1}) reflecting glycerol entry into the cells. Note that the treatment with 100 nM dDAVP significantly reduced glycerol permeability. A comparable effect was observed after cotreatment with 100 nM dDAVP and 100 nM tolvaptan for 72 h. By contrast, treatment with 100 nM SR49059 for 72 h prevented the dDAVP effect on glycerol uptake. Data are obtained from 35 to 56 different measurements of 3 independent experiments. A one-way ANOVA and Dunnett's Multiple Comparison test were performed (****$p < 0.0001$ vs. untreated; ####$p < 0.0001$ vs. DMSO).

TABLE 1 | Glycerol permeability, cell viability and total area of cell. Values represent the mean ± S.E.M. and analyzed by one-way ANOVA followed by Dunnett's Multiple Comparison test. *Significantly different versus Untreated (****$p < 0.0001$, **$p < 0.01$, *$p < 0.05$). #Significantly different versus DMSO (####$p < 0.0001$, ###$p < 0.001$, ##$p < 0.01$).

Parameters	Untreated	DMSO	dDAVP	dDAVP/TLV	dDAVP/SR49059	dDAVP/ SR49059/ DFP001	DFP00173	TLV	SR49059
Glycerol permeability	100 ± 2.72	94.14 ± 4.18	62.46 ± 3.27 **** ####	65.49 ± 2.56 **** ####	96.04 ± 4.15	42.30 ± 1.57 **** ####	45.72 ± 2.23 **** ####	88.67 ± 5.68	101.6 ± 4.94
	n = 428 cells	*n* = 181 cells	*n* = 87 cells	*n* = 108 cells	*n* = 160 cells	*n* = 138 cells	*n* = 93 cells	*n* = 96 cells	*n* = 71 cells
Cell Viability	100 ± 6.55	106.3 ± 7.00	71.14 ± 3.38 *** ####	64.59 ± 6.09 **** ####	102.9 ± 3.70	76.42 ± 2.99 ** ###	80.33 ± 1.2 * ##	98.3 ± 6.36	114.4 ± 2.97
	n = 6	*n* = 6	*n* = 6	*n* = 6	*n* = 6	*n* = 6	*n* = 6	*n* = 6	*n* = 6
Total Area of cell	100 ± 6.51	89.54 ± 5.31	47.07 ± 3.00 **** ####	46.12 ± 4.13 **** ####	86.16 ± 6.63	50.23 ± 1.82 **** ##	69.77 ± 8.07 *	88.38 ± 3.51	88.83 ± 11.94
	n = 6	*n* = 6	*n* = 6	*n* = 6	*n* = 6	*n* = 3	*n* = 3	*n* = 3	*n* = 3

HCT8 cells were used as an experimental model, and the expression of V1aR and V2R was evaluated. Immunoblotting analysis revealed immunoreactive bands of the expected mass of 45 kDa in homogenates isolated from HCT8 cells, indicating that V1aR and V2R are expressed in this cell model. Mouse kidney lysates were used as a positive control, whereas the negative control lanes are shown on the right of the panel (**Figure 1A**). Besides the expected bands, other few additional bands were detected which might correspond to variants or modified VRs. The expression of both receptors was further confirmed by immunohistochemistry (**Figure 1B**) revealing that HCT8 cells express V1aR and V2R. In particular, the xz scan suggests that V1aR is mainly localized at the plasma membrane. Conversely, V2R is expressed within the entire cell, including the plasma membrane. To test the functionality of the endogenous expressed V1aR, which is coupled to Gq (Thibonnier, 1992), changes in intracellular calcium were measured by single-cell epifluorescence imaging. Cells were loaded with Fluo-4 (4 μM) and exposed to dDAVP (1 μM) and ATP (100 μM) (**Figure 2**). Variations in intracellular calcium evoked by dDAVP were compared to the ATP response as a positive control. Statistical analysis of data revealed that stimulation with dDAVP caused a moderate increase in cytosolic calcium content (dDAVP = 10.17 ± 1.32% vs. ATP considered as 100%; n = 108 cells). The dDAVP triggered the increase in cytosolic calcium was prevented by preincubation with SR49059, a specific V1R

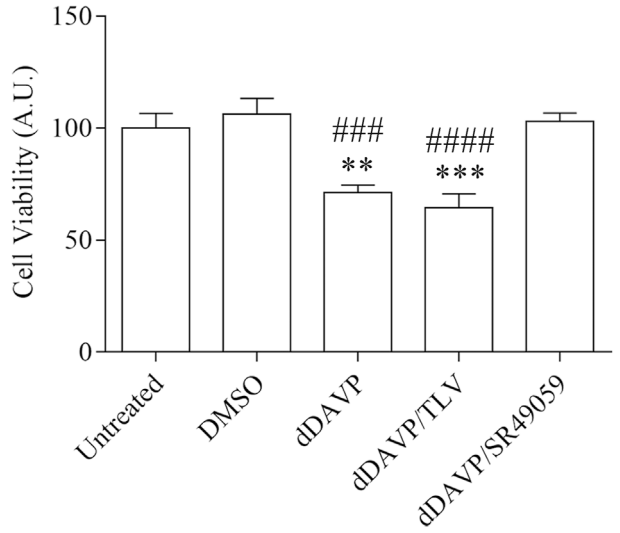

FIGURE 7 | Effect of Vasopressin receptors on cell viability. Cells were left under basal conditions or treated as described in the methods section and were stained with crystal violet solution. Treatment with 100 nM dDAVP significantly reduced cell viability compared with untreated cells. The same effect was observed in cells treated with 100 nM dDAVP and 100 nM tolvaptan for 72 h. In contrast, stimulation with 100 nM SR49059 did not affect dDAVP cell viability. Data are presented as means ± S.E.M. of six independent experiment and analyzed by one-way ANOVA followed by Dunnett's Multiple Comparison test (**$p < 0.01$ and ***$p < 0.001$ vs. untreated; ###$p < 0.001$ and ####$p < 0.0001$ vs. DMSO).

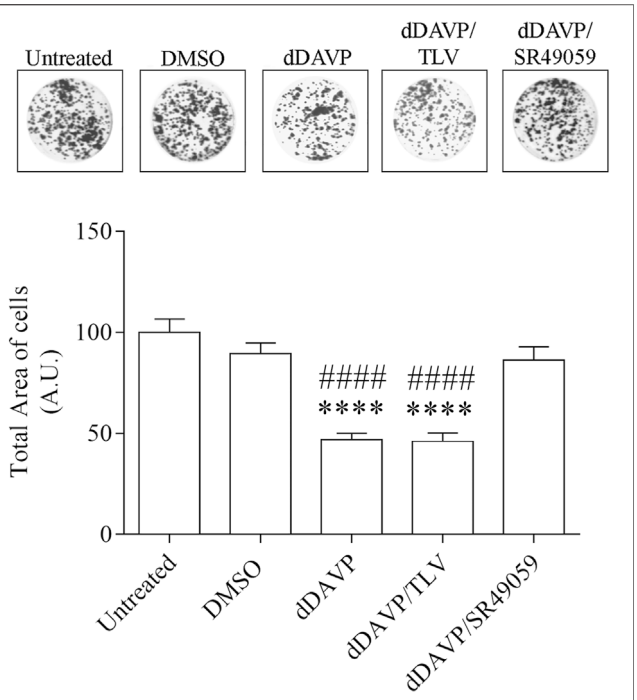

FIGURE 8 | Effect of Vasopressin receptors on cell growth. Cells were left under basal conditions or treated as described in the methods section, stained with 0.2% Coomassie Blue solution, and the total area of the growth cells was measured using Metamorph software. Compared to untreated cells, treatment with dDAVP significantly decreased the cell total growth area. A similar effect was observed when cells were treated with 100 nM dDAVP and 100 nM tolvaptan for 72 h. Incubation with 100 nM SR49059 abolished the effect of dDAVP on cell growth. Data are presented as means ± S.E.M. of 6 independent experiments and analyzed by one-way ANOVA followed by Dunnett's Multiple Comparison test (****$p < 0.0001$ vs. untreated; ####$p < 0.0001$ vs. DMSO).

antagonist (dDAVP/SR49059 = 5.32 ± 0.70% vs. ATP $n = 58$ cells), indicating that intracellular calcium increase occurs possibly through V1aR signaling. To evaluate the functionality of the endogenous expressed V2R, known to be coupled to Gs, (Birnbaumer et al., 1994), variations in intracellular cAMP, evoked by dDAVP stimulation, were measured using Fluorescence Resonance Energy Transfer (FRET) technology as previously described (Russo et al., 2017). HCT8 cells were transiently transfected with a plasmid encoding the H96 probe carrying the cAMP-binding motif of EPAC1 sandwiched between the CFP and Venus proteins (Ranieri et al., 2021). Compared to untreated cells, corrected netFRET signals are decreased with short-term (5 min) dDAVP stimulation (**Figure 3**, dDAVP = 68.52 ± 3.44%, $n = 100$ cells vs. untreated = 100 ± 7.72%, $n = 105$ cells), consistent with a significant increase in intracellular cAMP. Preincubation with tolvaptan, a selective V2R antagonist, abolished the dDAVP-induced increase in intracellular cAMP (dDAVP/TLV = 108.7 ± 8.13%, $n = 96$ cells). The treatment with tolvaptan did not alter intracellular cAMP levels (TLV = 112.6 ± 15.5%, $n = 51$ cells). Together these findings suggest that endogenous VRs are responding to dDAVP stimulation.

dDAVP Action on AQP3 Expression and Function

To test the possible involvement of dDAVP on AQP3 expression, Real-Time PCR experiments were performed (**Figure 4**). Cells were left untreated or incubated with DMSO as vehicle control. Alternatively, cells were stimulated with dDAVP or cotreated with dDAVP and tolvaptan (dDAVP/TLV) or with dDAVP and SR49059 (dDAVP/SR49059). Compared to untreated condition, stimulation with dDAVP significantly increases AQP3 mRNA expression (dDAVP = 1.23 ± 0.11 vs. untreated = 1.0 ± 0.02; $n = 6$). Importantly, cotreatment with dDAVP and SR49059 also increased AQP3 mRNA expression (dDAVP/SR49059 = 1.33 ± 0.06 vs. untreated = 1.0 ± 0.02, DMSO = 1.07 ± 0.03; $n = 6$), suggesting that the dDAVP-induced AQP3 expression is not regulated by V1aR signaling. By contrast, treatment with tolvaptan prevented the increase of AQP3 induced by dDAVP stimulation (dDAVP/TLV = 0.99 ± 0.04 vs. untreated = 1.0 ± 0.02, DMSO = 1.07 ± 0.03; $n = 6$), likely indicating that the increase of the AQP3 mRNA is dependent on V2R stimulation. No relevant change in AQP3 protein abundance was found under treatment with dDAVP (**Supplementary Figure S1**). Also, immunocytochemistry revealed that AQP3 is mainly expressed in the plasma membranes (**Figure 5**). However, a slight reduction of the membrane-stained AQP3 was detected in HCT8 cells treated with dDAVP or with dDAVP and tolvaptan (dDAVP/TLV). Whereas, the AQP3 staining in cells treated with dDAVP and SR49059 is similar to that observed in untreated cells. To further investigate the action of dDAVP on AQP3 function,

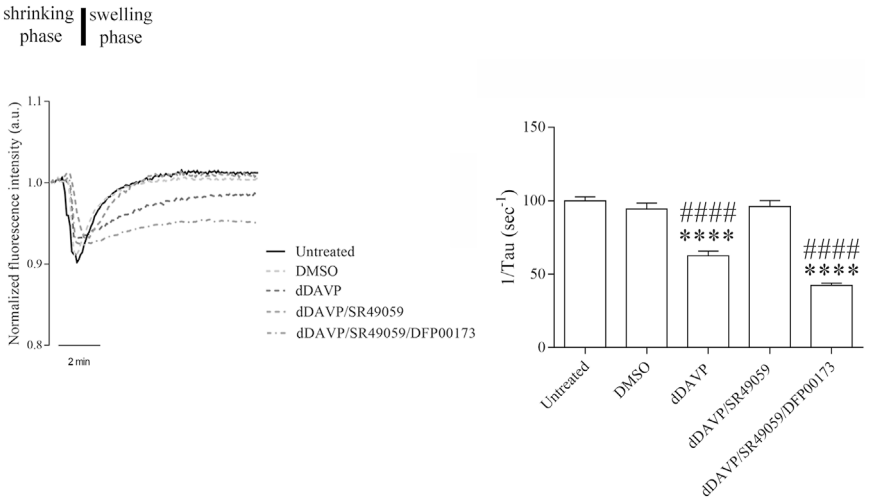

FIGURE 9 | Effect of AQP3 on glycerol permeability. Cells were grown, treated, and then labeled with calcein as described in the Methods section. The histogram shows that treatment with 2.5 μM DFP00173 for 48 h prevented the SR49059 action on dDAVP stimulation. Data are presented as means ± S.E.M. of 3 independent experiments and analyzed by one-way ANOVA followed by Dunnett's Multiple Comparison test (****$p < 0.0001$ vs. Untreated; $^{\#\#\#\#}p < 0.0001$ vs. DMSO).

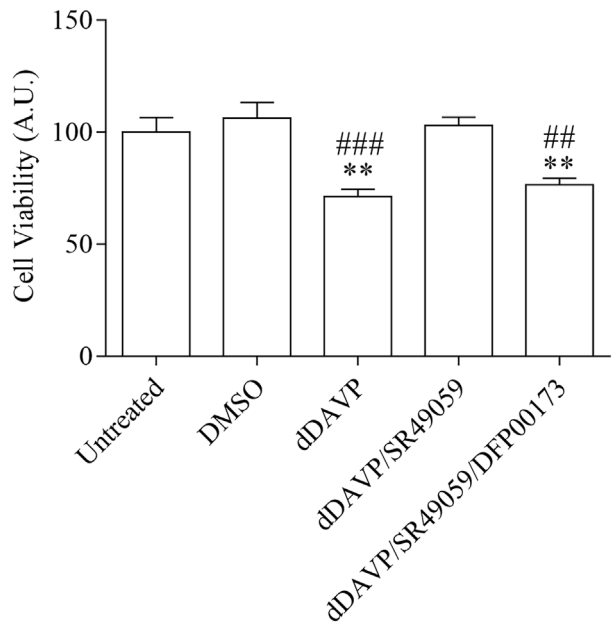

FIGURE 10 | Effect of AQP3 on cell viability. Cells were left under basal conditions or treated as described in the methods section and were stained with crystal violet solution. Compared to untreated cells, treatment with 2.5 μM DFP00173 for 48 h prevented the SR49059 action on dDAVP treatment. Data are presented as means ± S.E.M. of 6 independent experiments and analyzed by one-way ANOVA followed by Dunnett's Multiple Comparison test (**$p < 0.01$ vs. untreated; $^{\#\#}p < 0.01$ and $^{\#\#\#}p < 0.001$ vs. DMSO).

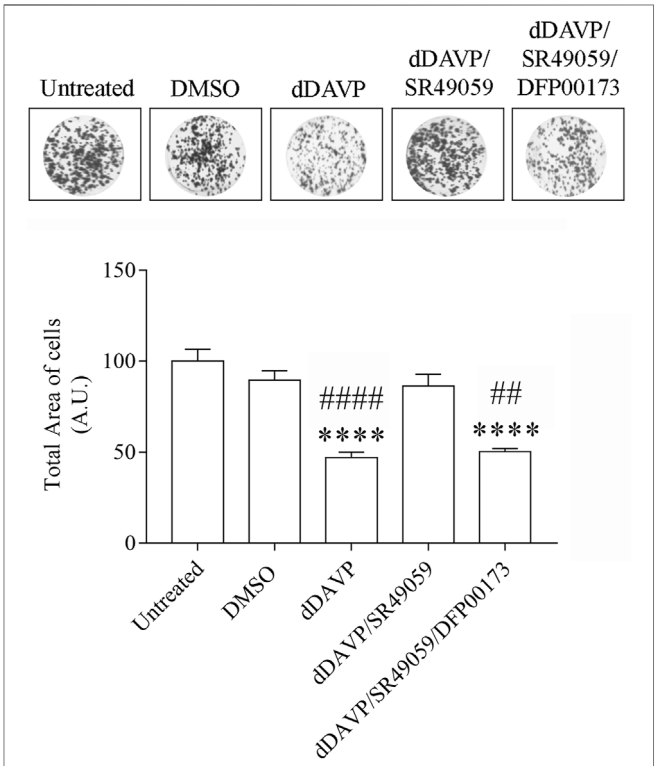

FIGURE 11 | Effect of AQP3 on cell growth. Cells were left under basal conditions or treated as described in the methods section, stained with 0.2% Coomassie Blue solution, and the total area of the growth cells was measured using Metamorph software. Compared to untreated cells, treatment with 2.5 μM DFP00173 for 48 h prevented the SR49059 action on dDAVP treatment. Data are presented as means ± S.E.M. of 3 independent experiments and analyzed by one-way ANOVA followed by Dunnett's Multiple Comparison test (****$p < 0.0001$ vs. untreated; $^{\#\#}p < 0.01$ and $^{\#\#\#\#}p < 0.0001$ vs. DMSO).

glycerol uptake was measured using a calcein-based assay (**Figure 6**). Stimulation with dDAVP significantly reduced the temporal osmotic response (reported as 1/τ) generated using a

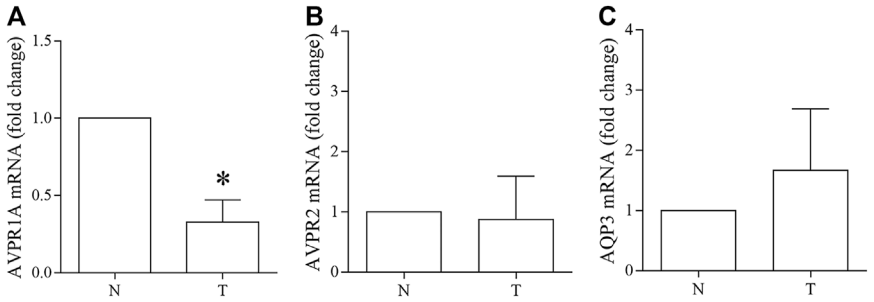

FIGURE 12 | Vasopressin receptors and AQP3 gene expression in human colon carcinoma biopsies. Real-Time PCR was performed as described in the methods **(A)** Real-time PCR experiments show that the V1aR expression is significantly downregulated in the tumor biopsies compared with the corresponding healthy mucosa. **(B–C)** No relevant changes were found in the expression of V2R and AQP3. Data are shown as mean ± S.E.M. and analyzed by Student's *t*-test (*$p < 0.05$ vs. untreated).

glycerol hyperosmotic solution (dDAVP = 62.46 ± 3.27, $n = 87$ cells vs. untreated = 100 ± 2.72, $n = 428$ cells). Similar results were obtained in cells treated with dDAVP and tolvaptan (dDAVP/TLV = 65.49 ± 2.56, $n = 108$ cells vs. untreated = 100 ± 2.72, $n = 428$ cells; DMSO = 94.14 ± 4.18, $n = 181$ cells). By contrast, selective inhibition of the V1aR, with SR49059, prevented the dDAVP action on glycerol intake rate (dDAVP/SR49059 = 96.04 ± 4.15, $n = 160$ cells vs. untreated = 100 ± 2.72, $n = 428$ cells; DMSO = 94.14 ± 4.18, $n = 181$ cells). Data are also summarized in **Table 1**. Parallel studies, however, revealed that dDAVP treatment slightly increased the water transport rate which might be due to the endogenous expression of the classical water channels AQP1, AQP4, and AQP5 (**Supplementary Figure S2**). Glycerol is an important metabolite playing a role in controlling cell growth and proliferation (Méndez-Giménez et al., 2014). In non-small cells, lung cancer downregulation of AQP3 is associated with a relevant suppression of cell growth (Xia et al., 2014). Moreover, dDAVP displays antimetastatic properties in a mouse model of mammary cancer (Alonso et al., 1999; Giron et al., 2002) and antiproliferative action in colon carcinoma cell lines (Ripoll et al., 2010). Here, the effect of dDAVP on cell viability was tested by the crystal violet assay (**Table 1**; **Figure 7**) in HCT8 cells. Compared to the control condition, treatment with dDAVP significantly reduced cell viability (dDAVP = 71.14 ± 3.38% vs. untreated = 100 ± 6.55%; $n = 6$). Similar observations were obtained in cells treated with dDAVP and tolvaptan (dDAVP/TLV = 64.59 ± 6.09% vs. untreated = 100 ± 6.55%, DMSO = 106.3 ± 7.00%; $n = 6$). Conversely, incubation with SR49059 abolished the effect of dDAVP on cell viability (dDAVP/SR49059 = 102.9 ± 3.70%; $n = 6$). To further investigate the action of dDAVP on cell growth, HCT8 cells were seeded and treated, as described in the methods. The total area of the growth cells was stained with 0.2% Coomassie Blue solution and measured using Metamorph software (**Table 1**; **Figure 8**). Compared to untreated cells, dDAVP significantly decreased the total growth area (dDAVP = 47.07 ± 3.00% vs. untreated = 100 ± 6.51%; $n = 6$). Similar observations were obtained in cells treated with dDAVP and tolvaptan (dDAVP/TLV = 46.12 ± 4.13% vs. untreated = 100 ± 6.51%, DMSO = 89.54 ± 5.13%; $n = 6$). Incubation with SR49059 prevented the action of dDAVP on cell viability (dDAVP/SR49059 = 86.16 ± 6.63%; $n = 6$). Moreover, dDAVP treatment did not alter the abundance of pCNA, a known proliferation marker (**Supplementary Figure S3**).

To evaluate whether the reduction of glycerol permeability observed under dDAVP stimulation can be ascribed to AQP3 function, glycerol uptake was measured in the presence of DFP00173, a selective inhibitor of AQP3 (**Table 1**; **Figure 9**). Incubation with DFP00173 abolished the effect exerted by SR49059 on dDAVP stimulation (dDAVP/SR49059/DFP00173 = 42.30 ± 1.57%, $n = 138$ vs. dDAVP/SR49059 = 96.04 ± 4.15%, $n = 160$) suggesting that AQP3 is committed for glycerol transport under these conditions. Crystal violet assay (**Figure 10**, dDAVP/SR49059/DFP00173 = 76.42 ± 2.99% vs. dDAVP/SR49059 = 102.9 ± 3.70%; $n = 6$) and the test to evaluate the total area of growth cells (**Figure 11**, dDAVP/SR49059/DFP00173 = 50.23 ± 1.82%, $n = 3$ vs. dDAVP/SR49059 = 86.16 ± 6.63%, $n = 6$) revealed and confirmed that selective inhibition of AQP3 using DFP00173 prevented the SR49059 action on dDAVP treatment.

Expression of VRs and AQP3 in Human Colon Carcinoma Biopsies and RNA-Seq Analysis

Specimens of neoplastic colon tissues and part of normal mucosa obtained from four patients were analyzed to investigate the expression of VRs and AQP3. Real-Time PCR experiments (**Figure 12**) showed significant downregulation of the V1aR expression in the tumor biopsies compared with the corresponding healthy mucosa (**Figure 12A**, $N = 1.0$ vs. $T = 0.33 \pm 0.14$; $n = 4$). By contrast, no relevant changes were found in the expression of V2R (**Figure 12B**, $N = 1.0$ vs. $T = 0.88 \pm 0.72$; $n = 4$) and AQP3 (**Figure 12C**, $N = 1.0$ vs. $T = 1.66 \pm 1.03$; $n = 4$). Similar observations were obtained by immunoblotting studies showing that compared with normal colon mucosa, in tumors specimens V1aR protein expression significantly decreased (**Figure 13A**, $N = 100$ vs. $T = 48.63 \pm 4.95$; $n = 4$) while no significant alterations in the abundance of V2R (**Figure 13B**, $N = 100$ vs. $T = 69.34 \pm 16.82$; $n = 4$) and AQP3 (**Figure 13C**, $N = 100$ vs. $T = 125.1 \pm 45.58$; $n = 4$) were detected.

Because of the small number of available human biopsies and to further validate the obtained data, publicly available pre-

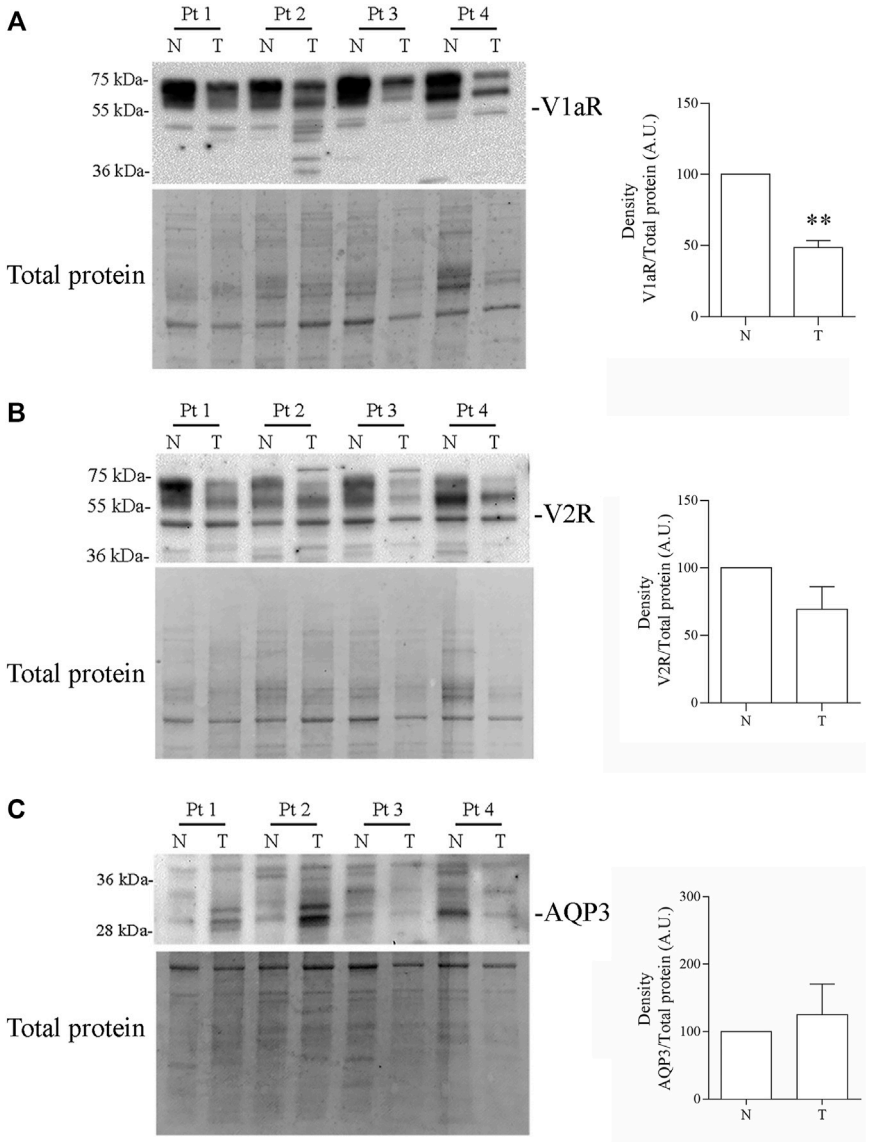

FIGURE 13 | Expression of Vasopressin receptors and AQP3 in human colon biopsy. Equal amount of proteins (20 μg) of total homogenates from human colon biopsies were blotted and probed with the indicated antibodies. **(A)** Immunodetection revealed that V1aR protein expression is significantly decreased in tumors compared to the normal colon mucosa. **(B–C)** Immunodetection revealed that V2R and AQP3 protein expression is not altered in human colon adenocarcinoma. Data are shown as mean ± S.E.M. and analyzed by Student's *t*-test (**p < 0.01 vs. normal colon mucosa).

analyzed gene expression data were downloaded for a total of 288 primary colon tumors from the TCGA RNA-Seq dataset and compared with 308 normal colon controls (GTExproject). Both genes AVPR1A and AVPR2 were significantly (Mann-Whitney p-value <0.0001) down-regulated in tumors, while AQP3 showed an opposite trend (**Figure 14**).

DISCUSSION

The major finding of this study is that the hormone vasopressin controls the expression and the function of AQP3 in human colon carcinoma cells. Specifically, long-term treatment with dDAVP increases AQP3 mRNA expression through V2R and decreases AQP3-mediated glycerol transport through V1aR signaling. Physiologically, vasopressin receptors are widely expressed in different tracts of the gastrointestinal tube including the colon (Monstein et al., 2008). Neoplastic tissue can express normal and abnormal forms of vasopressin and VRs which may exert distinct actions on cancer growth and metabolism (North, 2000) and a differentiated sensitivity to vasopressin (North et al., 1997). In MCF-7 breast cancer cells, an abnormal V2R mRNA coding for a V2R mutant has been detected. This mRNA contains a stop codon within the reading frame and therefore leads to a C-terminally truncated receptor similar to that causing the nephrogenic diabetes insipidus

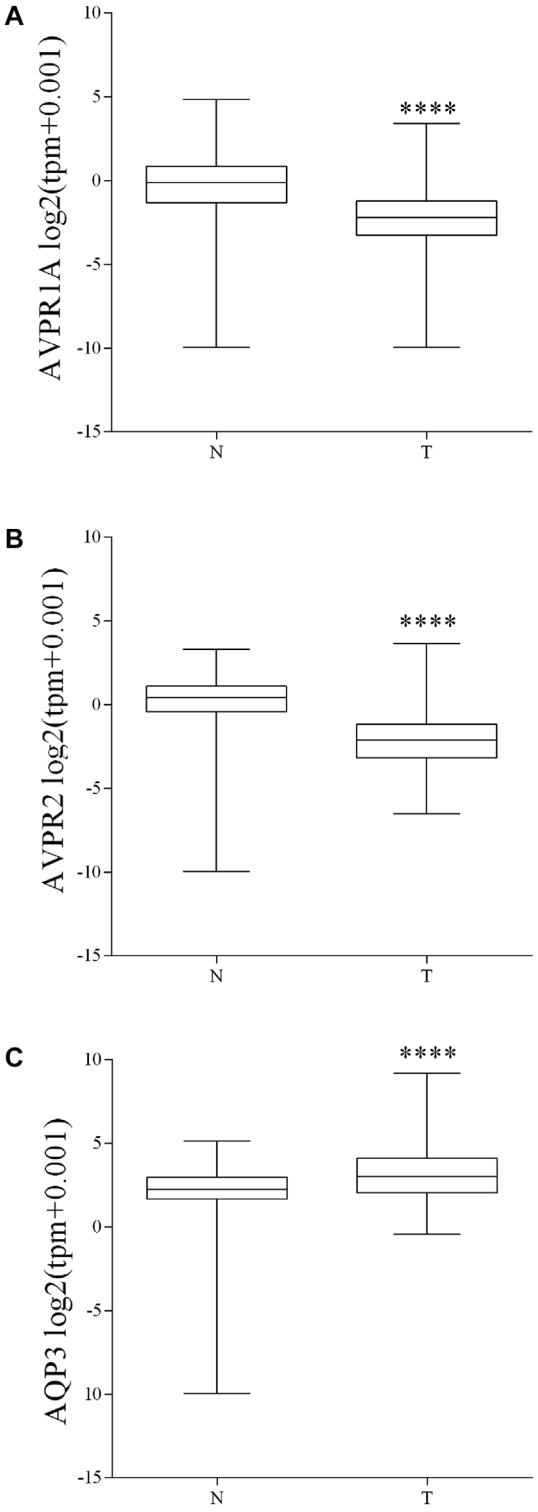

FIGURE 14 | Expression of Vasopressin receptors and AQP3 genes in human colon adenocarcinoma. Publicly available pre-analyzed gene expression (tpm) data from 288 primary colon tumors and 308 normal colon controls were downloaded and plotted as distribution in log2 (tpm+0.001) values. **(A–B)** Bioinformatic analysis of RNA-Seq showed that in colon cancer, gene expression of vasopressin receptors is significantly decreased. **(C)** Bioinformatic analysis of RNA-Seq showed that AQP3 gene expression is significantly increased in colon cancer compared to the normal colonic mucosa. Data are reported as box plot and analyzed by two-tailed Mann Whitney *U* test (****$p < 0.0001$).

(*Continued*)

(Rosenthal et al., 1994). Loss-of-function mutants of V2R are often located intracellularly and may also form heterodimers with wildtype V2R (Zhu and Wess, 1998) and V1aR (Terrillon et al., 2004). VRs mutants might be likely considered sponges for normal receptors and then act as negative regulators for VRs localization and function (Zhu and Wess, 1998; Terrillon et al., 2004). Moreover, the selectivity of the VRs antagonists, respect to these abnormal forms of VRs is unknown at moment. Immunolocalization experiments showed that V2R staining is widely distributed within the entire cells likely suggesting the expression of a non-canonical form of V2R, beyond the normal V2R and that may render the effect of vasopressin on cells expressing these receptors multifaceted. Also, western blotting studies reveal several few bands in HCT8 cells and tumor specimens compared with the healthy mucosa obtained from the same patient likely proposing the expression of post-translationally modified proteins or altered variants of the receptors. The possible expression and function of putative VRs variants have not been clarified here, nevertheless, in the present study, we report that HCT8 cells express functional V1a and V2 receptors which are sensitive to the action of dDAVP. dDAVP is a stable analog of vasopressin and it is widely applied clinically to treat bleeding disorders, nocturnal polyuria, and central diabetes insipidus due to the antidiuretic properties mediated by the V2R (Mannucci, 1997; Kapić et al., 2005; Weiss and Everaert, 2019). However, affinity binding assays showed that dDAVP exhibits differences in the affinity binding across species (Chini and Manning, 2007). dDAVP displayed a higher affinity for V2R in rats than in humans. In human receptor assays, dDAVP displays selectivity for V2R, V1aR, and V1bR (Cheng et al., 2004; Chini and Manning, 2007). Here, treatment with dDAVP increases the expression level of mRNA AQP3 through V2R but not *via* V1aR as demonstrated by using selective VRs antagonists. These findings, also, underline the distinct and opposite responses of the VRs to dDAVP action in terms of AQP3 mRNA expression level. Long-term regulation of AQP3 expression is complex and involves several transcription factors (Yde et al., 2021). In the context of inflammation, cytokines, and growth factors, such as IFNγ, TNFα, and hEGF can modulate AQP3 expression. In HT29 cells, IFNγ and TNFα reduce AQP3 expression through STAT1 and SP3 respectively (Peplowski et al., 2017; Peplowski et al., 2018). Conversely, in human colorectal carcinoma cells HCT116, hEGF upregulates AQP3 expression through PI3K/AKT signaling (Li et al., 2013). Furthermore, Mg^{2+} and the vasoactive intestinal polypeptide (VIP) upregulate AQP3 expression in a cAMP-dependent manner by involving the cAMP response element-binding protein (CREB) (Itoh et al., 2003; Okahira et al., 2008). In this study, however, the possible involvement of transcription factors in controlling the dDAVP dependent AQP3 expression was not investigated but based on

the data obtained with the VRs antagonists, we might propose that the increase in AQP3 expression elicited by dDAVP is dependent on a cAMP/PKA pathway.

Colon epithelium is mainly involved in water reabsorption through the paracellular route or the transcellular pathway *via* aquaporins (Iwata et al., 1997; Liao et al., 2021). Several studies report that AQP3 may play a key role in intestinal water uptake. A significant decrease in AQP3 protein abundance has been described in rectosigmoid specimens obtained by patients with diarrhea-predominant irritable bowel syndrome (IBS-D) compared with healthy subjects (Camilleri et al., 2019). However, our study shows that treatment with dDAVP does not alter the protein abundance of AQP3 despite the increase of the AQP3 mRNA. The discrepancy in AQP3 mRNA expression compared with AQP3 protein abundance has been found also in colonic epithelial cells isolated from rats fed with cholic acid (Yde et al., 2016) and might be due to post-transcriptional, or post-translational regulation mechanisms, and even the gating of the channel (Zeuthen and Klaerke, 1999) which might explain the reduction in glycerol permeability observed under dDAVP stimulation. On another hand, the intracellular trafficking of AQP3 might be controlled by a complex network of kinases such as PKC (Yasui et al., 2008). Alternatively, it cannot be excluded that the total abundance of AQP3 might be the result of two opposite forces mediated by V2R and V1aR respectively. In this respect, it has been shown that V1aR can limit the functions mediated by V2R (Bankir, 2001; Izumi et al., 2008).

In this study, incubation with dDAVP slightly but significantly increases the osmotic water permeability which might be not due to AQP3 that is instead functionally downregulated. Other aquaporins including AQP1, AQP4, and AQP5, that are expressed in HCT8 cells, might be involved in dDAVP dependent water transport. Further investigation is needed to clarify this aspect. On the other hand, functional studies reveal that treatment with dDAVP significantly decreases the glycerol uptake through V1aR. Glycerol is a key substrate for cell metabolism and is required for gluconeogenesis and lipid synthesis. However, whether the AQP3-dependent glycerol transport correlates with metabolic disorders and cancer progression remains to be better clarified (Li et al., 2016; Calamita et al., 2018). In gastric cells, inhibition of AQP3 reduces cell proliferation possibly *via* the PI3K/Akt pathway (Li et al., 2016). In this study, stimulation with dDAVP impairs cell growth regardless of V2R function. Also, we could not detect any significant changes in the expression level of PCNA, a known marker of cell proliferation. Conversely, specific inhibition of V1aR with SR49059 prevents the inhibitory action of dDAVP on cell growth. Inhibition of AQP3 with DFP00173 unmasks the inhibitory action of SR49059 on V1aR, likely supporting the notion that the effect of dDAVP on cell viability, mediated by V1aR signaling, occurs through inhibition of AQP3. In this respect, the incubation with DFP00173 alone also reduced the glycerol rate intake and cell growth (**Table 1**), likely suggesting AQP3 as a selective downstream effector of the combined actions of V1aR and V2R.

In the liver and renal polycystic disease, vasopressin increases the intracellular level of cAMP and cell proliferation (Wang et al., 2008; Mancinelli et al., 2016) *via* V2R signals. Targeting the V2R with tolvaptan has been, therefore, proposed for the therapeutical treatment of the autosomal dominant polycystic kidney disease (ADPKD) and renal carcinoma (van Gastel and Torres, 2017; Sinha et al., 2020). By contrast, in adrenocortical tumor cells, vasopressin blocks the cell cycle and reduces cell growth by inhibiting cyclin D1 (Schwindt et al., 2003). Adrenal tumors overexpress V1 receptors (Gagliardi et al., 2009). In adrenocortical carcinoma cells, stimulation with vasopressin, through V1R promotes cell senescence *via* RhoA signaling (Forti and Armelin, 2007). On another hand, dDAVP has been proposed to reduce tumor angiogenesis (Ripoll et al., 2013) and for the treatment of osteosarcoma, breast, and colon cancers for its ability to reduce cell growth and colony cell formation through V2R. Nevertheless, in these studies the expression and function of the V1aR have not been tested (Ripoll et al., 2010; Ripoll et al., 2013; Sobol et al., 2021), although vasopressin receptors, V1aR and V2R, are both expressed in neoplastic tissues, including colon mucosa (North, 2000). Inline, Real-Time PCR, and western blotting studies identified both VRs in HCT8 cells and colon cancer specimens. These findings were further supported by RNA-seq analysis showing that neoplastic colon specimens express VRs and AQP3. Although, RNAseq studies do not provide the relative expression of V1aR, V2R, and AQP3 in matching normal and tumor tissues from the same patient. However, the low number of biopsies does not allow us to propose a possible correlation between the relative expression of VRs and AQP3 functionality in the same tumor sample, which might be useful to design a therapeutic strategy and possibly to propose a classification of colon diseases based on differences in the expression and function of VRs and AQP3. To conclude in the present study, the action of dDAVP on human colon cells has been investigated by analyzing the relative contribution of V1aR and V2R on AQP3 expression and function using selective VRs antagonists. These findings indeed propose AQP3 as an effector of the orchestrated functions of V1aR and V2R. Several questions remain still open and needed to be further investigated. Nevertheless, the obtained data suggest that the AVP-dependent AQP3 pathway might represent a novel target in colon diseases associated with abnormal cell growth.

DATA AVAILABILITY STATEMENT

The original contributions presented in the study are included in the article/**Supplementary Material**, further inquiries can be directed to the corresponding author.

ETHICS STATEMENT

The studies involving human participants were reviewed and approved by the Ethical Committee of the University of Pisa (Protocol # 9989 from 2-20-2019). The patients/participants provided their written informed consent to participate in this study.

AUTHOR CONTRIBUTIONS

Conceptualization, MC, GT, and GV; Methodology, MC, MD, MM, PF, and PL; Investigation, GT, AD, MR, DS, and MV; Writing, GT, MC, MR, MD, and MM; Funding acquisition, GT. All authors have read and agree to the published version of the manuscript.

FUNDING

This work was supported by a project PRIN (2017R5ZE2C_002) to GT.

ACKNOWLEDGMENTS

We acknowledge Prof. Luana Poeta for her critical reading of the paper.

SUPPLEMENTARY MATERIAL

The Supplementary Material for this article can be found online at: https://www.frontiersin.org/articles/10.3389/fcell.2022.919438/full#supplementary-material

REFERENCES

Aburada, T., Ikarashi, N., Kagami, M., Ichikawa, Y., Sugitani, M., Maniwa, A., et al. (2011). Byakkokaninjinto Prevents Body Water Loss by Increasing the Expression of Kidney Aquaporin-2 and Skin Aquaporin-3 in KKAy Mice. *Phytother. Res.* 25 (6), 897–903. doi:10.1002/ptr.3358

Alonso, D. F., Skilton, G., Farías, E. F., Joffé, E. B. d. K., and Gomez, D. E. (1999). Antimetastatic Effect of Desmopressin in a Mouse Mammary Tumor Model. *Breast Cancer Res. Treat.* 57 (3), 271–275. doi:10.1023/a:1006291607871

Bankir, L. (2001). Antidiuretic Action of Vasopressin: Quantitative Aspects and Interaction between V1a and V2 Receptor-Mediated Effects. *Cardiovasc Res.* 51 (3), 372–390. doi:10.1016/s0008-6363(01)00328-5

Birnbaumer, M., Gilbert, S., and Rosenthal, W. (1994). An Extracellular Congenital Nephrogenic Diabetes Insipidus Mutation of the Vasopressin Receptor Reduces Cell Surface Expression, Affinity for Ligand, and Coupling to the Gs/adenylyl Cyclase System. *Mol. Endocrinol.* 8 (7), 886–894. doi:10.1210/mend.8.7.7984150

Boone, M., and Deen, P. M. T. (2008). Physiology and Pathophysiology of the Vasopressin-Regulated Renal Water Reabsorption. *Pflugers Arch. - Eur. J. Physiol.* 456 (6), 1005–1024. doi:10.1007/s00424-008-0498-1

Briley, E. M., Lolait, S. J., Axelrod, J., and Felder, C. C. (1994). The Cloned Vasopressin V1a Receptor Stimulates Phospholipase A2, Phospholipase C, and Phospholipase D through Activation of Receptor-Operated Calcium Channels. *Neuropeptides* 27 (1), 63–74. doi:10.1016/0143-4179(94)90017-5

Cabrijan, T., Skreb, F., and Susković, T. (1985). Syndrome of Inappropriate Secretion of Anti-diuretic Hormone (SIADH) Produced by an Adenocarcinoma of the Colon. Report of One Case. *Endocrinologie* 23 (3), 213–216.

Calamita, G., Perret, J., and Delporte, C. (2018). Aquaglyceroporins: Drug Targets for Metabolic Diseases? *Front. Physiol.* 9, 851. doi:10.3389/fphys.2018.00851

Camilleri, M., Carlson, P., Chedid, V., Vijayvargiya, P., Burton, D., and Busciglio, I. (2019). Aquaporin Expression in Colonic Mucosal Biopsies from Irritable Bowel Syndrome with Diarrhea. *Clin. Transl. Gastroenterology* 10 (4), e00019. doi:10.14309/ctg.0000000000000019

Carter, D. A., Fai, C. K., and Murphy, D. (1993). Neurohypophyseal Peptides as Regulators of Growth and Development. *J. Mol. Neurosci.* 4 (1), 11–19. doi:10.1007/bf02736686

Centrone, M., D'Agostino, M., Difonzo, G., De Bruno, A., Di Mise, A., Ranieri, M., et al. (2020a). Antioxidant Efficacy of Olive By-Product Extracts in Human Colon HCT8 Cells. *Foods* 10 (1), 11. doi:10.3390/foods10010011

Centrone, M., Gena, P., Ranieri, M., Di Mise, A., D'Agostino, M., Mastrodonato, M., et al. (2020b). *In Vitro* and *In Vivo* Nutraceutical Characterization of Two Chickpea Accessions: Differential Effects on Hepatic Lipid Over-Accumulation. *Antioxidants* 9 (3), 268. doi:10.3390/antiox9030268

Cheng, L. L., Stoev, S., Manning, M., Derick, S., Pena, A., Mimoun, M. B., et al. (2004). Design of Potent and Selective Agonists for the Human Vasopressin V1b Receptor Based on Modifications of [Deamino-Cys]arginine Vasopressin at Position 4. *J. Med. Chem.* 47 (9), 2375–2388. doi:10.1021/jm030611c

Chini, B., and Manning, M. (2007). Agonist Selectivity in the Oxytocin/vasopressin Receptor Family: New Insights and Challenges. *Biochem. Soc. Trans.* 35 (Pt 4), 737–741. doi:10.1042/bst0350737

Corciulo, S., Nicoletti, M. C., Mastrofrancesco, L., Milano, S., Mastrodonato, M., Carmosino, M., et al. (2019). AQP1-Containing Exosomes in Peritoneal Dialysis Effluent As Biomarker of Dialysis Efficiency. *Cells* 8 (4), 330. doi:10.3390/cells8040330

Di Giusto, G., Flamenco, P., Rivarola, V., Fernández, J., Melamud, L., Ford, P., et al. (2012). Aquaporin 2-increased Renal Cell Proliferation Is Associated with Cell Volume Regulation. *J. Cell. Biochem.* 113 (12), 3721–3729. doi:10.1002/jcb.24246

Di Mise, A., Venneri, M., Ranieri, M., Centrone, M., Pellegrini, L., Tamma, G., et al. (2019). Lixivaptan, a New Generation Diuretic, Counteracts Vasopressin-Induced Aquaporin-2 Trafficking and Function in Renal Collecting Duct Cells. *Int. J. Mol. Sci.* 21 (1), 183. doi:10.3390/ijms21010183

Forti, F. L., and Armelin, H. A. (2011). Arginine Vasopressin Controls p27Kip1 Protein Expression by PKC Activation and Irreversibly Inhibits the Proliferation of K-Ras-dependent Mouse Y1 Adrenocortical Malignant Cells. *Biochimica Biophysica Acta (BBA) - Mol. Cell Res.* 1813 (8), 1438–1445. doi:10.1016/j.bbamcr.2011.04.007

Forti, F. L., and Armelin, H. A. (2007). Vasopressin Triggers Senescence in K-Ras Transformed Cells via RhoA-dependent Downregulation of Cyclin D1. *Endocr. Relat. Cancer* 14 (4), 1117–1125. doi:10.1677/erc-07-0154

Gagliardi, L., Hotu, C., Casey, G., Braund, W. J., Ling, K.-H., Dodd, T., et al. (2009). Familial Vasopressin-Sensitive ACTH-independent Macronodular Adrenal Hyperplasia (VPs-AIMAH): Clinical Studies of Three Kindreds. *Clin. Endocrinol. (Oxf)* 70 (6), 883–891. doi:10.1111/j.1365-2265.2008.03471.x

Giron, S., Tejera, A. M., Ripoll, G. V., Gomez, D. E., and Alonso, D. F. (2002). Desmopressin Inhibits Lung and Lymph Node Metastasis in a Mouse Mammary Carcinoma Model of Surgical Manipulation. *J. Surg. Oncol.* 81 (1), 38–44. doi:10.1002/jso.10141

Gregoire, F., Lucidi, V., Zerrad-Saadi, A., Virreira, M., Bolaky, N., Delforge, V., et al. (2015). Analysis of Aquaporin Expression in Liver with a Focus on Hepatocytes. *Histochem Cell Biol.* 144 (4), 347–363. doi:10.1007/s00418-015-1341-3

Gupta, A., Sasarula, S., and Rao, P. V. (1986). The Syndrome of Inappropriate Secretion of Antidiuretic Hormone in a Case of Carcinoma of the Breast. *J. Assoc. Physicians India* 34 (6), 441–442.

Heasley, L. E. (2001). Autocrine and Paracrine Signaling through Neuropeptide Receptors in Human Cancer. *Oncogene* 20 (13), 1563–1569. doi:10.1038/sj.onc.1204183

Itoh, A., Tsujikawa, T., Fujiyama, Y., and Bamba, T. (2003). Enhancement of Aquaporin-3 by Vasoactive Intestinal Polypeptide in a Human Colonic Epithelial Cell Line. *J. Gastroenterol. Hepatol.* 18 (2), 203–210. doi:10.1046/j.1440-1746.2003.02949.x

Iwata, G., Iwai, N., and Nose, H. (1997). Segmental Difference of Water and Electrolyte Transport in Rat Colon *in Vivo*. *J. Basic Clin. Physiol. Pharmacol.* 8 (1-2), 13–29. doi:10.1515/jbcpp.1997.8.1-2.13

Izumi, Y., Nakayama, Y., Memetimin, H., Inoue, T., Kohda, Y., Nonoguchi, H., et al. (2008). Regulation of V2R Transcription by Hypertonicity and V1aR-V2R Signal Interaction. *Am. J. Physiology-Renal Physiology* 295 (4), F1170–F1176. doi:10.1152/ajprenal.00119.2008

Jayadeep, S., Nandakrishna, B., Varma, M., Vidyasagar, S, Khan, M. F., and Pai, K. (2020). Syndrome of Inappropriate Antidiuretic Hormone Release as the Initial Presentation of Adenocarcinoma of the Colon. *J. R. Coll. Physicians Edinb* 50 (3), 277–280. doi:10.4997/jrcpe.2020.312

Jung, H. J., Jang, H.-J., and Kwon, T.-H. (2021). Aquaporins Implicated in the Cell Proliferation and the Signaling Pathways of Cell Stemness. *Biochimie* 188, 52–60. doi:10.1016/j.biochi.2021.04.006

Jung, H. J., Park, J.-Y., Jeon, H.-S., and Kwon, T.-H. (2011). Aquaporin-5: a Marker Protein for Proliferation and Migration of Human Breast Cancer Cells. *PLoS One* 6 (12), e28492. doi:10.1371/journal.pone.0028492

Kapić, E., Bečić, F., and Todić, M. (2005). Modern Approach in Treatment of Diabetes Insipidus. *Bosn J Basic Med Sci* 5 (2), 38–42. doi:10.17305/bjbms.2005.3282

Klarenbeek, J. B., Goedhart, J., Hink, M. A., Gadella, T. W. J., and Jalink, K. (2011). A mTurquoise-Based cAMP Sensor for Both FLIM and Ratiometric Read-Out Has Improved Dynamic Range. *PLoS One* 6 (4), e19170. doi:10.1371/journal.pone.0019170

Kreda, S. M., Gynn, M. C., Fenstermacher, D. A., Boucher, R. C., and Gabriel, S. E. (2001). Expression and Localization of Epithelial Aquaporins in the Adult Human Lung. *Am. J. Respir. Cell Mol. Biol.* 24 (3), 224–234. doi:10.1165/ajrcmb.24.3.4367

Levin, M. H., and Verkman, A. S. (2006). Aquaporin-3-dependent Cell Migration and Proliferation during Corneal Re-epithelialization. *Invest. Ophthalmol. Vis. Sci.* 47 (10), 4365–4372. doi:10.1167/iovs.06-0335

Li, A., Lu, D., Zhang, Y., Li, J., Fang, Y., Li, F., et al. (2013). Critical Role of Aquaporin-3 in Epidermal Growth Factor-Induced Migration of Colorectal Carcinoma Cells and its Clinical Significance. *Oncol. Rep.* 29 (2), 535–540. doi:10.3892/or.2012.2144

Li, J., Zhang, X., He, Q., Feng, W., Ding, L., Wang, Z., et al. (2021). Pancreatic Neuroendocrine Tumor Producing Vasopressin. *Med. Baltim.* 100 (40), e27453. doi:10.1097/md.0000000000027453

Li, Z., Li, B., Zhang, L., Chen, L., Sun, G., Zhang, Q., et al. (2016). The Proliferation Impairment Induced by AQP3 Deficiency Is the Result of Glycerol Uptake and Metabolism Inhibition in Gastric Cancer Cells. *Tumor Biol.* 37 (7), 9169–9179. doi:10.1007/s13277-015-4753-8

Liao, S., Gan, L., Lv, L., and Mei, Z. (2021). The Regulatory Roles of Aquaporins in the Digestive System. *Genes & Dis.* 8 (3), 250–258. doi:10.1016/j.gendis.2019.12.011

Mancinelli, R., Franchitto, A., Glaser, S., Vetuschi, A., Venter, J., Sferra, R., et al. (2016). Vasopressin Regulates the Growth of the Biliary Epithelium in Polycystic Liver Disease. *Lab. Invest.* 96 (11), 1147–1155. doi:10.1038/labinvest.2016.93

Mannucci, P. M. (1997). Desmopressin (DDAVP) in the Treatment of Bleeding Disorders: the First 20 Years. *Blood* 90 (7), 2515–2521. doi:10.1182/blood.v90.7.2515.2515_2515_2521

Marlar, S., Jensen, H. H., Login, F. H., and Nejsum, L. N. (2017). Aquaporin-3 in Cancer. *Int. J. Mol. Sci.* 18 (10), 2106. doi:10.3390/ijms18102106

Méndez-Giménez, L., Rodríguez, A., Balaguer, I., and Frühbeck, G. (2014). Role of Aquaglyceroporins and Caveolins in Energy and Metabolic Homeostasis. *Mol. Cell. Endocrinol.* 397 (1-2), 78–92. doi:10.1016/j.mce.2014.06.017

Miller, R. L., Sandoval, P. C., Pisitkun, T., Knepper, M. A., and Hoffert, J. D. (2013). Vasopressin Inhibits Apoptosis in Renal Collecting Duct Cells. *Am. J. Physiology-Renal Physiology* 304 (2), F177–F188. doi:10.1152/ajprenal.00431.2012

Mobasheri, A., and Marples, D. (2004). Expression of the AQP-1 Water Channel in Normal Human Tissues: a Semiquantitative Study Using Tissue Microarray Technology. *Am. J. Physiology-Cell Physiology* 286 (3), C529–C537. doi:10.1152/ajpcell.00408.2003

Mobasheri, A., Wray, S., and Marples, D. (2005). Distribution of AQP2 and AQP3 Water Channels in Human Tissue Microarrays. *J. Mol. Hist.* 36 (1-2), 1–14. doi:10.1007/s10735-004-2633-4

Mola, M. G., Nicchia, G. P., Svelto, M., Spray, D. C., and Frigeri, A. (2009). Automated Cell-Based Assay for Screening of Aquaporin Inhibitors. *Anal. Chem.* 81 (19), 8219–8229. doi:10.1021/ac901526k

Mola, M. G., Saracino, E., Formaggio, F., Amerotti, A. G., Barile, B., Posati, T., et al. (2021). Cell Volume Regulation Mechanisms in Differentiated Astrocytes. *Cell Physiol. Biochem.* 55 (S1), 196–212. doi:10.33594/000000469

Monstein, H.-J., Truedsson, M., Ryberg, A., and Ohlsson, B. (2008). Vasopressin Receptor mRNA Expression in the Human Gastrointestinal Tract. *Eur. Surg. Res.* 40 (1), 34–40. doi:10.1159/000108655

Moon, C., Soria, J.-C., Jang, S. J., Lee, J., Hoque, M. O., Sibony, M., et al. (2003). Involvement of Aquaporins in Colorectal Carcinogenesis. *Oncogene* 22 (43), 6699–6703. doi:10.1038/sj.onc.1206762

Navarro-Almenzar, B., and Perianes, V. C. (2020). Syndrome of Inappropriate Antidiuretic Hormone Secretion in a Patient with Diffuse Large B-Cell Lymphoma. *Med. Clínica Engl. Ed.* 154 (11), 473. doi:10.1016/j.medcli.2019.06.031

North, W. G., Fay, M. J., and Du, J. (1999). MCF-7 Breast Cancer Cells Express Normal Forms of All Vasopressin Receptors Plus an Abnormal V2R☆. *Peptides* 20 (7), 837–842. doi:10.1016/s0196-9781(99)00070-4

North, W. G., Fay, M. J., Longo, K., and Du, J. (1997). Functional Vasopressin V1 Type Receptors Are Present in Variant as Well as Classical Forms of Small-Cell Carcinoma. *Peptides* 18 (7), 985–993. doi:10.1016/s0196-9781(97)00072-7

North, W. G. (2000). Gene Regulation of Vasopressin and Vasopressin Receptors in Cancer. *Exp. Physiol.* 85, 27s–40s. doi:10.1111/j.1469-445x.2000.tb00005.x

Okahira, M., Kubota, M., Iguchi, K., Usui, S., and Hirano, K. (2008). Regulation of Aquaporin 3 Expression by Magnesium Ion. *Eur. J. Pharmacol.* 588 (1), 26–32. doi:10.1016/j.ejphar.2008.03.063

Papadopoulos, M. C., Saadoun, S., and Verkman, A. S. (2008). Aquaporins and Cell Migration. *Pflugers Arch. - Eur. J. Physiol.* 456 (4), 693–700. doi:10.1007/s00424-007-0357-5

Pei, H. P., Liu, Z., Huang, L. S., and Zhu, H. (2011). Significance of Aquaporin-1 and Aquaporin-3 Expression in Colorectal Carcinoma. *Zhonghua Wei Chang. Wai Ke Za Zhi* 14 (4), 275–278.

Peplowski, M. A., Dicay, M., Baggio, C. H., Wysokinski, F., Renaux, B., Hollenberg, M. D., et al. (2018). Interferon Gamma Decreases Intestinal Epithelial Aquaporin 3 Expression through Downregulation of Constitutive Transcription. *J. Mol. Med.* 96 (10), 1081–1093. doi:10.1007/s00109-018-1681-2

Peplowski, M. A., Vegso, A. J., Iablokov, V., Dicay, M., Zaheer, R. S., Renaux, B., et al. (2017). Tumor Necrosis Factor α Decreases Aquaporin 3 Expression in Intestinal Epithelial Cells through Inhibition of Constitutive Transcription. *Physiol. Rep.* 5 (19), e13451. doi:10.14814/phy2.13451

Pifano, M., Garona, J., Capobianco, C. S., Gonzalez, N., Alonso, D. F., and Ripoll, G. V. (2017). Peptide Agonists of Vasopressin V2 Receptor Reduce Expression of Neuroendocrine Markers and Tumor Growth in Human Lung and Prostate Tumor Cells. *Front. Oncol.* 7, 11. doi:10.3389/fonc.2017.00011

Ranieri, M., Di Mise, A., Centrone, M., D'Agostino, M., Tingskov, S. J., Venneri, M., et al. (2021). Olive Leaf Extract (OLE) Impaired Vasopressin-Induced Aquaporin-2 Trafficking through the Activation of the Calcium-Sensing Receptor. *Sci. Rep.* 11 (1), 4537. doi:10.1038/s41598-021-83850-5

Ranieri, M., Di Mise, A., Tamma, G., and Valenti, G. (2019). Vasopressin-aquaporin-2 Pathway: Recent Advances in Understanding Water Balance Disorders. *F1000Res* 8, 149. doi:10.12688/f1000research.16654.1

Ripoll, G. V., Garona, J., Hermo, G. A., Gomez, D. E., and Alonso, D. F. (2010). Effects of the Synthetic Vasopressin Analog Desmopressin in a Mouse Model of Colon Cancer. *Anticancer Res.* 30 (12), 5049–5054.

Ripoll, G. V., Garona, J., Pifano, M., Farina, H. G., Gomez, D. E., and Alonso, D. F. (2013). Reduction of Tumor Angiogenesis Induced by Desmopressin in a Breast Cancer Model. *Breast Cancer Res. Treat.* 142 (1), 9–18. doi:10.1007/s10549-013-2724-6

Robben, J. H., Knoers, N. V. A. M., and Deen, P. M. T. (2005). Characterization of Vasopressin V2 Receptor Mutants in Nephrogenic Diabetes Insipidus in a Polarized Cell Model. *Am. J. Physiology-Renal Physiology* 289 (2), F265–F272. doi:10.1152/ajprenal.00404.2004

Rosenthal, W., Seibold, A., Antaramian, A., Gilbert, S., Birnbaumer, M., Bichet, D. G., et al. (1994). Mutations in the Vasopressin V2 Receptor Gene in Families with Nephrogenic Diabetes Insipidus and Functional Expression of the Q-2 Mutant. *Cell Mol. Biol. (Noisy-le-grand)* 40 (3), 429–436.

Russo, A., Ranieri, M., Di Mise, A., Dossena, S., Pellegrino, T., Furia, E., et al. (2017). Interleukin-13 Increases Pendrin Abundance to the Cell Surface in Bronchial NCI-H292 Cells via Rho/actin Signaling. *Pflugers Arch. - Eur. J. Physiol.* 469 (9), 1163–1176. doi:10.1007/s00424-017-1970-6

Schwindt, T. T., Forti, F. L., Juliano, M. A., Juliano, L., and Armelin, H. A. (2003). Arginine Vasopressin Inhibition of Cyclin D1 Gene Expression Blocks the Cell Cycle and Cell Proliferation in the Mouse Y1 Adrenocortical Tumor Cell Line. *Biochemistry* 42 (7), 2116–2121. doi:10.1021/bi026807g

Sinha, S., Dwivedi, N., Tao, S., Jamadar, A., Kakade, V. R., Neil, M. O., et al. (2020). Targeting the Vasopressin Type-2 Receptor for Renal Cell Carcinoma Therapy. *Oncogene* 39 (6), 1231–1245. doi:10.1038/s41388-019-1059-0

Sobol, N., Solernó, L., Beltrán, B., Vásquez, L., Ripoll, G., Garona, J., et al. (2021). Anticancer Activity of Repurposed Hemostatic Agent Desmopressin on AVPR2-expressing H-uman O-steosarcoma. *Exp. Ther. Med.* 21 (6), 566. doi:10.3892/etm.2021.9998

Terrillon, S., Barberis, C., and Bouvier, M. (2004). Heterodimerization of V1a and V2 Vasopressin Receptors Determines the Interaction with β-arrestin and Their Trafficking Patterns. *Proc. Natl. Acad. Sci. U.S.A.* 101 (6), 1548–1553. doi:10.1073/pnas.0305322101

Thibonnier, M., Conarty, D. M., and Plesnicher, C. L. (2000). Mediators of the Mitogenic Action of Human V1vascular Vasopressin Receptors. *Am. J. Physiology-Heart Circulatory Physiology* 279 (5), H2529–H2539. doi:10.1152/ajpheart.2000.279.5.H2529

Thibonnier, M. (1992). Signal Transduction of V1-Vascular Vasopressin Receptors. *Regul. Pept.* 38 (1), 1–11. doi:10.1016/0167-0115(92)90067-5

Valenti, G., and Tamma, G. (2021). The Vasopressin-Aquaporin-2 Pathway Syndromes. *Handb. Clin. Neurol.* 181, 249–259. doi:10.1016/b978-0-12-820683-6.00018-x

van Gastel, M. D. A., and Torres, V. E. (2017). Polycystic Kidney Disease and the Vasopressin Pathway. *Ann. Nutr. Metab.* 70 Suppl 1, 43–50. doi:10.1159/000463063

Wang, X., Wu, Y., Ward, C. J., Harris, P. C., and Torres, V. E. (2008). Vasopressin Directly Regulates Cyst Growth in Polycystic Kidney Disease. *J. Am. Soc. Nephrol.* 19 (1), 102–108. doi:10.1681/asn.2007060688

Weiss, J. P., and Everaert, K. (2019). Management of Nocturia and Nocturnal Polyuria. *Urology* 133, 24–33. doi:10.1016/j.urology.2019.09.022

Xia, H., Ma, Y.-F., Yu, C.-H., Li, Y.-J., Tang, J., Li, J.-B., et al. (2014). Aquaporin 3 Knockdown Suppresses Tumour Growth and Angiogenesis in Experimental Non-small Cell Lung Cancer. *Exp. Physiol.* 99 (7), 974–984. doi:10.1113/expphysiol.2014.078527

Yamamoto, N., Yoneda, K., Asai, K., Sobue, K., Tada, T., Fujita, Y., et al. (2001). Alterations in the Expression of the AQP Family in Cultured Rat Astrocytes during Hypoxia and Reoxygenation. *Mol. Brain Res.* 90 (1), 26–38. doi:10.1016/s0169-328x(01)00064-x

Yasir, M., and Mechanic, O. J. (2022). *Syndrome of Inappropriate Antidiuretic Hormone Secretion*. Treasure Island (FL): StatPearls StatPearls Publishing Copyright © 2022, StatPearls Publishing LLC.

Yasui, H., Kubota, M., Iguchi, K., Usui, S., Kiho, T., and Hirano, K. (2008). Membrane Trafficking of Aquaporin 3 Induced by Epinephrine. *Biochem. Biophysical Res. Commun.* 373 (4), 613–617. doi:10.1016/j.bbrc.2008.06.086

Yasui, M., Zelenin, S. M., Celsi, G., and Aperia, A. (1997). Adenylate Cyclase-Coupled Vasopressin Receptor Activates AQP2 Promoter via a Dual Effect on CRE and AP1 Elements. *Am. J. Physiology-Renal Physiology* 272 (4 Pt 2), F443–F450. doi:10.1152/ajprenal.1997.272.4.F443

Yde, J., Keely, S. J., and Moeller, H. B. (2021). Expression, Regulation and Function of Aquaporin-3 in Colonic Epithelial Cells. *Biochimica Biophysica Acta (BBA) - Biomembr.* 1863 (7), 183619. doi:10.1016/j.bbamem.2021.183619

Yde, J., Keely, S., Wu, Q., Borg, J. F., Lajczak, N., O'Dwyer, A., et al. (2016). Characterization of AQPs in Mouse, Rat, and Human Colon and Their Selective Regulation by Bile Acids. *Front. Nutr.* 3, 46. doi:10.3389/fnut.2016.00046

Zeuthen, T., and Klaerke, D. A. (1999). Transport of Water and Glycerol in Aquaporin 3 Is Gated by H+. *J. Biol. Chem.* 274 (31), 21631–21636. doi:10.1074/jbc.274.31.21631

Zhu, X., and Wess, J. (1998). Truncated V2 Vasopressin Receptors as Negative Regulators of Wild-type V2 Receptor Function. *Biochemistry* 37 (45), 15773–15784. doi:10.1021/bi981162z

Conflict of Interest: The authors declare that the research was conducted in the absence of any commercial or financial relationships that could be construed as a potential conflict of interest.

The handling editor SD declared a past collaboration with the author GT.

Publisher's Note: All claims expressed in this article are solely those of the authors and do not necessarily represent those of their affiliated organizations, or those of the publisher, the editors and the reviewers. Any product that may be evaluated in this article, or claim that may be made by its manufacturer, is not guaranteed or endorsed by the publisher.

frontiers | Frontiers in Cell and Developmental Biology

TYPE Original Research
PUBLISHED 02 September 2022
DOI 10.3389/fcell.2022.991659

OPEN ACCESS

EDITED BY
Alessia Remigante,
University of Messina, Italy

REVIEWED BY
Roberta De Zio,
University of Bari Aldo Moro, Italy
Teresa Pasqua,
University Magna Graecia of Catanzaro, Italy

*CORRESPONDENCE
Roberto Berra-Romani,
rberra001@hotmail.com
Francesco Moccia,
francesco.moccia@unipv.it

SPECIALTY SECTION
This article was submitted to Cellular Biochemistry, a section of the journal Frontiers in Cell and Developmental Biology

RECEIVED 11 July 2022
ACCEPTED 08 August 2022
PUBLISHED 02 September 2022

CITATION
Berra-Romani R, Vargaz-Guadarrama A, Sánchez-Gómez J, Coyotl-Santiago N, Hernández-Arambide E, Avelino-Cruz JE, García-Carrasco M, Savio M, Pellavio G, Laforenza U, Lagunas-Martínez A and Moccia F (2022), Histamine activates an intracellular Ca^{2+} signal in normal human lung fibroblast WI-38 cells. *Front. Cell Dev. Biol.* 10:991659. doi: 10.3389/fcell.2022.991659

Histamine activates an intracellular Ca^{2+} signal in normal human lung fibroblast WI-38 cells

Roberto Berra-Romani[1]*, Ajelet Vargaz-Guadarrama[1], Josué Sánchez-Gómez[1], Nayeli Coyotl-Santiago[1], Efraín Hernández-Arambide[1], José Everardo Avelino-Cruz[2], Mario García-Carrasco[3], Monica Savio[4], Giorgia Pellavio[4], Umberto Laforenza[4], Alfredo Lagunas-Martínez[5] and Francesco Moccia[6]*

[1]Department of Biomedicine, School of Medicine, Benemérita Universidad Autónoma de Puebla, Puebla, México, [2]Laboratory of Molecular Cardiology, Institute of Physiology, Benemérita Universidad Autónoma de Puebla, Puebla, México, [3]Department of Immunology, School of Medicine, Benemérita Universidad Autónoma de Puebla, Puebla, México, [4]Department of Molecular Medicine, University of Pavia, Pavia, Italy, [5]Direction of Chronic Infections and Cancer, Research Center in Infection Diseases, National Institute of Public Health, Morelos, México, [6]Laboratory of General Physiology, Department of Biology and Biotechnology "Lazzaro Spallanzani", University of Pavia, Pavia, Italy

Histamine is an inflammatory mediator that can be released from mast cells to induce airway remodeling and cause persistent airflow limitation in asthma. In addition to stimulating airway smooth muscle cell constriction and hyperplasia, histamine promotes pulmonary remodeling by inducing fibroblast proliferation, contraction, and migration. It has long been known that histamine receptor 1 (H1R) mediates the effects of histamine on human pulmonary fibroblasts through an increase in intracellular Ca^{2+} concentration ($[Ca^{2+}]_i$), but the underlying signaling mechanisms are still unknown. Herein, we exploited single-cell Ca^{2+} imaging to assess the signal transduction pathways whereby histamine generates intracellular Ca^{2+} signals in the human fetal lung fibroblast cell line, WI-38. WI-38 fibroblasts were loaded with the Ca^{2+}-sensitive fluorophore, FURA-2/AM, and challenged with histamine in the absence and presence of specific pharmacological inhibitors to dissect the Ca^{2+} release/entry pathways responsible for the onset of the Ca^{2+} response. Histamine elicited complex intracellular Ca^{2+} signatures in WI-38 fibroblasts throughout a concentration range spanning between 1 μM and 1 mM. In accord, the Ca^{2+} response to histamine adopted four main temporal patterns, which were, respectively, termed peak, peak-oscillations, peak-plateau-oscillations, and peak-plateau. Histamine-evoked intracellular Ca^{2+} signals were abolished by pyrilamine, which selectively blocks H1R, and significantly reduced by ranitidine, which selectively inhibits H2R. Conversely, the pharmacological blockade of H3R and H4R did not affect the complex increase in $[Ca^{2+}]_i$ evoked by histamine in WI-38 fibroblasts. In agreement with these findings, histamine-induced intracellular Ca^{2+} signals were initiated by intracellular Ca^{2+} release from the endoplasmic reticulum through inositol-1,4,5-trisphosphate ($InsP_3$) receptors ($InsP_3R$) and sustained by store-operated Ca^{2+} channels (SOCs). Conversely,

L-type voltage-operated Ca^{2+} channels did not support histamine-induced extracellular Ca^{2+} entry. A preliminary transcriptomic analysis confirmed that WI-38 human lung fibroblasts express all the three $InsP_3R$ isoforms as well as STIM2 and Orai3, which represent the molecular components of SOCs. The pharmacological blockade of $InsP_3$ and SOC, therefore, could represent an alternative strategy to prevent the pernicious effects of histamine on lung fibroblasts in asthmatic patients.

KEYWORDS

histamine, intracellular Ca^{2+}, lung fibroblasts, WI-38, Ca^{2+} oscillations, $InsP_3$ receptors, store-operated Ca^{2+} entry

Introduction

Asthma is a heterogeneous disease, generally characterized by chronic inflammation of the airways, defined by a clinical history of respiratory symptoms, such as wheezing, shortness of breath, chest tightness, and cough that vary in intensity and frequency, along with variable expiratory airflow (GBD Diseases and Injuries Collaborators, 2020). About 300 million people suffer from asthma worldwide and it is likely that, by 2025, another 100 million people will be affected by this disease (Dharmage et al., 2019).

The complex network of inflammatory responses in the pathophysiology of asthma involves the release of inflammatory mediators, such as cytokines, chemokines, proteases, and histamine (Murdoch and Lloyd, 2010). Histamine has been a widely recognized inflammatory mediator released from mast cells and could play a key role in the pathophysiology of asthma (Yamauchi and Ogasawara, 2019). Tomioka et al. (1984) estimated that the number of mast cells and the concentration of histamine in bronchoalveolar lavage fluid of asthmatic patients was higher than that of healthy subjects. In addition, Carroll et al. (2002) demonstrated that mast cell degranulation is related to the severity of asthma. Salomonsson et al. (2019) recently reported that elevated levels of circulating mast cell progenitors are related to reduced lung function in asthmatic patients.

In vitro studies demonstrated that histamine stimulated lung fibroblast collagen synthesis (Garbuzenko et al., 2004; Veerappan et al., 2013), migration (Kohyama et al., 2010), proliferation (Jordana et al., 1988; Veerappan et al., 2013) and human lung myofibroblast contraction (Horie et al., 2014). However, the transduction mechanisms whereby histamine leads to these effects in lung fibroblasts are still unclear. Histamine is thought to act by stimulating one or more of four types of plasmalemmal histaminergic receptor (HR) (H1R, H2R, H3R, and H4R) (Panula et al., 2015; Panula, 2021). The expression of H1R and, in less proportion, H2R has been reported in normal human lung fibroblasts (Veerappan et al., 2013) and their participation in promoting lung fibroblast activation has been proposed (Jordana et al., 1988; Garbuzenko et al., 2004; Kunzmann et al., 2007; Veerappan et al., 2013). In addition, H4R could promote lung fibroblast migration (Kohyama et al., 2010). Stimulation of H1R results in an increase in intracellular Ca^{2+} concentration ($[Ca^{2+}]_i$) in human valvular myofibrobasts (Liang et al., 2003), pteryglial derived fibroblasts (Maini et al., 2002), human gingival fibroblasts (Niisato et al., 1996; Ogata et al., 1999; Gutiérrez-Venegas and Rodríguez-Pérez, 2012), rheumatoid synovial fibroblasts (Zenmyo et al., 1995) human skin fibroblasts (Johnson et al., 1990), human subcutaneous fibroblasts (Pinheiro et al., 2013), and human lung fibroblasts (Zheng et al., 1994; Horie et al., 2014). While H3R are predominantly located in neurons (Abdulrazzaq et al., 2022), H4R are preferentially expressed in cells of the immune system and in blood forming organs, especially in mast cells, dendritic cells, basophils, eosinophils, monocytes, and T lymphocytes (Sarasola et al., 2021). However, immunostaining demonstrated that also human dermal fibroblasts express the H4R (Ikawa et al., 2008). Signaling mechanisms for the H4R receptor are much less well understood but appear to involve an increase in $[Ca^{2+}]_i$ (Panula et al., 2015).

An elevation in $[Ca^{2+}]_i$ in fibroblasts is key to protein synthesis, transcription factor activation, migration, progression through the cell cycle, and cell viability (Janssen et al., 2015). Resting $[Ca^{2+}]_i$ is maintained at very low levels (~100–200 nM), while the extracellular Ca^{2+} concentration is 1000-fold higher (> 1 mM) and the Ca^{2+} concentration in the primary intracellular Ca^{2+} store, the endoplasmic reticulum (ER), fluctuates between 100–800 μM (Sadras et al., 2021a). An array of agonists, such as bradykinin, thrombin, trypsin, adenosine trisphosphate, angiotensin II, and histamine, increases the $[Ca^{2+}]_i$ in pulmonary fibroblasts at concentrations ranging from approximately 100 nM to 0.1 mM (Janssen et al., 2015). The $[Ca^{2+}]_i$ can be increased by two main mechanisms upon cellular stimulation: the first one is through the release of Ca^{2+} from the ER and the second one is through the inflow of Ca^{2+} from the extracellular medium. In several cell types, histamine bind to the G_q-protein-coupled receptor (G_qPCR), H1R, which activates phospholipase C (PLC). PLC hydrolyzes a membrane phospholipid, phosphatidylinositol 4, 5 bisphosphate (PIP_2), to produce inositol-1, 4, 5-trisphosphate ($InsP_3$). $InsP_3$ triggers Ca^{2+} mobilization from the ER through $InsP_3$ receptors ($InsP_3R$) that

are located on the ER membrane and can in turn activate adjacent ryanodine receptors (RyR) through the process of Ca^{2+}-induced Ca^{2+} release (CICR) (Paltauf-Doburzynska et al., 2000; Clapham, 2007; Horie et al., 2014; Ishida et al., 2014; Berra-Romani et al., 2020). Extracellular Ca^{2+} can permeate the plasma membrane through a wide variety of ion channels, including voltage-operated channels (VOC) (Janssen et al., 2015; Rahman et al., 2016) and agonist-operated channels, which comprise three types of channels: 1) receptor-operated channels (ROC) (Saliba et al., 2015), which are ionotropic receptors stimulated by direct ligand binding, 2) second messenger-operated channels (SMOC), which are activated by intracellularly generated mediators, such as cyclic nucleotides, diacylglycerol (Hofmann et al., 2017), and arachidonic acid, and 3) store-operated Ca^{2+} channels (SOC), which are the main Ca^{2+} entry pathway in non-excitable cells. In the ER, Stromal Interaction Molecules (STIM1/2) act as sensors of ER Ca^{2+} concentration that, after a reduction in intraluminal Ca^{2+}, multimerize and translocate towards peripheral ER cisternae to functionally interact with the Ca^{2+} permeable Orai channels on the plasma membrane (Bendiks et al., 2020). The following influx of Ca^{2+} has been termed store-operated Ca^{2+} entry (SOCE) and mediates agonist-induced Ca^{2+} influx in human fibroblasts isolated from several tissues, including lungs (Guzmán-Silva et al., 2015; Vazquez-de-Lara et al., 2018).

It has been demonstrated that histamine triggers an increase in $[Ca^{2+}]_i$ also in human lung fibroblasts (Zheng et al., 1994; Horie et al., 2014). However, the molecular mechanisms implicated in this response, which are likely to regulate the multiple fibroblast function involved in asthma remodeling, remain to be elucidated. Therefore, this study aimed to examine for the first time the mechanisms underlying histamine-induced increase in $[Ca^{2+}]_i$ in fetal human pulmonary WI-38 fibroblasts.

Materials and methods

Cell culture

Human fetal lung fibroblast cell lines were purchased from American Type Culture Collection, Collection WI-38 (ATCC® CCL-75™) and cultured to 75% confluence in DMEM (Dulbecco's Modified Eagle Medium) culture medium supplemented with 10% fetal bovine serum and 1% penicillin-streptomycin at 37°C in an atmosphere of 95% O_2 and 5% CO_2. Fibroblasts from passages 5–10 were seeded on coverslips for 24 h and then incubated for 48 h in medium devoid of serum.

Physiological solutions

Physiological saline solution (PSS) with the following composition (in mM) 150 NaCl, 6 KCL, 1.5 CaCl2 1 MgCl2, 10 glucose, 10 HEPES was used for this study. To obtain Ca^{2+}-free physiological saline solution ($0Ca^{2+}$), Ca^{2+} was replaced with 2 mM NaCl and 0.5 mM EGTA was added as a Ca^{2+} chelator. Osmolarity was measured with an osmometer (Wescor 5500, Logan, UT, United States) solutions were adjusted to pH 7.4 with NaOH.

Measurement of $[Ca^{2+}]_i$

The technique for Ca^{2+} measurement in fibroblasts has been previously described (Guzmán-Silva et al., 2015), and is explained in detail below. Fibroblasts attached to coverslips were washed twice PSS and incubated with 3 μM FURA-2 acetoxymethyl ester (FURA-2/AM) in PSS for 30 min at room temperature (21°C–23°C). Cells were incubated for 30 min in PSS free of FURA-2/AM. The coverslips were washed and fixed to the bottom of a Petri dish using a drop of silicone. The Petri dish was mounted on a stage of the Axiolab upright epifluorescence microscope (Carl Zeiss, Oberkochen, Germany), equipped with a 100 W mercury lamp (OSRAM HBO 50). A Zeiss X63 Achroplan objective (water immersion, working distance 2.0 mm, numerical aperture 0.9) was used to visualize fibroblasts. Cells were alternately excited at 340 nm and 380 nm using a filter spinning wheel with a shutter (Lambda 10, Sutter Instrument, Novato, CA, United States) and light emitted was detected at 510 nm. The Ca^{2+} signal was measured in individual fibroblasts, using software that allows to delimit each cell by drawing on the acquired images a region of interest. To control the camera (Extended-ISIS camera, Photonic Science, Millham, United Kingdom), the filter rotating wheel, as well as to draw the regions of interest of the fluorescent signal to be measured, a customized software, previously validated, running in LINUX environment, was used. The signal measurement was captured every 3 s and the images obtained were stored on a hard disk and subsequently converted into 340/380 ratio images using ImageJ software (National Institutes of Health, United States, https://imagej.nih.gov/ij/). An increase in 340/380 is indicative of an elevation in $[Ca^{2+}]_i$ (Ferrera et al., 2021; Remigante et al., 2021). Experiments were performed at room temperature (21°C–23°C). All experiments were performed in triplicate using 3 different passages of fibroblasts for each of the conditions.

RT-qPCR

Total RNA was isolated from fibroblasts using QIAzol Lysis Reagent (Qiagen SpA, Milan, Italy), and reverse transcription was performed as described in (Ferrera et al., 2021; Negri et al., 2021). Reverse transcription was always performed in the presence (positive) or in the absence (negative control) of the reverse transcriptase enzyme (not shown), as shown elsewhere

TABLE 1 Primer sequences used for reverse transcription/polymerase chain reaction.

Gene	Primer sequences	Size (bp)	Accession number	
Orai1	Forward-5′-AGTTACTCCGAGGTGATGAG-3′	257	NM_032790.3	
	Reverse-5′-ATGCAGGTGCTGATCATGAG-3′			
Orai2	Forward-5′-CCATAAGGGCATGGATTACC-3′	334	NM_001126340.1	variant 1
	Reverse-5′-CAGGTTGTGGATGTTGCTCA-3′		NM_032831.2	variant 2
Orai3	Forward-5′-CCAAGCTCAAAGCTTCCAGCC-3′	159	NM_152,288.2	
	Reverse-5′-CAAAGAGGTGCACAGCCACCA-3′			
Stim1	Forward-5′-CCTCAGTATGAGGAGACCTT-3′	347	NM_003156.3	
	Reverse-5′-TCCTGAAGGTCATGCAGACT-3′			
Stim2	Forward-5′-AAACACAGCCATCTGCACAG-3′	186	NM_020860.2	
	Reverse-5′-GGGAAGTGTCGTTCCTTTGA -3′			
$InsP_3R1$	Forward 5′-TCAACAAACTGCACCACGCT-3′	180	ENSG00000150995	
	Reverse 5′-CTCTCATGGCATTCTTCTCC-3′			
$InsP_3R2$	Forward 5′-ACCTTGGG GTTAGTGGATGA-3′	158	ENSG00000123104	
	Reverse 5′-CCTTGTTTGGCTTGCTTTGC-3′			
$InsP_3R3$	Forward 5′-TGGCTTCATCAGCACTTTGG-3′	173	ENSG00000096433	
	Reverse 5′-TGTCCTGCTTAGTCTGCTTG-3′			
RyR1	Hs00166991 Thermo Fisher Scientific	75	NM_000540.3	
RyR2	Hs00181461 Thermo Fisher Scientific	65	NM_001035	
RyR3	Hs00168821 Thermo Fisher Scientific	63	NM_001036.6	
Trpc1	Forward 5′-ATCCTACACTGGTGGCAGAA-3′	307		
	Reverse 5′-AACAAAGCAAAGCAGGTGCC-3′			
Trpc3	Forward 5′-GGAGATCTGGAATCAGCAGA-3′	336	NM_001130698.1	v
	Reverse 5′-AAGCAGACCCAGGAAGATGA-3′		NM_003305.2	variant
Trpc4	Forward 5’-ACCTGGGACCTCTGCAAATA-3′	300	NM_016179.2	va
	Reverse 5′-ACATGGTGGCACCAACAAAC-3′		NM_001135955.1	va
			NM_001135956.1	v
			NM_001135957.1	va
			NM_003306.1	va
			NM_001135958.1	va
Trpc5	Forward 5′-GAGATGACCACAGTGAAGAG-3′	221	NM_012471.2	
	Reverse 5′-AGACAGCATGGGAAACAGGA-3′			
Trpc6	Forward 5′-AGCTGTTCCAGGGCCATAAA-3′	341	NM_004621.5	
	Reverse 5′-AAGGAGTTCATAGCGGAGAC-3′			
Trpc7	Forward 5′-CACTTGTGGAACCTGCTAGA-3′	387	NM_020389.1	
	Reverse 5′-CATCCCAATCATGAAGGCCA-3′			

(Zuccolo et al., 2019; Zuccolini et al., 2022). cDNA amplification was performed using KAPA SYBR FAST qPCR Master Mix (KAPA BIOSYSTEMS, United States), and the primers used for amplification are listed the Table 1. The conditions were as follows: initial denaturation at 95°C for 5 min; 40 cycles of denaturation at 95°C for 10 s; annealing and extension at 60°C for 30 s, PCR products were separated on a 3% Nusieve® (2:1) gel agarose, stained with ethidium bromide, and acquired with the iBrightTM CL1000 Imaging System (Thermo Fisher Scientific Inc., United States). The molecular weight of the PCR products was compared with the DNA molecular weight marker VIII (Roche Molecular Biochemicals, Italy).

Data analysis

For the acquisition of fluorescence values, ImageJ software was used, and Origin Pro 2021 and GraphPad Prism 8.0 were used for graphing and statistical analysis of the results.

Statistical design

Data were expressed as mean ± standard error (SE). Non-Gaussian data, identified by the D'Agostino and Pearson omnibus normality test ($p \leq 0.05$) were statistically analyzed by the nonparametric Mann-

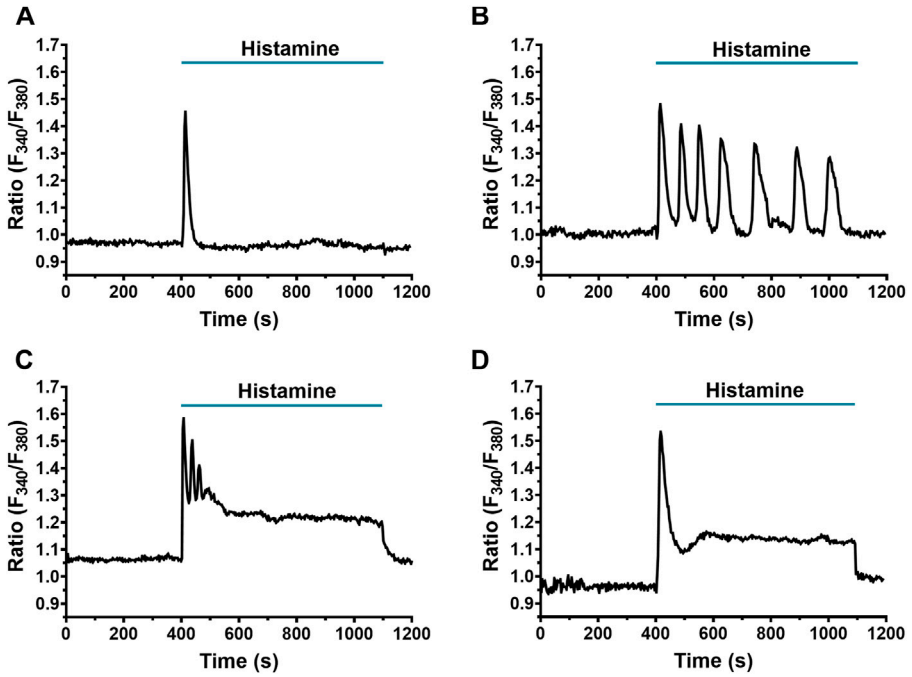

FIGURE 1
Heterogeneity in the Ca^{2+} response elicited by histamine in WI-38 human lung fibroblasts. Application of histamine (300 μM) elicited different Ca^{2+} signal patterns in FURA-2 AM-loaded WI-38 human lung fibroblasts. The intracellular Ca^{2+} signal consisted of **(A)** a rapid Ca^{2+} peak (spike) (19.28% of cells analyzed) which could be followed by **(B)** Ca^{2+} oscillations (64.70%) (peak-oscillations), **(C)** sustained plateau, superimposed by Ca^{2+} oscillations (13.39%) (peak-plateau-oscillations) or **(D)** only a plateau (0.65%) (peak-plateau). In this and the following figures, histamine was added at the time indicated by the horizontal bar drawn over the Ca^{2+} signal recording.

Whitney test for two groups and Kruskal–Wallis for more than two groups. For normal data, an unpaired Student *t*-test for two groups and ANOVA for more than two groups were used. A value of $p \leq 0.05$ was considered statistically significant.

Histamine concentration-response data were adjusted by the following Eq. 1:

$$Y = \frac{100}{1 + \frac{EC_{50}}{[Histamine]}} \quad (1)$$

where Y is the response (relative to the Ca^{2+} transient amplitude), [Histamine] is the histamine concentration and the mean maximal effective concentration (EC_{50}) is the [Histamine] that induced 50% of the maximal response.

Results

Histamine causes a heterogeneous Ca^{2+} signal in human lung fibroblasts of the WI-38 cell line

Using digital fluorescence imaging with FURA-2/AM $[Ca^{2+}]_i$ was measured simultaneously in several individual fibroblasts from the same population. A 22.5% of WI-38 fibroblasts displayed spontaneous Ca^{2+} oscillations, as also reported in human cardiac fibroblasts (Chen et al., 2010). These cells were, therefore, discarded from subsequent analysis (Faris et al., 2022). Application of histamine (300 μM), even in cells in the same microscopic field, elicited Ca^{2+} signals showing heterogeneous kinetics, which were classified into 4 different patterns: the first consisted of a rapid and transient increase in $[Ca^{2+}]_i$, termed peak (59/306 cells, 19.28%, Figure 1A); the second in a peak followed by cyclic increases and decreases in $[Ca^{2+}]_i$, termed peak-oscillations (198/306 cells, 64.70%, Figure 1B); the third in a peak with oscillations and a sustained increase in $[Ca^{2+}]_i$, termed peak-plateau-oscillations (41/306 cells, 13.39%, Figure 1C); and finally, the fourth pattern which was the least frequent, consisted of a peak accompanied by a plateau, and was termed peak-plateau (2/306 cells, 0.65%, Figure 1D). Only 1.96% (6/306 cells) of the analyzed fibroblasts did not respond to histamine 300 μM.

Histamine generates a Ca^{2+} signal in a concentration-dependent manner in WI-38 human lung fibroblasts

Typical recordings of the Ca^{2+} signals evoked by different histamine concentrations (100 nM–1 mM) are shown in Figure 2A. Histamine did not elicit any discernible increase in

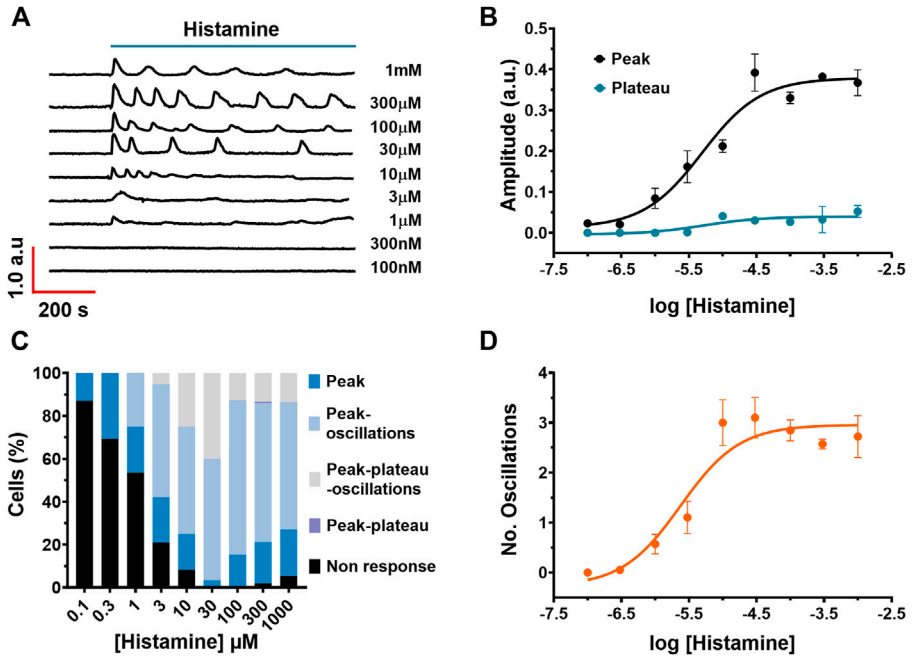

FIGURE 2
Concentration-dependent effect of histamine on Ca^{2+} signalling in WI-38 human lung fibroblasts. **(A)** Typical intracellular Ca^{2+} recordings in WI-38 cells loaded with FURA-2/AM exposed to different histamine concentrations ranging from 100 nM to 1 mM. The baseline of Ca^{2+} tracings has been shifted to avoid their overlapping for representation proposes. **(B)** Non-cumulative concentration-response relationship. Data points are the mean ± SE of the initial Ca^{2+} peak amplitude (black circles) or plateau amplitude (blue circles) plotted against the logarithm of histamine concentration. The continuous curves were obtained by fitting the data to Eq. 1, as shown in Materials and methods, which yielded EC_{50} values of 4.96 and 5.25 μM for peak amplitude (black line) and plateau amplitude (blue line), respectively. Data points were obtained of at least 19 cells. **(C)** Percentage of cells that presented each of the Ca^{2+} response patterns indicated in function of histamine concentrations applicated to WI-38 fibroblasts. **(D)** Data points are the mean ± SE of the number of oscillations measured over the first 400 s after histamine application, plotted against the logarithm of histamine concentration. The continuous curve was obtained by fitting the data to Eq. 1, as shown in Materials and methods, which yielded EC_{50} values of 2.38 μM.

$[Ca^{2+}]_i$ at very low concentrations, such as 100 and 300 nM. The Ca^{2+} response to histamine appeared at 1–3 μM; at these concentrations, the Ca^{2+} signal arising in most WI-38 cells displayed a single peak in response to agonist stimulation. However, at 10 μM histamine, the Ca^{2+} peak was followed by a short train of consecutive Ca^{2+} oscillations. The number of oscillations over 60 min of histamine application was increased at histamine concentrations ranging from 30 μM up to 1 mM. The non-cumulative concentration-response curve of histamine-induced elevation in $[Ca^{2+}]_i$ is depicted in Figure 2B (black circles), which shows that the increase in histamine concentration produces an increase in the amplitude of the initial Ca^{2+} response (peak). The maximum increase in the peak amplitude was observed at concentrations higher than 300 μM, whereas raising histamine concentration up to 1 mM did not significantly augment the magnitude of the response. Slight stimulation occurred at 3 μM, while no effect was detectable at concentrations lower than 1 μM (100 nM and 300 nM). The concentration of histamine required to produce a half maximal response (EC_{50}), which was calculated by fitting the concentration-response curve as described in Materials and Methods, was 4.96 μM (Figure 2B, black circles). Likewise, in cells that presented a plateau in the Ca^{2+} waveform, the EC_{50} of the plateau amplitude was equal to 5.25 μM (Figure 2B, blue circles). In order to assess whether the pattern of the Ca^{2+} signal was dependent on histamine concentration, the frequency of each Ca^{2+} signature detected at each histamine concentration (100 nM–1 mM) was calculated (Figure 2C). The data indicate that the spike pattern (see Figures 1A, 2C) is more common when fibroblasts are stimulated with low histamine concentrations (100 nM–1 μM), whereas the spike-oscillations patterns is more frequent as the histamine concentration is increased (3 μM–1 mM) (see Figures 1B,C, 2B). In accord, the number of oscillations recorded over the first 400 s after histamine application was increased in a histamine concentration-response manner with a EC_{50} = 2.37 μM (Figure 2D).

Desensitization of the Ca^{2+} response by repeated stimulation of WI-38 human lung fibroblasts with histamine

Homologous desensitization is a feature of GqPCRs, including H1R (Chen et al., 2014; Burghi et al., 2021).

10.3389/fcell.2022.991659

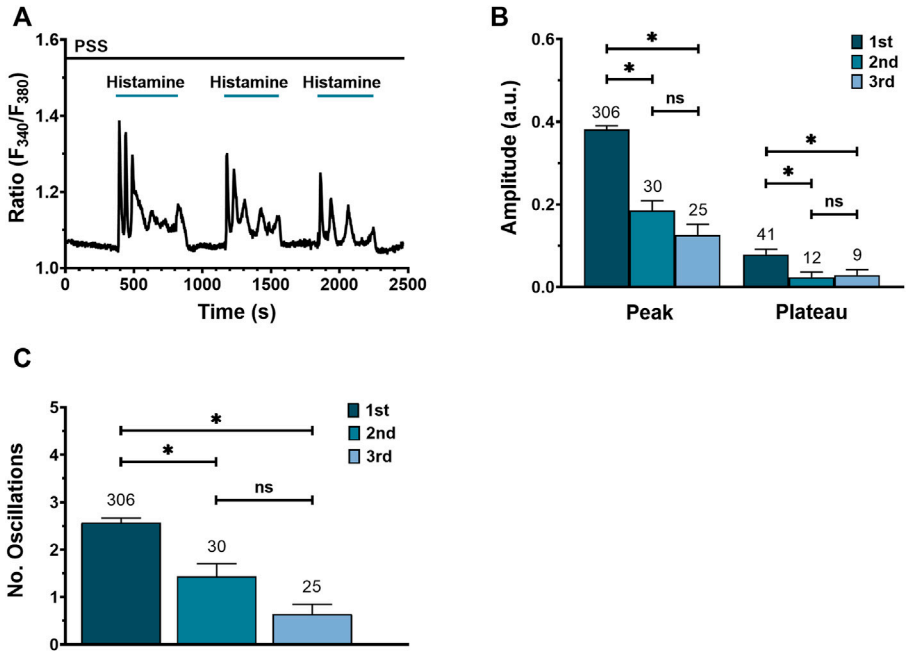

FIGURE 3
Effect of consecutive histamine applications on Ca^{2+} signal in WI-38 human lung fibroblasts WI-38. **(A)** Representative recording of a triple application of histamine (300 μM) in one cell, each followed by a washout with physiological saline solution (PSS). **(B)** Mean ± SE of peak and plateau amplitudes of the Ca^{2+} transient evoked by 3 consecutive histamine applications: first application (1st), second application (2nd), third application (3rd). **(C)** Mean ± SE of the number of oscillations measured over 400 s after each histamine application. The number in the figure represents the number of cells studied. Comparison between groups was performed using the Kruskal–Wallis test (* = $p \leq 0.05$; ns = no statistically relevant differences between groups).

Figure 3A shows a typical Ca^{2+} recording from a WI-38 fibroblast exposed to three consecutive applications of 300 μM histamine followed by PSS washout. Histamine elicited a similar Ca^{2+} response consisting in an initial Ca^{2+} peak followed by sustained plateau, superimposed by Ca^{2+} oscillations. However, the peak and plateau amplitudes (Figure 3B), as well as the number of oscillations (Figure 3C), were significatively reduced by repetitive histamine stimulation. These data suggest that the application of a maximal concentration of histamine (300 μM) to the same fibroblast leads to receptor desensitization.

Histamine-evoked elevation in $[Ca^{2+}]_i$ in WI-38 human lung fibroblasts is primarily mediated through activation of H1R and to a lesser extent through H2R

In order to elucidate the HR subtype through which histamine triggers an intracellular Ca^{2+} signal in WI-38 human lung fibroblasts, specific HR antagonists were used: for H1Rs pyrilamine (100 μM), for H2Rs ranitidine (50 μM), for H3R clobenpropit (50 μM) and, finally, for the H4R receptor, NJ7777120 (10 μM). After 30 min preincubation and in the continuous presence of the histaminergic antagonists, histamine (300 μM) was applied as indicated by the green bars. In order to confirm cell viability, arachidonic acid (AA) 50 μM was applied in cells in which histamine failed to induce an increase in $[Ca^{2+}]_i$ (Berra-Romani et al., 2019). Pharmacological manipulation of HR in WI-38 human lung fibroblasts revealed that H1R blockage completely abolished the histamine-evoked Ca^{2+} signal (Figure 4A), H2R blockage significantly decreased the amplitude of the Ca^{2+} signal (Figure 4B), while H3R (Figure 4C) and H4R blockage (Figure 4D) had no significant effect. In Figure 4E, the statistical comparison between the mean ± SE peak amplitude of the Ca^{2+} signals evoked by histamine 300 μM in the absence (Ctrl) and presence of the different antihistaminergic receptors antagonists (H1R, H2R, H3R, and H4R) are summarized. These results indicate that, for the $[Ca^{2+}]_i$ elevation to take place in the lung fibroblast cell line, WI-38, the activation of mainly H1R and, to a lesser extent, H2R is necessary, whereas H3R and H4R seem to play no role.

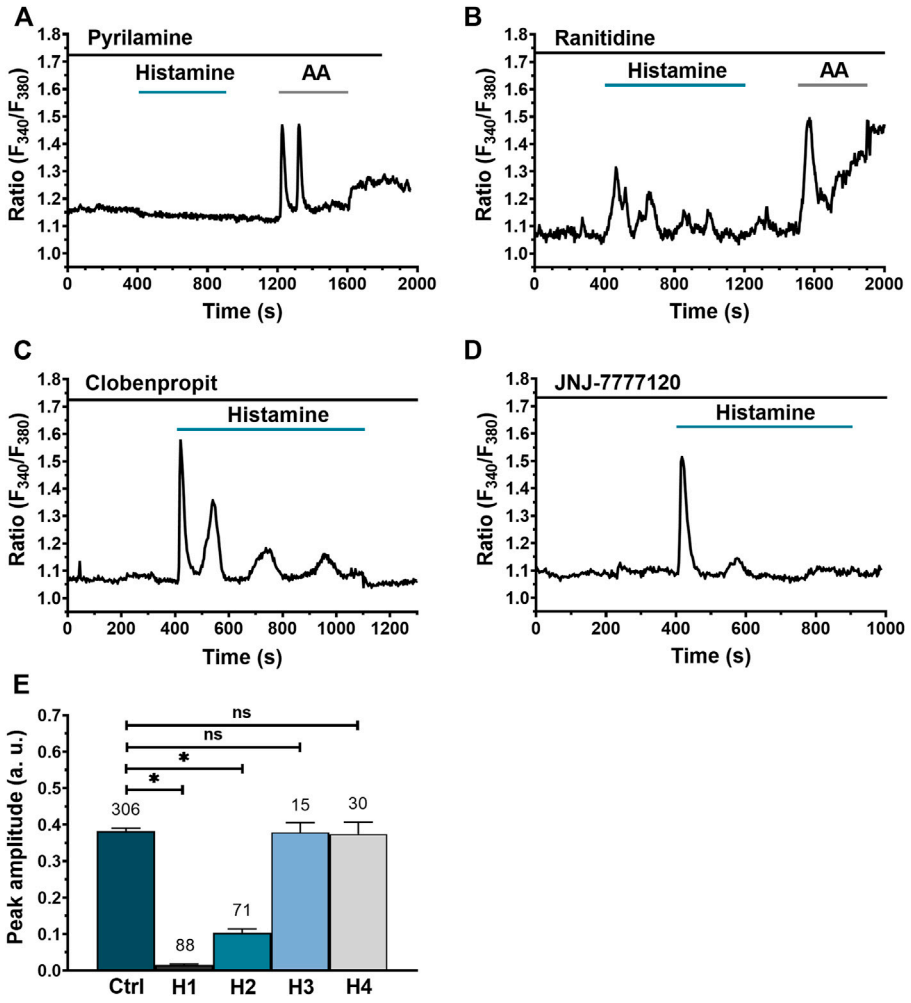

FIGURE 4
Dissection of histaminergic receptors (HR) responsible for histamine-evoked Ca^{2+} signal in WI-38 human lung fibroblasts. **(A)** Typical recording of histamine-evoked Ca^{2+} signal in the presence of the H1R antagonist, pyrilamine (100 μM). **(B)** Typical recording of the histamine-evoked Ca^{2+} signal in the presence of the H2R antagonist, ranitidine (50 μM). **(C)** Typical recording of the histamine-evoked Ca^{2+} signal in the presence of the H3R antagonist, clobenpropit (50 μM). **(D)** Typical recording of histamine-evoked Ca^{2+} signal in the presence of H4R antagonist, JNJ-7777120 (10 μM). All histaminergic antagonists were preincubated for 30 min prior to histamine application (incubation time not shown). For experiments showed in **(A,C)**, arachidonic acid (AA 50 μM) was applied after histamine application to corroborate cell viability. **(E)** Mean ± SE of the peak amplitude of the Ca^{2+} transient evoked by histamine (300 μM) in the absence (Ctrl) and presence of the HR antagonists: pyrilamine 100 μM (H1), ranitidine 50 μM (H2), clobenpropit 50 μM (H3) and JNJ-7777120 10 μM (H4). The numbers in the figure represents the number of cells studied. Comparison between groups was performed using the Kruskal–Wallis test (* = $p \leq 0.05$) (ns = no statistically relevant differences between groups).

Histamine-evoked Ca^{2+} signals in WI-38 lung fibroblasts do not involve $G\alpha_{i/o}$ activation but require PLCβ recruitment and ER Ca^{2+} release

The results shown in Figures 4C–E suggest that H3R and H4R do not participate in histamine-activated Ca^{2+} signaling. H3R and H4R are canonically coupled to $G\alpha_{i/o}$ proteins (Haas et al., 2008). Therefore, a reliable strategy to corroborate the lack of H3R and H4R involvement in histamine response would be to demonstrate that pertussis toxin (PT), a selective inhibitor of $G\alpha_{i/o}$ protein signalling, does not modify histamine-evoked Ca^{2+} signals. Indeed, as shown in Figure 5A, preincubation (30 min) with 100 ng/ml PT did not prevent histamine from increasing intracellular $[Ca^{2+}]_i$ in WI-38 fibroblasts. In accord, the amplitude of initial Ca^{2+} transient (peak) was not statistically different from untreated cells (Figure 5B). These results confirm that histamine-evoked increase in $[Ca^{2+}]_i$ in human lung WI-38 fibroblasts is insensitive to the inhibition of $G\alpha_{i/o}$ by PT (Figures 5A,B). After confirming that H1R and H2R are involved in the Ca^{2+} response to histamine, we turned to dissect out the molecular

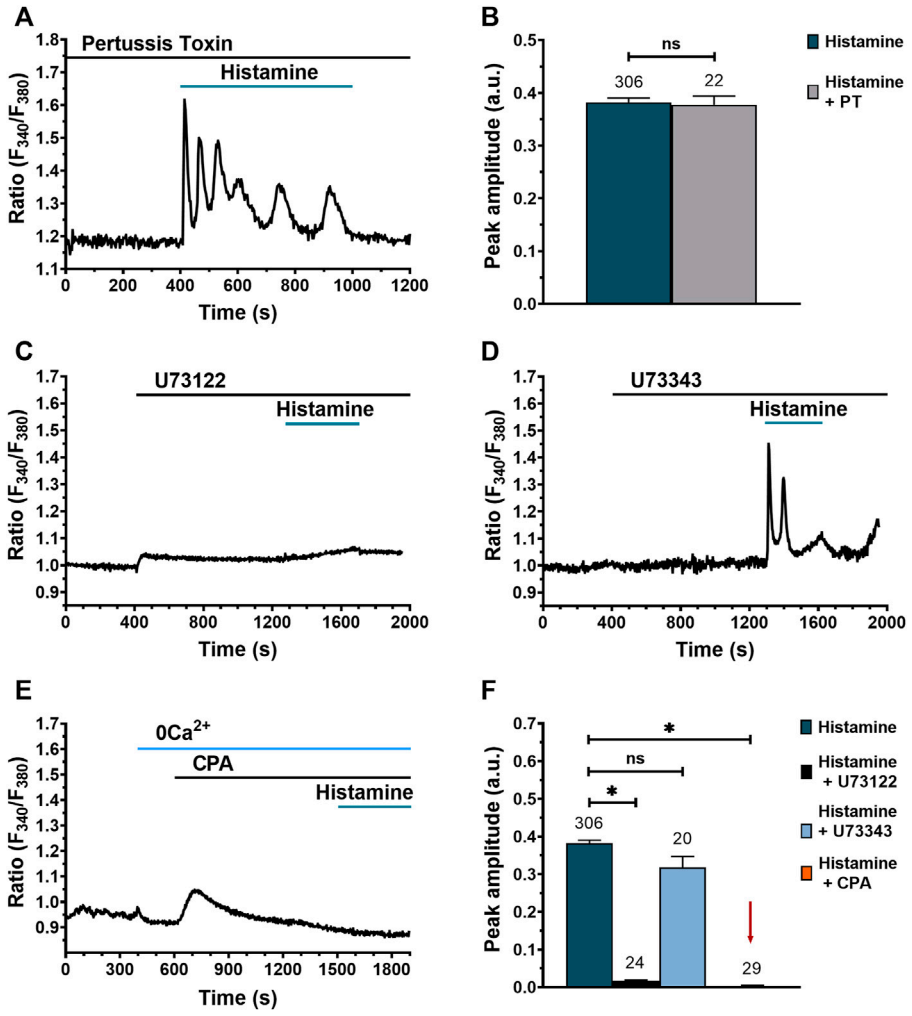

FIGURE 5
Histamine-evoked Ca^{2+} signals in WI-38 human lung fibroblasts do not involve $G\alpha_{i/o}$ activation but require PLC and ER Ca^{2+} release. **(A)** Typical recording of the Ca^{2+} response to histamine (300 μM) in fibroblasts preincubated for 30 min with 100 ng/ml pertussis toxin (PT). **(B)** Mean ± SE of the peak amplitude of histamine-evoked Ca^{2+} transients in the absence (green bar) and presence of pertussis toxin (gray bar). Comparison between groups was performed using the Student's t-test (ns = no statistically relevant differences between groups). **(C)** Typical recording of the effect of histamine (300 μM) on Ca^{2+} signal in cells pretreated for 15 min with U73122 (10 μM), a specific PLC inhibitor. **(D)** Typical recording of the Ca^{2+} response to histamine (300 μM) in cells pretreated for 15 min with U73343 (10 μM), an inactive analog of U73122. **(E)** Representative recording of the Ca^{2+} signal evoked by histamine (300 μM) in cells pretreated with CPA (10 μM) in the absence of extracellular Ca^{2+} ($0Ca^{2+}$). **(F)** Mean ± SE of the peak Ca^{2+} response to histamine (300 μM; green bar) in the presence of U73122 10 μM (black bar), U73343 10 μM (blue bar) and CPA 10 μM (orange bar not visible, marked with a red arrow). The numbers in the figure represent the number of cells studied. Statistical comparison between groups was performed using ANOVA test (* = $p \leq 0.05$).

underpinnings of the Ca^{2+} transient by using the following drugs: 1) U73122 (10 μM), a selective inhibitor of PLC (Moccia et al., 2006; Berra-Romani et al., 2012; Berra-Romani et al., 2020); 2) U73343 (10 μM), an inactive analogue of U73122 (Guzmán-Silva et al., 2015); and 3) cyclopiazonic acid (CPA) (10 μM), a selective inhibitor of sarco-edoplasmic reticulum calcium ATPase (SERCA) pump (Guzmán-Silva et al., 2015; Berra-Romani et al., 2020). The results obtained showed that PLC inhibition upon preincubation (15 min) with U73122 suppresses histamine-evoked Ca^{2+} signal (Figures 5C,F), whereas its inactive analog, U73343, does not affect the Ca^{2+} response (Figures 5D,F). Likewise, ER emptying *via* Ca^{2+} leak channels after SERCA inhibition with CPA in an extracellular Ca^{2+}-free environment ($0Ca^{2+}$) prevented the Ca^{2+} response to histamine (Figures 5E,F). These results indicate that the Ca^{2+} transient generated

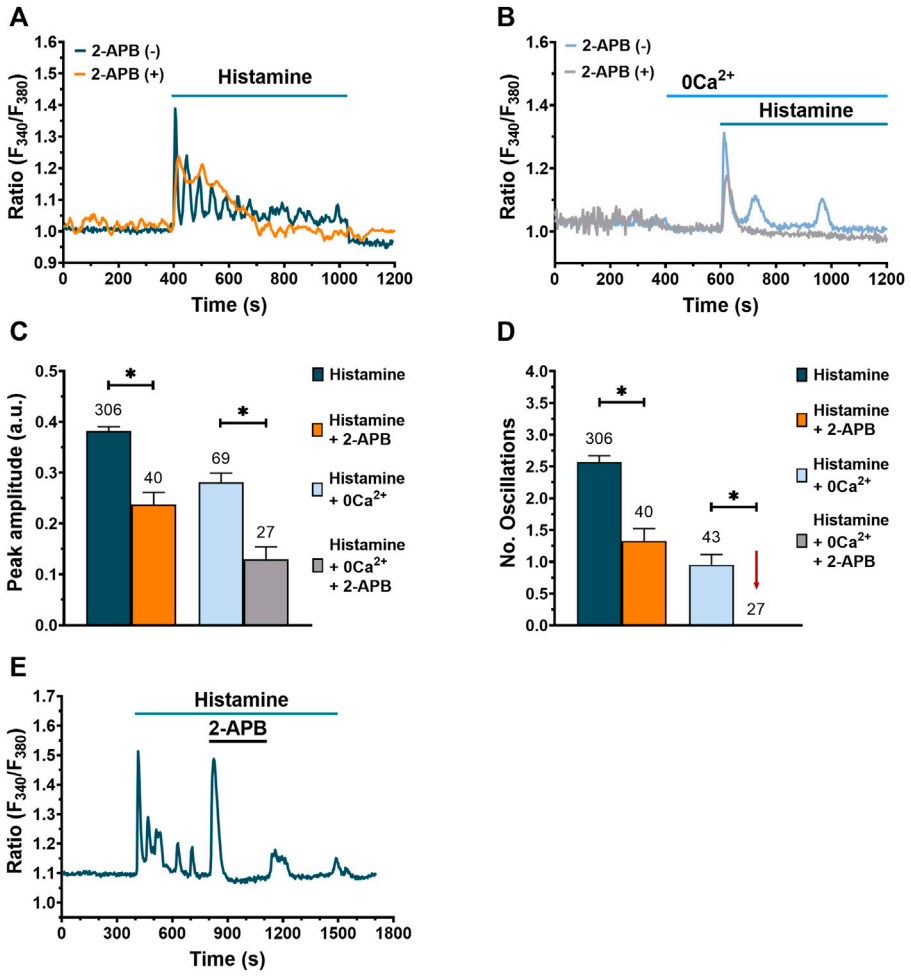

FIGURE 6
Involvement of $InsP_3R$ in histamine-evoked Ca^{2+} signals in WI-38 human lung fibroblasts. **(A)** Typical recording of the Ca^{2+} response to histamine (300 μM) in fibroblasts pre-incubated with 2-APB (50 μM) for 20 min [orange trace, 2-APB (+)] and its control [dark green trace, 2-APB (-)]. **(B)** Typical recording of histamine-evoked Ca^{2+} signal in absence of extracellular Ca^{2+} ($0Ca^{2+}$) after pre-incubation of fibroblasts for 20 min with 2-APB (50 μM) [gray trace, 2-APB (+)] and its control [blue trace, 2-APB (-)]. In (**A**,**B**) basal Ca^{2+} levels were aligned for comparative purposes. **(C)** Mean ± SE of the peak amplitude of the Ca^{2+} response to histamine (300 μM) in normal extracellular Ca^{2+} and in absence (dark green bar) or presence of 50 μM 2-APB (orange bar). Mean ± SE of the peak amplitude of the Ca^{2+} response to histamine (300 μM) in absence of extracellular Ca^{2+} ($0Ca^{2+}$) and in absence (blue bar) or presence of 50 μM 2-APB (gray bar). Statistic comparison between groups was performed using Mann-Whitney and t-Student test respectively (* = $p \leq 0.05$). **(D)** Mean ± SE of the number of oscillations evoked by histamine (300 μM) in normal extracellular Ca^{2+} and in absence (dark green bar) or presence of 50 μM 2-APB (orange bar). Mean ± SE of the number of oscillations evoked by histamine (300 μM) in the absence of extracellular Ca^{2+} ($0Ca^{2+}$) and in absence (blue bar) or presence of 50 μM 2-APB (gray bar, gray bar not visible, marked with a red arrow). Statistical comparison between groups was performed using Mann-Whitney and *t*-Student test respectively (* = $p \leq 0.05$). The numbers in the figure represents the number of cells studied. **(E)** Typical recording of the Ca^{2+} signal evoked by histamine and the effect of 2-APB application.

after histamine stimulation in WI-38 human lung fibroblasts is due to PLC activation and Ca^{2+} release from the ER.

$InsP_3R$ play an important role in histamine-evoked Ca^{2+} signaling in WI-38 human lung fibroblasts

Having demonstrated that the ER Ca^{2+} stores contributes to histamine-evoked Ca^{2+} signals upon PLC activation, we evaluated the involvement of $InsP_3R$, which provides the main pathway for ER Ca^{2+} release in fibroblasts (Horie et al., 2014; Berra-Romani et al., 2020). The results obtained demonstrate that, after incubation for 20 min with 2-aminoethoxydiphenyl borate (2-APB, 50 μM), a drug widely used as $InsP_3R$ inhibitor (Guzmán-Silva et al., 2015), the amplitude of histamine-evoked initial Ca^{2+} transient is significantly reduced compared to untreated cells, both in the presence (Figures 6A,C) and in the absence of extracellular Ca^{2+} (Figures 6B,C). In addition,

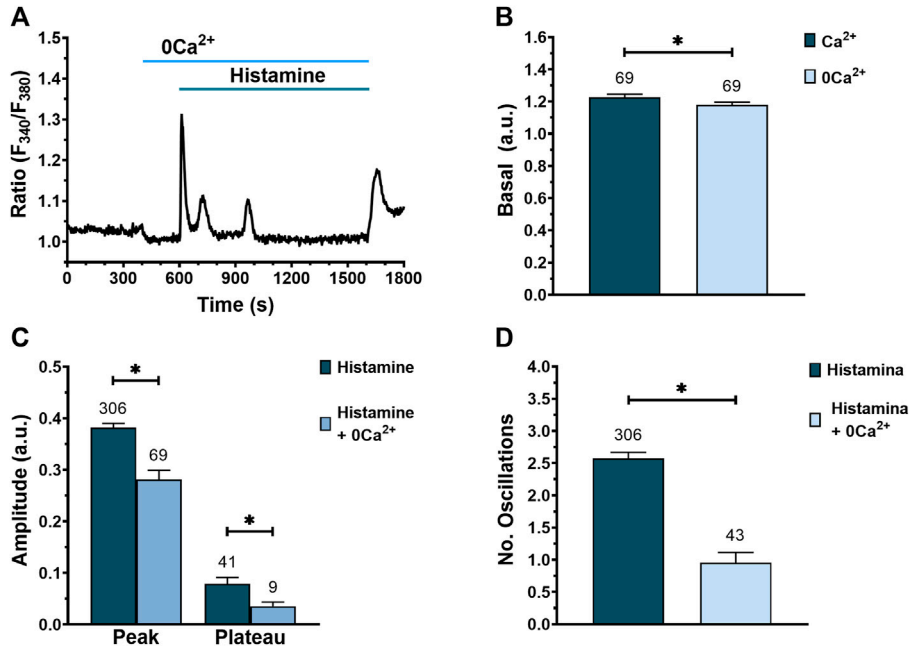

FIGURE 7
Effect of extracellular Ca^{2+} removal on histamine-evoked Ca^{2+} signal in WI-38 human lung fibroblasts. **(A)** Typical recording of histamine-evoked Ca^{2+} signals in the absence of extracellular Ca^{2+} ($0Ca^{2+}$). **(B)** Mean ± SE of basal $[Ca^{2+}]_i$ in fibroblasts exposed to an extracellular solution with (dark green bar) or without extracellular Ca^{2+} (blue bar). Comparison between groups was performed using the t-Student test (* = $p \leq 0.05$). **(C)** Mean ± SE of peak and plateau amplitudes of the Ca^{2+} signal evoked by histamine in fibroblasts expose to an extracellular solution with (dark green bar) or without extracellular Ca^{2+} (blue bar). Comparison between groups was performed using the *t*-Student test for peak amplitude data and Mann-Whitney test for plateau amplitude data (* = $p \leq 0.05$). **(D)** Mean ± SE of the number of oscillations recorded during the first 400 s after histamine application in an extracellular solution with (dark green bar) or without extracellular Ca^{2+} (blue bar). Comparison between groups was performed using the Mann-Whitney test (* = $p \leq 0.05$). The numbers in the figures represents the number of cells studied.

the number of oscillations was significantly decreased when fibroblasts were preincubated with 2-APB in normal Ca^{2+} (Figures 6A,D) and completely eliminated under $0Ca^{2+}$ conditions (Figures 6B,D). Even though 2-APB application during histamine-activated Ca^{2+} oscillations caused an immediate and transitory increase in $[Ca^{2+}]_i$, 2-APB subsequently erased the intracellular Ca^{2+} oscillations and plateau phase; this effect was reversible (Figure 6E). RyR could support $InsP_3$-induced intracellular Ca^{2+} oscillations through CICR, as reported in other cell types (Paltauf-Doburzynska et al., 2000). Nevertheless, the acute addition of caffeine (10 mM) mimicked the inhibitory effect of 2-APB by reversibly interrupting the oscillatory Ca^{2+} train (Supplementary Figure S1) in 92.3% of tested cells (60 out of 65 cells). This observation confirms that RyR, which are directly gated by caffeine (Pulina et al., 2010), do not contribute to histamine-induced intracellular Ca^{2+} waves in WI-38 fibroblasts and is consistent with the well-known phenomenon of $InsP_3R$ inhibition by caffeine (Parker and Ivorra, 1991; Moccia et al., 2003). Taken together, these results suggest a strong involvement of $InsP_3R$ in histamine-evoked Ca^{2+} transients in lung fibroblasts of the WI-38 cell line.

Extracellular Ca^{2+} influx contributes to histamine-induced intracellular Ca^{2+} signaling in WI-38 human lung fibroblasts

Next, we evaluated the contribution of extracellular Ca^{2+} to histamine-evoked Ca^{2+} signals by exposing the WI-38 fibroblasts to histamine in the absence of external Ca^{2+} to prevent Ca^{2+} entry across the plasma membrane (Berra-Romani et al., 2020). Histamine elicited an immediate increase in $[Ca^{2+}]_i$ in the absence of extracellular Ca^{2+} in 66 of 69 cells (Figure 7A). Of note, exposure of WI-38 cells to $0Ca^{2+}$ conditions caused a significative reduction in basal $[Ca^{2+}]_i$ (Figures 7A,B), which is consistent with the presence of a constitutive Ca^{2+} entry pathway (Zuccolo et al., 2018). When histamine (300 μM) was applied to fibroblasts under $0Ca^{2+}$ conditions, the peak and plateau amplitudes (Figure 7C), as well as the number of intracellular Ca^{2+}

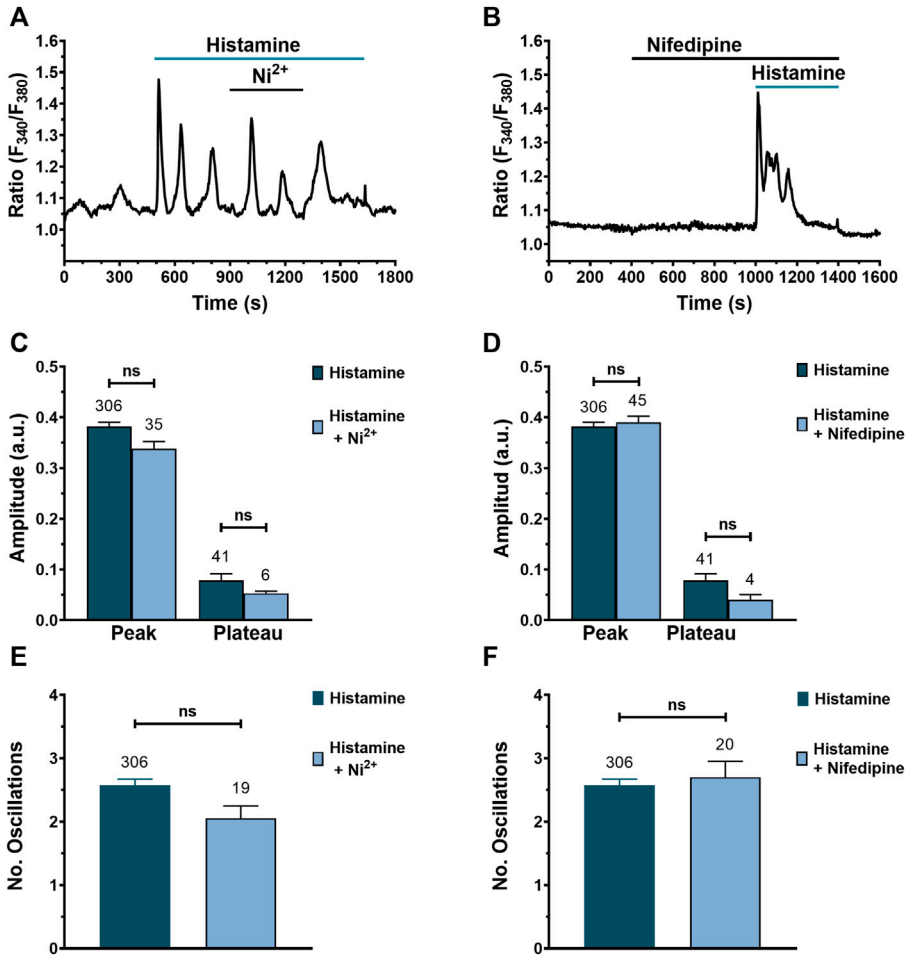

FIGURE 8
Blocking Ca^{2+} entry through VOCs does not affect histamine-evoked intracellular Ca^{2+} signals in WI-38 human lung fibroblasts. **(A)** Typical recording of histamine-evoked Ca^{2+} signals in the presence of nickel (10 μM). **(B)** Typical recording of histamine-evoked Ca^{2+} signals in the presence of nifedipine (10 μM). Comparison between groups was performed using the Mann-Whitney test (ns = not statistics differences between groups). **(C)** Mean ± SE of the peak and plateau amplitudes of the Ca^{2+} response to histamine (300 μM) in absence (dark green bar) or presence of the non-specific VOC inhibitor, nickel 10 μM (blue bar). **(D)** Mean ± SE of the peak and plateau amplitudes of the Ca^{2+} response to histamine (300 μM) in absence (dark green bar) or presence of the specific VOC inhibitor, nifedipine 10 μM (blue bar). **(E)** Mean ± SE of the number of oscillations recorded during the first 400 s after histamine application in presence (dark green bar) or presence of the unspecific VOC inhibitor, nickel 10 μM (blue bar). **(F)** Mean ± SE of the number of oscillations recorded during the first 400 s after histamine application in presence (dark green bar) or absence of the specific VOC inhibitor, nifedipine 10 μM (blue bar).

oscillations (Figure 7D), were significantly reduced compared to control conditions. In particular, Ca^{2+} oscillations rapidly run down in the absence of Ca^{2+} entry (Figure 7A). Furthermore, ongoing Ca^{2+} oscillations reversibly ceased upon removal of extracellular Ca^{2+} (Supplementary Figure S2) in 97.1% of tested cells (66 out of 68 cells). These results indicate that the peak and plateau amplitude as well the number of Ca^{2+} oscillations evoked by histamine are due to both Ca^{2+} release from the ER and Ca^{2+} influx from the extracellular medium.

Blocking Ca^{2+} entry through VOCs does not affect histamine-evoked intracellular Ca^{2+} signals

There is evidence for a key role of L-type VOCs in TGF-β-induced Ca^{2+} signaling in human lung fibroblasts (Mukherjee et al., 2015). We, therefore, evaluated their involvement in histamine-induced intracellular Ca^{2+} signaling in WI-38 cells. We exploited a non-specific L-type VOC antagonist (nickel, 10 μM) (Figures 8A,C,E) and a specific VOC antagonist

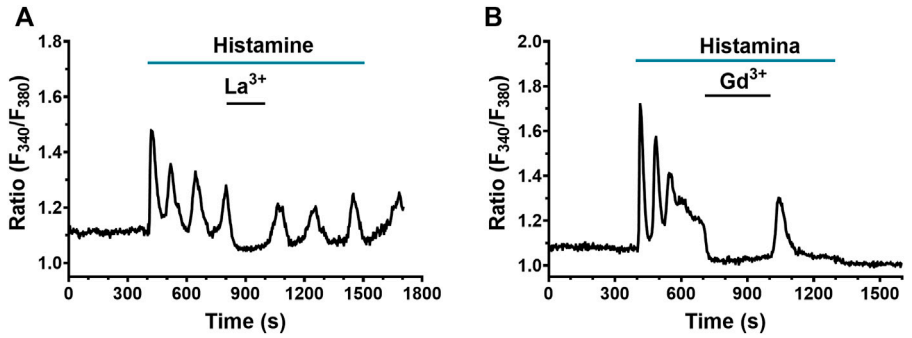

FIGURE 9
Effect of SOCE blockade on histamine-evoked Ca^{2+} signals in WI-38 human lung fibroblasts. **(A)** Typical recording of histamine-evoked Ca^{2+} signals and effect of the application of 10 μM La^{3+} (*n* = 79). **(B)** Typical recording of histamine-evoked Ca^{2+} signals and effect of the application of 10 μM Gd^{3+} (*n* = 40).

(nifedipine, 10 μM) (Figures 8B,D,F). The results show that there were no significant differences in the peak and plateau amplitudes, as well as in the number of oscillations, when Ca^{2+} entry through VOCs was inhibited with either nickel (Hobai et al., 2000) or nifedipine (Zhang et al., 2007), respectively.

Ca^{2+} influx through SOCs plays an important role in the plateau and oscillations of histamine-evoked Ca^{2+} transients in WI-38 lung fibroblasts

A recent investigation hinted at SOCE as the main Ca^{2+} entry pathway sustaining the Ca^{2+} response to chemical stimuli in human lung fibroblasts (Guzmán-Silva et al., 2015). Therefore, we evaluated the role of SOCs in the Ca^{2+} signal evoked by histamine in WI-38 fibroblasts. The pyrazole-derivative, BTP-2, which is widely employed to inhibit SOCE in non-excitable cells (Prakriya and Lewis, 2015; Moccia et al., 2016; Zhang et al., 2020), increases $[Ca^{2+}]_i$ in human lung fibroblasts (Guzmán-Silva et al., 2015) and cannot be reliably used to assess SOCE involvement in histamine-evoked extracellular Ca^{2+} entry. In accord, Supplementary Figure S3 shows that BTP-2 (20 μM) induced an immediate elevation in $[Ca^{2+}]_i$ upon application during the decay phase of the initial Ca^{2+} response to histamine. However, low micromolar doses of the trivalent cations, La^{3+} and Gd^{3+}, can also selectively inhibit Orai channels, which provides the main pore-forming subunits of SOCs in both excitable and non-excitable cells (Prakriya and Lewis, 2015; Moccia et al., 2016; Zhang et al., 2020), including human lung fibroblasts (Guzmán-Silva et al., 2015; Vazquez-de-Lara et al., 2018). The results showed that the application of both La^{3+} (10 μM) and Gd^{3+} (10 μM) abrogated the plateau and Ca^{2+} oscillations in 79 and 40 cells exposed to La^{3+} and Gd^{3+}, respectively (Figure 9A,B). This effect was reversible upon removal of La^{3+} or Gd^{3+}. Intriguingly, the acute addition of La^{3+} and Gd^{3+} also caused a decrease in resting Fura-2 fluorescence ratio below the baseline, which suggests that Orai channels are involved in constitutive Ca^{2+} entry (see Figure 6B). In summary, these results suggest a strong involvement of Ca^{2+} entry through SOCs in the histamine-evoked Ca^{2+} transient in lung fibroblasts of the WI-38 cell line.

Preliminary characterization of the Ca^{2+} handling machinery in in WI-38 fibroblast

No comprehensive information is available regarding the molecular composition of the Ca^{2+} handling toolkit in WI-38 fibroblasts. Therefore, we performed a preliminary qRT-PCR analysis of the main Ca^{2+}-permeable channels that are known to shape the Ca^{2+} response to histamine in other cell types. We used the specific primers described in Table 1, while negative controls were carried out by excluding the reverse transcription reaction, as shown in (Negri et al., 2021). Figure 10 displays that WI-38 lung fibroblasts express the transcripts encoding for all the $InsP_3R$ isoforms, i.e., $InsP_3R1$, $InsP_3R2$, and $InsP_3R3$, whereas, among the molecular players of the SOCE machinery, only STIM2 and Orai3 paralogues were present. In addition, the mRNAs encoding for RyR1 and most of the members of the Transient Receptor Potential Canonical (TRPC) subfamily, i.e., TRPC1, TRPC3, TRPC4, TRPC5, and TRPC6 (Negri et al., 2019), were also found (Figure 10). Therefore, these findings support the notion that the interaction between $InsP_3R$ and SOC drive histamine-induced intracellular Ca^{2+} signals in WI-38 human adult lung fibroblasts.

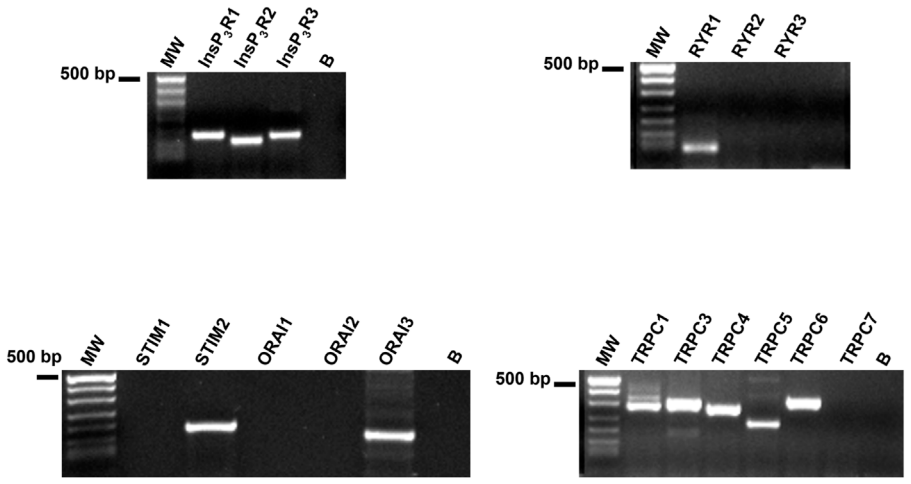

FIGURE 10
Transcriptomic characterization of the Ca^{2+} handling machinery in WI-38 fibroblasts. Gel electrophoresis of the PCR products are shown. Electrophoresis was performed as indicated in Materials and Methods. The PCR products were of the expected size: $InsP_3R1$, 180 bp; $InsP_3R_2$, 158 bp; $InsP_3R_3$, 173 bp; RyR_1, 75 bp; TRPC1, 307 bp; TRPC3, 336 bp; TRPC4, 300 bp; TRPC5, 221 bp; TRPC6, 341 bp; STIM2, 186 bp; and Orai3, 159 bp. No signal was observed for STIM1 and Orai1. MW, molecular weight markers. B, reaction without the template.

Discussion

Pulmonary remodeling is the main long-term complication of asthma and occurs as a compensatory response to a persistent inflammatory state of the lower airway epithelium that leads to an irreversible restriction in the airflow, and is a result of a multi-step process known as "scarring." Mast cells play a crucial pathogenic role in asthma by releasing the autacoid mediator histamine, which stimulates airway smooth muscle cell constriction and hyperplasia, and activates fibroblasts to acquire a contractile phenotype and support pulmonary remodelling. The molecular mechanisms whereby histamine promotes fibroblast proliferation and migration is still unclear, although preliminary evidence indicates that histamine-induced collagen gel contraction is mediated by an increase in $[Ca^{2+}]_i$ (Horie et al., 2014). Intriguingly, it has long been known that intracellular Ca^{2+} signaling can adopt multiple patterns to orchestrate many of the cellular events that contribute to pulmonary remodeling, including fibroblast proliferation and transformation into myofibroblasts (Janssen et al., 2015). Herein, we provided the first clear-cut characterization of the signaling pathways that shape histamine-induced intracellular Ca^{2+} signals in the WI-38 cell line, which is widely employed to study human lung fibroblasts. Our findings could pave the way towards an alternative strategy to target histamine signaling and thereby dampen airway remodeling in asthma.

Intracellular Ca^{2+} signals regulate a broad spectrum of cellular processes by adopting diverse spatiotemporal dynamics, ranging from single Ca^{2+} transient to repetitive Ca^{2+} transients whose frequency depends on agonist strength (Smedler and Uhlén, 2014). The introduction of high-speed microfluorimetry and high-resolution image analysis techniques have allowed researchers to monitor changes in $[Ca^{2+}]_i$ in individual cells simultaneously. These techniques have revealed a surprising degree of heterogeneity in the Ca^{2+} responses to the same agonist generated even by cells in the same field of view. Herein, we report that histamine evoked complex Ca^{2+} waveforms in WI-38 fibroblasts that could be classified according to the following patterns: 1) peak, 2) peak and oscillations, 3) peak plateau and oscillations, and 4) peak and plateau. Spatial and temporal heterogeneity of the Ca^{2+} signature can be a hallmark of the Ca^{2+} response evoked by both mechanical (Berra-Romani et al., 2008; Jing et al., 2013) and chemical cues (Dupont and Combettes, 2016; Wacquier et al., 2019). A recent investigation showed that, in normal human lung fibroblasts (NHLF), beractant (a natural surfactant) induced distinct patterns of intracellular Ca^{2+} signals, each comprising an initial Ca^{2+} spike that could be followed either by a) transient, by repetitive Ca^{2+} oscillations, c) a sustained Ca^{2+} plateau or d) a sustained plateau overlapped by repetitive Ca^{2+} oscillations (Guzmán-Silva et al., 2015). Similarly, ATP could elicit either a single Ca^{2+} transient or recurring Ca^{2+} oscillations in NHLF (Janssen et al., 2015), whereas an heterogenous array of agonist-induced intracellular Ca^{2+} signals has been described in fibroblasts deriving from other tissues (Chen et al., 2010; Kemény et al., 2013; Lembong et al., 2015). As expected (Ong et al., 2019), the diverse Ca^{2+} dynamics and the number of oscillations depend on histamine concentration, with the lower concentration being dominated by the peak pattern and the higher concentration being dominated by the peak, plateau

and oscillations pattern. In accord, low doses of histamine are predicted to elicit only intracellular Ca^{2+} release, while the Ca^{2+} response to higher doses can also involve extracellular Ca^{2+} entry (Ong et al., 2019). Likewise, a recent investigation showed that histamine was more eager to induce 1 or 2 Ca^{2+} spikes at low picomolar doses, whereas the number and frequency of repetitive Ca^{2+} transients progressively increased with histamine concentration (up to 300 μM) in human microvascular endothelial cells (Berra-Romani et al., 2020). The non-cumulative concentration-response relationship showed that the Ca^{2+} signal evoked by histamine in WI-38 human lung fibroblasts present an EC_{50} value of 4.96 μM, a maximum concentration of 300 μM, and a threshold concentration of 100 nM. Similarly, histamine induced collagen gel contraction and proliferation in, respectively, primary cultured human lung fibroblasts (Horie et al., 2014) and IMR-90 adult lung fibroblasts (Kunzmann et al., 2007) within a concentration range spanning from 100 nM up to 100 μM. Moreover, the pro-migratory effect of histamine on human lung fetal fibroblasts appeared at a threshold dose of 100 nM (Kohyama et al., 2010). These studies concur with the evidence that H1R mediates histamine-induced proliferation, migration, and collagen gel contraction in human lung fibroblasts. In agreement with these observations, pharmacological manipulation showed that histamine generates a complex increase in $[Ca^{2+}]_i$ in WI-38 fibroblasts mainly through H1R and, to a lesser extent, through H2R. Furthermore, short-term exposure of the cells to histamine reduced the responsiveness to subsequent applications of the agonist, which is a hallmark of H1R signalling (Smit et al., 1992). Homologous desensitization of H1R has also been reported in smooth muscle preparations (Leurs et al., 1990; Leurs et al., 1991), HeLa cells (Smit et al., 1992), and human gingival fibroblasts (Gutiérrez-Venegas and Rodríguez-Pérez, 2012). Conversely, H3R and H4R do not seem to play a crucial role in the onset of the Ca^{2+} signal. These results were supported by the evidence that histamine-evoked intracellular Ca^{2+} waves were not altered by the PT-dependent ribosylation of the $G\alpha_{i/o}$ subunit, which triggers the signalling cascades activated downstream of both H3R and H4R (Seifert et al., 2013). Consistent with our observations, Horie et al. (2014) previously reported the involvement of H1R in histamine-induced collagen gel contraction in primary cultured lung fibroblasts, whereas H2R could be responsible for a small Ca^{2+} response occurring in the presence of diphenhydramine, a specific H1R-antihistamine.

The mechanisms that control the mobilization of cytosolic Ca^{2+} are key to the regulation of numerous eukaryotic cell functions (Clapham, 2007). Therefore, after identifying the HR subtype responsible for histamine-evoked Ca^{2+} signaling, we set out to dissect the molecular underpinnings of the Ca^{2+} transient. H1R is a GqPCR that can signal an increase in $[Ca^{2+}]_i$ by stimulating PLCβ to synthesize $InsP_3$ and trigger ER Ca^{2+} release through $InsP_3R$ (Berra-Romani et al., 2012; Seifert et al., 2013; Berra-Romani et al., 2020). In accord, the Ca^{2+} response to histamine still occurred in the absence of extracellular Ca^{2+}, although it rapidly run down after 1-3 Ca^{2+} spikes. Furthermore, histamine-evoked intracellular Ca^{2+} signals were strongly reduced by blocking PLCβ activity with U73122, but not its inactive analog, U73343. Furthermore, the initial Ca^{2+} peak was significantly reduced as compared to control, i.e., untreated, cells upon inhibition of $InsP_3R$ with 2-APB. This inhibitory effect was observed both in the presence and in the absence of extracellular Ca^{2+}. 2-APB significantly decreased the number of oscillations under normal Ca^{2+} conditions, while it completely erased the spiking response under $0Ca^{2+}$ conditions. Of note, inhibition of $InsP_3Rs$ with 2-APB, despite decreasing the amplitude of the Ca^{2+} transients, did not completely eliminate histamine-induced Ca^{2+} signals, as previously reported both in fibroblasts (Horie et al., 2014) and in other cell types (Berra-Romani et al., 2020). Unlike histamine, the Ca^{2+} response to beractant in WI-38 fibroblasts was fully abrogated by 2-APB (Guzmán-Silva et al., 2015). This discrepancy can be explained by invoking several hypotheses. First, the ability of 2-APB to penetrate the cell membrane may significantly vary among different cell types: this feature could explain the high sensitivity to 2-APB observed in some cells, but not in others (Soulsby and Wojcikiewicz, 2002). Second, the degree of 2-APB-dependent inhibition could depend on the histamine concentration employed to characterize the Ca^{2+} response in WI-38 lung fibroblasts. For instance, early work carried out in HeLa cells showed that 100 μM 2-APB was able to completely inhibit the ATP-evoked Ca^{2+} response at all the tested concentrations, while histamine-evoked Ca^{2+} signals were only slightly reduced at high agonist doses (i.e., 100 μM) (Peppiatt et al., 2003). It is likely that a higher concentration of 2-APB is required to block $InsP_3R$ recruited by histamine in WI-38 lung fibroblasts. However, we did not increase 2-APB concentration to avoid the concentration-dependent side-effects that have been associated to this powerful $InsP_3R$ inhibitor, such as SOCE inhibition and SERCA modulation (Gambardella et al., 2021). The primary role of $InsP_3R$ in the Ca^{2+} response to histamine was further corroborated by caffeine, which reversibly inhibited, rather than enhancing, histamine-induced intracellular Ca^{2+} oscillations. At the concentration employed in the present investigation, caffeine can either stimulate RyR (Pulina et al., 2010) or inhibit $InsP_3R$ (Parker and Ivorra, 1991; Moccia et al., 2003). Therefore, the blocking effect of caffeine further confirms that $InsP_3R$ are the main responsible for the rhythmical ER Ca^{2+} release induced by caffeine in WI-38 fibroblasts.

While the complex increase in $[Ca^{2+}]_i$ is triggered by ER Ca^{2+} mobilization through $InsP_3R$, the Ca^{2+} response is maintained over time by extracellular Ca^{2+} entry. In accord, removal of external Ca^{2+} resulted in the decrease of the Ca^{2+} peak and Ca^{2+} plateau amplitudes, and in the number of Ca^{2+} oscillations evoked by histamine. These findings concur with previous studies showing that Ca^{2+} influx through the plasma membrane sustains intracellular Ca^{2+}

oscillations induced by H1R stimulation in several cell types, including cerebrovascular endothelial cells (Berra-Romani et al., 2020), HeLa cells (Sauvé et al., 1991), and vascular smooth muscle cells (Espinosa-Tanguma et al., 2011). SOCE is activated upon depletion of the ER Ca^{2+} pool and represents the Ca^{2+} entry pathway that sustains the Ca^{2+} signal induced by agonists stimulation in fibroblasts from different tissues, including human mammary gland (Sadras et al., 2021b), human heart (Chung et al., 2021), human skin (Wu et al., 2019), and human lungs (Guzmán-Silva et al., 2015). It has been nicely documented that low (1–10) micromolar doses of the trivalent cations, La^{3+} and Gd^{3+}, plug the access to the Orai channel inner pore, thereby specifically inhibiting SOCE (Prakriya and Lewis, 2015; Moccia et al., 2016; Zhang et al., 2020). In accord, the application of either SOC blocker at 400 s after histamine application completely abolished the oscillations and suppressed the Ca^{2+} plateau in WI-38 lung fibroblasts. Similar results were achieved by the acute addition of 10 μM La^{3+} and 10 μM Gd^{3+} on the long-lasting elevation in $[Ca^{2+}]_i$ evoked in the same cells by beractant (Guzmán-Silva et al., 2015). VOC represent an alternative pathway for extracellular Ca^{2+} entry in NHLF, as shown for the intracellular Ca^{2+} oscillations induced by transforming growth factor β (Mukherjee et al., 2015). However, two structurally unrelated VOC inhibitors, i.e., nickel and nifedipine, did not affect histamine-evoked intracellular Ca^{2+} signals in WI-38 cells. We hypothesize that histamine-dependent SOC activation does not depolarize the membrane potential to such an extent to induce VOC activation.

A preliminary qRT-PCR analysis of the Ca^{2+} handling machinery confirmed that WI-38 fibroblasts express all the three known $InsP_3R$ isoform and two of the molecular components required to activate SOCE, i.e., STIM2 and Orai3. These data are therefore consistent with the results provided by the pharmacological manipulation of the Ca^{2+} response. Conversely, all Orai and STIM isoforms were detected in human cardiac fibroblasts (Cendula et al., 2021), in which they support spontaneous Ca^{2+} oscillations (Chen et al., 2010). Intriguingly, Orai3 can be directly activated by 50 μM 2-APB independent from ER Ca^{2+} store depletion (Zhang et al., 2020), which might explain the immediate rise in $[Ca^{2+}]_i$ that occurs upon 2-APB application in the presence (see Figure 6F) but not in the absence (not shown) of extracellular Ca^{2+}. RyR1 transcript was also found, but it is unlikely to contribute to histamine-evoked intracellular Ca^{2+} signals, as shown by the inhibitory effect of caffeine. WI-38 fibroblasts also express the transcripts encoding for TRPC1-TRPC6, but the pharmacological sensitivity of histamine-evoked Ca^{2+} entry to 10 μM La^{3+} and Gd^{3+} argues against the involvement of TRPC isoforms. Moreover, a recent investigation demonstrated that TRPC channels do not support SOCE in primary murine lung fibroblasts (Bendiks et al., 2020). Conversely, TRPC channels, which present a single-channel conductance that is 1000-fold larger than Orai3, could be activated by transforming growth factor β and thereby lead to VOC activation via strong membrane depolarization (Mukherjee et al., 2015). Quite surprisingly, this was the first molecular characterization of the Ca^{2+} toolkit in human pulmonary fibroblasts. The selective expression of STIM2 as ER Ca^{2+} sensor might explain the rapid fall in resting $[Ca^{2+}]_i$ observed upon removal of external Ca^{2+}. In accord, STIM2 is activated only by a mild depletion of the ER Ca^{2+} store and can drive the activation of a constitutive Ca^{2+} influx (Brandman et al., 2007). In agreement with this hypothesis, preliminary evidence showed that μM La^{3+} and Gd^{3+} reduced the basal Ca^{2+} entry, thereby suggesting that SOC also support the resting Ca^{2+} permeability of WI-38 fibroblasts (Sanchez-Collado et al., 2020). It is worth of pointing out that the most frequent Ca^{2+} patterns evoked by high doses of histamine, i.e., mode 2) peak-oscillations, 64.7%, and mode 3) peak-plateau-oscillations, 13.39%, entail the occurrence of intracellular Ca^{2+} oscillations. In agreement with this observation, STIM2 and Orai3 can enhance the percentage of cells showing intracellular Ca^{2+} oscillations upon GqPCR stimulation (Yoast et al., 2020; Emrich et al., 2021). Furthermore, mathematical modelling has shown that, because of their distinct sensitivity to cytosolic Ca^{2+}, $InsP_3R3$ may provide a constant release of Ca^{2+} that stimulates $InsP_3R1$ and $InsP_3R2$ to rhythmically release ER stored Ca^{2+}, whereas SOCE maintains the Ca^{2+} response by ensuring ER Ca^{2+} refilling (Dupont and Croisier, 2010; Dupont, 2014). However, the periodic Ca^{2+} transients transition into a sustained plateau either when $InsP_3R3$ expression increases (Okumura et al., 2022) or when ER Ca^{2+} release through $InsP_3R3$ is enhanced by the tight coupling with the ER-embedded protein, Jaw1 (Okumura et al., 2022). Therefore, the molecular assortment of the distinct STIM/Orai and $InsP_3R$ isoform, as well as cell-to-cell variability in their expression, subcellular distribution, or posttranslational regulation, could contribute to pattern a heterogenous array of Ca^{2+} signatures in WI-38 adult lung fibroblast (Ishida et al., 2014; Guzmán-Silva et al., 2015; Bartok et al., 2019; Wilson et al., 2020). Conversely, cell cycle asynchrony is an unlikely explanation of the cell-to-cell heterogeneity of histamine-evoked Ca^{2+} waves because our experiments were performed in fibroblasts devoid of serum for 48 h, which causes cell cycle arrest in G0 phase (Santella, 1998). Similarly, previous studies in fibroblasts and other cell types have reported that this variability in the intracellular Ca^{2+} dynamics is not due to cell cycle asynchrony (Ambler et al., 1988; Byron and Villereal, 1989; Dragoni et al., 2011; Guzmán-Silva et al., 2015; Okumura et al., 2022).

In conclusion, the present investigation showed that histamine induces a dose-dependent increase in $[Ca^{2+}]_i$ in the widely employed human pulmonary fibroblast cell line, WI-38. The Ca^{2+} signal is mainly triggered by H1R and can adopt multiple signatures, the most common of which encompasses intracellular Ca^{2+} oscillations, which have long been known to stimulate gene expression, proliferation, contraction and migration in human pulmonary fibroblasts (Janssen et al., 2015). The Ca^{2+} response to histamine is triggered by ER Ca^{2+} release through $InsP_3R$ and maintained over time by SOCE activation. These data suggest that the Ca^{2+} handling machinery could provide an alternative molecular target to prevent the pernicious effects of histamine on lung fibroblasts in asthmatic patients, as recently suggested also

for pulmonary hypertension (Bikou et al., 2022), *Streptococcus* pneumoniae-induced lung injury (Ali et al., 2022), and asthma itself (Johnson et al., 2022). Much research remains therefore to be done to assess this issue, although the work presented here provides valuable information for understanding the mechanisms that regulate histamine-evoked Ca^{2+} signaling in lung fibroblasts. A limitation of the present study is that we did not use lung fibroblasts from an asthmatic model or from patients with asthma. Future work will have to compare the effect generated by histamine in lung fibroblasts from normal airways and in lung fibroblasts from asthmatic airways.

Data availability statement

The raw data supporting the conclusion of this article will be made available by the authors, without undue reservation.

Author contributions

RB-R and FM conceived and directed the project in collaboration with MG-C, AL-M, UL, and JA-C. AV-G, JS-G, NC-S, MS, GP, and EH-A performed the experiments and analyzed the data. All authors contributed to the article and approved the submitted version.

Acknowledgments

The authors thank CONCYTEP (Consejo de Ciencia y Tecnología del Estado de Puebla) for financing publication expenses.

Conflict of interest

The authors declare that the research was conducted in the absence of any commercial or financial relationships that could be construed as a potential conflict of interest.

Publisher's note

Supplementary material

The Supplementary Material for this article can be found online at: https://www.frontiersin.org/articles/10.3389/fcell.2022.991659/full#supplementary-material

SUPPLEMENTARY FIGURE S1
Effect of caffeine on histamine-evoked Ca^{2+} signals in WI-38 human lung fibroblasts. Typical recording of histamine-evoked Ca^{2+} signals and effect of the application of 10 mM caffeine.

SUPPLEMENTARY FIGURE S2
Effect of extracellular Ca^{2+} removal on histamine-evoked Ca^{2+} oscillations in WI-38 human lung fibroblasts. Typical recording of histamine-evoked Ca^{2+} oscillations and effect of extracellular Ca^{2+} removal.

SUPPLEMENTARY FIGURE S3
Effect of BTP-2 on histamine-evoked Ca^{2+} signals in WI-38 human lung fibroblasts. Typical recording of histamine-evoked Ca^{2+} signals and effect of BTP-2 (n = 76).

References

Abdulrazzaq, Y. M., Bastaki, S. M. A., and Adeghate, E. (2022). Histamine H_3 receptor antagonists - roles in neurological and endocrine diseases and diabetes mellitus. *Biomed. Pharmacother.* 150, 112947. doi:10.1016/j.biopha.2022.112947

Ali, M., Zhang, X., LaCanna, R., Tomar, D., Elrod, J. W., and Tian, Y. (2022). MICU1-dependent mitochondrial calcium uptake regulates lung alveolar type 2 cell plasticity and lung regeneration. *JCI Insight* 7 (4), e154447. doi:10.1172/jci.insight.154447

Ambler, S. K., Poenie, M., Tsien, R. Y., and Taylor, P. (1988). Agonist-stimulated oscillations and cycling of intracellular free calcium in individual cultured muscle cells. *J. Biol. Chem.* 263 (4), 1952–1959. doi:10.1016/S0021-9258(19)77971-X

Bartok, A., Weaver, D., Golenár, T., Nichtova, Z., Katona, M., Bánsághi, S., et al. (2019). IP_3 receptor isoforms differently regulate ER-mitochondrial contacts and local calcium transfer. *Nat. Commun.* 10 (1), 3726. doi:10.1038/s41467-019-11646-3

Bendiks, L., Geiger, F., Gudermann, T., Feske, S., and Dietrich, A. (2020). Store-operated Ca^{2+} entry in primary murine lung fibroblasts is independent of classical transient receptor potential (TRPC) channels and contributes to cell migration. *Sci. Rep.* 10 (1), 6812. doi:10.1038/s41598-020-63677-2

Berra-Romani, R., Faris, P., Negri, S., Botta, L., Genova, T., and Moccia, F. (2019). Arachidonic acid evokes an increase in intracellular Ca^{2+} concentration and nitric oxide production in endothelial cells from human brain microcirculation. *Cells* 8 (7), E689. doi:10.3390/cells8070689

Berra-Romani, R., Faris, P., Pellavio, G., Orgiu, M., Negri, S., Forcaia, G., et al. (2020). Histamine induces intracellular Ca^{2+} oscillations and nitric oxide release in endothelial cells from brain microvascular circulation. *J. Cell. Physiol.* 235 (2), 1515–1530. doi:10.1002/jcp.29071

Berra-Romani, R., Raqeeb, A., Avelino-Cruz, J. E., Moccia, F., Oldani, A., Speroni, F., et al. (2008). Ca^{2+} signaling in injured *in situ* endothelium of rat aorta. *Cell Calcium* 44 (3), 298–309. doi:10.1016/j.ceca.2007.12.007

Berra-Romani, R., Raqeeb, A., Torres-Jácome, J., Guzman-Silva, A., Guerra, G., Tanzi, F., et al. (2012). The mechanism of injury-induced intracellular calcium concentration oscillations in the endothelium of excised rat aorta. *J. Vasc. Res.* 49 (1), 65–76. doi:10.1159/000329618

Bikou, O., Tharakan, S., Yamada, K. P., Kariya, T., Aguero, J., Gordon, A., et al. (2022). Endobronchial aerosolized AAV1.SERCA2a gene therapy in a pulmonary hypertension pig model: Addressing the lung delivery bottleneck. *Hum. Gene Ther.* 33 (9-10), 550–559. doi:10.1089/hum.2021.274

Brandman, O., Liou, J., Park, W. S., and Meyer, T. (2007). STIM2 is a feedback regulator that stabilizes basal cytosolic and endoplasmic reticulum Ca^{2+} levels. *Cell* 131 (7), 1327–1339. doi:10.1016/j.cell.2007.11.039

Burghi, V., Echeverría, E. B., Zappia, C. D., Díaz Nebreda, A., Ripoll, S., Gómez, N., et al. (2021). Biased agonism at histamine H_1 receptor: Desensitization, internalization and MAPK activation triggered by antihistamines. *Eur. J. Pharmacol.* 896, 173913. doi:10.1016/j.ejphar.2021.173913

Byron, K. L., and Villereal, M. L. (1989). Mitogen-induced $[Ca^{2+}]_i$ changes in individual human fibroblasts. Image analysis reveals asynchronous responses which are characteristic for different mitogens. *J. Biol. Chem.* 264 (30), 18234–18239. doi:10.1016/s0021-9258(19)84702-6

Carroll, N. G., Mutavdzic, S., and James, A. L. (2002). Distribution and degranulation of airway mast cells in normal and asthmatic subjects. *Eur. Respir. J.* 19 (5), 879–885. doi:10.1183/09031936.02.00275802

Cendula, R., Chomaničová, N., Adamičková, A., Gažová, A., Kyselovič, J., and Máťuš, M. (2021). Altered expression of ORAI and STIM isoforms in activated human cardiac fibroblasts. *Physiol. Res.* 70 (1), S21–s30. doi:10.33549/physiolres.934771

Chen, T. R., Tao, R., Sun, H. Y., Tse, H. F., Lau, C. P., and Li, G. R. (2010). Multiple Ca^{2+} signaling pathways regulate intracellular Ca^{2+} activity in human cardiac fibroblasts. *J. Cell. Physiol.* 223 (1), 68–75. doi:10.1002/jcp.22010

Chen, X., Egly, C., Riley, A. M., Li, W., Tewson, P., Hughes, T. E., et al. (2014). PKC-dependent phosphorylation of the H_1 histamine receptor modulates TRPC6 activity. *Cells* 3 (2), 247–257. doi:10.3390/cells3020247

Chung, C. C., Chen, P. H., Lin, Y. F., Kao, Y. H., and Chen, Y. J. (2021). Lithium reduces migration and collagen synthesis activity in human cardiac fibroblasts by inhibiting store-operated Ca^{2+} entry. *Int. J. Mol. Sci.* 22 (2), E842. doi:10.3390/ijms22020842

Clapham, D. E. (2007). Calcium signaling. *Cell* 131 (6), 1047–1058. doi:10.1016/j.cell.2007.11.028

Dharmage, S. C., Perret, J. L., and Custovic, A. (2019). Epidemiology of asthma in children and adults. *Front. Pediatr.* 7, 246. doi:10.3389/fped.2019.00246

Dragoni, S., Laforenza, U., Bonetti, E., Lodola, F., Bottino, C., Berra-Romani, R., et al. (2011). Vascular endothelial growth factor stimulates endothelial colony forming cells proliferation and tubulogenesis by inducing oscillations in intracellular Ca^{2+} concentration. *Stem Cells* 29 (11), 1898–1907. doi:10.1002/stem.734

Dupont, G., and Combettes, L. (2016). *Fine tuning of cytosolic Ca (2+) oscillations*, 5, F1000Res. doi:10.12688/f1000research.8438.1*Review*

Dupont, G., and Croisier, H. (2010). Spatiotemporal organization of Ca^{2+} dynamics: A modeling-based approach. *HFSP J.* 4 (2), 43–51. doi:10.2976/1.3385660

Dupont, G. (2014). Modeling the intracellular organization of calcium signaling. *Wiley Interdiscip. Rev. Syst. Biol. Med.* 6 (3), 227–237. doi:10.1002/wsbm.1261

Emrich, S. M., Yoast, R. E., Xin, P., Arige, V., Wagner, L. E., Hempel, N., et al. (2021). Omnitemporal choreographies of all five STIM/Orai and IP_3Rs underlie the complexity of mammalian Ca^{2+} signaling. *Cell Rep.* 34 (9), 108760. doi:10.1016/j.celrep.2021.108760

Espinosa-Tanguma, R., O'Neil, C., Chrones, T., Pickering, J. G., and Sims, S. M. (2011). Essential role for calcium waves in migration of human vascular smooth muscle cells. *Am. J. Physiol. Heart Circ. Physiol.* 301 (2), H315–H323. doi:10.1152/ajpheart.00355.2010

Faris, P., Casali, C., Negri, S., Iengo, L., Biggiogera, M., Maione, A. S., et al. (2022). Nicotinic acid adenine dinucleotide phosphate induces intracellular Ca2+ signalling and stimulates proliferation in human cardiac mesenchymal stromal cells. *Front. Cell Dev. Biol.* 10, 874043. doi:10.3389/fcell.2022.874043

Ferrera, L., Barbieri, R., Picco, C., Zuccolini, P., Remigante, A., Bertelli, S., et al. (2021). TRPM2 oxidation activates two distinct potassium channels in melanoma cells through intracellular calcium increase. *Int. J. Mol. Sci.* 22 (16), 8359. doi:10.3390/ijms22168359

Gambardella, J., Morelli, M. B., Wang, X., Castellanos, V., Mone, P., and Santulli, G. (2021). The discovery and development of IP3 receptor modulators: An update. *Expert Opin. Drug Discov.* 16 (6), 709–718. doi:10.1080/17460441.2021.1858792

Garbuzenko, E., Berkman, N., Puxeddu, I., Kramer, M., Nagler, A., and Levi-Schaffer, F. (2004). Mast cells induce activation of human lung fibroblasts *in vitro*. *Exp. Lung Res.* 30 (8), 705–721. doi:10.1080/01902140490517809

GBD Diseases and Injuries Collaborators (2020). Global burden of 369 diseases and injuries in 204 countries and territories, 1990-2019: A systematic analysis for the global burden of disease study 2019. *Lancet* 396 (10258), 1204–1222. doi:10.1016/S0140-6736(20)30925-9

Gutiérrez-Venegas, G., and Rodríguez-Pérez, C. E. (2012). Toll-like receptor 3 activation promotes desensitization of histamine response in human gingival fibroblasts: Poly (I:C) induces histamine receptor desensitization in human gingival fibroblasts. *Cell. Immunol.* 273 (2), 150–157. doi:10.1016/j.cellimm.2011.12.005

Guzmán-Silva, A., Vázquez de Lara, L. G., Torres-Jácome, J., Vargaz-Guadarrama, A., Flores-Flores, M., Pezzat Said, E., et al. (2015). Lung beractant increases free cytosolic levels of Ca^{2+} in human lung fibroblasts. *PLoS One* 10 (7), e0134564. doi:10.1371/journal.pone.0134564

Haas, H. L., Sergeeva, O. A., and Selbach, O. (2008). Histamine in the nervous system. *Physiol. Rev.* 88 (3), 1183–1241. doi:10.1152/physrev.00043.2007

Hobai, I. A., Hancox, J. C., and Levi, A. J. (2000). Inhibition by nickel of the L-type Ca channel in Guinea pig ventricular myocytes and effect of internal cAMP. *Am. J. Physiol. Heart Circ. Physiol.* 279 (2), H692–H701. doi:10.1152/ajpheart.2000.279.2.H692

Hofmann, K., Fiedler, S., Vierkotten, S., Weber, J., Klee, S., Jia, J., et al. (2017). Classical transient receptor potential 6 (TRPC6) channels support myofibroblast differentiation and development of experimental pulmonary fibrosis. *Biochim. Biophys. Acta. Mol. Basis Dis.* 1863 (2), 560–568. doi:10.1016/j.bbadis.2016.12.002

Horie, M., Saito, A., Yamauchi, Y., Mikami, Y., Sakamoto, M., Jo, T., et al. (2014). Histamine induces human lung fibroblast-mediated collagen gel contraction via histamine H1 receptor. *Exp. Lung Res.* 40 (5), 222–236. doi:10.3109/01902148.2014.900155

Ikawa, Y., Shiba, K., Ohki, E., Mutoh, N., Suzuki, M., Sato, H., et al. (2008). Comparative study of histamine H4 receptor expression in human dermal fibroblasts. *J. Toxicol. Sci.* 33 (4), 503–508. doi:10.2131/jts.33.503

Ishida, S., Matsu-Ura, T., Fukami, K., Michikawa, T., and Mikoshiba, K. (2014). Phospholipase C-β1 and β4 contribute to non-genetic cell-to-cell variability in histamine-induced calcium signals in HeLa cells. *PLoS One* 9 (1), e86410. doi:10.1371/journal.pone.0086410

Janssen, L. J., Mukherjee, S., and Ask, K. (2015). Calcium homeostasis and ionic mechanisms in pulmonary fibroblasts. *Am. J. Respir. Cell Mol. Biol.* 53 (2), 135–148. doi:10.1165/rcmb.2014-0269TR

Jing, D., Lu, X. L., Luo, E., Sajda, P., Leong, P. L., and Guo, X. E. (2013). Spatiotemporal properties of intracellular calcium signaling in osteocytic and osteoblastic cell networks under fluid flow. *Bone* 53 (2), 531–540. doi:10.1016/j.bone.2013.01.008

Johnson, C. M., Johnson, C., Bazan, E., Garver, D., Gruenstein, E., and Ahluwalia, M. (1990). Histamine receptors in human fibroblasts: Inositol phosphates, Ca2+, and cell growth. *Am. J. Physiol.* 258 (1), C533–C543. doi:10.1152/ajpcell.1990.258.3.C533

Johnson, M. T., Xin, P., Benson, J. C., Pathak, T., Walter, V., Emrich, S. M., et al. (2022). STIM1 is a core trigger of airway smooth muscle remodeling and hyperresponsiveness in asthma. *Proc. Natl. Acad. Sci. U. S. A.* 119 (1), e2114557118. doi:10.1073/pnas.2114557118

Jordana, M., Befus, A. D., Newhouse, M. T., Bienenstock, J., and Gauldie, J. (1988). Effect of histamine on proliferation of normal human adult lung fibroblasts. *Thorax* 43 (7), 552–558. doi:10.1136/thx.43.7.552

Kemény, L. V., Schnúr, A., Czepán, M., Rakonczay, Z., Gál, E., Lonovics, J., et al. (2013). Na^+/Ca^{2+} exchangers regulate the migration and proliferation of human gastric myofibroblasts. *Am. J. Physiol. Gastrointest. Liver Physiol.* 305 (8), G552–G563. doi:10.1152/ajpgi.00394.2012

Kohyama, T., Yamauchi, Y., Takizawa, H., Kamitani, S., Kawasaki, S., and Nagase, T. (2010). Histamine stimulates human lung fibroblast migration. *Mol. Cell. Biochem.* 337 (1-2), 77–81. doi:10.1007/s11010-009-0287-y

Kunzmann, S., Schmidt-Weber, C., Zingg, J. M., Azzi, A., Kramer, B. W., Blaser, K., et al. (2007). Connective tissue growth factor expression is regulated by histamine in lung fibroblasts: Potential role of histamine in airway remodeling. *J. Allergy Clin. Immunol.* 119 (6), 1398–1407. doi:10.1016/j.jaci.2007.02.018

Lembong, J., Sabass, B., Sun, B., Rogers, M. E., and Stone, H. A. (2015). Mechanics regulates ATP-stimulated collective calcium response in fibroblast cells. *J. R. Soc. Interface* 12 (108), 20150140. doi:10.1098/rsif.2015.0140

Leurs, R., Smit, M. J., Bast, A., and Timmerman, H. (1990). Different profiles of desensitization dynamics in Guinea-pig jejunal longitudinal smooth muscle after stimulation with histamine and methacholine. *Br. J. Pharmacol.* 101 (4), 881–888. doi:10.1111/j.1476-5381.1990.tb14175.x

Leurs, R., Smit, M. J., Bast, A., and Timmerman, H. (1991). Homologous histamine H1 receptor desensitization results in reduction of H1 receptor agonist efficacy. *Eur. J. Pharmacol.* 196 (3), 319–322. doi:10.1016/0014-2999(91)90446-w

Liang, W., McDonald, P., McManus, B., van Breemen, C., and Wang, X. (2003). Histamine-induced Ca(2+) signaling in human valvular myofibroblasts. *J. Mol. Cell. Cardiol.* 35 (4), 379–388. doi:10.1016/s0022-2828(03)00010-5

Maini, R., Collison, D. J., Maidment, J. M., Davies, P. D., and Wormstone, I. M. (2002). Pterygial derived fibroblasts express functionally active histamine and epidermal growth factor receptors. *Exp. Eye Res.* 74 (2), 237–244. doi:10.1006/exer.2001.1116

Moccia, F., Berra-Romani, R., Tritto, S., Signorelli, S., Taglietti, V., and Tanzi, F. (2003). Epidermal growth factor induces intracellular Ca2+ oscillations in microvascular endothelial cells. *J. Cell. Physiol.* 194 (2), 139–150. doi:10.1002/jcp.10198

Moccia, F., Nusco, G. A., Lim, D., Kyozuka, K., and Santella, L. (2006). NAADP and InsP3 play distinct roles at fertilization in starfish oocytes. *Dev. Biol.* 294 (1), 24–38. doi:10.1016/j.ydbio.2006.02.011

Moccia, F., Zuccolo, E., Poletto, V., Turin, I., Guerra, G., Pedrazzoli, P., et al. (2016). Targeting Stim and Orai proteins as an alternative approach in anticancer therapy. *Curr. Med. Chem.* 23 (30), 3450–3480. doi:10.2174/0929867323666160607111220

Mukherjee, S., Ayaub, E. A., Murphy, J., Lu, C., Kolb, M., Ask, K., et al. (2015). Disruption of calcium signaling in fibroblasts and attenuation of bleomycin-induced fibrosis by nifedipine. *Am. J. Respir. Cell Mol. Biol.* 53 (4), 450–458. doi:10.1165/rcmb.2015-0009OC

Murdoch, J. R., and Lloyd, C. M. (2010). Chronic inflammation and asthma. *Mutat. Res.* 690 (1-2), 24–39. doi:10.1016/j.mrfmmm.2009.09.005

Negri, S., Faris, P., Berra-Romani, R., Guerra, G., and Moccia, F. (2019). Endothelial transient receptor potential channels and vascular remodeling: Extracellular Ca2+ entry for angiogenesis, arteriogenesis and vasculogenesis. *Front. Physiol.* 10, 1618. doi:10.3389/fphys.2019.01618

Negri, S., Faris, P., Maniezzi, C., Pellavio, G., Spaiardi, P., Botta, L., et al. (2021). NMDA receptors elicit flux-independent intracellular Ca^{2+} signals via metabotropic glutamate receptors and flux-dependent nitric oxide release in human brain microvascular endothelial cells. *Cell Calcium* 99, 102454. doi:10.1016/j.ceca.2021.102454

Niisato, N., Ogata, Y., Furuyama, S., and Sugiya, H. (1996). Histamine H1 receptor-induced Ca^{2+} mobilization and prostaglandin E2 release in human gingival fibroblasts. Possible role of receptor-operated Ca^{2+} influx. *Biochem. Pharmacol.* 52 (7), 1015–1023. doi:10.1016/0006-2952(96)00417-0

Ogata, Y., Nakao, S., Suzuki, T., Tsunoda, S., Furuyama, S., and Sugiya, H. (1999). Involvement of prostaglandins in histamine H1 receptor-operated Ca^{2+} entry in human gingival fibroblasts. *Life Sci.* 64 (4), Pl71–7. doi:10.1016/s0024-3205(98)00565-7

Okumura, W., Kozono, T., Sato, H., Matsui, H., Takagi, T., Tonozuka, T., et al. (2022). Jaw1/LRMP increases Ca^{2+} influx upon GPCR stimulation with heterogeneous effect on the activity of each ITPR subtype. *Sci. Rep.* 12 (1), 9476. doi:10.1038/s41598-022-13620-4

Ong, H. L., Subedi, K. P., Son, G. Y., Liu, X., and Ambudkar, I. S. (2019). Tuning store-operated calcium entry to modulate Ca^{2+}-dependent physiological processes. *Biochim. Biophys. Acta. Mol. Cell Res.* 1866 (7), 1037–1045. doi:10.1016/j.bbamcr.2018.11.018

Paltauf-Doburzynska, J., Frieden, M., Spitaler, M., and Graier, W. F. (2000). Histamine-induced Ca^{2+} oscillations in a human endothelial cell line depend on transmembrane ion flux, ryanodine receptors and endoplasmic reticulum Ca^{2+}-ATPase. *J. Physiol.* 524 (3), 701–713. doi:10.1111/j.1469-7793.2000.00701.x

Panula, P., Chazot, P. L., Cowart, M., Gutzmer, R., Leurs, R., Liu, W. L., et al. (2015). International union of basic and clinical pharmacology. XCIX. Angiotensin receptors: Interpreters of pathophysiological angiotensinergic stimuli [corrected]. *Pharmacol. Rev.* 67 (3), 601–655. doi:10.1124/pr.114.010249

Panula, P. (2021). Histamine receptors, agonists, and antagonists in health and disease. *Handb. Clin. Neurol.* 180, 377–387. doi:10.1016/b978-0-12-820107-7.00023-9

Parker, I., and Ivorra, I. (1991). Caffeine inhibits inositol trisphosphate-mediated liberation of intracellular calcium in Xenopus oocytes. *J. Physiol.* 433, 229–240. doi:10.1113/jphysiol.1991.sp018423

Peppiatt, C. M., Collins, T. J., Mackenzie, L., Conway, S. J., Holmes, A. B., Bootman, M. D., et al. (2003). 2-Aminoethoxydiphenyl borate (2-APB) antagonises inositol 1, 4, 5-trisphosphate-induced calcium release, inhibits calcium pumps and has a use-dependent and slowly reversible action on store-operated calcium entry channels. *Cell Calcium* 34 (1), 97–108. doi:10.1016/s0143-4160(03)00026-5

Pinheiro, A. R., Paramos-de-Carvalho, D., Certal, M., Costa, M. A., Costa, C., Magalhães-Cardoso, M. T., et al. (2013). Histamine induces ATP release from human subcutaneous fibroblasts, via pannexin-1 hemichannels, leading to Ca^{2+} mobilization and cell proliferation. *J. Biol. Chem.* 288 (38), 27571–27583. doi:10.1074/jbc.M113.460865

Prakriya, M., and Lewis, R. S. (2015). Store-operated calcium channels. *Physiol. Rev.* 95 (4), 1383–1436. doi:10.1152/physrev.00020.2014

Pulina, M. V., Zulian, A., Berra-Romani, R., Beskina, O., Mazzocco-Spezzia, A., Baryshnikov, S. G., et al. (2010). Upregulation of Na+ and Ca2+ transporters in arterial smooth muscle from ouabain-induced hypertensive rats. *Am. J. Physiol. Heart Circ. Physiol.* 298 (1), H263–H274. doi:10.1152/ajpheart.00784.2009

Rahman, M., Mukherjee, S., Sheng, W., Nilius, B., and Janssen, L. J. (2016). Electrophysiological characterization of voltage-dependent calcium currents and TRPV4 currents in human pulmonary fibroblasts. *Am. J. Physiol. Lung Cell. Mol. Physiol.* 310 (7), L603–L614. doi:10.1152/ajplung.00426.2015

Remigante, A., Zuccolini, P., Barbieri, R., Ferrera, L., Morabito, R., Gavazzo, P., et al. (2021). NS-11021 modulates cancer-associated processes independently of BK channels in melanoma and pancreatic duct adenocarcinoma cell lines. *Cancers (Basel)* 13 (23), 6144. doi:10.3390/cancers13236144

Sadras, F., Monteith, G. R., and Roberts-Thomson, S. J. (2021a). An emerging role for calcium signaling in cancer-associated fibroblasts. *Int. J. Mol. Sci.* 22 (21), 11366. doi:10.3390/ijms222111366

Sadras, F., Stewart, T. A., Robitaille, M., Peters, A. A., Croft, P. K., Soon, P. S., et al. (2021b). Altered calcium influx pathways in cancer-associated fibroblasts. *Biomedicines* 9 (6), 680. doi:10.3390/biomedicines9060680

Saliba, Y., Karam, R., Smayra, V., Aftimos, G., Abramowitz, J., Birnbaumer, L., et al. (2015). Evidence of a role for fibroblast transient receptor potential canonical 3 Ca^{2+} channel in renal fibrosis. *J. Am. Soc. Nephrol.* 26 (8), 1855–1876. doi:10.1681/ASN.2014010065

Salomonsson, M., Malinovschi, A., Kalm-Stephens, P., Dahlin, J. S., Janson, C., Alving, K., et al. (2019). Circulating mast cell progenitors correlate with reduced lung function in allergic asthma. *Clin. Exp. Allergy* 49 (6), 874–882. doi:10.1111/cea.13388

Sanchez-Collado, J., Lopez, J. J., Gonzalez-Gutierrez, L., Cantonero, C., Jardin, I., Salido, G. M., et al. (2020). Functional role of TRPC6 and STIM2 in cytosolic and endoplasmic reticulum Ca2+ content in resting estrogen receptor-positive breast cancer cells. *Biochem. J.* 477 (17), 3183–3197. doi:10.1042/BCJ20200560

Santella, L. (1998). The role of calcium in the cell cycle: Facts and hypotheses. *Biochem. Biophys. Res. Commun.* 244 (2), 317–324. doi:10.1006/bbrc.1998.8086

Sarasola, M. P., Táquez Delgado, M. A., Nicoud, M. B., and Medina, V. A. (2021). Histamine in cancer immunology and immunotherapy. Current status and new perspectives. *Pharmacol. Res. Perspect.* 9 (5), e00778. doi:10.1002/prp2.778

Sauvé, R., Diarra, A., Chahine, M., Simoneau, C., Morier, N., and Roy, G. (1991). Ca^{2+} oscillations induced by histamine H1 receptor stimulation in HeLa cells: Fura-2 and patch clamp analysis. *Cell Calcium* 12 (2-3), 165–176. doi:10.1016/0143-4160(91)90018-a

Seifert, R., Strasser, A., Schneider, E. H., Neumann, D., Dove, S., and Buschauer, A. (2013). Molecular and cellular analysis of human histamine receptor subtypes. *Trends Pharmacol. Sci.* 34 (1), 33–58. doi:10.1016/j.tips.2012.11.001

Smedler, E., and Uhlén, P. (2014). Frequency decoding of calcium oscillations. *Biochim. Biophys. Acta* 1840 (3), 964–969. doi:10.1016/j.bbagen.2013.11.015

Smit, M. J., Bloemers, S. M., Leurs, R., Tertoolen, L. G., Bast, A., de Laat, S. W., et al. (1992). Short-term desensitization of the histamine H1 receptor in human HeLa cells: Involvement of protein kinase C dependent and independent pathways. *Br. J. Pharmacol.* 107 (2), 448–455. doi:10.1111/j.1476-5381.1992.tb12766.x

Soulsby, M. D., and Wojcikiewicz, R. J. (2002). 2-Aminoethoxydiphenyl borate inhibits inositol 1, 4, 5-trisphosphate receptor function, ubiquitination and downregulation, but acts with variable characteristics in different cell types. *Cell Calcium* 32 (4), 175–181. doi:10.1016/s0143416002001525

Tomioka, M., Ida, S., Shindoh, Y., Ishihara, T., and Takishima, T. (1984). Mast cells in bronchoalveolar lumen of patients with bronchial asthma. *Am. Rev. Respir. Dis.* 129 (6), 1000–1005. doi:10.1164/arrd.1984.129.6.1000

Vazquez-de-Lara, L. G., Tlatelpa-Romero, B., Romero, Y., Fernández-Tamayo, N., Vazquez-de-Lara, F., M Justo-Janeiro, J., et al. (2018). Phosphatidylethanolamine induces an antifibrotic phenotype in normal human lung fibroblasts and ameliorates bleomycin-induced lung fibrosis in mice. *Int. J. Mol. Sci.* 19 (9), E2758. doi:10.3390/ijms19092758

Veerappan, A., O'Connor, N. J., Brazin, J., Reid, A. C., Jung, A., McGee, D., et al. (2013). Mast cells: A pivotal role in pulmonary fibrosis. *DNA Cell Biol.* 32 (4), 206–218. doi:10.1089/dna.2013.2005

Wacquier, B., Voorsluijs, V., Combettes, L., and Dupont, G. (2019). Coding and decoding of oscillatory Ca^{2+} signals. *Semin. Cell Dev. Biol.* 94, 11–19. doi:10.1016/j.semcdb.2019.01.008

Wilson, C., Zhang, X., Lee, M. D., MacDonald, M., Heathcote, H. R., Alorfi, N. M. N., et al. (2020). Disrupted endothelial cell heterogeneity and network organization impair vascular function in prediabetic obesity. *Metabolism.* 111, 154340. doi:10.1016/j.metabol.2020.154340

Wu, C. Y., Hsu, W. L., Tsai, M. H., Chai, C. Y., Yen, C. J., Chen, C. H., et al. (2019). A potential new approach for treating systemic sclerosis: Dedifferentiation of SSc fibroblasts and change in the microenvironment by blocking store-operated Ca^{2+} entry. *PLoS One* 14 (3), e0213400. doi:10.1371/journal.pone.0213400

Yamauchi, K., and Ogasawara, M. (2019). The role of histamine in the pathophysiology of asthma and the clinical efficacy of antihistamines in asthma therapy. *Int. J. Mol. Sci.* 20 (7), E1733. doi:10.3390/ijms20071733

Yoast, R. E., Emrich, S. M., Zhang, X., Xin, P., Johnson, M. T., Fike, A. J., et al. (2020). The native ORAI channel trio underlies the diversity of Ca^{2+} signaling events. *Nat. Commun.* 11 (1), 2444. doi:10.1038/s41467-020-16232-6

Zenmyo, M., Hiraoka, K., Komiya, S., Morimatsu, M., and Sasaguri, Y. (1995). Histamine-stimulated production of matrix metalloproteinase 1 by human rheumatoid synovial fibroblasts is mediated by histamine H1-receptors. *Virchows Arch.* 427 (4), 437–444. doi:10.1007/bf00199394

Zhang, J., Berra-Romani, R., Sinnegger-Brauns, M. J., Striessnig, J., Blaustein, M. P., and Matteson, D. R. (2007). Role of Cav1.2 L-type Ca^{2+} channels in vascular tone: Effects of nifedipine and Mg^{2+}. *Am. J. Physiol. Heart Circ. Physiol.* 292 (1), H415–H425. doi:10.1152/ajpheart.01214.2005

Zhang, X., Xin, P., Yoast, R. E., Emrich, S. M., Johnson, M. T., Pathak, T., et al. (2020). Distinct pharmacological profiles of ORAI1, ORAI2, and ORAI3 channels. *Cell Calcium* 91, 102281. doi:10.1016/j.ceca.2020.102281

Zheng, T., Nathanson, M. H., and Elias, J. A. (1994). Histamine augments cytokine-stimulated IL-11 production by human lung fibroblasts. *J. Immunol.* 153 (10), 4742–4752.

Zuccolini, P., Ferrera, L., Remigante, A., Picco, C., Barbieri, R., Bertelli, S., et al. (2022). The VRAC blocker DCPIB directly gates the BK channels and increases intracellular Ca^{2+} in melanoma and pancreatic duct adenocarcinoma cell lines. *Br. J. Pharmacol.* 179 (13), 3452–3469. doi:10.1111/bph.15810

Zuccolo, E., Laforenza, U., Ferulli, F., Pellavio, G., Scarpellino, G., Tanzi, M., et al. (2018). Stim and Orai mediate constitutive Ca^{2+} entry and control endoplasmic reticulum Ca^{2+} refilling in primary cultures of colorectal carcinoma cells. *Oncotarget* 9 (57), 31098–31119. doi:10.18632/oncotarget.25785

Zuccolo, E., Laforenza, U., Negri, S., Botta, L., Berra-Romani, R., Faris, P., et al. (2019). Muscarinic M5 receptors trigger acetylcholine-induced Ca(2+) signals and nitric oxide release in human brain microvascular endothelial cells. *J. Cell. Physiol.* 234 (4), 4540–4562. doi:10.1002/jcp.27234

Advantages of publishing in Frontiers

OPEN ACCESS
Articles are free to read for greatest visibility and readership

FAST PUBLICATION
Around 90 days from submission to decision

HIGH QUALITY PEER-REVIEW
Rigorous, collaborative, and constructive peer-review

TRANSPARENT PEER-REVIEW
Editors and reviewers acknowledged by name on published articles

Frontiers
Avenue du Tribunal-Fédéral 34
1005 Lausanne | Switzerland

Visit us: www.frontiersin.org
Contact us: frontiersin.org/about/contact

REPRODUCIBILITY OF RESEARCH
Support open data and methods to enhance research reproducibility

DIGITAL PUBLISHING
Articles designed for optimal readership across devices

FOLLOW US
@frontiersin

IMPACT METRICS
Advanced article metrics track visibility across digital media

EXTENSIVE PROMOTION
Marketing and promotion of impactful research

LOOP RESEARCH NETWORK
Our network increases your article's readership